TESIS DE LA UNIVERSIDAD DE ZARAGOZA

2015

41

Luis Hernando Cifuentes Rubio

Local flow topologies and scalar structures in turbulent combustion

Departamento

Ciencia y Tecnología de Materiales y Fluidos

Director/es

Dopazo García, César
Martín Yagüe, Jesús Joaquín

ISSN 2254-7606

Prensas de la Universidad Universidad Zaragoza

ISSN 2254-7606

Universidad Zaragoza
1542

Tesis Doctoral

LOCAL FLOW TOPOLOGIES AND SCALAR STRUCTURES IN TURBULENT COMBUSTION

Autor

Luis Hernando Cifuentes Rubio

Director/es

Dopazo García, César
Martín Yagüe, Jesús Joaquín

UNIVERSIDAD DE ZARAGOZA

Ciencia y Tecnología de Materiales y Fluidos

2015

Departamento de Ciencia y Tecnología de Materiales y Fluidos
Universidad Zaragoza

Escuela de Ingeniería y Arquitectura
Universidad Zaragoza

Universidad Zaragoza

Local flow topologies and scalar structures in turbulent combustion

A dissertation presented to the
University of Zaragoza

in partial fulfillment of the requirements for the Degree of
Doctor of Philosophy

by

Luis Hernando Cifuentes Rubio

Fluid Mechanics Area
Department of Science and Technology of Materials and Fluids
University of Zaragoza

Departamento de
Ciencia y Tecnología
de Materiales y Fluidos
Universidad Zaragoza

Escuela de
Ingeniería y Arquitectura
Universidad Zaragoza

Universidad
Zaragoza

Local flow topologies and scalar structures in turbulent combustion

A dissertation presented to the
University of Zaragoza

in partial fulfillment of the requirements for the Degree of
Doctor of Philosophy

by

Luis Hernando Cifuentes Rubio

Directors:

Dr. Cesar Dopazo
Professor
University of Zaragoza

Dr. Jesus Martin
Assistant Professor
University of Zaragoza

Fluid Mechanics Area
Department of Science and Technology of Materials and Fluids
University of Zaragoza
February, 2015

A mis dos amores
'Amanda y Andrea'

En primer lugar, mi agradecimiento va dirigido a mis dos supervisores, el Dr. César Dopazo y el Dr. Jesús Martín, por todos sus consejos, paciencia y guía durante el predoctorado. Al Dr. Juan Hierro, no solo por autorizarme al empleo de su código de DNS sino también por sus iluminadoras discusiones que se materializaron en esta memoria. A la Dra. Carmen Jiménez, por permitir usar su base de datos de DNS en una configuración de flujo de entrada-salida, y por su ayuda en el entendimiento de los problemas de combustión turbulenta premezclada. A los Dres. Luc Vervisch y Pascale Domingo, por autorizarme al empleo de su base de datos de DNS en una configuración de chorro con un co-flujo de productos calientes.

Hay un número de personas que he conocido a lo largo de los años en el Área de Mecánica de Fluidos de la Universidad de Zaragoza y en el Laboratorio de Investigación en Fluidodinámica y Tecnologías de la Combustión, los cuales han aportado no solo conocimiento sino también consuelo en muchas de las fases de la elaboración de esta tesis. Agradezco especialmente a los Dres. Norberto Fueyo y Javier Ballester, por aclarar muchos conceptos en Flujos reactivos y combustión durante mi fase de preparación. A los compañeros y amigos que en diversos momentos me ayudaron: Salvador Ochoa, Nidia Herrejón, Alberto Sánchez, Ramón Chorda, Ana Cubero, Antonio Gómez, Carlos Montañés, Cristina Gonzalo, Luis Manuel Cerecedo, Antonio Lozano, Félix Barreras, Luis Valiño, Jorge Barroso, Pilar Ezquerra, Olga Cebolla, Juan Antonio García, Antonio Pascau, Guillermo Hauke, Javier Murillo, Pilar García, Francisco Alcrudo, María García, Pedro Martín, Diego Irisarri, Carmelo Juez. Es muy probable que no haya mencionado a otros muchos que no caben en este espacio, a todos ellos mi más sincera gratitud por aportar directa o indirectamente a la realización de este proyecto.

Por último, pero no por ello menos importante, quiero agradecer a mi familia y amigos de Colombia por todo el apoyo, destacar a mi madre Amanda por todos los ánimos que me ha dado, y a mi compañera Andrea por su apoyo y comprensión durante estos años de predoctorado. A ellas dedico esta Tesis.

Contents

1
Abstract

The aim of this work is to investigate several turbulent mixing and combustion processes, through the study of the small-scale structures of the scalar and velocity fields, using direct numerical simulation (DNS) techniques. Different datasets for statistically homogeneous and stationary constant-density turbulence, and for turbulent premixed flames in an inflow-outflow configuration and in a jet with a co-flow of hot products, have been examined. The constant-density mixing and reaction cases have been analyzed for different Schmidt numbers. For the two turbulent premixed flames, the computational domain has been divided into four regions ('fresh reactants', 'preheat', 'burning' and 'hot products'), characterized by the values of the chemical reaction rate or, equivalently, of the scalar field. Small-scale scalar

structures have been identified in terms of the mean and Gauss curvatures, k_m and k_g. The kinematics of non-material iso-scalar surfaces has been theoretically analyzed; expressions for the propagation speed of an iso-scalar surface relative to the fluid and its derivative, with respect to the normal direction of the iso-surfaces, have been obtained. For constant-density mixing, the normal and tangential diffusion contributions to the displacement speed are essential; whereas for constant- and variable-density turbulent reacting flows, the propagation speed is controlled by the chemical process. Small-scale flow topologies interact with the local scalar structures. The time rate of change of the infinitesimal distance between two iso-surfaces is controlled by the value of the *'effective'* normal strain rate, which combines flow and diffusion-reaction induced effects. The value and sign of the *'effective'* normal strain rate determines whether the modulus of scalar gradients or, equivalently, the scalar fluctuation dissipation rate, increases or decreases with time. For turbulent premixed flames, chemical heat generation yields positive flow volumetric dilatation rates everywhere in the computational domain, $\nabla \cdot \mathbf{u} > 0$, which implies mostly positive flow strain rates normal to iso-scalar surfaces. An expression for $\nabla \cdot \mathrm{u}$, with additive contributions from molecular diffusion and chemical generation of the reaction progress variable defined from the temperature, has been obtained, assuming a one-dimensional flamelet; the differences between this expres-

sion and the computed dilatation rate are significantly high, which casts doubts on the validity of this approximation. The dilatation rate has also been decomposed into the tangential, a_T, and normal, a_N, strain rates. The joint pdf's of a_N and a_T, in the regions with high chemical activity, show that their most probable values are located above the line $a_N + a_T = 0$, regardless of the configuration under study. Small-scale structures of the velocity field, in terms of the invariants of the velocity-gradient tensor, have been examined. The universal teardrop shape of the joint pdf's of the second Q and third R invariants of the velocity-gradient tensor is apparent for the constant-density mixing and reaction cases, whereas it disappears in the turbulent premixed flames. The mean of the most extensive (compressive) eigenvalue of the strain rate tensor, $\langle\Lambda_1\rangle$ ($\langle\Lambda_3\rangle$), is always positive (negative), and the intermediate $\langle\Lambda_2\rangle$ remains on average positive. In the cases of turbulent premixed flames, Λ_3 has a high probability of being positive within the regions with significant chemical activity. The study of the alignment between the unit vector normal to the iso-scalar surfaces, $\mathbf{n}$, with respect to the strain rate eigenvectors, $\mathbf{e}_i$, and the local vorticity, $\boldsymbol{\omega}$, demonstrates that there is a specific orientation between the local flow topologies and the scalar structures. For turbulent premixed flames, the scalar gradient aligns preferentially with the strain rate tensor eigenvector corresponding to its most extensive eigenvalue, whereas in constant-

density mixing and reaction the scalar gradient is mainly parallel to the most compressive eigenvector. The analysis also revealed that the vorticity vector is predominantly tangential to the iso-scalar surfaces, regardless of the configuration under study. Furthermore, the results showed that a 'canonical' vortex, found perpendicular to the scalar gradient, contributes to curving and folding the iso-scalar surfaces. Studies on local enstrophy and strain rate, as well as on the production of enstrophy and dissipation, demonstrated that focal topologies are dominant in the 'fresh reactants' and tend to disappear in favor of nodal structures as moving towards the 'hot products', in turbulent premixed flames.

2
Resumen

El objetivo de este trabajo es investigar los procesos de mezcla y combustión turbulentas mediante el estudio de las estructuras de las pequeñas escalas de los campos de velocidad y escalar. Se usan varias simulaciones numéricas directas (SND) y diferentes bases de datos para turbulencia estadísticamente estacionaria, homogénea e incompresible, así como para llamas premezcladas turbulentas - una de las llamas con una configuración de flujo de entrada-salida, y otra en un chorro con un co-flujo de productos calientes. Los casos de flujos de densidad constante tanto con mezcla como reacción se han obtenido con diferentes números de Schmidt. Para las dos llamas premezcladas turbulentas, el dominio computacional se ha dividido en cuatro regiones ('reactantes frescos', 'región de precalentamiento',

'región de quemado' y 'productos calientes'), caracterizadas por los valores de la tasa de reacción química o, equivalentemente, del escalar. Se han identificado las estructuras de pequeñas escalas del campo escalar, en términos de las curvaturas media y de Gauss, k_m y k_g. Se ha analizado teóricamente la cinemática de las superficies iso-escalares no materiales; se han obtenido expresiones para la velocidad de propagación de una superficie iso-escalar relativa al fluido, y también para sus derivadas con respecto a la dirección normal de las superficies iso-escalares. Para el caso de mezcla con densidad constante, la velocidad de desplazamiento viene determinada por las contribuciones de difusión normal y tangencial; mientras que para el caso reactivo tanto de densidad variable como constante, la velocidad de propagación viene determinada por el proceso químico. Se obtienen también las velocidades locales de deformación del flujo y se estudia su interacción con las estructuras de pequeñas escalas del campo escalar. La variación temporal de la distancia infinitesimal entre dos iso-superficies depende del valor de la deformación normal *'efectiva'*, que suma las tasas de deformación inducidas por la reacción-difusión y las debidas al flujo. El valor y signo de la velocidad de deformación normal *'efectiva'* determina si el modulo del gradiente del escalar o, equivalentemente, la tasa de disipación de las fluctuaciones del escalar, aumenta o disminuye con el tiempo. Para llamas premezcladas turbulentas, la generación de calor pro-

duce tasas de dilatación volumétrica del flujo positivas en todo el dominio computacional, $\nabla \cdot \mathbf{u} > 0$, lo cual implica generalmente velocidades positivas de deformación del flujo perpendiculares a las superficies iso-escalares. Se ha obtenido una expresión para $\nabla \cdot \mathrm{u}$, con contribuciones aditivas de la difusión molecular y la generación química de la variable de progreso definida en términos de la temperatura, suponiendo un flamelet unidimensional; las diferencias entre esta expresión y la dilatación calculada son significativas, lo cual arroja dudas sobre la validez de las hipótesis usadas. Se ha descompuesto la tasa de dilatación volumétrica en sus componentes de deformación tangencial, a_T, y normal, a_N. Las pdfs conjuntas de a_N y a_T, en las regiones con alta actividad química, muestran sus valores más probables localizados por encima de la línea $a_N + a_T = 0$, independientemente de la configuración analizada. Se han examinado las estructuras de las pequeñas escalas del campo de velocidad, mediante los invariantes del tensor gradiente de velocidad. La forma universal de lágrima de las pdfs conjuntas del segundo y tercer invariante del tensor gradiente de velocidad permanece para los casos de mezcla y reacción de densidad constante, mientras que en las llamas premezcladas turbulentas desaparece. El promedio del autovalor más extensivo (compresivo) del tensor velocidad de deformación, $\langle \Lambda_1 \rangle$ ($\langle \Lambda_3 \rangle$), es siempre positivo (negativo), y el intermedio $\langle \Lambda_2 \rangle$ presenta promedio positivo. En los casos de llamas premezcladas turbulen-

tas, los valores positivos de Λ_3 presentan alta probabilidad en regiones con actividad química intensa. El estudio del alineamiento entre el vector unitario normal a las superficies iso-escalares, $\mathbf{n}$, y los autovectores del tensor velocidad de deformación, $\mathbf{e}_i$, o la vorticidad local $\boldsymbol{\omega}$, muestra que hay una correlación entre las orientaciones espaciales de las topologías del flujo local y de las estructuras del escalar. Para llamas premezcladas turbulentas, el gradiente del escalar se alinea preferentemente con el eje principal del tensor velocidad de deformación correspondiente al mayor autovalor positivo, mientras que en los casos de fluidos de densidad constante tanto con mezcla como reacción el gradiente del escalar resulta generalmente paralelo al eje principal correspondiente al autovalor negativo. El análisis también reveló que el vector vorticidad es predominantemente paralelo a las superficies iso-escalares, independientemente de la configuración analizada. Además, el análisis de un vórtice 'canónico', muestra que su orientación es perpendicular al gradiente del escalar y por lo tanto, contribuye a curvar y doblar las superficies iso-escalares. Estudios sobre la enstrofía y la tasa de deformación, así como también sobre la producción de enstrofía y disipación, demostraron que las topologías focales son dominantes en los 'reactantes frescos' y tienden a desaparecer en favor de estructuras nodales al desplazarse hacia los 'productos calientes', en llamas premezcladas turbulentas.

3
Introduction

3.1 Motivation

The turbulent mixing of spatially segregated scalar fields [i] (e.g., two regions of fluid with different temperatures, several inert or reactive chemical

[i] Scalar fields such as inert/reactive mass fraction, temperature, enthalpy, etc.

species) is a process which combines convection by large and medium scale velocity structures, straining of scalar geometries by the local flow and molecular diffusion. Should scalars be reactive, intimate contact at the molecular level is essential for them to be chemically converted into intermediate species or products. Large eddy convection beats heterogeneous scalars and brings them closer together, for example, by engulfment or entrainment, although retaining their distinct compositions, with segregation still at smaller spatial scales [1]. Local flow nodal and vortical structures fold and stretch scalar zones separating scalar fields, fostering scalar gradient enhancement and surface growth; the former increases molecular fluxes of scalars, whereas the latter promotes the global mixing.

The ubiquity of mixing in engineering and everyday devices is enormous. Combustion systems, chemical reactors, atmospheric pollution, domestic blending of liquids and solids are but a few examples of the relevance of mixing processes. Measuring the degree of mixing is thus an important issue. For example, in atmospheric applications, the forces that drive the turbulence can be dramatically affected as cool and warm air mix at the molecular level. In combustion applications, which generally take place in turbulent conditions, the heat released by combustion generates flow instability by buoyancy and gas expansion, which enhances the transition to turbulence, and turbulence increases the mixing processes and thereby

enhances combustion.

In a background of industrial breakthrough in developing and producing highly efficient and powerful internal combustion engines, the progress made by combustion science is much less impressive, especially as far as premixed turbulent flames are concerned. Premixed turbulent combustion is substantially a more difficult problem than non-premixed (diffusion) flames because the burning rate in diffusion flames is mainly controlled by mixing, whereas the burning rate in premixed flames is controlled by both chemical reactions and mixing. Turbulent mixing in combustion involves interaction of processes characterized by significantly different length scales and timescales. Even a laminar flame itself is a multi-scale nonlinear phenomenon. Because the rates of different reactions within the flame may differ by several orders of magnitudes and depend strongly nonlinearly on temperature, variations in the concentrations of different species are localized in spatial zones of significantly different widths. The problem is associated with a substantially wider range of important scales, because the largest scales characterizing a laminar flame are often of the order of or even less than the smallest scales of turbulence. Thus, it cannot be parametrized easily in terms of the large scale features of the flow. As a result, a detailed description of the scalar field at the smallest length scales of the flow and the local flow topologies is, in principle, necessary if

a reliable prediction of turbulent mixing is to be achieved.

This thesis aims at investigating the different turbulent mixing and combustion processes through the small-scale structures in the scalar and velocity fields using several direct numerical simulation datasets of premixed turbulent combustion. Among other things, the present work details a study of local scalar geometries and flow topologies for constant- and variable-density turbulent reacting flows which, to the best of our knowledge, has never been reported in turbulent flows with premixed reactants.

3.2 Turbulent flows

The majority of flows found in nature and in engineering applications are turbulent. Turbulence has a large influence on the transport properties of the flow and other engineering applications, and is thus a subject that has drawn a significant amount of attention. There are no general agreements on a definition of turbulence. From Von Kárman's [2] scholarly *'Turbulence is an irregular motion which in general makes its appearance in fluids, gaseous or liquid, when they flow past solid surfaces or even when neighboring stream of the same fluid flow past or over one another'*, to Bradshaw's [3] inspired *'invention of the Devil on the seventh day of Creation (when the Good Lord wasn't looking)'*. These interpretations and

the apparent frustrations come from the complex behavior of turbulence and from the consequence that there is no analytical solution for the three-dimensional non-linear Navier-Stokes equations, which describe the turbulent motion. A study of turbulence is incomplete without some mention of fluid stability and the transition to turbulence. From a historical perspective, the most well known experiment on hydrodynamic stability was carried out by Osborne Reynolds [4] in 1888. He performed a set of experiments in which he carefully studied the behavior of flow in a pipe under different flow conditions. Specially, by varying the diameter of the pipe, D, the velocity of the fluid, U, and the viscosity of the fluid, ν, Reynolds found that there was a relationship between these variables that indicated the transition from a smooth laminar stream, to a complex turbulent flow. Namely, when the value of UD/ν (which is called the Reynolds number) exceeded a particular value, the perturbations began to grow, and the instantaneous flow structure became very complex. The forces that upset this equilibrium can include buoyancy, inertia, or rotation to mention only a few. The viscous and inertial forces acting on the fluid are proportional to:

$$F_v \propto \mu U L \,, \tag{3.1}$$

$$F_i \propto \rho U^2 L^2 \,, \tag{3.2}$$

where μ is the fluid viscosity, ρ denotes density, and L and U are the characteristic velocity and length scales, respectively. If the viscous forces on the fluid are large compared with others, any disturbances introduced in the flow will tend to be damped out. If, on the other hand, the inertial forces become large, the flow will tend to break up into eddies.

For high Reynolds number flows, we can assume there are scales over which molecular forces are not significant. However, in any turbulent flow the molecular viscosity is always important at some scale. Turbulence is always a dissipative process, and if there is no source of energy to sustain the turbulence, it will decay as a result of the viscous small-scale motions. Richardson [5] was the first to qualitatively express the idea of an *energy cascade* in which the turbulent kinetic energy passes through the wavenumber spectrum before it is converted to heat by viscous dissipation. Later, Kolmogorov [6] extended this concept into his two famous hypotheses. These hypotheses, along with what they imply about the structure of turbulent flow, rank among the greatest contributions to turbulence theory.

Kolmogorov's 1^{st} Similarity Hypothesis: At sufficiently high Reynolds numbers there is a range of high wavenumbers where the turbulence is statiscally in equilibrium and uniquely determined by the parameter ε and ν. This state of equilibrium is universal.

The term universal is used here to emphasize that the character of the turbulence in this range does not depend on any specific mechanisms of the mean flow. The only parameters that play any role in the description of the turbulence are the dissipation, ε, and viscosity, ν. From this we can derive characteristic length, time and velocity scales of the small scales. The Kolmogorov length scale is defined using dimensional analysis as:

$$\eta = \left(\frac{\nu^3}{\varepsilon}\right)^{1/4} . \tag{3.3}$$

Using ν and ε to form a velocity scale gives:

$$v_\eta = (\nu\varepsilon)^{1/4} . \tag{3.4}$$

It is interesting to compute the Reynolds number based on these scales:

$$Re_\eta = \frac{\eta\, v_\eta}{\nu} = \nu^{-1} \left(\frac{\nu^3}{\varepsilon}\right)^{1/4} (\nu\varepsilon)^{1/4} = 1\,, \tag{3.5}$$

the value of $Re_\eta = 1$ is a constant independent of any flow parameters. This Reynolds number is characteristic only of the small viscous eddies (dissipation range) and is not characteristic of the turbulence throughout the equilibrium range.

For completeness, it is noted that a characteristic time scale can be defined:

$$\tau_\eta = \frac{\eta}{v_\eta} = \left(\frac{\nu}{\varepsilon^2}\right)^{1/4}\,. \tag{3.6}$$

If the Reynolds number of the flow is very high, it can be expected that there are length scales, l_i, much larger than η, but still within the equilibrium range, where the dissipation is very small compared with the energy flux through this region. Kolmogorov, in his second hypothesis specifically addressed this regime where $L \gg l_i \gg \eta$, where L is the integral scale and η is the Kolmogorov scale. In terms of wavenumbers, $\kappa = (2\pi)/Length$, this region corresponds to:

$$\kappa_L \ll \kappa_i \ll \kappa_\eta \,. \tag{3.7}$$

Kolmogorov's 2^{nd} Similarity Hypothesis: If the Reynolds number is sufficiently large, there exists a range of wavenumbers, $\kappa_L \ll \kappa_i \ll \kappa_\eta$, where the turbulence is independent of ν and is unambiguously defined by the value of the dissipation, ε.

In this range the inertial transfer of energy is the primary parameter characterizing the turbulence. Hence this range is called inertial subrange.

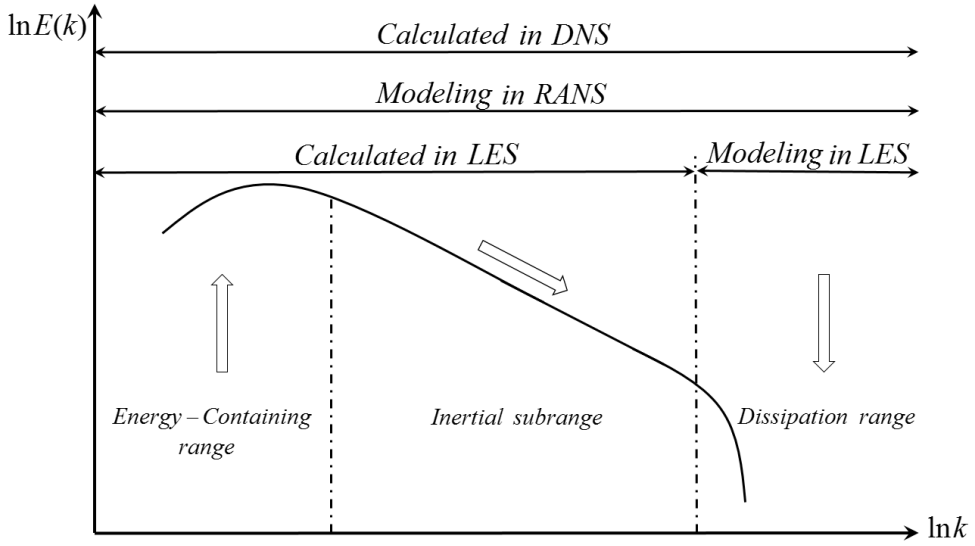

Figure 3.1: Typical turbulent kinetic energy spectrum. $E(\kappa)$ is the energy spectrum and κ is the wavenumber.

In any turbulent flow the turbulent energy is injected at the large scales. That energy is redistributed by pressure effects and cascades down towards

the intermediate (inertial) and small scales due to non-linear interactions. In the final stage of the turbulence life-cycle, energy is dissipated at the small scales by the action of molecular viscosity. The regions of energy production, redistribution, cascade and dissipation are shown schematically in Figure 3.1. The inertial of the spectrum enlarges with the increase of the Reynolds number, which displaces the dissipative zone to large wavenumbers and increases energy transfer. This interpretation allows distinguishing three zones in the wavenumber axis. The first is dominated by inertial forces (energy-containing range) in which the energy is introduced anisotropically; this zone belongs to small and intermediate wavenumbers. The second is localized in moderately high wavenumbers where energy transfer (inertial subrange) takes place; in this zone the statistic of the distribution of the velocity differences not depend on the viscosity. Finally, there is a zone with the largest wavenumbers where the kinetic energy dissipation (dissipation range) takes place.

3.3 Convection-Diffusion-Reaction processes

As mentioned above, mixing is intimately connected with turbulence, Earth and natural sciences, and various branches of engineering. However, in spite of its universality, to construct a general framework for its analysis

is not an easy task. A study requires deep knowledge in several fields of science, such as thermodynamics, chemical kinetics, molecular transport processes, and fluid dynamics. For example, consider a configuration that is initially composed of two distinct and segregated scalar constituents, which may be characterized by different chemical composition, different temperatures, contain different trace elements, or any other scalar marker. These constituents are brought together and interact at the molecular level. Unfortunately, accurately predicting their scalar structures is complex in turbulent flows. The governing equation that describes the above process is:

$$\frac{\partial \phi_\alpha}{\partial t} + \frac{\partial u_j \phi_\alpha}{\partial x_j} = \frac{\partial}{\partial x_j}\left(D_\alpha \frac{\partial \phi_\alpha}{\partial x_j}\right) + \dot{\omega}_\alpha \,, \tag{3.8}$$

where ϕ_α, D_α and $\dot{\omega}_\alpha$ represent the scalar concentration or mass fraction, the molecular diffusion coefficient and the reaction rate of species α, respectively. In this equation, there is no summation over α (only j). Equation (3.8) describes the following three physical processes:

- Tubulent convection,
- Molecular Diffusion,
- Chemical reaction rate.

Tubulent convection: Turbulent stirring redistributes or convects the scalar field throughout the flow domain. The action of this flow field on the scalar is to distort and increase the surface area of the interface between the constituents. Then, the scalar gradients and length scales will be increase and decrease, respectively. As a result of this convective process a complex structure of the scalar field evolves.

Molecular Diffusion: Mixing at the molecular level can only occur through the action of the molecular diffusion. Molecular diffusion is a result of the random motion (Brownian motion) of molecules. This process is most effective in regions of high gradients. Turbulent stirring increases the effectiveness of molecular diffusion by increasing the scalar gradient and the surface area over which the segregated constituents can diffuse.

Chemical reaction rate: Combustion and the cases with chemical conversion occur via multiple step chemical kinetic mechanisms that involve a huge number of chemical reactions. It is well known that often the expression for the mean species source terms due to chemical reaction are extremely simplified. Several models and numerical approaches have been developed in order to tackle this issue. All these models attempt to represent the essential features of the chemical kinetic mechanisms. Unfortunately, as the modeling becomes more sophisticated, there is a corresponding increase in the computational cost.

The redistribution the scalar throughout the flow field, the rate of molecular mixing, and the conversion of reacting species are a sample of multi-scale nonlinear phenomena and the interaction among the physical mechanisms present in turbulent reacting flows. The mathematical formulation for describing these different processes is presented in Chapter 2.

3.4 Local flow topology

In the chaotic behavior of turbulence there are regions with organized motions or topologies, which have been the focus of many discussions. Intuitively, a local topology is a three-dimensional region in the flow over which some properties of the flow exhibit significant correlation in the space and time. Theoretical studies and direct numerical simulations have been carried out to analyze and visualize these organized small-scale structures of turbulent flow. Kuo and Corrsin [7, 8] investigated the nature of small-scale turbulence and suggested that the small-scale vorticity structure is cylindrical rather than sheet-like as suggested by Betchov [9] and observed by Schwarz [10]. Siggia [11] observed cylindrical or tube-like structures of vorticity using a direct spectral simulation for a stationary, homogeneous, isotropic turbulence field. Kerr [12], She *et al.* [13], Vincent and Meneguzzi [14] confirmed the existence of organized structures in form of

tubes for the regions with intense vorticity. Other authors called the elongated coherent structures 'worms': Ruetsch and Maxey [15]; Jiménez *et al.* [16]. The worms present a high probability of having an extensional strain rate in the direction of the vorticity vector, i.e. along the axis of the vortex tube. Perry and Chong [17], and Chong *et al.* [18] proposed a general classification of the small-scale flow patterns, based on the three invariants of the velocity-gradient tensor, in order to study the local small-scale three-dimensional topologies for constant- and variable-density turbulent flows. In constant-density flows, the first invariant of the velocity-gradient tensor P is zero, then the turbulent flow can be described by the two-dimensional plane of the second, Q, and third, R, invariants of the velocity-gradient tensor. Following this methodology extensive numerical and experimental investigations of the flow statistical properties in the $Q-R$ plane have been performed. Perry and Chong [19], and Soria *et al.* [20] analyzed the fine-scale structures in time-developing mixing layers and found that motions with large positive values of Q are most likely to occur, with a topology of stable focus/stretching. Blackburn *et al.* [21] investigated the topological features of the velocity-gradient field of turbulent channel flow; the joint probability density functions (jpdf's) of Q and R were analyzed to indicate that topologies of stable focus/stretching and unstable node/saddle/saddle are the preferred ones away from the wall. Chong *et al.* [22] and Chacin

and Cantwell [23] revealed that the joint probability density functions of Q and R exhibit a teardrop shape. Ooi *et al.* [24], studied the fine-structure of several turbulent flows and found that the jpdf's of $Q - R$ were rather similar, which suggested a certain universality in the $Q - R$ plane of small-scale motions. The existence of the teardrop shape of the joint pdf was also confirmed experimentally in turbulent boundary layer by Andreopoulos and Honkan [25], and Elsinga and Marusic [26]. Recently, Elsinga and Marusic [27] provided an explanation for that universal teardrop shape, evaluating average flow patterns in the local coordinate system defined by the eigenvectors of the strain rate tensor. Tsinober [28] qualitatively summarized the local flow properties in the $Q - R$ plane and indicated that the enstrophy production is large in the stable focus/stretching topology and the total dissipation production is large in the unstable focus/compressing topology. Dopazo *et al.* [29] explored the correlations between the invariant Q and the structures of an inert dynamically passive scalar, in terms of the local mean and Gauss curvatures, k_m and k_g; the scalar saddle-point geometries are related with intense strain ($Q < 0$), while scalar concave or convex elliptic-points relate with focal motions corresponding to dominant vorticity ($Q > 0$). Lüthi *et al.* [30] expanded the $Q - R$ plane to three dimensions by the decomposition of R into its strain production and enstrophy production terms, and determined that the non-locality plays

an important role in the evolution of the velocity gradients. Da Silva and Pereira [31] and Khashehchi *et al.* [32] characterized the flow topology across the turbulent/non-turbulent (T/NT) interface in turbulent plane jets through the use of direct numerical simulation and experiments; the values of the invariants of the velocity-gradient tensor are all zero in the irrotational region and change rapidly when the T/NT interface is crossed; the universal teardrop shape of the joint pdf of $Q - R$ is not formed at the interface and it only exists inside the turbulent region. Gualtieri and Meneveau [33] studied the jpdf's of $Q - R$ for isotropic turbulence subjected to a straining and destraining cycle, and revealed the features of non-equilibrium turbulence. Bijlard *et al.* [34] investigated the local flow topology in a particle-laden turbulent channel flow and analyzed the effects of the particles on the flow field.

As noted, the investigation of flow topologies in variable-density turbulent flows is limited in comparison to the study of constant-density turbulence. Feiereisen *et al.* [35] conducted the first DNS of variable-density turbulence in 1981. However, serious studies were only undertaken a decade later. Chen *et al.* [36] examined the flow patterns of a variable density plane wake, applying the three-dimensional velocity critical point theory, in terms of P, Q and R. Sondergaard *et al.* [37] investigated the local flow geometry of a turbulent shear flow, studying scatter plots both in

the $P - Q - R$ and $P_S - Q_S - R_S$ invariant spaces, where P_S, Q_S, and R_S are the first, second and third invariants of the symmetric strain-rate tensor, respectively; the trends suggested that the second and third invariants of the symmetric strain-rate tensor correlate as $R_S \cong K(-Q_S)^{3/2}$, where the coefficient K is a function of the Reynolds number and the flow type. Maekawa *et al.* [38] studied the velocity-gradient invariants for decaying isotropic compressible turbulence, and revealed that the unstable node/saddle/saddle and stable focal/stretching topologies in the $Q - R$ plane prevailed over other topologies. Tanahashi *et al.* [39] used the Q invariant to separate strain dominated regions ($Q < 0$) from coherent fine-scale eddies ($Q > 0$) in a premixed flame; coherent fine-scale eddies are perpendicular to the flame front and can survive behind it. Suman and Girimaji [40] investigated the local flow topology in compressible isotropic turbulence. Grout *et al.* [41] studied the local flow topology of a reactive transverse fuel jet in cross-flow, and determined that the highest heat release rates of the flame are found in regions with node/node/node (unstable) topology. Wang and Lu [42] studied the behavior of flow topology in a compressible turbulent boundary layer identifying several topological preferences in the inner and outer layer.

3.5 Local structures of the scalar field

There have been many attempts to characterize the structure of scalar fields. In turbulent mixing of scalar fields, the points with constant values of scalar define the iso-scalar surfaces, which have their own dynamics with respect to the fluid that transports them. The first theoretical studies were about the material surface by Batchelor [43], Cocke [44] and Orszag [45], where by definition a material surface moves with the fluid. Gibson [46] analyzed in detail the local scalar geometries belonging for a turbulent scalar dynamically passive and concluded that the extremal points in a scalar field, which correspond to places where the scalar-gradient trajectories converge, are generated at scales of the Obukhov [47]-Corrsin [48] length. For premixed combustion, Clavin and Willian F. [49, 50] carried out an analytical study of the flamelet [ii] and obtained an influence of flame curvature on diffusive-thermal instability of flame. Henceforth the curvature, among other things, has been one of the most important features in the local structures of the scalar field.

Pope [51] derived the ordinary differential equations for the main curvatures, k_1 and k_2, of a material surface in homogeneous isotropic turbulence and observed that the second spatial derivative of the fluid velocity folds

[ii] Flamelet can be considered as 'flame sheet' where is assumed infinitely fast chemical reaction such that the reaction zone is an infinitely thin interface.

the material surfaces. Pope *et al.* [52] found that the most probable structures in the material surfaces with large curvatures are cylinders. Candel and Poinsot [53] deduced the flame surface stretch in terms of tangential strain rate, a_T, and the mean curvature of the flame, k_m; they proved that a_T and k_m correlate with the extinction mechanisms of turbulent flames. Rutland *et al.* [54] realized a study of premixed flame in a three-dimensional DNS and found that the positive and negative flame curvature are equally likely [iii]. Poinsot *et al.* [55] studied in a two-dimensional DNS the quenching processes in the flame; they observed that the interaction between small vortices and the flame front is controlled by the curvature of the flame and viscous effects. Haworth and Poinsot [56] realized a study of the structure of a premixed flame to different Lewis numbers, Le, using a two-dimensional DNS, and examined the relation between the displacement speed of the flame, V^Y, and mean curvature of the flame: the correlation between V^Y and k_m is positive for $Le < 1$, weak for $Le = 1$ and negative for $Le > 1$. Baum *et al.* [57] simulated a DNS of $H_2/O_2/N_2$ flame with complex chemistry in two-dimensional turbulent flow and found that for lean flames the local flame structure correlates with the flame curvature as predicted by DNS based on simple chemistry. Echekki and Chen [58] simulated turbulent premixed stoichiometric methane/air flames and eval-

[iii] For a positive (negative) flame curvature, $k_m > 0$ ($k_m < 0$), the scalar surface is convex (concave) towards the fresh gas side.

uated, among other things, the effects of strain rate and mean curvature of the flame upon radicals concentration and heat release. Gran *et al.* [59], using a two-dimensional DNS of a methane-air premixed flame, found that chemical effects on the displacement speed of the flame are negligible compared to molecular diffusion effects in regions with large flame curvature. Renou *et al.* [60] tested experimentally different mixtures (methane/air, propane/air, and hydrogen/air) to different Lewis numbers, and performed measurements of the flame curvature and tangential strain rate varying the turbulence conditions; they demonstrated that the local flame curvature and tangential strain rate are negatively correlated. Echekki and Chen [61] evaluated the influence of scalar geometry in the displacement speed using results from DNS of an unsteady stoichiometric methane-air flame embedded in a two-dimensional vortical flow field, and showed that the displacement speed is a balance of three components: reaction, normal diffusion, and local flame curvature. Chakraborty and Cant [62, 63] used three-dimensional DNS of premixed turbulent flames with single-step Arrhenius chemistry in a inflow-outflow configuration, and obtained a complete statistical analysis for the displacement speed, strain rate, dilatation rate and flame curvature; the mean curvature of the flame is negatively correlated with the local volumetric dilatation rate and the displacement speed of the iso-scalar surfaces. Dopazo *et al.* [64, 29] used results from

constant-density turbulent flow DNS to describe the local geometry of iso-scalar surfaces in terms of either main curvatures, k_1 and k_2, or mean and Gauss curvatures, k_m and k_g. Han and Huh [65] simulated turbulent premixed flames to different Karlovitz numbers, Ka, and found that in regions with convex flame curvature the displacement speed decreases when the Karlovitz number increases.

3.6 Strain rates in the turbulence-scalar interaction

A turbulent premixed flame acts as a propagating frontier between the fresh mixture and the burnt gases, which modifies both the upstream and downstream flows through aero-thermo-chemical processes. Far upstream of the flame, the flow turbulence, as well as the structure of the scalar fields will weakly sense the flame presence. As large- and small-scale structures of the velocity and scalar fields approach the flame, interactions become increasingly important and likely dominate in regions of intense chemical activity and thermal transport. The resulting flow and scalar structures downstream of the flame will be significantly different from those upstream of it. On the other hand, the wrinkling and stretching of iso-scalar surfaces by turbulent motion alter the statistical behavior of the scalar field. This turbulence-scalar interaction can be characterized by familiar quantities

such as the normal, a_N, and tangential, a_T strain rates, which appear in expansive and compressive flow regions, composing the local volumetric dilatation rate, $\nabla \cdot \mathbf{u}$.

The importance of the tangential strain rate on the propagation speed and stability of laminar, premixed flames has been widely investigated (Matalon [66], Chen and Im [67], Echekki and Chen [58], Chakraborty and Cant [62], among other references cited in previous sections). Transport equations for flame area and surface density function have been derived and they contain explicit dependences on tangential stretching [53, 68].

Flows with important density changes, due, for example, to chemical heat generation, will presumably undergo large volumetric dilatation rates. Intuitively, this situation may lead to mostly positive values for both tangential and normal strain rates [69]; the former will imply iso-scalar surface stretching, whereas the latter will, in principle, yield a reduction of the scalar-gradient modulus, as iso-surfaces separate. This fact seems at first glance to hamper scalar molecular fluxes and dissipation of composition inhomogeneities. Chakraborty [70] has documented, via DNS, the occurrence of positive normal strain rates in a 'corrugated flamelets' regime. and negative ones in a 'thin reaction zone regime'; while in the first case the scalar gradient aligns preferentially with the strain rate tensor eigenvector corresponding to its most extensive eigenvalue, in the second instance

the scalar gradient is mainly parallel to the most compressive eigenvector. This latter feature is coincident with that described for turbulent scalar mixing in constant density flows (Batchelor [43], Kerr [12], Ashur [71], and references therein). Chakraborty et al. [72] have scrutinized via DNS the Lewis number effect on the scalar gradient alignment in turbulent premixed flames; they have documented mainly positive normal strain rates and concluded that 'the most extensive principal strain rate' is preferentially perpendicular to iso-scalar surfaces and 'destroys the scalar gradient' with a 'magnitude' that 'increases with decreasing Lewis number for given turbulent Reynolds and Damköhler numbers'. It is apparent that small-scale flow and scalar structures strongly influence the turbulent mixing that, in turn, affect the thermal fields and the chemical kinetics. It is therefore important to know how small-scale flow and scalar structures, as momentum, mass and thermal molecular diffusion local enhancers, behave and evolve in front, within and behind the flame. Molecular mixing models for combusting flows, resulting from that knowledge, could incorporate more physical content and likely improve their accuracy and prediction capability.

3.7 Objectives and methodology

The study of turbulent mixing mechanisms in the dynamics of scalar fields requires to investigate different small-scale processes for both the scalar and the velocity fields. The knowledge of these features requires to solve exactly all physical spatial and time scales embedded in the flow equations without any model for turbulence. Thus, the direct numerical simulation (DNS) is the adequate tool to deal with this task. The goal of this dissertation is to investigate the different turbulent mixing and combustion processes through the small-scale structures in the scalar and velocity fields using several direct numerical simulation datasets. Specific objetives of this work are the following:

- Characterizing the small-scale structures of the scalar and velocity fields in turbulent mixing.
- Obtaining new information about the statistics of the invariants of the velocity-gradient tensor and to explore their role in turbulent mixing and combustion.
- Analyzing the geometric characteristics of the scalar field in combustion cases and its influence in the small-scale dynamics of turbulence.
- Investigating the reactive-diffusive characteristics of turbulent mixing

of scalar fields and their impacts in the displacement speed of the iso-scalar surfaces.

- Examining via DNS volumetric dilatation rates as functions of scalar micro-structures, and obtaining information of the expansive and compressive flow regions for several flame zones and different local scalar geometries.

To achieve these objectives, different direct numerical simulations of premixed systems have been conducted and the resulting datasets have been examined.

3.8 Outline

The thesis is organized as follows:

- **Chapter 4** details the governing equations of the constant- and variable-density turbulent reacting flows. It briefly reviews the velocity gradient tensor and its invariants, the non-material surfaces (specifically, scalar geometries and its characterization through curvatures) their propagation velocities and stretching, the turbulent premixed flame regimes and the chemical reaction rates used in this work.

- **Chapter 5** discusses the three-dimensional DNS results of constant-

density mixing and reaction. A single step Arrhenius-type chemistry is used. The simulation was performed using the FORTRAN code of the Fluid Mechanics Group at the University of Zaragoza. Scalar structures are obtained for different Schmidt numbers. Molecular diffusion effects on the scalar field are analyzed, as well as, the displacement speed of the iso-scalar surfaces. Flow strain rates are presented emphasizing the impact of their joint interactions with the small-scale scalar structures. Subsequently, invariants of the velocity gradient-tensor and local flow topologies are also obtained and analyzed. The effects of the flow strain rates upon the scalar iso-surfaces calculating the orientation of the unit vector normal to iso-scalar surfaces with respect to the strain rate eigenvectors and the local vorticity is scrutinized. Some preliminary conclusions and recommendations for future work are contained at the end of this Chapter.

- **Chapter 6** describes the three-dimensional DNS results of a variable-density turbulent premixed propagating flame in an inflow-outflow configuration using one-step Arrhenius chemistry. The simulation was performed using the fully parallel compressible solver NTMIX3D [73]. DNS code was programmed by the research group of the *'Departament of Energy - Centro de Investigaciones Energéticas, Medioambientales y Tecnológicas (CIEMAT)'*. Scalar structures are obtained in terms

of the mean and Gauss curvatures for several flame zones. Molecular diffusion effects on the scalar field are analyzed, as well as, the displacement speed of the iso-scalar surfaces in all reaction-conditioned regions. A kinematics of iso-scalar surfaces is presented and the local fluid volumetric dilatation and flow strain rates are analyzed and related with the small-scale scalar structures. Furthermore, invariants of the velocity gradient tensor and local flow topologies are also analyzed. The alignment between the unit vector normal to iso-scalar surfaces, the strain rate eigenvectors and the local vorticity is obtained. Some preliminary conclusions and recommendations for future work are contained at the end of this Chapter.

- **Chapter 7** analyzes the three-dimensional simulation results of a premixed turbulent jet flame in a hybrid Large Eddy Simulation (LES)/DNS approach, using a stoichiometric methane-air mixture injected through a central jet, surrounded by a co-flow of burned products. The fully parallel compressible solver SiTCom (Simulating Turbulent Combustion), programmed by the research group of the *'CORIA - CNRS - Normandie Université - INSA de Rouen'*, has been used to perform the simulation. Scalar structures are obtained in terms of the mean and Gauss curvatures. Molecular diffusion effects on the scalar field are analyzed, as well as, the displacement speed of the iso-scalar sur-

faces. The expansive and compressive flow regions for several flame zones and different local scalar geometries are studied through the local fluid volumetric dilatation and flow strain rates. Subsequently, invariants of the velocity gradient tensor and local flow topologies are also studied. The orientation of the strain rate eigenvectors respect to the local vorticity and the unit vector normal to iso-scalar surfaces is analyzed. Some preliminary conclusions and recommendations for future work are contained at the end of this Chapter.

- **Chapter 8** describes the main conclusions of the present work and some perspectives for further developments.

4

Dynamics of turbulent mixing and combustion

This chapter introduces the mathematical description in terms of the Navier-Stokes, species and energy transport equations, as well as the general de-

scription of the small-scale characteristic structures in turbulent mixing and reacting flow fields.

4.1 Governing equations

The basic set of conservation equations are given by the classical Navier-Stokes, species and energy transport equations. The following assumptions are made:

- The species and the mixture obeys the perfect gas law.
- The Mach number is much less than unity.
- There are no heat flux due to radiation.
- There are no body forces.
- The Soret and Dufour effects, pressure-gradient diffusion, and bulk viscosity are negligible.
- The molecular mass and heat fluxes are approximated by Fick's and Fourier's laws, respectively.

4.1.1 Variable-density turbulent reacting flows

Conservation of mass

The equation of mass conservation (or continuity equation) is written:

$$\frac{\partial \rho}{\partial t} + \frac{\partial (\rho u_i)}{\partial x_i} = 0 \,, \tag{4.1}$$

where ρ denotes density of the fluid, t is the time, x_i stands for the ith component of the position vector and u_i the ith component of hydrodynamic velocity.

Conservation of momentum

The balance equation for momentum in variable-density turbulent flows is as follows:

$$\frac{\partial (\rho u_i)}{\partial t} + \frac{\partial (\rho u_j u_i)}{\partial x_j} = -\frac{\partial p}{\partial x_i} + \frac{\partial \tau_{ij}}{\partial x_j} \,, \tag{4.2}$$

where p is the thermodynamic pressure and τ_{ij} is the viscous stress tensor defined as:

$$\tau_{ij} = 2\mu S_{ij} - \frac{2}{3}\mu S_{kk}\delta_{ij} \,, \tag{4.3}$$

μ is the dynamic viscosity, δ_{ij} is the Kronecker delta and S_{ij} is the strain rate tensor, which is defined as:

$$S_{ij} = \frac{1}{2}\left(\frac{\partial u_i}{\partial x_j} + \frac{\partial u_j}{\partial x_i}\right) \,. \tag{4.4}$$

S_{kk} in Eq. (4.3) stands for the local volumetric dilatation rate (velocity divergence $\nabla \cdot \mathrm{u}$), which is equal to zero for constant-density turbulent flows.

Viscous stress tensor and pressure are often combined into the stress tensor σ_{ij}, that reads:

$$\sigma_{ij} = -p\delta_{ij} + \tau_{ij} = -p\delta_{ij} + 2\mu S_{ij} - \frac{2}{3}\mu S_{kk}\delta_{ij} \,. \tag{4.5}$$

Conservation of species

In terms of the mass fraction for a chemical species, Y_α, in a mixture of N_s species, the balance equation for the species α is:

$$\frac{\partial(\rho Y_\alpha)}{\partial t} + \frac{\partial}{\partial x_i}(\rho u_i Y_\alpha) = -\frac{\partial q_{\alpha,i}}{\partial x_i} + \dot{\omega}_\alpha \,, \tag{4.6}$$

where $q_{\alpha,i}$ is the diffusive flux of the species α in the direction i and $\dot{\omega}_\alpha$ the mass reaction rate of the species α per unit time and volume. In this equation, there is no summation over α (only i).

In mixtures where one species has larger mass fraction than the other ones, the minority species fluxes are proportional to the concentration gradients. Taking into account only the diffusive flux by species gradient according to Fick's law, $q_{\alpha,i}$ is as follows:

$$q_{\alpha,i} = -\rho D_\alpha \frac{\partial}{\partial x_i} Y_\alpha \,, \tag{4.7}$$

where D_α is the molecular diffusivity of the α-th species in the mixture.

The Schmidt number of the species α can be written as:

$$Sc_\alpha = \frac{\mu}{\rho D_\alpha} \,, \tag{4.8}$$

thus, the diffusive flux of the species in terms of Schmidt number is:

$$q_{\alpha,i} = -\frac{\mu}{Sc_\alpha}\frac{\partial}{\partial x_i}Y_\alpha \,. \tag{4.9}$$

With the above considerations, the species conservation equation is recovered:

$$\frac{\partial(\rho Y_\alpha)}{\partial t} + \frac{\partial}{\partial x_i}(\rho u_i Y_\alpha) = \frac{\partial}{\partial x_i}\left(\frac{\mu}{Sc_\alpha}\frac{\partial Y_\alpha}{\partial x_i}\right) + \dot{\omega}_\alpha \,. \tag{4.10}$$

The species balance equation can also be written in its non-conservation form:

$$\frac{DY_\alpha}{Dt} = \frac{\partial Y_\alpha}{\partial t} + u_i\frac{\partial Y_\alpha}{\partial x_i} = \frac{1}{\rho}\frac{\partial}{\partial x_i}\left(\rho D_\alpha\frac{\partial Y_\alpha}{\partial x_i}\right) + \dot{\omega}^*_\alpha \,, \tag{4.11}$$

where D/Dt is the substantial derivative operator $\partial/\partial t + u_i\partial/\partial x_i$ and $\dot{\omega}^*_\alpha = \dot{\omega}_\alpha/\rho$.

Conservation of energy

Multiple forms can be derived for the balance equation for energy, depending on which variable is solved: enthalpy, internal energy, total energy,

etc.

Let us choose as first option total energy, e_t, at a fluid volume. e_t is the sum of internal energy, e ($e = C_v T$, where C_v is the specific heat at constant volume and T is the temperature), and kinetic energy, $u_i u_i/2$. The balance equation for e_t can be written as:

$$\frac{\partial(\rho e_t)}{\partial t} + \frac{\partial}{\partial x_i}(\rho u_i e_t) = \frac{\partial(\sigma_{ij} u_i)}{\partial x_j} - \frac{\partial q_i}{\partial x_i}\,, \tag{4.12}$$

where q_i is the diffusive flux of heat. q_i, considering only the Fourier's law, results in:

$$q_i = -\lambda \frac{\partial T}{\partial x_i}\,, \tag{4.13}$$

where λ stands for the thermal conductivity of the mixture.

The Prandtl number of the mixture, Pr, which compares the diffusive transport of momentum (viscous forces) and heat, can be written as:

$$Pr = \frac{C_p \mu}{\lambda} = \frac{\mu}{\rho D_{th}}\,, \tag{4.14}$$

where C_p is the specific heat at constant pressure and $D_{th} = \lambda/(\rho C_p)$ is the heat (thermal) diffusivity coefficient.

The diffusive flux of heat can be expressed in terms of Pr, such as follows:

$$q_i = -\frac{C_p \mu}{Pr} \frac{\partial T}{\partial x_i} \,. \tag{4.15}$$

With the above considerations, the balance equation for total energy is recovered:

$$\frac{\partial(\rho e_t)}{\partial t} + \frac{\partial}{\partial x_i}(\rho u_i e_t) = \frac{\partial(\sigma_{ij} u_i)}{\partial x_j} + \frac{\partial}{\partial x_i}\left(\frac{C_p \mu}{Pr} \frac{\partial T}{\partial x_i}\right) \,. \tag{4.16}$$

Other option of getting a balance equation for energy is to consider the total enthalpy, h_t. Using the continuity equation (4.1) and the relation between total energy and enthalpy: $h_t = e_t + p/\rho$, yields:

$$\rho \frac{De_t}{Dt} = \rho \frac{Dh_t}{t} - \frac{Dp}{Dt} - p \frac{\partial u_i}{\partial x_i} \,, \tag{4.17}$$

Equating the right sides of Eqs. (4.17) and (4.16), one can easily obtain a balance equation for the total enthalpy, h_t:

$$\frac{\partial(\rho h_t)}{\partial t} + \frac{\partial}{\partial x_i}(\rho u_i h_t) = \frac{\partial p}{\partial t} + \frac{\partial(\tau_{ij} u_i)}{\partial x_j} + \frac{\partial}{\partial x_i}\left(\frac{C_p \mu}{Pr}\frac{\partial T}{\partial x_i}\right) . \tag{4.18}$$

The kinetic energy equation is obtained multiplying the momentum equation (4.2) by u_i:

$$\frac{\partial}{\partial t}\left(\frac{1}{2}\rho u_i u_i\right) + \frac{\partial}{\partial x_j}\left(\frac{1}{2}\rho u_j u_i u_i\right) = \frac{\partial(u_i \sigma_{ij})}{\partial x_j} + p\frac{\partial u_i}{\partial x_i} - \phi\,, \tag{4.19}$$

where ϕ is the dissipation rate of kinetic energy:

$$\phi = 2\mu\left[\frac{\partial u_i}{\partial x_j} - \frac{1}{3}\frac{\partial u_k}{\partial x_k}\delta_{ij}\right]^2 . \tag{4.20}$$

ϕ is always positive and represents a rate of loss of mechanical energy due to viscous forces.

Subtracting Eq. (4.19) from (4.16) leads to the balance equation for the internal energy, e:

$$\frac{\partial(\rho e)}{\partial t} + \frac{\partial}{\partial x_i}(\rho u_i e) = \sigma_{ij}\frac{\partial u_i}{\partial x_j} + \frac{\partial}{\partial x_i}\left(\frac{C_p \mu}{Pr}\frac{\partial T}{\partial x_i}\right) . \tag{4.21}$$

Using the continuity equation (4.1), the balance equation for internal energy (4.21) and the relation between internal energy and specific enthalpy: $h = e + p/\rho$, one can easily obtain a balance equation for specific enthalpy, h:

$$\frac{\partial(\rho h)}{\partial t} + \frac{\partial}{\partial x_i}(\rho u_i h) = \frac{Dp}{Dt} + \tau_{ij}\frac{\partial u_i}{\partial x_j} - \frac{\partial q_i}{\partial x_i}\,. \tag{4.22}$$

The specific enthalpy is defined by:

$$h = h_s + h_q = h_s + \sum_{\alpha=1}^{N_s} h^o_{f,\alpha} Y_\alpha\,, \tag{4.23}$$

where h_s is the sensible enthalpy (commonly called the thermal enthalpy), h_q is the chemical enthalpy and $h^o_{f,\alpha}$ is the formation enthalpy of the species k. Using the balance equation for specific enthalpy (4.22), the balance equation for species (4.10) and canceling the pressure gradients, a balance equation for thermal enthalpy is obtained:

$$\frac{\partial(\rho h_s)}{\partial t} + \frac{\partial}{\partial x_i}(\rho u_i h_s) = \frac{Dp}{Dt} + \tau_{ij}\frac{\partial u_i}{\partial x_j} + \frac{\partial}{\partial x_i}\left(\frac{C_p \mu}{Pr}\frac{\partial T}{\partial x_i}\right) + \dot{\omega}_s\,, \tag{4.24}$$

where appears the term of heat release due to combustion: $\dot{\omega}_s = -\sum_{\alpha=1}^{N_s} h^o_{f,\alpha} W_\alpha$, which comes from the relation between the chemical enthalpy and the concentration of species.

The equation for the sensible energy e_s may be deduced from Eq. (4.24), the relation $e_s = h_s - p/\rho$ and deduction used in Eq. (4.17):

$$\frac{\partial(\rho e_s)}{\partial t} + \frac{\partial}{\partial x_i}(\rho u_i e_s) = \sigma_{ij}\frac{\partial u_i}{\partial x_j} + \frac{\partial}{\partial x_i}\left(\frac{C_p \mu}{Pr}\frac{\partial T}{\partial x_i}\right) + \dot{\omega}_s \,. \tag{4.25}$$

Other way is to work with the sum of sensible and kinetic energies, $E = e_s + u_i u_i/2$, adding Eq. (4.25) and (4.19):

$$\frac{\partial(\rho E)}{\partial t} + \frac{\partial}{\partial x_i}(\rho u_i E) = \frac{\partial(u_i \sigma_{ij})}{\partial x_j} + \frac{\partial}{\partial x_i}\left(\frac{C_p \mu}{Pr}\frac{\partial T}{\partial x_i}\right) + \dot{\omega}_s \,. \tag{4.26}$$

Based on the Schmidt number in Eq. (4.8) and Prandtl number in Eq. (4.14), it is possible to write the Lewis number as:

$$Le_\alpha = \frac{Sc_\alpha}{Pr} = \frac{\lambda}{\rho C_p D_\alpha} = \frac{D_{th}}{D_\alpha} \,. \tag{4.27}$$

Le_α compares the diffusion speeds of heat and species α.

The thermodynamic variables are related by the perfect gas equation of state:

$$p = \frac{\rho R T}{W} \,, \tag{4.28}$$

where R is the universal perfect gas constant and W is the mean molecular weight.

With the above definitions, the set of balance equations for reacting variable-density turbulent flows does not depend on any other additional thermodynamic variable.

Summary of conservation equations

Table 4.1 summarizes the equations to solve for reacting variable-density turbulent flows.

4.1.2 Constant-density turbulent reacting flows

If the fluid density ρ appearing in the governing equations is assumed to be constant. The governing equations can be written as:

Mass	$\frac{\partial \rho}{\partial t} + \frac{\partial (\rho u_i)}{\partial x_i} = 0$
Momentum	$\frac{\partial (\rho u_i)}{\partial t} + \frac{\partial (\rho u_j u_i)}{\partial x_j} = -\frac{\partial p}{\partial x_i} + \frac{\partial \tau_{ij}}{\partial x_j}$
Species	$\frac{\partial (\rho Y_\alpha)}{\partial t} + \frac{\partial (\rho u_i Y_\alpha)}{\partial x_i} = \frac{\partial}{\partial x_i}\left(\frac{\mu}{Sc}\frac{\partial Y_\alpha}{\partial x_i}\right) + \dot{\omega}_\alpha$
Energy (sum of sensible and kinetic, E)	$\frac{\partial (\rho E)}{\partial t} + \frac{\partial}{\partial x_i}(\rho u_i E) = \frac{\partial (u_i \sigma_{ij})}{\partial x_j} + \frac{\partial}{\partial x_i}\left(\frac{C_p \mu}{Pr}\frac{\partial T}{\partial x_i}\right) + \dot{\omega}_s$

Table 4.1: Conservation equations for reacting variable-density turbulent flows. The energy equation may be replaced by any of the Eqs. (4.16), (4.18), (4.21), (4.22), (4.24) or (4.25).

- Mass

$$\frac{\partial u_i}{\partial x_i} = 0 \tag{4.29}$$

- Momentum

$$\frac{\partial u_i}{\partial t} + u_j \frac{\partial u_i}{\partial x_j} = -\frac{1}{\rho}\frac{\partial p}{\partial x_i} + \nu \frac{\partial^2 u_i}{\partial x_j^2} \tag{4.30}$$

If the temperature, the specific heat at constant pressure and enthalpy are assumed constant, the scalar field obeys the following equation:

- Scalar:

$$\frac{\partial \phi}{\partial t} + u_i \frac{\partial \phi}{\partial x_i} = \frac{\partial}{\partial x_i}\left(D \frac{\partial \phi}{\partial x_i}\right) + \dot{\omega}^* \,, \tag{4.31}$$

where, ϕ could be the species concentration, D the chemical species diffusivity, and $\dot{\omega}^*$ the creation rate of species by chemical reaction.

The pressure field p, appearing on the right-hand side of Eq. (4.30), is governed by Poisson's equation:

$$\nabla^2 p = -\rho \frac{\partial u_i}{\partial x_j} \frac{\partial u_j}{\partial x_i} \,. \tag{4.32}$$

This expression is deduced from Eqs. (4.29) and (4.30), for the mass and momentum conservation, respectively.

For constant-density reacting flows the velocity field is not affected by the values of the mass fraction. The density is strictly constant and, if the viscosity coefficient is constants, the scalar mixing-reaction problem is decoupled from the dynamic one.

4.2 Velocity-gradient tensor

The deformation produced in fluids can be measured through the variation of the velocity field. In the kinematic study at a fluid point we get the following relation:

$$\frac{\partial \mathbf{r}}{\partial t} = \mathbf{u}(\mathbf{x}+\mathbf{r},t) - \mathbf{u}(\mathbf{x},t)\,, \tag{4.33}$$

where $\mathbf{r}$ is an infinitesimal fluid element (see Figure 4.1). If the velocity field in the neighborhood of $\mathbf{x}$ is approximated by Taylor series:

$$u_i(\mathbf{x}+\mathbf{r}) = u_i(\mathbf{x}) + r_j\frac{\partial u_i}{\partial x_j} + \frac{1}{2}r_j r_k\frac{\partial^2 u_i}{\partial x_j \partial x_k} + \ldots \tag{4.34}$$

Eq. (4.33) becomes:

$$\frac{\partial r_i}{\partial t} = r_j\frac{\partial u_i}{\partial x_j} + \mathcal{O}(r^2)\,, \tag{4.35}$$

where $\mathcal{O}(r^2)$ is the infinitesimal of second-order. The velocity-gradient tensor $\mathbf{A}$, with components $A_{ij} = \partial u_i/\partial x_j$, is the responsible of the variation

of $\mathbf{r}$.

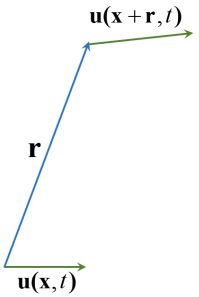

Figure 4.1: Deformation at a fluid point.

The velocity-gradient tensor can be split into its symmetric, S_{ij} (strain rate tensor), and skew-symmetric, W_{ij} (rotation rate tensor), components:

$$S_{ij} = \frac{1}{2}\left(A_{ij} + A_{ji}\right) , \tag{4.36}$$

$$W_{ij} = \frac{1}{2}\left(A_{ij} - A_{ji}\right) . \tag{4.37}$$

W_{ij} has an associated axial vector $\boldsymbol{\omega}$ (vorticity vector):

$$\boldsymbol{\omega} = \nabla \times \mathbf{u} . \tag{4.38}$$

Thus, the rotation rate tensor can be written as:

$$W_{ij} = -\frac{1}{2}\varepsilon_{ijk}\omega_k \,, \tag{4.39}$$

where ε_{ijk} is the Levi-Civitá tensor.

It is well known that S_{ij} has information about linear dilatation and angular deformation rates, and W_{ij} has information about angular velocities due to rotation with angular velocity $\boldsymbol{\omega}/2$.

4.2.1 Invariants and local flow topology

There is no doubt that flow patterns are strongly influenced by the strain and rotation rate tensors. Because of this, many studies of fluid motion are based on the description and understanding of the behavior of the velocity-gradient tensor.

One of the most important methods to explain and classify the features of flow patterns was proposed by Chong *et al.* [18]. Their critical point criteria, which are explained below, identify strong eddying or vortical regions, streaming zones, and stagnation points in the flow. The local flow topologies are characterized by the invariants of the velocity-gradient tensor, $\mathbf{A} = A_{ij} = \partial u_i/\partial x_j$; its three eigenvalues, λ_1, λ_2 and λ_3, are the

solutions of the characteristic equation,

$$\lambda^3 + P\lambda^2 + Q\lambda + R = 0\,, \tag{4.40}$$

P, Q, R are the three invariants of $\mathbf{A}$ [18], specified by

$$P = -tr(\mathbf{A}) = -(\lambda_1 + \lambda_2 + \lambda_3) = -S_{ii} = -\nabla \cdot \mathbf{u}\,, \tag{4.41}$$

$$Q = \frac{1}{2}\left([tr(\mathbf{A})]^2 - tr(\mathbf{A}^2)\right) = \frac{1}{2}\left(P^2 - S_{ij}S_{ij} + W_{ij}W_{ij}\right)\,, \tag{4.42}$$

$$R = -\det(\mathbf{A}) = \frac{1}{3}\left(-P^3 + 3PQ - S_{ij}S_{jk}S_{ki} - 3W_{ij}W_{jk}S_{ki}\right)\,, \tag{4.43}$$

where S_{ij} is the symmetric strain-rate tensor and W_{ij} is the skew-symmetric rotation-rate tensor.

$-P = \nabla \cdot \mathbf{u}$, represents the local volumetric dilatation rate, namely, the rate of change of an infinitesimal fluid volume per unit volume. $-P < 0$ implies element compression, $-P = 0$ means zero dilatation and $-P > 0$ entails local fluid expansion.

The discriminant D of Eq. (4.40) is defined by [18]

$$D = \frac{1}{108}\left[27R^2 + (4P^3 - 18PQ)R + 4Q^3 - P^2Q^2\right]\,. \tag{4.44}$$

The surface $D = 0$ divides the $P - Q - R$ phase space into two regions; for $D > 0$, $\mathbf{A}$ displays one real and two complex-conjugate eigenvalues (focal topologies), while in the region $D < 0$, $\mathbf{A}$ has three real eigenvalues (nodal topologies). The two surfaces, r_{1a} and r_{1b}, of $D = 0$ are given by

$$\frac{1}{3}P\left(Q - \frac{2}{9}P^2\right) - \frac{2}{27}\left(-3Q + P^2\right)^{3/2} - R = 0\,, \qquad [r_{1a}] \tag{4.45}$$

$$\frac{1}{3}P\left(Q - \frac{2}{9}P^2\right) + \frac{2}{27}\left(-3Q + P^2\right)^{3/2} - R = 0\,. \qquad [r_{1b}] \tag{4.46}$$

Further, in the region $D > 0$, $\mathbf{A}$ has purely imaginary eigenvalues on the surface r_2, which is described by

$$PQ - R = 0\,. \qquad [r_2] \tag{4.47}$$

For $P = 0$ the surface r_2 coincides with the $Q-$axis. Thus, the surfaces r_{1a}, r_{1b}, r_2 and $R = 0$ divide the $P - Q - R$ space into different regions, which correspond to distinct flow topologies, plotted, as reminder, in Figure 4.2 and explained pictorially in Table 4.2.

The invariants of S_{ij} and W_{ij} are given by

$$P_S = P = -S_{ii}\,,\;\; Q_S = \frac{1}{2}\left(P^2 - S_{ij}S_{ij}\right)\,,\;\; R_S = \frac{1}{3}\left(-P^3 + 3PQ_S - S_{ij}S_{jk}S_{ki}\right)\,, \tag{4.48}$$

$$P_W = 0\,, \quad Q_W = \frac{\boldsymbol{\omega}^2}{4} = \frac{1}{2}W_{ij}W_{ij}\,, \quad R_W = 0\,, \tag{4.49}$$

where $\boldsymbol{\omega}^2/2 = \omega_i\omega_i/2$ is the local enstrophy. ω_i is the ith component of the vorticity vector.

Both the turbulent kinetic energy dissipation and the volumetric dilatation rates contribute to Q_S. It is readily shown that

$$Q = Q_S + Q_W\,, \quad R = R_S + PQ_W - W_{ij}W_{jk}S_{ki} = R_S + PQ_W - \frac{1}{4}\omega_i S_{ij}\omega_j\,, \tag{4.50}$$

Q represents the additive contribution of enstrophy, Q_W, and dissipation/dilatation, Q_S. Enstrophy production, $PQ_W - (\omega_i S_{ij}\omega_j)/4$, and dissipation rate generation, $S_{ij}S_{jk}S_{ki}$, enter the definition of R [28].

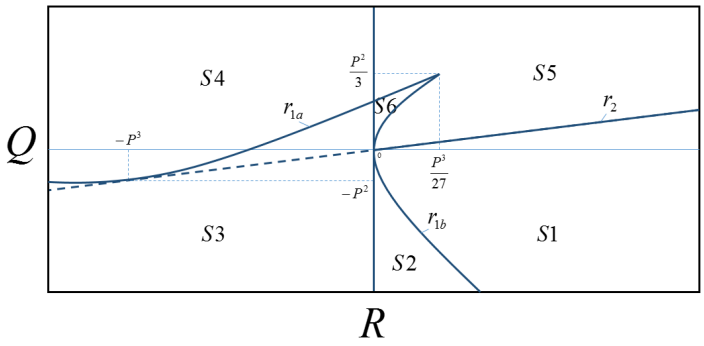

(a)

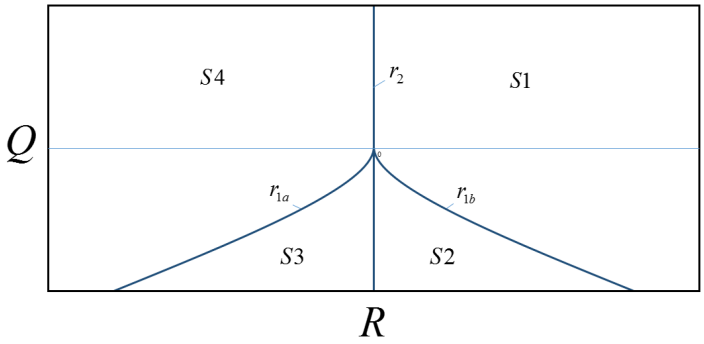

(b)

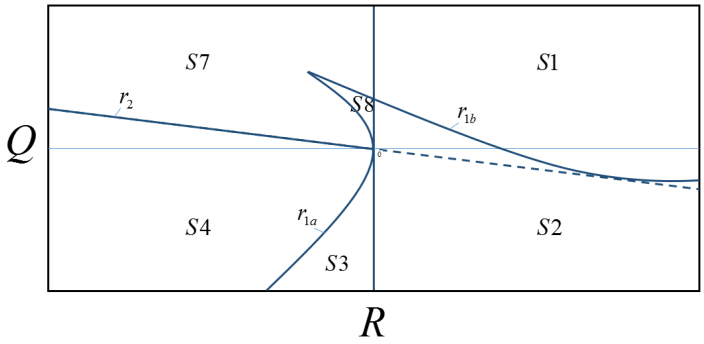

(c)

Figure 4.2: Classification of critical points in the $R - Q$ plane for: (a) $P > 0$, (b) $P = 0$, and (c) $P < 0$. Topologies and corresponding acronyms are listed in Table 4.2.

Sector	Acronym	Description	Sketch
S1	UFC	Unstable focus/compressing	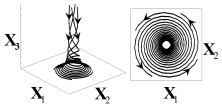
S2	UN/S/S	Unstable node/saddle/saddle	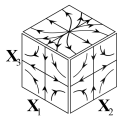
S3	SN/S/S	Stable node/saddle/saddle	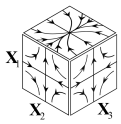
S4	SFS	Stable focus/stretching	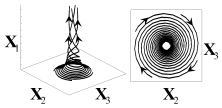
S5	SFC	Stable focus/compressing	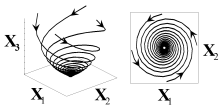
S6	SN/SN/SN	Stable node/stable node/stable node	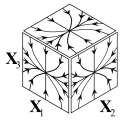
S7	UFS	Unstable focus/stretching	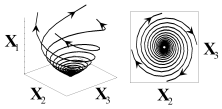
S8	UN/UN/UN	Unstable node/unstable node/unstable node	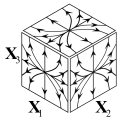

Table 4.2: Description of the flow topologies in $P - Q - R$ space.

4.3 Scalar geometries

The geometric structures of the scalar field have been essential in many studies of premixed systems. A clear example are the combustion instabilities where the scalar geometry helps to reproduce or increase these disturbances, despite the fact that the vorticity field creates instabilities [53, 74]. It is clear, at least locally, that the geometric structures of the scalar field are intrinsically related to the reactive-diffusion and mixing problems. Thus, it is important to detail the physical parameters describing the scalar geometries, not only to understand the premixed system problems but also to know the small-scale dynamics of turbulence.

4.3.1 Local geometry of iso-scalar surfaces

Iso-scalar surfaces, or iso-level surfaces [51], are surfaces on which the scalar value is constant. For the sake of simplicity in this section, iso-scalar surfaces are defined by $Y(\mathbf{x}, t) = \text{constant}$, where Y is the mass fraction of the scalar field [i]. The unit vector normal to an iso-surface is

$$\mathbf{n} = \frac{\nabla Y}{|\nabla Y|} \,. \tag{4.51}$$

[i] For non-passive scalar field, such as the studied in this thesis, Y could be the reduced fuel mass fraction, which goes from 1 in the fresh gases to 0 in the fully reacted products.

n points towards the fresh reactants. The local geometry of the scalar field is characterized by its value, $Y(\mathbf{x}, t)$, by its first and second derivatives, $\partial Y/\partial x_N$ and $\partial^2 Y/\partial x_N^2$, in the direction normal to the iso-surface, x_N, and also by its curvature tensor, $\partial n_i/\partial x_j = n_{i,j}$. The latter can be written in terms of the scalar field derivatives as [29, 64]

$$n_{i,j} = \frac{1}{|\nabla Y|}(\delta_{ik} - n_i n_k)\frac{\partial^2 Y}{\partial x_j \partial x_k}\,. \tag{4.52}$$

The relationship between $n_{i,j}$ and the intrinsic curvatures of isoscalar surfaces may be obtained from the Weingarten′s theorem [75]. The characteristic equation for $n_{i,j}$ is:

$$k^3 + I_1 k^2 + I_2 k + I_3 = 0\,. \tag{4.53}$$

The invariants of $n_{i,j}$ are given by

$$I_1 = -\nabla \cdot \mathbf{n}\,, \tag{4.54}$$

$$I_2 = (1/2)(n_{i,i}n_{j,j} - n_{i,j}n_{j,i})\,, \tag{4.55}$$

$$I_3 = -\det(n_{i,j})\,. \tag{4.56}$$

As $I_3 = 0$ [29], the two eigenvalues of $n_{i,j}$ are obtained from the equation

$$k^2 + I_1 k + I_2 = 0\,, \tag{4.57}$$

whose solutions are

$$k_1, k_2 = \frac{-I_1 \pm \sqrt{I_1^2 - 4I_2}}{2}\,, \tag{4.58}$$

k_1 and k_2 are the main curvatures.

The Gauss curvature, k_g, and the mean curvature, k_m, are

$$k_g = k_1 k_2\,, \tag{4.59}$$

$$k_m = \frac{k_1 + k_2}{2} = \frac{1}{2}\frac{\partial n_i}{\partial x_i}\,. \tag{4.60}$$

The zone $k_g > k_m^2$ in the $k_m - k_g$ plane implies non-physical complex curvatures. Figure 4.3 shows the different local geometries of isoscalar surfaces. For a positive (negative) mean curvature, $k_m > 0$ ($k_m < 0$), the surface is convex (concave) towards the fresh reactants.

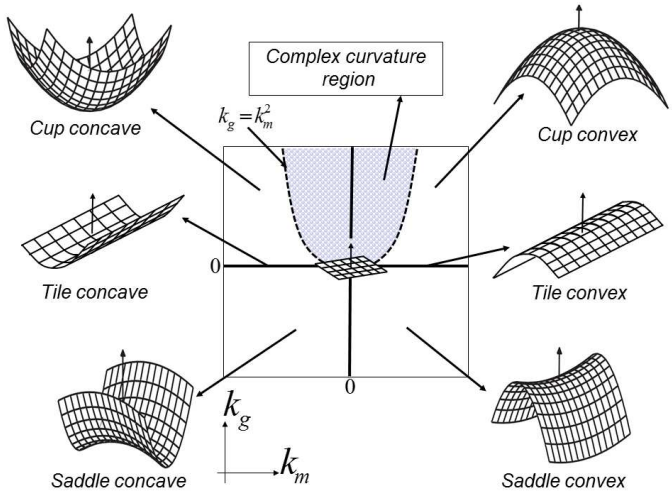

Figure 4.3: Classification of iso-scalar surface geometries in terms of their mean and Gauss curvatures, k_m and k_g.

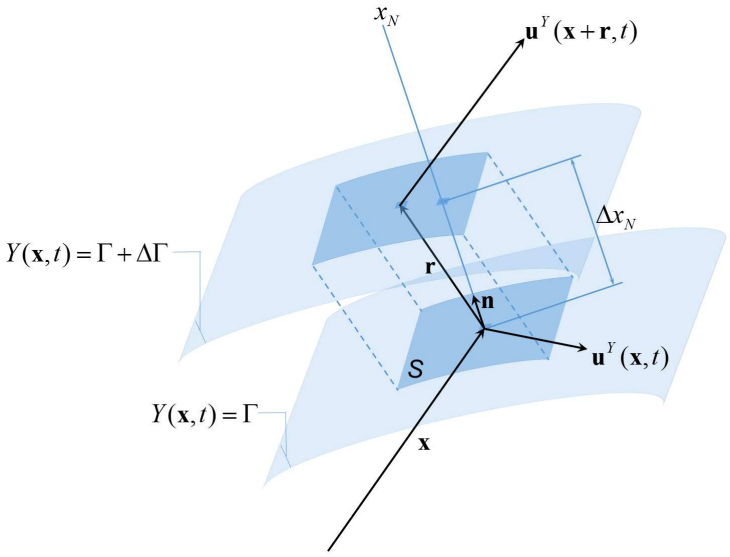

Figure 4.4: Schematic representation of two elements of flame surface.

4.3.2 Kinematics of iso-scalar surfaces

Scalar mixing can be viewed as a combination of iso-scalar surface stretching and scalar-gradient growth induced by the flow field. Figure 4.4 depicts

an infinitesimal surface, S, on the non-material iso-surface $Y(\mathbf{x},t) = \Gamma$, with a normal unit vector $\mathbf{n}(\mathbf{x},t) = \nabla Y/|\nabla Y|$.

$Y(\mathbf{x},t)$ is, for example, the normalized reactant mas fraction ($Y = 1$ in the 'fresh gases' and $Y = 0$ in the 'hot products').

An infinitesimal vector, $\mathbf{r}(\mathbf{x},t)$, joins a point $\mathbf{x}$ at the center of S to a point $\mathbf{x}+\mathbf{r}$ on a neighboring iso-scalar surface $Y(\mathbf{x},t) = \Gamma + d\Gamma$. The two extremes of $\mathbf{r}$ move with velocities $\mathbf{u}^Y(\mathbf{x},t)$ and $\mathbf{u}^Y(\mathbf{x}+\mathbf{r},t)$, where the velocity of a point of the non-material iso-scalar surface is decomposed as

$$\mathbf{u}^Y(\mathbf{x},t) = \mathbf{u}(\mathbf{x},t) + V^Y(\mathbf{x},t)\mathbf{n}\,, \tag{4.61}$$

$\mathbf{u}$ is the fluid velocity and V^Y is the normal displacement speed of $Y(\mathbf{x},t) = \Gamma$ relative to the local fluid. The time rate of change of $\mathbf{r}$ is

$$\frac{d\mathbf{r}}{dt} = (\mathbf{r}\cdot\nabla)\mathbf{u}^Y\,. \tag{4.62}$$

The right side of (4.62) can be expanded as

$$\frac{d\mathbf{r}}{dt} = \mathbf{r}\cdot\mathbf{s} + \mathbf{r}\cdot\mathbf{w} + (\mathbf{r}\cdot\nabla)V^Y\mathbf{n} + V^Y(\mathbf{r}\cdot\nabla)\mathbf{n}\,, \tag{4.63}$$

where $\mathbf{s}$ and $\mathbf{w}$ are the strain and rotation rate tensors, respectively, and $\nabla\mathbf{n}$ is the curvature tensor. $\mathbf{r}\cdot\mathbf{w}$ can be recast as $(\boldsymbol{\omega}\times\mathbf{r})/2$, in terms of

$\boldsymbol{\omega} = \nabla \times \mathbf{u}$, the vorticity vector.

If $\mathbf{r} = \Delta x_N \mathbf{n}$, one can readily obtain from (4.63)

$$\frac{1}{\Delta x_N}\frac{d\Delta x_N}{dt} = a_N + \frac{\partial V^Y}{\partial x_N}\,, \tag{4.64}$$

$$\frac{d\mathbf{n}}{dt} = (\boldsymbol{\delta} - \mathbf{nn})\cdot\mathbf{s}\cdot\mathbf{n} + \frac{1}{2}\boldsymbol{\omega}\times\mathbf{n} + V^Y(\mathbf{n}\cdot\nabla)\mathbf{n}\,, \tag{4.65}$$

where

$$a_N = \mathbf{n}\cdot\mathbf{s}\cdot\mathbf{n}\,, \tag{4.66}$$

is the flow strain rate normal to $Y(\mathbf{x}, t) = \Gamma$. $\partial V^Y/\partial x_N$ is the derivative of the propagation velocity in the normal direction to the iso-surface. $\boldsymbol{\delta}$ is the identity Kronecker delta tensor. While the vorticity has no influence on the variation of the modulus of $\mathbf{r}$, Δx_N, it obviously rotates its direction, $\mathbf{n}$.

The infinitesimal volume $V = S\Delta x_N$, between the two iso-scalar surfaces, changes in time according to

$$\frac{1}{V}\frac{dV}{dt} = tr(\mathbf{s}) + \frac{\partial V^Y}{\partial x_N} + 2k_m V^Y \,, \tag{4.67}$$

where $tr(\mathbf{s}) = \nabla \cdot \mathbf{u}$, the trace of the strain rate tensor, yields the flow volumetric dilatation rate, and k_m is the local mean curvature, $k_m = (\nabla \cdot \mathbf{n})/2$, of the iso-scalar surface. $k_m > 0$ for iso-surfaces convex towards 'fresh gases' and $k_m < 0$ for concave ones. The time rate of change of the infinitesimal surface S can thus be obtained from

$$\frac{1}{S}\frac{dS}{dt} = \frac{1}{V}\frac{dV}{dt} - \frac{1}{\Delta x_N}\frac{d\Delta x_N}{dt} \,, \tag{4.68}$$

and using (4.64) and (4.67)

$$\frac{1}{S}\frac{dS}{dt} = a_T + 2k_m V^Y \,, \tag{4.69}$$

with

$$a_T = (\boldsymbol{\delta} - \mathbf{nn}) : \mathbf{s} \,, \tag{4.70}$$

the flow strain rate tangential to $Y(\mathbf{x},t) = \Gamma$. This expression has been derived for flame stretch by several authors (Poinsot and Veynante [76], and references therein). a_N and a_T satisfy,

$$\nabla \cdot \mathbf{u} = a_N + a_T \,. \tag{4.71}$$

Surface stretching ($dS > 0$) occurs if $(a_T + 2k_m V^Y) > 0$, but seems to bear no direct influence on the local mixing rate. $(a_T + 2k_m V^Y)$ could be called the *'effective' tangential strain rate* to the iso-surface plane.

The mass flow rate per unit volume of $Y(\mathbf{x},t)$, which determines the local mixing rate, is

$$\frac{\mathbf{f}^Y \cdot S\mathbf{n}}{V} \sim -\rho D \frac{\Delta\Gamma}{(\Delta x_N)^2} \,, \tag{4.72}$$

where $\mathbf{f}^Y$ is the Fickian molecular flux, $\sum(\Gamma; x, t) = S/V = 1/\Delta x_N$ is the surface density function [68], and $|\nabla Y| = \partial Y/\partial x_N = \Delta\Gamma/\Delta x_N$.

For the two given iso-scalar surfaces, the local mixing rate increases with time if Δx_N diminishes. From (4.64) one concludes that $d\Delta x_N > 0$ if $a_N + \partial V^Y/\partial x_N > 0$ which increases the scalar gradient modulus, $|\nabla Y|$, and

$d\Delta x_N < 0$ if $a_N + \partial V^Y/\partial x_N < 0$, increasing $|\nabla Y|$. $\partial V^Y/\partial x_N$ measures the difference of propagation velocities of different iso-surfaces. $(a_N + \partial V^Y/\partial x_N)$ could be called the *'effective' normal strain rate* in the normal direction to the iso-surface.

For combusting flows with significant heat release ($\nabla \cdot \mathbf{u} > 0$), the probability of finding $a_N > 0$ in most of the flow domain might be large. Therefore, for the scalar-gradient and the mass flow rate per unit volume to increase, $\partial V^Y/\partial x_N$ should be negative and its absolute value greater than a_N.

On the other hand, the evolution of an iso-scalar surface obeys the equation

$$\frac{\partial Y}{\partial t} + (\mathbf{u} \cdot \nabla)Y = -V^Y |\nabla Y| \,. \tag{4.73}$$

An equation for the evolution of $|\nabla Y|$ can be readily obtained from (4.73),

$$\frac{\partial |\nabla Y|}{\partial t} + (\mathbf{u}^Y \cdot \nabla)|\nabla Y| = -\left(a_N + \frac{\partial V^Y}{\partial x_N}\right)|\nabla Y| \,. \tag{4.74}$$

The scalar-gradient associated to a point on a non-material iso-surface moving with velocity $\mathbf{u}^Y$ decreases or increases depending, once again, on positive or negative values, respectively, of the *'effective'* normal strain

rate, $(a_N + \partial V^Y/\partial x_N)$.

4.3.3 Non-material surface propagation velocity

The conservation equation for a reacting species mass fraction can be written as

$$\frac{D\,Y}{Dt} = \frac{1}{\rho}\nabla\cdot(\rho\,D\nabla Y) + \dot{\omega}_Y\,, \tag{4.75}$$

where D represents the Fickian molecular diffusivity coefficient for Y and $\dot{\omega}_Y = \dot{\omega}/\rho$ stands for its net production rate by chemical reaction.

Equating the right sides of Eq. (4.73) and (4.75), an expression for the displacement speed or propagation velocity relative to the fluid, V^Y, is easily obtained

$$V^Y = -\frac{1}{|\nabla Y|\rho}\nabla\cdot(\rho\,D\nabla Y) - \frac{\dot{\omega}_Y}{|\nabla Y|}\,. \tag{4.76}$$

V^Y is governed by the local balance between molecular diffusion and reaction rates.

The molecular diffusion contribution can be expressed as

$$\frac{1}{\rho}\nabla\cdot(\rho D\nabla Y) = \frac{|\nabla Y|}{\rho}\mathbf{n}\cdot\nabla(\rho D) + D\mathbf{n}\cdot\nabla|\nabla Y| + D|\nabla Y|\nabla\cdot\mathbf{n}\,. \quad (4.77)$$

Expanding expressions for (4.77)

$$MD_{(\rho D)} = (|\nabla Y|/\rho)\mathbf{n}\cdot\nabla(\rho D)\,, \quad (4.78)$$

$$MD_{|\nabla Y|} = D\mathbf{n}\cdot\nabla|\nabla Y|\,, \quad (4.79)$$

$$MD_{curv} = D|\nabla Y|\nabla\cdot\mathbf{n}\,. \quad (4.80)$$

$MD_{(\rho D)}$ and $MD_{|\nabla Y|}$ are the contributions due to the variation of ρD and $|\nabla Y|$ normal to the iso-surface, respectively. MD_{curv} is the contribution from tangential (due to the curvature) diffusion.

Equating the right sides of (4.73) and (4.75), and using (4.77), one can easily obtain

$$V^Y = -\frac{1}{\rho}\mathbf{n}\cdot\nabla(\rho D) - \frac{1}{|\nabla Y|}D\mathbf{n}\cdot\nabla|\nabla Y| - D(\nabla\cdot\mathbf{n}) - \frac{\dot{\omega}_Y}{|\nabla Y|}\,, \quad (4.81)$$

The first term in the right-hand side of (4.81) is the contribution to the displacement speed of the variation of ρD normal to the iso-surface

$$V^Y_{(\rho D)} = -\frac{1}{\rho}\mathbf{n}\cdot\nabla(\rho D)\,. \tag{4.82}$$

The second term represents the contribution due to the variation of $|\nabla Y|$ normal to the iso-surface

$$V^Y_{|\nabla\mathbf{Y}|} = -\frac{1}{|\nabla Y|}D\mathbf{n}\cdot\nabla|\nabla Y|\,. \tag{4.83}$$

Both (4.82) and (4.83) coincide in the normal direction to the iso-surface, thus, the contribution from normal molecular diffusion can be written as

$$V^Y_1 = -\frac{1}{\rho}\mathbf{n}\cdot\nabla(\rho D) - \frac{1}{|\nabla Y|}D\mathbf{n}\cdot\nabla|\nabla Y| = -D\frac{\partial}{\partial x_N}\left[\ln\left(\rho D\frac{\partial Y}{\partial x_N}\right)\right]\,. \tag{4.84}$$

The third term in the right-hand side of (4.81) describes the contribution to the displacement speed due to the spatial curvature of the iso-scalar surfaces:

$$V^Y_2 = -D(\nabla\cdot\mathbf{n}) = -2Dk_m\,, \tag{4.85}$$

for iso-surfaces convex (concave) towards the reactants the contribution of this term is negative (positive) since $\nabla\cdot\mathbf{n} > 0$ ($\nabla\cdot\mathbf{n} < 0$).

Finally, the last term in (4.81) is the contribution due to the chemical reaction:

$$V_3^Y = -\frac{\dot{\omega}_Y}{|\nabla Y|} = -\frac{\dot{\omega}_Y}{(\partial Y/\partial x_N)}\,. \tag{4.86}$$

The normal derivative of (4.81) yields

$$\frac{\partial V^Y}{\partial x_N} = -\frac{\partial}{\partial x_N}\left\{D\frac{\partial}{\partial x_N}\left[\ln\left(\rho D\frac{\partial Y}{\partial x_N}\right)\right]\right\} - 2\frac{\partial\left(Dk_m\right)}{\partial x_N} - \frac{\partial}{\partial x_N}\left[\frac{\dot{\omega}_Y}{(\partial Y/\partial x_N)}\right]\,. \tag{4.87}$$

The three terms on the right side of (4.87), $\left(\partial V^Y/\partial x_N\right)_1$, $\left(\partial V^Y/\partial x_N\right)_2$ and $\left(\partial V^Y/\partial x_N\right)_3$, quantify the contributions of normal and tangential diffusion, and chemistry, respectively. Note that $\partial V^Y/\partial x_N$ has dimensions of the inverse of a time scale, to which normal and tangential diffusion, as well as chemistry contributes.

For flows of constant ρ and D fluids,

$$D\nabla^2 Y = D\mathbf{n}\cdot\nabla|\nabla Y| + D|\nabla Y|\nabla\cdot\mathbf{n}\,. \tag{4.88}$$

Similarly

$$V^Y = -D\frac{\left(\partial^2 Y/\partial x_N^2\right)}{\left(\partial Y/\partial x_N\right)} - 2Dk_m - \left[\frac{\dot{\omega}_Y}{\left(\partial Y/\partial x_N\right)}\right], \tag{4.89}$$

and

$$\frac{\partial V^Y}{\partial x_N} = -\frac{\partial}{\partial x_N}\left[D\frac{\left(\partial^2 Y/\partial x_N^2\right)}{\left(\partial Y/\partial x_N\right)}\right] - 2\frac{\partial\left(Dk_m\right)}{\partial x_N} - \frac{\partial}{\partial x_N}\left[\frac{\dot{\omega}_Y}{\left(\partial Y/\partial x_N\right)}\right]. \tag{4.90}$$

4.4 Turbulent premixed flames

A turbulent premixed flame acts as a propagating frontier between the fresh mixture (fuel and oxidizer mixed at the molecular level) and the burnt gases (combustion products), which modifies both the upstream and downstream flows through aero-thermo-chemical processes. Far upstream of the flame the inlet mean flow and the turbulence structures, as well as the geometry of the scalar fields do not sense the flame presence. As large- and small-scale structures of the velocity and scalar fields approach the flame, mutual effects upon each other become increasingly important. This coupling leads to important modifications in the flame surface area, in the flame speed, in the consumption rate and in the flame thickness.

In order to carry out the numerical simulation of the complex phenomena described above there must be taken into account certain features of the

flame. Starting with the flame thickness, there must be enough points within it to reproduce its inner structure. There are many ways to define thicknesses for premixed flames and one of them is based on the temperature profile:

$$\delta_L^o = \frac{T_b - T_u}{\max(|\frac{\partial T}{\partial x}|)}\,, \tag{4.91}$$

δ_L^o is commonly called 'thermal thickness'. The subscripts u and b in (4.91) indicate variables in the unburned and the burnt gases, respectively. Usually this flame thickness is obtained after the computation of $\max(|\frac{\partial T}{\partial x}|)$. Thus, to calculate δ_L^o requires a first flame computation.

Assuming an analytical solution for the laminar flame speed, S_L, such as the Zeldovich/Frank-Kamenetshi and von Karman (ZFK) [74, 77], and considering also the fresh gases properties and the scaling laws [76], we can obtain the called 'diffusive thickness':

$$\delta = \frac{\lambda_u}{\rho_u C_p S_L} = \frac{D_{th_u}}{S_L}\,, \tag{4.92}$$

where the quantities $D_{th_u} = \lambda_u/(\rho_u C_p)$, ρ_u, C_p and λ_u are evaluated in the fresh gases. In this way, once S_L is known, δ may be evaluated before any computation.

It can be noted that the laminar flame speed, S_L, is other important feature in premixed flames. One of the ways to get S_L is integrating from $-\infty$ to $+\infty$ Eq. (4.10) for any species α in the reference frame of a premixed flame:

$$S_L = -\frac{1}{\rho_u(Y_{\alpha_u} - Y_{\alpha_b})} \int_{-\infty}^{+\infty} \dot{\omega}_\alpha \, dx \,, \tag{4.93}$$

where Y_{α_u} and Y_{α_b} are the values of Y_α at $x = -\infty$ and $+\infty$, respectively. This speed corresponds to a description of the flame as an interface moving at speed S_L against the local flow.

Using the flame thickness and the laminar flame speed we define a typical flame time scale τ_{ch}:

$$\tau_{ch} = \frac{\delta}{S_L} \,. \tag{4.94}$$

τ_{ch} is the time needed for the flame to move on a distance corresponding to its own thickness.

4.4.1 Combustion regimes

Combustion regimes are essential to the selection and development of the adequate combustion model for a given situation [76, 78, 79, 80]. The Damköhler number of the large scale and the Karlovitz number classify

the premixed turbulent combustion in regimes.

The Damköhler number can be written as:

$$Da = \frac{\tau_l}{\tau_c} = \frac{l}{\delta}\frac{S_L}{u'}\,, \tag{4.95}$$

and the Karlovitz number as:

$$Ka = \frac{\tau_c}{\tau_\eta} = \left(\frac{l}{\delta}\right)^{-1/2}\left(\frac{u'}{S_L}\right)^{3/2}\,, \tag{4.96}$$

where τ_l is the characteristic integral time scale and τ_η is the turbulent time associated to the Kolmogorov scales.

The turbulent premixed flames regimes are classified as follows:

- *Flamelet regime*, ($Ka < 1$ and $Da >> 1$): For low (large) values of the Karlovitz (Damköhler) number, chemical times are shorter than the Kolmogorov time and the integral turbulence time ($\tau_{ch} < \tau_\eta$ and $\tau_{ch} < \tau_l$). Hence, the flame is wrinkled by turbulence motions and the turbulence is not able to affect the inner flame structure. In this regime there are two subdivisions, depending on the velocity ratio u'/S_L:

  - *Wrinkled flamelet regime*, ($u' < S_L$): In this situation, the turbulence wrinkles the flame but it is not able to induce flame front

interactions.

- *Corrugated flamelet regime*, ($u' > S_L$): In this case, the turbulence wrinkles the flame and induces flame front interactions which creates pockets with fresh and burnt gases.

- *Thickened-wrinkled flame regime*, ($1 < Ka \leq 100$): In this regime, the smallest turbulence scales have a Kolmogorov time τ_η shorter than τ_{ch} but τ_{ch}, in turn, is larger than τ_l. Thus, the turbulent motions are able to affect and thicken the preheat zone of the flame, but cannot modify the reaction zone which remains thin and close to a laminar reaction zone.

- *Well-stirred reactor*, ($Ka > 100$ and $Da << 1$): In this situation, there is no laminar flame structure. Chemical time is larger than integral turbulent time and the preheat and reaction zones are strongly affected by turbulent motions.

Figure 4.5 shows a classical turbulent combustion diagram where all premixed turbulent combustion regimes have been represented in terms of length (l/δ) and velocity (u'/S_L) ratios.

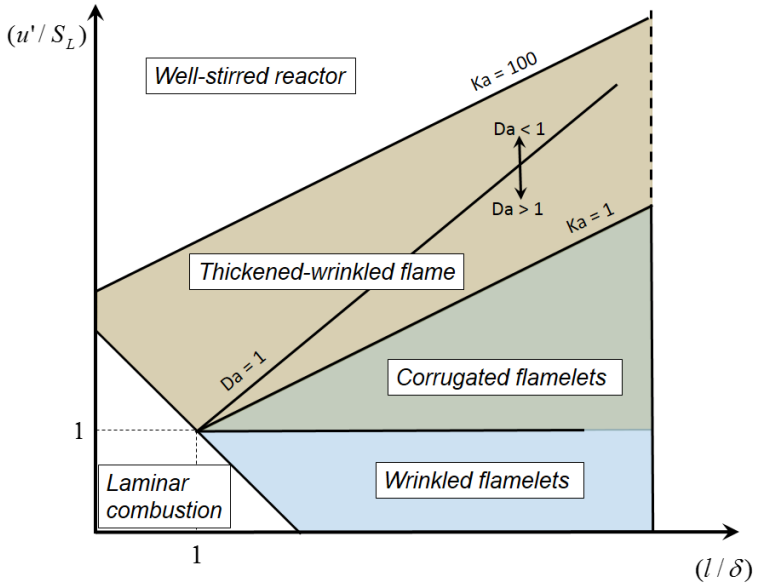

Figure 4.5: Classical turbulent combustion diagram. Combustion regimes are identified in terms of length (l/δ) and velocity (u'/S_L) ratios [76].

4.4.2 Description of chemistry

Premixed reacting flows have been investigated generally using simple one-step chemistry schemes or, at most, applying strategies to reduce kinetics by developing skeletal mechanisms and by manifold generation. All chemical models used in combustion share the same description of elementary chemical reactions, based on an Arrhenius law [74, 81, 82].

Consider a complete chemical system composed of N_s species reacting through N_r reversible elementary equations. Each elementary reaction can be written in the form:

$$\sum_{\alpha=1}^{N_s} \nu'_{\alpha j} \mathcal{M}_\alpha \rightleftharpoons \sum_{\alpha=1}^{N_s} \nu''_{\alpha j} \mathcal{M}_\alpha \quad (j = 1 \ldots N_r) \tag{4.97}$$

where $\nu'_{\alpha j}$ and $\nu''_{\alpha j}$ are the molar stoichiometric coefficients of species α in reaction j, and $\mathcal{M}_\alpha$ is a symbol for species α. Mass conservation implies:

$$\sum_{\alpha=1}^{N_s} \nu'_{\alpha j} W_\alpha = \sum_{\alpha=1}^{N_s} \nu''_{\alpha j} W_\alpha \,, \tag{4.98}$$

where W_α is the molecular weight of species α. Eq. (4.98) can also be written:

$$\sum_{\alpha=1}^{N_s} \nu_{\alpha j} W_\alpha = 0 \quad (j = 1 \ldots N_r) \tag{4.99}$$

with:

$$\nu_{\alpha j} = \nu''_{\alpha j} - \nu'_{\alpha j} \,. \tag{4.100}$$

Moreover, the stoichiometric coefficients also satisfy linear relations associated with the conservation of all individual chemical elements. The progress rate w_j of the jth reaction is defined as:

$$w_j = K_{fj} \prod_{\alpha=1}^{N_s} C_\alpha^{\nu'_{\alpha j}} - K_{bj} \prod_{\alpha=1}^{N_s} C_\alpha^{\nu''_{\alpha j}} \,, \tag{4.101}$$

where $C_\alpha = \rho Y_\alpha / W_\alpha$ denotes the molar concentration of the species α and the forward and backward constants K_{fj}, K_{bj} of the reaction j are expressed in the form:

$$K_{fj} = A_{fj} T^{\beta j} exp\left(\frac{E_{a,j}}{RT}\right) = A_{fj} T^{\beta j} exp\left(\frac{T_{a,j}}{T}\right) , \tag{4.102}$$

$$K_{bj} = \frac{K_{fj}}{\left(\frac{p_a}{RT}\right)^{\sum_{\alpha=1}^{N_s} \nu_{\alpha j}} exp\left(\frac{\Delta S_j^0}{R} - \frac{\Delta H_j^0}{RT}\right)} , \tag{4.103}$$

where A_f is the pre-exponential factor, T the temperature, β_j the temperature exponent, E_a the activation energy, R the universal gas constant, T_a the activation temperature, $p_a = 1$ bar, and ΔS_j^0 and ΔH_j^0 correspond, respectively, to entropy and enthalpy changes during the transition from reactants to products for the jth reaction. These quantities are obtained from tabulations based on experimental measurements. The mass reaction rate of species α is the sum of all contributions from the elementary reactions:

$$\dot{\omega}_\alpha = W_\alpha \sum_{\alpha=1}^{N_r} \nu_{\alpha j} w_j \, . \tag{4.104}$$

The fact that chemical reactions conserve the total mass is expressed by:

$$\sum_{\alpha=1}^{N_s} \dot{\omega}_\alpha = 0\,. \tag{4.105}$$

In this formulation, reactions are listed using a prescribed format, along with the values for A_j (in CGS units), β_j and $E_{a,j}$ (in cal/mol).

As an indication, the use of a complete kinetic scheme to describe the chemistry requires about eight species and 40 irreversible elementary reactions for hydrogen/oxygen combustion, typically around 50 species and a few hundred chemical reactions for methane, while more complex fuels like n-decane or cetane require several hundred species and several thousands of elementary reactions. Due to this high complexity, many works have been based on a simplified treatment of chemistry which permits simple analytical solutions.

One of them can be obtained assuming that the backward reaction rate $K_{b1} = 0$, for one irreversible reaction $N_r = 1$ in Eq. (4.97), and the forward reaction K_{f1} as follows:

$$K_{f1} = A_1 T^{\beta_1} exp\left(-\frac{E_{a1}}{RT}\right)\,, \tag{4.106}$$

the reaction rate can be written as (using (4.101) and (4.104)):

$$\dot{\omega}_F = B_1 T^{\beta_1} \rho Y_F exp\left(-\frac{E_{a1}}{RT}\right) = B_1 T^{\beta_1} \rho Y_F exp\left(-\frac{T_{a1}}{T}\right) , \qquad (4.107)$$

where

$$B_1 = A_1 \nu_{F1} . \qquad (4.108)$$

Eq. (4.107) gives a solution of $\dot{\omega}_\alpha$ by a single-step reaction.

Generally, the reaction rate is expressed in a more convenient form [74, 76]:

$$\dot{\omega} = B_1 T^{\beta_1} exp\left(\frac{-\beta}{\alpha}\right) \rho Y_F exp\left[-\frac{\beta Y_F}{(1-\alpha Y_F)}\right] , \qquad (4.109)$$

where $exp\left(\frac{-T_a}{T}\right)$ in Eq. (4.107) has been replaced by $exp\left(\frac{-\beta}{\alpha}\right) exp\left[-\frac{\beta Y_F}{(1-\alpha Y_F)}\right]$, and the values of α and β defined as,

$$\alpha = (T_b - T_u)/T_b , \quad \beta = \alpha E_a / R T_b , \qquad (4.110)$$

are parameters that measure the heat released by the flame and the activation temperature respectively.

The simplifications to a single-step reaction for reacting variable- and

constant-density flows often show unacceptable limitations for the prediction of pollutant emissions or of stability limits, which are probably the most important topics at present time in combustion research. But these models preserve features such as intense non-linear heat release, variable temperature, among other things, which are very important for theoretical studies.

Simulations of turbulent flames rely on complete reaction mechanisms, for instance complete hydrogen reaction schemes [83], often become cumbersome, and as a consequence new approaches have been derived. One of the approaches is the Intrinsic Low Dimensional Manifold (ILDM) approach proposed by Maas and Pope [84, 85]. ILDM approach tries to project the whole system with N + 2 degrees of freedom (N species, enthalpy and pressure) onto a lower dimensional system. An eigenvalue analysis of the species evolution helps to identify the fast and slow evolving species. Based on this eigensystem analysis, a small subset of variables is identified, which evolves slowly during combustion. These variables are then used to generate pre-computed look-up tables to be used during simulations for evaluating chemical kinetics. However this method has been shown to fail in regions of flow where diffusion processes are as important as chemical processes, and it generally does not produce good results in low temperature regions of flames since fast time scales have been neglected. An

improvement in the ILDM approach for the low temperature regions is the Flame-prolongation of ILDM (FPI) [86]. The basic idea is to generate look-up tables from simulations of one-dimensional laminar premixed flames using complex chemical schemes. A controlling parameter (for example, the sum of carbon monoxide and dioxide mass fraction $Y_{CO} + Y_{CO_2}$ for hydrocarbon combustion) is used to define the mapping between the tabulated solutions and local solutions within a combustion simulation. The FPI approach has been extended to diffusion flames by Vervisch *et al.* [87] and for non-adiabatic flames by Fiorina *et al.* [88].

5

Constant-density mixing and reaction

The physical systems simulated in this case are a collection of incompress-

ible, homogeneous and isotropic turbulent fields [i], which are started from a given spectrum, using a stochastic forcing scheme, to yield statistically stationary fields. Boundary conditions are periodic which means that the integrated volume is repeated up to infinity and the perturbations due to the boundary conditions are minima inside the simulation domain. Two scalars with identical initial statistical distributions, one inert and the other obeying a prescribed Arrhenius-like chemical reaction, evolve in homogeneous isotropic turbulence. Results have been analyzed when the scalar fields have a mean close to 0.7 and a variance close to 0.14 for the inert scalar cases, whereas for the reactive scalar cases the mean and the variance are close to 0.15 and 0.25, respectively.

5.1 Spectrum of the Scalar Field

The Kolmogorov scale, η, is the smallest velocity length scale in the flow. Below this scale, viscosity effectively damps out inhomogeneities in the flow. Analogously, there is a smallest scalar length scale which can be larger, smaller, or of the same scale as the Kolmogorov scale, depending on the relative magnitude of the kinematic viscosity of molecular diffusivity. This is parametrized by the Schmidt number, $Sc = \nu/D$. For a given flow

[i] The fluctuating quantities in this approach are considered as random functions, which are assumed to be statistically invariant under translations (homogeneity) and rotations (isotropy).

configuration the Kolmogorov scale will depend on the viscosity, ν. Similarly, the smallest scalar length scale will be determined by the molecular diffusivity, D.

First consider the case where $Sc > 1$ ($\nu > D$). The region over which we are applying the scale analysis is the smallest scalar length and is termed the Batchelor scale, l_B. In this region, the scalar field is subject to the complete range of strain-rate fluctuations since the Batchelor scale will be smaller than the Kolmogorov scale ($l_B < \eta$). In the inertial subrange, the velocity and scalar spectrum will behave similarity. Beyond the Kolmogorov wavenumber cut-off, velocity fluctuations vanish. Scalar fluctuations beyond this range will be reduced by the strain field, which below the Kolmogorov scale is $(\varepsilon/\nu)^{1/2}$. This reduction occurs until the Batchelor scale is reached. This region of wavenumbers for $\kappa_\eta < \kappa < \kappa_{l_B}$ is termed the 'viscous-convective subrange'. For wavenumbers $\kappa > \kappa_{l_B}$, the scalar fluctuation are effectively damped by molecular diffusion. In this region the scalar fluctuations are rapidly dissipated. This is called the 'viscous-diffusive subrange'.

Now for small $Sc < 1$, the scalar length scale is termed the Obukov-Corsin scale, l_C. The Obukov-Corsin scale will be greater than the Kolmogorov scale and may extend into the inertial subrange ($l_C > \eta$ or $\kappa_{l_C} < \kappa_\eta$). In this case, the diffusive cut-off for the scalar field will appear in the inertial

subrange. This subrange is referred to as the 'inertial-diffusive subrange'. Under this condition, the only parameters describing the scalar field will be the dissipation and the molecular diffusivity.

All of these features will be analyzed in this chapter using different Schmidt numbers ($Sc = 0.5$, $Sc = 1.0$, $Sc = 1.5$), in order to visualize and to obtain new information of the small-scale structures of the scalar field.

5.2 Numerical implementation

The numerical algorithms used to simulate the governing equations are a pseudo-spectral numerical code [89, 90] to advance in the spatial domain, and a second-order Runge-Kutta numerical scheme [91] to advance in time. A brief overview of these numerical methods is presented in this section.

Spatial integration

Let us consider a particular turbulent flow within a cubic box of size L, which contains all the spatial features of the flow. It is also assumed that the boundary conditions on the limits of the box are periodic. Once the periodic flow within the box is constructed, we fill the whole space with an infinite number of identical boxes, so that one obtains a periodic flow of wave-length L in the three directions of space. Thus, this flow within the

box is a periodic flow whose features for scales smaller than L are close to the features of the real flow.

Let $\vec{u}(\vec{x})$ be the periodic velocity field, (e.g. a velocity field at a given time). Since it is periodic of period L, it can be expanded as an infinite series:

$$\vec{u}(\vec{x}) = \sum_{n_1,n_2,n_3=-\infty}^{+\infty} e^{(i2\pi/L)(n_1x_1+n_2x_2+n_3x_3)}\widehat{\underline{u}}(n_1,n_2,n_3)\,, \tag{5.1}$$

where $\widehat{\underline{u}}(n_1,n_2,n_3)$ is known as the discrete Fourier transform of the function $\vec{u}(\vec{x})$, i is the imaginary unit $i=\sqrt{-1}$, $2\pi/L=\kappa_o$ is the lowest wavenumber, and n_1 n_2 n_3 are positive or negative integers. Introducing the wavenumber vector $\vec{\kappa}$ of components:

$$\vec{\kappa} = \kappa_o\vec{n} = \left[\frac{2\pi}{L}n_1, \frac{2\pi}{L}n_2, \frac{2\pi}{L}n_3\right]\,, \tag{5.2}$$

Eq. (5.1) can be written as:

$$\vec{u}(\vec{x}) = \sum_{\vec{\kappa}} e^{i\vec{\kappa}\cdot\vec{x}}\widehat{\underline{u}}(\vec{\kappa})\,, \tag{5.3}$$

where the sum is over the infinite number of discrete $\vec{\kappa} = \kappa_o \vec{n}$.

Thus, the derivative respect to space is:

$$\frac{\partial \vec{u}(\vec{x})}{\partial x_n} = \sum_{\vec{\kappa}} i\kappa_n e^{i\vec{\kappa}\cdot\vec{x}} \underline{\widehat{u}}(\vec{\kappa}) \,. \tag{5.4}$$

Using the notation $\left(\widehat{\frac{\partial \underline{u}}{\partial x_n}}\right)$ to indicate the Fourier transform of $\frac{\partial \vec{u}}{\partial x_n}$, yields:

$$\frac{\partial \vec{u}(\vec{x})}{\partial x_n} = \sum_{\vec{\kappa}} e^{i\vec{\kappa}\cdot\vec{x}} \left(\widehat{\frac{\partial \underline{u}}{\partial x_n}}\right) . \tag{5.5}$$

It can be seen that,

$$\left(\widehat{\frac{\partial \underline{u}}{\partial x_n}}\right) = i\kappa_n \widehat{f}(\vec{\kappa}) \,. \tag{5.6}$$

For the evolution of Fourier modes, the Navier-Stokes equations (4.30) and (4.31) are transformed to the wavenumber space or Fourier space using the Fast Fourier Transform (FFT) [92, 93]:

$$\frac{\partial \widehat{u}_i}{\partial t} = -i\kappa_j(\widehat{u_j u_i}) - \frac{i\kappa_i}{\kappa_j\kappa_j}\left(\widehat{\frac{\partial u_l}{\partial x_m}\frac{\partial u_m}{\partial x_l}}\right) - \nu\kappa_j\kappa_j\widehat{u}_i\,, \tag{5.7}$$

$$\frac{\partial \widehat{Y}}{\partial t} = -i\kappa_j(\widehat{u_j Y}) - D\kappa_j\kappa_j\widehat{Y} + \widehat{\dot{\omega}_Y}\,, \tag{5.8}$$

where in (5.7) is used the Fourier transform of Eq. (4.32) to solve the pressure. Y in Eq. (5.8) stands for the mass fraction of reactants, varying from 1 in the pure reactive mixture to 0 in the fully reacted products.

By definition, the turbulent kinetic energy k can be found directly from the turbulent energy spectrum by integrating over wavenumber space (see Figure 3.1):

$$k = \int_0^\infty E(\kappa)\mathrm{d}\kappa\,. \tag{5.9}$$

Thus, $E(\kappa)\mathrm{d}\kappa$ represents the amount of turbulent kinetic energy located between the wavenumbers κ and $\kappa + \mathrm{d}\kappa$.

For homogeneous isotropic turbulence, the turbulent energy dissipation rate, ε, and the integral length scale, l, are related to $E(\kappa)$ by [94]:

$$\varepsilon = 2\nu \int_0^\infty \kappa^2 E(\kappa) \mathrm{d}\kappa \,, \tag{5.10}$$

$$l = \frac{3\pi}{4k} \int_0^\infty \frac{E(\kappa)}{\kappa} \mathrm{d}\kappa \,. \tag{5.11}$$

There is another length scale widely used called the Taylor micro-scale, λ, and is defined by:

$$\lambda^2/\nu = 10k/\varepsilon \,. \tag{5.12}$$

It is important to note that at high Reynolds number λ lies at scales between l and η. Although the Taylor micro-scale does not have much physical meaning, λ has an important place in the study of homogeneous isotropic turbulent flow due to the fact that many characterizations of turbulent flows are based on this length scale.

The Taylor micro-scale is often used to define the Taylor-scale Reynolds number:

$$Re_\lambda \equiv \left(\frac{2k}{3}\right)^{1/2} \frac{\lambda}{\nu}\,. \tag{5.13}$$

Re_λ is traditionally used to characterize grid turbulence.

Time integration

A second-order Runge-Kutta numerical scheme [91] is used to provide time-marching from the nth time step to $(n+1)$th time step. This numerical method provide a good compromise between accuracy, stability, and computational efficiency. In order to illustrate the numerical method, we are going to consider a general governing equation given by:

$$U_t = R(U)\,, \tag{5.14}$$

where R represents a functional containing all spatial derivatives terms such as the one given on the right-hand side of Eq. (4.30). Let U^n denotes the numerical approximation of U at $t_n = n\Delta t$, where $t_0 = 0$ is the initial time. To obtain the solution U^{n+1} is necessary to build a series of 'stages' or 'sub-steps' that approximates the solution at various points using samples of $R(U)$ from the series of early stages. The numerical solution U^{n+1} is

constructed from a combination of U^n and all the approximations found at the precomputed stages. The second-order Runge-Kutta numerical scheme is as follows:

$$\begin{aligned} U^{(0)} &= U^{(n)}\,, \\ U^{(1)} &= U^{(n)} + \Delta t b_0 R(U^{(0)})\,, \\ U^{(2)} &= U^{(n)} + \Delta t b_1 R(U^{(1)})\,, \end{aligned} \tag{5.15}$$

where the coefficients are $b_0 = 1/2$, and $b_1 = 1$, respectively.

With the advance in time, it is necessary that a fluid particle move only a fraction of the grid spacing Δx in a time step Δt. To satisfy this requirement, the time step Δt is limited by the Courant number (C_o) defined by [95]:

$$C_o = \frac{\max\{|u_1|, |u_2|, |u_3|\}}{\Delta x/\Delta t}\,. \tag{5.16}$$

For most cases studied ([64, 95, 96] and others) to date $C_o \leq 0.3$ appeared to be sufficient to provide numerical stability. In the computation of Δt the Courant criterion limit becomes important. However, this time step is

also limited by the chemical reaction rate.

Reaction rate

The reaction term obeys a single step Arrhenius-type chemical reaction (*cf.* Eq. (4.109)):

$$\dot{\omega}_Y = -KY exp\left[-\frac{\beta Y}{(1-\alpha Y)}\right] . \tag{5.17}$$

This expresion has been used by Dopazo and co-workers [64] in order to numerically mimic the chemical term for a premixed system. In this case, $K = 30$ represents the factors: $B_1 T^{\beta_1} e^{-\beta/\alpha}$ of Eq. (4.109), $\rho_u = 1$, and the parameters that measure the heat released and the activation temperature, respectively, are: $\alpha = 0.7$ and $\beta = 4.5$.

5.3 Simulation parameters

As mentioned previously, three Direct Numerical Simulations have been performed with Schmidt numbers: $Sc = 0.5$, $Sc = 1.0$, and $Sc = 1.5$. All the simulations were carried out using the OpenMP (Open Multi-Processing) parallelized implementation [97, 98]. The computational do-

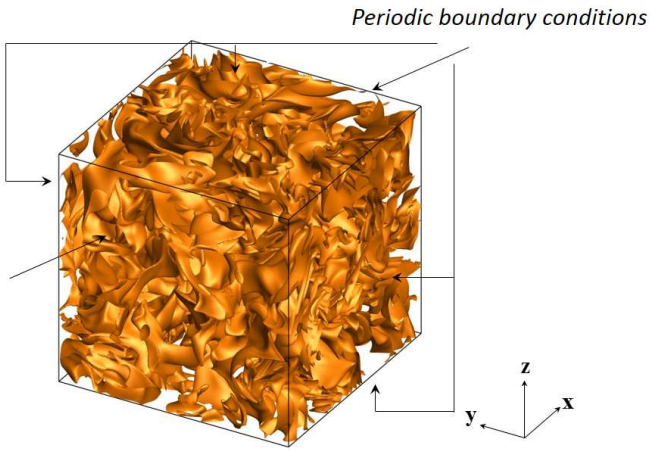

Figure 5.1: Computational domain showing the iso-scalar surface $Y = 0.5$ (Reactive scalar case, $Sc = 1.0$).

main, shown in Figure 5.1, contains 512 x 512 x 512 grid points uniformly distributed in the x, y and z directions. The length of each edge of this cube is 2π. In order to reduce the aliasing, a spherical filter is applied to the data in Fourier space: all nodes corresponding to a wave number larger than 512×0.471 are set to zero. This filter is chosen [89] in order to suppress the double and triple aliasing contribution [90] caused by convective terms. Due to the incompressibility condition the scalar fields do not affect the velocity field and evolve without forcing from an almost completely unmixed initial condition. Velocity fields undergo a random forcing producing statistically stationary flows without mean gradients. The forcing scheme is that of Eswaran and Pope [99, 100] with a zero correlation time of the forcing; all wave numbers with a modulus less than $2\sqrt{2}$, except the

zero mode which makes no contribution, receive a stochastic contribution at every time step, while their phase is adjusted to enforce incompressibility. On the other hand, the intensity of forcing takes values such that the integral length scale, l, is approximately the unit. Therefore, l is less than one-third of the length of each edge of the computational box, which guarantees the homogeneity of the resulting flow.

Velocity fields are characterized by the Taylor-scale Reynolds number ($Re_\lambda = 65$), the integral length scale ($l = 0.91$), the kinematic viscosity ($\nu = 0.0095$), the Taylor micro-scale ($\lambda = 0.408$), the Kolmogorov micro-scale ($\eta = 0.0257$), the total kinetic energy ($k = 3.42$), the kinetic energy dissipation rate ($\varepsilon = 1.951$), the root mean square velocity ($u' = 1.51$) and the maximum wave number times the Kolmogorov micro-scale ($\kappa_{max}\eta = 6.19$). Numerical values of the characteristic parameters of the simulations are presented in Table 5.1.

Description	Value
DNS grid points	512x512x512
Turbulent kinetic energy, k	3.42
Turbulent kinetic energy dissipation rate, ε	1.951
Kinematic viscosity, ν	0.0095
Integral length scale, l	0.91
rms of velocity fluctuations, u'	1.51
Kolmogorov micro-scale, η	0.0257
Integral eddy turnover time, τ_l	0.6
Kolmogorov time scale, τ_η	0.069
Taylor micro-scale, λ	0.408
Taylor-scale Reynolds number, Re_λ	65

Table 5.1: Characteristic parameters of the studied DNS fields.

5.4 Results and discussion

As mentioned previously, two scalars with identical initial distribution, one inert and the other obeying a prescribed Arrhenius-like chemical reaction, evolve in incompressible homogeneous isotropic turbulence. The probability density functions (pdf's) of the scalar mass fraction, Y, are shown in Figure 5.2 at the initial, t_i, and final, t_f, times. Initially, the scalar distribution displays two peaks near the extreme values 0 and 1, reminiscent of the starting partial segregation. For the inert scalar cases, the mixing process progresses from a partially mixed situation to the initiation of a well-mixed system, tending the pdf's asymptotically to a Gaussian distribution. In the final step of the reactive scalar cases, a large portion of the mass fraction has been consumed, so there is a final peak in the pdf's towards the value $Y = 0$. Results have been analyzed at t_f, where the scalar fields have a mean close to 0.7 and a variance close to 0.14 for the inert scalar cases, whereas for the reactive scalar cases the mean and the variance are close to 0.15 and 0.25, respectively. These values have been chosen taken into account that for the inert scalar cases the concentration must be as close as possible to diffuse the difference between solute and solvent, whereas in the reactive scalar cases the scalar value must be minimum but not zero so that the reaction rate does not disappear.

The evolution of the reaction rate, for the cases with chemical reaction, is given by Eq. (5.17). Figure 5.3 shows the reaction rate, $\dot{\omega}_Y$, as a function of the scalar value for the case $Sc = 1.0$. The reaction rate is always negative, which indicates a consumption of Y, as expected, and varies from one Y iso-surface to another across the mass fraction, reaching a maximum value when the scalar is close to the $Y = 0.18$.

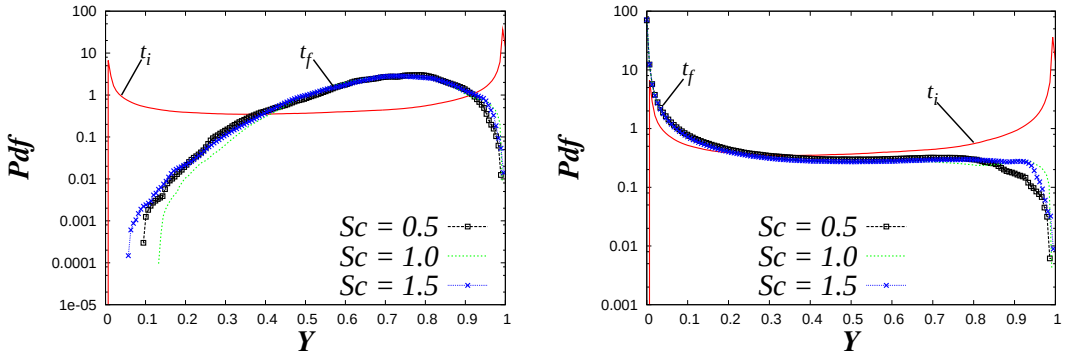

(a) Inert scalar cases. (b) Reactive scalar cases.

Figure 5.2: Pdf's of the mass fraction, Y, at different times and different Schmidt numbers.

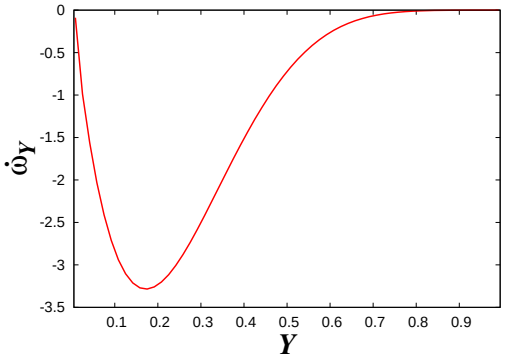

Figure 5.3: Reaction rate, $\dot{\omega}_Y$, conditional upon the scalar value.

5.4.1 Structure of the scalar field in terms of the Mean and Gauss curvatures

It can be seen in Figure 5.1 that the geometric structure of the iso-scalar surfaces are complicated. These structures can be classified though the local mean and Gauss curvatures, k_m and k_g, at every point of the iso-scalar surfaces.

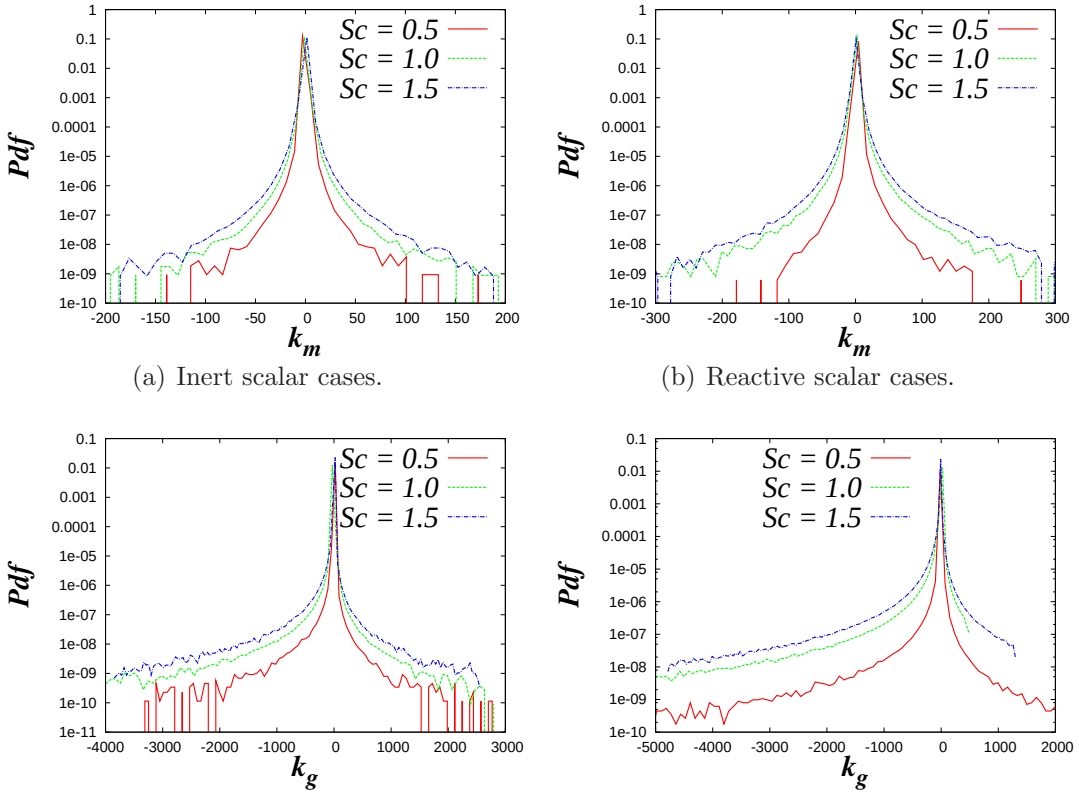

(a) Inert scalar cases. (b) Reactive scalar cases.

(c) Inert scalar cases. (d) Reactive scalar cases.

Figure 5.4: Pdf's of the mean and Gauss curvatures. (a), (b) k_m, and (a), (b) k_g.

Figure 5.4 shows the pdf's of the mean and Gauss curvatures for all the cases under study. k_m and k_g have been normalized with the mean of their

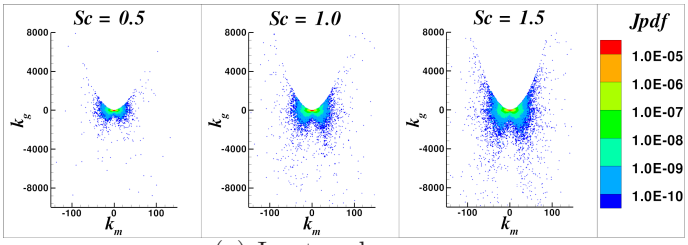

(a) Inert scalar cases.

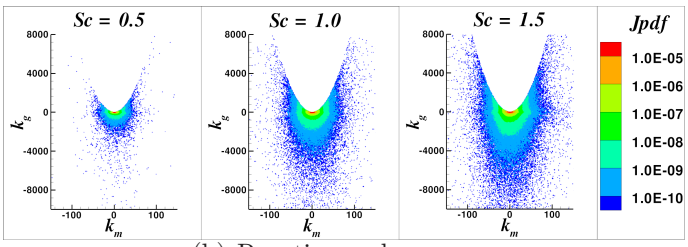

(b) Reactive scalar cases.

Figure 5.5: Joint pdf's of the mean and Gauss curvatures, k_m and k_g.

respective root-mean-square values, using all the samples of the inert cases and the reactive ones. A significant correlation between curvatures and Schmidt number is apparent. The curvature values grow with increasing Schmidt numbers. This is in connection with the dependence on the scalar length scale, as with increasing Schmidt numbers the smallest scalar length are obtained ($l_B < \eta$), thus, consequently, the curvature values increase. The statistical distributions for the mean curvatures in the inert scalar cases are approximately symmetric, with convex and concave iso-surfaces equally probable, whereas in the reactive scalar cases pdf's are skewed towards positive values of k_m. Referring to Gauss curvature, the probabilities are displaced towards negative values, which indicates that the saddle points are dominant over convex or concave ones. Values close to zero,

denoting flat or tile-like surfaces, are the most probable in all cases under study; these latter findings are in agreement with experimental results [60] and three-dimensional DNS calculations [63, 101] of premixed turbulent flames.

To obtain additional information about the shape of scalar geometry Figure 5.5 displays the joint pdf's of k_m and k_g for constant-density mixing and reaction. The resulting distributions are more widespread with increasing Schmidt numbers. The jpdf's in the inert scalar cases seem to be symmetric with respect to the k_g axis, whereas in the reactive scalar cases are slightly skewed towards the positive values of k_m. The statistical distribution in all cases display maxima values for nearly flat iso-scalar surfaces, in connection with the results in Figure 5.4. All samples are below the parabola $k_g = k_m^2$, separatrix of the prohibited region corresponding to complex curvatures (see Figure 4.3). Iso-contours present long tails on both sides of the limit curve $k_g = k_m^2$, and surround the origin spreading over increasing areas as the curvature magnitude increases. Furthermore, the distributions are skewed towards negative values of k_g, which indicates yet again that the saddle points are dominant over convex or concave ones. It is observed that the curvature values are larger in the reactive scalar cases than in the inert ones. This might be explained by the reactive-diffusive processes, as can increase or decrease the displacement speed of

the iso-scalar surfaces, which might, indirectly, fold the iso-surfaces creating larger curvature values compared to those produced in the inert scalar cases.

5.4.2 Non-material surface propagation velocity

For constant-density mixing the displacement speed, V^Y, of the iso-scalar surfaces depends on the molecular diffusion processes, whereas in the reaction cases is a balance between reactive-diffusive processes. Thus, to evaluate V^Y it is important to check the behavior of the molecular diffusion rate.

Figure 5.6 shows the molecular diffusion rate, $D\nabla^2 Y$, and its normal and curvature contributions (see Eq.(4.88)) conditional upon the mass fraction, Y. The molecular diffusion rate and its contributions have been normalized with the mean of the rms values of $D\nabla^2 Y$, using all the samples of the inert cases and the reactive ones. It can be noted that in each case (inert and reactive) the behavior of the conditional means seems to be the same. Varying from one iso-surface to another across the mass fraction, $D\nabla^2 Y$ is much greater in the reactive scalar cases than those of the inert ones. In the inert (reactive) scalar cases, there are positive molecular diffusion rates for $Y < 0.7$ ($Y < 0.3$) and negative for $Y > 0.7$ ($Y > 0.3$). Regardless of the Schmidt number, $D\nabla^2 Y$ attains a maximum value close

to the $Y \approx 0.25$ value, and a minimum value about $Y \approx 0.9$, in the inert scalar cases; whereas the maxima and minima values of $D\nabla^2 Y$, in the reactive scalar cases, are close to the $Y \approx 0.12$ and $Y \approx 0.55$ values, respectively. The contributions to the molecular diffusion rates due to the curvature, $MD_{curv}(= D|\nabla Y|\nabla \cdot \mathbf{n})$, seem to have a negative correlation with the mass fraction Y in the constant-density mixing cases, whereas in the reactive scalar cases do not; negative (positive) values of MD_{curv} increase in the (opposite) direction of the scalar gradient for $Y \approx 0.75$ in the inert scalar cases. The most important contribution to the molecular diffusion rates comes from $MD_{|\nabla Y|}(= D\mathbf{n} \cdot \nabla|\nabla Y|)$, which is the variation of $|\nabla Y|$ normal to the iso-surface. $D\nabla^2 Y$ displays an almost identical variation to that $MD_{|\nabla Y|}$ for all cases under study. As the reaction rate does not depend on the Schmidt number, and $D\nabla^2 Y$ seems to have the same behavior to different Schmidt numbers, hereafter, the results will be only analyzed for $Sc = 1.0$.

Figure 5.7 presents the propagation velocity V^Y of iso-scalar surfaces, given by equation (4.89), conditional upon the mass fraction Y. The separate contributions of the normal and tangential (due to iso-surface curvature) molecular diffusion rates are also presented, as well as the chemical source term in the reactive scalar case. The displacement speed and its contributions have been normalized with the mean of the rms values of V^Y, using

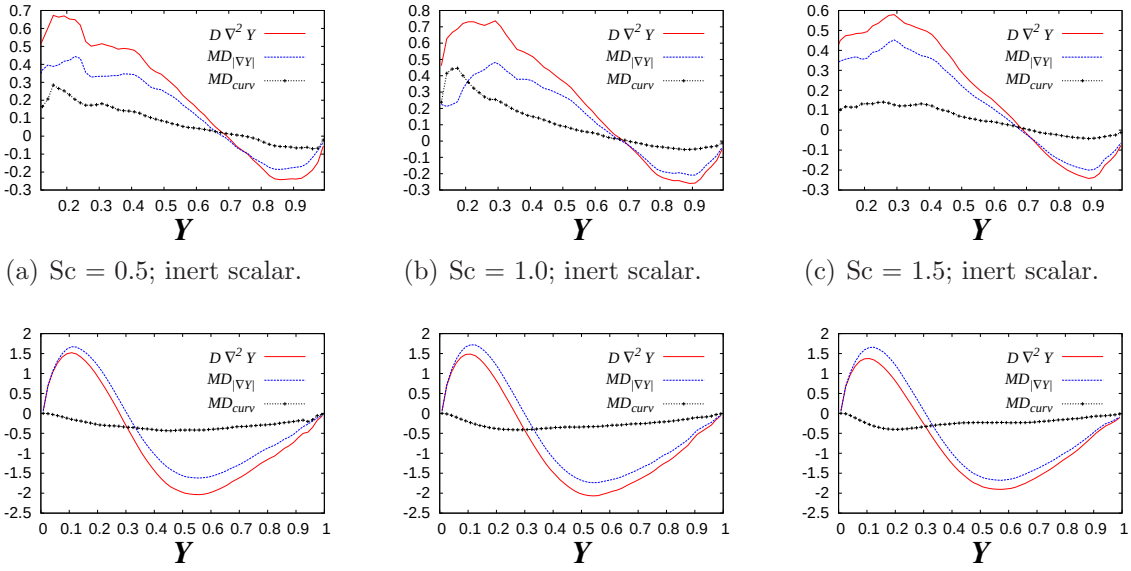

(a) Sc = 0.5; inert scalar. (b) Sc = 1.0; inert scalar. (c) Sc = 1.5; inert scalar.

(d) Sc = 0.5; reactive scalar. (e) Sc = 1.0; reactive scalar. (f) Sc = 1.5; reactive scalar.

Figure 5.6: Molecular diffusion rate, $D\nabla^2 Y$, and its contributions [Eq.(4.88)] conditional upon the mass fraction, Y.

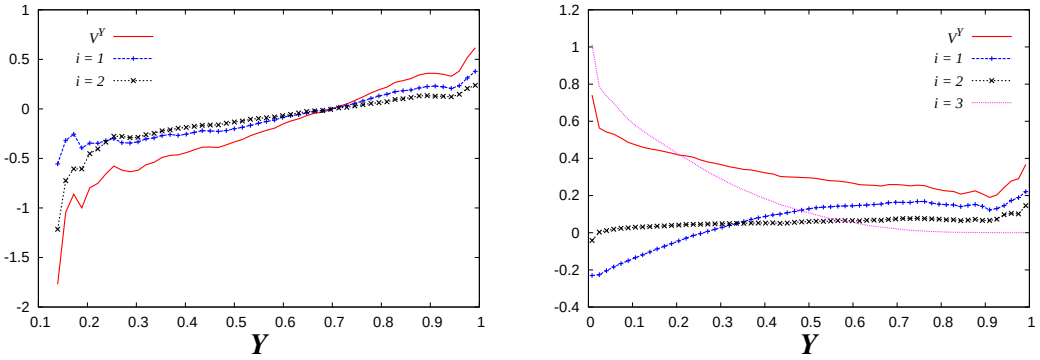

(a) Inert scalar case; $Sc = 1.0$. (b) Reactive scalar case; $Sc = 1.0$.

Figure 5.7: Iso-scalar surface normal propagation speed, V^Y, relative to the fluid and its contributions as a function of the reactant mass fraction. Hereafter, the results will be only analyzed for $Sc = 1.0$.

the inert and reactive scalar fields. For the inert scalar, it is important to note that the iso-surfaces propagate in the opposite direction of the scalar gradient when $Y < 0.7$ and in the same direction when $Y > 0.7$; V^Y dis-

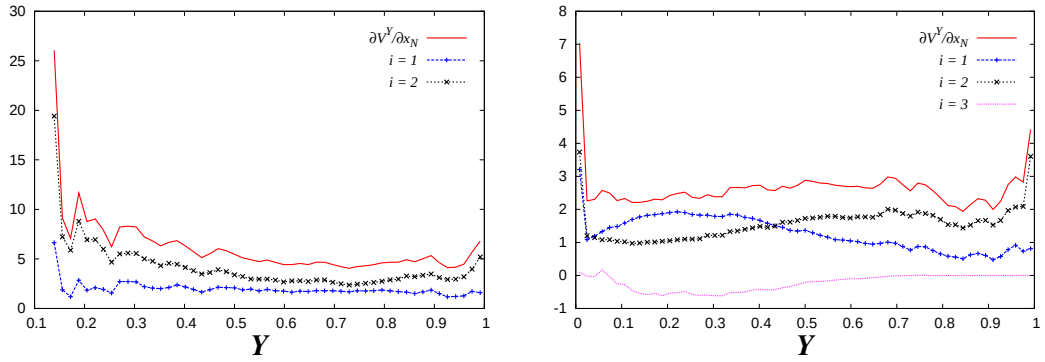

(a) Inert scalar case. (b) Reactive scalar case.

Figure 5.8: Derivative of V^Y in the direction normal to iso-scalar surfaces, x_N, and contributions to $\partial V^Y/\partial x_N$ due to normal diffusion, $(\partial V^Y/\partial x_N)_1$, tangential diffusion (curvature), $(\partial V^Y/\partial x_N)_2$, and chemical reaction, $(\partial V^Y/\partial x_N)_3$.

plays an almost identical variation to those of the normal and tangential diffusion contributions. Chemistry causes a drastic change with respect to the inert scalar case, with all iso-surfaces propagating in the direction of the scalar gradient, $V^Y > 0$. The propagation velocity is higher at the scalar extrema and displays a minimum at $Y \approx 0.9$, only the normal diffusion contributes negatively for $Y < 0.25$, and the tangential diffusion velocity is comparable to the normal one over most scalar values. The contribution of chemistry to the propagation speed is greater that those of diffusion for $Y < 0.47$.

Figure 5.8 shows $\partial V^Y/\partial x_N$, given by the equation (4.90), conditional upon the mass fraction Y. The normal and curvature diffusion contributions are also presented, as well as the chemical contribution in the reactive scalar case. The variables have been normalized with the mean of the rms values

of $\partial V^Y/\partial x_N$, using the inert and reactive scalar fields. $\partial V^Y/\partial x_N$ can be interpreted as an added normal strain rate due to the combined action of diffusion and chemistry (Eqs. (4.64) and (4.74)). The mixing of an inert scalar case yields a concave curve, with comparable contributions of normal and tangential diffusion and positive added strain for all compositions; chemistry shows a modest and negative contribution for $0.07 < Y < 0.7$, while the diffusion shares are modified with respect to the inert scalar over all values of the mass fraction. The two constant density cases produce only positive values of $\partial V^Y/\partial x_N$. In this context, $\partial V^Y/\partial x_N > 0$ means that two adjacent iso-surfaces separate as time increases, whereas a negative value indicates that they get closer to each other.

5.4.3 Local strain rates

In the interaction of the scalar field and the turbulent velocity field the flow strain rates play an important role in the scalar structures, and in the local mixing rates. As mentioned previously (see Section 4.3.2), the flow strain rates tangential, a_T, and normal, a_N, to the iso-surface compose the volumetric dilatation rate, $\nabla \cdot \mathbf{u} = -P = a_T + a_N$ [53, 70, 72, 76]. For the incompressible case, the local dilatation rate is zero, $-P = \nabla \cdot \mathbf{u} = 0$, thus,

$$a_T = -a_N \, . \tag{5.18}$$

Figure 5.9 represents the normal and tangential strain rates, a_N and a_T, conditional upon the mass fraction Y. a_N and a_T have been normalized with the mean of the rms values of $\partial V^Y/\partial x_N$, using the inert and reactive scalar fields. It can be seen that the average of a_N remains predominantly negative ($a_N < 0$ and $a_T = -a_N > 0$). The local flow approaches iso-scalar surfaces and, simultaneously, stretches them. The chemistry slightly modifies the strain values at different constant composition surfaces. a_N increases slightly its modulus in the regions with negative molecular diffusion rate for the inert scalar case, and the same happens in the regions with high chemical activity for the reactive one.

Figure 5.10 is a plot of $(a_N+\partial V^Y/\partial x_N)$ conditional upon the mass fraction Y. The summation $a_N + \partial V^Y/\partial x_N$ is termed the *'effective'* normal strain rate and enters equations (4.64), describing the time evolution of the infinitesimal distance separating two adjacent iso-scalar surfaces, and (4.74), governing the scalar gradient modulus. The latter depends on the *'effective'* normal strain rate, with negative values leading to gradient enhancement as time evolves, and positive ones implying gradient reduction. Scatter plots in Figure 5.10 show that positive *'effective'* normal strain rates dominate, and hence gradients should be destroyed as time progresses. The latter is apparent in Figure 5.11 where the tails of the scalar gradient modulus pdf extends to a wider range of values for increasing times in the reactive

scalar case.

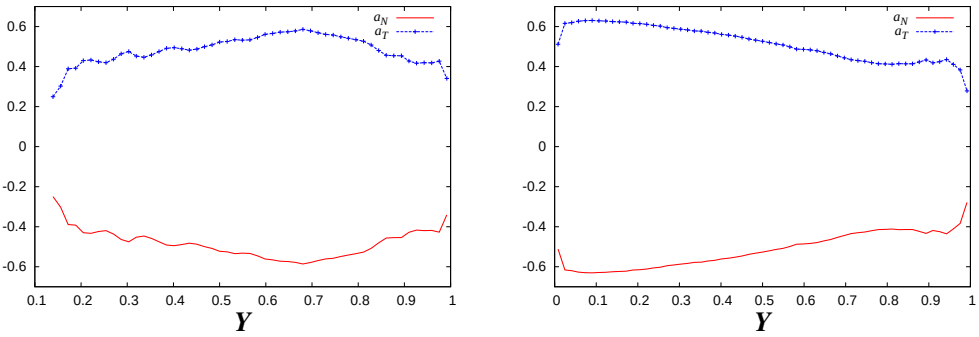

(a) Inert scalar case. (b) Reactive scalar case.

Figure 5.9: Flow strain rates normal, a_N, and tangential, a_T, to the iso-scalar surfaces.

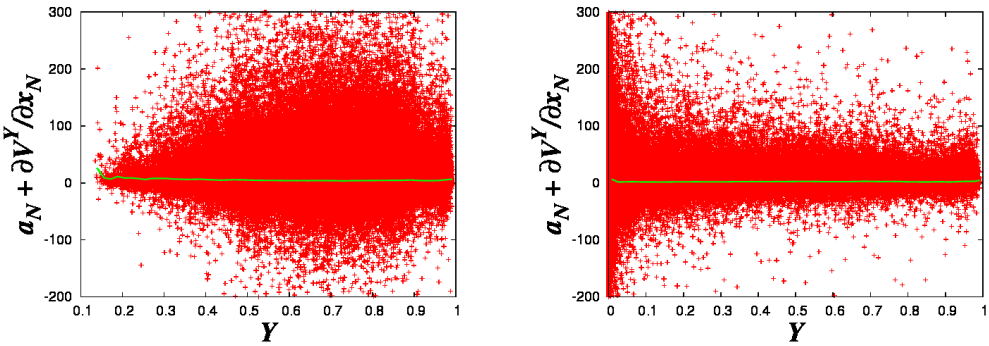

(a) Inert scalar case. (b) Reactive scalar case.

Figure 5.10: *'Effective'* strain rate normal to iso-scalar surfaces, $(a_N + \partial V^Y/\partial x_N)$.

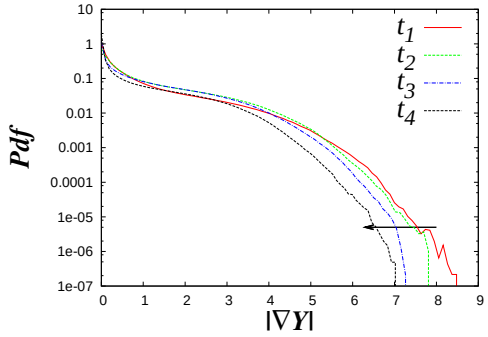

Figure 5.11: Scalar gradient modulus pdf's at several simulation times, for the reactive scalar case.

5.4.4 Small-scale flow structures

The strain-rate tensor, S_{ij}, symmetric, has three real eigenvalues, which sum zero due to the solenoidal condition of the incompressible velocity field. The eigenvalues are denoted by Λ_1, Λ_2 and Λ_3, where Λ_1 corresponds to the most extensive direction, whereas Λ_3 correspond to the most compressive one, ($\Lambda_1 > 0$ and $\Lambda_3 < 0$). Λ_2 is the intermediate eigenvalue, which could take any sign. Betchov [102] demonstrated for the incompressible case that the mean $\langle \Lambda_1 \Lambda_2 \Lambda_3 \rangle$ is proportional to the skewness of $\partial u_1 / \partial x_1$, which is typically negative. This has been confirmed in many numerical [14, 71] and experimental [103, 104] results. Thus, the intermediate eigenvalue Λ_2 should be, in average, positive.

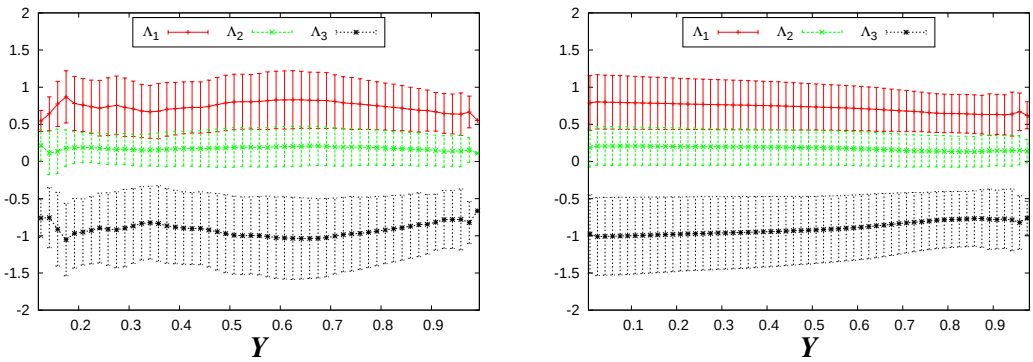

(a) Inert scalar case. (b) Reactive scalar case.

Figure 5.12: Eigenvalues of the symmetric strain-rate tensor, Λ_1, Λ_2 and Λ_3, as a function of the mass fraction. The eigenvalues have been normalized with $\langle Q_W \rangle^{1/2}$.

Figure 5.12 shows the eigenvalues of the symmetric-strain rate tensor as functions of the mass fraction for the inert and reactive scalar cases with

$Sc = 1.0$; vertical solid bars indicate their respective rms values. In both cases the sum of eigenvalues is zero, which is in agreement with the solenoidal condition. It can be seen that the average of the eigenvalues Λ_1 and Λ_3 their modulus in the regions close to the average of the scalar field (see Figure 5.2 to compare with the pdf's of the mass fraction, Y), whereas Λ_2 remains constant. The eigenvalue Λ_1 (Λ_3) is always positive (negative), while the average of Λ_2 remains positive with minimum negative values; this result confirms the predictions of Betchov [102] indicating that the mean $\langle\Lambda_2\rangle$ is positive. For constant-density reacting flows the velocity field is not affected by the values of the mass fraction nor by the temperature, as the thermal problem is decoupled from the dynamic one. However, it is important to note that in the region with high chemical activity, the modulus of eigenvalues corresponding to the most extensive and compressive directions increase. This indicates that towards $Y = 0$ there are zones with high strain rates in the reactive scalar case.

The three eigenvalues have associated three corresponding eigenvectors, which define the "principal directions" of the strain rate. A way to explore the effects of the flow strain rates upon the scalar iso-surfaces is calculating the orientation of the unit vector normal to iso-scalar surfaces, $\mathbf{n}$, with respect to the strain rate eigenvectors, $\mathbf{e}_i$, and the local vorticity, $\boldsymbol{\omega}$.

The alignment between the principal directions of the strain rate and the

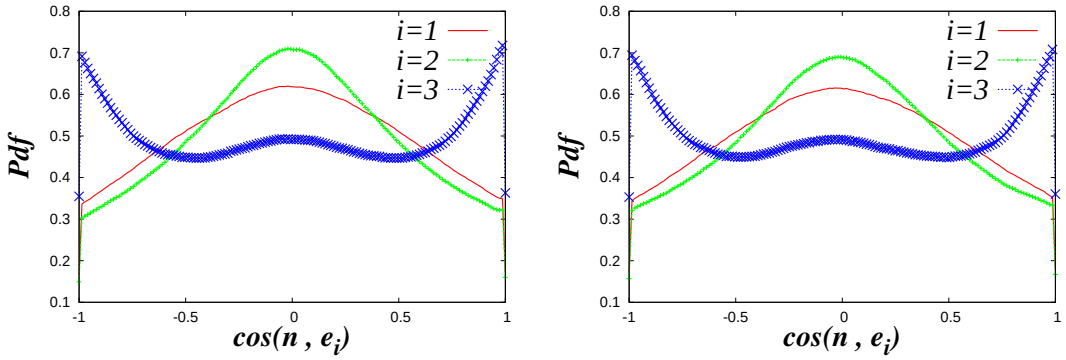

(a) Inert scalar case. (b) Reactive scalar case.

Figure 5.13: Pdf's of cos($\mathbf{n}$, $\mathbf{e}_i$). $\mathbf{n}$ is the unit vector normal to iso-scalar surfaces and $\mathbf{e}_i$ is the eigenvector of S_{ij}. The subindex of $\mathbf{e}_i$ denotes one of the three eigenvalues, ordered by decreasing values. $i = 1$ corresponds to the most extensive (positive) eigenvalue.

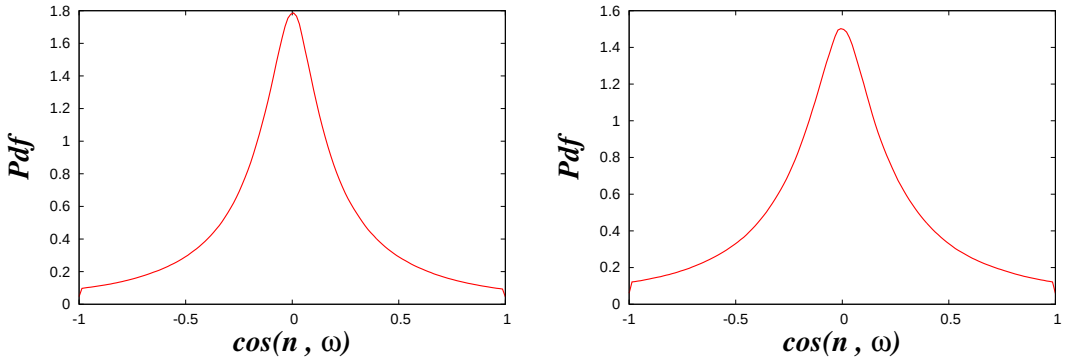

(a) Inert scalar case. (b) Reactive scalar case.

Figure 5.14: Pdf's of cos($\mathbf{n}$, $\boldsymbol{\omega}$). $\mathbf{n}$ is the unit vector normal to iso-scalar surfaces. $\boldsymbol{\omega}$ is the local vorticity vector.

iso-scalar surfaces is investigated by calculating the pdf's of the cosines of the angles between the unit vector normal at every point of the iso-scalar surface and the eigenvectors of the strain rate tensor over the flow domain, as shown in Figure 5.13. $\mathbf{e}_1$ is the eigenvector corresponding to the most extensive eigenvalue; the subindex i orders the eigenvectors by decreasing order. It can be seen that both for constant-density mixing and reaction

the trend is similar. All the iso-scalar surfaces are predominantly aligned with the most compressive eigenvalue of the strain rate tensor, $\mathbf{e}_3$, which is in agreement with studies of reacting [105] and non-reacting [71, 12] constant-density turbulent flows. The compressive effects in the direction of $\mathbf{e}_3$ and its alignment with the scalar gradient represent the flow strain rate normal to iso-surface, a_N.

Figure 5.14 plots the pdf's of the cosine between $\mathbf{n}$ and the local vorticity vector, $\boldsymbol{\omega}$. Values computed over all the flow domain are used. It can be seen that both for constant-density mixing and reaction the trend is similar. The vorticity vector is preferentially tangential to iso-scalar surfaces and, therefore, it contributes to curve and fold them. The joint action of two vortical structures, either co-rotating or counter-rotating, may also stretch and/or bend the surface. $\boldsymbol{\omega}$ lies in the plane of the iso-surface causes compressive effects, which also contribute to $a_N < 0$. These results are in agreement with three-dimensional DNS calculations [105], where the vorticity vector is found to lie preferentially in the plane of the flame.

5.4.4.1 Invariants of the velocity-gradient tensor and local flow topologies

Turbulence dynamics formally is determined by the strain and vorticity fields. However, to obtain a detailed picture of turbulence is complicated due to the nonlocal relation between the strain-rate tensor and vorticity. A way to deepen in this subject is to investigate the behavior of every local flow topologies, which constitute the flow (see Table 4.2).

First of all, to study the flow topologies it is important to understand the behavior of the invariants of the velocity-gradient tensor. For incompressible flows their definitions are as follows [18]:

$$P = P_S = -S_{ii} = -(\Lambda_1 + \Lambda_2 + \Lambda_3) = 0\,, \tag{5.19}$$

$$Q = Q_S + Q_W = -S_{ij}S_{ij}/2 + \omega_i\omega_i/4 = (\Lambda_1\Lambda_2 + \Lambda_1\Lambda_3 + \Lambda_2\Lambda_3) + \omega^2/4\,, \tag{5.20}$$

$$R = R_S - \omega_i S_{ij}\omega_j/4 = -S_{ij}S_{jk}S_{ki}/3 - \omega_i S_{ij}\omega_j/4 = -\Lambda_1\Lambda_2\Lambda_3 - \omega_i S_{ij}\omega_j/4\,. \tag{5.21}$$

The terms $S_{ij}S_{ij} \equiv \mathbf{s}^2$ and $\omega_i\omega_i \equiv \boldsymbol{\omega}^2$ in (5.20) are the total strain and enstrophy, respectively. The dynamical equations for $\mathbf{s}^2$ and $\boldsymbol{\omega}^2$ are as follows [28]:

$$\frac{1}{2}\frac{D\boldsymbol{\omega}^2}{Dt} = \omega_i S_{ij}\omega_j + \nu\omega_j\nabla^2\omega_j \,, \tag{5.22}$$

$$\frac{1}{2}\frac{D\mathbf{s}^2}{Dt} = -S_{ik}S_{kj}S_{ji} - \frac{1}{4}\omega_i\omega_j S_{ij} - S_{ij}\frac{\partial^2 p}{\partial x_i \partial x_j} + \nu S_{ij}\nabla^2 S_{ij} \,, \tag{5.23}$$

the term $\omega_i S_{ij}\omega_j$ in (5.22) is called the enstrophy production and the vector $S_{ij}\omega_j$ is the vortex stretching [28], which expresses the interaction between vorticity and strain rate tensor. $S_{ij}\omega_j$ is responsible for stretching (compressing) and tilting of vorticity. The term $-S_{ik}S_{kj}S_{ji} - \frac{1}{4}\omega_i\omega_j S_{ij} - S_{ij}\frac{\partial^2 p}{\partial x_i \partial x_j}$ in (5.23) is known as the (inviscid) production of total strain [103].

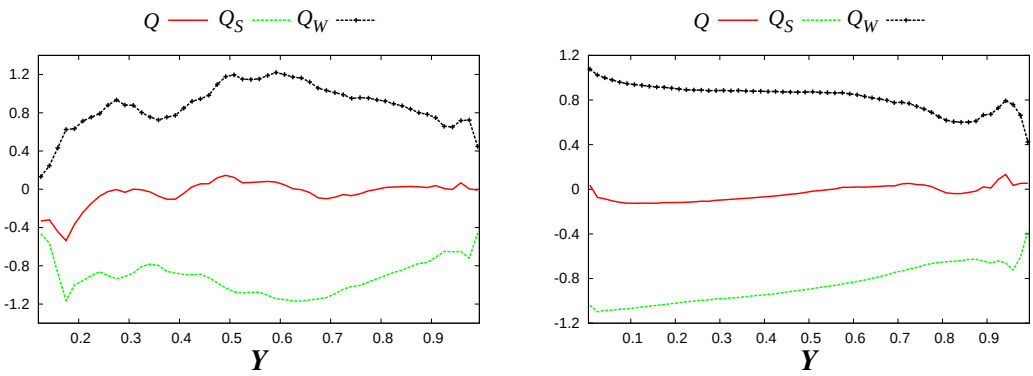

(a) Inert scalar case. (b) Reactive scalar case.

Figure 5.15: Invariants Q, Q_S, and Q_W as a function of the mass fraction.

Figures 5.15 and 5.16 depict the invariants Q, Q_S, Q_W, R, R_S, and $-(\omega_i S_{ij}\omega_j)/4$ as a function of the mass fraction, Y. The seconds and thirds invariants have been normalized with $\langle Q_W\rangle$ and $\langle Q_W\rangle^{3/2}$, respectively.

It can be seen in Figure 5.15 that $Q_W > 0$ and $Q_S < 0$ since $Q_W(\equiv$

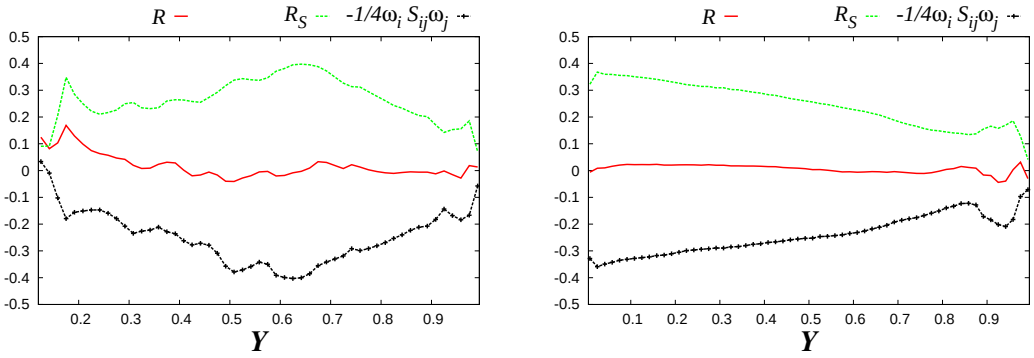

(a) Inert scalar case. (b) Reactive scalar case.

Figure 5.16: R, R_S, $-\omega_i S_{ij}\omega_j/4$ as a function of the mass fraction.

$\omega_i\omega_i/4$) and $-Q_S(\equiv S_{ij}S_{ij}/2)$ are positive definite in incompressible flows (Eq. (5.20)). The local enstrophy and strain rate increase their modulus in the regions close to the average of the scalar field (see Figure 5.2 to compare with the pdf's of the mass fraction, Y) and in regions with intense chemical activity. Q_S's negative values come from $\Lambda_3 < 0$, since $\Lambda_1 > 0$ and Λ_2 is positively skewed (see Figure 5.12). Although the volumen integral of $-Q_S$ is equal to the volumen integral of Q_W, i.e. $\langle Q \rangle = 0$ over all the domain in homogeneous turbulent flows with semi-infinite or doubly infinite domains [106], the local values of $-Q_S$ and Q_W are not necessarily equal. It can be noted that, e.g. for $Y = 0.2$ value, the local value of $-Q_S$ is different to that of Q_W, both for constant-density mixing and reaction. These findings are in agreement with the results shown in Soria *et al.* [106].

It is important to note in Figure 5.16 that, both for constant-density mixing and reaction, the total strain production, R_S, and the enstrophy produc-

tion, $-\omega_i S_{ij} \omega_j/4$, undergo an increase in their modulus in the regions close to the average of the scalar field and in regions with intense chemical activity; these results are in connection with the increase of the modulus of the eigenvalues Λ_1 and Λ_3 in the zones with high strain rates (see Figure 5.12). The total strain production, R_S, is positive because the product $\langle \Lambda_1 \Lambda_2 \Lambda_3 \rangle$ is negative, due to the fact that $\langle \Lambda_3 \rangle < 0$ (see Eq. (5.21)). The more negative is the enstrophy production ($-\omega_i S_{ij} \omega_j/4$), the more local enstrophy (Q_W) is observed. The term $-\omega_i S_{ij} \omega_j$ turns into positive in Eq. (5.22) producing high values of Q_W. Although the volumen integral of the total strain production is equal to the volumen integral of the enstrophy production, i.e. $\langle R \rangle = 0$ over all the domain, the two components making up the third invariant of the velocity-gradient tensor do not have equal local values. It can be seen that there are regions where the local values of R_S and $-\omega_i S_{ij} \omega_j/4$ are quite different. These findings are in agreement with DNS results of incompressible turbulent flows *et al.* [106].

Figure 5.17 shows the joint pdf's of Q and R both for constant-density mixing and reaction. The seconds and thirds invariants have been normalized with $\langle Q_W \rangle$ and $\langle Q_W \rangle^{3/2}$, respectively. The resulting distributions are skewed towards negative values of Q, and displays a maximum near to the origin. Nevertheless, there are complex topologies with large modulus (towards $Q > 0$), which balance the skew of the statistical distributions,

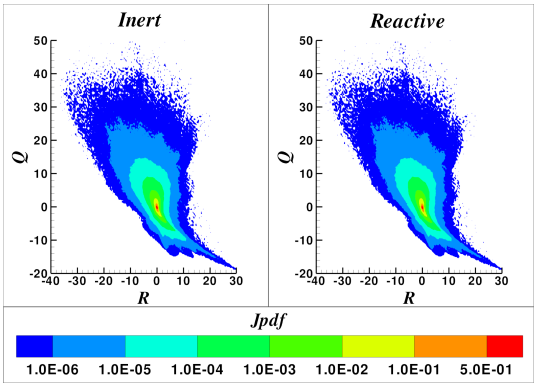

Figure 5.17: Joint pdf of $R - Q$, for the inert and reactive scalar cases. Joint pdf magnitudes decrease from the center to the circumference.

and keep the local enstrophy and strain rate close to zero ($\langle Q \rangle \approx 0$, and $\langle R \rangle \approx 0$), such as shown in Figures 5.15 and 5.16. It is important to note that the universal teardrop remains in both cases, and seems to be the same. The nodal topology S3 (SN/S/S) has a modest participation in the small-scale dynamics and mixing, therefore, the changes in the strain rate are represented by the nodal topology S2 (UN/S/S). On the other hand, the probability of finding the stable focus/stretching topology S4 (SFS) is greater than that of the complex topologies S1 (UFC).

5.5 Summary and conclusions

Results of 512^3 grid DNS for inert and reactive scalars to three different Schmidt numbers, $Sc = 0.5$, $Sc = 1.0$, $Sc = 1.5$, in a constant density fluid forced by a statistically homogeneous field of turbulence have been used

to study mixing characteristics, scalar structures and local flow topologies. The scalar field geometries, using the $k_m - k_g$ plane, have been identified. A significant correlation between the curvature magnitude and Schmidt number is apparent. With the increasing of the Schmidt number the curvature values increase; for $Sc > 1$, the smallest scalar length are obtained ($l_B < \eta$), consequently, the curvature values increase. The joint pdf's of k_m and k_g are more widespread with the increase of Schmidt number, and the curvature values are larger in the reactive scalar cases than in the inert ones. Nearly flat scalar iso-surfaces are the most probable geometries in all cases under study, and the saddle points are dominant over convex or concave ones.

The kinematics of non-material iso-scalar surfaces has been analyzed. The molecular diffusion rate is much greater in the reactive scalar cases than those of the inert ones, and its maxima and minima values for the inert (reactive) scalar cases correlate with the $Y \approx 0.25$ ($Y \approx 0.12$) and $Y \approx 0.9$ ($Y \approx 0.55$) iso-surfaces, respectively, independently of Schmidt number. The contribution to $D\nabla^2 Y$ due to the tangential diffusion is important in the inert scalar cases, whereas in the reactive scalar cases is negligible. In all cases, the most important contribution to the molecular diffusion rates comes from the normal diffusion through the variation of $|\nabla Y|$ normal to the iso-surfaces.

Expressions for the propagation speed of an iso-scalar surface relative to the fluid and its derivative, with respect to the normal direction of the iso-scalar surfaces have been obtained. The displacement speed of the iso-scalar surfaces, V^Y, displays an almost identical variation to those of the normal and tangential diffusion contributions for the inert scalar case, with iso-surfaces propagating in the same (opposite) direction of the scalar gradient for $Y > 0.7$ ($Y < 0.7$). In the reactive scalar case the iso-surfaces propagate in the direction of the scalar gradient, $V^Y > 0$, and the contribution of chemistry to the propagation speed is greater that those of diffusion for $Y < 0.47$. The term $\partial V^Y/\partial x_N$, interpreted as an added normal strain rate due to the combined action of diffusion and chemistry, is always positive, which means that two adjacent iso-surfaces separate as time increases.

Negative normal strain rates, a_N, dominate in all cases under study ($a_N < 0$ and $a_T = -a_N > 0$). High negative normal strain rates correlate with negative molecular diffusion rate for the inert scalar case, and with high chemical activity for the reactive one. The added normal strain rate, $\partial V^Y/\partial x_N$, allows the *'effective'* normal strain rate, $a_N + \partial V^Y/\partial x_N$, to be positive. $a_N + \partial V^Y/\partial x_N > 0$ indicates that iso-scalar separate as time increases, which destroys scalar gradients; scalar gradient pdf clearly shows this last feature, since the likelihood of high values of $|\nabla Y|$ decreases with time.

The eigenvalues, Λ_1, Λ_2 and Λ_3, of the strain rate tensor conditional upon

the mass fraction Y have been obtained. Λ_1 (Λ_3) is always positive (negative), and Λ_2 remains in average positive with few negative values; these findings are in agreement with previous investigations [14, 71, 103, 104]. The eigenvalues Λ_1 and Λ_3 undergo an increase in their modulus in the regions close to the average of the scalar field, and in regions with intense chemical activity.

Regardless of the case under study, the scalar gradient is predominantly aligned with the eigenvector corresponding to the most compressive eigenvalue, $\mathbf{e}_3$, which is in good agreement with studies of reacting [105], non-reacting [12, 71] constant-density turbulent flows, and the compressive effects due to the normal strain rate, a_N. The vorticity vector, $\boldsymbol{\omega}$, contributes to curve and fold the iso-scalar surfaces, and it is found to lie preferentially in the plane of the flame. This feature can cause compressive effects, which also contribute to the negative values of a_N.

The local enstrophy and strain rate, Q_W and Q_S, as well as the production of enstrophy and strain, $\omega_i S_{ij} \omega_j$ and R_S, increase in the regions close to the average of the scalar field and in regions with intense chemical activity. Although the volumen integral of the second and third invariants of the velocity-gradient tensor are zero over all the domain, their local values are not necessarily equal. These findings are in agreement with DNS results of incompressible turbulent flows *et al.* [106]. The well known universal

teardrop shape of the joint pdf's of Q and R is obtained in the results, and seems to be the same both for constant-density mixing and reaction. Local strain rates are dominated by the nodal topologies S2 (UN/S/S) since S3 (SN/S/S) has a modest participation in the small-scale flow, whereas the vorticity field is mostly represented by the stable focus/stretching topology S4 (SFS) instead of the complex topologies S1 (UFC).

Future development of mixing models for constant density fluid could mimic some features of scalar structures and local flow topologies found in this study. All conclusions reached in this study pertain to small-scale features and thus should display a certain degree of universality. Correlations of two point micro-structures and two-times (of the order of the Kolmogorov time micro-scale) could also be relevant to continue characterizing scalar structures, mixing characteristics, and local flow topologies in reacting flows.

6

Turbulent premixed flame in an inlet-outlet configuration

The physical system simulated in this case is a premixed turbulent flame using an inflow-outflow configuration at moderate turbulent Reynolds number and with single-step Arrhenius chemistry (see Figure 6.1). A planar

laminar flame used as initial condition interacts with a turbulent field of fresh gases, which wrinkles the iso-scalar surfaces; simultaneously, the velocity field undergoes the influence of thermal processes. The set of conservation equations for mass, momentum, energy and chemical species, are solved using the fully parallel compressible solver NTMIX3D [73]. The domain is considered as periodic in the y and z directions, while non-reflecting inlet-outlet boundary conditions are imposed in the x direction, using the Navier-Stokes Characteristic Boundary Condition (NSCBC) method [107].

6.1 Numerical implementation

The fully parallel compressible solver [73] uses a 6th order compact Finite-Differences (FD) scheme for space discretization, and integrates in time the conservation equations through a third-order Runge-Kutta explicit method [108]. The boundary conditions are imposed by the NSCBC method, which allows to use non-reflecting boundary conditions. A brief overview of these numerical techniques is presented below.

Spatial integration

In order to describe the method for the advance in the spatial domain, let us consider φ as a generic scalar quantity over the domain and the notation

for its first and second derivatives respectively as follows:

$$\partial\varphi/\partial x = \varphi' \,, \tag{6.1}$$

$$\partial^2\varphi/\partial x^2 = \varphi'' \,. \tag{6.2}$$

The development of FD schemes for the first and second derivatives, based on the compact FD scheme, are as follows:

- First derivative

$$3\varphi'_{i+1} + 9\varphi'_i + 3\varphi'_{i-1} = \frac{1}{\Delta x}\left(\frac{1}{4}\varphi_{i+2} + 7\varphi_{i+1} - 7\varphi_{i-1} - \frac{1}{4}\varphi_{i-2}\right) \,. \tag{6.3}$$

- Second derivative

$$2\varphi''_{i-1} + 11\varphi''_i + 2\varphi''_{i+1} = \frac{1}{(\Delta x)^2}\left(\frac{3}{4}\varphi_{i+2} + 12\varphi_{i+1} - \frac{51}{2}\varphi_i + 12\varphi_{i-1} + \frac{3}{4}\varphi_{i-2}\right) \,. \tag{6.4}$$

The solver starts with given initial conditions for the scalar fields (e.g. mass fraction, temperature, and other scalar fields), and uses an initial turbulent velocity field generated by an independent pseudo-spectral numerical code

to evolve all the spatial derivative accordingly to the rule above. The pseudo-spectral method is described in detail in Chapter 3, Section 5.2.

Time integration

The time integration is solved using the third-order Runge-Kutta method [108]. In order to illustrate the numerical method, we are going to solve Eq. (5.14) as follows:

$$\begin{aligned} U^{(0)} &= U^{(n)}\,, \\ U^{(1)} &= U^{(n)} + \Delta t b_0 R(U^{(0)})\,, \\ U^{(2)} &= U^{(n)} + \Delta t b_1 R(U^{(1)})\,, \\ U^{(3)} &= U^{(n)} + \Delta t \sum_{j=0}^{1} a_j R(U^{(2j)})\,, \end{aligned} \tag{6.5}$$

where the coefficients are $a_0 = 1/4$, $a_1 = 3/4$; $b_0 = 1/3$, and $b_1 = 2/3$, respectively.

The maximum time step, Δt, is given by two classical criteria: The Courant-Friedrichs-Lewys-number (CFL) and the Fourier number (Fo). The first criteria takes into account the convective part and limits the fluid particle moves only a fraction of Δx in a time step Δt, and the second one takes

into account the diffusive part and limits the momentum transport due to the viscosity does not move more than a fluid-cell in a time step Δt:

$$CFL = \frac{\max\{|u+a|, |u-a|\}}{\Delta x/\Delta t}\,, \tag{6.6}$$

$$Fo = \frac{\max(\nu/Re_a)}{(\Delta x)^2/\Delta t}\,, \tag{6.7}$$

where a is the speed of sound, ν is the kinematic viscosity, and Re_a (defined in Eq. (6.37)) is the acoustical Reynolds number. In this study, the Courant-Friedrichs-Lewys and Fourier numbers have been taken $CFL \leq 0.6$, $Fo \leq 0.1$ since for most cases studied ([73, 108, 109] and others) this limits are sufficient to provide numerical stability.

Description of characteristic boundary conditions

The computational domain is treated as non-periodic in the x direction and periodic in the y and z directions. Thus, the numerical instabilities in the y and z directions are minima. Despite the high order numerical method used to compute the spatial derivatives, in the x direction the numerical dissipation is too small to damp high wavenumber instabilities. These numerical waves propagate into the domain and are reflected at boundaries, which generates new physical waves that lead to unphysical

oscillations unacceptable in a DNS computation. Hence, non-reflecting inlet-outlet boundary conditions are enforced in the x direction, using the Navier-Stokes Characteristic Boundary Condition (NSCBC) method [107]. The NSCBC technique is based on the idea that any hyperbolic system can be associated with a corresponding system of propagating waves. At the boundaries, some of these waves leave the domain while others penetrate into it. Determining the waves requires a transformation between the conservative system in which the integration is generally conducted, and a primitive system where the wave structures, and the propagation direction of these waves, can be computed.

In order to give a brief overview of the NSCBC method let us consider that the outlet is located in x_1. Under the NSCBC assumptions, the fluid dynamics equations for the boundaries located at x_1 can be written as:

$$\frac{\partial \rho}{\partial t} + d_1 + \frac{\partial}{\partial x_2}(\rho u_2) + \frac{\partial}{\partial x_3}(\rho u_3) = 0\,, \tag{6.8}$$

$$\frac{\partial(\rho E)}{\partial t} + \frac{1}{2}(u_k u_k)d_1 + \frac{d_2}{\gamma - 1} + \rho u_1 d_3 + \rho u_2 d_4 + \rho u_3 d_5 + \frac{\partial}{\partial x_2}[u_2(\rho e_s + p)] + \frac{\partial}{\partial x_3}[u_3(\rho e_s + p)] = \frac{\partial}{\partial x_i}\left(\lambda \frac{\partial T}{\partial x_i}\right) + \frac{\partial}{\partial x_i}(u_i \tau_{ij}) + \dot{\omega}_s\,, \tag{6.9}$$

$$\frac{\partial(\rho u_1)}{\partial t} + u_1 d_1 + \rho d_3 + \frac{\partial}{\partial x_2}(\rho u_2 u_1) + \frac{\partial}{\partial x_3}(\rho u_3 u_1) = \frac{\partial \tau_{1j}}{\partial x_j}\,, \tag{6.10}$$

$$\frac{\partial(\rho u_2)}{\partial t} + u_2 d_1 + \rho d_4 + \frac{\partial}{\partial x_2}(\rho u_2 u_2) + \frac{\partial}{\partial x_3}(\rho u_3 u_2) + \frac{\partial p}{\partial x_2} = \frac{\partial \tau_{2j}}{\partial x_j}\,, \quad (6.11)$$

$$\frac{\partial(\rho u_3)}{\partial t} + u_3 d_1 + \rho d_5 + \frac{\partial}{\partial x_2}(\rho u_2 u_3) + \frac{\partial}{\partial x_3}(\rho u_3 u_3) + \frac{\partial p}{\partial x_3} = \frac{\partial \tau_{3j}}{\partial x_j}\,, \quad (6.12)$$

$$\frac{\partial(\rho Y)}{\partial t} + Y d_1 + \rho d_6 + \frac{\partial}{\partial x_2}(\rho u_2 Y) + \frac{\partial}{\partial x_3}(\rho u_3 Y) = \frac{\partial}{\partial x_j}\left(\rho D \frac{\partial Y}{\partial x_j}\right) - \dot{\omega}\,, \quad (6.13)$$

where E is the total energy without chemical term:

$$E = e_s + \frac{1}{2} u_k u_k = h_s + \frac{1}{2} u_k u_k - \frac{p}{\rho}\,, \quad (6.14)$$

and d_1 to d_6 are the derivatives normal to the x_1 boundary. The vector $\mathbf{d}$ is given by characteristic analysis [107, 110]:

$$\mathbf{d} = \begin{pmatrix} d_1 \\ d_2 \\ d_3 \\ d_4 \\ d_5 \\ d_6 \end{pmatrix} = \begin{pmatrix} \frac{1}{a^2}\left[L_2 + \frac{1}{2}(L_2 + L_1)\right] \\ \frac{1}{2}(L_5 + L_1) \\ \frac{1}{2\rho a}(L_5 - L_1) \\ L_3 \\ L_4 \\ L_6 \end{pmatrix} = \begin{pmatrix} \dfrac{\partial(\rho u_1)}{\partial x_1} \\ \rho a^2 \dfrac{\partial u_1}{\partial x_1} + u_1 \dfrac{\partial p_1}{\partial x_1} \\ u_1 \dfrac{\partial u_1}{\partial x_1} + \frac{1}{\rho} \dfrac{\partial p_1}{\partial x_1} \\ u_1 \dfrac{\partial u_2}{\partial x_1} \\ u_1 \dfrac{\partial u_3}{\partial x_1} \\ u_1 \dfrac{\partial Y}{\partial x_1}\,, \end{pmatrix} \quad (6.15)$$

where the L_i's are the amplitudes of characteristic waves associated with each characteristic velocity λ_i. These velocities are given by [110]:

$$\lambda_1 = u_1 - a \,, \tag{6.16}$$

$$\lambda_2 = \lambda_3 = \lambda_4 = u_1 \,, \tag{6.17}$$

$$\lambda_5 = u_1 + a \,. \tag{6.18}$$

The L_i's in Eq. (6.15) are as follows:

$$L_1 = \lambda_1 \left(\frac{\partial p}{\partial x_1} - \rho a \frac{\partial u_1}{\partial x_1} \right) \,, \tag{6.19}$$

$$L_2 = \lambda_2 \left(a^2 \frac{\partial \rho}{\partial x_1} - \frac{\partial p}{\partial x_1} \right) \,, \tag{6.20}$$

$$L_3 = \lambda_3 \frac{\partial u_2}{\partial x_1} \,, \tag{6.21}$$

$$L_4 = \lambda_4 \frac{\partial u_3}{\partial x_1} \,, \tag{6.22}$$

$$L_5 = \lambda_5 \left(\frac{\partial p}{\partial x_1} + \rho a \frac{\partial u_1}{\partial x_1} \right) \,, \tag{6.23}$$

$$L_6 = \lambda_6 \frac{\partial Y}{\partial x_1} \,. \tag{6.24}$$

Thus, we get the solution in time on the boundaries by using the system of Eqs. (6.8) to (6.13). Most quantities are estimated using points inside

the domain and values at previous time steps. Terms involving derivatives along x_2 or x_3 are obtained on the boundaries with the same approximation.

Reaction rate

A reactive scalar interacts with a three-dimensional turbulent velocity field. The reaction rate is a single step Arrhenius-type irreversible reaction, Reactants $\rightarrow$ Products, to maintain the computational cost within reasonable limits. The reaction rate expression is (*cf.* Eq. (4.109)):

$$\dot{\omega} = \frac{\dot{\omega}_R}{Y_R^u} = \rho Y B_o \, exp\left(-\frac{\beta}{\alpha}\right) exp\left[\frac{-\beta(1-\theta)}{1-\alpha(1-\theta)}\right] , \tag{6.25}$$

where ρ is the density of the mixture; $Y = Y_R/Y_R^u$ is the reduced mass fraction, defined with Y_R, the reactants mass fraction and its value in the fresh gasses, Y_R^u; B_o is the pre-exponential factor; the ratio $\alpha = (T_b - T_u)/T_b$ is defined with the temperature, T, in the unburned, T_u, and burnt gases, T_b; β is the reduced activation energy or Zel′dovich number, $\beta = \alpha E_a/RT_b$, E is the activation energy and R the universal gas constant; and $\theta = (T - T_u)/(T_b - T_u)$ is the reduced temperature.

Dimensionless equations

The full set of governing equations is made dimensionless using reference characteristic variables and molecular transport coefficients in the fresh gases, namely,

$$a_{ref} = a_u \quad T_{ref} = (\gamma - 1)T_u \quad \rho_{ref} = \rho_u \quad p_{ref} = \rho_u a_u^2 = \gamma p_u$$

$$\lambda_{ref} = \lambda_u \quad \mu_{ref} = \mu_u \quad \nu_{ref} = \mu_{ref}/\rho_{ref} \quad C_{p_{ref}} = C_{p_u}$$

$$D_{thref} = \lambda_{ref}/\rho_{ref}C_{p_{ref}} \quad D_{ref} = D_u \quad t_{ref} = L_{ref}/a_{ref}$$

where the sub-index u denotes the variable value in the fresh gases. a_{ref}, T_{ref}, ρ_{ref}, p_{ref}, λ_{ref}, μ_{ref}, ν_{ref}, $C_{p_{ref}}$, D_{thref}, D_{ref}, L_{ref} and t_{ref}, are the reference speed of sound, temperature, density, pressure, thermal conductivity, dynamic viscosity, kinematic viscosity, specific heat at constant pressure (assumed constant), thermal diffusivity, mass diffusivity, length scale and time. γ is the ratio of specific heats at constant pressure and volume, respectively. The full set of dimensionless governing equations can be written in Cartesian tensor notation as [76],

mass continuity:

$$\frac{\partial \rho^+}{\partial t^+} + \frac{\partial}{\partial x_i^+}(\rho^+ u_i^+) = 0\,, \tag{6.26}$$

momentum:

$$\frac{\partial \rho^+ u_i^+}{\partial t^+} + \frac{\partial}{\partial x_j^+}(\rho^+ u_i^+ u_j^+) + \frac{\partial p^+}{\partial x_i^+} = \frac{1}{Re_a} \cdot \frac{\partial \tau_{ij}^+}{\partial x_j^+} \,, \tag{6.27}$$

energy:

$$\begin{aligned} \frac{\partial \rho^+ e_t^+}{\partial t^+} + \frac{\partial}{\partial x_i^+}\left[(\rho^+ e_t^+ + p^+) u_i^+\right] =& \frac{1}{Re_a} \cdot \frac{\partial}{\partial x_j^+}(u_i^+ \cdot \tau_{ij}^+) \\ & - \frac{1}{Re_a \cdot Pr} C_p^+ \frac{\partial q_i^+}{\partial x_i^+} \\ & - \alpha' T_u^+ \dot{\omega}^+ \,, \end{aligned} \tag{6.28}$$

and reactant mass fraction:

$$\frac{\partial(\rho^+ Y)}{\partial t^+} + \frac{\partial}{\partial x_i^+}(\rho^+ Y u_i^+) = \frac{1}{Re_a Sc} \frac{\partial}{\partial x_i^+}\left(\mu^+ \frac{\partial Y}{\partial x_i^+}\right) + \dot{\omega}^+ \,, \tag{6.29}$$

The superscript + denotes a dimensionless variable or property. Dimensionless density, $\rho^+ = \rho/\rho_{ref}$, ith component of the velocity vector, $u_i^+ = u_i/a_{ref}$, pressure, $p^+ = p/p_{ref}$, temperature, $T^+ = T/T_{ref}$, time, $t^+ = t/t_{ref}$, and ith component of the position vector, $x_i^+ = x_i/L_{ref}$ are used. Moreover, the following constitutive relations and the perfect gas law complete the system definition,

$$\tau_{ij}^{+} = 2\mu^{+}\left(S_{ij}^{+} - \frac{1}{3}\delta_{ij}S_{kk}^{+}\right), \tag{6.30}$$

$$S_{ij}^{+} = \frac{1}{2}\left(\frac{\partial u_i^{+}}{\partial x_j^{+}} + \frac{\partial u_j^{+}}{\partial x_i^{+}}\right), \tag{6.31}$$

$$e_t^{+} = \frac{1}{2}\cdot\sum_{k=1}^{3} u_k^{+2} + \frac{p^{+}}{(\gamma-1)\rho^{+}}, \tag{6.32}$$

$$q_j^{+} = -\lambda^{+}\frac{\partial T^{+}}{\partial x_j^{+}}, \tag{6.33}$$

$$p^{+} = \rho^{+}T^{+}C_p^{+}\frac{\gamma-1}{\gamma}, \tag{6.34}$$

$$\alpha' = \frac{\alpha}{1-\alpha}, \tag{6.35}$$

$$\dot{\omega}^{+} = -\rho^{+}YRe_aPrDaS_L^{+2}\cdot exp\left[\frac{-\beta(1-\theta)}{1-\alpha(1-\theta)}\right]. \tag{6.36}$$

where τ_{ij}^{+} is the viscous stress tensor, given by the Navier-Poisson relation, and S_{ij}^{+} is the rate of strain tensor. e_t^{+} is the total (kinetic plus internal) specific energy. q_j^{+} is the heat conduction vector, given by the Fourier constitutive relation. The perfect gas law relates p^{+}, ρ^{+} and T^{+}. The dimensionless parameters, entering the conservation equations, (6.26)-(6.29), and the reaction rate (6.36), are defined as

$$Re_a = \frac{a_{ref} L_{ref}}{\nu_u} , \tag{6.37}$$

$$Pr = \frac{C_{p_u} \cdot \mu_u}{\lambda_u} , \tag{6.38}$$

$$Sc = \frac{\mu_u}{\rho_u D_u} , \tag{6.39}$$

$$Da = \frac{D_{th}^+}{S_L^{+2}} B_o \, exp(-\beta/\alpha) \tag{6.40}$$

where Re_a stands for the acoustical Reynolds number, Pr for the Prandtl number, Sc for the Schmidt number and Da for the Damköhler number.

S_L^+ in Eqs. (6.36) and (6.40) denotes the non stretched laminar flame speed, defined by

$$S_L^+ = \frac{1}{a_{ref} \rho_u Y_u} \int_{-\infty}^{+\infty} \dot{\omega} \, dx . \tag{6.41}$$

The laminar flame thickness is then given by

$$\delta_L^+ = \frac{D_{th}^+}{S_L^+} , \tag{6.42}$$

where the thermal diffusivity, D_{th}^+, is evaluated in the hot products.

The turbulent Reynolds number Re, based on the fluctuating velocity rms value, u', and the integral length scale, l, is expressed as

$$Re = \frac{u'l}{\nu_u} \,. \tag{6.43}$$

In this study, the acoustical and turbulent Reynolds numbers are 5066 and 61, respectively, at the end of the simulation. The dynamic viscosity is modeled as

$$\mu^+ = \mu_u^+ \left(\frac{T}{T_u} \right)^b \,, \tag{6.44}$$

with $b = 0.6$. The thermal conductivity and mass diffusivity are functions of dynamic viscosity and density, via the assumption of constant C_p, Prandtl and Schmidt numbers, with $Pr = 0.75$ and $Sc = 0.7$. The Lewis number is unity.

To simplify the notation, dimensionless variables will be written hereafter without the superscript +.

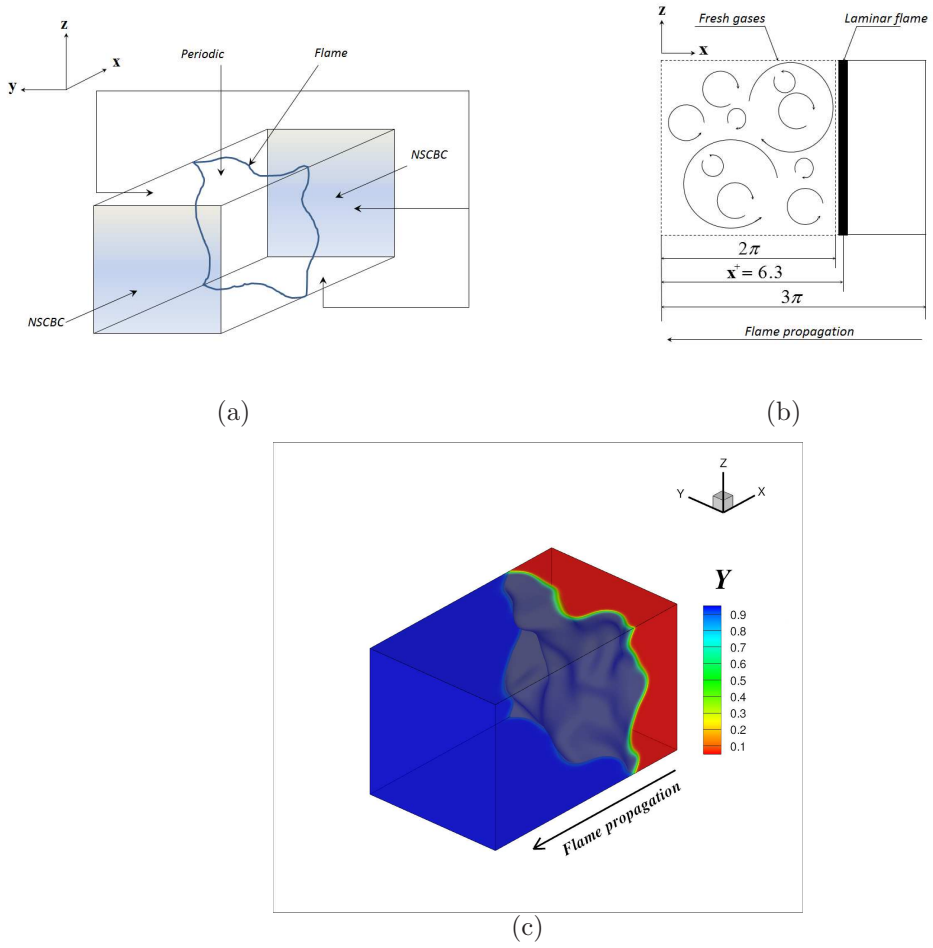

Figure 6.1: (a) Description of the computational domain, (b) initial conditions and (c) scalar field from simulation at $t = 90$.

6.2 Simulation parameters

The Direct Numerical Simulation has been performed using the MPI (Message Passing Interface) parallelized implementation [111, 112]. The computational domain, shown schematically in Figure 6.1, has a size 3π in the x direction and 2π in the y and z directions, and contains 768 x 512 x 512 grid points, uniformly distributed, which gives a spatial resolution $\Delta x = 0.0122$.

Initial conditions correspond to a planar premixed flame propagating in the negative x direction with a laminar flame speed S_L and width $\delta_L = D_{th}/S_L$, so that fresh gases (corresponding to $Y = 1$) are located to the left of the x axis and burnt products ($Y = 0$) to the right. A constant-density isotropic turbulent velocity field is initially superposed to the velocity in the fresh gases side and evolves without forcing in the compressible solver NTMIX3D. In the subsequent propagation towards fresh gases the flame encounters a decaying turbulent field, which wrinkles it as it progresses. The initial constant-density isotropic turbulence is generated with an independent pseudo-spectral numerical code [89, 90], starting from a given spectrum and using a stochastic forcing scheme, to yield a statistically stationary field. In the zero correlation-time forcing scheme [99, 100], all wave numbers with a modulus less than $2\sqrt{2}$, except the zero mode which makes

no contribution, receive a stochastic contribution at every time step, while their phase is adjusted to enforce incompressibility.

The computational domain, of size $Lx \times Ly \times Lz = 1.5L \times L \times L$ with $L/\delta_L = 119.45$ is discretized in a $768 \times 512 \times 512$ uniform grid with periodic boundary conditions in the cross-flow directions, y and z, and non-reflecting inlet-outlet boundary conditions in the x direction, imposed using the Navier-Stokes Characteristic Boundary Condition (NSCBC) method [107].

In this study the gas parameters introduced above are chosen as $b = 0.6$, $Pr = 0.75$, $Sc = 0.75$, $\gamma = 1.4$, and the chemical rate parameters are $\alpha = 0.8$, and $\beta = 6.0$. The rms velocity fluctuations in the 'fresh reactants' decay from $u'_0 = 0.016$ in $t = 0$ to $u' = 0.010$ in t_{final}, in which our data are presented. To estimate the integral length scale, l, in the 'fresh reactants', the transverse autocorrelation coefficients in cross-stream planes, $y-z$, are obtained. The integral scale increases from $l_0 = 1.058$ in $t = 0$ to $l = 1.200$ in t_{final}. The turbulent Reynolds number, $Re = u'l/\nu_u$, decreases from $Re_{t_0} = 86$ in $t = 0$ to $Re_t = 61$ in t_{final}. The initial eddy turnover time is $\tau_0 = l_0/u'_0 = 66.13$. In this study, the initially planar laminar flame is allowed to interact with the turbulence field up to a time $t_{final} = 90$, 1.36 times greater than the initial eddy turnover time.

The Kolmogorov length micro-scales at the beginning and the end of the simulation, are $\eta_0 = 0.0370$ and $\eta = 0.0550$, respectively, which guarantee

an adequate spatial resolution with the current domain and mesh sizes along the simulation time. The turbulent Damköhler number, defined as $Da = (l/\delta_L)/(u'/S_L)$, is 11.41 at t_{final}. Therefore, combustion takes place in the 'corrugated flamelets' regime [76, 78], as shown in Figure 6.2. Numerical values of the aero-thermo-chemical variables and dimensionless parameters for this simulation are presented in Tables 6.1.

Parameter	Value
Prandtl number, Pr	0.75
Schmidt number, Sc	0.75
Lewis number, Le	1.0
$\alpha = (T_b - T_u)/T_b$	0.8
Zel′dovich number, β	6.0
rms of velocity fluctuations, u'	0.01
Integral length scale, l	1.20
Turbulent kinetic energy dissipation rate, ε	8.333e-7
Kolmogorov length micro-scale, η	0.055
Kolmogorov time micro-scale, τ_η	15.36
Non stretched laminar flame velocity, S_L	0.005
Laminar flame thickness, δ_L	0.0526
Chemical time scale, τ_{ch}	10.40
Velocity ratio, u'/S_L	2.0
Length ratio, l/δ_L	22.81
Turbulent Reynolds number, Re	61
Damköhler number, $Da = (l/\delta_L)/(u'/S_L)$	11.41
Karlovitz number, $Ka = \tau_{ch}/\tau_\eta$	0.68

Table 6.1: Values of dimensionless parameters and physical variables at the end of the simulation.

6.3 Results and discussion

Figure 6.3 shows the reactant mass fraction iso-lines in planes $x - y$ and $x - z$, in a zoom of the computational domain, at different times $t = 10$, $t = 50$ and $t = 90$. The initially flat flame bends under the influence of the turbulence and the images are consistent with the current 'corrugated

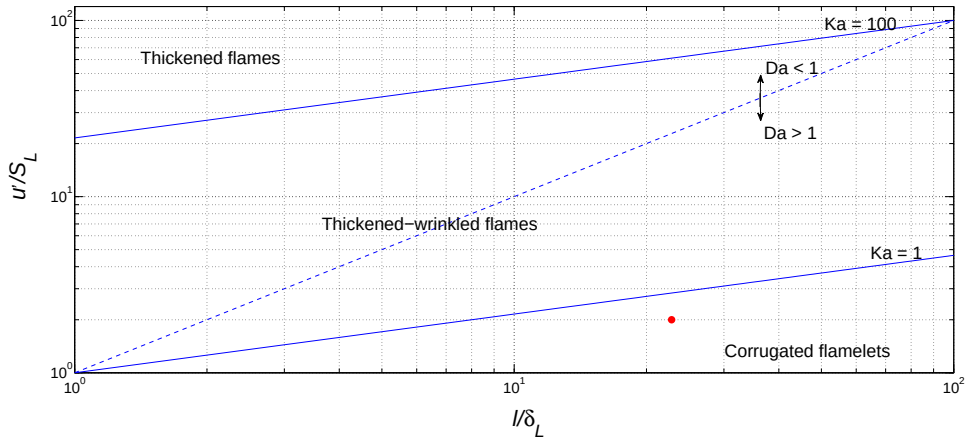

Figure 6.2: Turbulent combustion diagram. The point indicates the case under study.

flamelets' regime (Figure 6.2). Hereafter, we analyze DNS data at $t = 90$.

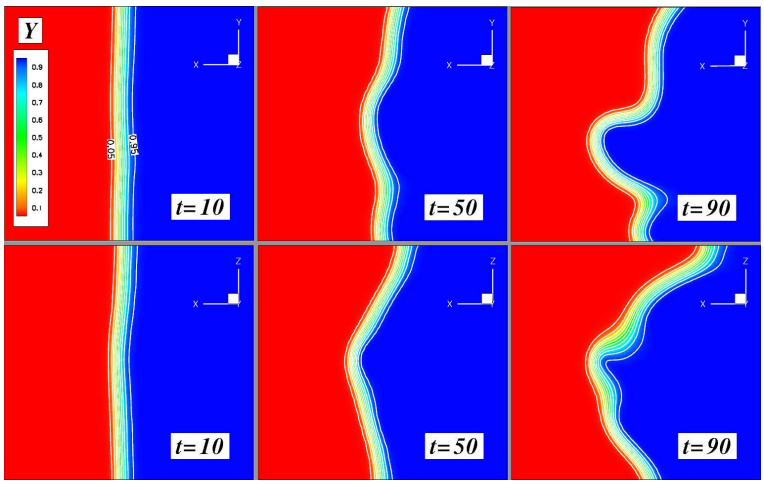

Figure 6.3: Iso-lines of reactant mas fraction at $t = 10$, 50 and 90, in the $x-y$ and $x-z$ planes.

As mentioned in Chapter 3, local scalar geometries and flow topologies interact with thermochemical processes, specific of different parts of the computational domain, which is then divided into four regions depending on the value of the reaction rate, $\dot{\omega}_Y$, and mass fraction, Y. Parts of the domain where $|\dot{\omega}_Y| < 0.001|\dot{\omega}_{Y_{max}}| = 0.0004$ (or, equivalently, $0.700 <$

$Y < 0.999$) are termed 'fresh reactants'. The 'preheat' region extends over $0.253 < Y < 0.700$ or $0.001|\dot{\omega}_{Y_{max}}| < |\dot{\omega}_Y| < 0.7|\dot{\omega}_{Y_{max}}| = 0.336$. $|\dot{\omega}_Y| > 0.7|\dot{\omega}_{Y_{max}}|$ or $0.053 < Y < 0.253$ characterizes the 'burning' region. Finally, $0.001 < Y < 0.053$, which corresponds to $|\dot{\omega}_Y| < 0.7|\dot{\omega}_{Y_{max}}|$, defines the 'hot products'. These four regions are depicted in Figure 6.4 and summarized in Table 6.2.

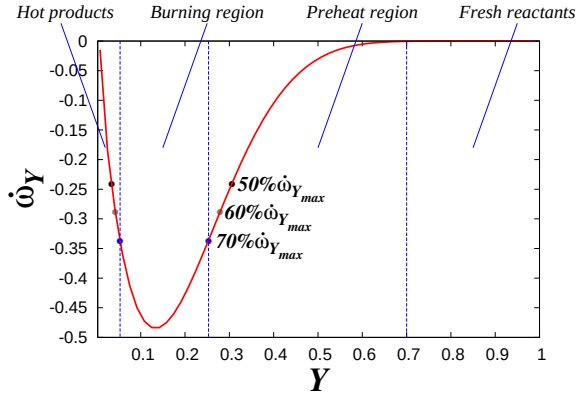

Figure 6.4: Reaction rate, $\dot{\omega}_Y$, conditional upon the mass fraction, Y. The dots upon the red line mark the limits of the reaction rate to evaluate the sensitivity of the 'burning' region. Vertical dotted lines mark the limits of the four regions of the computational domain.

Fresh reactants	$0.700 < Y < 0.999$
Preheat region	$0.253 < Y < 0.700$
Burning region	$0.053 < Y < 0.253$
Hot products	$0.001 < Y < 0.053$

Table 6.2: Ranges corresponding to scalar values for the different regions of the computational domain.

In order to evaluate the adequate limit of $\dot{\omega}_Y$ for the 'burning' region, the joint pdf of the mean and Gauss curvatures, k_m and k_g, selecting $|\dot{\omega}_Y| > 0.5|\dot{\omega}_{Y_{max}}|$, $|\dot{\omega}_Y| > 0.6|\dot{\omega}_{Y_{max}}|$, and $|\dot{\omega}_Y| > 0.7|\dot{\omega}_{Y_{max}}|$ have been calculated

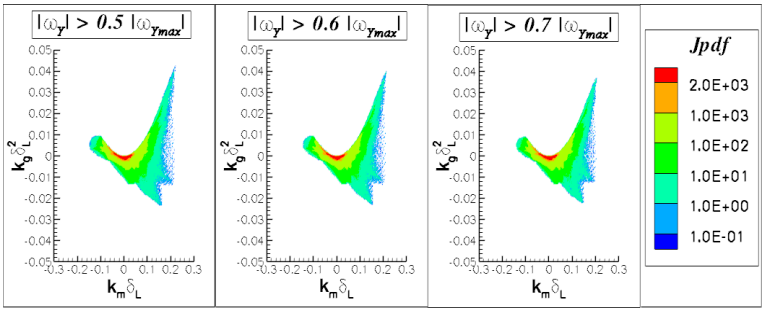

Figure 6.5: Joint pdf of the mean and Gauss curvatures, k_m and k_g, characterized by different limits of the reaction rate to evaluate the 'burning' region. k_m and k_g have been normalized with the flame thickness, δ_L. Joint pdf magnitudes decrease from the center to the circumference.

and the result is shown in Figure 6.5. These reaction-conditioned limits are also depicted like points upon the red line of $\dot{\omega}_Y$ in Figure 6.4. All the joint pdf's of k_m and k_g display maxima for nearly flat iso-scalar surfaces and are skewed towards positive values of k_m. It can be noted that the sensitivity of results is small to changes in the definition of the 'reacting' region. As $|\dot{\omega}_Y| > 0.7|\dot{\omega}_{Y_{max}}|$ is the nearest the maximum reaction rate value, hereafter, results of 'burning' region will be analyzed using this limit.

6.3.1 Structure of the scalar field in terms of the mean and Gauss curvatures

In order to provide information about the shape of the iso-scalar surfaces and their curvature, Figure 6.6 shows the joint pdf of the mean and Gauss curvatures, k_m and k_g, calculated in the four regions of the computational

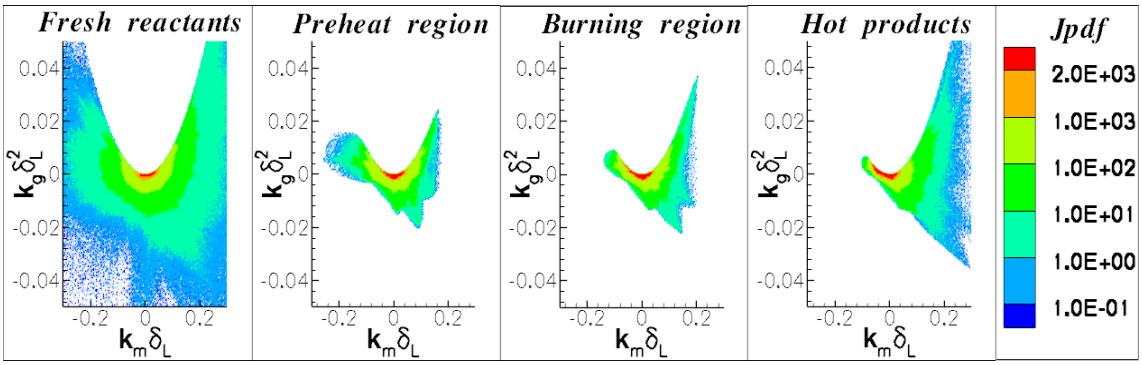

Figure 6.6: Joint pdf of the mean and Gauss curvatures, k_m and k_g. Joint pdf magnitudes decrease from the center to the circumference. k_m and k_g have been normalized with the flame thickness, δ_L.

domain. k_m and k_g have been normalized with the flame thickness, δ_L. In the 'fresh reactants', the joint pdf is slightly skewed towards positive values of k_m, reflecting the features of initially imposed and evolving small-scale turbulent structures and scalar field upstream of zones of intense heat and mass diffusive/reactive activity. These processes drastically discriminate against large values of k_m and k_g in both the 'preheat' and 'burning' regions; the probability of highly concave and convex iso-scalar surfaces, of a marked either elliptic or hyperbolic nature, significantly decreases as the heat transfer and chemical reaction become important. Nearly flat scalar geometries are the most probable ones in all four regions. Slightly concave scalar iso-surfaces occur in the 'preheat' region, but they become less probable in the 'burning' zone and 'hot products', very likely due to the heat conduction enhancement or focusing, with a reduction of $k_m < 0$, by concave geometries. Convex iso-surfaces with moderate values of k_m, pre-

dominantly of an elliptic cup-like structure, survive in the 'hot products'.

6.3.2 Non-material surface propagation velocity

Before studying the non-material surface propagation velocity or displacement speed of the iso-scalar surfaces, V^Y, it is important to check the contribution due to the molecular diffusion processes. The balance between these molecular diffusion processes and the chemical reaction rate determines the behavior of the displacement speed of the iso-scalar surfaces.

The molecular diffusion rate and its contributions conditional upon the mass fraction, Y, have been calculated and the result is shown in Figure 6.7. It can be seen that the contribution to the diffusion due to the variation of ρD, $MD_{(\rho D)}$, is not negligible in the regions with high chemical activity. The term ρD decreases from $Y = 0$ to $Y = 1$ thus the derivative in the normal direction to the iso-scalar surfaces is negative and attains a maximum value in the 'preheat region'. It is important to note that the average of the spatial curvature term is close to zero, $\langle MD_{curv} \rangle \approx 0$, which implies that the influence of the curvature of the iso-scalar surfaces is negligible. The most important contribution to the molecular diffusion rate comes from $MD_{|\nabla Y|} (= D\mathbf{n} \cdot \nabla |\nabla Y|)$, which is the variation of $|\nabla Y|$ normal to the iso-surface. As D is always positive, the sign of $MD_{|\nabla Y|}$

depends on that of $\mathbf{n} \cdot \nabla|\nabla Y| = \partial|\nabla Y|/\partial x_N$. $MD_{|\nabla Y|}$, with the increasing progress variable, attains a broad maximum within the 'burning region', which indicates that the scalar gradient, $|\nabla Y|$, increases in the x_N direction; then $MD_{|\nabla Y|}$ starts decreasing and changes sign until attains a local minimum in the 'preheat region'; $MD_{|\nabla Y|} = 0$ and its change of sign point out the maximum value of $|\nabla Y|$ and its subsequent decreasing, respectively, in the x_N direction, as shown in Figure 6.8 ($|\nabla Y|$ in function of Y). Finally, in Figure 6.7, it can be noted that $(1/\rho)\nabla \cdot (\rho D \nabla Y)$ displays an almost identical variation to that of $MD_{|\nabla Y|}$, thus, the molecular diffusion rate is governed by the variation of $|\nabla Y|$ normal to the iso-surfaces.

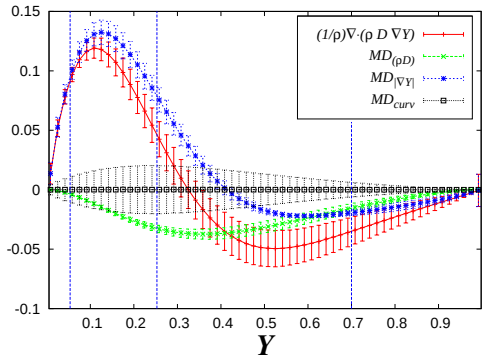

Figure 6.7: Molecular diffusion rate, $(1/\rho)\nabla \cdot (\rho D \nabla Y)$, and its contributions [Eqs.(4.77) - (4.80)] conditional upon the mass fraction, Y. Vertical solid bars in the terms indicate their respective root-mean-square values and the vertical dotted lines in figure mark the four regions of the computational domain.

The displacement speed, V^Y, and its different contributions are plotted against the mass fraction in Figure 6.9. V^Y monotonically decreases from the 'hot products' to the 'fresh gases'. It can be seen that the contribution

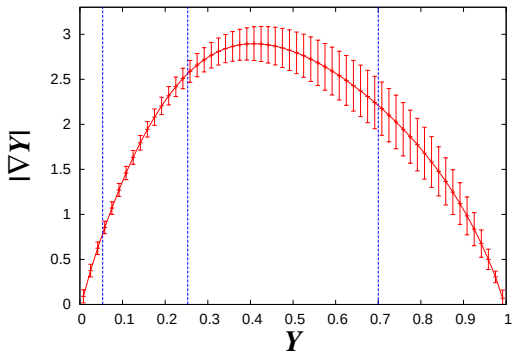

Figure 6.8: Scalar gradient modulus, $|\nabla Y|$, as a function of the reactant mass fraction. Dotted lines mark the limits of the four regions of the computational domain. $|\nabla Y|$ has been normalized with its rms value using all iso-scalar surfaces.

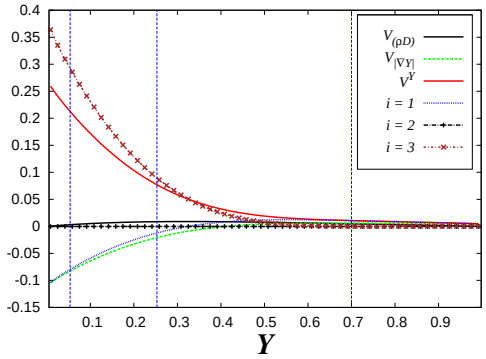

Figure 6.9: Normal propagation velocity, V^Y, and its contributions as a function of the reactant mass fraction. Vertical dotted lines mark the limits of the four regions of the computational domain.

due to the normal diffusion by variation of (ρD) is not very strong, thus, the behavior of $V_1^Y (= V_{\rho D} + V_{|\nabla Y|})$ is governed by $V_{|\nabla Y|}$. The contribution of the tangential diffusion (due to the curvature) is negligible, $V_2^Y \approx 0$, whereas the chemical contribution, V_3^Y, is always positive, as expected; only the normal diffusion, V_1^Y, contributes negatively for $Y < 0.3$. All iso-surfaces propagate in the direction of the scalar gradient, $V^Y > 0$; the increase of

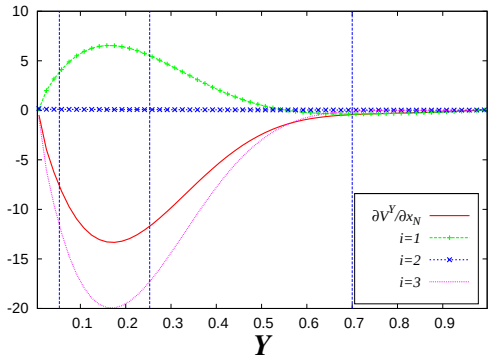

Figure 6.10: Derivative of V^Y in the direction normal to iso-scalar surfaces, x_N, and contributions to $\partial V^Y/\partial x_N$ due to normal diffusion, $(\partial V^Y/\partial x_N)_1$, tangential diffusion (curvature), $(\partial V^Y/\partial x_N)_2$, and chemical reaction, $(\partial V^Y/\partial x_N)_3$. Vertical dotted lines mark the limits of the four regions of the computational domain.

V^Y towards the burnt gases is due to the fact that the large positive values of V_3 are greater in magnitude than the large negative V_1, this allows that iso-scalar surfaces located in the 'hot products' and the 'burning' region propagate faster than those in the 'fresh gases', which reduces the distance between iso-surfaces and increases the scalar gradient.

Figure 6.10 shows $\partial V^Y/\partial x_N$ conditioned on the mass fraction Y, as well as the normal and curvature diffusions and the chemical contributions. $\partial V^Y/\partial x_N$ can be interpreted as an added normal strain rate due to the combined action of diffusion and chemistry. The time rate of change of an infinitesimal area on an iso-scalar surface and the infinitesimal distance between two iso-surfaces depend on their propagation speed relative to the fluid, according to Eqs. (4.64) and (4.69). $\partial V^Y/\partial x_N$ is negative for all values of Y, thus, two iso-scalar surfaces tend to get closer to each other

enhancing the mixing rate. Mean curvature effects are negligible, whereas the chemical term, $(\partial V^Y/\partial x_N)_3$ is the main drivers of $\partial V^Y/\partial x_N$ since the term involving normal derivative of the diffusion coefficient, $(\partial V^Y/\partial x_N)_1$, has only a minor contribution.

6.3.3 Local strain rates

Local scalar molecular fluxes are proportional to mass fraction gradients, which depend on the flow strain rate normal to the iso-scalar surfaces, a_N, whereas tangential strain rate, a_T, influences the surface stretching. Flows with significant density changes, due, for example, to chemical heat generation, will presumably undergo large volumetric dilatation rates. Intuitively, this situation may lead to mostly positive values for both tangential and normal strain rates [69]; the former will imply iso-scalar surface stretching, whereas the latter will, in principle, yield a reduction of the scalar-gradient modulus, as iso-surfaces separate. This fact seems to contradict the notion of dissipation of composition inhomogeneities by scalar molecular transport. In order to discuss this latter physical explanation, it is important to analyze the stretching induced by the turbulent velocity field through a_N, a_T and the correlations of the local volumetric dilatation with the scalar field features.

Figure 6.11(a) shows a zoom of a $x - y$ plane of the computational do-

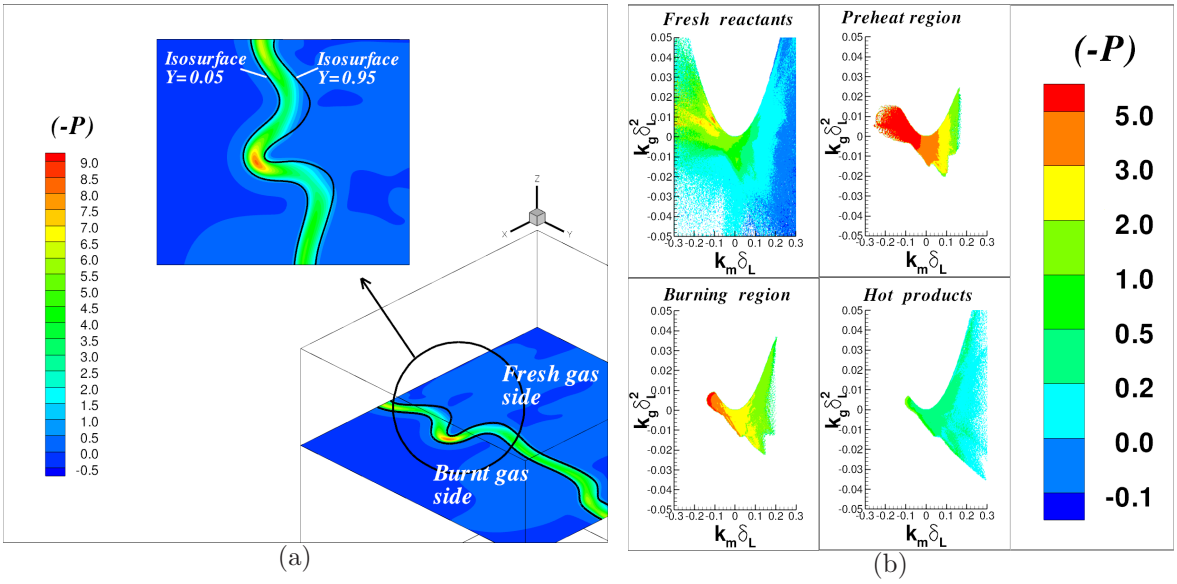

Figure 6.11: (a) Fluid element dilatation rate, $-P = \nabla \cdot \mathbf{u}$, in the computational domain. (b) $-P$ conditional upon the mean and Gauss curvatures, k_m and k_g. The volumetric dilatation rate has been normalized with $\langle Q_W \rangle^{1/2}$.

main, which displays two scalar iso-lines and the volumetric dilatation rate, $-P = \nabla \cdot \mathbf{u}$. Figure 6.11(b) shows $-P$ conditional upon the mean and Gauss curvatures, k_m and k_g. In both figures, there is a correlation between the local dilatation rate and scalar geometries. Expansive (compressive) volumetric dilatations rates are mainly associated to concave and flat (convex) iso-scalar surfaces, in agreement with previous results [63]. Cup-like elliptic concave geometries in the 'preheat' and 'burning' regions correlate with the highest values of $-P$; this behavior can be explained by the heat conduction focussing (defocussing) by concave (convex) geometries. It should also be noted that small compressive rates prevail for convex and concave iso-surfaces in both the 'fresh reactants' and the

'hot products' zones, while this tendency disappears in the 'preheat' and 'burning' regions due to the high chemical heat release.

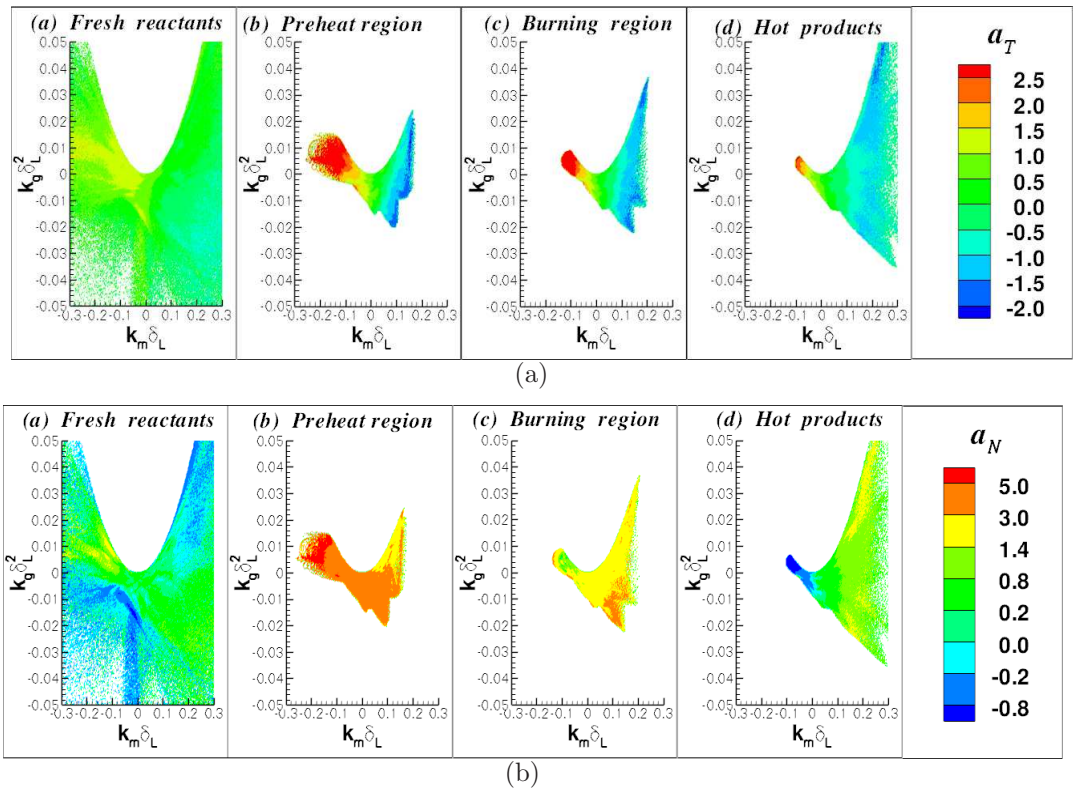

Figure 6.12: (a) Tangential a_T, and (b) normal a_N strain rates conditional upon the mean and Gauss curvatures, k_m and k_g. The terms have been normalized with $\langle Q_W \rangle^{1/2}$.

The correlations between the local volumetric dilatation rate, $-P$, and the iso-scalar surfaces can be analyzed through the strain rates. As mentioned previously in Section 4.3.2, the volumetric dilatation rate can be decomposed as: $-P = a_T + a_N = \nabla \cdot \mathbf{u}$ [53, 76, 70, 72]. Generally, the tangential strain rate, a_T, has been used to explain some premixed and non-premixed flame features [76, 53]. Figure 6.12 plots the tangential and the normal strain rates, a_T and a_N, as functions of k_m and k_g in the four regions of

the computational domain. a_T exhibits similar curvature dependent features to $-P$, although negative strain-rates do appear for convex scalar iso-surfaces. Thermal transport yields only positive values of a_N in the 'preheating' and 'burning' regions; negative a'_Ns occur for both concave (mainly hyperbolic) and convex structures in the 'fresh reactants', and for concave geometries in the 'hot products'. In the zones with high chemical activity there is no a strong curvature dependence of a_N. Thus, the correlations between local dilatation rate and scalar geometries come from the dependence of a_T on the curvature.

Figure 6.13 represents $-P$, a_T and a_N as a function of Y. Vertical dotted lines mark the limits of the four $\dot{\omega}_Y$-conditioned regions of the computational domain. The average of a_T remains almost constant, with large fluctuations, whereas a_N displays an almost identical variation to that of $-P$. Positive values of all three variables are predominant, with some probability of negative values of a_T for all values of Y and of a_N for $Y > 0.94$ ('fresh reactants') and $Y < 0.06$ ('hot products'); Chakraborty *et al.* [72] show similar results in DNS of turbulent premixed flames with Lewis number unity. Mainly positive values of a_N in Figure 6.13(c) should, in principle, lead to diminishing scalar gradients [72, 113], particularly in the 'preheat' ($0.253 < Y < 0.700$) and 'burning' ($0.053 < Y < 0.253$) regions where maxima of $|\nabla Y|$ occur (Figure 6.8, $|\nabla Y|$ in function of Y). This result

seems counterintuitive and difficult to interpret in the absence of the 'additional' normal strain rate, $\partial V^Y/\partial x_N$.

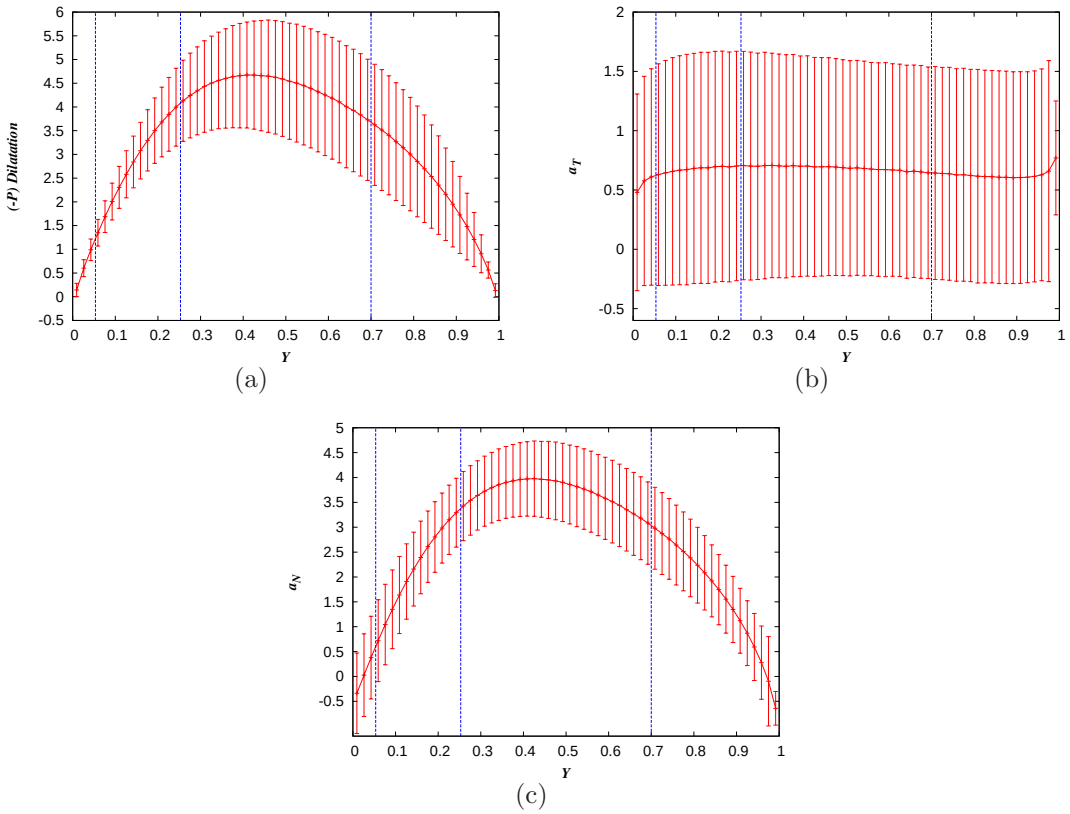

Figure 6.13: (a) Local fluid volumetric dilatation rate, (b) tangential strain rate and (c) normal strain rate as a function of the reactant mass fraction. Vertical bars indicate the rms values of the variables. Dotted lines mark the limits of the four regions of the computational domain.

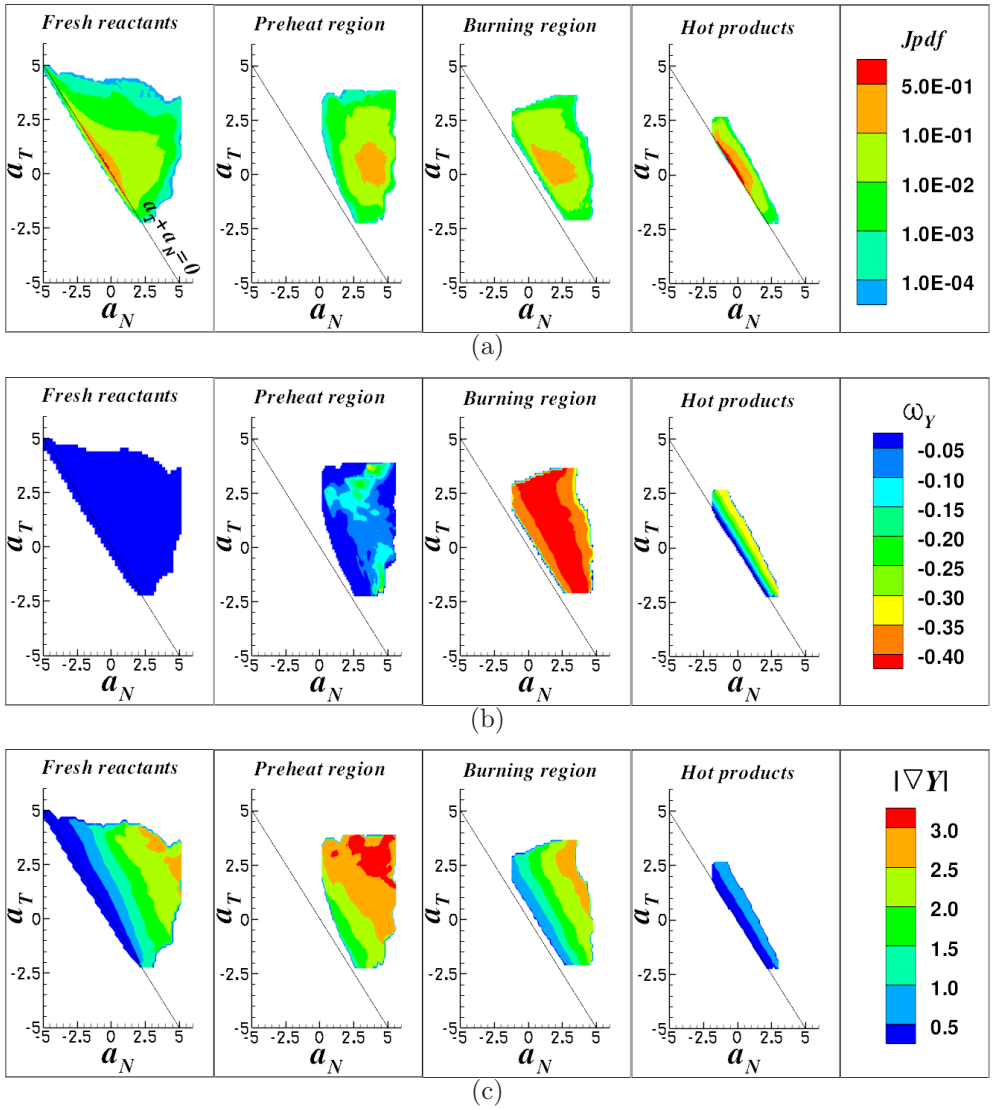

Figure 6.14: (a) Joint pdf of the normal and tangential strain rates, a_N and a_T. (b) Reaction rate, $\dot{\omega}_Y$, and (c) scalar gradient modulus, $|\nabla Y|$, conditional upon the normal and tangential strain rates.

Figure 6.14 depicts the joint pdf of a_N and a_T, and $\dot{\omega}_Y$ and $|\nabla Y|$ conditioned to a_N and a_T in the four regions defined for different levels of reaction rate. The regions with the most probable values are mainly located above the line $a_N + a_T = 0$, consistent with the fact that most fluid elements

undergo expansion; both 'fresh reactants' and 'hot products' share the highest probabilities for low volumetric dilatation rates with zone under $a_N + a_T = 0$ indicating that there are regions with fluid elements undergo compression; significant expansions in the 'preheating' and 'burning' regions imply positive normal strain, with both signs for a_T. Maximum reaction rates occur, mainly for $a_N > 0$ and a_T either positive or negative, in the 'burning' region, which is a proof of consistency in the definition of that zone. Maxima of $|\nabla Y|$, or equivalently the scalar dissipation rate, are coincident with $a_N > 0$; this unexpected result seems counterintuitive and can only be explained by the chemical enhancement of existing scalar gradients which might balance the reduction due to positive a'_Ns. The combination of a_N and a_T can also be useful to detect certain flow topologies in the flame zones, for instance in the regions above the line $a_N + a_T = 0$ could exist flow topologies with expansive features, such as S2 (UN/S/S) and S8 (UN/UN/UN).

Figure 6.15 depicts the flow strain rates, a_T and a_N, the additional contributions due to V^Y and $\partial V^Y/\partial x_N$, respectively, and the *'effective'* tangential, $(a_T + 2k_m V^Y)$, and normal, $(a_N + \partial V^Y/\partial x_N)$, strain rates for nonmaterial iso-surfaces. Vertical rms bars indicate very large fluctuations of $2k_m V^Y$ compared to its mean value, whereas variations associated to a_T, a_N and $\partial V^Y/\partial x_N$ are rather small. This is likely due to significant

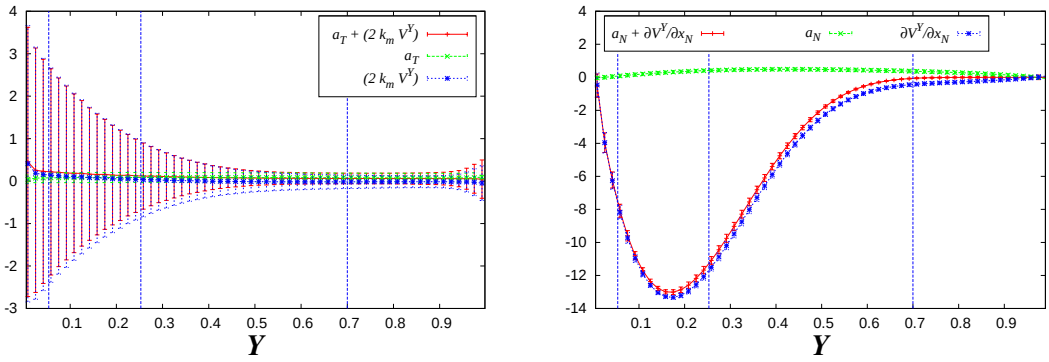

(a) (b)

Figure 6.15: Variables as functions of the mass fraction. (a) *'Effective'* tangential strain rate and its contributions, a_T and $2k_mV^Y$ and (b) *'effective'* normal strain rate and its contributions, a_N and $\partial V^Y/\partial x_N$. Vertical dotted lines mark the limits of the four regions of the computational domain. The variables have been normalized with τ_η.

iso-surface corrugation. The curvature-propagation contribution, implies surface generation by the displacement of convex iso-scalar surfaces and yields surface reduction for concave iso-scalar surface propagation. The contributions of a_T and $2k_mV^Y$ to the 'effective tangential strain rate' are apparently comparable, except in the 'hot products'. $\partial V^Y/\partial x_N$ is large, compared to a_N, and negative for all values of Y, which makes the *'effective'* normal strain rate, $(a_N + \partial V^Y/\partial x_N)$, negative everywhere. While $a_N > 0$ tends to separate two neighboring iso-scalar surfaces and diminishes $|\nabla Y|$, $\partial V^Y/\partial x_N < 0$ will draw them closer to each other and enhance scalar-gradients. Eqs.(4.64) and (4.69) provide strong mathematical bases to designate $(a_T + 2k_mV^Y)$ and $(a_N + \partial V^Y/\partial x_N)$ *'effective'* tangential and normal strain rates, respectively. They stretch non-material infinitesimal surfaces located on $Y(\mathbf{x}, t) = \Gamma$ and dilate infinitesimal normal distances

between $Y = \Gamma$ and $Y = \Gamma + \Delta\Gamma$.

Figure 6.16 depicts the joint PDF of the *'effective'* normal and tangential strain rates, and $\dot{\omega}_Y$ and $(1/\rho)\nabla \cdot (\rho D \nabla Y)$ conditioned upon $(a_N + \partial V^Y/\partial x_N)$ and $(a_T + 2k_m V^Y)$ in the four 'reacting' regions. In the 'fresh reactants' $(a_N + \partial V^Y/\partial x_N)$ is mostly positive and $(a_T + 2k_m V^Y)$ is mainly negative with most probable values near the origin; this implies separation of iso-surfaces with their area elements shrinking. In the 'preheat' and 'burning' regions and in the 'hot products' the *'effective'* normal strain rate is always negative; $(a_T + 2k_m V^Y)$ displays both positive and negative values in the 'preheating' zone showing some degree of symmetry about the zero value, while positive quantities become more probable in the 'burning' region; most probable normal and tangential *'effective'* strain rates locate also near the origin in the 'hot' products. The reaction rate in the 'preheat' and 'burning' regions depends solely on the *'effective'* normal strain rate; this is also true to some extent in the 'hot' products for significant values of the chemical conversion. The molecular diffusion rate depends on both strain rates as it is apparent from Eq.(4.77); significant values of molecular transport occur always for large negative *'effective'* normal strain rates and both positive and negative *'effective'* tangential strain rates. Any infinitesimal non-material volume element appended to an iso-scalar surface will undergo contraction in the direction normal to the iso-surface and ei-

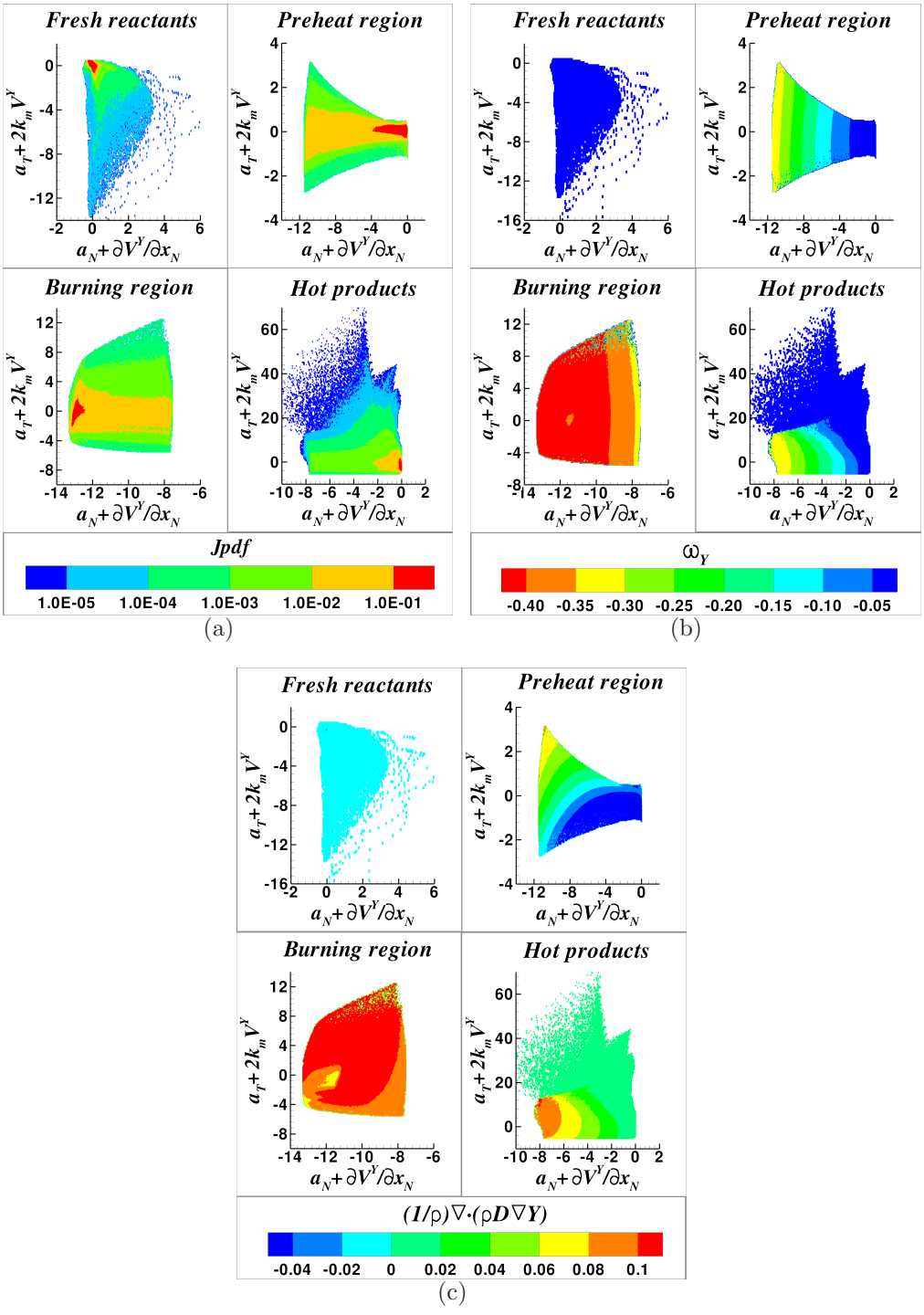

Figure 6.16: (Color online) (a) Joint pdf of the line and surface stretches, $a_N + \partial V^Y/\partial x_N$ and $a_T + 2k_m V^Y$. (b) Reaction rate, $\dot{\omega}_Y$, and (c) molecular diffusion rate, $(1/\rho)\nabla\cdot(\rho D\nabla Y)$, conditional upon the line and surface stretches.

ther positive or negative area tangential stretching. The thermal expansion and scalar conversion, resulting from the chemical reaction rate, given by Eq.(6.25) and Fickian molecular diffusion, Eq.(4.77), yield the previously described behavior.

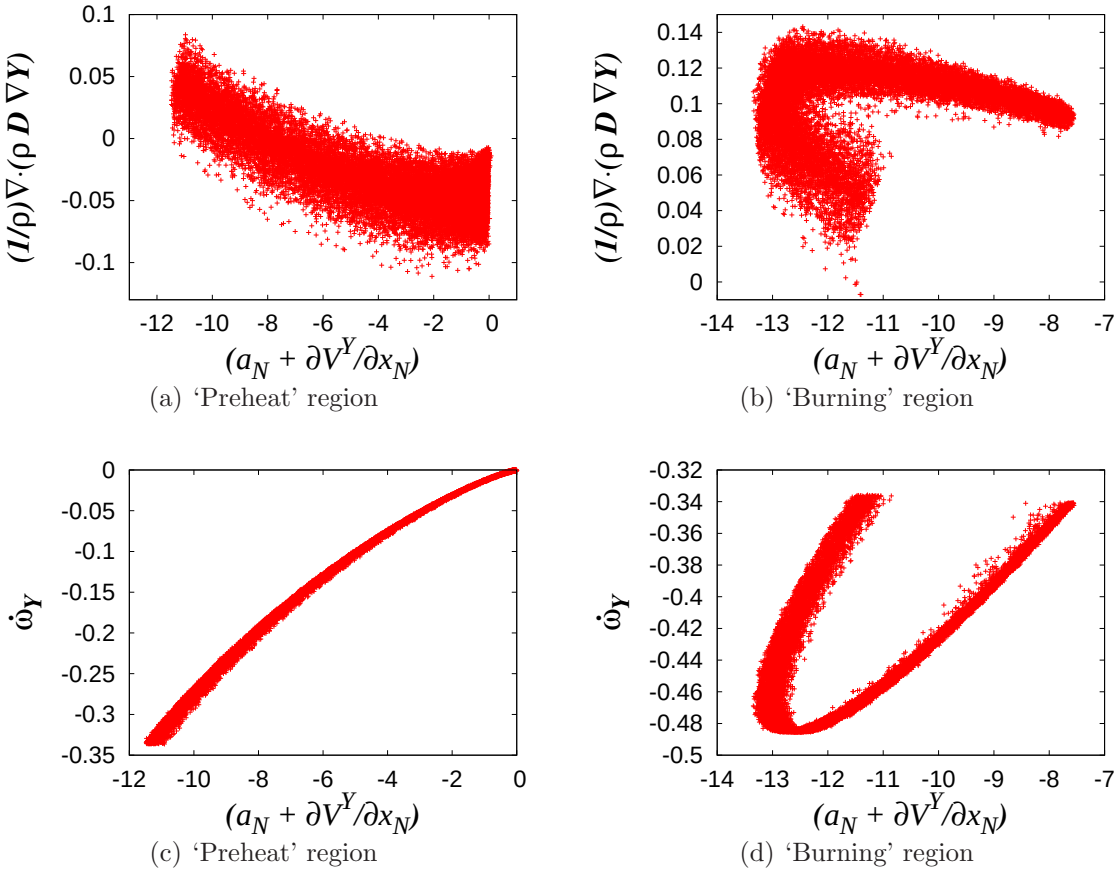

(a) 'Preheat' region (b) 'Burning' region

(c) 'Preheat' region (d) 'Burning' region

Figure 6.17: (a), (b) Molecular diffusion and (c), (d) chemical reaction rates as functions of the *'effective'* normal strain rate in the 'preheat' and 'burning' regions.

Figure 6.17 presents scatter plots of the molecular diffusion and the chemical reaction terms as functions of the *'effective'* normal strain rate in both the 'preheat' and the 'burning' regions. Correlations are apparent

between diffusion or reaction and the *'effective'* normal strain rates in the preheat region; the additional functional dependence of the diffusion term on the scalar mass fraction should be such that its sign changes at around $(a_N + \partial V^Y/\partial x_N) = -7.5$ in the 'preheat' region; the larger the absolute value of the *'effective'* normal strain rate the higher the reaction rate in the preheat zone. On the other hand, the two branches observed in the 'burning' region obviously correspond to values to the left and the right sides of the minimum of $(a_N + \partial V^Y/\partial x_N)$ as a function of Y (Figure 6.15); the upper branch of the molecular diffusion belongs to values of strain rates to the left of that minimum, whereas the lower branch pertains to those to its right; the upper (lower) branch of the chemical conversion correlates with effective normal strain rates to the right (left) side of its minimum. The lower (upper) branch of the molecular diffusion (chemical source) term in the burning region could be easily assigned to the preheat zone by redefining the limit between the two.

6.3.4 Small-scale flow structures

The orientation of the unit vector normal to iso-scalar surfaces with respect to the strain rate eigenvector and the local vorticity will be investigated in this section. First of all, we turn our attention in the eigenvalues of the strain rate tensor Λ_1, Λ_2 and Λ_3, which are ordered from the largest to the

smallest value. For combusting flows with significant heat release the sum of the eigenvalues ($\Lambda_1+\Lambda_2+\Lambda_3 = \nabla\cdot\mathbf{u}$) is distinct of zero (see Eq. (4.41)).

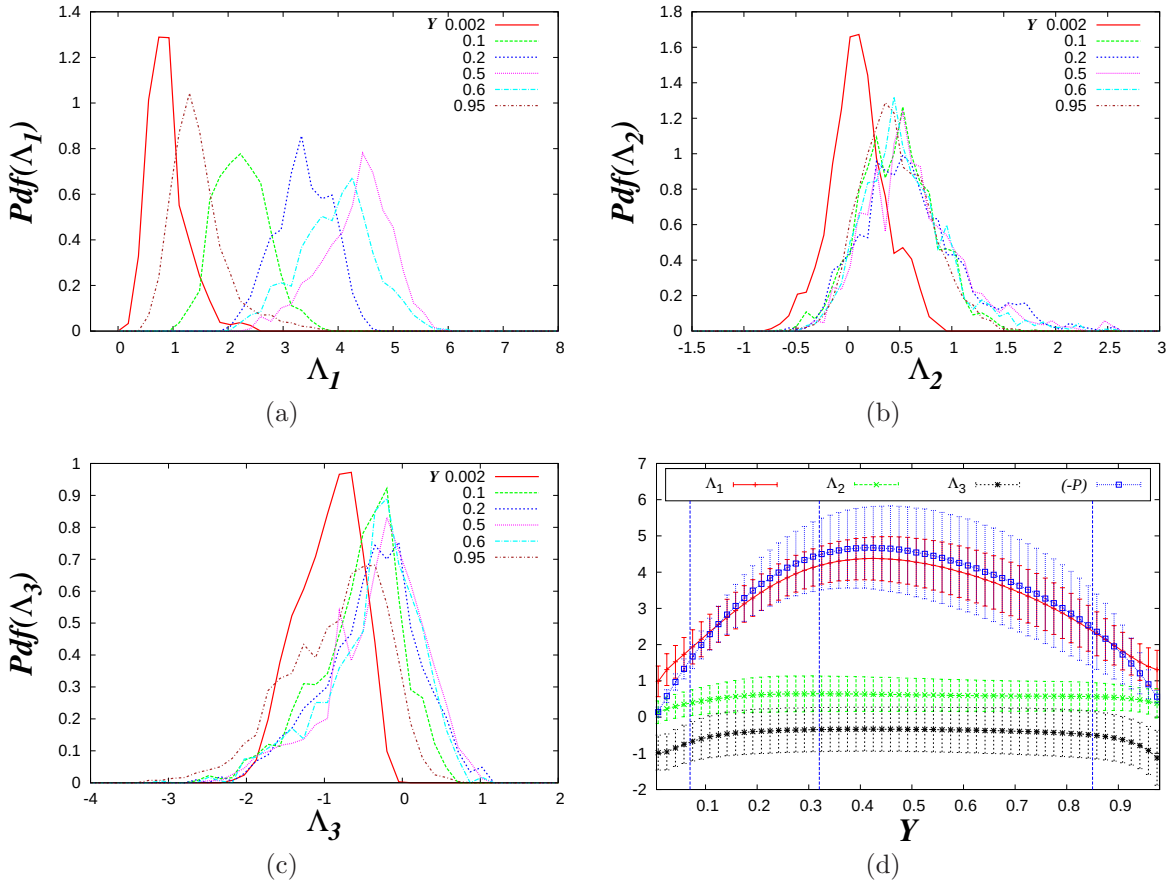

Figure 6.18: Eigenvalues of the strain rate tensor. (a) Pdf of Λ_1, (b) Λ_2 and (c) Λ_3 for different levels of Y. (d) Eigenvalues as a function of Y. The eigenvalues have been normalized with $\langle Q_W\rangle^{1/2}$.

The resulting probability density functions of the eigenvalues of the strain rate tensor for different levels of mass fraction are shown in Figure 6.18. The eigenvalues have been normalized with $\langle Q_W\rangle^{1/2}$. It can be noticed as the distributions of the most extensive and compressive eigenvalues, Λ_1 and Λ_3, are more affected than the intermediate eigenvalue, Λ_2, as fluid elements

move towards the regions with high chemical activity. There is a high probability of finding positive values of Λ_3 in the 'preheat' and 'burning' regions. It can be seen as the 'fresh' reactants and 'hot' products share the highest probability for low volumetric dilatation rates since the sum of the averages of the three eigenvalues tends to zero. This facts indicates a decrease of the strain rates in the 'fresh' and 'burnt' gases regions of the computational domain. Figure 6.18(d) summarizes the previous results since it shows the eigenvalues as a function of the mass fraction; vertical solid bars indicate their respective rms values. It is interesting to note that Λ_1 displays an almost identical variation to those of $-P$ and a_N of Figure 6.13, which is in agreement with the fact that most fluid elements undergo expansion.

As every eigenvalue of the strain rate tensor have its corresponding eigenvector, it is important to examine how the eigenvectors are oriented with respect to iso-scalar surfaces; the alignment of the eigenvectors with the normal unit vector indicates how are aligned the nodal topologies of the turbulent flow with respect to iso-scalar surfaces. Figure 6.19 depicts the pdf's of the cosine of the angle between the normal vector to the iso-scalar surfaces, $\mathbf{n}$, and the strain rate principal directions, $\mathbf{e}_i$, calculated for the whole flow domain. $\mathbf{e}_1$ is the eigenvector corresponding to the most extensive eigenvalue; the subindex i orders the eigenvectors by decreasing

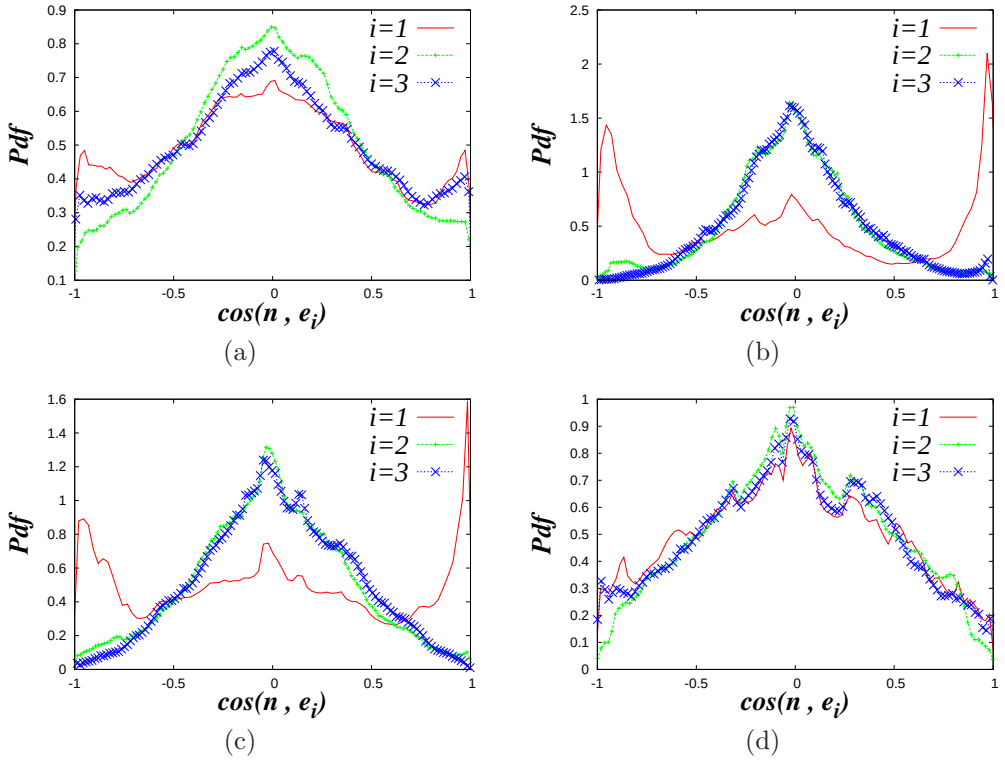

Figure 6.19: Pdf's of cos($\mathbf{n}$, $\mathbf{e}_i$). $\mathbf{n}$ is the unit vector normal to the iso-scalar surfaces and $\mathbf{e}_i$ stands for the eigenvectors of S_{ij}. The subindex of $\mathbf{e}_i$ denotes one of the three eigenvalues, ordered by decreasing values. $i = 1$ corresponds to the most extensive (positive) eigenvalue. (a) Fresh reactants, (b) preheat region, (c) burning region, (d) hot products.

corresponding eigenvalues. $\mathbf{n}$ is predominantly aligned with the eigenvector corresponding to the most extensive eigenvalue in the 'preheating' and 'burning' regions, which is in agreement with recent numerical [72, 113, 114] and experimental results [115]. $\mathbf{n}$ exhibits a slight alignment with the most compressive eigenvalue, $\mathbf{e}_3$, in the 'fresh reactants', where the heat release is weak and iso-scalar surfaces behave like those in non-reacting constant-density turbulent flows [12, 71]. There is no preferred alignment in the 'hot products' region.

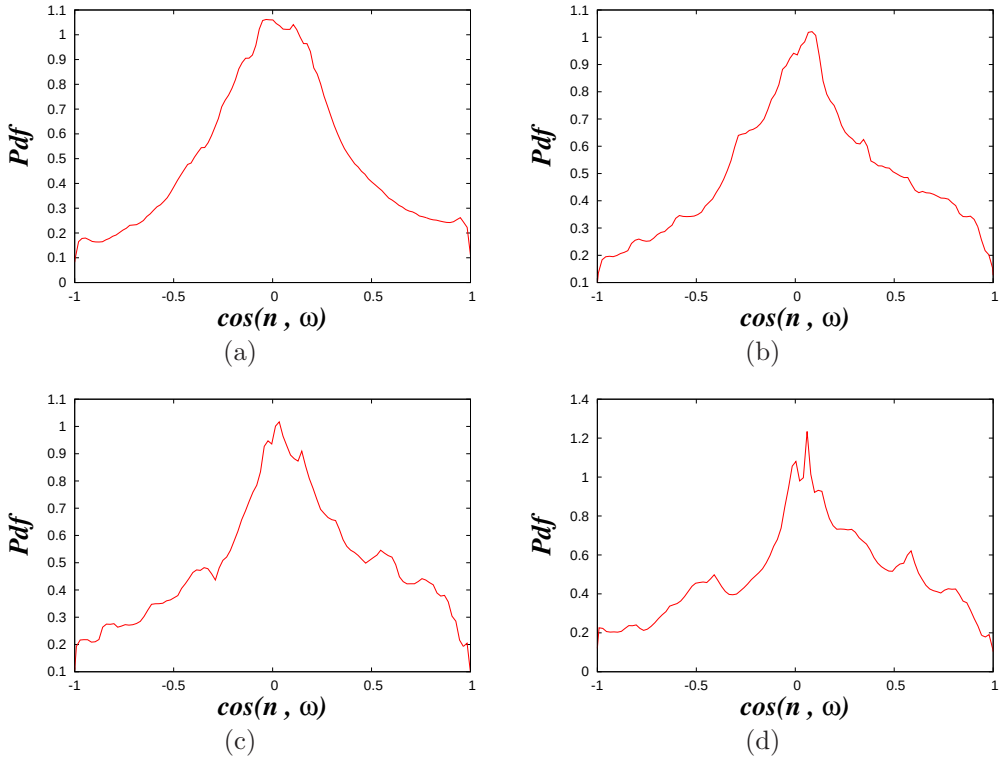

Figure 6.20: Pdf's of cos(**n**, $\boldsymbol{\omega}$). **n** is the unit vector normal to iso-scalar surfaces. $\boldsymbol{\omega}$ is the local vorticity vector. (a) Fresh reactants, (b) preheat region, (c) burning region, (d) hot products.

In order to study the alignment of the focal topologies of the turbulent flow with the iso-scalar surfaces, the alignment of vorticity vector, $\boldsymbol{\omega}$, with the normal vector, **n**, has been calculated. Figure 6.20 plots the pdf's of the cosine between **n** and the local vorticity vector. It can be seen that the vorticity vector results preferentially tangential to the iso-scalar surfaces, as it results in the incompressible case (see Figure 5.14). Thus, it contributes to curve and fold the iso-surfaces. This process can be more complex, as the joint action of two vortical structures, either co-rotating or counter-rotating, may also stretch and/or bend the surface.

6.3.4.1 Invariants of the velocity-gradient tensor and local flow topologies

Nodal and focal topologies can be investigated through the study of the invariants of the velocity-gradient tensor. As mentioned in Chapter 2, Section 4.2.1, for combusting flows with significant heat release there are four more flow topologies (from S5 to S8, see Table 4.2), which have not yet been analyzed to the best of our knowledge. In this section, the first invariant of the velocity-gradient tensor, P, will not be analyzed since it was scrutinized in Section 6.3.3. We now turn our attention to the other invariants as well as in the interaction of local flow topologies with the iso-scalar geometries.

The second invariant of the velocity-gradient tensor, Q, represents the additive contribution of enstrophy, $Q_W(\equiv \omega_i\omega_i/4)$, and dilatation/dissipation, $Q_S(\equiv (P^2 - S_{ij}S_{ij})/2)$. For flows with non constant density, the dynamical equations for the enstrophy and the strain are as follows [103]:

$$\frac{1}{2}\frac{D\boldsymbol{\omega}^2}{Dt} = \omega_i S_{ik}\omega_k - \omega_i\omega_i S_{kk} - \frac{\omega_i}{\rho^2}\nabla\rho\times\nabla p + \omega_i\, curl\left(\frac{1}{\rho}\frac{\partial\tau_{ik}}{\partial x_k}\right), \quad (6.45)$$

$$\frac{1}{2}\frac{D\mathbf{s}^2}{Dt} = -S_{ik}S_{ij}S_{jk} - \frac{1}{4}\omega_i S_{ik}\omega_k + \frac{1}{4}\omega_i\omega_i S_{kk} - \frac{S_{ik}}{2}\left[\frac{\partial}{\partial x_k}\left(\frac{1}{\rho}\frac{\partial p}{\partial x_i}\right) + \frac{\partial}{\partial x_i}\left(\frac{1}{\rho}\frac{\partial p}{\partial x_k}\right)\right] + \frac{S_{ik}}{2}\left[\frac{\partial}{\partial x_k}\left(\frac{1}{\rho}\frac{\partial \tau_{ij}}{\partial x_j}\right) + \frac{\partial}{\partial x_i}\left(\frac{1}{\rho}\frac{\partial \tau_{kj}}{\partial x_j}\right)\right] . \quad (6.46)$$

The terms $\omega_i S_{ik}\omega_k - \omega_i\omega_i S_{kk}$ in (6.45) are the enstrophy production and enter the definition of the third invariant of the velocity-gradient tensor, R, as well as the dissipation rate generation, $-S_{ik}S_{ij}S_{jk}(\equiv -\Lambda_1\Lambda_2\Lambda_3)$, of Eq. (6.46) (*cf.* Chapter 2, Section (4.2.1)). Figure 6.21 depicts Q, Q_S, Q_W, R, R_S, and $(\omega_i\omega_i S_{kk} - \omega_i S_{ij}\omega_j)/4$ as a function of the reactant mass fraction. The seconds and thirds invariants have been normalized with $\langle Q_W\rangle$ and $\langle Q_W\rangle^{3/2}$, respectively.

As shown Figure 6.21(a) the mean of Q_S is negative in the 'fresh' reactants, where the heat release is weak; it behaves like those of turbulent mixing to constant-density. With decreasing of mass fraction, Q_S attains a maximum within the 'preheat' region and then starts decreasing; the maximum value is due to the dilatation term, P^2, which enter its definition. Q_S changes sign in the 'burning' region and attains a minimum within the 'hot' products region. The local enstrophy, Q_W, is always positive and attains a maximum towards the 'fresh' gases and starts decreasing as fluid elements move towards the regions with high chemical activity; obviously,

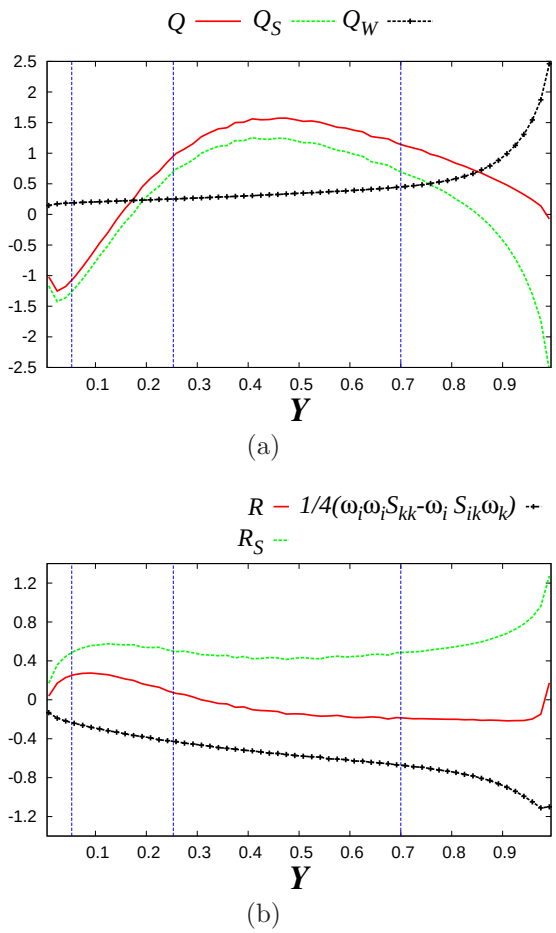

Figure 6.21: (a) Q, Q_S, Q_W, and (b) R, R_S, $1/4(\omega_i\omega_i S_{kk} - \omega_i S_{ik}\omega_k)$ as functions of the reactant mass fraction. Vertical dotted lines mark the limits of the four regions of the computational domain.

the increments of dynamic viscosity with increasing temperature destroy vorticity. The balance of these two quantities, along the mass fraction, determines the magnitude of the second invariant of the velocity-gradient tensor, Q. The magnitude of the mean of Q_W is small compared with that of Q_S through mass fraction, and the change in sign of the mean of Q is governed entirely by the behavior of Q_S; moreover, Q displays an almost

identical variation to those of Q_S.

It can be seen in Figure 6.21(b) that the average of R remains near zero, as it happens in the constant-density case (see Figure 5.16). The third invariant of the symmetric strain-rate tensor, R_S, is defined as: $R_S = (-P^3+3PQ_S-S_{ik}S_{ij}S_{jk})/3$. According to previous results of Figure 6.13(a) $\langle P\rangle < 0$ from 'fresh' reactants to 'hot' products, thus, $-P^3 > 0$ and the term $3PQ_S$ is positive except in the 'fresh' and 'burnt' gases, where Q_S is negative. On the other hand, the mean of dissipation rate generation, $-S_{ik}S_{ij}S_{jk}$, is always positive because the product $\langle\Lambda_1\Lambda_2\Lambda_3\rangle$ is negative due to $\langle\Lambda_3\rangle < 0$. Thus, the balance for R_S is positive, as shown Figure 6.21(b). The enstrophy production, $\omega_i S_{ik}\omega_k - \omega_i\omega_i S_{kk}$, is positive towards the 'fresh' reactants and starts decreasing as fluid elements move towards the regions with high chemical activity; this results is related to the high values of the local enstrophy, Q_W, towards the 'fresh' gas side.

Figure 6.22 shows the resulting joint pdf's of R and Q in the four reaction rate conditioned regions of the computational domain. It is interesting to note that the universal teardrop shape remains in the 'fresh' reactants region, where the heat transfer and chemical reaction are weak, whereas the statistical distributions move towards the left side in the regions with high chemical activity; the latter result is in connection with the high volumetric dilatation rates, $P < 0$, of these regions (see Figure 4.2(c)). Jpdf's tails

decrease with decreasing of mass fraction the , which indicates that the local dissipation and enstrophy decrease towards the 'hot' products.

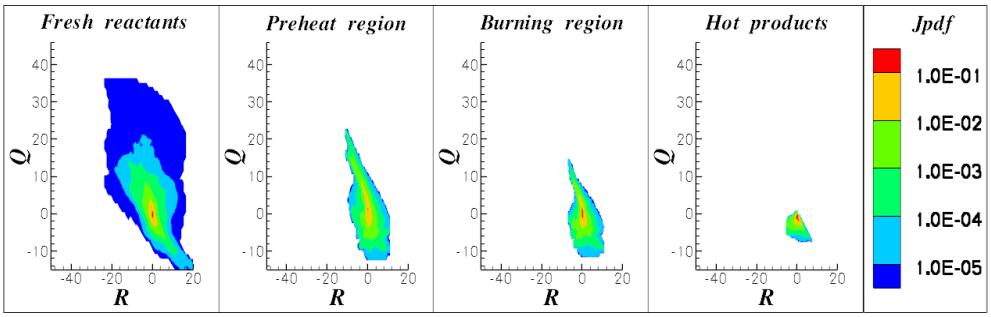

Figure 6.22: Joint pdf of $R-Q$. Joint pdf magnitudes decrease from the center to the circumference.

Zone	Description	Ranges
1	Geometries with flat curvature	$[\|k_m\delta_L\| < 0.02$ and $\|k_g\delta_L^2\| < 0.004]$
2	Geometries with predominant negative curvature	$k_m\delta_L < 0$ excluding the zone 1
3	Geometries with predominant positive curvature	$k_m\delta_L > 0$ excluding the zone 1

Table 6.3: Description of zones 1, 2 and 3 in the k_m - k_g plane.

In order to reduce the number of combinations of scalar field structures and flow topologies, we have considered only three zones in the $k_m - k_g$ plane of Figure 4.3: nearly flat (zone 1), concave (zone 2) and convex (zone 3), which are characterized by the ranges given in Table 6.3.

Figure 6.23 shows the different joint pdf's of R and Q calculated in the three curvature conditioned zones of the k_m-k_g plane and for every reaction rate region of the computational domain. S5 (SFC) and S6 (SN/SN/SN), typical of flows with local negative volumetric dilatation rates, are absent in this premixed combustion study. About 50% of the topologies in the

'fresh reactants' are focal and tend to disappear, in favor of nodal micro-structures, as the scalar value move through the 'preheating' and 'burning' regions towards the 'hot products'; obviously, positive volumetric dilatation rates and flow laminarization mechanism, due to increments of dynamic viscosity with increasing temperature, destroy enstrophy. Joint pdf's look similar to the teardrop shape of constant density flows ($P = 0$) in the 'fresh reactants', with occurrence of both stretching/compressing focuses and stable/unstable nodes; however, local topologies, characteristic of flows with volumetric expansion, S7 (UFS) and S8 (UN/UN/UN), contribute about 25%, this can be interpreted as a sign of a moderate interaction of the propagating flame with the initially imposed constant density turbulence.

Two nodal topologies, S2 (UN/S/S, 51%) and S8 (UN/UN/UN, 26%), and two focal ones, S4 (SFS, 8%) and S7 (UFS, 10%), add up to 95% over the flow domain in the 'preheat' region. Nodal, S2 (UN/S/S, 61%), S3 (SN/S/S, 7%) and S8 (UN/UN/UN, 14%), and focal, S4 (SFS, 10%), structures account for 92% of local flow topologies in the 'burning' region. Vortical structures S4 (SFS) and S7 (UFS) start both from 20% contributions in the 'fresh reactants', and decrease through the 'preheating' and 'burning' regions; however, whereas the S4 maintains a 13% share in the 'hot products', S7 almost vanishes. This could be due to the alignment of

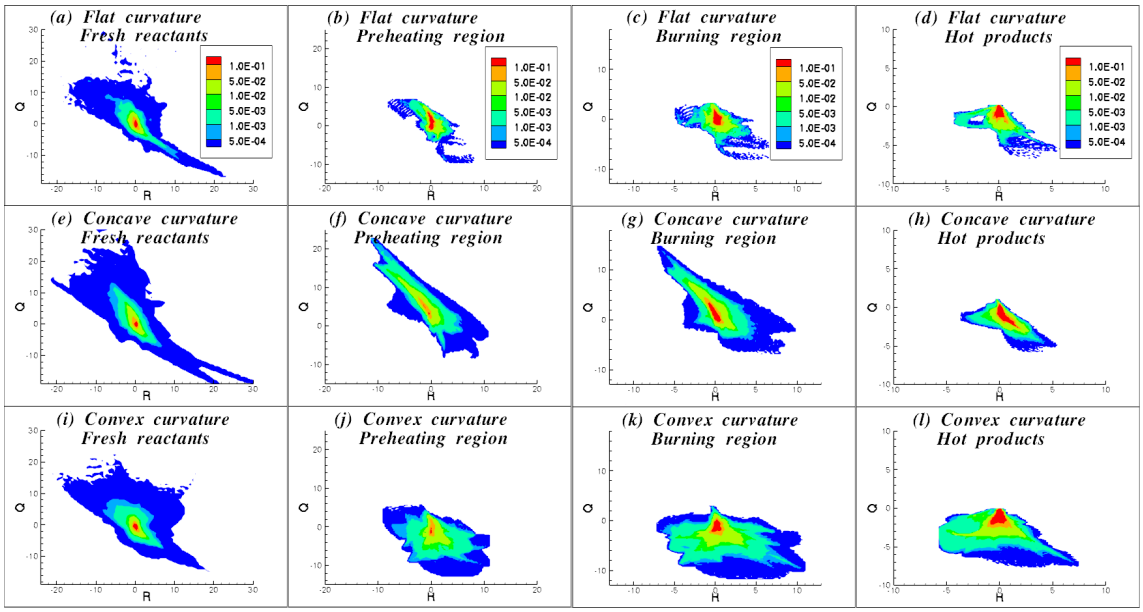

Figure 6.23: Joint pdf of $R-Q$: (a), (b), (c) and (d) zone 1 (Flat iso-surfaces); (e), (f), (g) and (h) zone 2 (Concave iso-surfaces); (i), (j), (k) and (l) zone 3 (Convex iso-surfaces). Joint pdf magnitudes decrease from the center to the circumference.

the former vorticity with an extensive eigenvector.

Figure 6.24 shows the volume fractions of the flow domain pertaining to different flow topologies, calculated for the three curvature conditioned zones. The S2 (UN/S/S) topology dominates the local flow dynamics for all three scalar geometries and all reaction-conditioned regions, with some significant contribution of S8 (UN/UN/UN) for concave iso-surfaces (in the 'preheating' and 'burning' regions). S3 (SN/S/S) for flat and convex geometries has a modest to moderate share, mainly in the 'hot products'. Figure 6.24 confirms that S7 and S8 topologies associate more likely to concave iso-scalar surfaces, where heat-conduction focusing effects enhance chemical reaction.

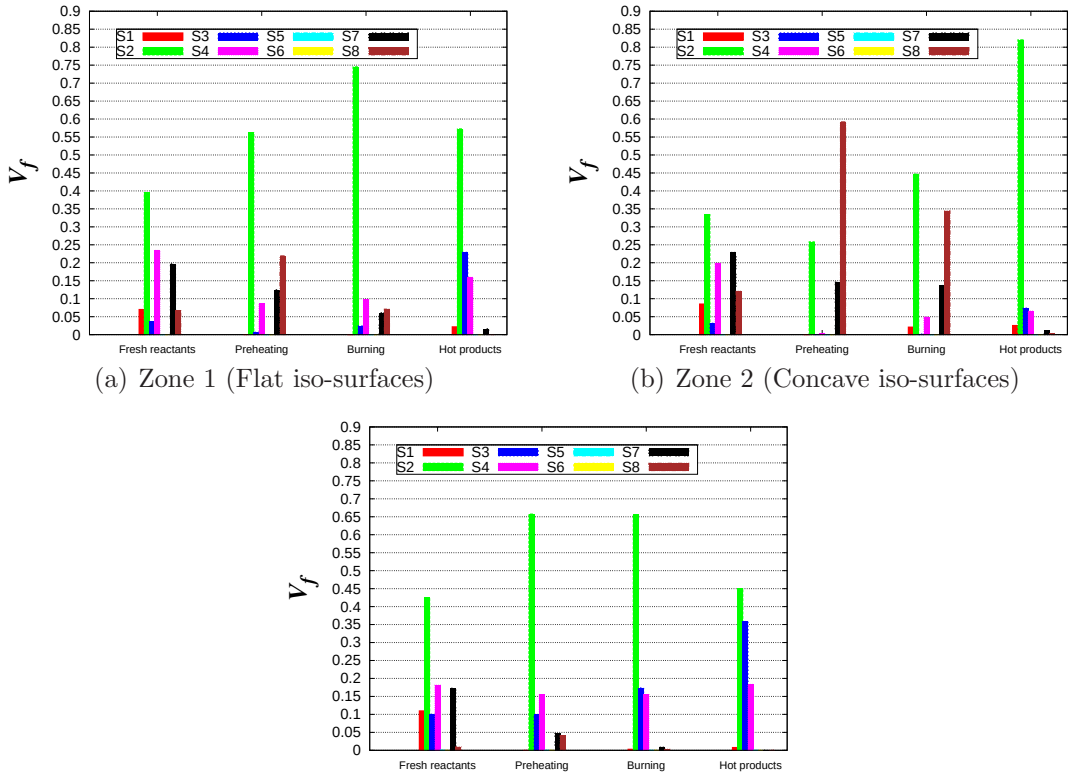

(a) Zone 1 (Flat iso-surfaces)

(b) Zone 2 (Concave iso-surfaces)

(c) Zone 3 (Convex iso-surfaces)

Figure 6.24: Topologies ($S1 - S8$) belonging to $P - Q - R$ space: (a) zone 1 (Flat iso-surfaces); (b) zone 2 (Concave iso-surfaces); (c) zone 3 (Convex iso-surfaces).

Two nodal topologies, S2 (UN/S/S) and S8 (UN/UN/UN), and two focal ones, S4 (SFS) and S7 (UFS), dominate for well over 90% of the samples in the 'preheating' and 'burning' regions. The key scalar mixing variable, $|\nabla Y|$, conditioned to a_N and a_T is shown in Figure 6.25 for the previous four topologies and for the three scalar geometries. These topologies for flat and concave scalar geometries are characterized by $a_N > 0$ and $a_T > 0$ with maxima of $|\nabla Y|$ far from the constant density line $a_T + a_N = 0$. Only S2 and S4 topologies associated to convex iso-surfaces produce

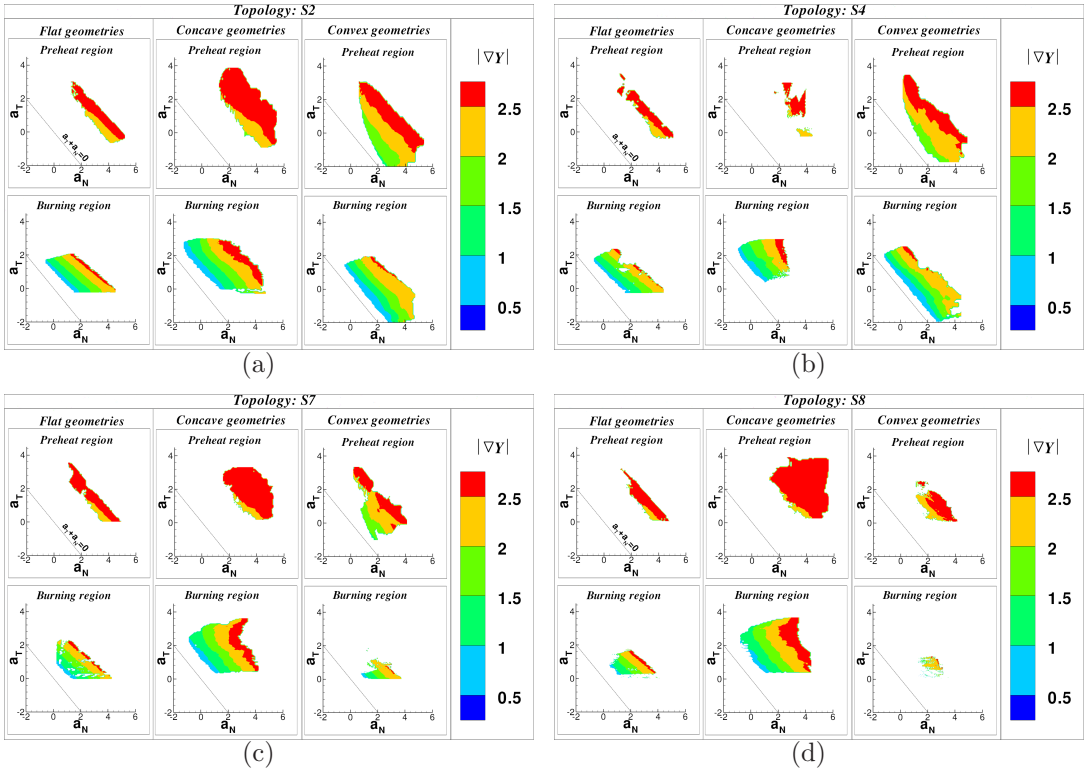

Figure 6.25: Scalar gradient modulus, $|\nabla Y|$, conditioned to $a_T - a_N$ in the 'preheating' and 'burning' regions. (a) S2, (b) S4, (c) S7, (d) S8.

$a_T < 0$, with modest values of $|\nabla Y|$. Concave geometries under flow topologies S2, S7 and S8 in both the 'preheating' and 'burning' regions display large gradients for a wide range of a_N and a_T. All the features of the nodal topologies S2 and S8 could be easily incorporated to the formulation of molecular mixing models. Focal structures S4 and S7 require further investigation to relate the probable region on the $a_N - a_T$ plane to pairs of counter- and co-rotating vortices.

6.4 Summary and conclusions

The DNS of a three-dimensional variable-density turbulent premixed propagating flame has been performed in an inflow-outflow configuration using one-step Arrhenius chemistry. The interaction of the thermochemical processes in the flame with scalar field geometries and flow topologies has been studied from the resulting database. The computational domain has been divided into four regions, corresponding to 'fresh reactants', 'preheat', 'burning' and 'hot products', depending on the reaction rate value. The scalar field structures, in terms of the mean and Gauss curvatures, have been identified. Nearly flat scalar iso-surfaces result the most probable geometries in all four regions. Thermochemical processes in the 'preheating' and 'burning' regions smooth out highly contorted iso-scalar surfaces, present in the 'hot reactants', and annihilate large curvatures. Convex structures with moderate mean curvatures are regenerated in the 'hot products'.

The molecular diffusion rate and its contributions have been analyzed. The contribution to the diffusion due to the variation of ρD, $MD_{(\rho D)}$, is not negligible in the regions with high chemical activity, whereas the contribution due to the spatial curvature term is close to zero. The most important contribution to the molecular diffusion rate comes from the variation of

$|\nabla Y|$ normal to the iso-surface.

Expressions for the propagation speed of the iso-scalar surfaces and its contributions, and its derivative with respect to x_N have been obtained. The contributions to displacement speed due to the variation of (ρD) and the curvature are negligible. All iso-surfaces propagate in the direction of the scalar gradient, $V^Y > 0$; the balance between the chemical contribution and the contribution due to the variation of $|\nabla Y|$ normal to the iso-surfaces governs, mainly, the behavior of V^Y.

Chemical heat generation yields positive flow volumetric dilatation rates everywhere in the computational domain, which imply mostly positive flow strain rates normal to iso-scalar surfaces. This tends to separate iso-surfaces and diminish scalar-gradients. On the other hand, flow strain rates in a plane tangential to the iso-scalar surfaces can be either positive, stretching infinitesimal areas, or negative, leading to surface reduction. Therefore, flow strain rates do not explain the intense molecular diffusive transports occurring in turbulent premixed flames.

Positive volumetric dilatation rates, $-P = \nabla \cdot \mathbf{u}$, display maxima (minima) for concave (convex) scalar micro-structures due to heat conduction focusing (defocusing) effects. Minima of $-P$ are associated with convex scalar geometries in the 'fresh reactants' and maxima with slightly concave tile- and cup-like geometries in the 'preheat' and 'burning' regions.

For the latter two regions of the computational domain a_N does not show correlation with the scalar geometries. Thus, the correlations between local dilatation rate and iso-scalar surfaces are represented by a strong curvature dependence of a_T. Average tangential strain rates are approximately constant with large fluctuations throughout the flow domain, whereas normal strain rates follow the trends of volumetric dilatation rates in the different reaction rate conditioned regions.

The most probable values of a_N and a_T are predominantly located above $a_N + a_T = 0$, corresponding to positive values of $\nabla \cdot \mathbf{u}$ which are most of the points of the computational domain. Most probable values occur in the neighborhood of $a_N + a_T = 0$ in the 'fresh reactants' and 'hot products', with positive or negative values of both strain rates, and for $a_N + a_T > 0$ in the 'preheat' and 'burning' regions, with $a_N > 0$. A positive a_N implies a reduction of $|\nabla Y|$ and hampers scalar mixing, as pointed out by Chakraborty and coworkers [113, 72]. This effect must be definitely balanced by the reactive-diffusive processes since the added normal strain rate acts negatively in the normal direction to the iso-scalar surfaces. The increase of normal propagation speed, monotonically from 'fresh gases' to 'hot products', causes two iso-scalar surfaces to get closer together, and, therefore, increase scalar-gradients. This variation in propagation speed, due to both chemistry and molecular diffusive transport, acts like a nega-

tive normal strain rate, ($\partial V^Y/\partial x_N < 0$). Its values are much greater than the flow normal strain rate over most part of the computational domain. Thus,

The values of the principal strain rates, Λ_1, Λ_2 and Λ_3, conditional upon the mass fraction have been obtained. In accordance with high volumetric dilatation rates ($\nabla \cdot \mathbf{u} > 0$) all eigenvalues have a high probability of positive values towards the regions with high chemical activity. In 'fresh' reactants and 'hot' products the sum of the averages of eigenvalues tends to zero, which points out a decrease of the strain rates in those regions of the computational domain.

The scalar gradient results predominantly aligned with the eigenvector corresponding to the most extensive eigenvalue in the 'preheating' and 'burning' regions, which is in agreement with recent numerical [113, 72, 114] and experimental results [115]. $\mathbf{n}$ exhibits a slight alignment with the most compressive eigenvalue, $\mathbf{e}_3$, in the 'fresh reactants', where the heat release is weak and iso-surfaces behave like those in constant-density turbulent flows [71, 12].

The enstrophy production, $\omega_i S_{ik} \omega_k - \omega_i \omega_i S_{kk}$, results intense towards the 'fresh' reactants and starts decreasing as fluid elements move towards the regions with high chemical activity. This results can be explained by the high local enstrophy, Q_W, towards the 'fresh' gas side. The average of the

third invariant of the velocity-gradient tensor, R, is close to zero such as in constant-density mixing and reaction. The magnitude of the mean of Q_W is small compared with that of local strain, Q_S, for all values of mass fraction. Thus, the second invariant of the velocity-gradient tensor, Q, is governed entirely by the behavior of Q_S.

Focal topologies are dominant in the 'fresh reactants' and tend to disappear in favor of nodal structures as moving towards the 'hot products'. Positive volumetric dilatation rates, which are more intense in the 'preheating' and 'burning' regions, effectively destroy enstrophy. Further, these destructive trends are also associated to increments of viscosity due to temperature increases which fosters flow laminarization.

Joint pdf's of R and Q look similar to the teardrop shape of constant density flows in the 'fresh reactants'; however, a 25% share of the samples correspond to local topologies S7 (UFS) and S8 (UN/UN/UN), characteristic of flows with volumetric expansion, a sign of a moderate interaction of the propagating flame with the initially imposed constant density turbulence. Nodes S2 (UN/S/S, 51%) and S8 (UN/UN/UN, 26%), and focuses S4 (SFS, 8%) and S7 (UFS, 10%) add up to 95% and 92% of the topologies in the 'preheating' and the 'burning' regions, respectively. Vortical structures S4 (SFS) and S7 (UFS) start both from 20% contributions in the 'fresh reactants', and decrease through the 'preheating' and 'burning'

regions. However, whereas the S4 maintains a 13% share in the 'hot products', S7 almost vanishes. This could be due to the alignment of the vorticity with an extensive eigenvector in the S4 structures. The S2 (UN/S/S) topology dominates the local flow dynamics for all three scalar geometries and all reactive regions. S8 (UN/UN/UN) has a significant contribution for concave iso-surfaces (in the 'preheating' and 'burning' regions). S7 and S8 topologies associate more likely to concave iso-scalar surfaces, where heat-conduction focusing effects enhance the chemical reaction.

The conclusions reached in this study pertain to small-scale features and thus should display a certain degree of universality. Future development of mixing models should incorporate some representation of the dependences of $|\nabla Y|$ and area element variations in terms of a_T, a_N and some thermochemical parameters. The relative importance of thermal and mass diffusivities as measured by the Lewis number should be studied. The influence of the Karlovitz number should also be explored. Turbulent mixing in the absence of chemical phenomena for constant density flows and for variable density, due to external heat addition, should also be further investigated.

7

Premixed turbulent jet flame

The physical system simulated here is a jet-flame configuration with a hybrid Large Eddy Simulation (LES)/DNS approach (see Figure 7.2). A stoichiometric methane-air mixture is injected through a central jet, surrounded by a co-flow of burned products. The simulation has been ad-

vanced in time long enough to obtain statistical stationarity. The fully parallel compressible solver SiTCom (Simulating Turbulent Combustion) is used to solve the mass, momentum, energy and reaction progress variable conservation equations (*cf.* Table 4.1). Viscosity, thermal conductivity, and mass diffusion coefficients are given functions of the temperature.

7.1 Numerical implementation

The numerical schemes used within the code are based on the Finite Volume (FV) approach, thus, the physical domain is then subdivided in small polyhedral control volumes $V_{i,j,k}$, which are delimited by a finite number of plane surfaces, S_k, where k represent the surface element's component in the kth direction. The governing transport equations are rewritten in integral formulation by integrating over a control volume V-with frontier S-and applying the Gauss' Theorem to the divergence-like terms, as shown in Tabla 7.1.

The equations are solved resorting to the approximations [i]

[i] In order to explain the *spatial integration* the Einstein summation convention will not be used. We will stick to the convention that i, j, k indices refer to the discretization (in general, cell numbering along the three coordinate directions) and we will use m, l indices to refer to vector components.

Mass $\iiint_V \frac{\partial \rho}{\partial t}\, dV + \iint_S \rho u_i\, dS_i = 0$
Momentum $\iiint_V \frac{\partial (\rho u_i)}{\partial t}\, dV + \iint_S (\rho u_j u_i)\, dS_j + \iint_S p\, dS_i = \iint_S \tau_{ij}\, dS_j\ , \qquad (i = 1, 2, 3)$
Species $\iiint_V \frac{\partial (\rho Y_\alpha)}{\partial t}\, dV + \iint_S (\rho u_i Y_\alpha)\, dS_i = \iint_S \left(\frac{\mu}{Sc} \frac{\partial Y_\alpha}{\partial x_i} \right) dS_i + \iiint_V \dot{\omega}_\alpha\, dV$
Energy (sum of sensible and kinetic, E) $\iiint_V \frac{\partial (\rho E)}{\partial t}\, dV + \iint_S (\rho u_i E)\, dS_i = \iint_S (u_i \sigma_{ij})\, dS_j + \iint_S \left(\frac{C_p \mu}{Pr} \frac{\partial T}{\partial x_i} \right) dS_i + \iiint_V \dot{\omega}_s\, dV$

Table 7.1: Integral form of the governing equations for reacting variable-density turbulent flows.

$$\int_{V_{i,j,k}} \varphi\, dV \simeq \hat{\varphi} V_{i,j,k}\ , \quad \text{and} \quad \int_S \varphi\, dS_m \simeq \sum_i [\varphi]_i S_i^m\ , \tag{7.1}$$

where $\hat{\varphi}$ is the average value of a generic scalar quantity φ over the control volume $V_{i,j,k}$ and the summation in the second equation is extended to all the elementary plane surfaces delimiting the control volume; $[\varphi]_i$ is a measure of the value of φ over the ith surface S_i^m delimiting the discrete control volume $V_{i,j,k}$.

The solver approximates the convective terms resorting to a fourth-order centered skew-symmetric-like scheme [116] and the diffusive terms with a

fourth-order centered scheme. Time integration is performed via a third-order Runge-Kutta scheme [117].

All boundary conditions are imposed using the non-reflecting 3D-Navier-Stokes Characteristic Boundary Condition (3D-NSCBC) approach [118], which means that the perturbations due to the boundary conditions are minima inside the simulation region. The 3D-NSCBC is an improvement of the NSCBC method discussed in Chapter 4, Section 6.1, therefore the 3D-NSCB will not be repeated here. A brief overview of the spatial and time integration is presented in this section.

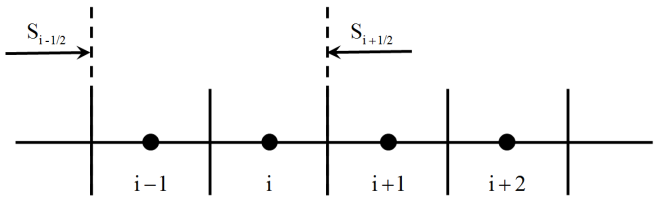

Figure 7.1: Schematic representation of four-nodes used for surface integral approximations.

Spatial integration

The mathematical details of spatial integration can be conveniently analyzed considering one coordinate direction at a time, as shown in Figure 7.1. Considering the uniform spacing Δx, *i.e.* $V_i = S\Delta x$, the volume averaged value of φ at cell i can be computed as:

$$\hat{\varphi}_i = \frac{1}{V_i}\int_{V_i} \varphi \, dV = \frac{1}{\Delta x}\int_{\Delta x} \varphi(x)\, dx \, . \tag{7.2}$$

With the suitable coefficients and integrating the Taylor expansion of $\varphi(x)$ around the interface location $x_{i+1/2}$, the centered fourth- and second-order approximations of the interface value $[\varphi]_{i+1/2}$ can be determined [119]:

$$[\varphi]^{\mathcal{O}4}_{i+1/2} = \frac{7}{12}(\hat{\varphi}_i + \hat{\varphi}_{i+1}) - \frac{1}{12}(\hat{\varphi}_{i+2} + \hat{\varphi}_{i-1}) + \mathcal{O}(\Delta x^4) \, , \tag{7.3}$$

$$[\varphi]^{\mathcal{O}2}_{i+1/2} = \frac{1}{2}(\hat{\varphi}_i + \hat{\varphi}_{i+1}) + \mathcal{O}(\Delta x^2) \, , \tag{7.4}$$

The following one-sided third-order approximations are applying to compute boundary gradients:

$$[\varphi]^{\mathcal{O}3}_{i+1/2} = \frac{1}{3}\hat{\varphi}_{i+1} + \frac{5}{6}\hat{\varphi}_i - \frac{1}{6}\hat{\varphi}_{i-1} + \mathcal{O}(\Delta x^3) \, , \tag{7.5}$$

$$[\varphi]^{\mathcal{O}3}_{i+3/2} = \frac{11}{6}\hat{\varphi}_{i+1} - \frac{7}{6}\hat{\varphi}_i + \frac{1}{3}\hat{\varphi}_{i-1}\mathcal{O}(\Delta x^3) \, , \tag{7.6}$$

the last relation has been obtained by deriving the FV Taylor expansion around the interface point $[\varphi]_{i+3/2}$.

Considering the ith control V_i, the 1D-FV transport equation results as

follows:

$$\frac{\partial \hat{\varphi}_i}{\partial t} + \frac{FC_{i+1/2}S_{i+1/2} - FC_{i-1/2}S_{i-1/2}}{V_i} = \frac{FD_{i+1/2}S_{i+1/2} - FD_{i-1/2}S_{i-1/2}}{V_i}\,, \tag{7.7}$$

where $FC_{i\pm1/2}$ and $FD_{i\pm1/2}$ are respectively generic convective and viscous discrete fluxes for the transported quantity $\varphi = \rho\phi$ computed on the cell interfaces, and κ represents the diffusion coefficient for the relevant primitive variable ϕ.

The convective flux, $FC_{i+1/2}$, into the domain is computed using the fourth-order skew-symmetric-like FV formulation proposed by Ducros *et al.* [116]:

$$FC^{\mathcal{O}4}_{i+1/2} = [\varphi]^{\mathcal{O}4}_{i+1/2}[u]^{\mathcal{O}4}_{i+1/2}\,, \tag{7.8}$$

whereas on the frontier of the domain $FC_{i+1/2}$ is computed switching the scheme to second-order skew-symmetric-like formulation and using an additional exterior boundary node computed with the 3D-NSCBC:

$$FC^{\mathcal{O}2}_{i+1/2} = [\varphi]^{\mathcal{O}2}_{i+1/2}[u]^{\mathcal{O}2}_{i+1/2}\,. \tag{7.9}$$

Diffusive flux, $FD_{i+1/2}$, into the computational domain is computed using a fourth-order centered scheme such as follows:

$$FD^{\mathcal{O}4}_{i+1/2} = \frac{7}{12}\left(\left[\kappa\frac{\partial\hat{\phi}}{\partial x}\right]_i + \left[\kappa\frac{\partial\hat{\phi}}{\partial x}\right]_{i+1}\right) - \frac{1}{12}\left(\left[\kappa\frac{\partial\hat{\phi}}{\partial x}\right]_{i+2} + \left[\kappa\frac{\partial\hat{\phi}}{\partial x}\right]_{i-1}\right), \tag{7.10}$$

where $[\kappa\partial\hat{\phi}/\partial x]_i = \kappa_i[\partial\hat{\phi}/\partial x]_i$ and $[\partial\hat{\phi}/\partial x]_i$ is the cell-averaged value of the gradient:

$$\left[\frac{\partial\hat{\phi}}{\partial x}\right]_i = \frac{[\phi]^{\mathcal{O}4}_{i+1/2}S_{i+1/2} - [\phi]^{\mathcal{O}4}_{i-1/2}S_{i-1/2}}{V_i}\,. \tag{7.11}$$

$[\phi]^{\mathcal{O}4}_{1\pm1/2}$ are evaluated resorting to the fourth-order average, with Eq. (7.3). Numerical diffusive fluxes at the last cell interface before the boundary are computed with a third-order approximation:

$$FD^{\mathcal{O}3}_{i+1/2} = \frac{1}{3}\left[\kappa\frac{\partial\hat{\phi}}{\partial x}\right]_{i+1} + \frac{5}{6}\left[\kappa\frac{\partial\hat{\phi}}{\partial x}\right]_i - \frac{1}{6}\left[\kappa\frac{\partial\hat{\phi}}{\partial x}\right]_{i-1}, \tag{7.12}$$

where the gradients in cell i and the external node $i+1$ are respectively:

$$\left[\frac{\partial\hat{\phi}}{\partial x}\right]_i = \frac{[\phi]^{\mathcal{O}3}_{i+1/2} S_{i+1/2} - [\phi]^{\mathcal{O}4}_{i-1/2} S_{i-1/2}}{V_i}\,, \tag{7.13}$$

$$\left[\frac{\partial\hat{\phi}}{\partial x}\right]_{i+1} = \frac{[\phi]^{\mathcal{O}3}_{i+3/2} S_{i+1/2} - [\phi]^{\mathcal{O}3}_{i+1/2} S_{i-1/2}}{V_{i+1}}\,. \tag{7.14}$$

Normal diffusive fluxes at the boundary node $i+1$ are computed by $FD^{\mathcal{O}3}_{i+3/2}$, which leads to the second-order one side difference approximation:

$$\begin{aligned}\left[\frac{\partial}{\partial x}\left(\kappa\frac{\partial\hat{\phi}}{\partial x}\right)\right]_{i+1} =& \frac{FD^{\mathcal{O}3}_{i+3/2} S_{i+3/2} - FD^{\mathcal{O}3}_{i-3/2} S_{i-3/2}}{V_i} \\ &= \frac{1}{2\,\Delta x}\left(3\left[\kappa\frac{\partial\hat{\phi}}{\partial x}\right]_{i+1} - 4\left[\kappa\frac{\partial\hat{\phi}}{\partial x}\right]_i + \left[\kappa\frac{\partial\hat{\phi}}{\partial x}\right]_{i-1}\right)\,.\end{aligned} \tag{7.15}$$

Time integration

The time integration is solved using the third-order TVD (Total Variation Diminishing) Runge-Kutta scheme proposed by Gottlieb and Shu [117]. Applying Eq. (5.14) the time integration results in:

$$
\begin{aligned}
U^{(0)} &= U^{(n)}\,, \\
U^{(1)} &= U^{(n)} + \Delta t R(U^{(0)})\,, \\
U^{(2)} &= \frac{3}{4}U^{(n)} + \frac{1}{4}[U^{(1)} + \Delta t R(U^{(1)})]\,, \\
U^{(3)} &= \frac{1}{3}U^{(n)} + \frac{2}{3}[U^{(2)} + \Delta t R(U^{(2)})]\,.
\end{aligned}
\tag{7.16}
$$

The maximum time step, Δt, is given by the Courant-Friedrichs-Lewys-number limit (CFL) involving an inviscid time Δt_I and a viscous time Δt_V:

$$
CFL = \frac{\Delta t}{\min\{\Delta t_I, \Delta t_V\}}\,, \tag{7.17}
$$

where the inviscid and viscous time-steps are given by:

$$
\Delta t_I = \frac{V_{i,j,k}}{\sum_m (|\hat{u}_m| + \hat{a}) S^m_{i,j,k}}\,, \tag{7.18}
$$

$$\Delta t_V = \frac{\hat{\rho} V_{i,j,k}^2}{2\hat{\mu}_{\text{eff}} \sum_m (S_{i,j,k}^m S_{i,j,k}^m)} \,, \tag{7.19}$$

where the *hat* operator implies volume averaging within $V_{i,j,k}$, $a = \sqrt{\gamma p/\rho}$ is the speed of sound and $\hat{\mu}_{\text{eff}}$ is the effective dynamic viscosity. In the present work $CFL \leq 1$ [117].

Reaction progress variable, reaction rate and flame thickness

The chemistry is tabulated with the FPI (Flame-Prolongation of ILDM) flamelet approach [86] (*cf.* Chapter 2, Section (4.4.2)). A reaction progress variable, c, based on a single progress variable Y_c defined by Godel *et al.* [120], $Y_c = Y_{CO} + Y_{CO_2} + (Y_{N_2} - Y_{N_2}^0) + (Y_{H_2O} - Y_{H_2O}^0) + Y_{NO} + Y_{NO_2} + Y_{N_2O}$, is used in this case. c is defined as follows:

$$c = \frac{Y_c}{Y_c^{eq}} \,, \tag{7.20}$$

where the 'eq' superscript designates the value of the corresponding variable in the burnt state of the laminar-premixed flame. $Y_{N_2}^0$ and $Y_{H_2O}^0$ are, respectively, the mass fractions of N_2 and H_2O in fresh gases. $Y_{N_2}^0$ and $Y_{H_2O}^0$ ensures that $Y_c = 0$ in fresh gases for all mixing conditions. This tabulation approach actually provides the best fit for the burning rate of a

single-step chemistry, with all the species of the detailed scheme involved in the thermochemistry. Thermodynamic variables are related by the perfect gas equation of state, $p = \rho RT/W$, where R is the universal perfect gas constant and W is the mean molecular weight. The flame thickness is based on the maximum temperature gradient, (*cf.* Eq. (4.91)).

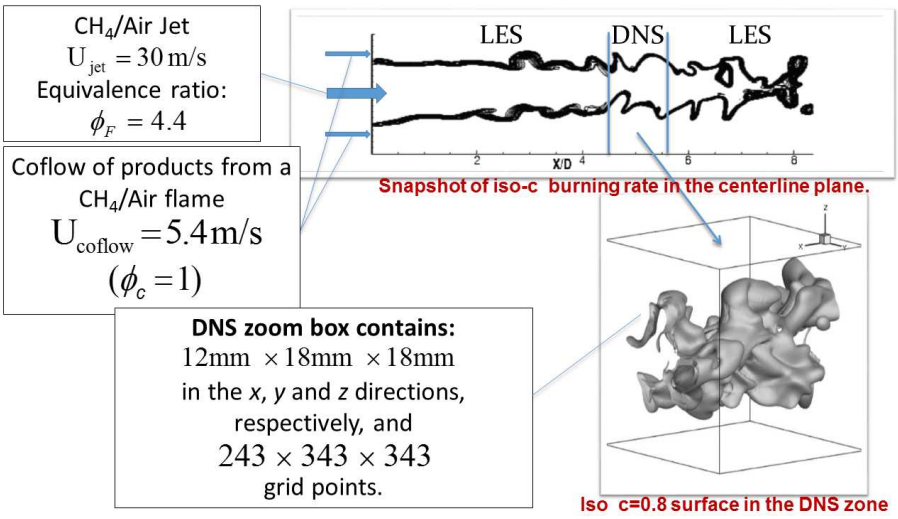

Figure 7.2: Description of the computational domain.

7.2 Simulation parameters

The analysis is performed in a jet-flame configuration simulated with a hybrid Large Eddy Simulation (LES)/DNS approach. A stoichiometric methane-air mixture is injected through a central jet with a mean velocity $U_{jet} = 30$ m/s, and equivalence ratio $\phi_F = 4.4$, surrounded by a co-flow of burned products with a mean velocity $U_{coflow} = 5.4$ m/s, and equivalence

ratio $\phi_c = 1$. Turbulence parameters are those experimentally studied by Chen *et al.* [121]. The nozzle diameter is $D = 12$ mm and the computational domain extends 192 mm in the streamwise (x), 66 mm in the crosswise (y) and 66 mm in the spanwise (z) directions, with 802, 466 and 466 grid points, uniformly spaced, in the x, y, and z directions, respectively. Therefore a LES mesh of about 171 million nodes is used, with a resolution varying between 150 μm and 200 μm. An imbedded zone within the LES mesh features a much higher resolution of 50 μm (see Figure 7.2), where small scales can rapidly develop to complete the turbulence cascade of the already well-resolved LES. Results are analyzed in this zoom box located at $x/D = 4.5$ from the nozzle, which corresponds essentially to the potential core of the jet [121], and at $t = 80$ ms, which is much greater that one initial integral eddy turnover time, $\tau_l = 1.13$ ms. The DNS zoom box under study contains $243 \times 343 \times 343$ grid points where the resolution is of the order of 50 micrometer in the x, y and z directions, respectively, and has physical domain dimensions of 12 mm ×18 mm ×18 mm (see Figure 7.2).

A presumed probability density function closure [122] is used in the LES part, close to the burner injection and downstream of the fully resolved flow part. In the DNS zone, the probability density function reduces to a Dirac delta function, thus ensuring full resolution of the reaction zone

and that of its interaction with turbulence. This is visible in Figure 7.2, where the reaction zone thickness strongly decreases within the DNS zone starting at $x/D = 4.5$. This simple approach allows for generating DNS data embedded within a turbulent flow featuring most of the properties of shear-flows found in real burners.

The turbulent Reynolds number, Re, based on the characteristic DNS velocity fluctuations rms, $u' = 2.12$ m/s, and the integral length scale, $l = 2.4$ mm, reads:

$$Re = \frac{\rho u' l}{\mu} \, , = 300 \, . \tag{7.21}$$

On the other hand, the Lewis number,

$$Le = \frac{\lambda}{\rho C_p D} = 1 \ . \tag{7.22}$$

C_p is the specific heat at constant pressure.

Turbulence is introduced by injecting a correlated random noise [123] with uniform rms, u', throughout the jet inlet. The dimensionless characteristic velocity fluctuations rms, u'/S_L, and the integral length scale, l/δ_L, of the premixed flame turbulent jet flame are used, where S_L is the non stretched laminar flame velocity and δ_L is the flame thickness based on the maximum temperature gradient. In this study, $u'/S_L = 5.43$ and $l/\delta_L = 6.31$, with combustion taking place in the 'thickened-wrinkled flame' regime [78, 76],

as shown in Figure 7.3. Numerical values of the aero-thermo-chemical variables for this simulation are presented in Table 7.2.

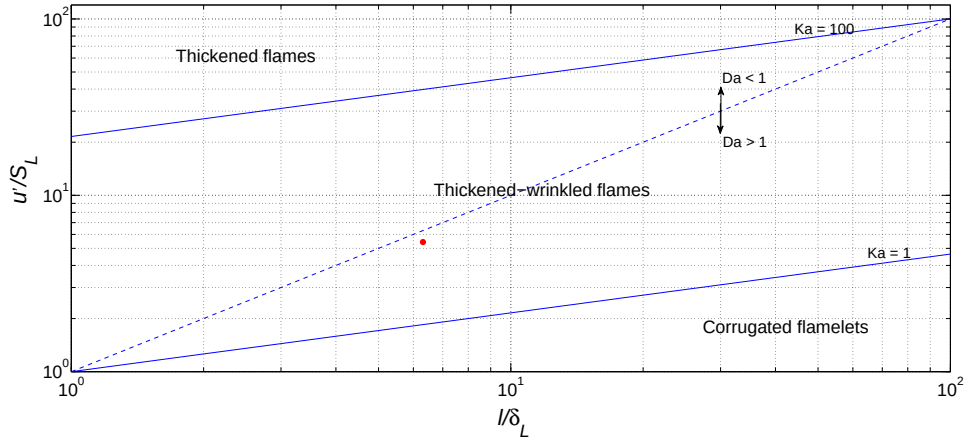

Figure 7.3: Turbulent combustion diagram. The point indicates the case under study.

Parameter	Value
Prandtl number, Pr	0.72
Schmidt number, Sc	0.72
Lewis number, Le	1.0
rms of velocity fluctuations, u'	2.12 (m/s)
Integral length scale, l	2.4 (mm)
Turbulent kinetic energy dissipation rate, ε	4.0e3 (m^2/s^3)
Kolmogorov length micro-scale, η	0.0332 (mm)
Kolmogorov time micro-scale, τ_η	6.5192e-2 (ms)
Non stretched laminar flame velocity, S_L	0.39 (m/s)
Laminar flame thickness, δ_L	0.38 (mm)
Chemical time scale, τ_{ch}	0.97 (ms)
Velocity ratio, u'/S_L	5.43
Length ratio, l/δ_L	6.31
Turbulent Reynolds number, Re	300
Damköhler number, $Da = (l/\delta_L)/(u'/S_L)$	1.16
Karlovitz number, $Ka = \tau_{ch}/\tau_\eta$	5.03

Table 7.2: Values of dimensionless parameters and physical variables of the simulation.

7.3 Results and discussion

As mentioned in Chapter 4, the geometrical structures of the scalar field change in the normal direction to the iso-surfaces (see Figure 7.4). Thus,

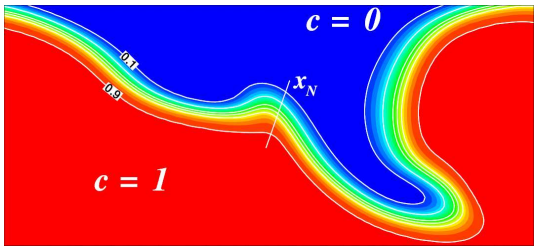

Figure 7.4: Iso-contours of the progress variable c.

results will be analyzed considering four different regions of the computational domain based on the reaction rate and the progress variable values. The regions are termed as follows: 'fresh reactants', 'preheat region', 'burning region' and 'hot products'. Figure 7.5 shows the reaction rate, $\dot{\omega}_c = \dot{\omega}/\rho$, as a function of the progress variable, c; $\dot{\omega}_c$ has been normalized with its rms using all the samples in the domain. As the progress variable is monotonically increasing toward the hot products, the reaction rate is always positive. $\dot{\omega}_c$ attains a maximum about $c \approx 0.78$. In Figure 7.5, vertical dotted lines split the four regions of the computational domain under study. The dots upon the red line mark the limits of the reaction rate between 50%, 60% and 70% of its maximum value to evaluate the sensitivity of the 'burning' region. Figure 7.6 shows the joint probability density functions of the mean and Gauss curvatures, k_m and k_g, using the different limits of the 'burning' region. It can be noted that there are no changes in the features of the scalar geometries, as the jpdf's are very similar. Then, the 'burning' region is defined using the limit $0.7\dot{\omega}_{c_{max}}$ as it is the nearest

value to the maximum reaction rate. Tabla 7.3 resumes the intervals for 'fresh reactants', 'preheat region', 'burning region' and 'hot products' depending on the values of the progress variable. Hereafter, results will be analyzed in these four regions of the computational domain.

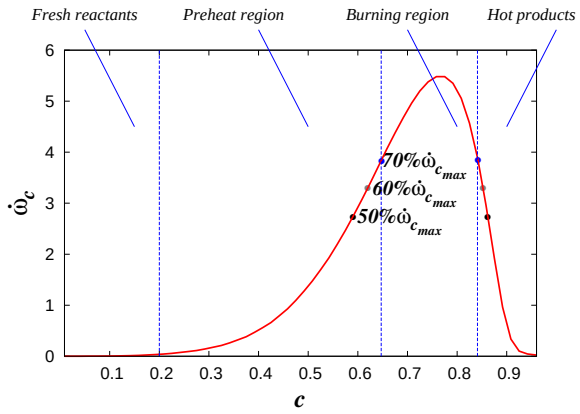

Figure 7.5: Reaction rate, $\dot{\omega}_c$, conditional upon the progress variable, c. The dots upon the red line mark the limits of the reaction rate to evaluate the sensitivity of the 'burning' region. Vertical dotted lines mark the limits of the four regions of the computational domain.

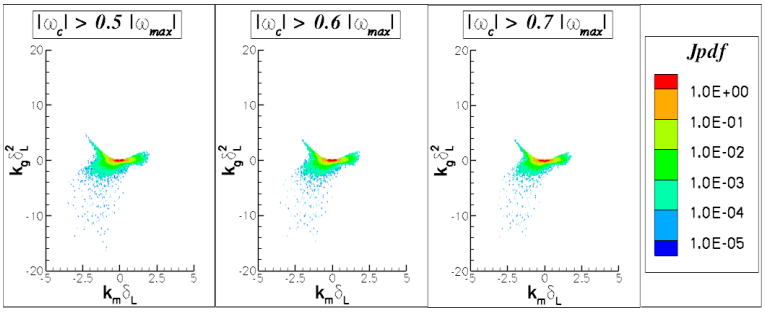

Figure 7.6: Joint pdf of the mean and Gauss curvatures, k_m and k_g, in the 'burning' region characterized by $\dot{\omega}_c > 0.5\dot{\omega}_{c_{max}}$, $\dot{\omega}_c > 0.6\dot{\omega}_{c_{max}}$, and $\dot{\omega}_c > 0.7\dot{\omega}_{c_{max}}$. k_m and k_g have been normalized with the flame thickness, δ_L. Joint pdf magnitudes decrease from the center to the circumference.

Fresh reactants	$0.001 < c < 0.200$
Preheat region	$0.200 < c < 0.647$
Burning region	$0.647 < c < 0.841$
Hot products	$0.841 < c < 0.960$

Table 7.3: Ranges corresponding to scalar values for the different regions of the computational domain.

7.3.1 Structure of the scalar field in terms of the Mean and Gauss curvatures

To explore the scalar structure, the geometries of the scalar field through the mean and Gauss curvatures of the iso-scalar surfaces in the different regions of the computational domain have been calculated. Figure 7.7 shows the joint pdf of the mean and Gauss curvatures, k_m and k_g, for the four regions of the computational domain. k_m and k_g have been normalized with the laminar flame thickness, δ_L. All the joint pdf's display maxima for nearly flat iso-scalar surfaces, in agreement with the results of Chapters 3 and 4, experimental results [60] and three-dimensional DNS calculations [63, 101] of premixed turbulent flames. It is important to note that concave iso-surfaces are much more probable than convex ones both in the 'fresh reactants' and 'preheat' regions; this result seems to agree with the intuitive notion that concave geometries are predominant in zones enclosed within the jet flame. It seems that the high chemical activity smooth the large curvatures of the iso-scalar surfaces as fluid elements move from the 'preheating' to the 'burning region' the large curvatures decrease. This

behavior is similar to that obtained in Figure 6.6 of Chapter 4. The scalar structures curved positively increase in the 'hot' products and are dominant over other structures. The radius of convex geometries decrease towards the 'burnt' gases, which could be induced by the vortices that survive in this region of the computational domain; Tanahashi *et al.* [39] argue that strong coherent fine-scale eddies, perpendicular to the flame front, can survive behind it and create low pressure zones, which increase the probability of finding convex geometries in the 'hot' products region.

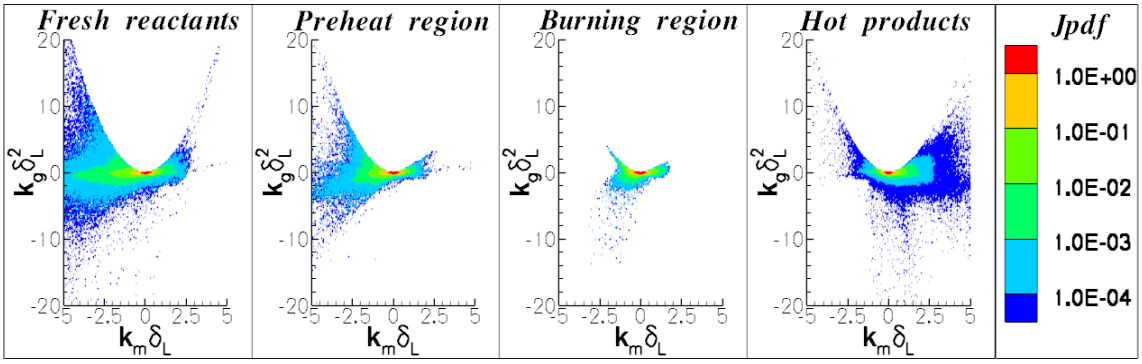

Figure 7.7: Joint pdf of the mean and Gauss curvatures, k_m and k_g. Joint pdf magnitudes decrease from the center to the circumference. k_m and k_g have been normalized with the flame thickness, δ_L.

7.3.2 Non-material surface propagation velocity

As mentioned in Chapter 2, Section 4.3.3, the displacement speed of the iso-scalar surfaces, V^c [ii], is governed by the local balance between molecular diffusion and reaction rates. Thus, before studying the behavior of V^c

[ii] For this case, we are working with the progress variable c, thus, the displacement speed symbol is termed: V^c.

it is important to check the contribution due to the molecular diffusion processes.

Scalar structures play an important role in the molecular diffusion rate, $(1/\rho)\nabla\cdot(\rho D\nabla c)$, since the geometry of the iso-surfaces could become a source/sink from the mass flow rate, which enhances or hampers the molecular diffusive transport. Using the definition of the unit vector normal to the iso-scalar surfaces, $\mathbf{n} = -\nabla c/|\nabla c|$, the various contributions to $(1/\rho)\nabla\cdot(\rho D\nabla c)$ can be estimated, namely,

$$MD_{(\rho D)} = -\frac{|\nabla c|}{\rho}\mathbf{n}\cdot\nabla(\rho D) = -\frac{|\nabla c|}{\rho}\frac{\partial(\rho D)}{\partial x_N}\,, \tag{7.23}$$

$$MD_{|\nabla c|} = -D\mathbf{n}\cdot\nabla|\nabla c| = -D\frac{\partial|\nabla c|}{\partial x_N}\,, \tag{7.24}$$

$$MD_{curv} = -D|\nabla c|\nabla\cdot\mathbf{n} = -2D|\nabla c|k_m\,. \tag{7.25}$$

The total molecular diffusion rate and its contributions conditional upon the progress variable have been calculated and the result is shown in Figure 7.9. All variables in this figure have been normalized with the rms values of $(1/\rho)\nabla\cdot(\rho D\nabla c)$.

It can be seen in Figure 7.9 that the contribution to the diffusion due to the variation of ρD, $MD_{(\rho D)}$, is not negligible in the regions with high chemical activity. The term ρD decreases from $c = 1$ to $c = 0$ thus the

derivative in the normal direction to the iso-scalar surfaces is negative; this term turns $MD_{(\rho D)}$ into positive and attains a maximum value in the 'preheat region'. It is important to note that the average of the spatial curvature term is close to zero, $\langle MD_{curv} \rangle \approx 0$. It can be noted that the most important contribution to the molecular diffusion rate comes from the variation of $|\nabla Y|$ normal to the iso-surface, $MD_{|\nabla c|}$. $(1/\rho)\nabla \cdot (\rho D \nabla c)$ displays an almost identical variation to that $MD_{|\nabla c|}$; this finding is in agreement with the results of Chapter 4, Section 6.3.2. $MD_{|\nabla c|}$, with the increasing progress variable, attains a broad maximum within the 'preheat' region and then starts decreasing and changes sign until attains a local minimum in the 'burning' region. The sign of $MD_{|\nabla c|}$ depends on that of $\partial^2 c/\partial x_N^2$. If there is an inflection point of $c(x_N)$ at x_N^*, where $\partial^2 c/\partial x_N^2 = 0$, this occurs for a particular iso-surface $c(x,t) = c(x_N^*, t)$, $MD_{|\nabla c|}$ will be zero. For monotonically varying $c(x_N)$: $\partial^2 c/\partial x_N^2 < 0$ for $0 < c(x_N) < c(x_N^*)$, and $MD_{|\nabla c|}$ will be positive; $\partial^2 c/\partial x_N^2 > 0$ for $c(x_N^*) < c(x_N) < 1$, and $MD_{|\nabla c|}$ will be negative. It might be tempting to define a normal characteristic length scale, δ_N, as

$$\delta_N = \frac{\partial c/\partial x_N}{|\partial^2 c/\partial x_N^2|} \,. \tag{7.26}$$

For $(\partial c/\partial x_N) \to 0$, results show that δ_N is finite, as shown in Figure 7.8.

δ_N reaches a maximum value of 20 mmat $c \approx 0.56$ ('preheat region'), with much smaller values in the 'fresh' and 'burning' regions.

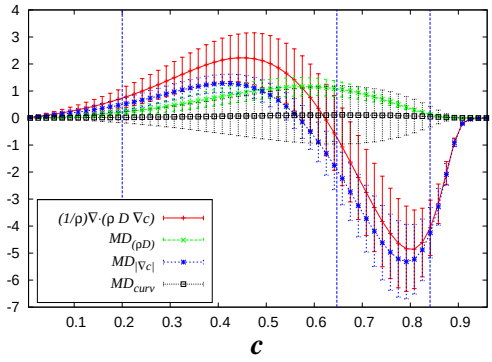

Figure 7.8: Characteristic iso-scalar surface separation length, δ_N (mm).

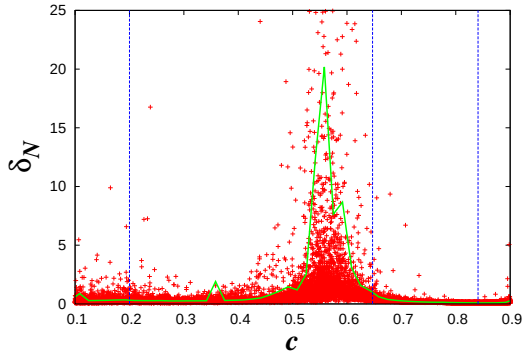

Figure 7.9: Molecular diffusion rate, $(1/\rho)\nabla \cdot (\rho D \nabla c)$, and its contributions conditional upon the progress variable, c. Variables in this figure have been normalized with the rms values of $(1/\rho)\nabla \cdot (\rho D \nabla c)$. Vertical solid bars in the terms indicate their respective root-mean-square values and the vertical dotted lines in figure mark the four regions of the computational domain.

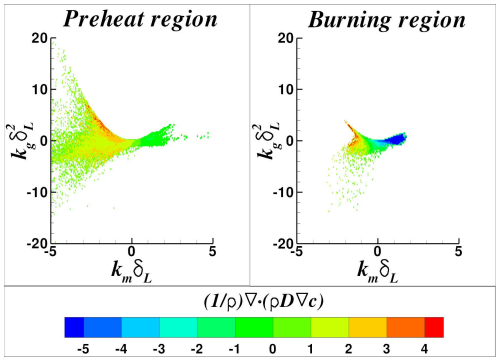

Figure 7.10: Molecular diffusion rate, $(1/\rho)\nabla\cdot(\rho D\nabla c)$, conditional upon the mean and Gauss curvatures, k_m and k_g.

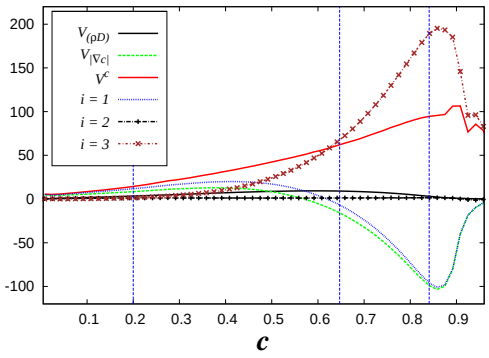

Figure 7.11: Normal propagation velocity, V^c, and its contributions as a function of the reactant mass fraction. Vertical dotted lines mark the limits of the four regions of the computational domain.

In order to examine the correlation between the iso-scalar surface geometries and the molecular diffusion rate, the term $(1/\rho)\nabla\cdot(\rho D\nabla c)$ has been calculated upon the mean and Gauss curvatures, k_m and k_g, for the 'preheat' and 'burning' regions. The result is shown in Figure 7.10; these regions of the computational domain have been selected because they contain the maximum and minimum values of the molecular diffusion term according to the results in Figure 7.9. The results shows that there is a

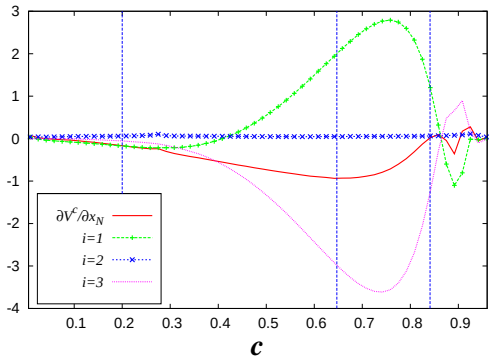

Figure 7.12: Derivative of V^c in the direction normal to iso-scalar surfaces, x_N, and contributions to $\partial V^c/\partial x_N$ due to normal diffusion, $(\partial V^c/\partial x_N)_1$, tangential diffusion (curvature), $(\partial V^c/\partial x_N)_2$, and chemical reaction, $(\partial V^c/\partial x_N)_3$. Vertical dotted lines mark the limits of the four regions of the computational domain.

correlation between these variables; concave structures of the scalar field correlate with positive values of $(1/\rho)\nabla\cdot(\rho D\nabla c)$, whereas for nearly flat and convex geometries correlate with negative values of the molecular diffusion term. These effects could be explained by the diffusive removal of the heat of reaction, generated near concave iso-surfaces; convex geometries could tend to enhance the heat removal through the defocusing of thermal conduction.

The displacement speed, V^c, and its different contributions are plotted against the progress variable in Figure 7.11. V^c and its contributions have been normalized with (D_0/δ_L), where D_0 is the value of the molecular mass diffusivity in the fresh gases, and δ_L is the laminar flame thickness. In this case the contributions due to the variation of (ρD) is positive and the contribution due to the spatial curvature is negligible, $\langle V_2^c\rangle \approx 0$. The most

important term in $V_1^c (= V_{(\rho D)} + V_{|\nabla c|})$ comes from the the variation of $|\nabla Y|$ normal to the iso-surface; V_1^c displays an almost identical variation to that of $V_{|\nabla c|}$. The propagation velocity induced by the chemical conversion is always positive, as expected $V_3^c > 0$, and reaches the highest values towards the 'hot' products, which is consistent with the reaction rate plot shown in Figure 7.5. V^c, always positive, monotonically increases towards the burnt gases since the large positive values of V_3 are greater in magnitude than the large negative V_1. The iso-scalar surfaces located in the 'hot products' and 'burning' regions propagate faster than those in the 'fresh' gases due to the chemical reaction effects. Consequently, two iso-surfaces, $c(\mathbf{x}, t) = \Gamma$ and $c(\mathbf{x}, t) = \Gamma + \Delta\Gamma$, for example, in the 'preheating' region will move toward the 'fresh' zone and tend to narrow the gap, Δx_N, among themselves. This finding is consistent with the small values of δ_N in the 'fresh gases' of Figure 7.8.

Figure 7.12 shows $\partial V^Y / \partial x_N$ and its contributions conditioned on the progress variable. It can be seen that $\partial V^Y / \partial x_N < 0$ in the regions with high chemical activity. $\partial V^Y / \partial x_N$ can be interpreted as an added normal strain rate due to the combined action of diffusion and chemistry, and in this context, $\partial V^Y / \partial x_N < 0$ means that two adjacent iso-surfaces get closer to each other as time increases. Curvature effects are negligible while normal diffusion (positive) and chemistry (negative) contributions are comparable

in absolute value; for $c > 0.85$ the chemistry and normal diffusion almost balancing.

7.3.3 Local strain rates

This section aims at explaining the local mixing rate thorough the flow strain rates, which enhance or hamper the molecular diffusion processes.

Figure 7.13(a) shows a zoom of a $y - z$ plane of the computational domain, which displays two scalar iso-lines and the volumetric dilatation rate, $-P = \nabla \cdot \mathbf{u}$. Figure 7.13(b) shows $-P$ conditional upon the mean and Gauss curvatures, k_m and k_g. The behavior of $-P$ with scalar geometries are consistent with those results shown in Chapter 4, Section 6.3.3 since zones with scalar geometries positively (negatively) curved or with concave (convex) geometries connect with positive (negative) dilatation rates. Thus, there seems to be a universal behavior between the local dilatation rate and scalar geometries regardless of the configuration under study. Expansive (compressive) volumetric dilatations rates are mainly associated to concave and flat (convex) iso-scalar surfaces. The heat conduction focussing (defocussing) by concave (convex) geometries enhance (hamper) the local volumetric dilatation rate. Thus, it can be seen that for geometries with small radius of curvature like cup elliptic concave (convex) geometries are obtained the highest positive (negative) values of $\nabla \cdot \mathbf{u}$

in the 'preheat' and 'burning' regions. It is clear, at least locally, that scalar molecular transport effects through the scalar structures can influence the rate of change of an infinitesimal fluid volume per unit volume, which, in turn, would affect directly the flow strain rates tangential, a_T, and normal, a_N, to the iso-surfaces.

On the other hand, the reactive-diffusive processes can be linked to the local volumetric dilatation rate through the Low Mach number flamelet assumption. Assuming constant-pressure in the flow domain, under the flamelet hypothesis, it exists a progress variable based on the temperature,

$$c_T = \frac{T - T_u}{T_b - T_u} \,, \tag{7.27}$$

so that the state of law ($P = \rho RT/W$) can be replaced by [124]

$$\rho = \rho(c_T) = \frac{\rho_u}{(1 + \tau c_T)} \,, \tag{7.28}$$

with

$$\tau = \frac{(T_b - T_u)}{T_u} \,, \tag{7.29}$$

subscripts 'u' and 'b' indicate variables corresponding to the unburned and the burnt gases, respectively, and $\tau = 6.4$ [124].

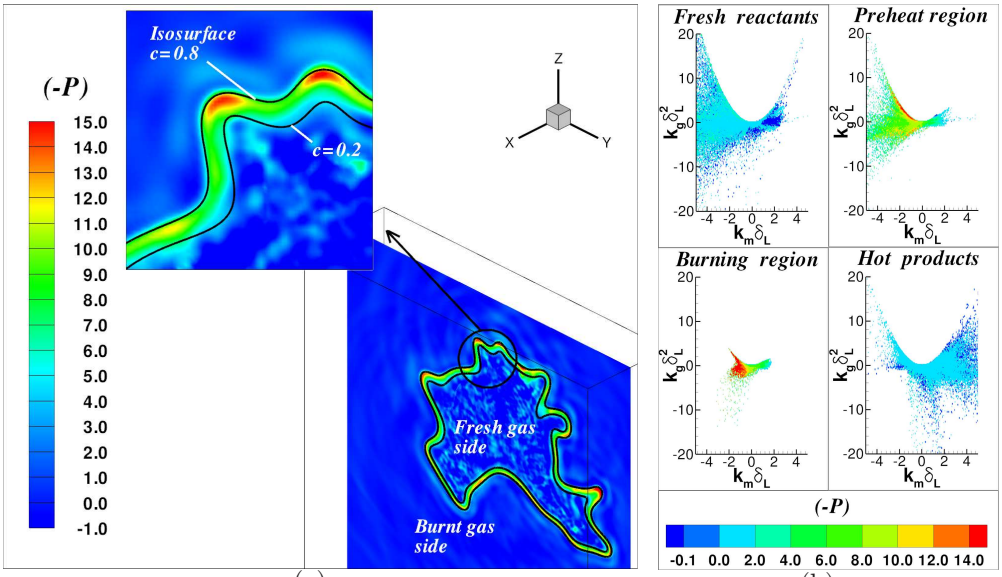

Figure 7.13: (a) Fluid element dilatation rate, $-P = \nabla \cdot \mathbf{u}$, in the computational domain. (b) $-P$ conditional upon the mean and Gauss curvatures, k_m and k_g. The volumetric dilatation rate has been normalized with $\langle \nabla \cdot \mathbf{u} \rangle$, using all the samples in the domain.

Then, from Eq. (4.1):

$$\nabla \cdot \mathrm{u}_{c_T} = -\frac{1}{\rho}\left(\frac{\partial \rho}{\partial t} + \mathrm{u} \cdot \nabla \rho\right) = -\frac{1}{\rho}\frac{D\rho}{Dt}\,, \tag{7.30}$$

$$= -\left(\frac{1}{\rho}\frac{d\rho}{dc_T}\right)\frac{Dc_T}{Dt} = \left(\frac{\tau}{1+\tau c_T}\right)\frac{Dc_T}{Dt}\,. \tag{7.31}$$

According to the flamelet formalism, the progress variable verifies an equation of the form:

$$\frac{Dc_T}{Dt} = \frac{1}{\rho}\left[\nabla \cdot (\rho D \nabla c_T) + \dot{\omega}\right]\,, \tag{7.32}$$

leading to the low Mach number approximation:

$$\nabla \cdot \mathrm{u}_{c_T} = \frac{\tau}{\rho_u} \left[\nabla \cdot (\rho D \nabla c_T) + \dot{\omega} \right] , \tag{7.33}$$

where $\dot{\omega}$ is the chemical source of c_T.

In a fully compressible and multi-species formulation, the energy equation cannot be cast in temperature equation without assuming numerous hypotheses [76]. Even when this is done, there are additional terms due to pressure gradient, molar weights and C_P variations, acting on temperature used to define c_T. Therefore, (Dc_T/Dt), the substantial derivative of c_T, does not equal exactly the summation $\nabla \cdot (\rho D \nabla c) + \dot{\omega}$.

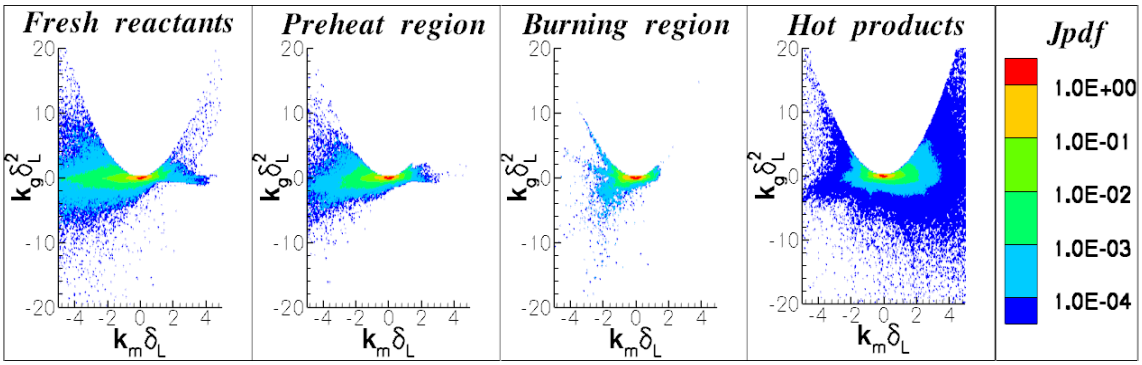

Figure 7.14: Joint pdf of the mean and Gauss curvatures, k_m and k_g, using the scalar field c_T. Joint pdf magnitudes are maxima in the origin, and decrease as curvature values increase. k_m and k_g have been normalized with the flame thickness, δ_L.

One way to see the effects of the approximation of the Low Mach number is computing the joint pdf of the mean and Gauss curvatures using the progress variable based on the temperature, c_T. Figure 7.14 shows the

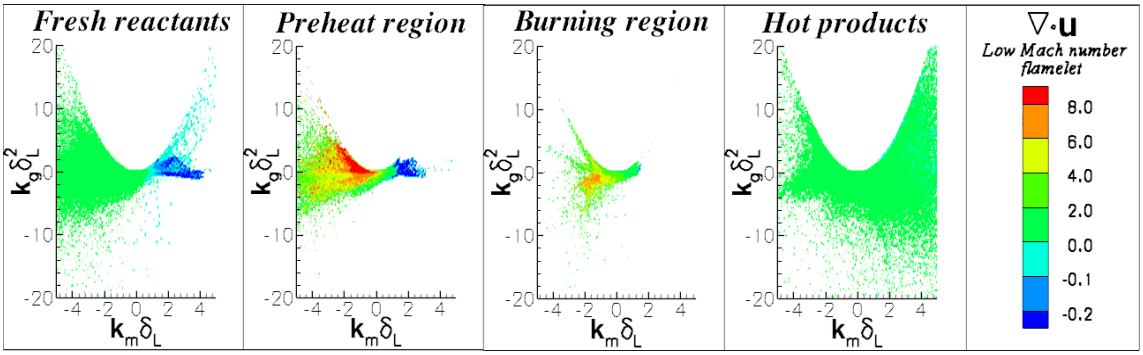

Figure 7.15: Volumetric dilatation rate obtained from Eq. (7.33), conditional upon the mean and Gauss curvatures, k_m and k_g.

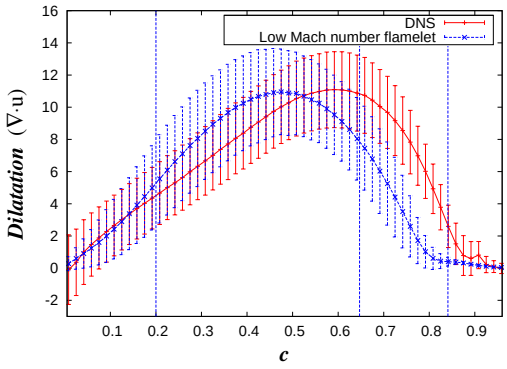

Figure 7.16: Dilatation, $\nabla \cdot \mathrm{u}$, obtained from the present DNS and that calculated using Eq. (7.33), across the progress variable. Vertical solid bars in the terms indicate their respective root-mean-square values and the vertical dotted lines in figure mark the four regions of the computational domain.

joint pdf's of the mean and Gauss curvatures, k_m and k_g, calculated in the four regions of the computational domain using the scalar field c_T. These results look almost identical to those of Figure 7.7, but it can be noted that in some parts of Figure 7.14 the curvature values are larger than those shown in Figure 7.7. Both figures show the same trends. Nearly flat iso-scalar surfaces are the most probable local scalar structures. Concave scalar geometries towards 'fresh reactants' and 'preheat region' prevail and

convex scalar structures, with large values of the mean curvatures, are dominant over the concave ones in the 'hot products'.

In order to analyze the relation between $\nabla \cdot \mathrm{u}_{c_T}$ obtained with the low Mach number flamelet approximation [124] and the small-scales scalar structures, Figure 7.15 shows the plot of $\nabla \cdot \mathrm{u}_{c_T}$ conditional upon k_m and k_g. It can be seen that the dilatation rate has the same trend with scalar micro-structures to those results shown in Figure 7.13(b) but there is no a perfect match between them. To measure the relative differences between these dilatation rates, Figure 7.16 plots the values of $\nabla \cdot \mathrm{u}$ obtained from the DNS and those calculated using Eq. (7.33). Variables in this figure have been normalized with $\langle \nabla \cdot \mathbf{u} \rangle$, using all the points in the domain. Vertical solid bars indicate their respective rms values. High volumetric dilatation rates occur in the 'preheat' and 'burning' regions. Part of the 'fresh reactants' and 'hot products' regions can display small negative values of dilatation rates. While relative differences of the two volumetric dilatation rates remain between 0 and 4.5% for $c < 0.17$, they notably increase for $c > 0.18$. This is not surprising, since the effects neglected in the simplified diffusive and reactive budget of the temperature-based progress variable discussed above, occur mainly in regions with high chemical activity. The high relative differences between dilatation rates casting doubts on the validity of the progress variables defined without a perfect match with the

form of the primitive equations solved.

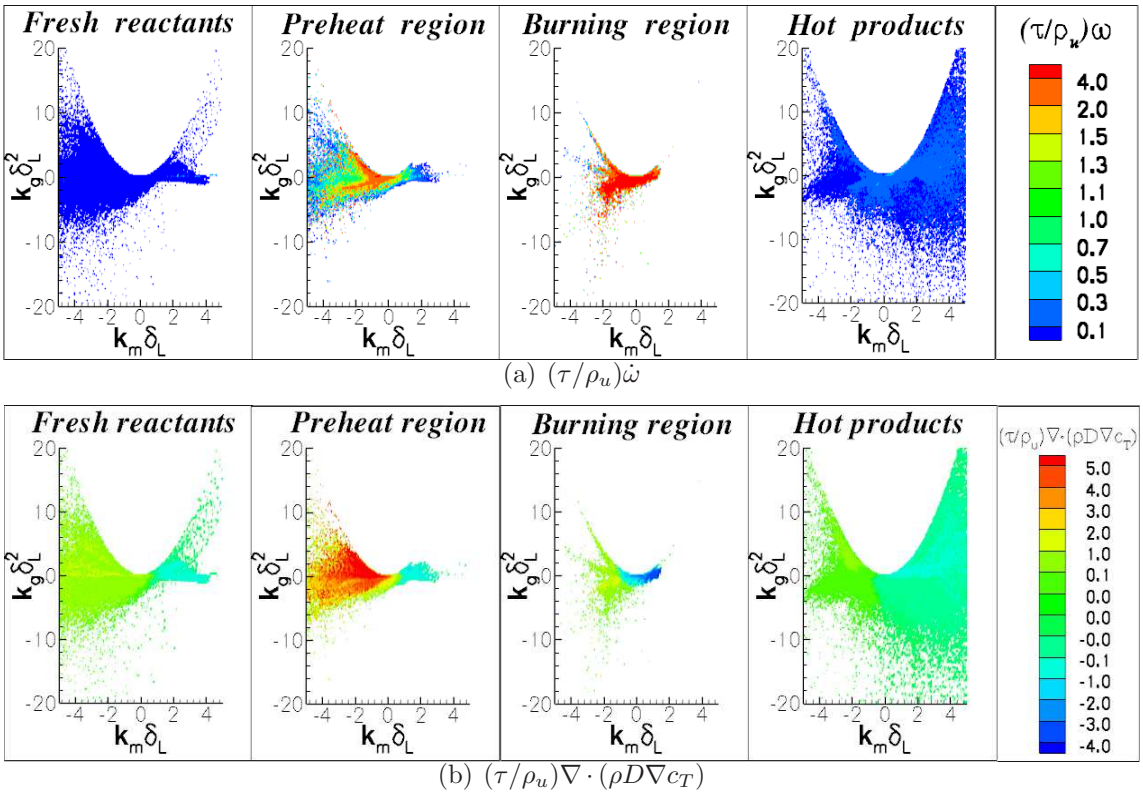

Figure 7.17: Different terms of dilatation rate, $\nabla\cdot\mathrm{u}$ (Eq. 7.33), conditional upon the mean and Gauss curvatures, k_m and k_g. (a) $(\tau/\rho_u)\dot{\omega}$, (b) $(\tau/\rho_u)\nabla\cdot(\rho D\nabla c_T)$. The terms have been normalized with $\langle\nabla\cdot\mathbf{u}\rangle$ using all the samples of the computational domain.

In order to explain the discrepancies between the values of $\nabla\cdot\mathrm{u}$ obtained from the jet flame DNS and that calculated using Eq. (7.33), the diffusive and reactive contributions to the latter have been analyzed. Figure 7.17 shows the chemical and molecular diffusion contributions to $\nabla\cdot\mathrm{u}_{c_T}$, conditional upon k_m and k_g, for the four regions of the domain. All terms in this figure have been normalized with $\langle\nabla\cdot\mathbf{u}\rangle$, using all samples of the domain. While the chemical contribution is always positive, as expected,

the molecular diffusion term is negative for nearly flat and slightly convex geometries in the burning region. This feature can be explained by the diffusive removal of the heat of reaction, generated near flat and slightly concave iso-surfaces; convex geometries tend to enhance the heat removal through the already mentioned defocussing of thermal conduction. The reactive contribution is small in the 'fresh reactants' and the 'hot products' regions, displays moderate values in the 'preheat region' and exhibits maxima in the 'burning' region. Cup-like and tile-like elliptic concave geometries yield the highest positive diffusive contributions to $\nabla \cdot \mathrm{u}_{c_T}$, which, once more, can be explained by the focussing effect of the scalar molecular transport in concave structures.

The previous results show that high (low) volumetric dilatation rates, $\nabla \cdot \mathbf{u}$, are present in the 'preheat' and 'burning' regions ('fresh' and 'burnt' gases), but now it will be analyzed which of the parts of the volumetric dilatation rate ($\nabla \cdot \mathbf{u} = a_T + a_N$; the tangential, a_T, or normal, a_N strain rates) is dominant in all of these regions since this information will indicate how the strain enhances or hampers the mixing rate of scalar field. Figure 7.18 shows the dilatation rate and the normal and tangential strain rates for different values of the progress variable. The terms in this figure have been normalized with $\langle \nabla \cdot \mathbf{u} \rangle$, using all the iso-scalar surfaces. These results are similar to those obtained in Figure 6.13. It can be noted in Figure 7.18(a)

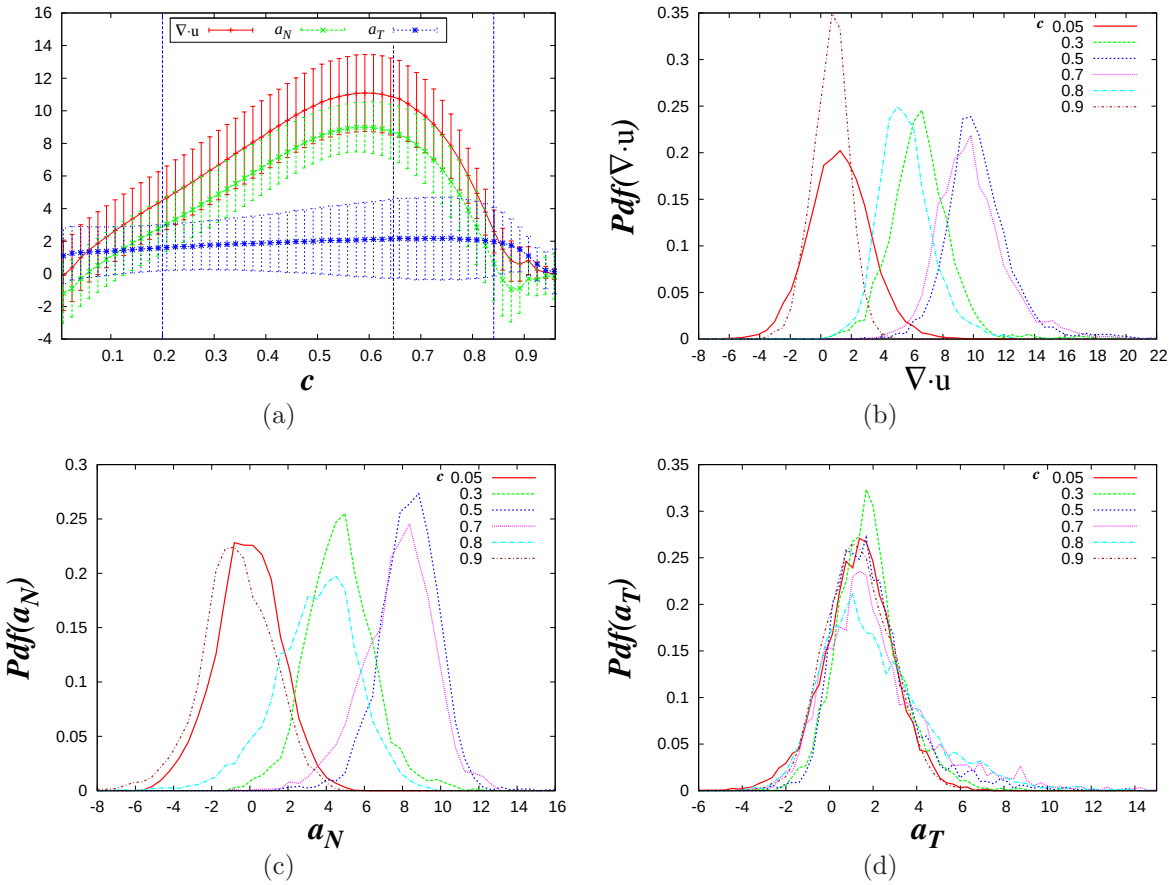

Figure 7.18: (a) $\nabla \cdot \mathbf{u}$, a_N and a_T conditional upon the progress variable, c. (b) Pdf of $\nabla \cdot \mathbf{u}$, (c) a_N and (d) a_T for different values of c. For Figure 7.18(a), vertical solid bars in the curves indicate the standard deviation of the value at every point and the vertical dotted lines in figure mark the four regions of the computational domain.

that approximately for $c > 0.88$ the values of $\nabla \cdot \mathbf{u}$, a_T and a_N have not a dependence on c. This behavior might be explained on account of the fact that there is a co-flow of burned products in the jet flame where a mixing layer is developed around $c \approx 0.999$, which allows that the variables decorrelate with the scalar value. Figure 7.18(b) shows that the probability of high dilatation rate is greater towards the regions with high chemical ac-

tivity. Referring to Figure 7.18(c) is evident that the probability of finding high positive a_N is larger in the 'preheat' and 'burning' regions. It is possible also to have negative a_N in the 'fresh' and 'burnt' gases where the reaction rate is negligible. It can be seen in Figure 7.18(a) that a_T is constant with an average value about 1.8, whereas a_N displays an almost identical variation to that of dilatation rate. Thus, regardless of the configuration (premixed turbulent jet flame and premixed planar turbulent flame), the trend of high dilatation rates across the progress variable is mimicked by a_N, which means that locally the rate of change of an infinitesimal fluid volume per unit volume is stronger in the normal direction to the iso-surface than in the tangent plane to it. However, there is no correlation between the flow strain rate normal to the iso-scalar and the iso-scalar surface geometries as shown in Figure 7.19(a). Despite a_T remains almost constant through the progress variable it shows in Figure 7.19(b) a correlation with the small-scale scalar geometries. This last feature is consistent with the result shown in Figure 6.12(a) where a_T exhibits similar curvature dependent features to $\nabla \cdot \mathbf{u}$. Thus, once again, it is important to highlight that the correlations between local dilatation rate and scalar geometries (see Figure 7.13) come from the dependence of a_T on the curvature.

Figure 7.20 depicts the joint pdf of the flow strain rates, a_N and a_T, and also $|\nabla c|$ conditioned to a_N and a_T in the four regions defined for differ-

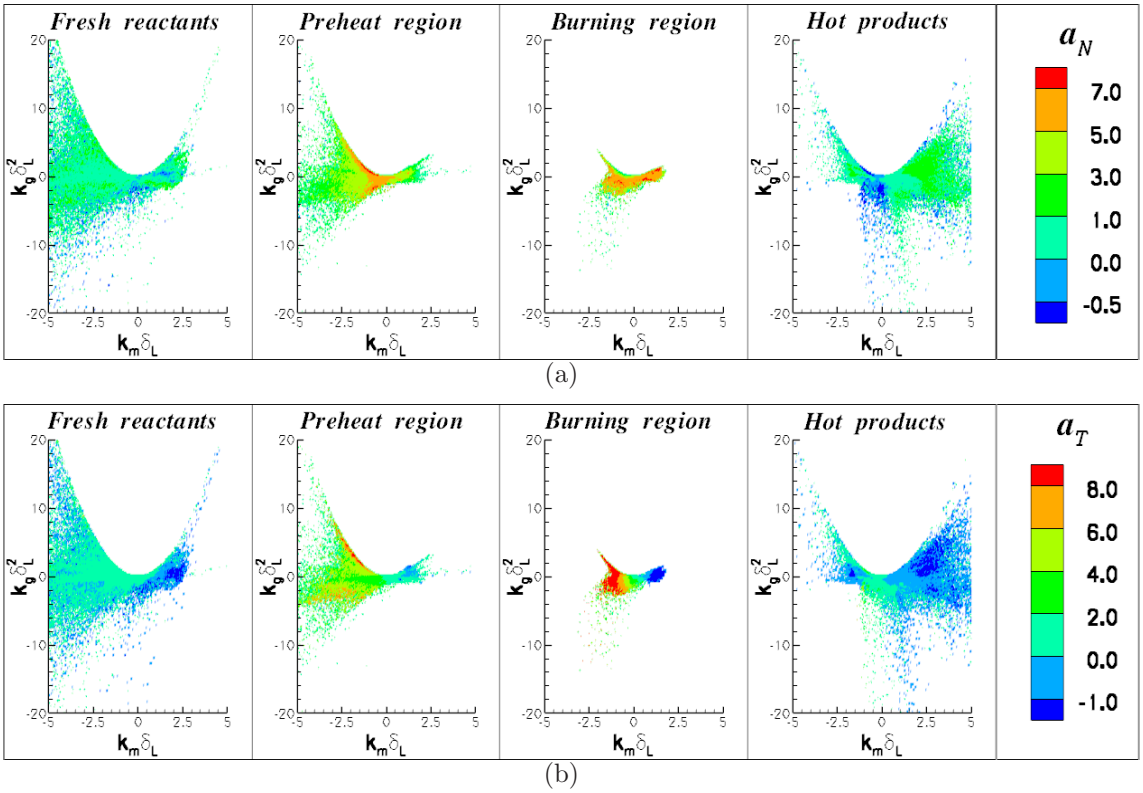

Figure 7.19: (a) Normal, and (b) tangential strain rates conditional upon the mean and Gauss curvatures, k_m and k_g. The terms have been normalized with $\langle \nabla \cdot \mathbf{u} \rangle$ using all the samples of the computational domain.

ent levels of reaction rate. a_N and a_T have been normalized with $\langle \nabla \cdot \mathbf{u} \rangle$ and $|\nabla c|$ with its own rms using all the values of the domain. Referring to a_T, there seems to be the same likelihood of positive and negative values in all regions of computational domain, whereas only in the 'fresh' and 'burnt' gases a_N has the same likelihood of positive and negative values. The statistical probabilities are above the line $a_T + a_N = 0$ in the 'preheat' and 'burning' regions, which indicates that in these regions fluid elements undergo expansion. The latter finding is in connection with the

results shown in Figure 6.14(a) and the positive dilatation rates belonging to these flame zones. As this study pertain to small-scale features and has a certain degree of universality, one can affirm that the joint statistical probabilities of a_N and a_T should always be above the line $a_T + a_N = 0$ in the regions with high chemical activity and regardless of the configuration under study. On the other hand, it is interesting to note that positive values of a_N are dominant over negative ones in the 'preheat' and 'burning' regions. $a_N > 0$ indicates positive stretching in the normal direction to the iso-surface, which means that the infinitesimal distance between two iso-surfaces increases. This finding is surprising looking at Figure 7.20(b) where $|\nabla c|$ is maxima for the 'preheat' and 'burning' regions.

The iso-scalar surfaces must move closer to each other to produce an increase of $|\nabla c|$. Thus, the 'additional' part of the normal strain rate, $\partial V^c/\partial x_N$, must be acting in a negative way so that $|\nabla c|$ increases. The 'additional' part of the normal strain rate was analyzed in Figure 7.12, and measures the difference of propagation velocities of different iso-surfaces. The competition between a_N and $\partial V^c/\partial x_N$ determines the magnitude of the *'effective'* normal strain rate $a_N+\partial V^c/\partial x_N$. Figure 7.21 depicts the *'effective'* normal strain rate, a_N and $\partial V^c/\partial x_N$, for nonmaterial iso-surfaces. Vertical solid bars in the curves indicate the respective root-mean-square value at every point and the vertical dotted line marks the limit of the

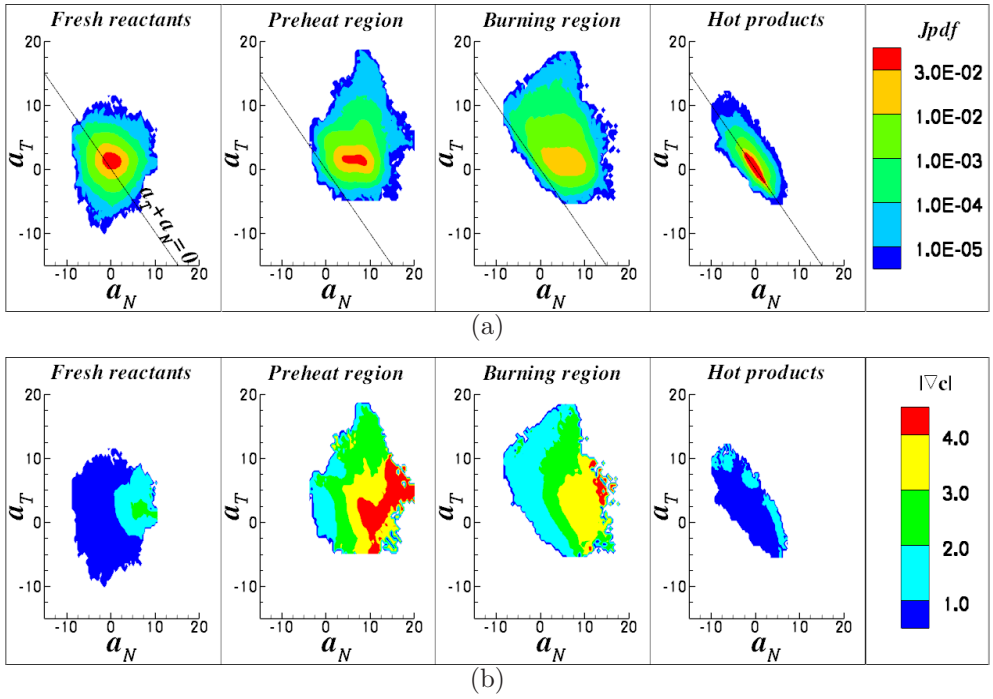

Figure 7.20: (a) Joint pdf of the normal and tangential strain rates, a_N and a_T. (b) Scalar gradient modulus, $|\nabla c|$, conditional upon the normal and tangential strain rates.

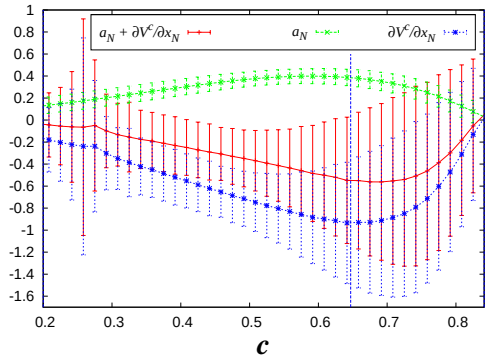

Figure 7.21: *'Effective'* normal strain rate and its contributions, a_N and $\partial V^c/\partial x_N$, across the progress variable. The variables have been normalized with τ_η. Vertical solid bars in the curves indicate their respective root-mean-square values and the vertical dotted line marks the limit of the 'preheat' and 'burning' regions.

'preheat' and 'burning' regions. This figure only shows the 'preheat' and 'burning' regions because in the 'fresh gases' and 'hot products' the val-

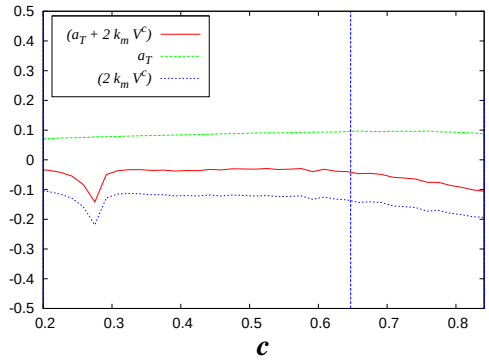

Figure 7.22: *'Effective'* tangential strain rate and its contributions, a_T and $2k_mV^c$, across the progress variable. The variables have been normalized with τ_η. Vertical dotted lines mark the limits of the four regions of the computational domain.

ues of a_N and the difference of propagation velocities are very low, thus, the competition between a_N and $\partial V^c/\partial x_N$ is near zero. It can be seen that $\partial V^c/\partial x_N$ is negative, with its absolute value greater than a_N. The mean value of $a_N + \partial V^c/\partial x_N$ is negative and displays an almost identical variation to that of $\partial V^c/\partial x_N$. It is possible also to have positive $a_N + \partial V^c/\partial x_N$ where a_N displays its maxima values and also towards the 'fresh' and 'burnt' gases. It is interesting to note that with increasing values of the progress variable the mean of the *'effective'* normal strain rate starts decreasing and attains a minimum value within the 'burning' region. This finding is consistent with the decreasing of V^c when iso-scalar surfaces move from the 'burning' region to the 'preheat' region (as shown in Figure 7.11).

It seems that regardless of the configuration under study in combusting

flows with significant density variations, the *'effective'* normal strain rate is negative. This is owing to the term $\partial V^c/\partial x_N$, which is also negative due to the fact that the difference of propagation velocities belonging to the chemical term are negative and dominant over the contributions of the molecular diffusion term. $a_N + \partial V^c/\partial x_N < 0$ allows that the iso-scalar surfaces move closer to each other, thus, scalar gradients and scalar fluctuation dissipation rates will increase with time. The latter is apparent in Figure 7.23 where the tails of the scalar gradient modulus pdf extends to a wider range of values for increasing times; the opposite is true for the mixing of a reactive scalar in a field of statistically homogeneous and stationary turbulence in a constant density fluid (see Figure 5.11).

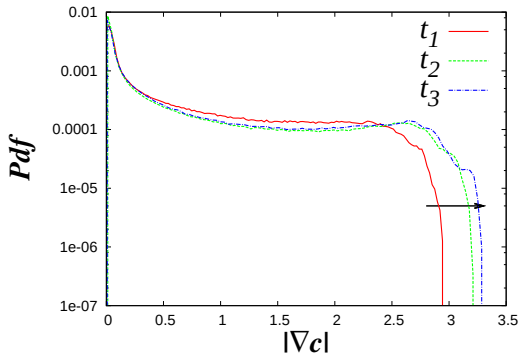

Figure 7.23: Scalar gradient modulus pdf's at several simulation times.

The *'effective'* tangential strain rate, $(a_T + 2k_m V^c)$, and its contributions, a_T and $(2k_m V^c)$, have been calculated upon the progress variable and plotted together in Figure 7.22. It is important to note that these variables have an almost constant mean value ranging from 'fresh' reactants to 'hot'

products. On the other hand, $(a_T + 2k_m V^c)$ is negative and displays an almost identical variation to that of $(2k_m V^c)$ which is also negative. The latter finding yields surface reduction due to concave iso-scalar surfaces propagation. Finally, it is also remarkable that $(a_T + 2k_m V^c) < 0$ in these 'preheat' and 'burning' regions has compressive effects that reduce the iso-surface infinitesimal area, which implies separation of iso-surfaces with their area elements shrinking.

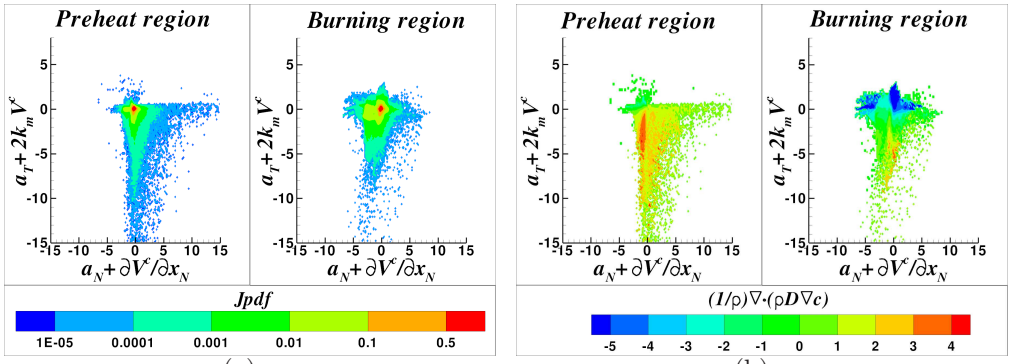

(a) (b)

Figure 7.24: (a) Joint pdf of the line and surface stretches, $a_N + \partial V^c/\partial x_N$ and $a_T + 2k_m V^c$, and (b) molecular diffusion rate, $(1/\rho)\nabla \cdot (\rho D \nabla c)$, conditional upon the line and surface stretches.

Figure 7.24 depicts the joint PDF of the *'effective'* normal and tangential strain rates, and $(1/\rho)\nabla \cdot (\rho D \nabla Y)$ conditioned upon $(a_N + \partial V^Y/\partial x_N)$ and $(a_T + 2k_m V^Y)$ in the 'preheat' and 'burning' regions. In the 'preheat region' $(a_N + \partial V^Y/\partial x_N)$ has a high likelihood of positive and negative values with a long tail extending along its positive axis, whereas $(a_T + 2k_m V^Y)$ is mainly negative with most probable values near the origin; this implies separation of iso-surfaces with their area elements shrinking. In the 'burning'

region the *'effective'* normal strain rate is mainly negative; $(a_T + 2k_m V^Y)$ displays both positive and negative values with a long tail extending along its negative axis; most probable normal and tangential *'effective'* strain rates locate also near the origin.

The molecular diffusion rate depends on both strain rates; significant values of molecular transport occur always for large negative *'effective'* normal strain rates. Positive values of $(1/\rho)\nabla \cdot (\rho D \nabla c)$ correlate with negative $(a_T + 2k_m V^Y)$, which points out a enhance of molecular diffusion process by area elements shrinking. Any infinitesimal non-material volume element appended to an iso-scalar surface will undergo contraction in the direction normal to the iso-surface. These findings are in agreement with the results of Chapter 4, Section 6.3.3. The thermal expansion and scalar conversion, resulting from the chemical reaction rate and Fickian molecular diffusion, given by Eq. (4.77), yield the previously described behavior.

7.3.4 Small-scale flow structures

According to Eq. (4.41), the local volumetric dilatation rate, $\nabla \cdot \mathbf{u}$, results from the summation of the eigenvalues of the strain rate tensor Λ_1, Λ_2 and Λ_3, which are ordered from the largest to the smallest value. As the case under study is with variable-density the sum of the eigenvalues can be distinct of zero, $\nabla \cdot \mathbf{u} = \Lambda_1 + \Lambda_2 + \Lambda_3 \neq 0$. The latter statement has

not only been observed in the results analyzed in Section 7.3.3 but also is confirmed by the pdf's shown in Figure 7.25 for the three eigenvalues of the strain rate tensor.

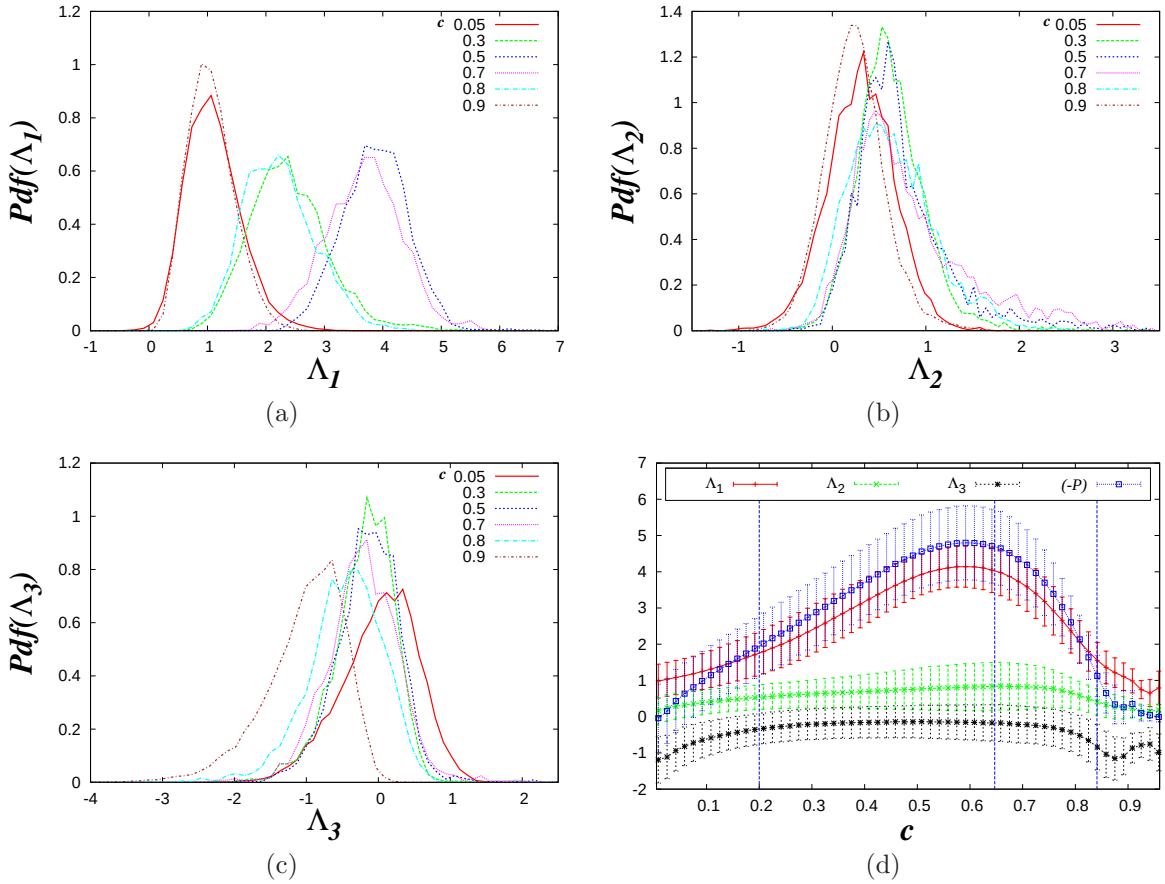

Figure 7.25: Eigenvalues of the strain rate tensor. (a) Pdf of Λ_1, (b) Λ_2 and (c) Λ_3 for different levels of c. (d) Eigenvalues conditional upon the progress variable. For Figure 7.25(d), vertical solid bars in the terms indicate their respective root-mean-square values and the vertical dotted lines in figure mark the four regions of the computational domain.

In this figure the eigenvalues have been normalized with $\langle Q_W \rangle^{1/2}$. It can be seen that the probability of positive values for Λ_1, Λ_2 and Λ_3 (which turn into flow expansion effects) is greater in the 'preheat' and 'burning' regions. This is related to the high chemical reaction rates located in these regions of the computational domain that foster the divergent features in the flow. On the other hand, negative values for the eigenvalues (which indicate compressive effects) increase their likelihood in the 'fresh' and 'burnt' gases. The mean value of the most extensive eigenvalue, Λ_1, is positive for all regions of the computational domain, and it increases as progress variable c does, reaching its maximum value in the 'preheat' region. The pdf's for Λ_2 are similar, with positive mean values, and small (large) tails toward negative (positive) values. Referring to Figure 7.25(c), it is evident that the probability of finding high negative Λ_3 is greater towards the 'fresh' and 'burnt' gases where the reaction rate is negligible. $\nabla \cdot \mathbf{u}$ increases from 'fresh' gases, reaches a maximum in the 'preheat' region and after decreases toward the 'hot' products. Then, Λ_1 is the eigenvalue that best represents its behavior across the progress variable.

As mentioned in Chapters 3 and 4, the eigenvalues have associated their corresponding eigenvectors, $\mathbf{e}_1$, $\mathbf{e}_2$, and $\mathbf{e}_3$; the subindex i orders the eigenvectors by decreasing corresponding eigenvalues. The alignment between the strain principal directions and the flame normal, $\mathbf{n}$, indicate how are

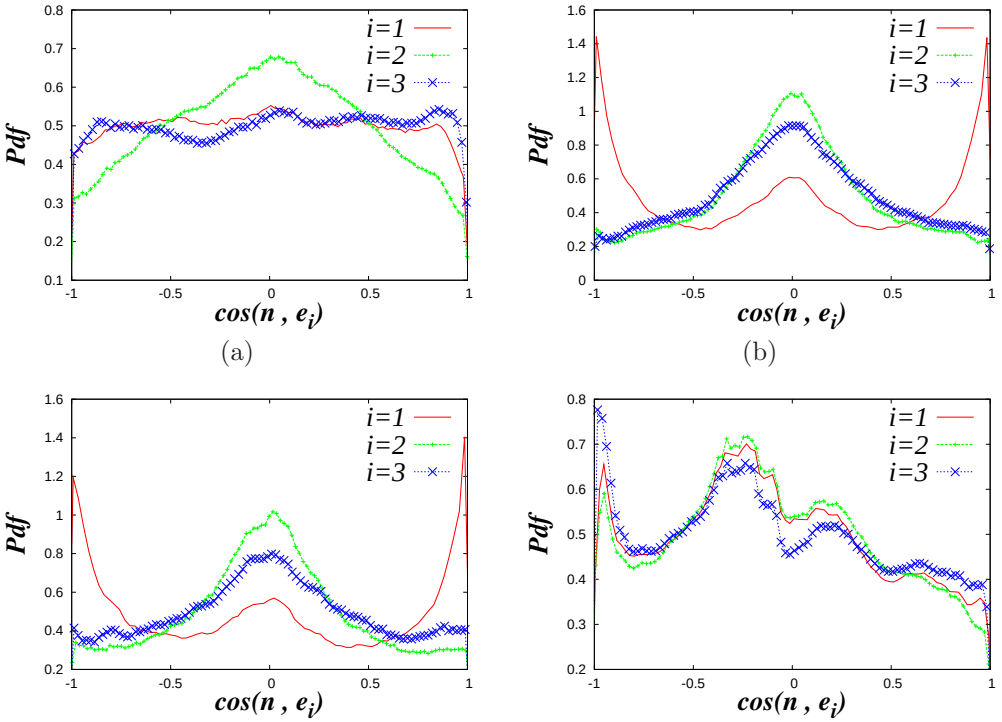

Figure 7.26: Pdf's of cos($\mathbf{n}$, $\mathbf{e}_i$). $\mathbf{n}$ is the unit vector normal to the iso-scalar surface and $\mathbf{e}_i$ are the eigenvectors corresponding to the three eigenvalues of S_{ij}. $i = 1$ corresponds to the most positive (extensive) eigenvalue, $i = 2$ the intermediate and $i = 3$ the most negative. (a) Fresh reactants, (b) preheat region, (c) burning region, (d) hot products.

located the nodal topologies of the turbulent flow respect to the iso-scalar surfaces. Figure 7.26 depicts the pdf's of the cosines of the angles between the normal vector to the iso-scalar surfaces and the strain rate principal directions. There seems to be a slight alignment between the normal vector and the most extensive and compressive eigenvectors in 'fresh' gases, which means that in this part of the computational domain the fluid elements undergo both expansion and compressive effects. In the 'preheat' and 'burning' regions the flame normal has a strong alignment with $\mathbf{e}_1$,

which is in agreement with results analyzed in Chapter 4, Section 6.3.4, and recent numerical [72, 113, 114] and experimental results [115]. Here, it is important to highlight the following: Λ_1 is the eigenvalue that best represents $\nabla \cdot \mathbf{u}$ which, in turn, displays an almost identical variation to that of a_N, thus, Λ_1 is related to a_N; in accordance with this, the alignment of $\mathbf{e}_1$ with the normal flame confirms that the distance between iso-scalar surfaces increase due to positive a_N's, which hamper scalar-gradients. Finally, in the 'hot' products there is no alignment, which might be explained by the decorrelation of the variables with the scalar value due to the mixing layer created by the co-flow of burned products in the jet flame.

Another way to study the alignment is to see how are located the focal topologies (related to the vorticity) with respect to iso-scalar surfaces. For this study is pertinent to examine the alignment of the vorticity vector, $\boldsymbol{\omega}$, with the normal vector, $\mathbf{n}$. Figure 7.27 plots the pdf's of the cosine between the flame normal and the local vorticity vector for all regions of the computational domain. It seems that, regardless of the configuration under study, the results for this alignment do not change. As detailed in Sections 5.4.4 and 6.3.4, the probability of finding the vorticity vector lying in the plane of the iso-scalar surfaces is high. Thus, there will be the same likelihood of positive and negative values of surface stretching in the tangent plane to the iso-scalar surfaces. This results is consistent with the

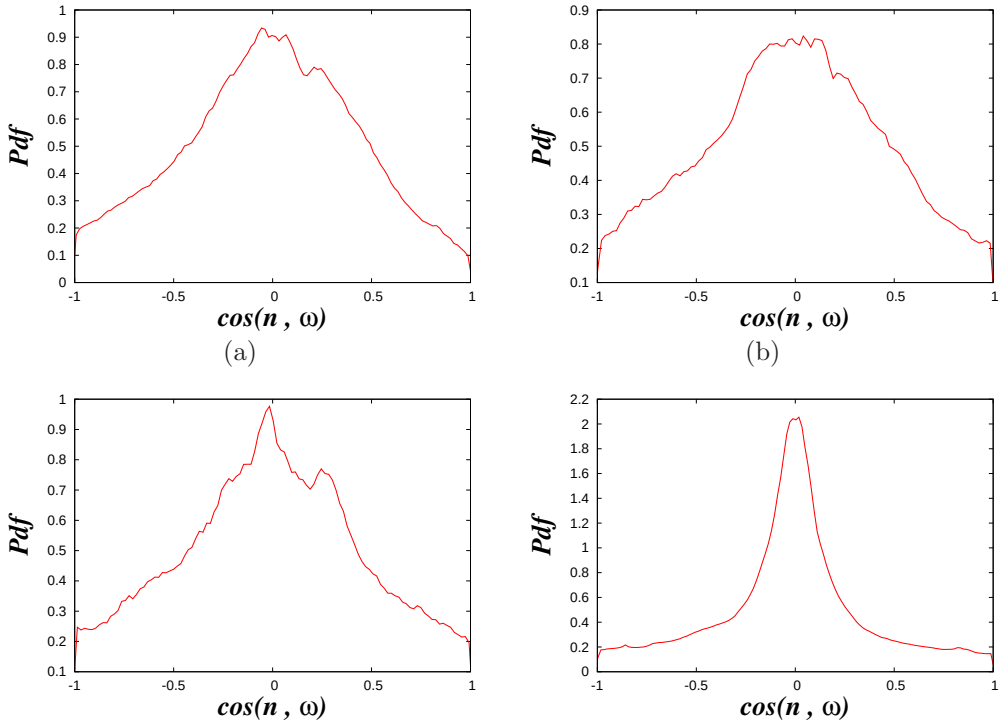

Figure 7.27: Pdf's of cos(**n**, $\boldsymbol{\omega}$). **n** is the unit vector normal to iso-scalar surfaces. $\boldsymbol{\omega}$ is the local vorticity vector. (a) Fresh reactants, (b) preheat region, (c) burning region, (d) hot products.

constant behavior of the tangential strain rate across the progress variable (see Figures 7.18(a) and 7.18(d)).

7.3.4.1 Invariants of the velocity-gradient tensor and local flow topologies

Combustion instabilities can be created, in particular, by the diffusion effects, thermal expansion, or heat losses. For premixed flames, thermal expansion plays an important role in the hydrodynamic instability: it creates sharp folds in the flame front. On the other hand, in reacting turbulent flows there are external perturbations, different from diffusive-thermal ef-

fects, coming from the turbulent field in which the flame front propagates. The effects of these perturbations might be due to the small-scale local flow topologies [18], which in interaction with the flame front could create different small-scale scalar structures. Thus, it is of considerable interest to study these turbulent flow topologies and their influence upon the iso-scalar surfaces.

As mentioned in previous Chapters, one way to provide information on this subject is to study the local flow topology and to analyze the behavior of the invariants, P, Q, R, of the velocity-gradient tensor [18]. The first invariant of the velocity-gradient tensor, $P = -\nabla \cdot \mathbf{u}$, will not be consider in this section since it was scrutinized in Section 7.3.3. Here, the attention is put in the other invariants, as well as in the production/annihilation terms of the transport equations for the enstrophy and the total strain [Eqs. (6.45) and (6.46)].

Figure 7.28 depicts the invariants Q, Q_S, Q_W, R, R_S, and $1/4(\omega_i\omega_i S_{kk} - \omega_i S_{ij}\omega_j)$ conditional upon the progress variable c. The seconds and thirds invariants have been normalized with $\langle Q_W \rangle$ and $\langle Q_W \rangle^{3/2}$, respectively, using all the iso-scalar surfaces. Referring to Figure 7.28(a), it is evident that Q displays an almost identical behavior to that of the local dissipation/dilatation, Q_S. This trend is due to the fact that Q_S is larger in magnitude than the local enstrophy, Q_W, which is consistent with the

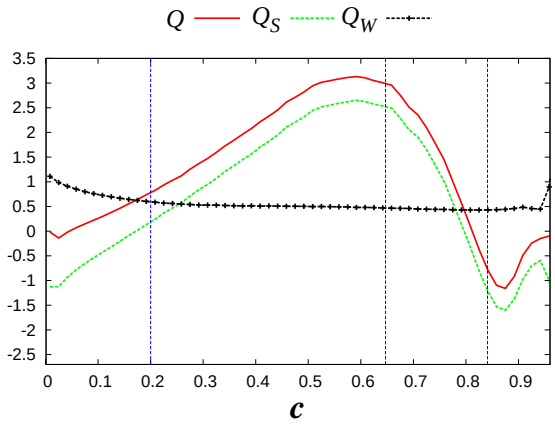

(a)

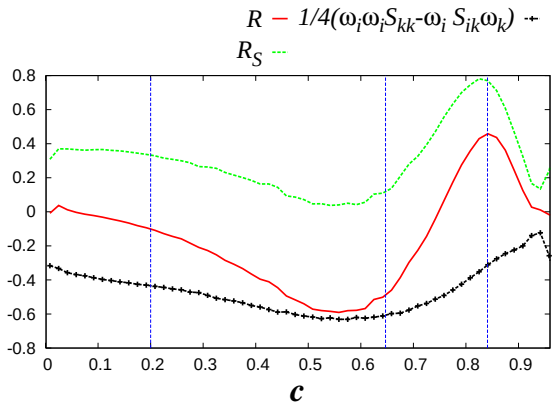

(b)

Figure 7.28: (a) Q, Q_S, Q_W, and (b) R, R_S, $1/4(\omega_i\omega_i S_{kk} - \omega_i S_{ik}\omega_k)$ conditional upon the progress variable. Vertical dotted lines mark the limits of the four regions of the computational domain.

behavior of dissipation/dilatation analyzed in Section 7.3.3. The nodal topologies are related to $Q_S(\equiv (P^2 - S_{ij}S_{ij})/2))$, thus, the budget of these topologies in the 'preheat' and 'burning' might be due to the action of the high dilatation rates. On the other hand, the budget of nodal topologies in the 'fresh' and 'burnt' gases might be governed by the dissipation process, $S_{ij}S_{ij}$, since the negative values of $Q_S(\equiv (P^2 - S_{ij}S_{ij})/2))$ predominate

in these regions of the computational domain. This finding is consistent with the fact that $\langle P^2 \rangle \approx 0$ in these flame regions (see Figures 7.18(a) and 7.18(b)). The above seems to indicate a universality in the behavior of nodal topologies and their budgets in reacting turbulent flows since the same trend is observed in the results shown in Figure 6.21(a). Referring to Q_W, it has a slight decreasing from 'fresh reactants' to regions with high chemical activity, which can be related to the increments of dynamic viscosity due to the increasing temperature that destroy vorticity. The almost constant behavior of Q_W in the regions with high chemical activity means that there is the same likelihood of increasing or reducing an iso-surface infinitesimal area by the action of the complicated turbulent motions of the vortices. If the vorticity budget is constant in these regions the a_T budget there will be constant too, since the vorticity vector is lying in the tangent plane to the iso-scalar surfaces keeping the values of a_T constant. This finding is related to the constant values of the tangential strain rate across the progress variable (see Figures 7.18(a) and 7.18(d)).

R_S has a mean value always positive. Despite the fact that $R_S (\equiv (-P^3 + 3PQ_S - S_{ik}S_{ij}S_{jk})/3)$ includes several dynamically significant complex processes, it can be seen in Figure 7.28(b) that is governed by $-\langle P \rangle^3 > 0$ (since $\langle P \rangle = -\langle \nabla \cdot \mathbf{u} \rangle < 0$) and $-S_{ik}S_{ij}S_{jk} (\equiv -\Lambda_1\Lambda_2\Lambda_3)$. The latter is always positive due to the fact that $\langle \Lambda_1 \rangle > 0$, $\langle \Lambda_2 \rangle > 0$ and $\langle \Lambda_3 \rangle < 0$ according

to results in Figure 7.25. On the other hand, the enstrophy production, $\omega_i S_{ik} \omega_k - \omega_i \omega_i S_{kk}$, defined in Eq. (6.45) is always positive. The balance between this term and the annihilation of enstrophy due to the increments of dynamic viscosity, leads to a constant budget of Q_W across the progress variable. It can be seen in Figure 7.28(b) that $\omega_i S_{ik} \omega_k - \omega_i \omega_i S_{kk}$ has lower magnitude than that of R_S. Thus, the balance for R (Eq. (4.50)) has the same trend and sign than that of R_S.

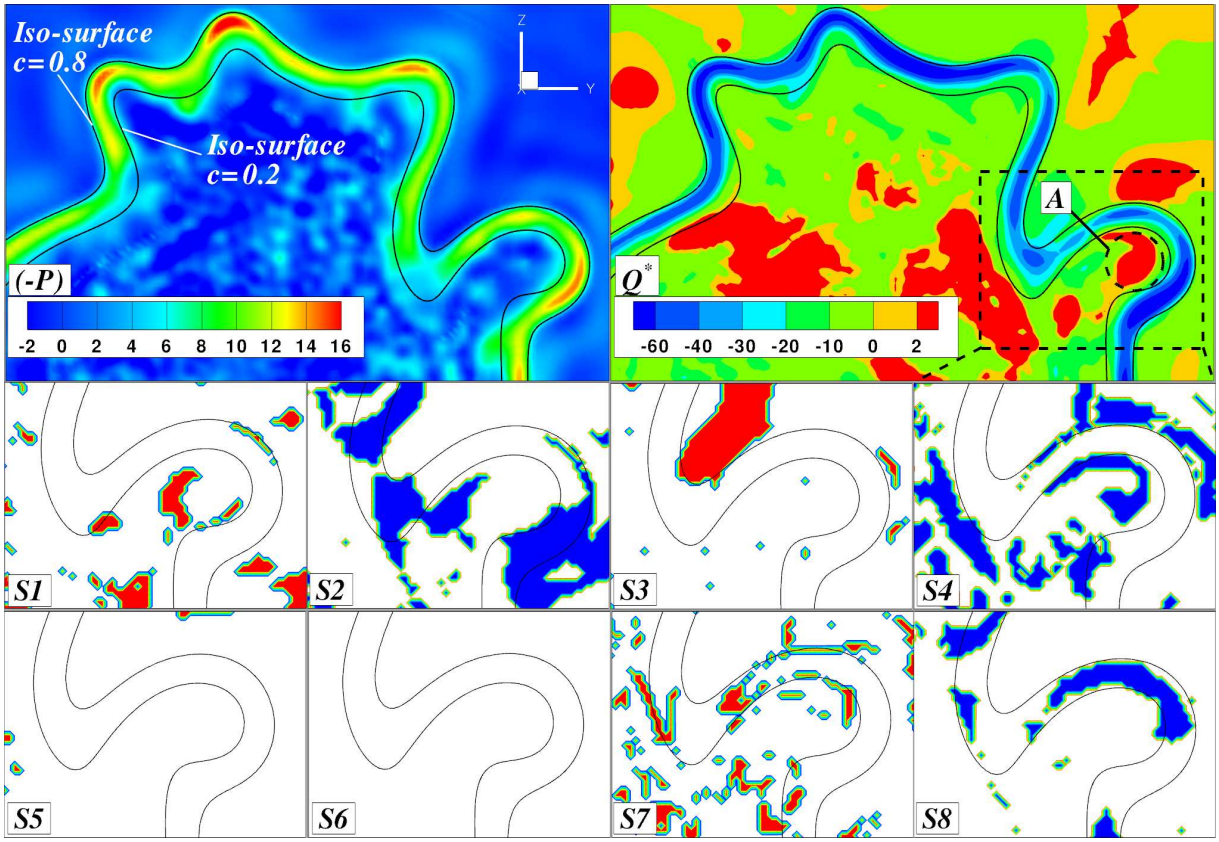

Figure 7.29: $(-P) = \nabla \cdot \mathbf{u}$, Q^* and flow topologies $(S1 - S8)$ in the computational domain. $(-P)$ and Q^* have been normalized with $\langle \nabla \cdot \mathbf{u} \rangle$ and $\langle \nabla \cdot \mathbf{u} \rangle^2$, respectively. $\langle \nabla \cdot \mathbf{u} \rangle$ has been obtained using all the samples of the four reaction-rate conditioned regions

Flow topology effects upon the iso-scalar surfaces can be examined if we

track the topologies around the flame. Figure 7.29 shows the zoom of a $y-z$ plane of the computational domain. This zoom displays two scalar iso-lines, the volumetric dilatation rate $(-P) = \nabla \cdot \mathbf{u}$, the flow topologies from S1 to S8 and the Q^* invariant used by Hunt *et al.* [125],

$$Q^* \equiv (-S_{ij}S_{ij} + W_{ij}W_{ij})/2\,. \tag{7.34}$$

Q^* separates strain dominated regions ($Q^* < 0$) from coherent fine scale eddies ($Q^* > 0$). It can be seen in Figure 7.29 that local expansion ($-P < 0$) is significant between the iso-lines, with maximum (minimum) values associated to concave (convex) scalar geometries. These processes can be explained by the heat conduction focussing (defocussing) effect of the scalar concave (convex) structures. High positive values of $(-P)$ also highlight a zone between the scalar iso-lines where an intense thermo-chemical activity prevails. The dotted black circle 'A' marks a zone with $Q^* > 0$, which can be considered like a 'canonical' vortex. The identified vortex tends to fold the flame front. It can also be noted high stretching zones ($Q^* < 0$) found into the flame with joint interactions of unstable topologies, such as S2 (UN/S/S) and S8 (UN/UN/UN). The latter has been identified as a typical topology of combusting flows with significant heat release [126]. It is apparent that the S3 (SN/S/S), S5 (SFC) and S6 (SN/SN/SN) topologies

are absent in this flame.

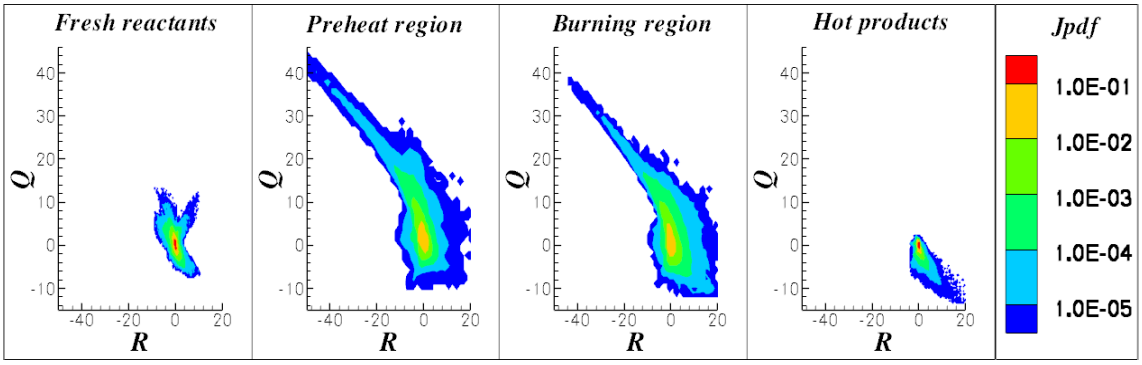

Figure 7.30: Joint pdf of $R - Q$. Joint pdf magnitudes decrease from the center to the circumference.

Figure 7.30 shows the joint pdf's of R and Q in the four regions of the computational domain. It is interesting to note that in this case, with chemical effects acting on the flow, the universal teardrop shape typical of constant-density turbulent flows disappears. Instead, the statistical distributions are displaced towards the left side and are sharper in the regions where high chemical activity exists, which is consistent with the statistical distributions corresponding to $P < 0$ (see Figure 4.2(c)). Referring to 'fresh' and 'burnt' gases, there are zones of the statistical distributions displaced towards the right, which indicates flow compressive effects due to the low values of the reaction rate. S6 (SN/SN/SN), typical of flows with local negative volumetric dilatation rates, is absent in all the statistical distributions. The unstable topology S2 (UN/S/S) is the most probable, whereas the stable compressive topologies S3 (SN/S/S) and S5 (SFC) have the low-

est share. Focal topologies such as S1 (UFC) and S4 (SFS) decrease their shares about 15%, in the 'preheating' and 'burning' regions, whereas the divergent topologies S7(UFS) and S8 (UN/UN/UN) increase their shares up to about 10% and 30%, respectively. In general, it is observed how focal topologies tend to disappear in favor of nodal micro-structures towards the 'hot products'. This latter can explain the slight decreasing of Q_W observed from 'fresh reactants' to regions with high chemical activity.

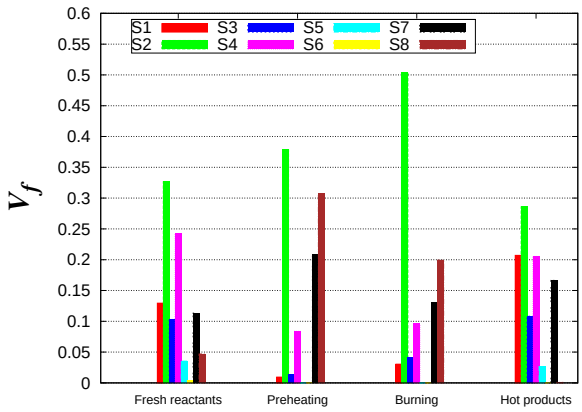

Figure 7.31: Topologies ($S1 - S8$) belonging to $P - Q - R$ space in the four regions of the computational domain.

Figure 7.31 shows volume fractions of the flow domain pertaining to different flow topologies. It can be seen that S5 (SFC) and S6 (SN/SN/SN) topologies, typical of flows with local negative volumetric dilatation rates, have the lowest share. Topologies S2 (UN/S/S), S4 (SFS), S7 (UFS) and S8 (UN/UN/UN) dominate in the 'preheat' and 'burning' regions, whereas the topologies S1 (UFC), S3 (SN/S/S) and S4 (SFS) are important in the

'fresh reactants' and tend to disappear as moving towards the regions with high chemical activity. The above is consistent with previous results [126]. In the 'hot products' the share of focal topologies is high, but the shape of the joint pdf of R and Q shown in Figure 7.30 suggests that in these topologies the vorticity is very low. Moreover, the focal topologies in this region might be created by the co-flow of burned products in the jet flame with values of local enstrophy.

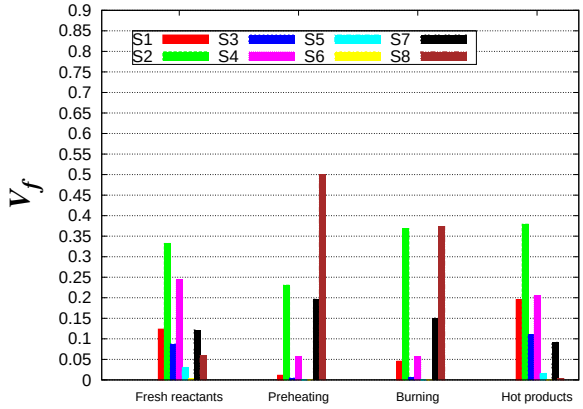

(a) Zone 2 (Concave iso-surfaces)

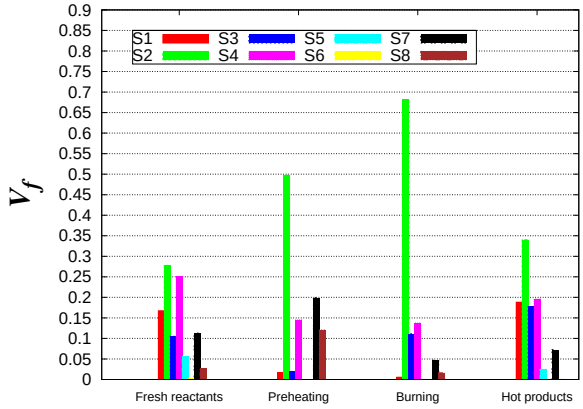

(b) Zone 3 (Convex iso-surfaces)

Figure 7.32: Topologies ($S1-S8$) belonging to $P-Q-R$ space: (a) zone 2 (Concave iso-surfaces); (b) zone 3 (Convex iso-surfaces).

In order to reduce the number of combinations of scalar field structures and flow topologies, the analysis of flow topologies has been restricted to only two zones of the $k_m - k_g$ plane of Figure 4.3: concave (zone 2) and convex (zone 3) geometries. This zones are characterized by the ranges given in Table 6.3. Figure 7.32 shows the volume fractions of the domain corresponding to the different flow topologies. These fractions have been calculated for the two curvature conditioned zones. The S2 (UN/S/S) topology dominates the local flow dynamics for the two zones and for all reaction-conditioned regions, but there is also some significant contribution of S8 (UN/UN/UN) for concave iso-surfaces (in the 'preheating' and 'burning' regions). S1 (UFC) and S3 (SN/S/S) have a low to moderate share, from 'preheat' region to 'hot' products, whereas S5 (SFC) and S6 (SN/SN/SN) topologies, typical of flows with local negative volumetric dilatation rates, are absent. Figure 7.32(a) confirms that unstable topologies S7 and S8 are associated more likely to concave iso-scalar surfaces, where heat-conduction focusing effects enhance the chemical reaction and increase the dilatation.

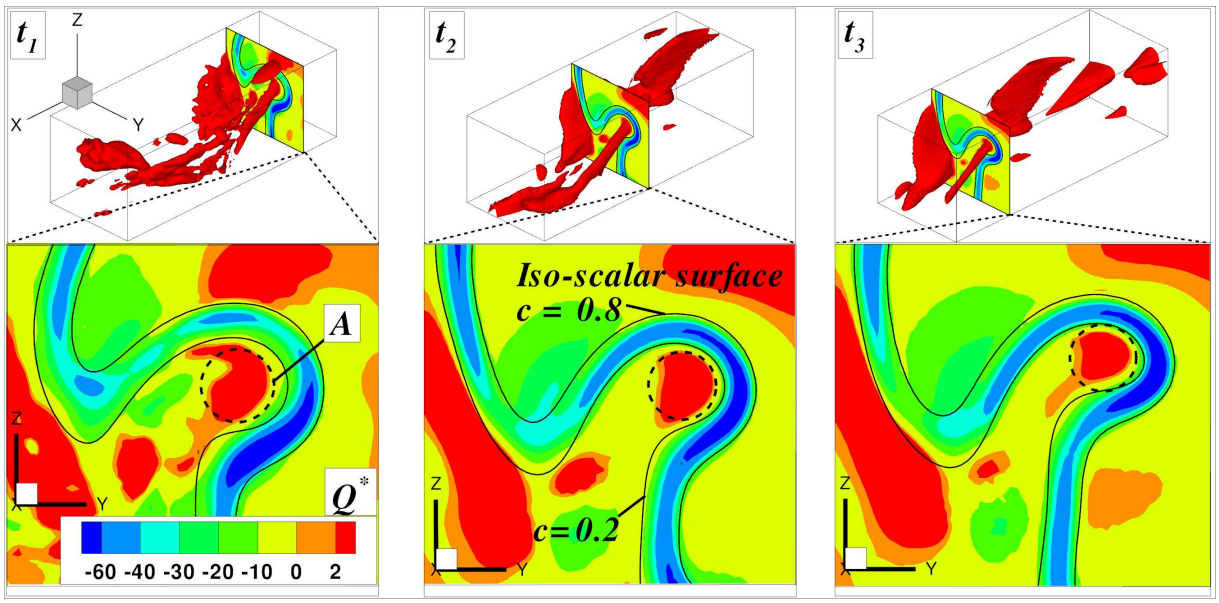

Figure 7.33: Contour surfaces of Q^* at three different times. The three dimensional surfaces shown at the top of the picture correspond to a value $Q^* = 3$. This zoom box coincides with the 'canonical' vortex marked with a dotted black circle 'A' in Figure 7.29.

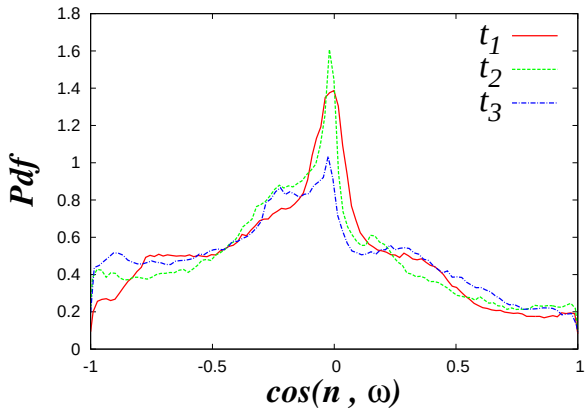

Figure 7.34: Pdf's of the cosine between the flame normal, $\mathbf{n}$, and the local vorticity vector, $\boldsymbol{\omega}$. These pdf's have been calculated for the zoom box of Figure 7.33.

Contour surfaces of Q^* are shown in Figure 7.33 at three different times separated by time increments of the order of the Kolmogorov micro-scale. This zoom box captures the 'canonical' vortex shown in Figure 7.29. The

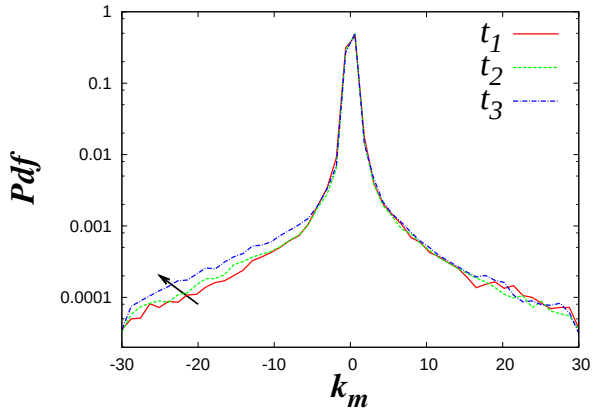

Figure 7.35: Pdf's of the mean curvature, k_m. These pdf's have been calculated for the zoom box of Figure 7.33.

red iso-surfaces at the top of the picture have a value $Q^* = 3$. It can be seen that the 'canonical' vortex (dotted black circle 'A') interacts with the iso-lines of the progress variable, c. It is important to remark that the diameter of the vortex decreases as well as its length as it evolves; Tsinober *et al.* [127] argue that in the enstrophy dominated regions the curvature radius of vortex lines increases. Visually, it seems that all these iso-surfaces $Q^* = 3$ are preferentially perpendicular to the unit vector normal to the iso-scalar surfaces: $\mathbf{n} = -\nabla c/|\nabla c|$. To calculate the alignment of these focal topologies respect to the iso-scalar surfaces, Figure 7.34 plots the pdf's of the cosine between the flame normal, $\mathbf{n}$, and the local vorticity vector, $\boldsymbol{\omega}$, at the three different times. The results of this alignment do not change and the probability of finding the vorticity vector parallel to the plane of the iso-scalar surfaces is high. These findings are in agreement with the

results of Chapter 4, Section 6.3.4 and DNS calculations [105], where the vorticity vector is found to lie preferentially in the plane of the flame.

It can also be seen in Figure 7.33 that where the identified vortex acts the concavity of the iso-scalar surface geometries increases. In order to quantify the increase of curvature of the iso-scalar surfaces, Figure 7.35 shows the pdf's of the mean curvature, k_m (For a positive (negative) flame curvature, $k_m > 0$ ($k_m < 0$), the scalar surface is convex (concave) towards the fresh gas side. $k_m = 0$ are flat iso-scalar structures). k_m has been made non-dimensional by the laminar flame thickness, δ_L. All the pdf's display maxima for nearly flat iso-scalar surfaces, in agreement with experimental results [60] and three-dimensional DNS calculations [126, 63, 101] of premixed turbulent flames. It is important to note that concave iso-surfaces increase their probability as they evolves, whereas convex ones remains equal for the three times under study. These results provide evidence that the local flow topologies have an influence in the geometry of flame structure apart from its diffusive-thermal effects.

7.4 Summary and conclusions

A three-dimensional DNS of a premixed methane-air turbulent jet flame in a piloted Bunsen burner configuration has been performed. The com-

putational domain has been divided into four regions ('fresh reactants', 'preheat', 'burning' and 'hot products'), characterized by the value of the chemical reaction rate and the progress variable. The scalar field geometries, in terms of the curvatures k_m and k_g, have been identified. Nearly flat iso-surfaces are the most probable local scalar structures. The high chemical activity smooths the large curvatures in the 'preheat' and 'burning' regions. Concave geometries towards 'fresh reactants' prevail in this jet flame configuration in front of the 'burning region', while convex structures are more probable in the 'hot products'. Some explanations for the latter feature, anticipated in the literature, in terms of small-scale eddies perpendicular to the iso-scalar surfaces must be carefully scrutinized in future research.

Molecular diffusion rate and its effects on the scalar field have also been analyzed. The tangential diffusion (due to the curvature) is negligible, whereas the contribution to the molecular diffusion rate due to the variation of $|\nabla Y|$ normal to the iso-surface is the strongest; the variation of ρD is not negligible in the regions with high chemical activity and has a positive contribution in the normal molecular diffusion. The total diffusion rate conditional upon the k_m and k_g suggests that convex geometries could enhance the heat removal through the defocusing of thermal conduction, whereas the concave iso-surfaces could enhance the diffusive removal

through the focusing of the heat of reaction.

The kinematics of non-material iso-scalar surfaces has been analyzed; a characteristic length scale normal to an iso-scalar surface emerges from that analysis. The infinitesimal distance between to iso-surfaces, δ_N, in the 'fresh gases' indicates that the mixing rate can be dominated by the small-scale flow features.

Expressions for the propagation speed of an iso-scalar surface relative to the fluid and its derivative, with respect to the normal direction to the constant composition surface and negative in the direction of the scalar gradient, have been obtained. The displacement speed of the iso-scalar surfaces, V^c, and its contributions due to the normal molecular diffusion variation, V_1 and chemical processes, V_3, are found to be consistent with the results reported by Chakraborty and Cant [62]. However, the contributions due to the variation of (ρD) and to the spatial curvature, V_2, are negligible. The displacement speed is governed by the chemical contribution, V_3, and it suggests that the iso-scalar surfaces located in the 'hot products' and 'burning' regions propagate faster than those in the 'fresh' gases.

The volumetric dilatation rate, $\nabla \cdot \mathrm{u}$, conditional upon k_m and k_g, has been obtained for the four regions. Maxima (minima) of $\nabla \cdot \mathrm{u}$ correspond to concave and flat (convex) scalar structures. This finding was also found in the analysis of Chapter 4, which suggests a universal behavior for the

dilatation and the scalar geometries regardless of the configuration under study.

An expression for $\nabla \cdot \mathrm{u}$, with additive contributions from molecular diffusion and chemical generation of the reaction progress variable, has been obtained, formulating a one-dimensional flamelet assumption based on a progress variable defined from temperature, as in a low Mach number approximation, but solving for a fully compressible energy equation in the DNS. A comparison of this expression with values of the volumetric dilatation rate, computed from the present DNS results, shows that differences are relatively small or moderate for $c < 0.5$. However, for $c > 0.5$, relative differences are significantly high, casting doubts on the validity of progress variables defined without a perfect match with the form of the primitive equations solved, in the case of a highly wrinkled flame surface.

The diffusive and reactive contributions to the flamelet model for $\nabla \cdot \mathrm{u}$, conditional upon k_m and k_g, have been analyzed for the four flow regions. The chemical term is positive and yields high values for slightly concave isosurfaces, cup-like and tile-like structures. Molecular diffusion contributes negatively to the volumetric dilatation rate in nearly flat and slightly convex geometries within the 'burning' region; defocussing of heat conduction by convex structures can explain this feature. Diffusive fluxes display high positive values for elliptic concave geometries in the 'preheat' region.

The dilatation rate has been disaggregated in the tangential, a_T, and normal, a_N, strain rates. Average tangential strain rates are approximately constant across the progress variable, whereas normal strain rates follow the trends of volumetric dilatation rates in the different regions of the computational domain. This means that locally the rate of change of an infinitesimal fluid volume per unit volume is stronger in the normal direction to the iso-surface than in the tangent plane to it. The tangential and normal strain rates conditional upon the k_m and k_g indicate that the correlations between local dilatation rate and scalar geometries come from the dependence of a_T on the curvature. The joint pdf's of a_N and a_T in the 'preheat' and 'burning' regions show their most probable values located above the line $a_N + a_T = 0$. This finding was also found in Chapter 4, which suggests a universal behavior for a_T and a_N in the regions with high chemical activity regardless of the configuration under study. The normal strain rate has the same likelihood of positive and negative values in the 'fresh' and 'burnt' gases, whereas in the 'preheat' and 'burning' regions is always positive. This indicates that the infinitesimal distance between two iso-surfaces by the a_N effects increases in the 'preheat' and 'burning' regions. The latter is balanced by the action of the *'additional'* part of the normal strain rate $\partial V^c/\partial x_N$, which is dominant and always negative for the four reaction-level regions. $\partial V^c/\partial x_N$ allows the *'effective'*

normal strain rate, $a_N + \partial V^c/\partial x_N$, to be negative and attains a minimum value within the 'burning' region. This is due to the fact that V^c decreases when iso-surfaces move from the 'burning' region to 'preheat' region. $a_N + \partial V^c/\partial x_N < 0$ allows that iso-scalar surfaces move closer to each other and then the scalar-gradients is enhanced; scalar gradient pdf clearly shows enhancement with time. The molecular diffusion rate depends on both *'effective'* strain rates; significant values of molecular transport occur always for large negative *'effective'* normal strain rates. Positive values of $(1/\rho)\nabla \cdot (\rho D \nabla c)$ correlate with negative $(a_T + 2k_m V^Y)$, which points out a enhance of molecular diffusion process by area elements shrinking.

The values of the principal strain rates, Λ_1, Λ_2 and Λ_3, have been obtained in the four regions of the computational domain. In this case, with chemical effects acting on the flow, $\langle \Lambda_2 \rangle > 0$, contrarily to constant-density turbulent flows [14, 71, 103, 104] (*cf.* Chapter 3, Section 5.4.4); furthermore, $\langle \Lambda_1 \rangle > 0$, and $\langle \Lambda_3 \rangle < 0$. All eigenvalues have a high probability of being positive towards the regions with high chemical activity, which is in agreement with $\nabla \cdot \mathbf{u} > 0$. The most extensive eigenvalue, Λ_1, represents clearly the behavior of $\nabla \cdot \mathbf{u}$. The eigenvector corresponding to most extensive eigenvalue, $\mathbf{e}_1$, is preferentially aligned with the unit vector normal to the iso-scalar surfaces, $\mathbf{n}$. This alignment was also found in Chapter 4 and in recent numerical [113, 72, 114] and experimental results [115] of turbulent

premixed flames. This fact suggests that the most extensive direction of nodal flow topologies is always aligned with the normal direction to the iso-surfaces. On the other hand, the focal flow topologies are predominantly lying in the tangent plane to the iso-scalar surfaces, thus, there will be the same likelihood of positive and negative values of surface stretching in these tangent planes. This result is consistent with the constant behavior of the tangential strain rate across the progress variable.

The production/annihilation terms of the transport equations for the enstrophy and the total strain have been studied. The dissipation/dilatation processes related to nodal topologies are governed by the high dilatation rates in the 'preheat' and 'burning', whereas in the 'fresh' and 'burnt' gases are governed by the dissipation process, $S_{ij}S_{ij}$. This seems to indicate a universality in the behavior of nodal topologies and their budgets in reacting turbulent flows since the same trend is observed in the results of Chapter 4. The local enstrophy, Q_W, decrease slightly towards the regions with high chemical activity and in these regions keeps its budget constant. This finding is consistent with the constant values of the tangential strain rate found across the progress variable: as the vorticity vector is lying in the tangent plane to the iso-scalar surfaces there will be the same likelihood of increasing or reducing an iso-surface infinitesimal area in these tangent planes. Furthermore, the dissipation production, R_S, is mainly governed

by the dilatation rates and its mean value is always positive across the progress variable. The enstrophy production, $\omega_i S_{ik} \omega_k - \omega_i \omega_i S_{kk}$, is always positive and competes with the annihilation of enstrophy due to the increments of dynamic viscosity leading to a constant budget of Q_W across the progress variable.

The universal teardrop shape of the joint pdf's of R and Q typical of constant-density turbulent flows disappears. Instead, the statistical distributions are displaced towards the left side and are sharper in the regions where high chemical activity exists. Stable flow topologies, such as S3 (SN/S/S), S5 (SFC) and S6 (SN/SN/SN), are negligible or have the lowest share across the progress variable. Focal topologies, such as S1 (UFC) and S4 (SFS), tend to disappear in favor of nodal micro-structures, such as S2 (UN/S/S) and S8 (UN/UN/UN), from 'fresh reactants' to the 'hot products'. This finding explains the slight decreasing of Q_W observed towards the 'hot products'. The study of the type of flow topologies conditional upon the scalar geometries suggests that nodal topologies S2 (UN/S/S) dominates the local flow dynamics in all reaction-conditioned regions, and that unstable and divergent topologies S7 (UFS) and S8 (UN/UN/UN) are more likely associated to concave iso-scalar surfaces, where heat-conduction focusing effects enhance the chemical reaction and increase the flow dilatation. Flow topology effects upon the iso-scalar surfaces have been examined

tracking the flow topologies around the flame. A 'canonical' vortex has been identified and its time evolution has been analyzed considering three different times separated by increments of the order of the Kolmogorov time micro-scale. This vortex is found to lie most probably in the plane of the iso-scalar surfaces. The local concave scalar structures increases where the identified vortex acts. These results provide evidence that local flow topologies have a strong influence in the geometry of flame structure apart from its diffusive-thermal effects.

The molecular diffusion effects upon the scalar field investigated in this work are a topic of interest, mainly to include them, if relevant, in new molecular mixing models of reacting turbulent flows. The relative importance of thermal and mass diffusivities as measured by the Lewis number should be investigated in future work, as well as the influence of the Karlovitz number in these phenomena. Future work should address the investigation of the fields in two close times with a difference of the order of Kolmogorov time micro-scale, where the nodal and focal flow topologies can be located around the flame. This will give information about the low pressure zones which could strongly affect the modulus of the flame curvature.

8
Conclusions

The most important findings of this work have been summarized at the end of every chapter, with the exceptions of Chapters 1 and 2. This last chapter aims at summarizing the main results of the research presented in this dissertation, as well as at comparing the four cases considered. Finally, some suggestions for future work are outlined.

Scalar mixing and turbulent reacting flows have been revisited through the study of three-dimensional DNS experiments and datasets for different turbulent flows of constant and variable density fluids. Statistically homogeneous and stationary isochoric turbulence, as well as turbulent premixed flames in an inflow-outflow configuration and in a jet with a co-flow of hot products have been investigated. Small-scale processes for both the scalar

and the velocity fields have been analyzed through of the study of the local flow topologies and scalar structures.

Small-scale structures of the scalar field, in terms of the mean and Gauss curvatures, k_m and k_g, of the scalar iso-surfaces, have been identified. The computational domain for the combusting flows has been divided into four regions: 'fresh reactants', 'preheat', 'burning' and 'hot products', characterized by the values of both the chemical reaction rate and the scalar field. For constant-density mixing and reaction, the curvature values of the iso-scalar surfaces grow as the Schmidt number increases. Nearly flat scalar iso-surfaces are the most probable geometries in all cases. For variable-density turbulent premixed flames, the thermochemical processes in regions with high chemical activity smooth out highly contorted iso-scalar surfaces, and annihilate large curvatures; convex scalar structures with moderate mean curvatures are regenerated in the 'hot products'.

The effects of the molecular diffusion rate on the scalar have also been analyzed. For constant-density mixing and reacting fields, the molecular diffusion rate is much greater for the reactive scalars than for the inert ones. The contribution to the tangential molecular diffusion rate due to the curvature effects is important for inert scalars, whereas it results negligible for reacting cases. This is also true for the variable-density turbulent combusting flows. While the product of the fluid density and the molec-

ular diffusion coefficient is constant for isochoric flows, it may vary for turbulent premixed flames and contributes to the molecular diffusion rate. However, the most important contribution to the molecular diffusion rate comes from the diffusion normal to the iso-scalar surfaces in all the cases studied. The molecular diffusion rate conditional upon k_m and k_g suggests that convex geometries could foster the heat removal through the defocusing of thermal conduction, whereas concave iso-surfaces could increase the local temperature through the focusing of the heat of reaction.

Understanding the transport of iso-scalar surfaces by turbulence and by molecular diffusion is tantamount to grasp the building blocks of scalar mixing. The kinematics of non-material iso-scalar surfaces has been theoretically analyzed. The time rate of change of the infinitesimal distance between two iso-surfaces is controlled by the value of the *'effective'* normal strain, which combines flow and diffusion-reaction induced strain rates. The value and sign of the *'effective'* normal strain rate determines whether the modulus of scalar gradients or, equivalently, the scalar fluctuation dissipation rate, increases or decreases with time.

Expressions for the propagation speed of an iso-scalar surface relative to the fluid and its derivative, with respect to the normal direction of the iso-scalar surfaces, have been obtained. Flows with constant and variable values of the product of the fluid density and the molecular diffusion coefficient

are distinguished. For the former, the displacement speed displays an almost identical variation to those of the normal and tangential diffusion contributions, whereas for the latter the propagation speed is governed by the chemical process.

For the turbulent premixed flames studied, heat generation by chemical reaction yields positive flow volumetric dilatation rates, $-P = \nabla \cdot \mathbf{u} > 0$, in the whole computational domain, which indicates the prevalence of positive flow strain rates normal to the iso-scalar surfaces. $\nabla \cdot \mathbf{u}$ displays maxima (minima) for concave (convex) micro-scalar structures due to heat conduction focusing (defocusing) effects. An expression for $\nabla \cdot \mathrm{u}$, with additive contributions from molecular diffusion and chemical generation of the reaction progress variable, has been obtained under a one-dimensional flamelet assumption based on a progress variable defined from temperature, as in a low Mach number approximation, but solving for a fully compressible energy equation in the DNS. A comparison of that expression with the dilatation rate values, obtained from the present DNS results, shows that differences between them are significantly high. These results casts doubts on the validity of this approximation. The dilatation rate has been decomposed into the tangential, a_T, and normal, a_N, strain rates. Average tangential strain rates are approximately constant for all values of the progress variable, whereas normal strain rates follow the trends of volumet-

ric dilatation rates in the different regions of the computational domain. The local rate of change of an infinitesimal fluid volume per unit volume seems dominated by variations in the normal direction to the iso-surface. The joint pdf's of a_N and a_T, in the combusting flow regions with high chemical activity, show that the most probable values are located above the line $a_N + a_T = 0$ regardless of the configuration under study. This indicates that a_N causes an increasing of the infinitesimal distance between two iso-surfaces in regions with high chemical activity. This is balanced by the 'induced' normal strain rate due to the term $\partial V^Y/\partial x_N$, which is dominant and always negative.

Flow normal strain rates, iso-surfaces propagation speeds and normal derivatives are radically different for the constant-density turbulence and for the premixed flames. While the flow normal strain rate is mainly negative for constant density flows, heat release causes its values to be positive in most of the computational flow domain for combusting flows. The profiles of the propagation speed and its derivative as functions of composition are also drastically different for constant and variable density flows. As a consequence, the *'effective'* normal strain rates, whose sign determines the temporal growth or decay of scalar gradients and dissipation rates, are predominantly positive for constant density turbulence and mostly negative in the cases of premixed flames. Pdf's of the modulus of the scalar

gradient clearly show the enhancement of the scalar gradients with time for turbulent premixed flames, and destruction for constant density mixing-reaction.

Small-scale structures of the velocity field have been investigated using the invariants of the velocity gradient tensor. The eigenvalues, Λ_1, Λ_2 and Λ_3, of the strain rate tensor have been obtained, where Λ_1 is the largest and Λ_3 the smallest. For all cases, $\langle\Lambda_1\rangle$ is always positive, $\langle\Lambda_3\rangle$ is negative, and the intermediate $\langle\Lambda_2\rangle$ remains positive; in the cases of turbulent premixed flames, Λ_3 has a high probability of being positive in regions with intense chemical activity, which is in agreement with the fact that $\nabla \cdot \mathbf{u} > 0$. The eigenvector corresponding to the largest eigenvalue, $\mathbf{e}_1$, is preferentially aligned with the unit vector normal to the iso-scalar surfaces, $\mathbf{n}$, in the 'preheat' and 'burning' regions for turbulent premixed flames; this fact suggests that the most extensive direction of nodal flow topologies is always aligned with the normal direction to the iso-surfaces. In the cases of constant-density mixing and reaction, $\mathbf{n}$ is aligned with the eigenvector corresponding to the smallest eigenvalue, $\mathbf{e}_3$, which enhances the local scalar gradient. On the other hand, for all cases considered in this work, the vorticity vector contributes to curve and fold the iso-surfaces as it is found to lie preferentially in the tangent plane to iso-scalar surfaces.

The local enstrophy and strain rate, as well as their production terms,

increase their magnitudes in the regions where the scalar value is close to the average and in regions with intense chemical activity in the statistically homogeneous turbulence cases. On the contrary, for turbulent premixed flames, these processes are annihilated as fluid elements move towards the 'hot products'. Positive volumetric dilatation rates, which are more intense in the 'preheating' and 'burning' regions, effectively destroy enstrophy. Furthermore, these destructive trends can also be associated to increments of viscosity due to temperature increments which fosters flow laminarization. The dissipation/dilatation processes, related to nodal topologies, are dominated by the high dilatation rates in the 'preheat' and 'burning' regions, whereas in the 'fresh' and 'burnt' gases are governed by the local dissipation of kinetic energy. The universal teardrop shape of the joint pdf's of Q and R appears for constant-density mixing and reaction, but this shape changes drastically for the cases of variable-density turbulent reacting flows: the joint pdf is displaced towards the left side and it becomes sharper in regions with high chemical activity. The statistical study of flow topologies suggests that focal topologies are dominant in the 'fresh reactants' and tend to disappear in favor of nodal structures as moving towards the 'hot products'. A 'canonical' vortex, identified in the simulation domain, has been studied: it is found to lie most probably in the plane of the iso-scalar surfaces. Its time evolution has also been

analyzed considering three different times separated by increments of the order of the Kolmogorov time micro-scale: the local concavity of scalar structures increases where the identified vortex acts. This result seems to provide evidence that local flow topologies have a strong influence in the flame structure geometry.

The contributions to the physical understanding of turbulent mixing resulting from this study should be incorporated to the development of molecular mixing models or used to improve the existing ones, particularly those for combusting turbulent flows. The functional dependence of the molecular diffusion term on the mass fraction and the relevance of the *'effective'* normal strain rate as a characteristic mixing rate should be scrutinized. The implementation in the molecular mixing models of the dimensional or dimensionless equations for the time rate of change of the infinitesimal distance between two adjacent iso-surfaces should be one of the main objectives of further research in the short term. All reaction-conditioned regions pointed out in our analysis, and the usefulness of the characteristic normal distance defined in this research must be investigated. Future work should also address the study of all these features in diffusion flames, and their applications in the non-premixed turbulent combustion.

9
Conclusiones

Los resultados más importantes se han resumido al final de cada capítulo, excepto en los Capítulos 1 y 2. Este último capítulo tiene como objetivos sintetizar los principales resultados de la investigación presentada en esta tesis, comparar los cuatro casos considerados y proponer algunas sugerencias para el trabajo futuro.

Se han analizado la mezcla escalar y los flujos reactivos turbulentos a través del estudio de experimentos numéricos de SND tridimensional y los datos resultantes para flujos turbulentos de densidad constante y variable. Se ha investigado turbulencia isócora estadísticamente estacionaria y homogénea, así como también llamas premezcladas turbulentas en una configuración de entrada-salida y en un jet con un co-flujo de productos calientes. Se

han analizado también los procesos de las pequeñas escalas, tanto para el campo escalar como para el campo de velocidades, mediante del estudio de las topologías del flujo local y las estructuras locales del escalar.

Se han identificado las estructuras de las pequeñas escalas del campo escalar, en términos de las curvaturas media y de Gauss, k_m y k_g. Se ha dividido el dominio computacional para los flujos con combustión en cuatro regiones: 'reactantes frescos', 'región de precalentamiento', 'región de quemado' y 'productos calientes', caracterizadas por los valores de la tasa de reacción y el campo escalar. Para mezcla y reacción con densidad constante, las curvaturas de las superficies iso-escalares crecen cuando el número Schmidt aumenta. Las geometrías más probables de las iso-superficies del escalar son prácticamente planas en todos los casos. Para las llamas premezcladas turbulentas de densidad variable, los procesos termoquímicos en regiones con alta actividad química suavizan las superficies iso-escalares muy arrugadas y eliminan las altas curvaturas; las estructuras del escalar convexas con curvaturas medias moderadas aparecen de nuevo en los 'productos calientes'.

Se han analizado también los efectos de la difusión molecular sobre el campo escalar. Para los campos de mezcla y reacción con densidad constante, la tasa de difusión molecular es mucho mayor para los casos de escalares reactivos que para los inertes. La contribución de la tasa de di-

fusión molecular tangencial debida a los efectos de curvatura es importante para escalares inertes, mientras que para los casos reactivos es despreciable. Esto último también sucede en los casos de flujos con combustión turbulenta de densidad variable. Si bien para flujos isócoros el producto de la densidad del fluido por el coeficiente de difusión molecular es constante, éste puede variar para llamas premezcladas turbulentas contribuyendo a la tasa de difusión molecular. Sin embargo, la contribución más importante a la difusión molecular viene dada por la difusión normal a las superficies iso-escalares en todos los casos analizados. La tasa de difusión molecular condicionada a k_m y k_g sugiere que las geometrías del escalar convexas podrían fomentar la eliminación de calor por la desfocalización de la conducción térmica, mientras que las iso-superficies cóncavas podrían aumentar la temperatura local a través de la focalización del calor de reacción.

Conocer bien el transporte de las superficies iso-escalares por turbulencia y difusión molecular equivale a comprender los elementos básicos de la mezcla escalar. Se ha analizado teóricamente la cinemática de las superficies iso-escalares, no materiales. La variación temporal de la distancia infinitesimal entre dos iso-superficies viene dada por el valor de la deformación normal *'efectiva'*, la cual suma las tasas de deformación inducidas por la reacción-difusión y las debidas al flujo. El valor y el signo de la deformación normal *'efectiva'* determinan si los módulos de los gradientes

del escalar o, equivalentemente, las tasas de disipación de las fluctuaciones del escalar, aumentan o disminuyen con el tiempo.

Se han obtenido las expresiones para la velocidad de propagación de una superficie iso-escalar relativa al fluido, y su derivadas con respecto a la dirección normal de las superficies iso-escalares. Se distinguen aquí los flujos con valores constantes o variables del producto de la densidad de fluido y el coeficiente de difusión molecular. Para los primeros, la velocidad de desplazamiento resulta casi idéntica a las contribuciones de difusión normal y tangencial, mientras que para los últimos la velocidad de propagación aparece gobernada por el proceso químico.

Para las llamas premezcladas turbulentas estudiadas, la generación de calor por reacción química produce tasas de dilatación volumétricas positivas en todo el dominio computacional, $-P = \nabla \cdot \mathbf{u} > 0$, lo cual indica el predominio de tasas de deformación positivas normales a las superficies iso-escalares. $\nabla \cdot \mathbf{u}$ muestra máximos (mínimos) para micro-estructuras del escalar cóncavas (convexas) debido a la focalización (desfocalización) de los efectos por conducción de calor. Se ha obtenido una expresión para $\nabla \cdot \mathrm{u}$, con las contribuciones aditivas de la difusión molecular y de la generación química de la variable de progreso definida en términos de la temperatura, suponiendo un flamelet unidimensional similar a la de una aproximación para bajo número de Mach, pero resuelta en la SND para una ecuación

de la energía del caso totalmente compresible. Una comparación entre esa expresión y la tasa de dilatación calculada con la SND muestra diferencias significativas, lo cual cuestiona la validez de las hipótesis usadas. Se ha descompuesto la tasa de dilatación volumétrica en sus componentes de deformación tangencial, a_T, y normal, a_N. El promedio de la tasa de deformación tangencial es aproximadamente constante para todos los valores de la variable de progreso, mientras que la velocidad de deformación normal sigue la tendencia de la dilatación volumétrica en las diferentes regiones del dominio computacional. La variación local de un volumen fluido infinitesimal por unidad de volumen parece dominada por variaciones en la dirección normal a la iso-superficie. Las pdfs conjuntas de a_N y a_T, en las regiones con alta actividad química, muestran sus valores más altos localizados por encima de la línea $a_N + a_T = 0$, independientemente de la configuración analizada. Esto indica que a_N causa un incremento de la distancia infinitesimal entre dos iso-superficies en regiones con actividad química alta. Este fenómeno se compensa con la velocidad 'inducida' de deformación normal debida al término $\partial V^Y/\partial x_N$, la cual es dominante y siempre positiva.

Las tasas de deformación normal, las velocidades de propagación y las derivadas normales son radicalmente diferentes en los casos de turbulencia con densidad constante y en llamas premezcladas. Mientras que la

velocidad de deformación normal del flujo es generalmente negativa para los casos de densidad constante, la liberación de calor hace que sus valores sean positivos en la mayor parte del dominio computacional para los flujos con combustión. Los perfiles de la velocidad de propagación y su derivadas como funciones de la composición son también diferentes para los casos de flujo de densidad constante y los de densidad variable. Como consecuencia, las velocidades de deformación normal *'efectiva'*, cuyo signo determina el crecimiento temporal o decaimiento de los gradientes del escalar y tasas de disipación, son predominantemente positivas para los casos de turbulencia con densidad constante y mayoritariamente negativas en los casos de las llamas premezcladas. Las pdfs del módulo del gradiente del escalar muestran claramente el crecimiento de los gradientes del escalar con el tiempo para llamas premezcladas turbulentas, y su disminución para los casos de mezcla y reacción con densidad constante.

Se han investigado las estructuras de las pequeñas escalas del campo de velocidad mediante los invariantes del tensor gradiente de velocidad. Se han obtenido los valores propios, Λ_1, Λ_2 y Λ_3, del tensor velocidad de deformación, donde Λ_1 es el más grande y Λ_3 el más pequeño. Para todos los casos, el promedio de Λ_1 es siempre positivo, el promedio de Λ_3 es negativo, y el promedio del intermedio Λ_2 resulta positivo; en los casos de llamas premezcladas, Λ_3 tiene una alta probabilidad de ser positivo

en las regiones con actividad química intensa, lo cual concuerda con el hecho que $\nabla \cdot \mathbf{u} > 0$. El vector propio correspondiente al autovalor más grande, $\mathbf{e}_1$, está preferentemente alineado con el vector normal unitario a las superficies iso-escalares, $\mathbf{n}$, en las regiones de 'precalentamiento' y 'quemado' para llamas premezcladas turbulentas; este hecho sugiere que la dirección más extensiva de las topologías nodales del flujo esté siempre alineada con la dirección normal a las superficies iso-escalares. En los casos de densidad constante tanto con mezcla como reacción, $\mathbf{n}$ resulta alineado con el vector propio correspondiente al autovalor más pequeño, $\mathbf{e}_3$, lo cual aumenta el gradiente del escalar local. Por otra parte, para todos los casos analizados en este trabajo, la vorticidad contribuye a curvar y doblar las iso-superficies ya que resulta casi siempre paralela al plano tangente a las superficies iso-escalares.

La enstrofía local y la velocidad de deformación así como sus términos de producción, para los casos de turbulencia estadísticamente homogénea, crecen significativamente en las regiones donde el valor del escalar es cercano al promedio y también en las regiones con actividad química intensa. Por el contrario, para las llamas premezcladas, estos procesos son muy atenuados al desplazarse los elementos fluidos hacia los 'productos calientes'. Las tasas de dilatación volumétrica positivas, que son más intensas en las regiones de 'precalentamiento' y 'quemado', efectivamente destruyen

la enstrofía. Además, estas tendencias disipativas también pueden asociarse a incrementos de viscosidad, ya que el aumento de la temperatura fomenta la laminarización del flujo. Los procesos de disipación/dilatación, relacionados con topologías nodales, están dominados por las altas tasas de dilatación en las regiones de 'precalentamiento' y 'quemado', mientras que en los gases 'frescos' y 'productos calientes' se rigen por el proceso de disipación de energía cinética local. La forma universal de lágrima de las pdfs conjuntas de Q y R aparece para los casos de mezcla y reacción de densidad constante, pero cambia drásticamente para los casos de flujos reactivos turbulentos con densidad variable: la pdf conjunta se desplaza hacia el lado izquierdo y se afila en las regiones con alta actividad química. El estudio estadístico de las topologías del flujo sugiere que las topologías focales son dominantes en los 'reactivos frescos' y tienden a desaparecer en favor de estructuras nodales al desplazarse hacia los 'productos calientes'. Se ha estudiado en detalle un vórtice 'canónico' identificado en el dominio de la simulación: éste aparece prácticamente paralelo al plano de las superficies iso-escalares. Su evolución temporal se ha analizado utilizando tres tiempos diferentes separados por incrementos del orden de la micro-escala de Kolmogorov y se ha encontrado que la concavidad local de las estructuras escalares aumenta donde el vórtice identificado actúa. Este resultado parece indicar que las topologías locales del flujo tienen una fuerte

influencia en la geometría de la estructura de la llama.

Las contribuciones a la comprensión física de la mezcla y combustión turbulentas resultantes de este estudio deberían ser incorporadas al desarrollo de modelos de mezcla molecular o utilizadas para mejorar los ya existentes, particularmente los de flujos con combustión turbulenta. La dependencia funcional del término de difusión molecular de la fracción de masa y la importancia de la velocidad de deformación normal *'efectiva'* considerada como una tasa de mezcla característica deberían ser analizadas. La implementación en los modelos de mezcla molecular de ecuaciones dimensionales o adimensionales para la variación temporal de la distancia infinitesimal, entre dos iso-superficies cercanas, debería ser uno de los principales objetivos a corto plazo. Todas las regiones condicionadas a los valores del escalar y la reacción indicadas en nuestro análisis y la utilidad de la distancia normal característica definida en este trabajo deben ser examinadas. El trabajo futuro también debería abordar la investigación de todos estos aspectos en llamas de difusión y sus aplicaciones a la combustión turbulenta no premezclada.

A

List of Publications

Journal

1. *L. Cifuentes*, C. Dopazo, J. Martin, and C. Jimenez. Local flow topologies and scalar structures in a turbulent premixed flame. *Phys. Fluids*, 26 (6), 065108-1/24, (2014).

   Abstract: A three-dimensional direct numerical simulation (DNS) of

a propagating turbulent premixed flame is performed using one-step Arrhenius model chemistry. The interaction of the flame thermochemical processes with the local geometries of the scalar field and flow topologies is studied. Four regions ('fresh reactants', 'preheating', 'burning' and 'hot products'), characterized by their reaction rate and mass fraction values, are examined. Thermochemical processes in the 'preheating' and 'burning' regions smooth out highly contorted iso-scalar surfaces, present in the 'fresh reactants', and annihilate large curvatures. Positive volumetric dilatation rates, $-P = \nabla \cdot \mathbf{u}$, display maxima for elliptic concave and minima for convex scalar micro-structures. Constant average tangential strain rates, a_T, with large fluctuations, occur throughout the flow domain, whereas normal strain rates, a_N, follow the trends of volumetric dilatation rates. Focal topologies, present in the 'fresh reactants', tend to disappear in favor of nodal structures as moving towards the 'hot products'. The vorticity vector is predominantly tangential to the iso-scalar surfaces. The Unstable Node/Saddle/Saddle and Stable Focus/Stretching topologies, present in the 'fresh reactants', correlate with large values of a_N and a_T providing hints on the flow topologies fostering scalar mixing.

2. *L. Cifuentes*, C. Dopazo, J. Martin, P. Domingo, and L. Vervisch. Local volumetric dilatation rate and scalar geometries in a premixed

methane-air turbulent jet flame. *Proc. Combust. Inst.*, 35, (2014).

Abstract: The local volumetric dilatation rate, namely, the rate of change of an infinitesimal fluid volume per unit volume, $\nabla \cdot \mathrm{u}$, is an important variable particularly in flows with heat release. Its tangential and normal strain rate components, a_T and a_N, respectively, account for stretching and partially for separation of iso-scalar surfaces. A three-dimensional direct numerical simulation (DNS) of a turbulent premixed methane-air flame in a piloted Bunsen burner configuration has been performed by solving the full conservation equations for mass, momentum, energy and chemical species using tabulated chemistry. Results for the volumetric dilatation rate as a function of the iso-scalar surface geometry, characterized by the mean and Gauss curvatures, k_m and k_g, are obtained in several zones (reactants, preheat, reacting and products) of the computational domain. Flat iso-scalar surfaces are the most likely geometries in agreement with previous DNS. The relationship between density and a reaction progress variable, under a low Mach number flamelet assumption, leads to an expression for $\nabla \cdot \mathrm{u}$ with contributions from progress variable source and molecular diffusion budget, with a significant contribution from the latter; this approximate expression for the volumetric dilatation rate is studied with DNS results. The joint pdf of a_N and a_T confirms that the line

$a_T + a_N = 0$ separates mostly expansive flow regions from compressive zones.

3. C. Dopazo, *L. Cifuentes*, J. Martin, and C. Jimenez. Strain rates normal to approaching iso-scalar surfaces in a turbulent premixed flame. *Combustion and Flame*, (2014). 2014.

   Abstract: A Direct Numerical Simulation (DNS) dataset of a turbulent premixed propagating flame with an Arrhenius one-step chemistry in an input-output configuration is examined. Combustion takes place in the 'corrugated flamelets' regime. Heat release causes the flow volumetric dilatation rate to be positive over most of the computational domain, with associated positive strain rates normal to iso-scalar surfaces and both positive or negative strain rates tangent to them. The normal propagation of convex and concave iso-surface infinitesimal area elements produces stretching and reduction, respectively, superposed to tangential flow strain rate effects. The normal propagation speed of iso-surfaces increases monotonically from 'fresh gases' to 'hot products', which draws two adjacent ones closer; this contribution, due to both chemistry and molecular diffusive transport, is much greater than that of the normal flow strain, and enhances mixing and chemical conversion. Many aspects of turbulent premixed flames traditionally explained in terms of tangential strain rates can

likely be well understood using the normal ones.

4. C. Dopazo, *L. Cifuentes*, J. Hierro and J. Martin. Still mixing after all these years. *Flow, Turbulence and Combustion* (Under review), (2015).

Abstract: DNS datasets for inert and reactive scalars in statistically homogeneous and stationary turbulence of constant density fluid, and for turbulent premixed flames in an inflow-outflow configuration and in a jet are examined. The objective is to gain a better physical understanding of mixing to use in modeling molecular diffusion terms. Classical descriptions in term of either scalar fluctuation moments or pdf conservation equations can be related to transport of iso-scalar surfaces by turbulent convection and molecular diffusion. The kinematics and propagation speeds of iso-surfaces are theoretically analyzed. The effective normal strain rate, which combines flow and diffusion-reaction induced processes, emerges as an essential variable; scalar gradients and dissipation rates increase for negative effective normal strains and decrease for positive ones. It is argued that the characteristic mixing time should be proportional to the inverse of the effective normal strain rate. The latter displays drastically different behaviors for constant density turbulence, with predominantly positive values, and for flows with significant heat release, with mostly

positive ones. The former turbulent flows cause scalars to become less dissipative as time progresses, whereas the latter increase scalar dissipation. Functional dependences of the molecular diffusion rate conditioned on composition are sought. It is suggested that the characteristic mixing time is determined by the different interrelated processes, mainly in the limits of very low and very high Karlovitz numbers.

5. *L. Cifuentes*, C. Dopazo, J. Martin, P. Domingo and L. Vervisch. Effects of the local flow topologies upon the structure of a premixed methane-air turbulent jet flame. *Flow, Turbulence and Combustion* (Under review), (2015).

   Abstract: Local flow topologies have been identified and the interactions of them with the iso-scalar surfaces geometries have been investigated using the results of a three-dimensional direct numerical simulation (DNS) of a turbulent premixed methane-air flame in a piloted Bunsen burner configuration with tabulated chemistry. The universal teardrop shape of the joint probability density function (jpdf) of the second and third invariants of the velocity-gradient tensor disappears in the different flame regions under study. A 'canonical' vortex, which affects the fine-scale structure of the turbulent premixed flame, has been identified and analyzed at three times, differing by increments of the order of the Kolmogorov time micro-scale.

Conferences

1. J. Martin, C. Dopazo, J. Hierro and *L. Cifuentes*. Effects of scalar isosurfaces curvatures on turbulent combustion. *13th International Conference on Numerical Combustion*, (2011).

   Abstract: Turbulent scalar mixing and combustion phenomena are investigated in terms of the local principal curvatures of the scalar field isosurfaces. Direct numerical simulations of both inert and reactive scalars at three different Schmidt numbers have been performed with a mesh size 256^3. Results show that high chemical reaction rates occur for small curvature values -isosurface flat zones- and for 'tile'-like structures convex towards the isosurface propagation direction. Further work is in progress, using 512^3 DNS databases, to investigate with greater detail this behavior, and also to explore its correlations with the velocity field small scale structures.

2. J. Hierro, *L. Cifuentes* and J. Martin. An analysis of the correlation of chemically active scalar fields. *SPEIC14-Towards Sustainable Combustion*, (2014).

   Abstract: Direct Numerical Simulation (DNS) data about the different terms which appear in the evolution of the scalar correlation function is presented. The behavior of a previous model, which had

been initially proposed to handle passive scalars, is studied.

3. *L. Cifuentes*, C. Dopazo, J. Martin, P. Domingo, L. Vervisch and C. Jimenez. 'Effective' normal strain rate and scalar gradient enhancement. *15th International Conference on Numerical Combustion* (Accepted for oral presentation), (2015).

   Abstract: Two DNS datasets for turbulent premixed flames (Flame-A: inflow-outflow configuration; Flame-B: Jet in a co-flow) are used to investigate local flow topologies and scalar iso-surface geometries [126]. The scalar-gradient modulus, $|\nabla Y|$, evolution depends on the sign of $(a_N + \partial V^Y/\partial x_N)$, the 'effective' strain rate normal to the iso-scalar surfaces [128]. This study aims at characterizing the 'effective' normal strain rate for different scalar field geometries and flow topologies for Flame-A [126] and Flame-B [69].

4. *L. Cifuentes*, C. Dopazo, J. Martin, C. Jimenez, P. Domingo and L. Vervisch. Scalar field geometries and small-scale flow features in turbulent premixed flames. *Ninth Mediterranean Combustion Symposium* (Accepted for oral presentation), (2015).

   Abstract: Direct Numerical Simulation (DNS) datasets of turbulent premixed flames (inflow-outflow and jet in a co-flow) are used to study interactions of the flame thermochemical processes with scalar field

geometries in terms of their mean and Gauss curvatures, k_m and k_g, and local flow topologies characterized by the three invariants of the velocity-gradient tensor. Four regions ('fresh reactants', 'preheating', 'burning' and 'hot products'), singled out by their reaction rate levels, are examined. Nearly flat scalar iso-surfaces are the most probable geometries in all four regions. The second invariant of the velocity-gradient tensor, Q, which represents the balance between the physical enstrophy and local dissipation of kinetic energy, is governed by the second invariant of the symmetric strain-rate tensor, S_{ij}. Focal topologies tend to disappear in favor of nodal micro-structures towards the 'hot products'.

B

Local flow topologies and scalar structures in a turbulent premixed flame

PHYSICS OF FLUIDS **26**, 065108 (2014)

Local flow topologies and scalar structures in a turbulent premixed flame

Luis Cifuentes,[1,a)] Cesar Dopazo,[1] Jesus Martin,[1] and Carmen Jimenez[2]
[1]*LIFTEC, CSIC – University of Zaragoza, Zaragoza, Spain*
[2]*Department of Energy, CIEMAT, Madrid, Spain*

(Received 4 February 2014; accepted 5 June 2014; published online 25 June 2014)

A three-dimensional direct numerical simulation of a propagating turbulent premixed flame is performed using one-step Arrhenius model chemistry. The interaction of the flame thermochemical processes with the local geometries of the scalar field and flow topologies is studied. Four regions ("fresh reactants," "preheating," "burning," and "hot products"), characterized by their reaction rate and mass fraction values, are examined. Thermochemical processes in the "preheating" and "burning" regions smooth out highly contorted iso-scalar surfaces, present in the "fresh reactants," and annihilate large curvatures. Positive volumetric dilatation rates, $-P = \nabla \cdot \mathbf{u}$, display maxima for elliptic concave and minima for convex scalar micro-structures. Constant average tangential strain rates, a_T, with large fluctuations, occur throughout the flow domain, whereas normal strain rates, a_N, follow the trends of volumetric dilatation rates. Focal topologies, present in the "fresh reactants," tend to disappear in favor of nodal structures as moving towards the "hot products." The vorticity vector is predominantly tangential to the iso-scalar surfaces. The Unstable Node/Saddle/Saddle and Stable Focus/Stretching topologies, present in the "fresh reactants," correlate with large values of a_N and a_T providing hints on the flow topologies fostering scalar mixing. © *2014 AIP Publishing LLC*. [http://dx.doi.org/10.1063/1.4884555]

I. INTRODUCTION

A turbulent premixed flame acts as a propagating frontier between the fresh mixture and the burnt gases, which modifies both the upstream and downstream flows through aero-thermo-chemical processes. Far upstream of the flame, the flow turbulence, as well as the structure of the scalar fields will weakly sense the flame presence. As large- and small-scale structures of the velocity and scalar fields approach the flame, interactions become increasingly important and likely dominate in regions of intense chemical activity and thermal transport. The resulting flow and scalar structures downstream of the flame will be significantly different from those upstream of it.

It is apparent that small-scale flow and scalar structures strongly influence the turbulent mixing that, in turn, affect the thermal fields and the chemical kinetics. It is therefore important to know how small-scale flow and scalar structures, as momentum, mass, and thermal molecular diffusion local enhancers, behave and evolve in front, within and behind the flame. Molecular mixing models for combusting flows, resulting from that knowledge, could incorporate more physical content and likely improve their accuracy and prediction capability.

The study of scalar field local topologies in turbulent flows is an old subject. Gibson[1,2] analyzed the features of zero-gradient points and minimal gradient surfaces of a passive scalar in a turbulent flow. Moffatt[3] classified the scalar field critical points (zero scalar-gradient points) in terms of the eigenvalues of the scalar Hessian (second-derivative) tensor; depending on the index of the critical points, elliptic extremal points (maxima and minima), or saddle points of two types are encountered. Wang and Peters[4] investigated small-scale passive scalar statistics through the use of direct numerical

[a)]Electronic mail: lcifuentes@unizar.es

simulation (DNS) and introduced the concept of dissipation elements. Dopazo *et al.*[5,6] used DNS results for constant-density turbulent flow to describe the local geometry of iso-scalar surfaces in terms of either main curvatures k_1 and k_2 or mean and Gauss curvatures, k_m and k_g.

Candel and Poinsot[7] obtained an expression for the flame stretch and relate it to previous derivations; they also present a balance equation for the flame surface density function. Chakraborty and co-workers[8,9] dissected various aspects of turbulent premixed flame curvature and its propagation speed as a function of Lewis number; the preferential alignments of the reaction progress variable gradient and the strain rate eigenvectors, for thin reaction zone and corrugated flamelet regimes, implied different dependence of the former on strain rates tangential to the iso-surface and its curvature; that preferred alignment also changed with Damköhler number, with scalar gradients parallel to the most compressive eigenvector for low values and to the most extensive one for high values and intense heat release zones;[10] the occurrence and importance of positive strain rates normal to the iso-scalar surfaces remarkably and distinctly emerged from these works.[9,11]

Chong *et al.*[12] studied and classified the local small-scale three-dimensional topologies for both compressible and incompressible flows, based on the velocity-gradient tensor invariants. Distinct surfaces in the 3D invariant space separate stable and unstable, nodal and focal topologies. Extensive numerical and experimental investigations of statistical properties in the plane of the second and third invariants have been performed for constant density flows; Perry and Chong[13] and Soria *et al.*[14] analyzed the fine-scale structures in time-developing mixing layers and found that most probable motions display large positive values of the second invariant, associated with a stable focus/stretching topology. Chong *et al.*[15] and Chacin and Cantwell[16] revealed that the joint probability density functions (jpdf's) of the second and third invariants exhibit a teardrop shape. Ooi *et al.*[17] studied the fine-structure of several turbulent flows and found that their jpdf's were rather similar, which suggested a certain universality of small-scale motions. Recently, Elsinga and Marusic[18] provided an explanation for that universal teardrop shape, evaluating average flow patterns in the local coordinate system defined by the eigenvectors of the strain-rate tensor.

The investigation of flow topologies in variable-density turbulent flows is limited in comparison with that of incompressible turbulence. Feiereisen *et al.*[19] conducted the first DNS of variable-density turbulence; however, extensive studies were only undertaken a decade later. Chen *et al.*[20] studied the geometry of flow patterns of a numerically simulated compressible mixing layer; data suggested that the third invariant of the strain rate tensor correlates with a 3/2 power of the second invariant, with a Reynolds number dependent proportionality factor. Maekawa *et al.*[21] studied the velocity-gradient invariants for decaying isotropic compressible turbulence and observed that unstable node/saddle/saddle and stable focal/stretching topologies prevailed over other topologies. Tanahashi *et al.*[22] used the second invariant of the velocity-gradient tensor to separate strain dominated regions from coherent fine scale eddies in a premixed flame DNS with an inflow-outflow configuration; the latter are perpendicular to the flame front and can survive behind it. Suman and Girimaji[23] investigated the local flow topology in compressible isotropic turbulence. Grout *et al.*[24] studied the local flow topology of a reactive transverse fuel jet in cross-flow; the highest heat release rates of the flame are found in regions with node/node/node (unstable) topology. Wang and Lu[25] studied a compressible turbulent boundary layer identifying several most probable topologies in the inner and outer layer.

To the best of our knowledge, a detailed joint study of local scalar geometries and flow topologies for variable-density turbulent reacting flows has never been reported. This study aims at exploring the interactions of a flame with the small-scale geometry of the scalar field and the flow fine-structure, as well as obtaining new information on the features of invariants of the velocity-gradient tensor. Section II describes the partial differential equations governing mass, momentum, scalar, and energy transports; it includes brief summaries of local geometries of iso-scalar surfaces in terms of their curvatures, k_m and k_g, and of local flow topologies with regard to the velocity-gradient tensor invariants. The DNS numerical implementation is described in Sec. III. Section IV analyzes the results and discusses their physical meaning and implications. Some concluding remarks and suggestions for future work are finally presented in Sec. V.

II. MATHEMATICAL FORMULATION

We solve the set of conservation equations for mass, momentum, energy, and chemical species, using the fully parallel compressible solver NTMIX3D.[26,27] A single step Arrhenius-type irreversible reaction, Reactants → Products, to maintain the computational cost within reasonable limits, interacts with a three-dimensional turbulent velocity field. The reaction rate expression is

$$\dot{\omega} = \frac{\dot{\omega}_R}{Y_R^u} = \rho Y B_o \, exp\left(-\frac{\beta}{\alpha}\right) exp\left[\frac{-\beta(1-\theta)}{1-\alpha(1-\theta)}\right], \tag{1}$$

where ρ is the density of the mixture; $Y = Y_R/Y_R^u$ is the reduced mass fraction, defined with Y_R, the reactants mass fraction and its value in the fresh gasses, Y_R^u; B_o is the pre-exponential factor; the ratio $\alpha = (T_b - T_u)/T_b$ is defined with the temperature, T, in the unburned, T_u, and burnt gases, T_b; β is the reduced activation energy or Zel'dovich number, $\beta = \alpha E_a/RT_b$, E is the activation energy and R the universal gas constant; and $\theta = (T - T_u)/(T_b - T_u)$ is the reduced temperature.

A. Dimensionless equations

The full set of governing equations is made dimensionless using reference characteristic variables and molecular transport coefficients in the fresh gases, namely,

$$a_{ref} = a_u, \qquad T_{ref} = (\gamma - 1)T_u, \qquad \rho_{ref} = \rho_u, \qquad p_{ref} = \rho_u a_u^2 = \gamma p_u,$$

$$\lambda_{ref} = \lambda_u, \qquad \mu_{ref} = \mu_u, \qquad \nu_{ref} = \mu_{ref}/\rho_{ref}, \qquad C_{p_{ref}} = C_{p_u},$$

$$D_{th_{ref}} = \lambda_{ref}/\rho_{ref} C_{p_{ref}}, \qquad D_{ref} = D_u, \qquad t_{ref} = L_{ref}/a_{ref},$$

where the sub-index u denotes a variable value in the fresh gases. a_{ref}, T_{ref}, ρ_{ref}, p_{ref}, λ_{ref}, μ_{ref}, ν_{ref}, C_{pref}, D_{thref}, D_{ref}, L_{ref}, and t_{ref} are the reference speed of sound, temperature, density, pressure, thermal conductivity, dynamic viscosity, kinematic viscosity, specific heat at constant pressure (assumed constant), thermal diffusivity, mass diffusivity, length scale, and time. γ is the ratio of specific heats at constant pressure and volume, respectively. The full set of dimensionless governing equations can be written in Cartesian tensor notation as[28], mass continuity:

$$\frac{\partial \rho^+}{\partial t^+} + \frac{\partial}{\partial x_i^+}(\rho^+ u_i^+) = 0, \tag{2}$$

momentum:

$$\frac{\partial \rho^+ u_i^+}{\partial t^+} + \frac{\partial}{\partial x_j^+}(\rho^+ u_i^+ u_j^+) + \frac{\partial p^+}{\partial x_i^+} = \frac{1}{Re_a} \cdot \frac{\partial \tau_{ij}^+}{\partial x_j^+}, \tag{3}$$

energy:

$$\begin{aligned}\frac{\partial \rho^+ e_t^+}{\partial t^+} + \frac{\partial}{\partial x_i^+}\left[(\rho^+ e_t^+ + p^+)u_i^+\right] = {} & \frac{1}{Re_a} \cdot \frac{\partial}{\partial x_j^+}(u_i^+ \cdot \tau_{ij}^+) \\ & - \frac{1}{Re_a \cdot Pr} C_p^+ \frac{\partial q_i^+}{\partial x_i^+} \\ & - \alpha' T_u^+ \dot{\omega}^+,\end{aligned} \tag{4}$$

and reactant mass fraction:

$$\frac{\partial(\rho^+ Y)}{\partial t^+} + \frac{\partial}{\partial x_i^+}(\rho^+ Y u_i^+) = \frac{1}{Re_a Sc} \frac{\partial}{\partial x_i^+}\left(\mu^+ \frac{\partial Y}{\partial x_i^+}\right) + \dot{\omega}^+ . \tag{5}$$

The superscript + denotes a dimensionless variable or property. Dimensionless density, $\rho^+ = \rho/\rho_{ref}$, ith component of the velocity vector, $u_i^+ = u_i/a_{ref}$, pressure, $p^+ = p/p_{ref}$, temperature, $T^+ = T/T_{ref}$, time, $t^+ = t/t_{ref}$, and ith component of the position vector, $x_i^+ = x_i/L_{ref}$ are

used. Moreover, the following constitutive relations and the perfect gas law complete the system definition:

$$\tau_{ij}^{+} = 2\mu^{+}\left(S_{ij}^{+} - \frac{1}{3}\delta_{ij}S_{kk}^{+}\right), \tag{6}$$

$$S_{ij}^{+} = \frac{1}{2}\left(\frac{\partial u_i^{+}}{\partial x_j^{+}} + \frac{\partial u_j^{+}}{\partial x_i^{+}}\right), \tag{7}$$

$$e_t^{+} = \frac{1}{2}\cdot\sum_{k=1}^{3} u_k^{+2} + \frac{p^{+}}{(\gamma-1)\rho^{+}}, \tag{8}$$

$$q_j^{+} = -\lambda^{+}\frac{\partial T^{+}}{\partial x_j^{+}}, \tag{9}$$

$$p^{+} = \rho^{+}T^{+}C_p^{+}\frac{\gamma-1}{\gamma}, \tag{10}$$

$$\alpha' = \frac{\alpha}{1-\alpha}, \tag{11}$$

$$\dot{\omega}^{+} = -\rho^{+}Y Re_a Pr Da S_L^{+2}\cdot exp\left[\frac{-\beta(1-\theta)}{1-\alpha(1-\theta)}\right] \tag{12}$$

τ_{ij}^{+} is the viscous stress tensor, given by the Navier-Poisson relation, and S_{ij}^{+} is the rate of strain tensor. e_t^{+} is the total (kinetic plus internal) specific energy. q_j^{+} is the heat conduction vector, given by the Fourier constitutive relation. The perfect gas law relates p^{+}, ρ^{+}, and T^{+}. The dimensionless parameters, entering the conservation equations, (2)–(5), and the reaction rate (12), are defined as

$$Re_a = \frac{a_{ref}L_{ref}}{\nu_u}, \tag{13}$$

$$Pr = \frac{C_{p_u}\cdot\mu_u}{\lambda_u}, \tag{14}$$

$$Sc = \frac{\mu_u}{\rho_u D_u}, \tag{15}$$

$$Da = \frac{D_{th}^{+}}{S_L^{+2}}B_o\, exp(-\beta/\alpha), \tag{16}$$

where Re_a stands for the acoustical Reynolds number, Pr for the Prandtl number, Sc for the Schmidt number, and Da for the Damköhler number.

S_L^{+} in Eqs. (12) and (16) denotes the non-stretched laminar flame speed, defined by

$$S_L^{+} = \frac{1}{a_{ref}\rho_u Y_u}\int_{-\infty}^{+\infty}\dot{\omega}\,dx\ . \tag{17}$$

The laminar flame thickness is then given by

$$\delta_L^{+} = \frac{D_{th}^{+}}{S_L^{+}}, \tag{18}$$

where the thermal diffusivity, D_{th}^{+}, is evaluated in the hot products.

The turbulent Reynolds number Re_t, based on the fluctuating velocity rms value, u', and the integral length scale, l, is expressed as

$$Re_t = \frac{u'l}{\nu_u}\ . \tag{19}$$

In this study, the acoustical and turbulent Reynolds numbers are 5066 and 64.28, respectively. The dynamic viscosity is modeled as

$$\mu^+ = \mu_u^+ \left(\frac{T}{T_u}\right)^b, \tag{20}$$

with $b = 0.6$. The thermal conductivity and mass diffusivity are functions of dynamic viscosity and density, via the assumption of constant C_p, Prandtl and Schmidt numbers, with $Pr = 0.75$ and $Sc = 0.7$. The Lewis number is unity.

To simplify the notation, dimensionless variables will be written hereafter without the superscript $+$.

B. Local geometry of isoscalar surfaces

In this paper, an iso-scalar surface is defined by $Y(\mathbf{x}, t) =$ constant. The unit vector normal to an iso-surface is

$$\mathbf{n} = \frac{\nabla Y}{|\nabla Y|}. \tag{21}$$

The local geometry of the scalar field is characterized by its value, $Y(\mathbf{x}, t)$, by its first and second derivatives, $\partial Y/\partial x_n$ and $\partial^2 Y/\partial x_n^2$, in the direction normal to the iso-surface, x_n, and also by its curvature tensor, $\partial n_i/\partial x_j = n_{i,j}$. The latter can be written in terms of the scalar field derivatives as[5,6],

$$n_{i,j} = \frac{1}{|\nabla Y|}(\delta_{ik} - n_i n_k)\frac{\partial^2 Y}{\partial x_j \partial x_k}. \tag{22}$$

The invariants of $n_{i,j}$ are given by

$$I_1 = -\nabla \cdot \mathbf{n}, \tag{23}$$

$$I_2 = (1/2)(n_{i,i}n_{j,j} - n_{i,j}n_{j,i}), \tag{24}$$

$$I_3 = -\det(n_{i,j}). \tag{25}$$

As $I_3 = 0$[6], the two eigenvalues of $n_{i,j}$ (main curvatures, k_1 and k_2) are obtained from the equation

$$k^2 + I_1 k + I_2 = 0. \tag{26}$$

The Gauss curvature, k_g, and the mean curvature, k_m, are

$$k_g = k_1 k_2, \tag{27}$$

$$k_m = \frac{k_1 + k_2}{2} = \frac{1}{2}\frac{\partial n_i}{\partial x_i}. \tag{28}$$

The zone $k_g > k_m^2$ in the $k_m - kg$ plane implies non-physical complex curvatures. Figure 1 shows the different local geometries of isoscalar surfaces and may be presented in a dimensionless form with $k_m\delta_L$ and $k_g\delta_L^2$. For a positive (negative) mean curvature, $k_m\delta_L > 0$ ($k_m\delta_L < 0$), the surface is convex (concave) towards the fresh reactants.

C. Local flow topology

The local flow topologies are characterized by the invariants of the velocity-gradient tensor, $\mathbf{A}$, with components $A_{ij} = \partial u_i/\partial x_j$; its three eigenvalues, λ_1, λ_2, and λ_3, are the solutions of the

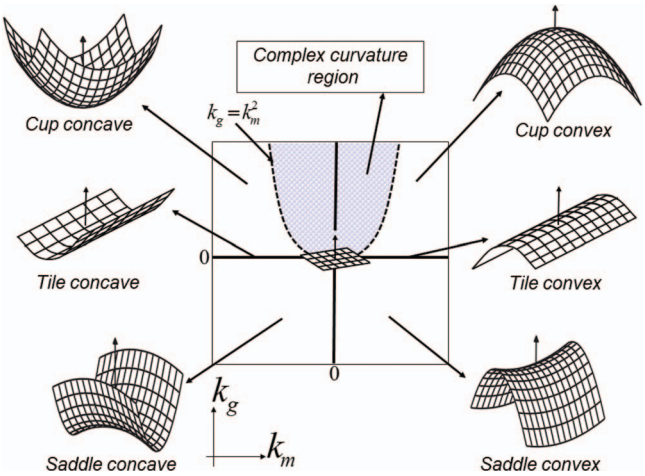

FIG. 1. Classification of iso-scalar surface geometries in terms of their mean and Gauss curvatures, k_m and k_g.

characteristic equation,

$$\lambda^3 + P\lambda^2 + Q\lambda + R = 0, \tag{29}$$

P, Q, R are the three invariants of $\mathbf{A}$[12], specified by

$$P = -tr(\mathbf{A}) = -(\lambda_1 + \lambda_2 + \lambda_3) = -S_{ii}, \tag{30}$$

$$Q = \frac{1}{2}\left([tr(\mathbf{A})]^2 - tr(\mathbf{A}^2)\right) = \frac{1}{2}\left(P^2 - S_{ij}S_{ij} + W_{ij}W_{ij}\right), \tag{31}$$

$$R = -\det(\mathbf{A}) = \tfrac{1}{3}\left(-P^3 + 3PQ - S_{ij}S_{jk}S_{ki} - 3W_{ij}W_{jk}S_{ki}\right), \tag{32}$$

where S_{ij} is the symmetric strain-rate tensor and W_{ij} is the skew-symmetric rotation-rate tensor.

$-P = \nabla \cdot \mathbf{u}$, represents the local volumetric dilatation rate, namely, the rate of change of an infinitesimal fluid volume per unit volume. $-P < 0$ implies element compression, $-P = 0$ means zero dilatation, and $-P > 0$ entails local fluid expansion.

The discriminant D of Eq. (29) is defined by[12]

$$D = \frac{1}{108}\left[27R^2 + (4P^3 - 18PQ)R + 4Q^3 - P^2Q^2\right]. \tag{33}$$

The surface $D = 0$ divides the $P - Q - R$ phase space into two regions; for $D > 0$, $\mathbf{A}$ displays one real and two complex-conjugate eigenvalues (focal topologies), while in the region $D < 0$, $\mathbf{A}$ has three real eigenvalues (nodal topologies). The two surfaces, r_{1a} and r_{1b}, of $D = 0$ are given by

$$\frac{1}{3}P\left(Q - \frac{2}{9}P^2\right) - \frac{2}{27}\left(-3Q + P^2\right)^{3/2} - R = 0\,, \qquad [r_{1a}] \tag{34}$$

$$\frac{1}{3}P\left(Q - \frac{2}{9}P^2\right) + \frac{2}{27}\left(-3Q + P^2\right)^{3/2} - R = 0\,. \qquad [r_{1b}] \tag{35}$$

Further, in the region $D > 0$, $\mathbf{A}$ has purely imaginary eigenvalues on the surface r_2, which is described by

$$PQ - R = 0. \qquad [r_2] \tag{36}$$

For $P = 0$ the surface r_2 coincides with the Q −axis. Thus, the surfaces r_{1a}, r_{1b}, r_2 and $R = 0$ divide the $P - Q - R$ space into different regions, which correspond to distinct flow topologies, plotted, as reminder, in Figure 2 and explained pictorially in Table I.

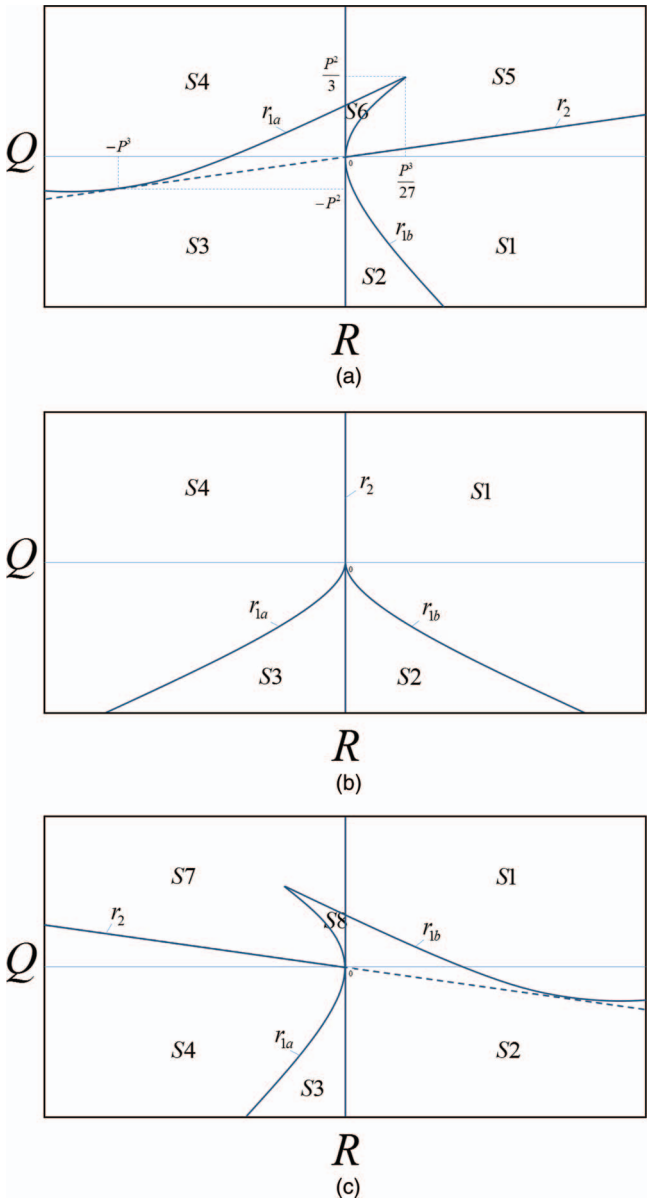

FIG. 2. Classification of critical points in the $Q - R$ plane for: (a) $P > 0$, (b) $P = 0$, and (c) $P < 0$. Topologies and corresponding acronyms are listed in Table I.

The invariants of S_{ij} and W_{ij} are given by

$$P_S = P = -S_{ii}, \qquad Q_S = \frac{1}{2}\left(P^2 - S_{ij}S_{ij}\right), \qquad R_S = \frac{1}{3}\left(-P^3 + 3PQ_S - S_{ij}S_{jk}S_{ki}\right), \tag{37}$$

$$P_W = 0, \qquad Q_W = \frac{\omega^2}{4} = \frac{1}{2}W_{ij}W_{ij}, \qquad R_W = 0, \tag{38}$$

where $\omega^2/2 = \omega_i\omega_i/2$ is the local enstrophy. ω_i is the ith component of the vorticity vector. Both the turbulent kinetic energy dissipation and the volumetric dilatation rates contribute to Q_S. It is readily shown that

$$Q = Q_S + Q_W, \qquad R = R_S + PQ_W - W_{ij}W_{jk}S_{ki} = R_S + PQ_W - \frac{1}{4}\omega_i S_{ij}\omega_j, \tag{39}$$

TABLE I. Description of the flow topologies in $P - Q - R$ space.

Sector	Acronym	Description	Sketch
S1	UFC	Unstable focus/compressing	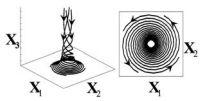
S2	UN/S/S	Unstable node/saddle/saddle	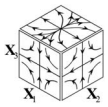
S3	SN/S/S	Stable node/saddle/saddle	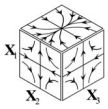
S4	SFS	Stable focus/stretching	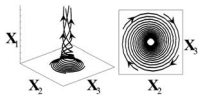
S5	SFC	Stable focus/compressing	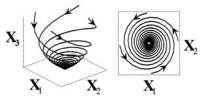
S6	SN/SN/SN	Stable node/stable node/stable node	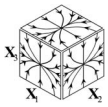
S7	UFS	Unstable focus/stretching	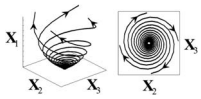
S8	UN/UN/UN	Unstable node/unstable node/unstable node	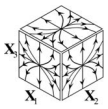

Q represents the additive contribution of enstrophy, Q_W, and dissipation/dilatation, Q_S. Enstrophy production, $PQ_W - (\omega_i S_{ij} \omega_j)/4$, and dissipation rate generation, $S_{ij}S_{jk}S_{ki}$, enter the definition of R.[29]

III. NUMERICAL SIMULATION

The DNS solver[26,27] uses a 6th order compact finite-differences scheme for space discretization and time integrates the conservation Eqs. (2)–(5) with a third order Runge-Kutta explicit method. The computational domain, shown schematically in Figure 3, has a size 3π in the x direction and 2π in the y and z directions, and contains $768 \times 512 \times 512$ grid points, uniformly distributed. The domain is treated as periodic in the y and z directions, while non-reflecting inlet-outlet boundary conditions are imposed in the x direction, using the Navier-Stokes Characteristic Boundary Condition (NSCBC) method.[30]

A planar laminar flame, located at $x = 6.3$, is used as initial condition. At $t = 0$, an incompressible turbulent velocity field is imposed on the fresh reactants region of size $(2\pi)^3$, as shown in Figure 3(b). The flame then propagates with a velocity S_L towards the fresh gases, interacting with the turbulence, which wrinkles iso-scalar surfaces; simultaneously, the velocity field undergoes the influence of thermal processes. The initial incompressible isotropic turbulence is generated with an independent pseudo-spectral numerical code,[31,32] starting from a given spectrum and using a stochastic forcing scheme, to yield a statistically stationary field. In the zero correlation-time forcing scheme,[33,34] all wave numbers with a modulus less than $2\sqrt{2}$, except the zero mode which makes

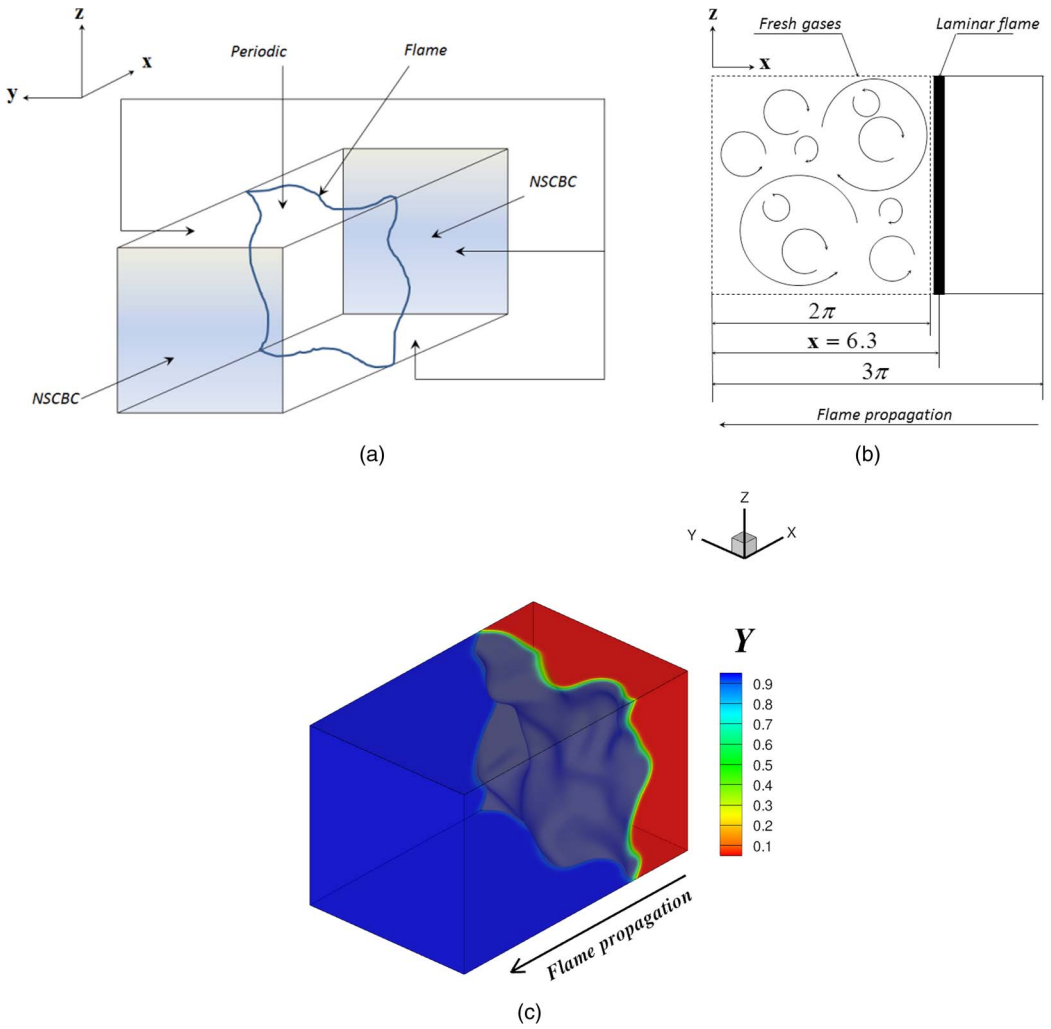

FIG. 3. (a) Description of the computational domain, (b) initial conditions, and (c) computational domain from simulation at $t = 90$.

no contribution, receive a stochastic contribution at every time step, while their phase is adjusted to enforce incompressibility.

Numerical values of the aero-thermo-chemical variables and dimensionless parameters for this simulation are presented in Tables II and III. The initial ratio of the rms velocity fluctuations, u', to the non-stretched laminar flame velocity is $u'/S_L = 3$. The eddy turnover time, l/u', is $\tau = 56.40$. In this study, the initially planar laminar flame is allowed to interact with the turbulence field up to a time $t = 90$, greater than the eddy turnover time. The Kolmogorov micro-scale, $\eta = 0.0372$, guarantees an adequate spatial resolution with the current domain and mesh sizes. The laminar flame thickness, $\delta_L = 0.0526$, is also sufficiently well resolved. The initial integral length scale to flame thickness ratio is $l/\delta_L = 16.084$. Therefore, combustion takes place in the "thickened-wrinkled flame" regime,[28,35,36] as shown in Figure 4.

IV. RESULTS AND DISCUSSION

Figure 5 shows the reactant mass fraction iso-lines in planes $x - y$ and $x - z$, in a zoom of the computational domain, at $t = 10$, $t = 50$, and $t = 90$. The initially flat flame bends under the influence of the turbulence and images are consistent with the current thickened-wrinkled flame regime (Figure 4). Hereafter, we analyze DNS data at $t = 90$.

TABLE II. Values of dimensionless parameters.

Parameter	Value
Acoustical Reynolds number, Re_a	5066
Turbulent Reynolds number, Re_t	64.28
Prandtl number, Pr	0.75
Schmidt number, Sc	0.75
Lewis number, Le	1.0
Damköhler number, Da	93.64
Karlovitz number, $Ka = \tau_{ch}/\tau_\eta$	1.49
$\alpha = (T_b - T_u)/T_b$	0.8
Zel′dovich number, β	6.0

TABLE III. Values of physical variables.

Physical variable	Value
DNS grid points	$768 \times 512 \times 512$
Integral length scale, l	0.846
rms of velocity fluctuations, u'	0.015
Turbulent kinetic energy dissipation rate, ε	3.9894×10^{-6}
Kolmogorov scale, η	0.0372
Kolmogorov time scale, τ_η	7.03
Integral eddy turnover time, τ	56.40
Non stretched laminar flame velocity, S_L	0.005
Laminar flame thickness, δ_L	0.0526
Chemical time scale, τ_{ch}	10.52
Initial turbulence intensity, u'/S_L	3
Initial integral length scale to flame thickness ratio, l/δ_L	16.084

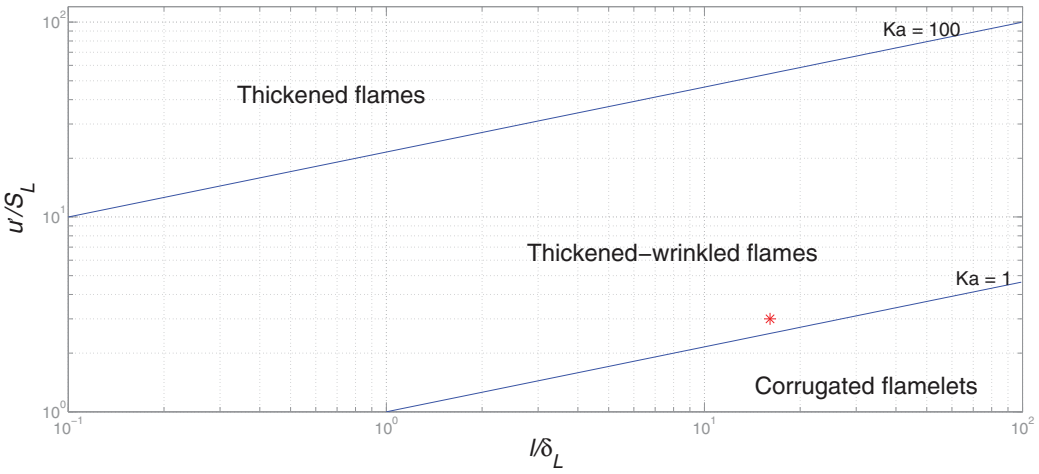

FIG. 4. Turbulent combustion diagram. The point indicates the case under study.

Local scalar geometries and flow topologies interact with thermochemical processes, specific of different parts of the computational domain, which is then divided into four regions depending on the value of the reaction rate, $\dot{\omega}_Y$. Parts of the domain where $|\dot{\omega}_Y| < 0.001|\dot{\omega}_{Y_{max}}| = 0.0004$ (or, equivalently, $0.700 < Y < 0.999$) are termed "fresh reactants." The "preheating" region extends over $0.253 < Y < 0.700$ or $0.001|\dot{\omega}_{Y_{max}}| < |\dot{\omega}_Y| < 0.7|\dot{\omega}_{Y_{max}}| = 0.336$. $|\dot{\omega}_Y| > 0.7|\dot{\omega}_{Y_{max}}|$ or $0.053 < Y < 0.253$ characterizes the "burning" region. Finally, $0.001 < Y < 0.053$, which corresponds

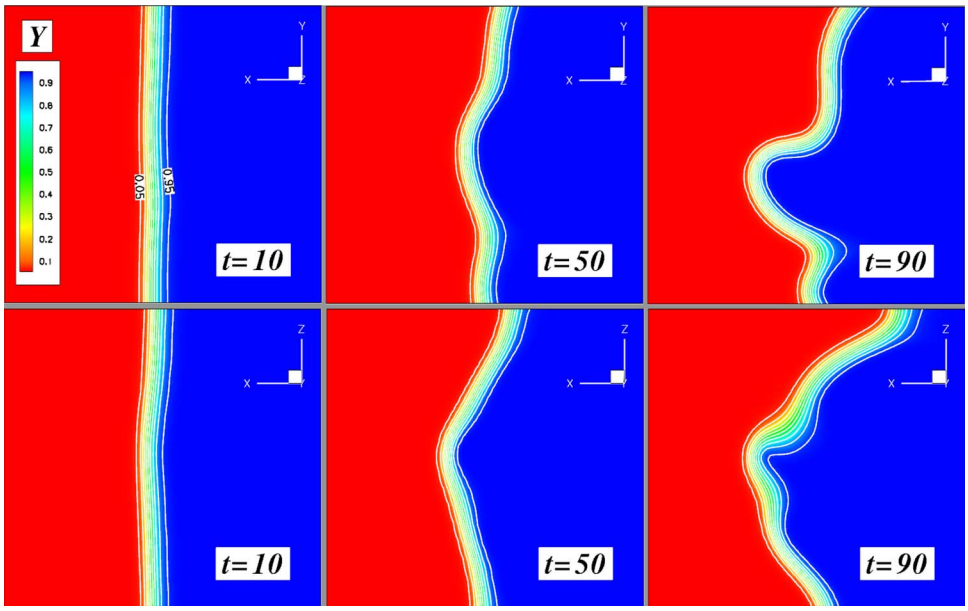

FIG. 5. Iso-lines of reactant mas fraction at $t = 10$, 50, and 90, in the $x - y$ and $x - z$ planes.

to $|\dot{\omega}_Y| < 0.7|\dot{\omega}_{Y_{max}}|$, defines the "hot products." These four regions are depicted in Figure 6. The sensitivity of results is small to changes in the definition of the "reacting" region (e.g., selecting 0.5 or $0.6|\dot{\omega}_{Y_{max}}|$ instead of $0.7|\dot{\omega}_{Y_{max}}|$).

Figure 7 shows the joint pdf of the mean and Gauss curvatures, k_m and k_g, for the four regions of the computational domain. k_m and k_g have been normalized with the thickness flame, δ_L. In the "fresh reactants," the joint pdf is slightly skewed towards positive values of k_m, reflecting the features of initially imposed and evolving small-scale turbulent structures and scalar field upstream of zones of intense heat and mass diffusive/reactive activity. These processes drastically discriminate against large values of k_m and k_g in both the "preheating" and "burning" regions; the probability of highly concave and convex iso-scalar surfaces, of a marked either elliptic or hyperbolic nature, significantly decreases as the heat transfer and chemical reaction become important. Nearly flat scalar geometries

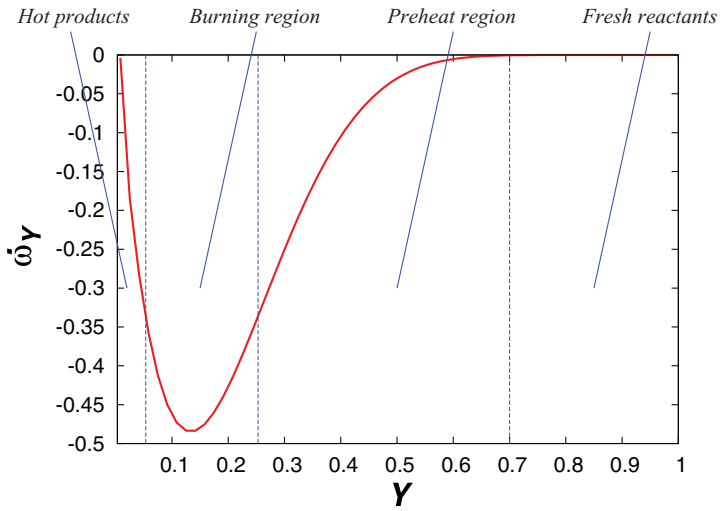

FIG. 6. Reaction rate, $\dot{\omega}_Y$, as a function of the reactant mass fraction. Dotted lines mark the limits of the four regions of the computational domain.

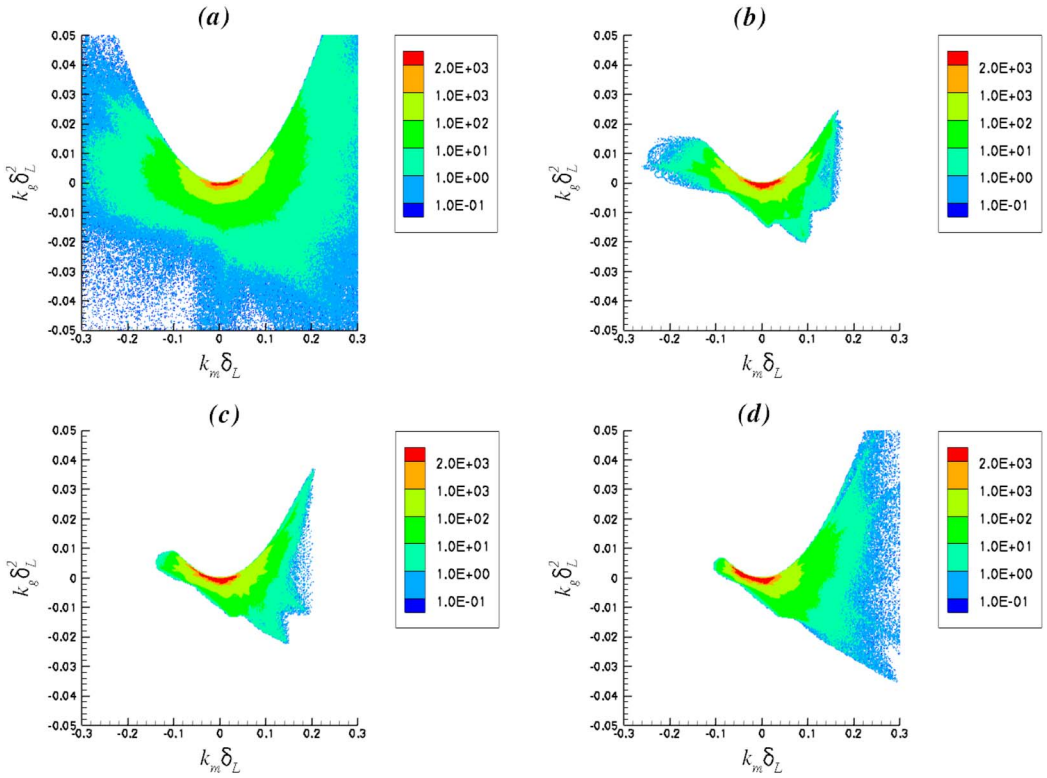

FIG. 7. Joint pdf of the mean and Gauss curvatures, k_m and k_g. Joint pdf magnitudes decrease from the center to the circumference. (a) Fresh reactants, (b) preheating region, (c) burning region, (d) hot products.

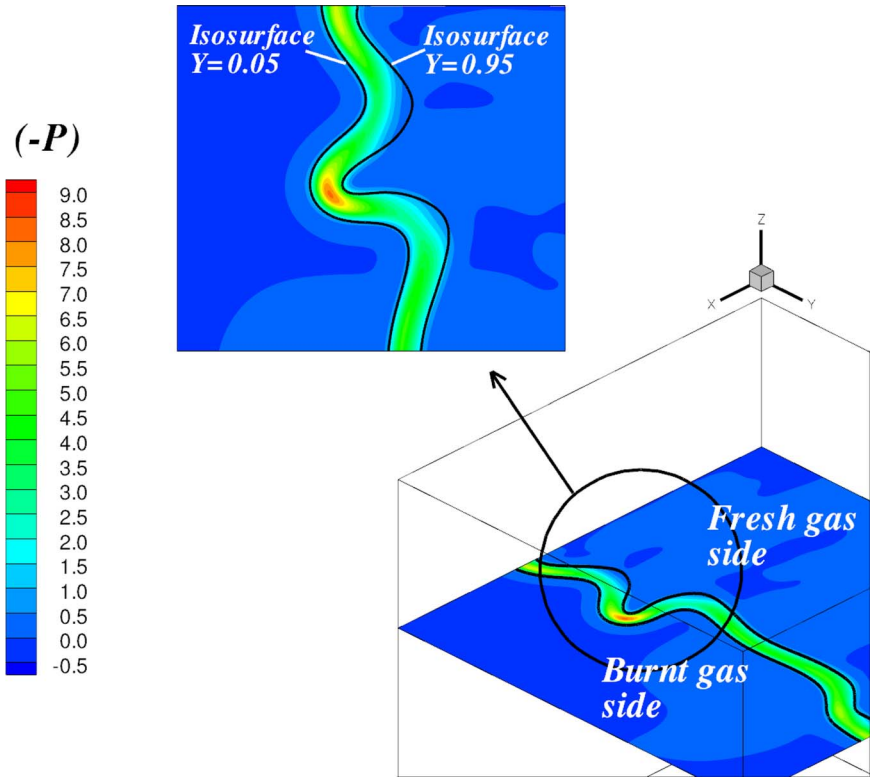

FIG. 8. Fluid element dilatation rate, ($-P$), in the computational domain.

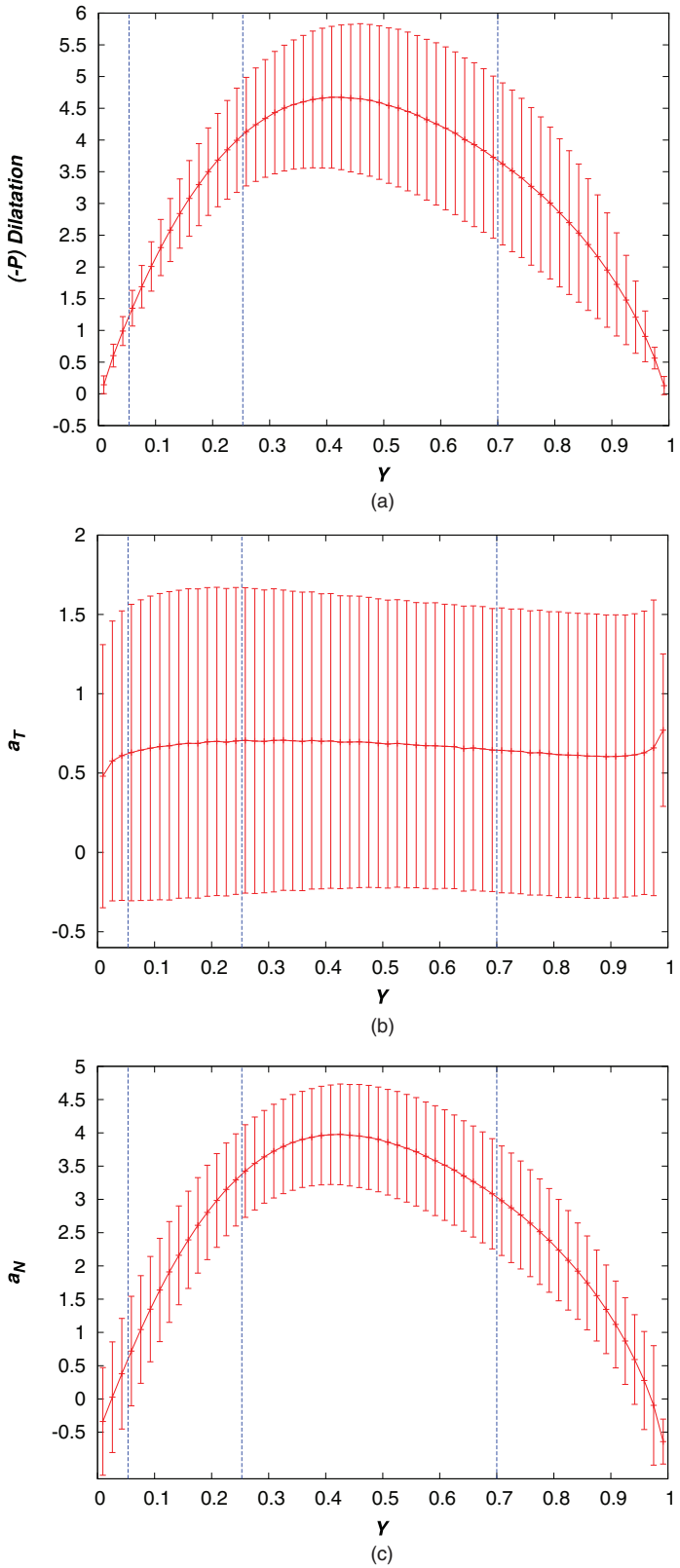

FIG. 9. (a) Local fluid volumetric dilatation rate, (b) tangential strain rate, and (c) normal strain rate as a function of the reactant mass fraction. Vertical bars indicate the rms values of the variables. Dotted lines mark the limits of the four regions of the computational domain.

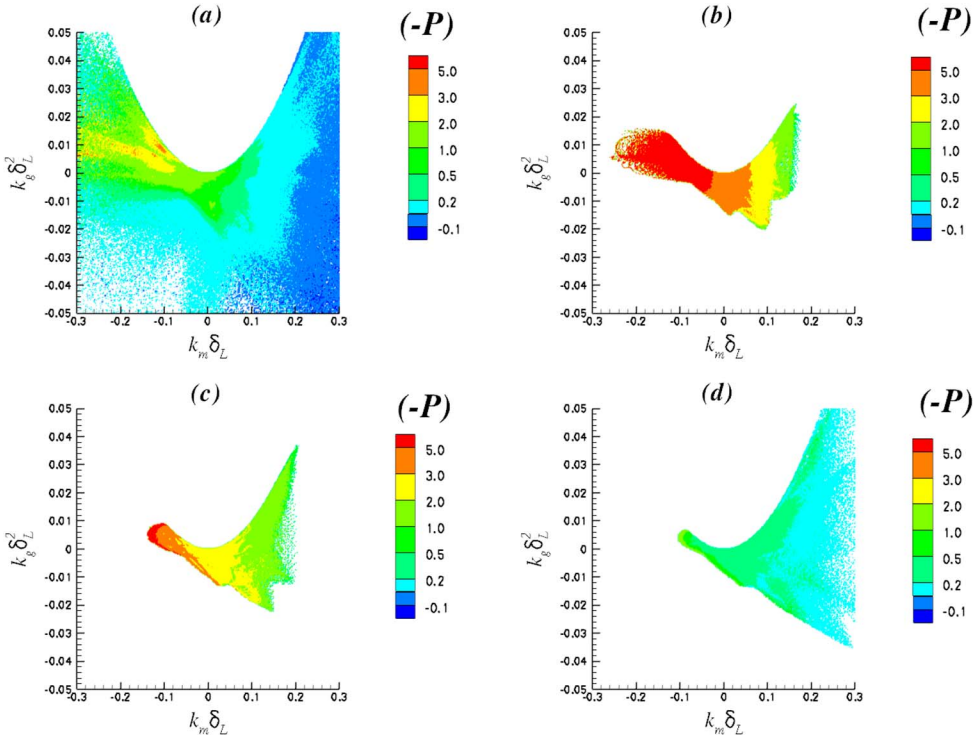

FIG. 10. Fluid element dilatation rate, $(-P)$, conditional upon the mean and Gauss curvatures, k_m and k_g. (a) Fresh reactants, (b) preheating region, (c) burning region, (d) hot products.

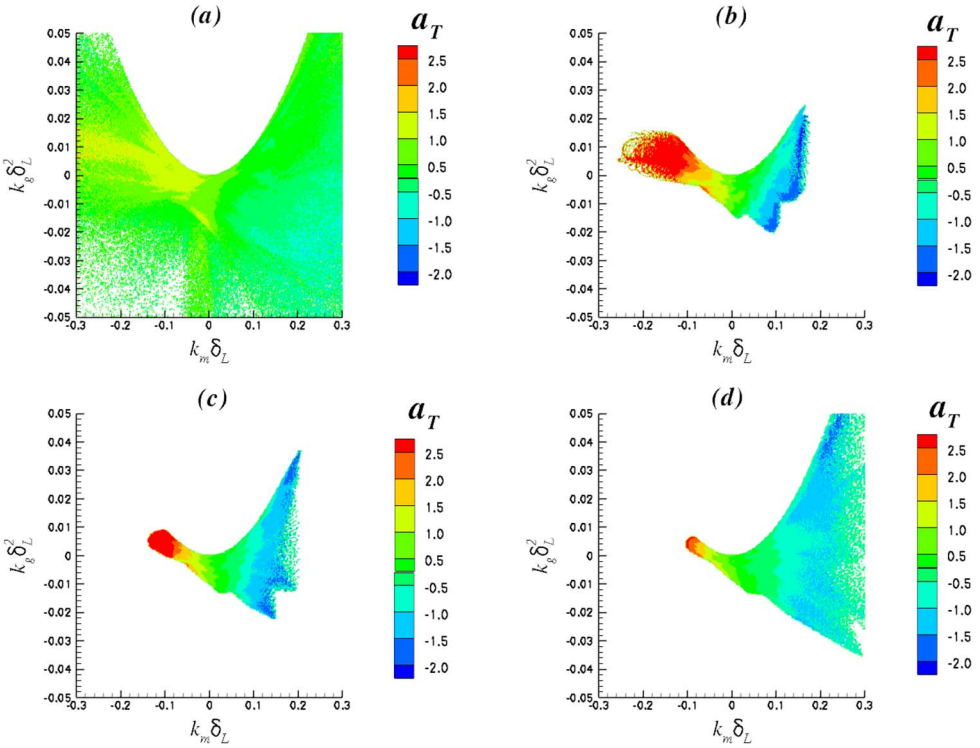

FIG. 11. Tangential strain rate, a_T, conditional upon the mean and Gauss curvatures, k_m and k_g. (a) Fresh reactants, (b) preheating region, (c) burning region, (d) hot products.

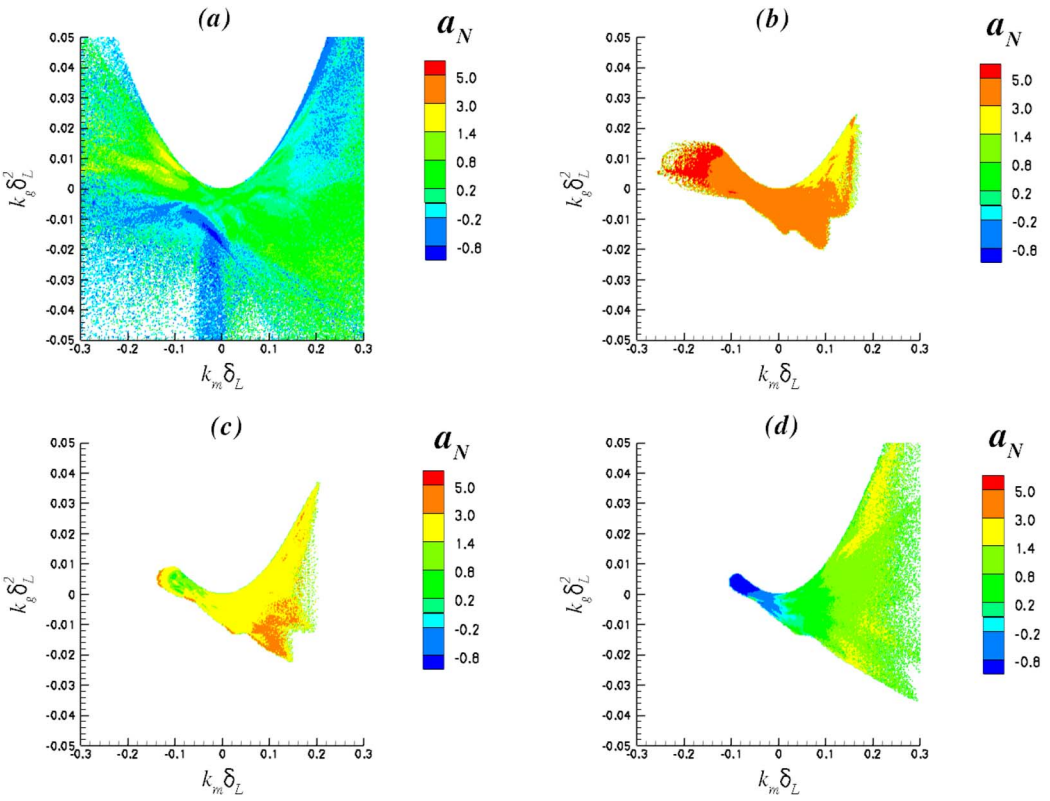

FIG. 12. Normal strain rate, a_N, conditional upon the mean and Gauss curvatures, k_m and k_g. (a) Fresh reactants, (b) preheating region, (c) burning region, (d) hot products.

are the most probable ones in all four regions. Slightly concave scalar iso-surfaces occur in the "preheating" region, but they become less probable in the "burning" zone and "hot products," very likely due to the heat conduction enhancement or focusing, with a reduction of $k_m < 0$, by concave geometries. Convex iso-surfaces with moderate values of k_m, predominantly of an elliptic cup-like structure, survive in the "hot products."

Figure 8 shows a zoom of a $x - y$ plane of the computational domain, which displays two scalar iso-lines and the volumetric dilatation rate, $-P = \nabla \cdot \mathbf{u}$. Local expansion predominates between the iso-lines, with maximum (minimum) values associated to concave (convex) scalar geometries. The volumetric dilatation rate can be decomposed as[7,10,11,28]

$$\nabla \cdot \mathbf{u} = -P = a_T + a_N, \tag{40}$$

where

$$a_T = (\delta_{ij} - n_i n_j) S_{ij}, \tag{41}$$

is the scalar iso-surface tangential strain-rate and

$$a_N = n_i S_{ij} n_j, \tag{42}$$

is the corresponding normal strain-rate. The use of a_T to explain some premixed and non-premixed flame features prevails in the literature.[7,28]

Figure 9 represents $-P$, a_T, and a_N as a function of Y in the four $\dot{\omega}_Y$-conditioned regions of the computational domain. $-P$, a_T, and a_N are normalized with $\langle Q_W \rangle^{1/2}$. The average of a_T remains almost constant, with large fluctuations, whereas a_N displays an almost identical variation to that of $-P$. Positive values of all three variables are predominant, with minimum negative values of a_T for all values of Y and of a_N only for $Y > 0.94$ ("fresh reactants") and $Y < 0.06$ ("hot products"); Chakraborty *et al.*[11] show similar trends for Lewis number unity. Figures 10–12 plot the values of

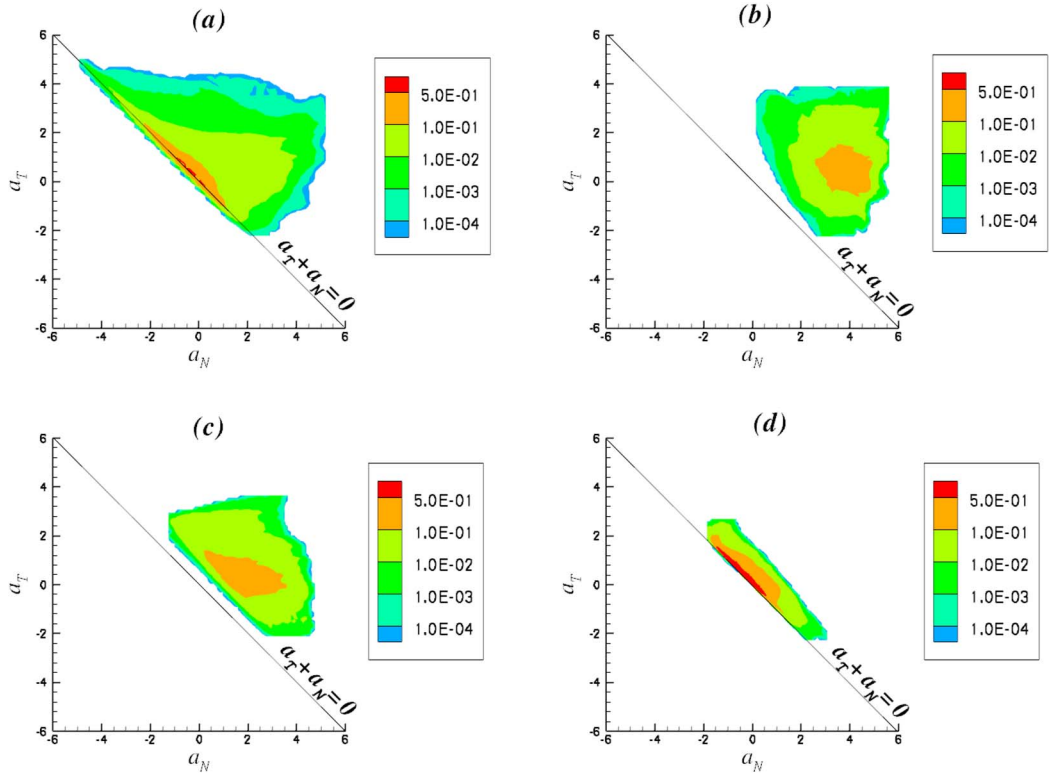

FIG. 13. Joint pdf of the normal and tangential strain rate, a_N and a_T. Joint pdf magnitudes decrease from the center to the circumference. (a) Fresh reactants, (b) preheating region, (c) burning region, (d) hot products.

$-P$, a_T, and a_N as functions of k_m and k_g in the four regions of the computational domain. In the "fresh reactants," moderate positive values (expansions) of $-P$ occur for concave geometries, while nearly zero and low negative values (compressions) are associated with convex structures. High positive values of $-P$ associated with intense thermo-chemical activity, are apparent in the "preheating" and "burning" regions, for low values of k_m and k_g. a_T exhibits similar curvature dependent features

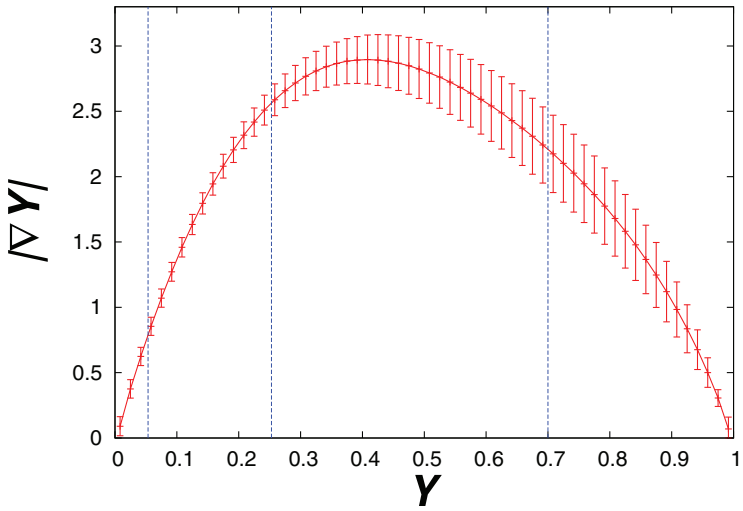

FIG. 14. Scalar gradient modulus, $|\nabla Y|$, as a function of the reactant mass fraction. Dotted lines mark the limits of the four regions of the computational domain.

TABLE IV. Description of zones 1, 2, and 3 in the k_m–k_g plane.

Zone	Description	Ranges
1	Geometries with flat curvature	$[\lvert k_m\delta_L\rvert < 0.02$ and $\lvert k_g\delta_L^2\rvert < 0.004]$
2	Geometries with predominant negative curvature	$k_m\delta_L < 0$ excluding the zone 1
3	Geometries with predominant positive curvature	$k_m\delta_L > 0$ excluding the zone 1

to $\nabla \cdot \mathbf{u}$, although negative strain-rates do exist for convex scalar iso-surfaces. Thermal transport yields only positive values of a_N in the "preheating" and "burning" regions; negative a'_Ns occur for both concave (mainly hyperbolic) and convex structures in the "fresh reactants," and for concave geometries in the "hot products."

The joint pdf of a_N and a_T is shown in Figure 13; the domain of probable values is mainly located above $a_N + a_T = 0$, consistent with the fact that most fluid elements undergo expansion; both "fresh reactants" and "hot products" share the highest probabilities for low volumetric dilatation rates. Significant expansions in the "preheating" and "burning" regions imply positive normal strain, with both signs for a_T.

Mixing rates of scalar fields are in part determined by a_T and a_N. Local scalar molecular fluxes are proportional to mass fraction gradients, which depend on a_N, whereas a_T influences surface stretching. Mainly positive values of a_N should, in principle, lead to diminishing scalar gradients,[9,11] particularly in the "preheating" ($0.253 < Y < 0.700$) and "burning" ($0.053 < Y < 0.253$) regions where maxima of $|\nabla Y|$ occur (Figure 14, $|\nabla Y|$ en function de Y). This result seems counterintuitive and can only be explained by the chemical enhancement of existing scalar gradients which might well balance the reduction due to positive a'_Ns.

To reduce the number of relevant combinations of scalar field structures and flow topologies, we propose to split the $k_m - k_g$ plane of Figure 1 into three zones: nearly flat (zone 1), concave (zone 2), and convex (zone 3), which are characterized by the ranges given in Table IV.

Figure 15 shows the joint pdf's of R and Q in the three curvature conditioned zones of the $k_m - k_g$ plane and the four reaction rate conditioned regions of the computational domain. S5 (SFC) and S6 (SN/SN/SN), typical of flows with local negative volumetric dilatation rates, are absent in this premixed combustion study. About 50% of the topologies in the "fresh reactants" are focal

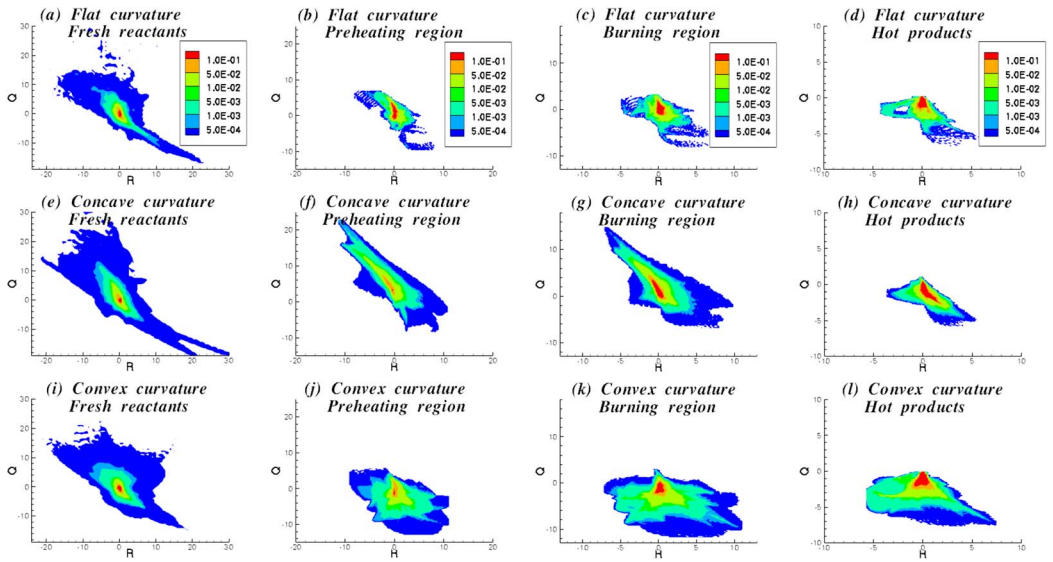

FIG. 15. Joint pdf of $R - Q$: (a)–(d) zone 1 (Flat iso-surfaces); (e)-(h) zone 2 (Concave iso-surfaces); (i)-(l) zone 3 (Convex iso-surfaces). Joint pdf magnitudes decrease from the center to the circumference.

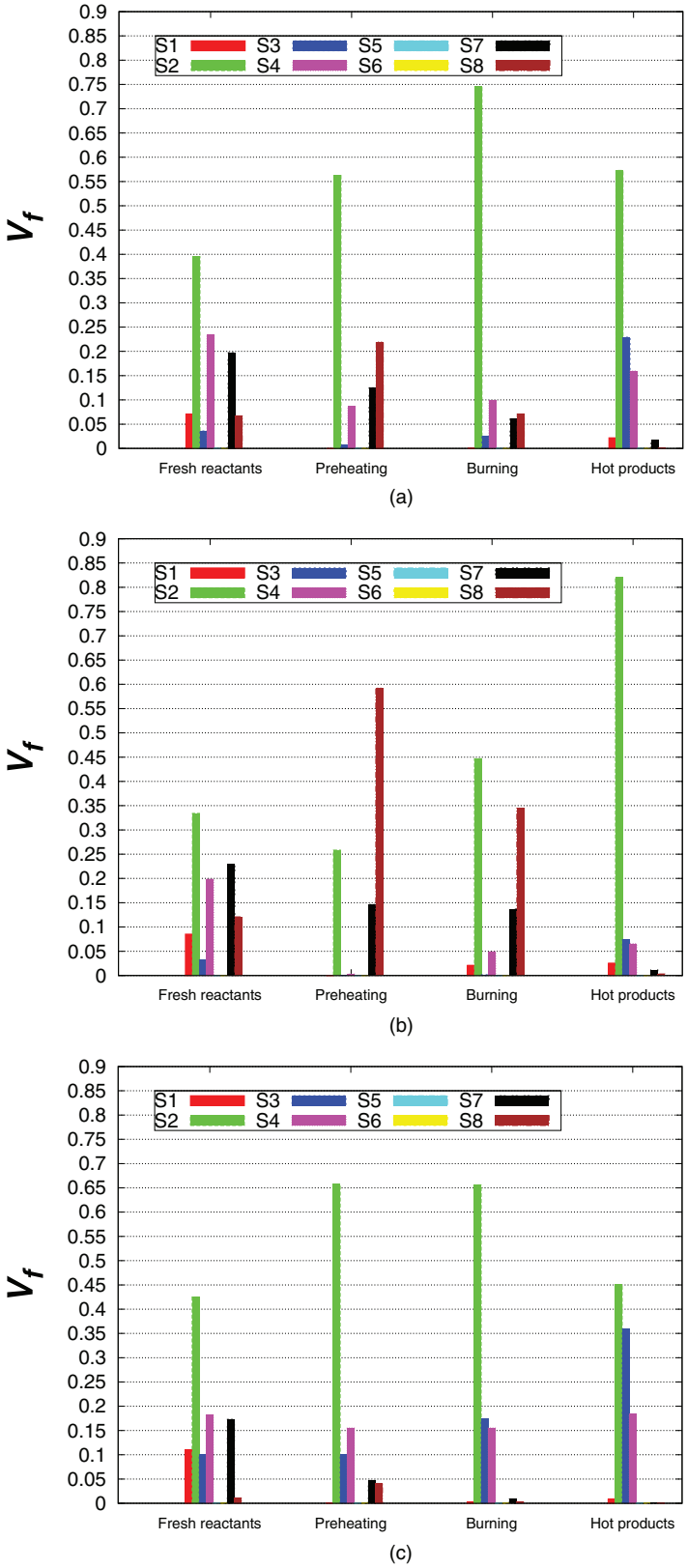

FIG. 16. Topologies ($S1 - S8$) belonging to $P - Q - R$ space: (a) zone 1 (flat iso-surfaces); (b) zone 2 (concave iso-surfaces); (c) zone 3 (convex iso-surfaces).

and tend to disappear, in favor of nodal micro-structures, as moving through the "preheating" and "burning" regions towards the "hot products"; obviously, positive volumetric dilatation rates and flow laminarization, due to increments of dynamic viscosity with increasing temperature, destroy vorticity. Joint pdf's look similar to the teardrop shape of constant density flows ($P = 0$) in the "fresh reactants," with occurrence of both stretching/compressing focuses and stable/unstable nodes; however, local topologies, characteristic of flows with volumetric expansion, S7 (UFS) and S8 (UN/UN/UN), contribute about 25%, a sign of a moderate interaction of the propagating flame with the initially imposed constant density turbulence.

Two nodal topologies, S2 (UN/S/S, 51%) and S8 (UN/UN/UN, 26%), and two focal ones, S4 (SFS, 8%) and S7 (UFS, 10%), add up to 95% over the flow domain in the "preheating" region. Nodal, S2 (UN/S/S, 61%), S3 (SN/S/S, 7%), and S8 (UN/UN/UN, 14%), and focal, S4 (SFS, 10%), structures account for 92% of local flow topologies in the "burning" region. Vortical structures S4 (SFS) and S7 (UFS) start both from 20% contributions in the "fresh reactants," and decrease through the "preheating" and "burning" regions; however, whereas the S4 maintains a 13% share in the "hot products," S7 almost vanishes. This could be due to the alignment of the former vorticity with an extensive eigenvector.

Figure 16 shows volume fractions of the flow domain pertaining to different flow topologies also disaggregated for the three curvature conditioned zones. The S2 (UN/S/S) topology dominates the local flow dynamics for all three scalar geometries and all reaction-conditioned regions, with some significant contribution of S8 (UN/UN/UN) for concave iso-surfaces (in the "preheating" and "burning" regions). S3 (SN/S/S) for flat and convex geometries has a modest to moderate share, mainly in the "hot products." Figure 16 confirms that S7 and S8 topologies associate more likely to concave iso-scalar surfaces, where heat-conduction focusing effects enhance chemical reaction.

It is important to examine the alignment of both nodal and focal topologies with respect to iso-scalar surfaces. Figure 17 depicts the pdf's of the cosine of the angle between the unit vector

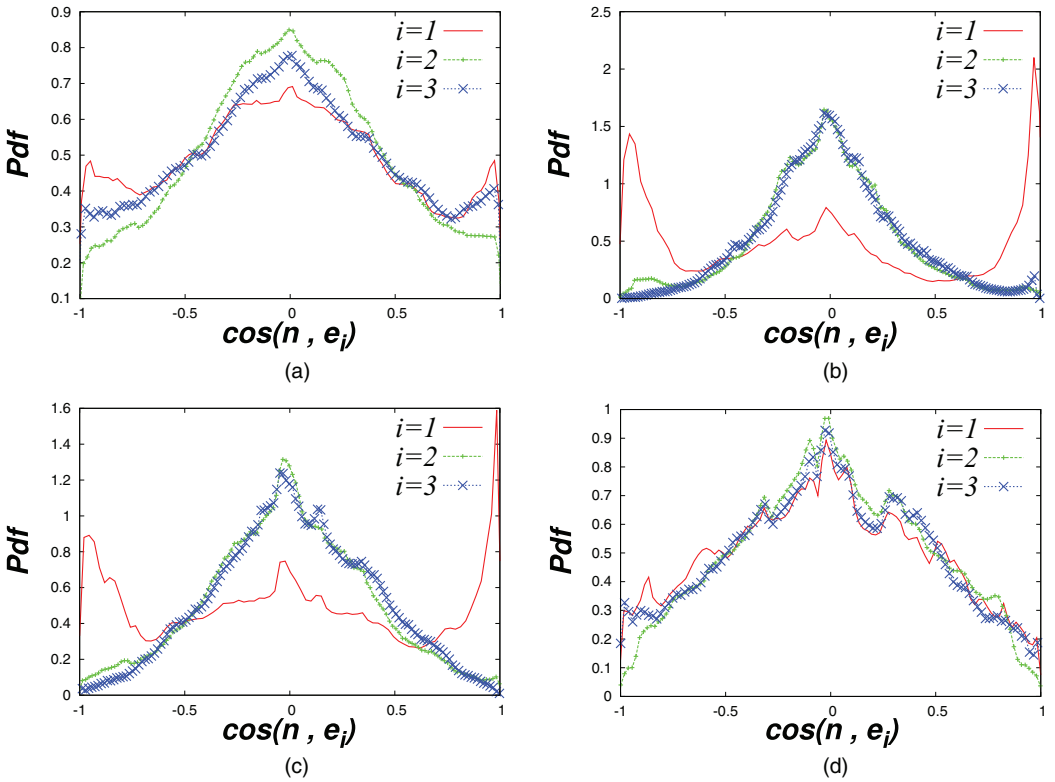

FIG. 17. Pdf's of cos($\mathbf{n}$, $\mathbf{e}_i$). $\mathbf{n}$ is the unit vector normal to iso-scalar surfaces and $\mathbf{e}_i$ is the eigenvector of S_{ij}. The subindex of $\mathbf{e}_i$ denotes one of the three eigenvalues, ordered by decreasing values. $i = 1$ corresponds to the most extensive (positive) eigenvalue. (a) Fresh reactants, (b) preheat region, (c) burning region, (d) hot products.

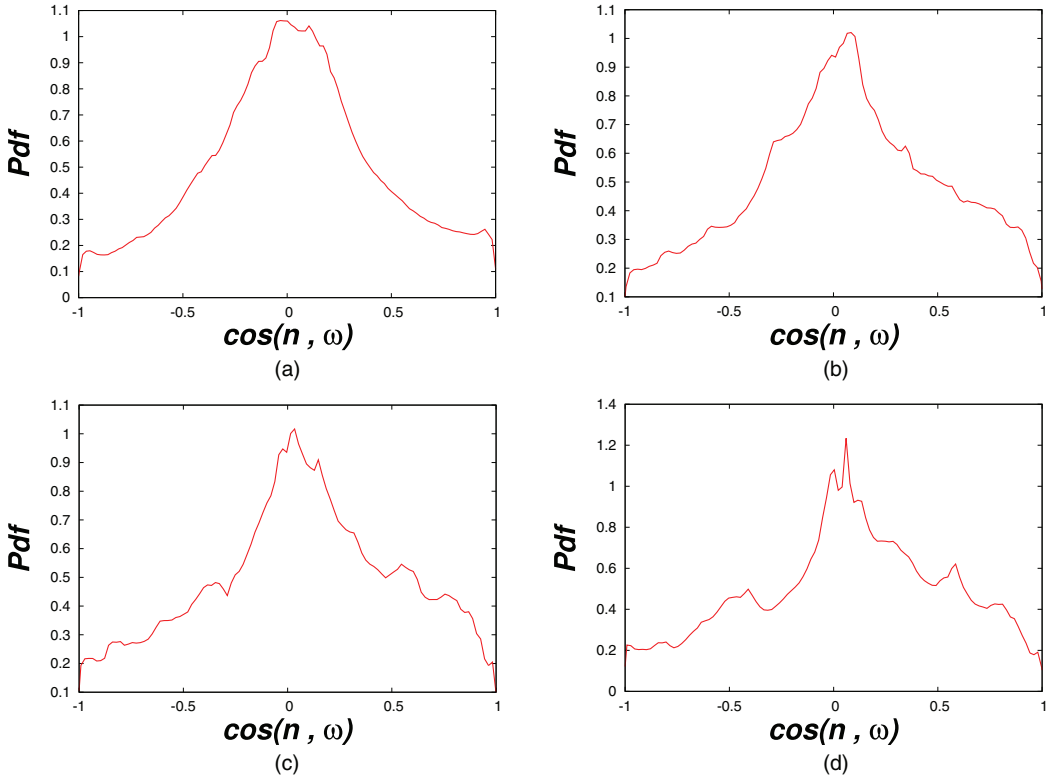

FIG. 18. Pdf's of cos(**n**, $\boldsymbol{\omega}$). **n** is the unit vector normal to iso-scalar surfaces. $\boldsymbol{\omega}$ is the local vorticity vector. (a) Fresh reactants, (b) preheat region, (c) burning region, (d) hot products.

normal to iso-scalar surfaces, **n**, and the eigenvectors of the strain rate tensor, $\mathbf{e}_i$, all over the flow domain. $\mathbf{e}_1$ is the eigenvector corresponding to the most extensive eigenvalue; the subindex i orders the eigenvectors by decreasing corresponding eigenvalues. **n** is predominantly aligned with the eigenvector corresponding to the most extensive eigenvalue in the "preheating" and "burning" regions, which is in agreement with recent numerical[9,11,37] and experimental results.[38] **n** exhibits a slight alignment with the most compressive eigenvalue, $\mathbf{e}_3$, in the "fresh reactants," where the heat

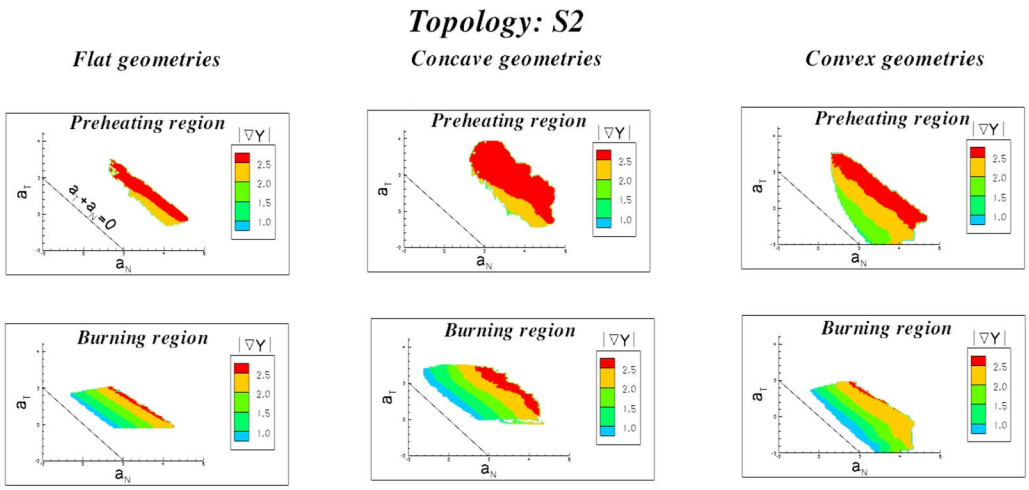

FIG. 19. Scalar gradient modulus, $|\nabla Y|$, conditioned to $a_T - a_N$ for nodal topology S2 in the "preheating" and "burning" regions.

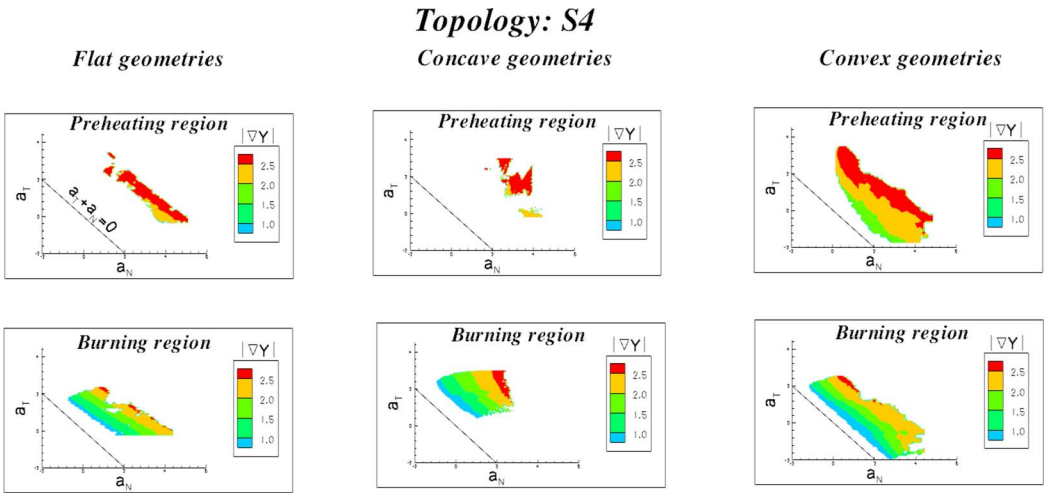

FIG. 20. Scalar gradient modulus, $|\nabla Y|$, conditioned to $a_T - a_N$ for focal topology S4 in the "preheating" and "burning" regions.

release is weak and iso-scalar surfaces behave like those in non-reacting constant-density turbulent flows.[39,40] There is no preferred alignment in the "hot products."

Figure 18 plots the pdf's of the cosine between **n** and the local vorticity vector, $\boldsymbol{\omega}$. Values computed over all the flow domain are used. The vorticity vector is preferentially tangential to iso-scalar surfaces and, therefore, it contributes to curve and fold them. The joint action of two vortical structures, either co-rotating or counter-rotating, may also stretch and/or bend the surface. These results are in agreement with three-dimensional DNS calculations,[41] where the vorticity vector is found to lie preferentially in the plane of the flame.

Two nodal topologies, S2 (UN/S/S) and S8 (UN/UN/UN), and two focal ones, S4 (SFS) and S7 (UFS), account for well over 90% of the samples in the "preheating" and "burning" regions. The key scalar mixing variable, $|\nabla Y|$, conditioned to a_N and a_T is shown in Figures 19–22 for the previous four topologies and for the three scalar geometries. These topologies for flat and concave scalar geometries are characterized by $a_N > 0$ and $a_T > 0$ with maxima of $|\nabla Y|$ far from the constant density line $a_T + a_N = 0$. Only S2 and S4 topologies associated to convex iso-surfaces can produce

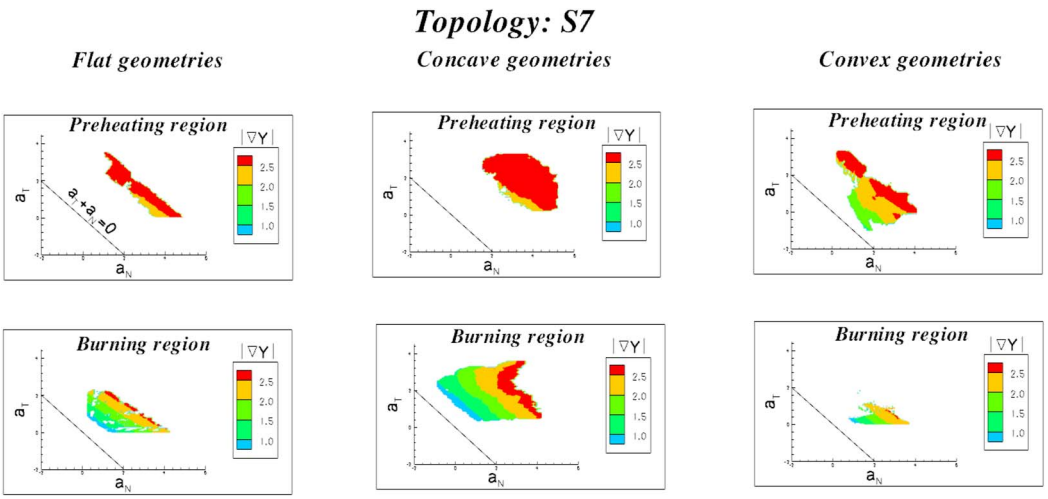

FIG. 21. Scalar gradient modulus, $|\nabla Y|$, conditioned to $a_T - a_N$ for focal topology S7 in the "preheating" and "burning" regions.

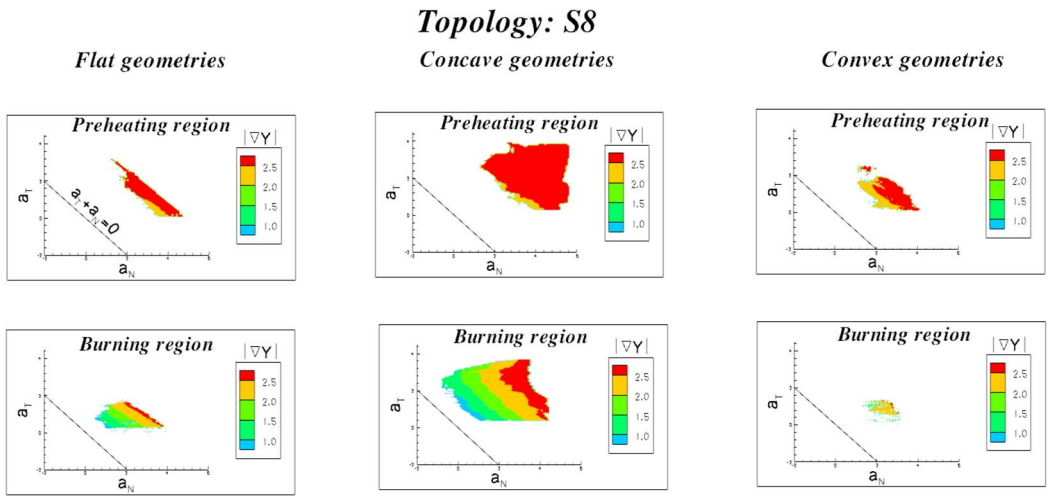

FIG. 22. Scalar gradient modulus, $|\nabla Y|$, conditioned to $a_T - a_N$ for nodal topology S8 in the "preheating" and "burning" regions.

$a_T < 0$ with modest values of $|\nabla Y|$. Concave geometries under flow topologies S2, S7, and S8 in both the "preheating" and "burning" regions display large gradients for a wide range of a_N and a_T. The features of nodal topologies S2 and S8 should be easy to incorporate in the formulation of molecular mixing models. Focal structures S4 and S7 require further investigation to relate the probable region on the $a_N - a_T$ plane to pairs of counter- and co-rotating vortices.

V. CONCLUSIONS

A three-dimensional variable-density DNS of a turbulent premixed propagating flame has been performed in an inflow-outflow configuration using one-step Arrhenius chemistry. The interaction of the flame thermochemical processes with scalar field geometries and flow topologies has been studied. The computational domain has been divided into four regions, corresponding to "fresh reactants," "preheating," "burning," and "hot products," depending on the value of the reaction rate. Nearly flat scalar iso-surfaces are the most probable geometries in all four regions. Thermochemical processes in the "preheating" and "burning" regions smooth out highly contorted iso-scalar surfaces, present in the "hot reactants," and annihilate large curvatures; convex structures with moderate mean curvatures are regenerated in the "hot products."

Positive volumetric dilatation rates, $-P = \nabla \cdot \mathbf{u}$, display maxima (minima) for concave (convex) scalar micro-structures due to heat conduction focusing (defocusing) effects. Minima of $-P$ are associated with convex scalar geometries in the "fresh reactants" and maxima with slightly concave tile- and cup-like geometries in the "preheating" and "burning" regions. Average tangential strain rates are approximately constant with large fluctuations throughout the flow domain, whereas normal strain rates follow the trends of volumetric dilatation rates in the different reaction rate conditioned regions.

Probable values of a_N and a_T are predominantly located above $a_N + a_T = 0$, corresponding to positive values of $\nabla \cdot \mathbf{u}$ throughout most points of the computational domain. Most probable values occur in the neighborhood of $a_N + a_T = 0$ in the "fresh reactants" and "hot products," with positive or negative values of both strain rates, and for $a_N + a_T > 0$ in the "preheating" and "burning" regions, with $a_N > 0$.

Focal topologies are important in the "fresh reactants" and tend to disappear in favor of nodal structures as moving towards the "hot products." Positive volumetric dilatation rates, which are more intense in the "preheating" and "burning" regions, effectively destroy enstrophy; further, these destructive trends are also associated to increments of viscosity due to temperature increases which fosters flow laminarization.

Joint pdf's of R and Q look similar to the teardrop shape of constant density flows in the "fresh reactants"; however, a 25% share of the samples correspond to local topologies S7 (UFS) and S8 (UN/UN/UN), characteristic of flows with volumetric expansion, a sign of a moderate interaction of the propagating flame with the initially imposed constant density turbulence. Nodes S2 (UN/S/S, 51%) and S8 (UN/UN/UN, 26%), and focuses S4 (SFS, 8%) and S7 (UFS, 10%) add up to 95% and 92% of the topologies in the "preheating" and the "burning" regions, respectively. Vortical structures S4 (SFS) and S7 (UFS) start both from 20% contributions in the "fresh reactants," and decrease through the "preheating" and "burning" regions; however, whereas the S4 maintains a 13% share in the "hot products," S7 almost vanishes. This could be due to the alignment of the vorticity with an extensive eigenvector in the former. The S2 (UN/S/S) topology dominates the local flow dynamics for all three scalar geometries and all reactive regions. S8 (UN/UN/UN) has a significant contribution for concave iso-surfaces (in the "preheating" and "burning" regions). S7 and S8 topologies associate more likely to concave iso-scalar surfaces, where heat-conduction focusing effects enhance chemical reaction.

The scalar gradient is predominantly aligned with the eigenvector corresponding to the most extensive eigenvalue in the "preheating" and "burning" regions, which is in agreement with recent numerical[9,11,37] and experimental results.[38] $\mathbf{n}$ exhibits a slight alignment with the most compressive eigenvalue, $\mathbf{e}_3$, in the "fresh reactants," where the heat release is weak and iso-surfaces behave like those in constant-density turbulent flows.[39,40]

Future development of mixing models should incorporate some representation of the dependences of $|\nabla Y|$ and area element variations in terms of a_T, a_N and some thermochemical parameters. A positive a_N implies a reduction of $|\nabla Y|$ and hampers scalar mixing, as pointed out by Chakraborty and co-workers;[9,11] this effect must be definitely balanced by thermochemical processes. It is straightforward to show that a chemical source term cannot generate scalar gradients, but can increase or decrease existing ones.

The conclusions reached in this study pertain to small-scale features and thus should display a certain degree of universality; however, this should be confirmed in other flows, like turbulent premixed jet flames. Local flow topologies at a single point cannot unambiguously be related to iso-scalar surface geometries. Two point micro-structures might also be required to characterize local deformations of non-material surfaces. Two-time studies, with time lags of the order of the Kolmogorov time micro-scale could also be relevant.

ACKNOWLEDGMENTS

The authors would like to thank Professor Luc Vervisch and Professor Pascale Domingo of the CORIA-CNRS, Normandie Université, INSA de Rouen for some interesting discussions on the conditioned regions of the computational domain, and also to Dr. Juan Hierro, of the "Centro Universitario de la Defensa/University of Zaragoza" for his help with the pseudo-spectral numerical code. The Spanish Ministry of Science and Innovation initially sponsored this research through Project No. ENE2008-01404/CON. The late support of Project No. CS D2010-00011-SCORE, funded under the CONSOLIDER-INGENIO Program of the Spanish Ministry of Economy and Competitiveness, is also acknowledged.

[1] C. Gibson, "Fine structure of scalar fields mixed by turbulence: I. Zero-gradient points and minimal gradient surfaces," Phys. Fluids **11**, 2305–2315 (1968).
[2] C. Gibson, "Fine structure of scalar fields mixed by turbulence: II. Spectral theory," Phys. Fluids **11**, 2316–2327 (1968).
[3] H. Moffatt, *New Trends in Turbulence. Turbulence: Nouveaux Aspects: Les Houches*, edited by M. Lesieur, A. Yaglom, and F. David (Springer, Berlin, 2001), pp. 319–340.
[4] L. Wang and N. Peters, "The length-scale distribution function of the distance between extremal points in passive scalar turbulence," J. Fluid Mech. **554**, 457–475 (2006).
[5] C. Dopazo, J. Martín, and J. Hierro, "Iso-scalar surfaces, mixing and reaction in turbulent flows," C. R. Mec. **334**, 483–492 (2006).
[6] C. Dopazo, J. Martín, and J. Hierro, "Local geometry of isoscalar surfaces," Phys. Rev. E **76**, 056316 (2007).
[7] S. Candel and T. Poinsot, "Flame stretch and the balance equation for the flame area," Combust. Sci. Technol. **70**, 1–15 (1990).
[8] N. Chakraborty and R. Cant, "Influence of Lewis number on curvature effects in turbulent premixed flame propagation in the thin reaction zones regime," Phys. Fluids **17**, 105105 (2005).

[9] N. Chakraborty and N. Swaminathan, "Influence of the Damköhler number on turbulence-scalar interaction in premixed flames. I. Physical insight," Phys. Fluids **19**, 045103 (2007).
[10] N. Chakraborty, "Comparison of displacement speed statistics of turbulent premixed flames in the regimes representing combustion in corrugated flamelets and thin reaction zones," Phys. Fluids **19**, 105109 (2007).
[11] N. Chakraborty, M. Klein, and N. Swaminathan, "Effects of Lewis number on reactive scalar gradient alignment with local strain rate in turbulent premixed flames," Proc. Combust. Inst. **32**, 1409–1417 (2009).
[12] M. Chong, A. Perry, and B. Cantwell, "A general classification of three-dimensional flow fields," Phys. Fluids **2**, 765–777 (1990).
[13] A. Perry and M. Chong, "Topology of flow patterns in vortex motions and turbulence," Appl. Sci. Res. **53**, 357–374 (1994).
[14] J. Soria, R. Sondergaard, B. Cantweel, M. Chong, and A. Perry, "A study of the fine-scale motions of incompressible time-developing mixing layers," Phys. Fluids **6**, 871–884 (1994).
[15] M. Chong, A. Perry, J. Chacin, and B. Cantweel, "Turbulence structures of wall-bounded shear flows found using DNS data," J. Fluid Mech. **357**, 225–247 (1998).
[16] J. Chacin and B. Cantwell, "Dynamics of a low Reynolds number turbulent boundary layer," J. Fluid Mech. **404**, 87–115 (2000).
[17] A. Ooi, J. Martín, J. Soria, and M. Chong, "A study of the evolution and characteristics of the invariants of the velocity-gradient tensor in isotropic turbulence," J. Fluid Mech. **381**, 141–174 (1999).
[18] E. Elsinga and I. Marusic, "Universal aspects of small-scale motions in turbulence," J. Fluid Mech. **662**, 514–539 (2010).
[19] W. Feiereisen, W. Reynolds, and J. Ferziger, "Numerical simulation of a compressible, homogeneous turbulent shear flow," Report No. TF-13 (Thermoscience Division, Department of Mechanical Engineering, Stanford University, Stanford, 1981).
[20] J. Chen, M. Chong, J. Soria, R. Sondergaard, A. Perry, M. Rogers, R. Moser, and B. Cantwell, "A study of the topology of dissipating motions in direct numerical simulations of time-developing compressible and incompressible mixing layers," Center for Turbulence Research, 1990, pp. 141–164.
[21] H. Maekawa, T. Hiyama, and Y. Matsuo, "Study of the geometry of flow patterns in compressible isotropic turbulence," JSME Int. J. Ser. B. **42**(3), 336–343 (1999), available at https://www.jstage.jst.go.jp/browse/jsmeb/42/3/_contents.
[22] M. Tanahashi, M. Fujimura, and T. Miyauchi, "Coherent fine-scale eddies in turbulent premixed flames," Proc. Combust. Inst. **28**, 529–535 (2000).
[23] S. Suman and S. Girimaji, "Velocity gradient invariants and local flow field topology in compressible turbulence," J. Turbul. **11**(2), N2, 1–24 (2010).
[24] R. Grout, A. Gruber, C. Yoo, and J. Chen, "Direct numerical simulation of flame stabilization downstream of a transverse fuel jet in cross-flow," Proc. Combust. Inst. **33**, 1629–1637 (2011).
[25] L. Wang and X. Lu, "Flow topology in compressible turbulent boundary layer," J. Fluid Mech. **703**, 255–278 (2012).
[26] T. Poinsot, D. Haworth, and G. Bruneaux, "Direct simulation and modelling of flame-wall interaction for premixed turbulent combustion," Combust. Flame **95**, 118–132 (1993).
[27] B. Cuenot and T. Poinsot, "Asymptotic and numerical study of diffusion flames with variable Lewis number and finite rate chemistry," Combust. Flame **104**, 111–137 (1996).
[28] T. Poinsot and D. Veynante, *Theoretical and Numerical Combustion* (Edwards, Philadelphia, 2005).
[29] A. Tsinober, *Turbulence Structure and Vortex Dynamics* (Cambridge University Press, 2000), pp. 164–191.
[30] T. Poinsot and S. Lele, "Boundary conditions for direct simulations of compressible viscous flows," J. Comput. Phys. **101**, 104–129 (1992).
[31] S. Orszag and G. Patterson, "Numerical simulation of three-dimensional homogeneous isotropic turbulence," Phys. Rev. Lett. **28**, 76–79 (1972).
[32] R. Rogallo, "Numerical experiments in homogeneous turbulence," NASA TM 81315, NASA Ames Research Center, CA 1981.
[33] V. Eswaran and S. Pope, "An examination of forcing in direct numerical simulations of turbulence," Comput. Fluids **16**(3), 257–278 (1988).
[34] V. Eswaran and S. Pope, "Direct numerical simulations of the turbulent mixing of a passive scalar," Phys. Fluids **31**(3), 506–520 (1988).
[35] R. Borghi, *Recent Advances in Aerospace Sciences: In Honor of Luigi Crocco on his Seventy-fifth Birthday*, edited by C. Casci and C. Bruno (Plenum Press, New York, 1985), pp. 117–138.
[36] D. Veynante and L. Vervisch, "Turbulent combustion modeling," Prog. Energy Combust. Sci. **28**, 193–266 (2002).
[37] S. Kim and H. Pitsch, "Scalar gradient and small-scale structure in turbulent premixed combustion," Phys. Fluids **19**, 115104 (2007).
[38] G. Hartung, J. Hult, C. Kaminski, J. Rogerson, and N. Swaminathan, "Effect of heat release on turbulence and scalar-turbulence interaction in premixed combustion," Phys. Fluids **20**, 035110 (2008).
[39] W. Ashurst, A. Kerstein, R. Kerr, and C. Gibson, "Alignment of vorticity and scalar gradient in simulated Navier-Stokes turbulence," Phys. Fluids **30**, 2343–2353 (1987).
[40] R. Kerr, "Higher-order derivative correlations and the alignment of small-scale structures in isotropic numerical turbulence," J. Fluid Mech. **153**, 31–58 (1985).
[41] C. Rutland and A. Trouvé, "Direct simulations of premixed turbulent flames with nonunity Lewis numbers," Combust. Flame **94**, 41–57 (1993).

C

Local volumetric dilatation rate and scalar geometries in a premixed methane-air turbulent jet flame

Available online at www.sciencedirect.com

ScienceDirect

Proceedings of the Combustion Institute 35 (2015) 1295–1303

Proceedings of the Combustion Institute

www.elsevier.com/locate/proci

Local volumetric dilatation rate and scalar geometries in a premixed methane–air turbulent jet flame

Luis Cifuentes [a,*], César Dopazo [a], Jesús Martín [a], Pascale Domingo [b], Luc Vervisch [b]

[a] LIFTEC, CSIC – University of Zaragoza, Spain
[b] CORIA – CNRS, Normandie Université, INSA de Rouen, France

Available online 28 June 2014

Abstract

The local volumetric dilatation rate, namely, the rate of change of an infinitesimal fluid volume per unit volume, $\nabla \cdot \mathbf{u}$, is an important variable particularly in flows with heat release. Its tangential and normal strain rate components, a_T and a_N, respectively, account for stretching and partially for separation of iso-scalar surfaces. A three-dimensional direct numerical simulation (DNS) of a turbulent premixed methane–air flame in a piloted Bunsen burner configuration has been performed by solving the full conservation equations for mass, momentum, energy and chemical species using tabulated chemistry. Results for the volumetric dilatation rate as a function of the iso-scalar surface geometry, characterized by the mean and Gauss curvatures, k_m and k_g, are obtained in several zones (reactants, preheat, reacting and products) of the computational domain. Flat iso-scalar surfaces are the most likely geometries in agreement with previous DNS. The relationship between density and a reaction progress variable, under a low Mach number flamelet assumption, leads to an expression for $\nabla \cdot \mathbf{u}$ with contributions from progress variable source and molecular diffusion budget, with a significant contribution from the latter; this approximate expression for the volumetric dilatation rate is studied with DNS results. The joint pdf of a_N and a_T confirms that the line $a_T + a_N = 0$ separates mostly expansive flow regions from compressive zones.

Keywords: Volumetric dilatation rate; Iso-scalar surface curvature; Tangential and normal strain rates; Premixed flame; Direct numerical simulation

1. Introduction

Turbulent reacting flows are ubiquitous in chemical processes, energy systems and multiple engineering and environmental problems. Their interest stems from both technical applications and an incomplete understanding of the underlying physical fundamental mechanisms. Small-scale flow structures and scalar geometries strongly interact in front, within and behind highly reacting zones and determine mixing, combustion and heat release rates. Turbulent mixing models should incorporate correct physical features to improve their predictive accuracy.

* Corresponding author.
E-mail address: lcifuentes@unizar.es (L. Cifuentes).

http://dx.doi.org/10.1016/j.proci.2014.06.026
1540-7489/

Haworth and Poinsot [1], through the use of two-dimensional direct numerical simulations (DNS), investigated Lewis number effects in the structure of a premixed flame front with single-step Arrhenius chemistry; they found that the local flame structure of non-unity Lewis number flames correlates more strongly with local flame curvature than with tangential strain rate. The two-dimensional DNS of a turbulent premixed methane–air flame by Echekki and Chen [2] showed that the correlation of radical species with mean curvature, k_m, of the flame surface is strongly dependent upon their individual mass diffusion rates. Tanahashi et al. [3] studied, via DNS, the local flame structure of hydrogen/air premixed turbulent flames propagating in three-dimensional homogeneous isotropic turbulence; they found that the probability density function (pdf) of k_m is far from Gaussian, with exponential tails, and that flame elements with large curvatures, convex towards the burned side, display high heat release rates. Chakraborty and Cant [4] used three-dimensional DNS of premixed turbulent flames with single-step Arrhenius chemistry to investigate the effect of k_m on flame propagation and obtained that the mean curvature is negatively correlated with the local volumetric dilatation rate, $\nabla \cdot \mathrm{u}$, and with the displacement speed of the iso-scalar surfaces. Sankaran et al. [5] conducted three-dimensional DNS of a turbulent premixed methane–air Bunsen turbulent flame with a reduced chemistry; they concluded that the volumetric dilatation rate decreases with k_m and that k_m exhibits a longer tail for positive curvatures.

To the best of our knowledge, a detailed characterization for variable-density turbulent reacting flows of the rate of change of an infinitesimal fluid volume per unit volume for different local scalar geometries, described in terms of k_m and k_g [6], the mean and Gauss curvatures, respectively, has never been undertaken. Moreover in flame zones, how molecular diffusion and reaction of scalars are related with $\nabla \cdot \mathrm{u}$ are also of interest. The present work aims at investigating these issues through DNS of a premixed methane–air turbulent jet flame.

Section 2 provides an overview of the conservation equations, of the numerical method and of the DNS properties. Section 3 briefly summarizes the mathematical description of local geometries of iso-scalar surfaces in the $k_m - k_g$ plane. Section 4 analyzes and discusses the results for different regions of the flow domain (reactant, preheat, reacting and product zones); $\nabla \cdot \mathrm{u}$ directly calculated from DNS and that obtained formulating a so-called 'flamelet' assumption are examined with tangential and normal strain rates characterizing expansive and compressive flow regions. Section 5 summarizes the main findings and recommends some future work.

2. Mathematical description and imbedded DNS in LES

The analysis is performed in a jet-flame configuration simulated with a hybrid Large Eddy Simulation (LES)/DNS approach.

A stoichiometric methane–air mixture is injected through a central jet, surrounded by a co-flow of burned products. Turbulence parameters are those experimentally studied by Chen et al. [7]. The nozzle diameter is $D = 12$ mm and the computational domain extends 192 mm in the streamwise (x), 66 mm in the crosswise (y) and 66 mm in the spanwise (z) directions, with 802, 466 and 466 grid points, uniformly spaced, in the x, y, and z directions, respectively. Therefore a LES mesh of about 171 million nodes is used, with a resolution varying between 150 μm and 200 μm. An imbedded zone within the LES mesh features a much higher resolution of 50 μm (Fig. 1(a)), where small scales can rapidly develop to complete the turbulence cascade of the already well-resolved LES. Results are analyzed in this zoom box located at $x/D = 4.5$ from the nozzle, which corresponds essentially to the potential core of the jet [7], and at $t = 80$ ms, which is much greater that one initial integral eddy turnover time, $t_l = 1.13$ ms. The DNS zoom box under study contains $243 \times 343 \times 343$ grid points where the resolution is of the order of 50 micrometer in

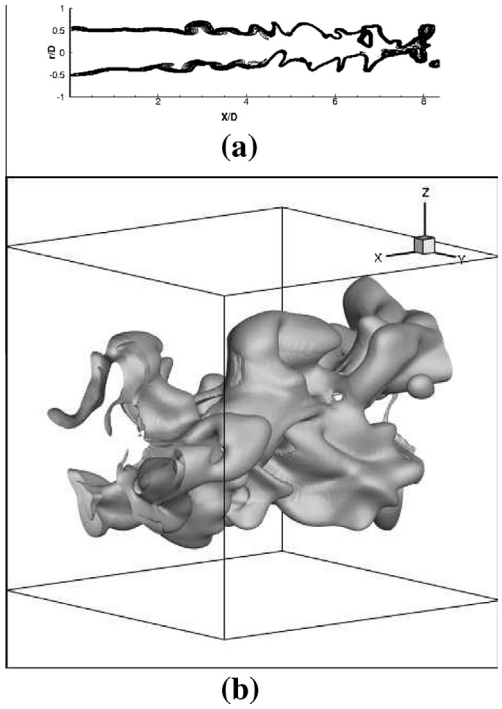

Fig. 1. (a) Snapshot of iso-c burning rate in the centerline plane. (b): Iso $c = 0.8$ surface in the DNS zone.

the x, y and z directions, respectively, and has physical domain dimensions of 12 mm × 18 mm ×18 mm (Fig. 1(b)).

A presumed probability density function closure [8] is used in the LES part, close to burner injection and downstream of the fully resolved flow part. In the DNS zone, the probability density function reduces to a Dirac delta function, thus ensuring full resolution of the reaction zone and of its interaction with turbulence. This is visible in Fig. 1(a), where the reaction zone thickness strongly decreases within the DNS zone starting at $x/D = 4.5$. This simple approach allows for generating DNS data embedded within a turbulent flow featuring most of the properties of shear-flows found in real burners.

Turbulence is introduced by injecting a correlated random noise [9] with uniform rms, u', throughout the jet inlet. The dimensionless characteristic velocity fluctuations rms, u'/S_L, and the integral length scale, l/δ_L, of the premixed flame turbulent jet flame are used, where S_L is the non stretched laminar flame velocity and δ_L is the flame thickness based on the maximum temperature gradient. In this study, $u'/S_L = 5.43$ and $l/\delta_L = 6.31$, with combustion taking place in the 'thickened-wrinkled flame' regime [10,11].

The fully parallel compressible solver SiTCom (Simulating Turbulent Combustion) is used to solve the mass, momentum, energy and reaction progress variable conservation equations. This solver approximates the convective terms resorting to a fourth-order centered skew-symmetric-like scheme [12] and the diffusive terms with a fourth-order centered scheme. Time integration is performed via a third-order Runge–Kutta scheme [13]. All boundary conditions are imposed using the 3D-NSCBC approach [14]. External forces, Soret and Dufour effects, thermal diffusive fluxes of chemical species, pressure gradient diffusion, bulk viscosity and radiative heat transfer are assumed negligible. Viscosity, thermal conductivity, and mass diffusion coefficients are given functions of the temperature.

The chemistry is tabulated with the FPI flamelet approach (Flame-Prolongation of ILDM) [15] using a single progress variable Y_c as defined by Godel et al. [16], which includes CO, CO_2, H_2O and some nitrogen species. This tabulation approach actually provides the best fit for the burning rate of a single-step chemistry, with all the species of the detailed scheme involved in the thermochemistry.

The governing equations can then be written in Cartesian tensor notation as mass continuity:

$$\frac{\partial \rho}{\partial t} + \frac{\partial}{\partial x_i}(\rho u_i) = 0, \tag{1}$$

momentum equation:

$$\frac{\partial (\rho u_i)}{\partial t} + \frac{\partial (\rho u_j u_i)}{\partial x_j} = -\frac{\partial p}{\partial x_i} + \frac{\partial \tau_{ij}}{\partial x_j}, \tag{2}$$

energy equation in the form of $E = e_s + 0.5 u_i u_i$, sensible plus kinetic energy:

$$\frac{\partial (\rho E)}{\partial t} + \frac{\partial}{\partial x_i}(\rho u_i E) = -\frac{\partial}{\partial x_j}(p u_j) + \frac{\partial}{\partial x_j}(\tau_{ij} u_i) + \frac{\partial}{\partial x_i}\left(\lambda \frac{\partial T}{\partial x_i}\right) + \dot{\omega}_T, \tag{3}$$

and reaction progress variable Y_c:

$$\frac{\partial (\rho Y_c)}{\partial t} + \frac{\partial}{\partial x_i}(\rho u_i Y_c) = \frac{\partial}{\partial x_i}\left(\rho D \frac{\partial Y_c}{\partial x_i}\right) + \dot{\omega}_{Y_c}. \tag{4}$$

In these balance equations, t and x_i stand for time and ith component of the position vector, respectively. ρ denotes density, u_i is the ith component of velocity, p is the pressure, τ_{ij} is the ij component of the viscous stress tensor, given by the Navier–Poisson constitutive relation [11], λ is the thermal conductivity, D is the mass diffusivity computed with a Schmidt number of 0.7, $\dot{\omega}_{Y_c}$ is the reaction rate of the progress variable and $\dot{\omega}_T$ is the heat release due to combustion. Thermodynamic variables are related by the perfect gas equation of state, $p = \rho RT/W$, where R is the universal perfect gas constant and W is the mean molecular weight.

The turbulent Reynolds number, R_e, based on the characteristic DNS velocity fluctuations rms, $u' = 2.12$ ms, and the integral length scale, $l = 2.4$ mm, reads:

$$Re = \frac{\rho u' l}{\mu}, = 300. \tag{5}$$

On the other hand, the Lewis number,

$$Le = \frac{\lambda}{\rho C_p D} = 1. \tag{6}$$

C_p is the specific heat at constant pressure.

Formally, the volumetric dilatation rate can be split into strain rates tangential, a_T, to iso-scalar surfaces (c = constant) and normal, a_N, to them [1,17]:

$$\nabla \cdot \mathrm{u} = \frac{\partial u_i}{\partial x_i} = a_N + a_T, \tag{7}$$

where a_N and a_T are defined by,

$$a_N = n_i n_j \frac{\partial u_i}{\partial x_j}, \tag{8}$$

$$a_T = (\delta_{ij} - n_i n_j)\frac{\partial u_i}{\partial x_j}, \tag{9}$$

n is the unit normal vector at each point of the iso-scalar surfaces.

Assuming constant-pressure in the flow domain, under the flamelet hypothesis, it exists a progress variable $c = (T - T_u)/(T_b - T_u)$, based on temperature, so that the state of law ($P = \rho RT/W$) can be replaced by $\rho = \rho(c) = \rho_u/(1 + \tau c)$, with $\tau = (T_b - T_u)/T_u$ [18]. Subscripts '$_u$' and '$_b$' indicate variables in the unburned and

the burnt gases, respectively, and $\tau = 6.4$. Then, from Eq. (1):

$$\nabla \cdot \mathbf{u} = -\frac{1}{\rho}\left(\frac{\partial \rho}{\partial t} + \mathbf{u} \cdot \nabla \rho\right) = -\frac{1}{\rho}\frac{D\rho}{Dt}, \tag{10}$$

$$= -\left(\frac{1}{\rho}\frac{d\rho}{dc}\right)\frac{Dc}{Dt} = \left(\frac{\tau}{1+\tau c}\right)\frac{Dc}{Dt}. \tag{11}$$

According to the flamelet formalism, the progress variable verifies a balance equation of the form:

$$\frac{Dc}{Dt} = \frac{1}{\rho}(\nabla \cdot (\rho D \nabla c) + \dot{\omega}), \tag{12}$$

leading to the low Mach number approximation:

$$\nabla \cdot \mathbf{u} = \frac{\tau}{\rho_u}(\nabla \cdot (\rho D \nabla c) + \dot{\omega}), \tag{13}$$

where $\dot{\omega}$ is the chemical source of c.

In a fully compressible and multi-species formulation, the energy equation cannot be cast in temperature equation without formulating numerous hypotheses [11]. Even when this is done, there are additional terms due to pressure gradient, molar weights and C_P variations, acting on temperature used to define c. Therefore, (Dc/Dt), the substantial derivative of c, does not equal exactly $\nabla \cdot (\rho D \nabla c) + \dot{\omega}$. Expressing $\nabla \cdot \mathbf{u}$ with relation (13), thus neglecting these additional terms, allows for measuring their impact and how they relate to the scalar field topology through relation (7).

3. Geometries of scalar fields

Iso-scalar surfaces, $c(x,t) = \text{constant}$, can be described in terms of their mean and Gauss curvatures, k_m and k_g, respectively [6]. The unit normal vector to those surfaces, pointing towards the reactants, is given by $\mathbf{n} = -\nabla c/|\nabla c|$.

The expressions for k_g and k_m are,

$$k_g = k_1 k_2, \tag{14}$$

$$k_m = \frac{k_1 + k_2}{2} = \frac{1}{2}\nabla \cdot \mathbf{n}, \tag{15}$$

where k_1 and k_2 are the main surface curvatures, namely, the eigenvalues of the curvature tensor, $\partial n_i/\partial x_j$, corresponding to its eigenvectors, the main directions of curvature. Figure 2 characterizes iso-scalar surface geometries in the $k_m - k_g$ plane [6]; the region $k_g > k_m^2$ implies non-physical complex curvatures. Positive mean curvatures entail convex surfaces towards the fresh reactants, while $k_m < 0$ indicate concave ones. The $k_m - k_g$ plane may be presented in a dimensionless form with $k_m \delta_L$ and $k_g \delta_L^2$.

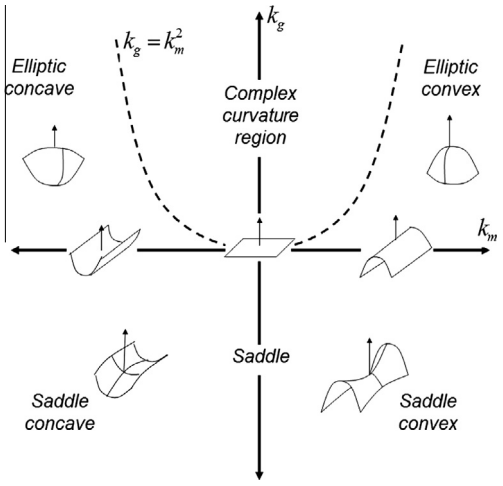

Fig. 2. Classification of iso-scalar surface geometries in terms of their mean and Gauss curvatures, k_m and k_g.

4. Results and discussion

The interaction of small-scale flow structures with the scalar geometries locally modifies reaction progress variable iso-surfaces [19]. Presumably, that interaction will be different for various flow regions, characterized, among other things, by their volumetric dilatation rates. In this study, results are separately obtained for four zones, defined in terms of their reaction rate or progress variable values. Reaction rates smaller than 0.1% of the maximum value, $\dot{\omega}_{c_{max}} = \dot{\omega}_{max}/\rho = 5.626$ (for $c \approx 0.708$), define the 'fresh reactants' region $(0.001 < c < 0.100)$. The region characterized by $\dot{\omega}_c$ between 0.1% and 70% of $\dot{\omega}_{c_{max}}$ is termed the 'preheat' zone $(0.100 < c < 0.5856)$. The 'burning' region is the highly reactive zone with $\dot{\omega}_c > 0.7\dot{\omega}_{c_{max}}$ or, equivalently, $0.5856 < c < 0.7747$. The 'hot products' region is typified by reaction progress variable values greater than 0.7747 and smaller than 0.999. Setting the reaction rate limit for the 'burning' region

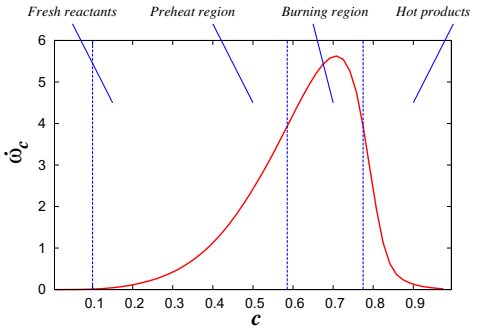

Fig. 3. Reaction rate, $\dot{\omega}_c$, as a function of the progress variable, c. Vertical dotted lines mark the four regions of the computational domain.

between 50% and 70% only slightly modify the analyzed features. Figure 3 shows graphically the reaction rate as a function of the reaction progress variable and defines the ranges of c for the 'fresh reactants', 'preheat', 'burning' and 'hot products' regions; $\dot{\omega}_c$ has been normalized with its rms using all iso-scalar surfaces. Hereafter, results will be analyzed in these four regions of the computational domain.

Figure 4 shows the joint pdf of the mean and Gauss curvatures in the four regions previously defined. k_m and k_g have been normalized with the thickness flame, δ_L. The joint pdfs display maxima for nearly flat iso-scalar surfaces, in agreement with experimental results [20] and three-dimensional DNS calculations [4,5] of premixed turbulent flames. Concave iso-surfaces are much more probable than convex ones both in the fresh reactants and preheat regions; this result seems to agree with the intuitive notion that concave geometries are predominant in zones enclosed within the jet flame. The statistical distribution of k_m and k_g in the burning region is only slightly skewed towards negative values of mean curvature. Convex scalar geometries, with large values of the mean curvatures, are probable in the 'hot products' region; Tanahashi et al. [3] argue that strong coherent fine-scale eddies, perpendicular to the flame front, can survive behind it and create low pressure zones, which increase the probability of finding convex geometries in the 'hot products' region. This explanation should be carefully scrutinized, since vorticity is efficiently destroyed in regions of high volumetric dilatation rates.

$\nabla \cdot u$, conditional upon the mean and Gauss curvatures, is shown in Fig. 5 for the four regions of the domain. The volumetric dilatation rate has been normalized with its rms value, using all the iso-scalar surfaces. A negative correlation between $\nabla \cdot u$ and k_m is observed, in agreement with previous results [4]. Expansive (compressive)

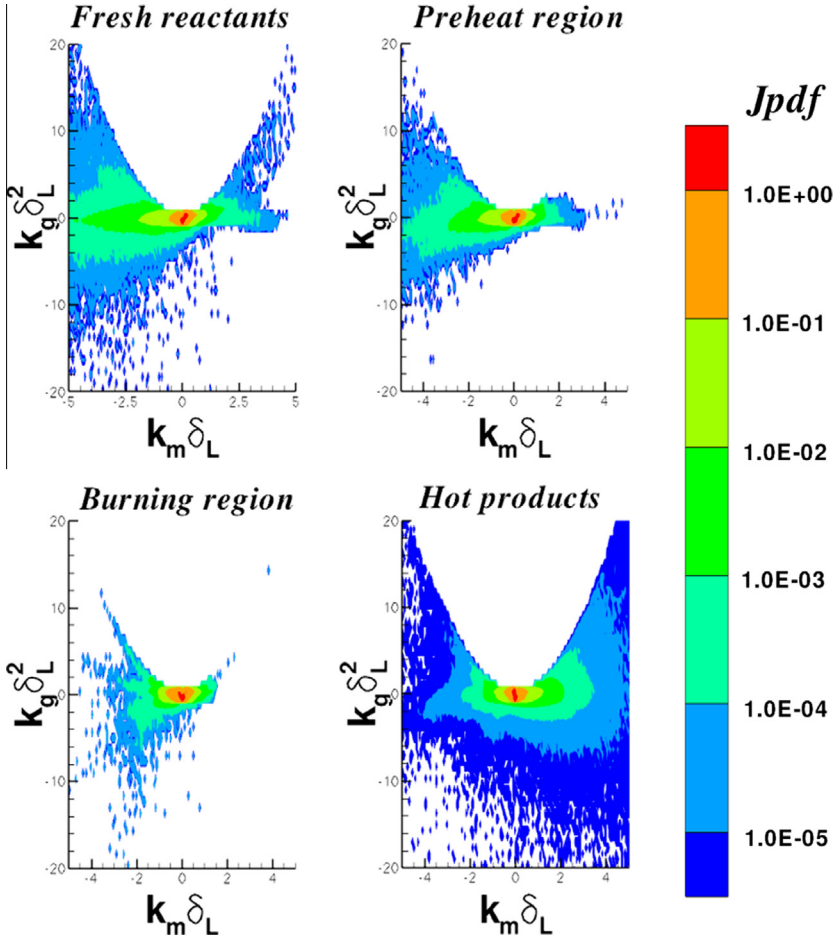

Fig. 4. Joint pdfs of mean and Gauss curvatures, k_m and k_g, for the four regions of the computational domain: Fresh reactants, preheat region, burning region and hot products.

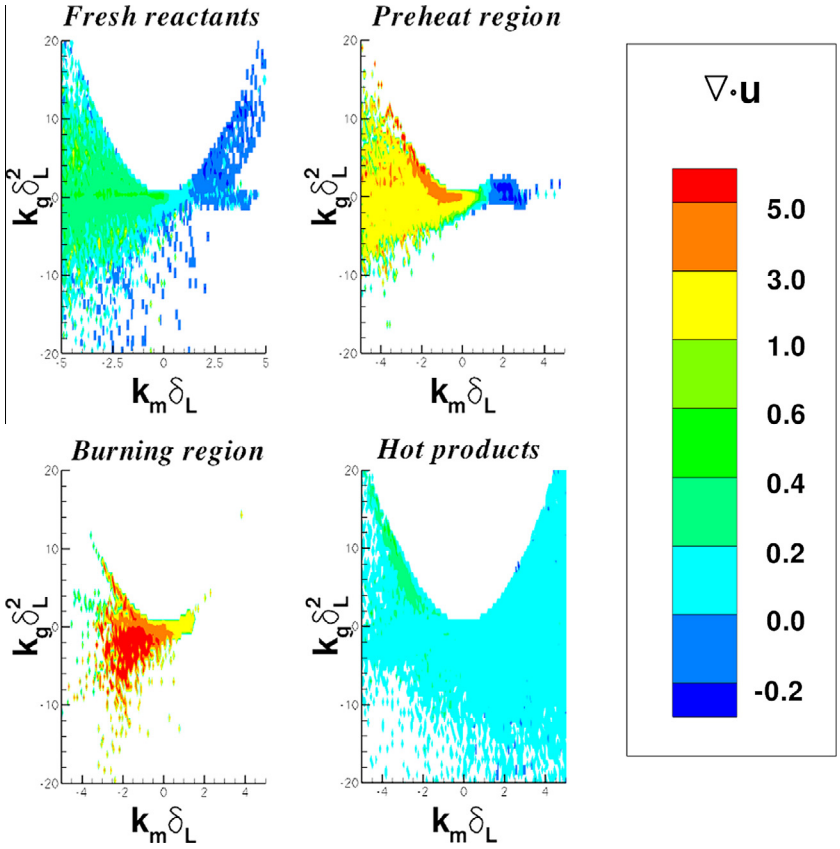

Fig. 5. Fluid element dilatation rate, $\nabla \cdot u$, conditional upon the mean and Gauss curvatures, k_m and k_g.

volumetric dilatations rates are mainly associated to concave and flat (convex) iso-scalar surfaces. Cup-like elliptic concave geometries in the 'preheat' and 'burning' regions correlate with the highest values of $\nabla \cdot u$; this behavior can be explained by the heat conduction focussing (defocussing) by concave (convex) geometries. It should also be noted that small compressive rates prevail for convex and concave iso-surfaces in both the 'fresh reactants' and the 'hot products' zones, while this tendency disappears in the 'preheat' and 'burning' regions due to the high chemical heat release.

The comparison between $\nabla \cdot u$ obtained from the present DNS and that calculated using Eq. (13), which corresponds to the low Mach number flamelet approximation [18], is shown in Fig. 6. Variables in this figure have been normalized with the rms values of $\nabla \cdot u$, using all the iso-scalar surfaces. Vertical solid bars indicate their respective rms values. While relative differences of the two volumetric dilatation rates remain between 0% and 4.5% for $c < 0.5$, their disagreement notably increase for $c > 0.54$. This is expected, since the effects neglected in the simplified diffusive and

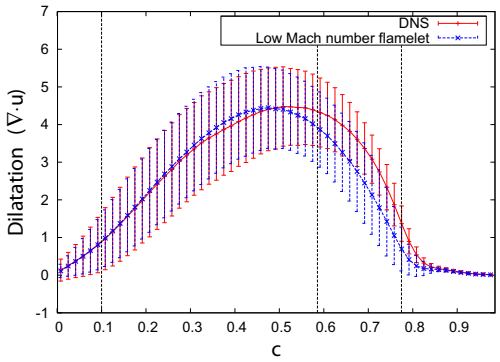

Fig. 6. Dilatation, $\nabla \cdot u$, obtained from the present DNS and that calculated using Eq. (13), across the progress variable. Vertical solid bars in the terms indicate their respective root-mean-square values and the vertical dotted lines in figure mark the four regions of the computational domain.

reactive budget of the temperature-based progress variable discussed above, occur mainly in burnt gases. Also, high volumetric dilatation rates occur

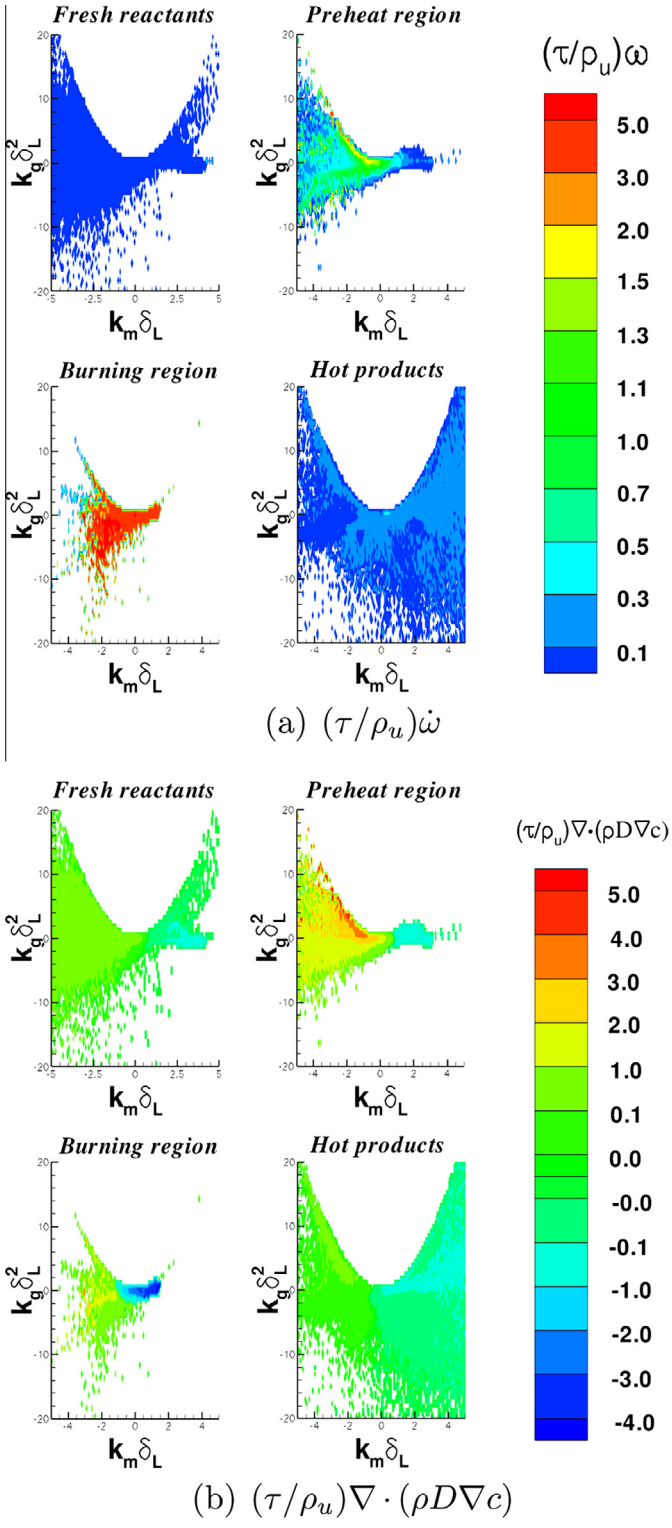

Fig. 7. Different terms of dilatation rate, $\nabla \cdot u$ (Eq. 13), conditional upon the mean and Gauss curvatures, k_m and k_g. (a) $(\tau/\rho_u)\dot{\omega}$, (b) $(\tau/\rho_u)\nabla\cdot(\rho D\nabla c)$. The terms have been normalized with the rms of $\nabla \cdot u$ using all the iso-scalar surfaces.

in the 'preheat' and 'burning' regions. Part of the 'fresh reactants' and 'hot products' regions can display small negative values of $\nabla \cdot u$. A plot of the volumetric dilatation rate obtained from Eq. (13), conditional to k_m and k_g, looks almost identical to that of Fig. 5.

Notwithstanding the discrepancies between the values of $\nabla \cdot u$ obtained from the current DNS and that calculated using Eq. (13), it is of interest to analyze the diffusive and reactive contributions to the latter. Figure 7 shows the chemical and molecular diffusion contributions to $\nabla \cdot u$, conditional upon k_m and k_g, for the four regions of the domain. The terms in this figure have been normalized with the rms value of $\nabla \cdot u$, using all the iso-scalar surfaces. While the chemical contribution is always positive, the molecular diffusion term is negative for nearly flat and slightly convex geometries in the burning region. The latter effect can be explained by the diffusive removal of the heat of reaction, generated near flat and slightly concave iso-surfaces; convex geometries tend to enhance the heat removal through the already mentioned defocussing of thermal conduction. The reactive contribution is small in the 'fresh reactants' and the 'hot products' regions, displays moderate values in the 'preheat region' and exhibits maxima in the 'burning' region. Cup-like and tile-like elliptic concave geometries yield the highest positive diffusive contributions to $\nabla \cdot u$, which, once more, can be explained by the focussing effect of the scalar molecular transport in concave structures.

Figure 8 shows the joint pdf of the normal and tangential strain rates, a_N and a_T, using all the iso-scalar surfaces for the complete domain. a_N and a_T have been normalized with the rms values of $\nabla \cdot u$. The straight line $a_T + a_N = 0$ separates the expansive zones (above the line) from the compressive ones (below the line). High probabilities of finding zones with $\nabla \cdot u = 0$ might be misleading; although expansive zones are certainly more probable, mixing together values for the 'fresh reactants', 'preheat', 'burning' and 'hot products' regions yield this statistically averaged picture.

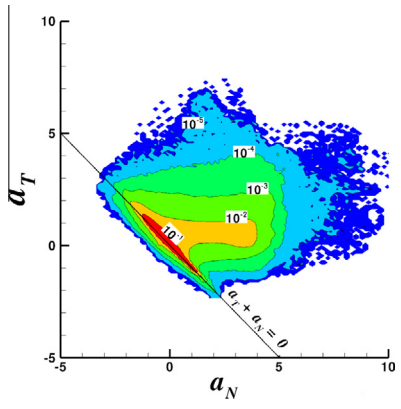

Fig. 8. Joint pdfs of the normal and tangential strain rates, a_N and a_T, using all the iso-scalar surfaces.

5. Conclusions

A three-dimensional DNS of a premixed methane–air turbulent jet flame has been performed in a piloted Bunsen burner configuration. The computational domain has been divided into four regions ('fresh reactants', 'preheat', 'burning' and 'hot products'), characterized by the value of the chemical reaction rate. The scalar field geometries, using the $k_m - k_g$ plane, have been identified. Nearly flat iso-surfaces are the most probable local scalar structures. Concave geometries towards 'fresh reactants' prevail in this jet flame configuration in front of the 'burning region', while convex structures are more probable in the 'hot products'. Some explanations for the latter feature, anticipated in the literature, in terms of small-scale eddies perpendicular to the iso-scalar surfaces must be carefully scrutinized in future research.

The volumetric dilatation rate, $\nabla \cdot u$, conditional upon k_m and k_g, has been obtained for the four regions. Maxima (minima) of $\nabla \cdot u$ correspond to concave and flat (convex) scalar structures.

An expression for $\nabla \cdot u$, with additive contributions from molecular diffusion and chemical generation of the reaction progress variable, has been obtained, formulating a one-dimensional flamelet assumption based on a progress variable defined from temperature, as in a low Mach number approximation, but solving for a fully compressible energy equation in the DNS. A comparison of this expression with values of the volumetric dilatation rate, computed from the present DNS results, shows that differences are relatively small or moderate for $c < 0.5$. However, for $c > 0.5$, relative differences are significantly high, casting doubts on the validity of progress variables defined without a perfect match with the form of the primitive equations solved, in the case of a highly wrinkled flame surface.

The diffusive and reactive contributions to the flamelet model for $\nabla \cdot u$, conditional upon k_m and k_g, have been disaggregated for the four flow regions. The chemical term is positive and yields high values for slightly concave iso-surfaces, cup-like and tile-like structures. Molecular diffusion contributes negatively to the volumetric dilatation rate in nearly flat and slightly convex geometries within the 'burning' region; defocussing of heat conduction by convex structures can explain this feature. Diffusive fluxes display high positive values for elliptic concave geometries in the 'preheat' region.

The joint pdf of the strain rates normal and tangential to scalar iso-surfaces for the overall computational domain combines different behaviors in the four regions. Mixing all four regions most likely masks the peculiarities of every one. Future work should address the investigation of a_N and a_T statistics, conditional upon k_m and k_g, and for the four reaction-level regions.

Acknowledgments

The Spanish Ministry of Science and Innovation initially sponsored this research through Project *ENE2008-01404/CON*. The late support of Project *CSD2010-00011-SCORE*, funded under the *CONSOLIDER-INGENIO* Program of the Spanish Ministry of Economy and Competitiveness, is also acknowledged. L. Cifuentes is grateful for the hospitality and scientific environment provided by the investigators of *CORIA – CNRS – INSA* of Rouen during his visit. This work was granted access to the HPC resources of IDRIS-CNRS under the allocation 2014-02b152 made by GENCI (Grand Equipement National de Calcul Intensif).

References

[1] D. Haworth, T. Poinsot, *J. Fluid Mech.* 244 (1992) 405–436.
[2] T. Echekki, J. Chen, *Combust. Flame* 106 (1996) 184–202.
[3] M. Tanahashi, M. Fujimura, T. Miyauchi, *Proc. Combust. Inst.* 28 (2000) 529–535.
[4] N. Chakraborty, R. Cant, *Phys. Fluids* 17 (2005) 105105/1–105105/20.
[5] R. Sankaran, E. Hawkes, J. Chen, T. Lu, C. Law, *Proc. Combust. Inst.* 31 (2007) 1291–1298.
[6] C. Dopazo, J. Martín, J. Hierro, *Phys. Rev. E* 76 (2007) 056316/1–056316/11.
[7] Y. Chen, N. Peters, G. Schneemann, N. Wruck, U. Renz, M. Mansour, *Combust. Flame* 107 (1996) 223–244.
[8] P. Domingo, L. Vervisch, D. Veynante, *Combust. Flame* 152 (2008) 415–432.
[9] M. Klein, A. Sadiki, J. Janicka, *J. Comput. Phys.* 186 (2003) 652–665.
[10] R. Borghi, in: C. Bruno, C. Casci (Eds.), Recent Advances in Aerospace Science, 1985, pp. 117–138.
[11] T. Poinsot, D. Veynante, *Theoretical and Numerical Combustion*, Edwards, Philadelphia, 2005.
[12] F. Drucos, T. Laporte, F. Souléres, V. Guinot, P. Moinat, B. Caruelle, *J. Comput. Phys.* 161 (2000) 114–139.
[13] S. Gottlieb, C. Shu, *Math. Comput.* 67 (1998) 73–85.
[14] G. Lodato, P. Domingo, L. Vervisch, *J. Comput. Phys.* 227 (2008) 5105–5143.
[15] O. Gicquel, N. Darabiha, D. Thévenin, *Proc. Comsbust. Inst.* 28 (2000) 1901–1908.
[16] G. Godel, P. Domingo, L. Vervisch, *Proc. Combust. Inst.* 32 (2008) 1555–1561.
[17] S. Candel, T. Poinsot, *Combust. Sci. Tech.* 70 (1990) 1–15.
[18] K. Bray, P. Libby, J. Moss, *Combust. Flame* 61 (1985) 87–102.
[19] K. Bray, A. Paul, G. Libby, G. Masuya, J. Moss, *Combust. Sci. Tech.* 70 (1990) 1–15.
[20] B. Renou, A. Boukhalfa, D. Puechberty, M. Trinite, *Proc. Combust. Inst.* 27 (1998) 841–847.

D

Strain rates normal to approaching iso-scalar surfaces in a turbulent premixed flame

Combustion and Flame xxx (2014) xxx–xxx

Contents lists available at ScienceDirect

Combustion and Flame

journal homepage: www.elsevier.com/locate/combustflame

Strain rates normal to approaching iso-scalar surfaces in a turbulent premixed flame

Cesar Dopazo [a], Luis Cifuentes [a,*], Jesus Martin [a], Carmen Jimenez [b]

[a] LIFTEC, CSIC-University of Zaragoza, Spain
[b] Department of Energy, CIEMAT, Spain

ARTICLE INFO

Article history:
Received 5 June 2014
Received in revised form 13 November 2014
Accepted 25 November 2014
Available online xxxx

Keywords:
Turbulent premixed flames
Tangential strain rate
Normal strain rate
Flame stretch
Iso-scalar surface kinematics
Propagation speed

ABSTRACT

A Direct Numerical Simulation (DNS) dataset of a turbulent premixed propagating flame with an Arrhenius one-step chemistry in an input–output configuration is examined. Combustion takes place in the 'corrugated flamelets' regime. Heat release causes the flow volumetric dilatation rate to be positive over most of the computational domain, with associated positive strain rates normal to iso-scalar surfaces and both positive or negative strain rates tangent to them. The normal propagation of convex and concave iso-surface infinitesimal area elements produces stretching and reduction, respectively, superposed to tangential flow strain rate effects. The normal propagation speed of iso-surfaces increases monotonically from 'fresh gases' to 'hot products', which draws two adjacent ones closer; this contribution, due to both chemistry and molecular diffusive transport, is much greater than that of the normal flow strain, and enhances mixing and chemical conversion. Many aspects of turbulent premixed flames traditionally explained in terms of tangential strain rates can likely be well understood using the normal ones.

1. Introduction

The importance of the tangential strain rate on the propagation speed and stability of laminar, premixed flames has been investigated for some time (Matalon [1], and references therein). Interpretations of turbulent mixing in terms of the iso-scalar surface evolution have also been proposed [2,3].

Transport equations for flame area and surface density function have been derived with an explicit dependence on tangential stretching [4,5].

Flows with important density changes, due, for example, to chemical heat generation, will presumably undergo large volumetric dilatation rates. Intuitively, this situation may lead to mostly positive values for both tangential and normal strain rates [6]; the former will imply iso-scalar surface stretching, whereas the latter will, in principle, yield a reduction of the scalar-gradient modulus, as iso-surfaces separate. This fact seems at first glance to hamper scalar molecular fluxes and dissipation of composition inhomogeneities. Chakraborty [7] has documented, via DNS, the occurrence of positive normal strain rates in a 'corrugated flamelets' regime. and negative ones in a 'thin reaction zone regime'; while in the first case the scalar gradient aligns preferentially with the strain rate tensor eigenvector corresponding to its most extensive eigenvalue, in the second instance the scalar gradient is mainly parallel to the most compressive eigenvector. This latter feature coincides with that described for turbulent scalar mixing in constant density flows [8,9]. Chakraborty et al. [10] have scrutinized via DNS the Lewis number effect on the scalar gradient alignment in turbulent premixed flames; they have documented mainly positive normal strain rates and concluded that 'the most extensive principal strain rate' is preferentially perpendicular to iso-scalar surfaces and 'destroys the scalar gradient' with a 'magnitude' that 'increases with decreasing Lewis number for given turbulent Reynolds and Damköhler numbers'.

This works aims at explaining why scalar-gradients can grow and mixing is not hampered under mostly positive flow strain rates normal to iso-surfaces. DNS results for a propagating turbulent premixed flame with one-step Arrhenius chemistry in an input–output configuration are examined. Normal strain rates caused by changes in iso-scalar surface propagation speed in the normal direction, due to both molecular transport and chemistry, are negative and lead to 'effective' strain rates that bring iso-surfaces closer together and enhance scalar-gradients.

Section 2 describes the kinematics of non-material iso-scalar surfaces and summarizes the assumptions underlying the direct numerical simulations. The practical execution of the latter is presented briefly in Section 3. Numerical results are discussed in Section 4 and some conclusions are drawn in Section 5.

* Corresponding author.
E-mail address: lcifuentes@unizar.es (L. Cifuentes).

http://dx.doi.org/10.1016/j.combustflame.2014.11.034
0010-2180/

2. Formulation

2.1. Kinematics of iso-scalar surfaces

Scalar mixing can be viewed as a combination of iso-scalar surface stretching and scalar-gradient growth induced by the flow field. Figure 1 depicts an infinitesimal surface, S, on the non-material iso-surface $Y(\mathbf{x},t)=\Gamma$, with a normal unit vector $\mathbf{n}(\mathbf{x},t)=\nabla Y/|\nabla Y|$.

$Y(\mathbf{x},t)$ is, for example, the normalized reactant mas fraction ($Y=1$ in the 'fresh gases' and $Y=0$ in the 'hot products').

An infinitesimal vector, $\mathbf{r}(\mathbf{x},t)$, joins a point $\mathbf{x}$ at the center of S to a point $\mathbf{x}+\mathbf{r}$ on a neighboring iso-scalar surface $Y(\mathbf{x},t)=\Gamma+d\Gamma$. The two extremes of $\mathbf{r}$ move with velocities $\mathbf{v}^Y(\mathbf{x},t)$ and $\mathbf{v}^Y(\mathbf{x}+\mathbf{r},t)$, where the velocity of a point of the non-material iso-scalar surface is decomposed as

$$\mathbf{v}^Y(\mathbf{x},t)=\mathbf{v}(\mathbf{x},t)+V^Y(\mathbf{x},t)\mathbf{n}, \tag{1}$$

$\mathbf{v}$ is the fluid velocity and V^Y is the normal displacement speed of $Y(\mathbf{x},t)=\Gamma$ relative to the local fluid. The time rate of change of $\mathbf{r}$ is

$$\frac{d\mathbf{r}}{dt}=(\mathbf{r}\cdot\nabla)\mathbf{v}^Y. \tag{2}$$

The right side of (2) can be expanded as

$$\frac{d\mathbf{r}}{dt}=\mathbf{r}\cdot\mathbf{s}+\mathbf{r}\cdot\mathbf{w}+(\mathbf{r}\cdot\nabla)V^Y\mathbf{n}+V^Y(\mathbf{r}\cdot\nabla)\mathbf{n}, \tag{3}$$

where $\mathbf{s}$ and $\mathbf{w}$ are the strain and rotation rate tensors, respectively, and $\nabla\mathbf{n}$ is the curvature tensor. $\mathbf{r}\cdot\mathbf{w}$ can be recast as $1/2(\boldsymbol{\omega}\times\mathbf{r})$, in terms of $\boldsymbol{\omega}=\nabla\times\mathbf{v}$, the vorticity vector.

If $\mathbf{r}=\Delta x_N\mathbf{n}$, one can readily obtain from (3)

$$\frac{1}{\Delta x_N}\frac{d\Delta x_N}{dt}=a_N+\frac{\partial V^Y}{\partial x_N}, \tag{4}$$

$$\frac{d\mathbf{n}}{dt}=(\boldsymbol{\delta}-\mathbf{nn})\cdot\mathbf{s}\cdot\mathbf{n}+\frac{1}{2}\boldsymbol{\omega}\times\mathbf{n}+V^Y(\mathbf{n}\cdot\nabla)\mathbf{n}, \tag{5}$$

where

$$a_N=\mathbf{n}\cdot\mathbf{s}\cdot\mathbf{n}, \tag{6}$$

is the flow strain rate normal to $Y(\mathbf{x},t)=\Gamma$. $\partial V^Y/\partial x_N$ is the derivative of the propagation velocity in the normal direction to the iso-surface. $\boldsymbol{\delta}$ is the identity Kronecker delta tensor. While the vorticity has no influence on the variation of the modulus of $\mathbf{r}$, Δx_N, it obviously rotates its direction, $\mathbf{n}$.

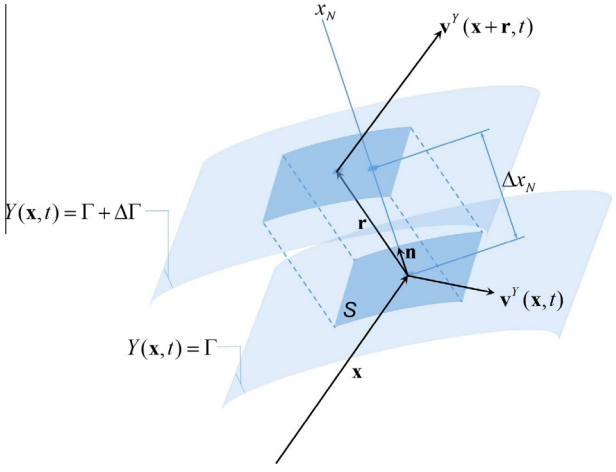

Fig. 1. Schematic representation of two elements of flame surface.

The infinitesimal volume $V=S\Delta x_N$, between the two iso-scalar surfaces, changes in time according to

$$\frac{1}{V}\frac{dV}{dt}=tr(\mathbf{s})+\frac{\partial V^Y}{\partial x_N}+2k_mV^Y, \tag{7}$$

where $tr(\mathbf{s})=\nabla\cdot\mathbf{v}$, the trace of the strain rate tensor, yields the flow volumetric dilatation rate, and k_m is the local mean curvature, $k_m=(\nabla\cdot\mathbf{n})/2$, of the iso-scalar surface. $k_m>0$ for iso-surfaces convex towards 'fresh gases' and $k_m<0$ for concave ones. The time rate of change of the infinitesimal surface S can thus be obtained from

$$\frac{1}{S}\frac{dS}{dt}=\frac{1}{V}\frac{dV}{dt}-\frac{1}{\Delta x_N}\frac{d\Delta x_N}{dt}, \tag{8}$$

and using (4) and (7)

$$\frac{1}{S}\frac{dS}{dt}=a_T+2k_mV^Y, \tag{9}$$

with

$$a_T=(\boldsymbol{\delta}-\mathbf{nn}):\mathbf{s}, \tag{10}$$

the flow strain rate tangential to $Y(\mathbf{x},t)=\Gamma$. This expression has been derived for flame stretch by several authors (Poinsot and Veynante [11], and references therein). a_N and a_T satisfy $a_N+a_T=\nabla\cdot\mathbf{v}$.

The mass flow rate per unit volume of $Y(\mathbf{x},t)$, which determines the local mixing rate, is

$$\frac{\mathbf{f}^Y\cdot S\mathbf{n}}{V}\sim-\rho D\frac{S}{V}\frac{\Delta\Gamma}{\Delta x_N}, \tag{11}$$

where $\mathbf{f}^Y$ is the Fickian molecular flux, $\sum(\Gamma;x,t)=S/V=1/\Delta x_N$ is the surface density function [5], and $|\nabla Y|=\partial Y/\partial x_N=\Delta\Gamma/\Delta x_N$.

For the two given iso-scalar surfaces, the local mixing rate increases with time if Δx_N diminishes. From (4) one concludes that $d\Delta x_N>0$ if $(a_N+\partial V^Y/\partial x_N)>0$, and $d\Delta x_N<0$ if $(a_N+\partial V^Y/\partial x_N)<0$.

For combusting flows with significant heat release $\nabla\cdot\mathbf{v}>0$, and the probability of finding $a_N>0$ in most of the flow domain might be large. Therefore, for the scalar-gradient and the mass flow rate per unit volume to increase, $\partial V^Y/\partial x_N$ should be negative and its absolute value greater than a_N.

Surface stretching ($dS>0$) occurs if $(a_T+2k_mV^Y)>0$, but seems to bear no direct influence on the local mixing rate.

On the other hand, the evolution of an iso-scalar surface obeys the equation

$$\frac{\partial Y}{\partial t}+(\mathbf{v}^Y\cdot\nabla)Y=0, \tag{12}$$

which can be rephrased as

$$\frac{\partial Y}{\partial t}+(\mathbf{v}\cdot\nabla)Y=-V^Y|\nabla Y|. \tag{13}$$

An equation for the evolution of $|\nabla Y|$ can be readily obtained from (12),

$$\frac{\partial|\nabla Y|}{\partial t}+(\mathbf{v}^Y\cdot\nabla)|\nabla Y|=-\left(a_N+\frac{\partial V^Y}{\partial x_N}\right)|\nabla Y|, \tag{14}$$

The scalar-gradient associated to a point on a non-material iso-surface moving with velocity $\mathbf{v}^Y$ decreases or increases depending, once again, on positive or negative values, respectively, of the 'effective' normal strain rate, $(a_N+\partial V^Y/\partial x_N)$.

2.2. Non-material surface propagation velocity

The conservation equation for a reacting species mass fraction can be written as

$$\frac{DY}{Dt}=\frac{1}{\rho}\nabla\cdot(\rho D\nabla Y)+\frac{\dot{\omega}}{\rho}, \tag{15}$$

where D represents the Fickian molecular diffusivity coefficient for Y and $\dot{\omega}$ stands for its net production rate by chemical reaction.

The molecular diffusion contribution can be expressed as

$$\frac{1}{\rho}\nabla\cdot(\rho D\nabla Y)=D\frac{\partial Y}{\partial x_N}\left\{\frac{\partial}{\partial x_N}\left[\ln\left(\rho D\frac{\partial Y}{\partial x_N}\right)\right]+2k_m\right\}, \tag{16}$$

in terms of derivatives normal to the iso-surface and its mean curvature.

Equating the right sides of (13) and (15), and using (16), an expression for V^Y is easily obtained

$$V^Y=-D\frac{\partial}{\partial x_N}\left[\ln\left(\rho D\frac{\partial Y}{\partial x_N}\right)\right]-2Dk_m-\frac{(\dot{\omega}/\rho)}{(\partial Y/\partial x_N)}. \tag{17}$$

The contributions from molecular diffusion normal and tangential (due to curvature) to an iso-surface and from chemical reaction correspond to the three terms on the right side of (17). Its normal derivative is

$$\frac{\partial V^Y}{\partial x_N}=-\frac{\partial}{\partial x_N}\left\{D\frac{\partial}{\partial x_N}\left[\ln\left(\rho D\frac{\partial Y}{\partial x_N}\right)\right]\right\}-2\frac{\partial(Dk_m)}{\partial x_N}-\frac{\partial}{\partial x_N}\left[\frac{(\dot{\omega}/\rho)}{(\partial Y/\partial x_N)}\right]. \tag{18}$$

3. Numerical simulation

A dataset from a Direct Numerical Simulation of a propagating premixed turbulent flame with an inflow-outflow configuration at moderate turbulent Reynolds number is used to examine and compare the different terms in the propagation speed of iso-scalar surfaces defined above.

The conservation equations for mass, momentum, energy and species mass fractions are integrated with the fully parallel compressible solver NTMIX3D [12,13], using a 6th order compact finite-differences scheme for space discretization and a third-order Runge–Kutta explicit method for time advancement. The full set of governing equations is made dimensionless using reference characteristic variables and molecular transport coefficients in the fresh gases. Dimensionless density, $\rho^+=\rho/\rho_{ref}$, ith component of the velocity vector, $u_i^+=u_i/a_{ref}$, pressure, $p^+=p/p_{ref}$, temperature, $T^+=T/T_{ref}$, time, $t^+=t/t_{ref}$, and ith component of the position vector, $x_i^+=x_i/L_{ref}$ are used. The superscript $+$ denotes a dimensionless variable or property, and a_{ref} and L_{ref}, are the reference speed of sound and length, respectively [12,13]. To simplify the notation, dimensionless variables will be written hereafter without the superscript $+$.

The formulation, as presented, for example, in (Poinsot and Veynante [11]), assumes a lean fuel mixture in which the deficient reactant is the fuel and a single step Arrhenius expression as a model for combustion chemical kinetics. The rate of consumption of the reduced fuel mass fraction $Y=Y_F/Y_F^0$ is then written as

$$\left(\frac{dY}{dt}\right)_{ch}=-\dot{\omega}=-\rho YB_0 exp\left(\frac{-T_a}{T}\right), \tag{19}$$

where ρ is the density of the mixture, B_0 is the pre-exponential factor and T_a is the activation temperature. The heat release rate is related to omega by the heat release factor $Q=C_p(T_b-T_u)/Y_F^0$, so that

$$\left(\frac{dT}{dt}\right)_{ch}=Q\dot{\omega}. \tag{20}$$

The chemical reaction rate is then completely determined by the parameters $\alpha=(T_b-T_u)/T_b, \beta=\alpha T_a/T_b$ and B_0. The sub-index u and b denote a variable value in the unburned and burnt gases, respectively.

The fluid density follows a perfect gas equation of state, with constant molecular mass and constant specific heat ratio γ. The transport coefficients are considered temperature dependent, via a model for the molecular viscosity

$$\mu=\mu_u\left(\frac{T}{T_u}\right)^b, \tag{21}$$

and constant Schmidt and Prandtl numbers so that the mass diffusivity D and the thermal diffusivity D_{th} are given by

$$D=\frac{\mu}{\rho Sc}, \tag{22}$$

$$D_{th}=\frac{\lambda}{\rho C_p}=\frac{\mu}{\rho Pr}. \tag{23}$$

Initial conditions correspond to a planar premixed flame propagating in the negative x direction with a laminar flame speed S_L and width $\delta_L=D_{th}/S_L$, so that fresh gases (corresponding to $Y=1$) are located to the left of the x axis and burnt products ($Y=0$) to the right. A constant-density isotropic turbulent velocity field is initially superposed to the velocity in the fresh gases side and evolves without forcing in the compressible solver NTMIX3D. In the subsequent propagation towards fresh gases the flame encounters a decaying turbulent field, which wrinkles it as it progresses. The initial constant-density isotropic turbulence is generated with an independent pseudo-spectral numerical code [14,15], starting from a given spectrum and using a stochastic forcing scheme, to yield a statistically stationary field. In the zero correlation-time forcing scheme [16,17], all wave numbers with a modulus less than $2\sqrt{2}$, except the zero mode which makes no contribution, receive a stochastic contribution at every time step, while their phase is adjusted to enforce incompressibility.

The computational domain, of size $Lx\times Ly\times Lz=1.5L\times L\times L$ with $L/\delta_L=119.45$ is discretized in a $768\times512\times512$ uniform grid with periodic boundary conditions in the cross-flow directions, y and z, and non-reflecting inlet–outlet boundary conditions in the x direction, imposed using the Navier–Stokes Characteristic Boundary Condition (NSCBC) method [18].

In this study the gas parameters introduced above are chosen as $b=0.6, Pr=0.75, Sc=0.75, \gamma=1.4$, and the chemical rate parameters are $\alpha=0.8$, and $\beta=6.0$. The rms velocity fluctuations in the 'fresh reactants' decay from $u'_0=0.016$ in $t=0$ to $u'=0.010$ in t_{final}, in which our data are presented. To estimate the integral length scale, l, in the 'fresh reactants', the transverse autocorrelation coefficients in cross-stream planes, $y-z$, are obtained. The integral scale increases from $l_0=1.058$ in $t=0$ to $l=1.200$ in t_{final}. The turbulent Reynolds number, $\mathrm{Re}_t=u'l/\nu_u$, decreases from $Re_{t_0}=86$ in $t=0$ to $Re_t=61$ in t_{final}. The initial eddy turnover time is $\tau_0=l_0/u'_0=66.13$. In this study, the initially planar laminar flame is allowed to interact with the turbulence field up to a time $t_{final}=90$, 1.36 times greater than the initial eddy turnover time.

The Kolmogorov length micro-scales at the beginning and the end of the simulation, are $\eta_0=0.0370$ and $\eta=0.0550$, respectively, which guarantee an adequate spatial resolution with the current domain and mesh sizes along the simulation time. The turbulent Damköhler number, defined as $\mathrm{Da}=(l/\delta_L)/(u'/S_L)$, is 11.41 at t_{final}. Therefore, combustion takes place in the 'corrugated flamelets' regime [11,19]. Numerical values of the aero-thermo-chemical variables and dimensionless parameters for this simulation are presented in Table 1.

Please cite this article in press as: C. Dopazo et al., Combust. Flame (2014), http://dx.doi.org/10.1016/j.combustflame.2014.11.034

Table 1
Values of dimensionless parameters and physical variables at the end of the simulation.

Parameter	Value
Prandtl number, Pr	0.75
Schmidt number, Sc	0.75
Lewis number, Le	1.0
$\alpha = (T_b - T_u)/T_b$	0.8
Zel'dovich number, β	6.0
rms of velocity fluctuations, u'	0.01
Integral length scale, l	1.20
Turbulent kinetic energy dissipation rate, ε	8.333e−7
Kolmogorov length micro-scale, η	0.055
Kolmogorov time micro-scale, τ_η	15.36
Non stretched laminar flame velocity, S_L	0.005
Laminar flame thickness, δ_L	0.0526
Chemical time scale, τ_{ch}	10.40
Velocity ratio, u'/S_L	2.0
Length ratio, l/δ_L	22.81
Turbulent Reynolds number, Re_t	61
Damköhler number, $Da = (l/\delta_L)/(u'/S_L)$	11.41
Karlovitz number, $Ka = \tau_{ch}/\tau_\eta$	0.68

The local interaction of small-scale flow structures with scalar geometries will probably vary in different flow regions. Thus, results are separately obtained for four regions, defined in terms of their reaction rate $\dot{\omega}_Y = \dot{\omega}/\rho$, and mass fraction Y, values. The zones of the computational domain where $|\dot{\omega}_Y| < 0.001|\dot{\omega}_{Y_{max}}| = 0.0004$ (or, equivalently, $0.700 < Y < 0.999$) is termed the 'fresh reactants'. The 'preheating' region extends over $0.253 < Y < 0.700$ or $0.001|\dot{\omega}_{Y_{max}}| < |\dot{\omega}_Y| < 0.7|\dot{\omega}_{Y_{max}}| = 0.336$. The 'burning' region is characterized by $|\dot{\omega}_Y| > 0.7|\dot{\omega}_{Y_{max}}|$ or $0.053 < Y < 0.253$. Finally, $0.001 < Y < 0.053$, which corresponds to $|\dot{\omega}_Y| < 0.7|\dot{\omega}_{Y_{max}}|$, defines the 'hot products'. Figure 2 demarcates these four reaction-conditioned regions.

4. Numerical results

Figure 3 shows the volumetric dilatation rate, $\nabla \cdot \mathbf{v}$, and the tangential, a_T, and normal, a_N, strain rates as functions of the reactant mass fraction, Y. Vertical error bars display root-mean-square (rms) values of these variables, which depict large fluctuations. Intense heat release causes positive values of $\nabla \cdot \mathbf{v}$ all over the computational domain. a_T is constant for most values of Y, except in the neighborhood of $Y = 0$ and $Y = 1$. The evolution of a_N resembles that of $\nabla \cdot \mathbf{v}$, with positive values everywhere, in agreement with previous results [7], except near $Y = 0$ and $Y = 1$, where $\nabla \cdot \mathbf{v} \approx 0$ and $a_N \approx -a_T$.

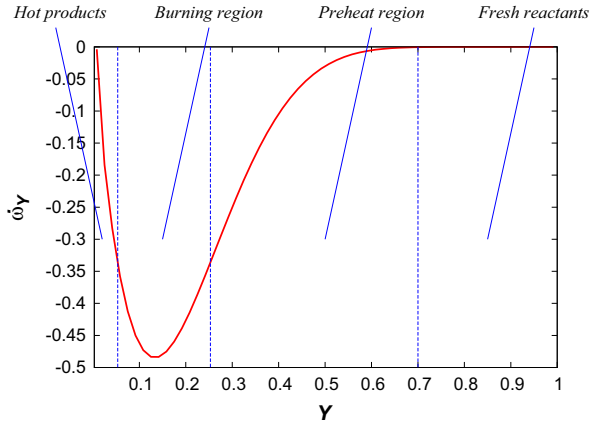

Fig. 2. Reaction rate, $\dot{\omega}_Y = \dot{\omega}/\rho$, as a function of the reactant mass fraction. Dotted lines mark the limits of the four regions of the computational domain.

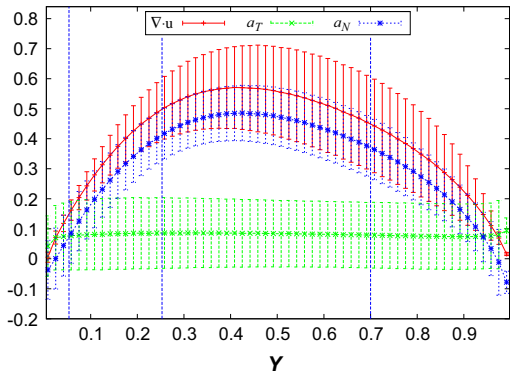

Fig. 3. Local fluid volumetric dilatation rate, tangential strain rate and normal strain rate as a function of the reactant mass fraction. The variables have been normalized with the Kolmogorov time scale, τ_η. Vertical bars indicate the rms values of the variables. Dotted lines mark the limits of the four regions of the computational domain.

The time rate of change of an infinitesimal area on an iso-scalar surface and the infinitesimal distance between two iso-surfaces depend on their propagation speed relative to the fluid, according to Eqs. (4) and (9). Figure 4 shows V^Y and $\partial V^Y/\partial x_N$ as functions of Y. Expanding expressions for V^Y and $\partial V^Y/\partial x_N$, the various contributions to both can be estimated, namely,

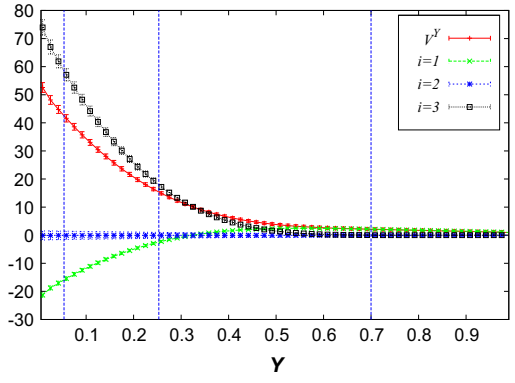

(a)

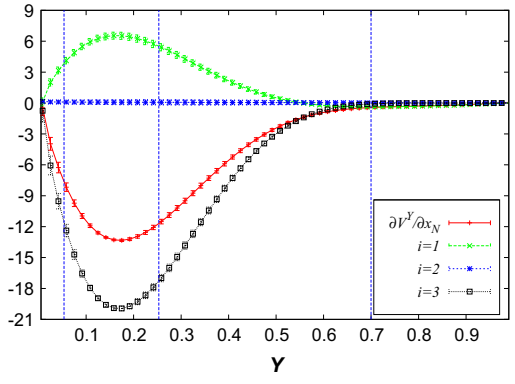

(b)

Fig. 4. Variables as a function of the reactant mass fraction. (a) Normal propagation velocity, V^Y, and its contributions (Eqs. (24)–(26)), and (b) derivative of V^Y in the normal direction $x_N, \partial V^Y/\partial x_N$, and its contributions (Eqs. (27)–(29)). Vertical bars indicate the rms values of the variables. Dotted lines mark the limits of the four regions of the computational domain. V^Y and its contributions have been normalized with (D_0/δ_L), where D_0 is the value of the molecular mass diffusivity in the fresh gases, and δ_L is the laminar flame thickness. $\partial V^Y/\partial x_N$ and its contributions have been normalized with τ_η.

$$V_1^Y = -D\frac{\partial}{\partial x_N}\left[\ln\left(\rho D\frac{\partial Y}{\partial x_N}\right)\right], \tag{24}$$

$$V_2^Y = -2Dk_m, \tag{25}$$

$$V_3^Y = -\frac{\dot{\omega}_Y}{(\partial Y/\partial x_N)}, \tag{26}$$

$$\left(\frac{\partial V^Y}{\partial x_N}\right)_1 = -\frac{\partial}{\partial x_N}\left\{D\frac{\partial}{\partial x_N}\left[\ln\left(\rho D\frac{\partial Y}{\partial x_N}\right)\right]\right\}, \tag{27}$$

$$\left(\frac{\partial V^Y}{\partial x_N}\right)_2 = -2\frac{\partial(Dk_m)}{\partial x_N}, \tag{28}$$

$$\left(\frac{\partial V^Y}{\partial x_N}\right)_3 = -\frac{\partial}{\partial x_N}\left[\frac{\dot{\omega}_Y}{(\partial Y/\partial x_N)}\right]. \tag{29}$$

V^Y is positive whereas $\partial V^Y/\partial x_N$ is negative for all values of Y. Mean curvature effects are negligible for both V^Y and $\partial V^Y/\partial x_N$. Chemistry is the leading positive contributor to V^Y, while the normal diffusion term yields a negative V_1^Y for $Y < 0.3$ and a small positive contribution for $Y > 0.3$. The chemical term, $(\partial V^Y/\partial x_N)_3$ is the main driver of $\partial V^Y/\partial x_N$ while the normal diffusion term, $(\partial V^Y/\partial x_N)_1$, has a smaller contribution. Vertical error bars included in the figure render very small variations of both propagation velocity and its normal derivative, with insignificant variable fluctuations. Iso-scalar surfaces increase their normal velocity of propagation, relative to the fluid, from 'fresh gases' to 'hot products'. Consequently, two iso-surfaces, $Y(\mathbf{x},t) = \Gamma$ and $Y(\mathbf{x},t) = \Gamma + \Delta\Gamma$, for example, in the 'burning' region will move toward the 'preheating' zone and tend to narrow the gap, Δx_N, among themselves.

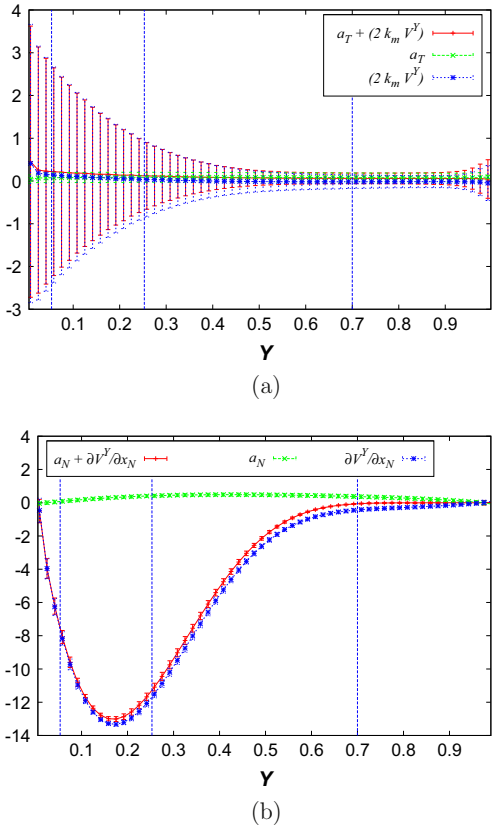

Fig. 5. Variables as a function of the reactant mass fraction. (a) 'Effective' tangential strain rate and its contributions, a_T and $2k_mV^Y$ and (b) 'effective' normal strain rate and its contributions, a_N and $\partial V^Y/\partial x_N$. Vertical bars indicate the rms values of the variables. Dotted lines mark the limits of the four regions of the computational domain. The variables have been normalized with τ_η.

$\partial V^Y/\partial x_N$ can be viewed as a 'normal strain rate', which enhances the scalar-gradient, $\Delta\Gamma/\Delta x_N$, through the reduction of Δx_N.

Figure 5 depicts the flow strain rates, a_T and a_N, the additional contributions due to V^Y and $\partial V^Y/\partial x_N$, respectively, and the 'effective' tangential, $(a_T + 2k_mV^Y)$, and normal, $(a_N + \partial V^Y/\partial x_N)$, strain rates for nonmaterial iso-surfaces. Vertical rms bars indicate very large fluctuations of $2k_mV^Y$ compared to its mean value, whereas variations associated to a_T, a_N and $\partial V^Y/\partial x_N$ are rather small. This is likely due to significant iso-surface corrugation. The curvature-propagation contribution, implies surface generation by the displacement of convex iso-scalar surfaces and yields surface reduction for concave iso-scalar surface propagation. The contributions of a_T and $2k_mV^Y$ to the 'effective tangential strain rate' are apparently comparable, except in the 'hot products'. $\partial V^Y/\partial x_N$ is large, compared to a_N, and negative for all values of Y, which makes the 'effective' normal strain rate, $(a_N + \partial V^Y/\partial x_N)$, negative everywhere. While $a_N > 0$ tends to separate two neighboring iso-scalar surfaces and diminishes $|\nabla Y|, \partial V^Y/\partial x_N < 0$ will draw them closer to each other and enhance scalar-gradients. Eqs. (4) and (9) provide strong mathematical bases to designate $(a_T + 2k_mV^Y)$ and $(a_N + \partial V^Y/\partial x_N)$ 'effective' tangential and normal strain rates, respectively. They stretch non-material infinitesimal surfaces located on $Y(\mathbf{x},t) = \Gamma$ and dilate infinitesimal normal distances between $Y = \Gamma$ and $Y = \Gamma + \Delta\Gamma$.

Figure 6 plots the joint PDF of a_N and a_T, in the four regions defined for different levels of the reaction rate. The most probable values locate near $a_N + a_T = 0$, both in the 'fresh reactants' and in the 'hot products' where $\nabla\cdot\mathbf{v} \approx 0$; in the 'preheat' and 'burning' regions the maximum probability corresponds to $a_N > 0$ and a_T takes both positive and negative values, consistent with $\nabla\cdot\mathbf{v} > 0$.

Figure 7 depicts the joint PDF of the 'effective' normal and tangential strain rates, and $\dot{\omega}_Y$ and $(1/\rho)\nabla\cdot(\rho D\nabla Y)$ conditioned upon $(a_N + \partial V^Y/\partial x_N)$ and $(a_T + 2k_mV^Y)$ in the four 'reacting' regions. In the 'fresh reactants' $(a_N + \partial V^Y/\partial x_N)$ is mostly positive and $(a_T + 2k_mV^Y)$ is mainly negative with most probable values near

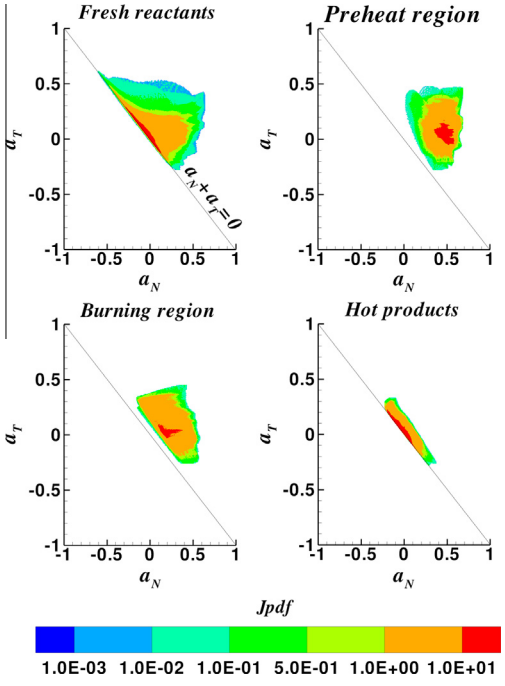

Fig. 6. Joint pdf of the normal and tangential strain rates, a_N and a_T. Joint pdf magnitudes decrease from the center to the circumference.

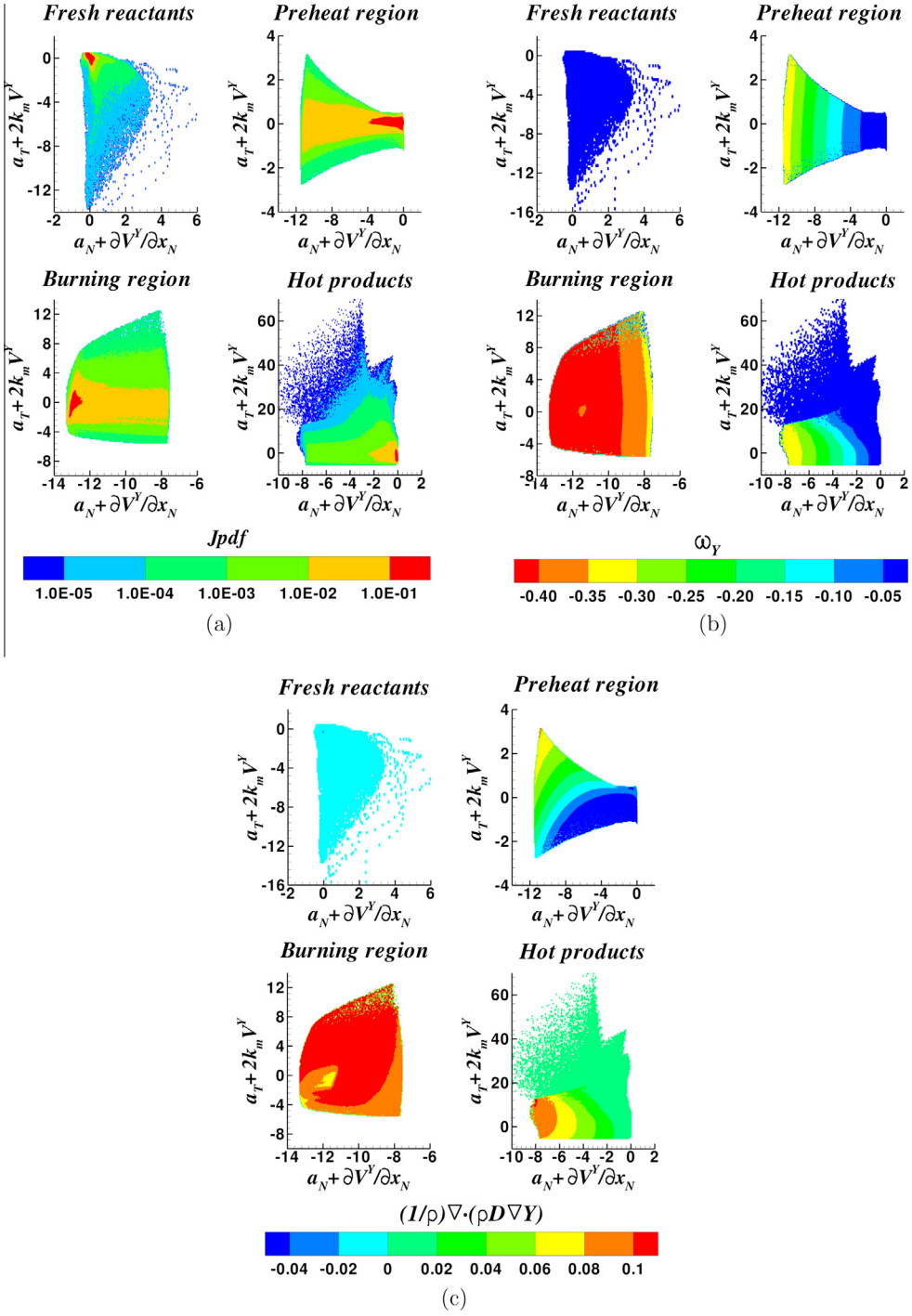

Fig. 7. (a) Joint pdf of the line and surface stretches, $a_N + \partial V^Y/\partial x_N$ and $a_T + 2k_m V^Y$. (b) Reaction rate, $\dot{\omega}_Y$, and (c) molecular diffusion rate, $(1/\rho)\nabla\cdot(\rho D\nabla Y)$, conditional upon the line and surface stretches.

the origin; this implies separation of iso-surfaces with their area elements shrinking. In the 'preheat' and 'burning' regions and in the 'hot products' the 'effective' normal strain rate is always negative; $(a_T + 2k_m V^Y)$ displays both positive and negative values in the 'preheating' zone showing some degree of symmetry about the zero value, while positive quantities become more probable in the 'burning' region; most probable normal and tangential 'effective' strain rates locate also near the origin in the 'hot' products. The reaction rate in the 'preheat' and 'burning' regions depends solely on the 'effective' normal strain rate; this is also true to some extent in the 'hot' products for significant values of the chemical conversion. The molecular diffusion rate depends on both strain rates as it is apparent from Eq. (16); significant values of molecular transport occur always for large negative 'effective' normal strain rates and both positive and negative 'effective' tangential strain rates. Any infinitesimal non-material volume element appended to an iso-scalar surface will undergo contraction in the direction normal to the iso-surface and either positive or negative area tangential stretching. The thermal expansion and scalar conversion, resulting from the chemical reaction rate, given by Eq. (19) and Fickian molecular diffusion, Eq. (16), yield the previously described behavior.

Please cite this article in press as: C. Dopazo et al., Combust. Flame (2014), http://dx.doi.org/10.1016/j.combustflame.2014.11.034

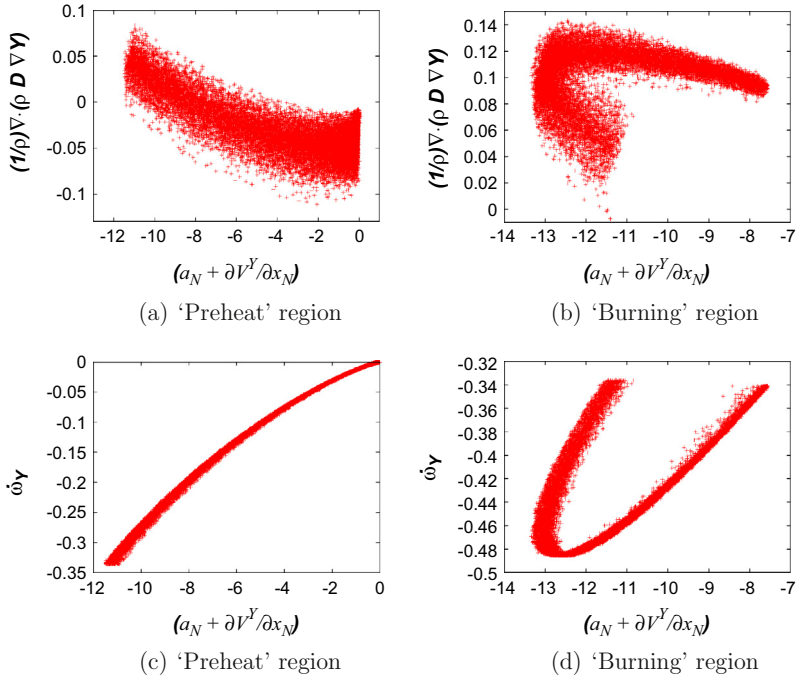

Fig. 8. (a), (b) Molecular diffusion and (c), (d) chemical reaction rates as functions of the 'effective' normal strain rate in the 'preheat' and 'burning' regions.

Figure 8 presents scatter plots of the molecular diffusion and the chemical reaction terms as functions of the 'effective' normal strain rate in both the 'preheat' and the 'burning' regions. Correlations are apparent between diffusion or reaction and the 'effective' normal strain rates in the preheat region; the additional functional dependence of the diffusion term on the scalar mass fraction should be such that its sign changes at around $(a_N + \partial V^Y/\partial x_N) = -7.5$ in the 'preheat' region; the larger the absolute value of the 'effective' normal strain rate the higher the reaction rate in the preheat zone. On the other hand, the two branches observed in the 'burning' region obviously correspond to values to the left and the right sides of the minimum of $(a_N + \partial V^Y/\partial x_N)$ as a function of Y (Fig. 5); the upper branch of the molecular diffusion belongs to values of strain rates to the left of that minimum, whereas the lower branch pertains to those to its right; the upper (lower) branch of the chemical conversion correlates with effective normal strain rates to the right (left) side of its minimum. The lower (upper) branch of the molecular diffusion (chemical source) term in the burning region could be easily assigned to the preheat zone by redefining the limit between the two.

5. Concluding remarks

A simple kinematic derivation of the mechanisms that cause two adjacent non-material iso-scalar surfaces to move apart or closer together, and infinitesimal areas to stretch or contract in a domain containing a propagating turbulent premixed flame in the 'corrugated flamelets' regime has been presented. Chemical heat generation yield positive flow volumetric dilatation rates everywhere in the computational domain, which imply mostly positive flow strain rates normal to iso-scalar surfaces; this tends to separate iso-surfaces and diminish scalar-gradients. On the other hand, flow strain rates in a plane tangential to the iso-scalar surfaces can be either positive, stretching infinitesimal areas, or negative, leading to surface reduction. Therefore, flow strain rates do not explain the intense molecular diffusive transports occurring in turbulent premixed flames.

The normal propagation velocity of iso-surfaces increases an infinitesimal convex area, producing a flame stretch-like effect, and reduces a concave one, implying a surface contraction. This curvature-propagation effect is comparable to the flow tangential strain rate in most regions of the computational domain and superposes to it.

The normal propagation speed increases monotonically from 'fresh gases' to 'hot products', and causes two iso-scalar surfaces to get closer together, and, therefore, increase scalar-gradients. This variation in propagation speed, due to both chemistry and molecular diffusive transport, acts like a negative normal strain rate. Its values are much greater than the flow normal strain rate over most part of the computational domain.

The 'effective' tangential and normal strain rates, thus, enhance molecular diffusive transport and chemical conversion.

The importance of the normal strain rates in turbulent premixed flame phenomena has been recognized in the existing literature by a limited number of authors. Some phenomena can probably be better explained in term of the normal strain rate rather than the tangential one.

The relative importance of thermal and mass diffusivities as measured by the Lewis number will be studied in future work. The influence of the Karlovitz number should also be explored. Similar features to those presented in this work are currently under investigation in turbulent jet premixed flames. Turbulent mixing in the absence of chemical phenomena for constant density flows and for variable density, due to external heat addition, is also under scrutiny.

Acknowledgments

This research was sponsored through Project CS D2010-00011-SCORE, funded under the CONSOLIDER-INGENIO Program of the Spanish Ministry of Economy and Competitiveness. DNS datasets were generated with the support of the Project ENE2008-01404/CON funded by the former Spanish Ministry of Science and Innovation.

References

[1] M. Matalon, Proc. Combust. Inst. 32 (2009) 57–82.

[2] C. Dopazo, P. Calvo, F. Petriz, Phys. Fluids 11 (1999) 2952–2956.
[3] S. Kim, R. Bilger, J. Fluid Mech. 590 (2007) 381–409.
[4] S. Candel, T. Poinsot, Combust. Sci. Tech. 70 (1990) 1–15.
[5] L. Vervisch, E. Bidaux, K. Bray, W. Kollmann, Phys. Fluids 7–10 (1995) 2496–2503.
[6] L. Cifuentes, C. Dopazo, J. Martin, P. Domingo, L. Vervisch, Proc. Combust. Inst. 35 (2014).
[7] N. Chakraborty, Phys. Fluids 19 (2007) 105109/1–045103/20.
[8] R. Kerr, J. Fluid Mech. 153 (1985) 31–58.
[9] W. Ashurst, A. Kerstein, R. Kerr, C. Gibson, Phys. Fluids 30 (1987) 2343–2353.
[10] N. Chakraborty, M. Klein, N. Swaminathan, Proc. Combust. Inst. 32 (2009) 1409–1417.
[11] T. Poinsot, D. Veynante, Theoretical and Numerical Combustion, Edwards, Philadelphia, 2001.
[12] T. Poinsot, D. Haworth, G. Bruneaux, Combust. Flame 95 (1993) 118–132.
[13] B. Cuenot, T. Poinsot, Combust. Flame 104 (1996) 111–137.
[14] S. Orszag, G. Patterson, Phys. Rev. Lett. 12 (1972) 76–79.
[15] R. Rogallo, NASA TM 81315, NASA Ames Research Center, CA, 1981.
[16] V. Eswaran, S. Pope, Comp. Fluids 16 (N3) (1988) 257–278.
[17] V. Eswaran, S. Pope, Phys. Fluids 31 (N3) (1988) 506–520.
[18] T. Poinsot, S. Lele, J. Comput. Phys. 101 (1992) 104–129.
[19] R. Borghi, On the Structure and Morphology of Turbulent Premixed Flames, Plenum Press, New York, 1985.

Please cite this article in press as: C. Dopazo et al., Combust. Flame (2014), http://dx.doi.org/10.1016/j.combustflame.2014.11.034

E

Still mixing after all these years

SPEIC14 – Towards Sustainable Combustion
November 19-21, 2014, Lisboa, Portugal

Still mixing after all these years

Cesar Dopazo*, Luis Cifuentes*, Juan Hierro, Jesus Martin***

*LIFTEC, CSIC - University of Zaragoza, C/ Maria de Luna 3, 50018, Zaragoza – Spain
**Centro Universitario de la Defensa, AGM. Crta. Huesca s/n, 50090, Zaragoza – Spain,
E-mail: dopazo@unizar.es

ABSTRACT

DNS datasets for inert and reactive scalars in statistically homogeneous and stationary turbulence of constant density fluid, and for turbulent premixed flames in an inflow-outflow configuration and in a jet are examined. The objective is to gain a better physical understanding of mixing to use in modeling molecular diffusion terms. Classical descriptions in term of either scalar fluctuation moments or pdf conservation equations can be related to transport of iso-scalar surfaces by turbulent convection and molecular diffusion. The kinematics and propagation speeds of iso-surfaces are theoretically analyzed. The effective normal strain rate, which combines flow and diffusion-reaction induced processes, emerges as an essential variable; scalar gradients and dissipation rates increase for negative effective normal strains and decrease for positive ones. It is argued that the characteristic mixing time should be proportional to the inverse of the effective normal strain rate. The latter displays drastically different behaviors for constant density turbulence, with predominantly positive values, and for flows with significant heat release, with mostly positive ones. The former turbulent flows cause scalars to become less dissipative as time progresses, whereas the latter increase scalar dissipation. Functional dependences of the molecular diffusion rate conditioned on composition are sought. It is suggested that the characteristic mixing time is determined by the different interrelated processes, mainly in the limits of very low and very high Karlovitz numbers.

***Keywords**: Turbulent premixed flames, tangential and normal strain rates, flame, iso-scalar surface kinematics, propagation speed, inert and reactive scalars, homogeneous turbulence*

1. INTRODUCTION

The ubiquity of mixing in engineering and everyday devices is enormous. Combustion systems, chemical reactors, atmospheric pollution, domestic blending of liquids and solids are but a few examples of the relevance of mixing processes. Measuring the degree of mixing is thus an important issue. Some authors choose entropy considerations and definitions to quantify mixing [1]-[2].

The turbulent mixing of spatially segregated scalar fields (e.g., two regions of fluid with different temperatures, several inert or reactive chemical species) is a process, which combines convection by large and medium scale velocity structures, straining of scalar geometries by the local flow topologies and molecular diffusion. Should scalars be reactive, intimate contact at the molecular level is indispensable for them to be chemically converted into intermediate species or products. Large eddy convection beats heterogeneous scalars and brings them closer together, for example, by engulfment or entrainment, although retaining their distinct compositions, with segregation still at smaller spatial scales [3]. Local flow nodal and vortical structures fold and stretch scalar zones separating scalar fields, fostering scalar gradient enhancement and surface growth; the former increases molecular fluxes of scalars, whereas the latter promotes the global mixing.

Average scalar fluctuations (e.g., the standard deviation, $\langle (Y - \langle Y \rangle)^2 \rangle^{1/2}$, or this value normalized with the mean $\langle Y \rangle$) are good indicators of mixing. The shape of scalar probability density functions (pdf), displaying either two Dirac δ spikes for an initially segregated scalar with two possible values, or a single spike for asymptotically perfect mixing, can also serve to evaluate mixing.

Oboukhov [4], Corrsin [5] and Batchelor [6] pioneered work on scalar mixing, emphasizing spectra and length micro-scale estimates. Experiments on scalar mixing has been the subject of many experimental studies [7]-[10]. Numerical studies are also numerous [11]-[12].

Organized vorticity large structures experimentally, first observed by Brown and Roshko [13], caused a temporary change in the mind-sets of traditional mixing researchers. Vortex growth by pairing seemed to clash with conventional cascade processes. The experimentally well documented interaction between span-wise and stream-wise vortices [14] and the discovery of the 'mixing transition', from predominant large span-wise vortices to a three-dimensional flow with small scale structures ([15] and references therein), also numerically corroborated [16], were important milestones to reconcile classical viewpoints on mixing with newly proposed models [17].

The geometric interpretation of mixing and turbulence is physically and mathematically appealing [18]-[20]. Local geometries of iso-scalar surfaces can be classified using the eigenvalues of the curvature tensor [21] and [22]. Some attempts at explaining small scale mixing in terms of zero gradient points have been suggested [23]. A model using the extremal points of a fluctuating scalar field and its gradient trajectories serves to define 'dissipation elements', which are parameterized in terms of minima-maxima distance and scalar value differences [24]. A technique to obtain critical points of geometric fields is used to determine three-dimensional flow topologies of turbulent premixed flame interactions, analyzing the eigenvalues of the

scalar Hessian tensor [25]. Investigations on the alignment of passive scalar gradients were performed via DNS [26] and [27].

Local flow topologies have been investigated using critical point concepts. The nature of the three eigenvalues, P, Q and R, of the velocity gradient tensor allows the separation of nodal (strain dominated) and focal (vorticity dominated) points in the Q-R plane for constant density flows (P = 0) for any type of homogeneous and inhomogeneous turbulence [28]-[30]. For variable density flows, $P \neq 0$ is the third axis to categorize up to eight local flow topologies [31]-[33].

Local flow topologies and iso-scalar surface geometries are therefore two basic building blocks, which interact in the mixing process in statistically homogeneous flows. In shear flow turbulence, engulfment or entrainment of fluids is a previous step, with some limited mixing at the molecular level taking place at that stage.

Reynolds averaged transport equations in the physical and spectral spaces for reactive scalars were first formulated by Corrsin [3], [34] and [35], and O'Brien [36]-[38].

Dopazo and O'Brien [39] proposed a closed formalism using the probability density (PD) functional of a scalar field. They projected the PD functional transport equation into a one-dimensional composition space to obtain the scalar pdf conservation equation [40], with no closure needed for the highly nonlinear chemical source term; they applied it to the evolution of the temperature in a statistically homogeneous exothermic mixture. A different technique was used by Lundgren [41] to obtain the turbulent velocity pdf transport equation.

Modelling the 'conditional diffusion' (molecular mixing) became a central problem in pdf methodologies. A linear mean square estimation (LMSE) model was first proposed [40], and the hyperbolic PDE for the pdf was readily integrated. This model relaxes all the scalar values in the flow field towards the scalar mean; however, the relaxation in unphysical, and, for example, two initial Dirac δ's, corresponding to two segregated values of the scalar, remain asymptotically separated for large times, indicating inadequate mixing behavior. Aiming at a more physically sound relaxation towards the scalar mean, Dopazo [42] and Janicka et al. [43] independently developed a two 'scalar value' interaction model, inspired on the coalescence/dispersion model of Curl [44]. A combination of a LMSE model and a Langevin stochastic composition change was proposed by Valino and Dopazo [45] to correctly relax any initial pdf.

Flagan and Appleton [46] first introduced particle methods in a plug-flow burner to predict NOx. Pope [47] formalized the use of MonteCarlo particle methods for mixing/reactive systems with turbulent flows to integrate multidimensional pdf transport equations; six basic principles were also enunciated to guide the development of molecular mixing models (MMM): i) dimensional consistency; ii) coordinate system independence; iii) Galilean invariance; iv) realizability; v) linearity and independence of conserved passive scalars; and vi) boundedness of compositions.

Some review papers [48]-[50] and a textbook [51] illustrate aspects of the pdf methodology. Over the last 30 years, many molecular mixing models have been proposed, that perform with different degrees of success [52]-[55]. However, none is completely satisfactory at present. In general, the existing models are statistically-based and the current physical understanding of mixing, through DNS and experiments, has little reflection in them. Models are becoming increasingly complicated, supposedly 'to predict situations of practical, industrial interest'.

Distinct approaches, which try to address the molecular mixing modeling have been proposed. The joint pdf transport equation of one scalar and its gradient modulus was studied by Meyers and O'Brien [56]. Valino [57] replaced MonteCarlo particles by fields that vary closer to the real scalar evolution. The linear eddy model [58] and the one-dimensional turbulence model [59] aimed at mimicking the effects of small scale vortices on scalar fields.

The mixing of inert and reactive scalars by statistically stationary and homogeneous turbulence in a constant density fluid has been investigated via DNS in a box with 256^3grid points [21] and [22]. The pseudo-spectral method was analogous to those previously developed [60] and [61] and a classical forcing scheme [62] was used.

Laminar and turbulent premixed flames have been investigated for some time [63]-[66]. Transport equations for flame area and surface density function have been derived with a explicit dependence on tangential stretching [67] and [68]. Flows with important density changes, due, for example, to chemical heat generation, undergo large volumetric dilatation rates [69]. This situation leads to mostly positive values for both tangential and normal strain rates [70]; the former will imply iso-scalar surface stretching, whereas the latter will, in principle, yield a reduction of the scalar-gradient modulus, as iso-surfaces separate.

Chakraborty [71] and [72] has conducted direct numerical simulations to document the existence of positive normal strain rates in a 'corrugated flamelet regime' and negative ones in a 'thin reaction zone regime'; while in the first case the scalar gradient aligns preferentially with the strain rate tensor eigenvector corresponding to its most extensive eigenvalue, in the second instance the scalar gradient is mainly parallel to the most compressive eigenvector. This latter result is identical to findings in turbulent scalar mixing in constant density flows [26] and [27]. Chakraborty et al. [73] have examined the Lewis number effect on the scalar gradient alignment in turbulent premixed flames; mainly positive normal strain rates exist and "the most extensive principal strain rate" is preferentially perpendicular to iso-scalar surfaces and "destroys the scalar gradient" with a "magnitude" that "increases with decreasing Lewis number for given turbulent Reynolds and Damköhler numbers". Predominant local flow topologies and scalar geometries in turbulent premixed flames have recently been investigated [74] and [75].

Section 2 contains some mathematical descriptions of the mixing process of inert and reactive scalars; moment formulation and characteristic mixing times are discussed; the transported pdf methodology is briefly described and the closure problems are described; a kinematic analysis of iso-scalar surfaces allows a simple explanation for the enhancement and destruction of

scalar gradients. The DNS datasets examined in this work are summarily presented in Section 3. A comparison of results for inert and reactive scalars in constant density turbulence, and for two turbulent premixed flames is scrutinized in Section 4. Some conclusions are drawn in Section 5.

2. THE MATHEMATICS OF MIXING PROCESSES

2.1 Scalar conservation equation

The problem of mixing can be illustrated with a single scalar. The reduced reactants mass fraction, $Y(\mathbf{x},t)$, is governed by

$$\partial Y/\partial t + v_j\,\partial Y/\partial x_j = (1/\rho)\,\partial/\partial x_j\,[\rho D\,(\partial Y/\partial x_j)] + [\dot{\omega}(Y)/\rho], \quad (1)$$

where v_j is the *j*th component of the velocity vector, **v**, mean plus fluctuation, ρ is the density, D is the molecular diffusion coefficient and $[\dot{\omega}(Y)/\rho]$ is the chemical reaction rate, with dimensions of the inverse of a chemical time. For variable density flows, (1) is coupled with the continuity, momentum and energy conservation equations, the gas state equation and appropriate thermodynamic relations. Should ρ and D be constants, **v** is independently determined and is a known 'driver' for (1), which is also separately treated. The molecular diffusion contribution can be expressed as

$$(1/\rho)\,\partial/\partial x_j\,[\rho D\,(\partial Y/\partial x_j)] = D(\partial Y/\partial x_N)\,[\partial \ln(\rho D\,\partial Y/x_N)/\partial x_N + 2\,k_m], \quad (2)$$

where x_N is the coordinate normal to the iso-surface, $Y(x,t) = \Gamma$, and $k_m = (\partial n_i/\partial x_i)/2$ is its mean curvature. For $\rho D = $ constant,

$$(1/\rho)\,\partial/\partial x_j[\rho D\,(\partial Y/\partial x_j)] = D\nabla^2 Y = D(\partial^2 Y/\partial x_N^2) + 2\,k_m D(\partial Y/\partial x_N). \quad (3)$$

The first and second derivatives of the scalar profile with respect to x_N, and the mean curvature of the iso-scalar surface emerge as important features.

For constant ρ and D, and statistically homogeneous velocity (zero mean) and scalar fields, the Reynolds average of (1) yields

$$d\langle Y\rangle/dt = \langle[\dot{\omega}(Y)/\rho]\rangle, \quad (4)$$

where angular brackets denote either ensemble or spatial averages. Splitting the scalar field as

$$Y(\mathbf{x},t) = \langle Y\rangle(t) + y(\mathbf{x},t), \quad (5)$$

where $y(\mathbf{x},t)$ stands for scalar fluctuations, leads to

$$\partial y/\partial t + v'_j\partial y/\partial x_j = D\partial x_j(\partial y/\partial x_j) + [\dot{\omega}(Y)/\rho] - \langle[\dot{\omega}(Y)/\rho]\rangle, \quad (6)$$

$\mathbf{v}'$ is the fluctuating turbulent velocity vector. The time evolution equation for the variance of $y(\mathbf{x},t), \langle y^2\rangle(t)$, is

$$d[(1/2)\langle y^2\rangle]/dt = -\langle\varepsilon_Y\rangle + \langle y[\dot{\omega}(Y)/\rho]\rangle, \quad (7)$$

where $\langle\varepsilon_Y\rangle = \langle D\,(\partial y/\partial x_j)\,(\partial y/\partial x_j)\rangle$ is the scalar fluctuation dissipation rate, analogous to the turbulent kinetic energy dissipation rate, $\langle\varepsilon\rangle$, which appears in the equation

$$d[(1/2)\langle v'_i\,v'_i\rangle]/dt = -\langle\varepsilon\rangle, \quad (8)$$

for the time evolution of the average turbulent kinetic energy. For statistically stationary turbulence the characteristic macroscopic time $\tau = [(1/2)\,\langle v'_i\,v'_i\rangle]/\langle\varepsilon\rangle$ is constant. On the other hand, the fluctuations of an inert scalar field will have a characteristic decay time, $\tau_Y(t) = [(1/2)\,\langle y^2\rangle]/\langle\varepsilon_Y\rangle$, which will, in general, vary with time according to $d\tau_Y(t)/dt = -[1 + \tau_Y(t)\,(1/\langle\varepsilon_Y\rangle)\,d\langle\varepsilon_Y\rangle/dt]$; depending on the sign and value of $[\tau_Y(t)\,(1/\langle\varepsilon_Y\rangle)\,d\langle\varepsilon_Y\rangle/dt]$, $\tau_Y(t)$ can increase or decrease with time.

For a chemically inert scalar, $\langle\varepsilon_Y\rangle > 0$ dictates the mixing rate. For example, for a completely segregated scalar with two possible values, 0 and 1, at $t = 0$, $\langle Y\rangle(0) = 1/2$, whereas $\langle Y^2\rangle(0) = 1/4$; as time becomes asymptotically large, $\langle Y\rangle(t) = 1/2$ and $\langle y^2\rangle(t) \longrightarrow 0$. An indicator of scalar 'mixedness' is $\langle y^2\rangle^{1/2}(t)/\langle Y\rangle(t)$, which in the previous case will vary from unity for the completely segregated state, to zero for a perfectly mixed composition. Obviously, the mixing rate or, equivalently, the characteristic mixing time will change with time; the latter, of the order of $\langle y^2\rangle/\langle\varepsilon_Y\rangle$, will be very large for small times due to huge scalar gradients, and it will decrease as mixing progresses.

A conservation equation for the instantaneous variable ε_Y can be readily obtained,

$$\partial[(1/2)\,\varepsilon_Y]/\partial t + v'_j\,\partial[(1/2)\,\varepsilon_Y]/\partial x_j = -(n_i\,s_{ij}\,n_j)\,\varepsilon_Y + D\,\partial/\partial x_j\,\{\partial[(1/2)\,\varepsilon_Y]/\partial x_j)\} - D\,[\partial(\partial y/\partial x_N)/\partial x_j]\,[\partial(\partial y/\partial x_N)/\partial x_j] - D\,\varepsilon_Y\,(\partial n_i/\partial x_j)\,(\partial n_i/\partial x_j) + \varepsilon_Y\,d[\dot{\omega}(Y)/\rho]/dY, \quad (9)$$

where **n** is the unit vector normal to the iso-scalar surface $Y(\mathbf{x},t) = \Gamma$, defined by

$$n_i(\mathbf{x},t) = (\partial Y/\partial x_i)/\,[(\partial Y/\partial x_k)(\partial Y/\partial x_k)]^{1/2}, \quad (10)$$

s_{ij} is (i,j) component of the turbulent flow strain rate tensor, $\partial y/\partial x_N = \partial Y/\partial x_N = n_j\,\partial Y/\partial x_j$ is the scalar gradient modulus, and $\partial n_i/\partial x_j$ is the iso-surface curvature tensor. The first term on the right side of (9) is the gradient enhancement or destruction by the flow strain rate normal to the iso-surface,

$$a_N = n_i\,s_{ij}\,n_j, \quad (11)$$

$a_N > 0$ will reduce ε_Y, whereas $a_N < 0$ will tend to increase ε_Y. The second term is the molecular transport of ε_Y. The third and fourth terms are the dissipation rate of ε_Y due to molecular diffusion of gradient modulus and to changes in iso-surface orientations and curvatures. The last term represents the enhancement or destruction of ε_Y due to chemistry.

2.2 Probability density function (PDF) methodology

An alternative way to describe mixing is through the use the probability density function (pdf) methodology. This formalism is illustrated with a simple pdf transport equation, corresponding to the scalar field governed by (1) with constant ρ and D. The fine-grained probability density function is defined by

$$\delta[\Gamma - Y(\mathbf{x},t)] = (1/\Delta\Gamma)\{H + [\Gamma\Delta\Gamma - Y(\mathbf{x},t)] - H[\Gamma - Y(\mathbf{x},t)]\}\ , \tag{12}$$

when $\Delta\Gamma \longrightarrow 0$. δ and H are the Dirac-delta and the Heaviside-step functions. The term within curly brackets is unity only when $\Gamma \leq Y(\mathbf{x},t) < \Gamma + \Delta\Gamma$. $\delta[\Gamma - Y(\mathbf{x},t)]$ can loosely be viewed as the pdf of a fine-grained distribution function, $H[\Gamma - Y(\mathbf{x},t)]$, a scalar variable that obeys the transport equation [49].

$$D\delta/Dt = -(\partial/\partial\Gamma)\,[D(\nabla^2 Y)\,\delta] - (\partial/\partial\Gamma)\,\{[\dot{\omega}(\Gamma)/\rho]\,\delta\}. \tag{13}$$

Ensemble average of (13) yields

$$\partial P/\partial t + V_j\,(\partial P/\partial x_j) + (\partial/\partial x_j)\,[\langle v'_j \mid Y(\mathbf{x},t) = \Gamma\rangle P] = -(\partial/\partial\Gamma)[\langle D\,(\nabla^2 Y)\mid Y(\mathbf{x},t) = \Gamma\rangle\,P] - (\partial/\partial\Gamma)\,\{[\dot{\omega}(\Gamma)/\rho]\,P\}\ , \tag{14}$$

where $P = P_Y(\Gamma;\mathbf{x},t) = \langle\delta[\Gamma - Y(\mathbf{x},t)]\rangle$ is the pdf of $Y(\mathbf{x},t)$ and $\boldsymbol{V}$ is the mean flow velocity vector. The closure problem is apparent in two transport terms of the iso-scalar surface $Y(\mathbf{x},t) = \Gamma$:

· $\langle v'j \mid Y(\mathbf{x},t) = \Gamma\rangle$, the average turbulent convection, and

· $\langle D\,(\nabla^2 Y)\mid Y(\mathbf{x},t) = \Gamma\rangle$, the average 'conditional diffusion' or 'molecular mixing'.

On the positive side, the chemical source term is closed in this transported PDF methodology. The turbulent convection of P vanishes in statistically homogeneous flows. The main difficulty for the last forty years has thus been the modeling of the 'conditional diffusion'. A 'molecular mixing model' should implicitly involve not only the molecular transport, but the concomitant evolution of iso-scalar surface geometries undergoing the straining due directly to small scale flow topologies or that induced by chemistry and diffusion.

Using (3), the 'conditional diffusion' can be rephrased as

$$\langle D\,(\nabla^2 Y)\mid Y(\mathbf{x},t) = \Gamma\rangle = \langle D\,(\partial^2 Y/\partial x_N^2)\mid Y(\mathbf{x},t) = \Gamma\rangle + \langle 2\,k_m\,D(\partial\,Y/\partial\,x_N)\mid Y(\mathbf{x},t) = \Gamma\rangle\ , \tag{15}$$

The 'conditional normal and tangential diffusion' terms, respectively. The shape of the profile $Y(x_N,t)$ as a function of x_N, normal to iso-surfaces, as well as the local mean curvature of the iso-surfaces influence the mixing term. Since, $\partial\,Y/\partial x_N \geq 0$, convex (concave) iso-surfaces will yield a positive (negative) contribution to 'conditional diffusion' due to curvature, whereas convexity (concavity) of profiles $Y(x_N,t)$ will negatively (positively) contribute to it.

Let Δx_N be an infinitesimally small distance between the iso-surface $Y(\mathbf{x},t) = \Gamma$ and the ones in front and behind it, following $\mathbf{n}$. $D(\partial^2 Y/\partial x_N^2)$ is then approximated as

$$D\,(\partial^2 Y/\partial x_N^2) = -\{1/[(\Delta x_N)^2/6\,D]\}\,[\Gamma - \langle Y(x_N,t)\rangle_{2(\Delta xN)}] \tag{16}$$

where $\langle Y(x_N,t)\rangle_{2(\Delta xN)}$ is the average of $Y(x_N,t)$ in the interval $(-\Delta x_N, +\Delta x_N)$ about x_N, on $Y(\mathbf{x},t) = \Gamma$. $(\Delta x_N)^2/6\,D$ is interpreted as a 'scalar mixing time', dependent on the time evolution of Δx_N. On the other hand, the deviation $[\Gamma - \langle Y(x_N,t)\rangle_{2(\Delta xN)}]$ will be negative (positive) for concave (convex) profiles of $Y(x_N,t)$.

Modelling the molecular mixing term encompasses several difficulties:

- Determining the functional dependence on Γ. When $\langle Y(x_N,t)\rangle_{2(\Delta xN)}$ is replaced by $\langle Y(\mathbf{x},t)\rangle$, the local mean in either a LES or a RANS methodology, the dependence on Γ will be likely nonlinear. Nonlinear mean square estimations can provide cubic dependences, but adds complexity to the use of the model.
- The characteristic mixing time or mixing rate varies with $\mathbf{x}$ and t, and is dictated by the relative separation of iso-scalar surfaces. The latter might well depends not only on the local flow strain rate but also on the molecular transport and chemical reactions. The limits of $Ka \gg 1$ and $Ka \ll 1$, in a combusting flow, might have widely different characteristic mixing times. The traditional choice of a mixing time proportional to $\langle k\rangle/\langle\varepsilon\rangle$ in RANS methodologies seems extremely simplistic.
- Most 'molecular mixing models' have been developed for turbulent mixing in constant density fluids. Flow and heat release in combustion can jointly induce normal strain rates totally different from those for constant density turbulent velocity fields. Significant changes in ρD with x_N should certainly modify physical mechanisms of molecular transport.

2.3 Kinematics of iso-scalar surfaces

It is clear from the two previous sub-sections that scalar mixing can viewed from a vantage point in terms of evolution of iso-scalar surfaces. Figure 1 shows an infinitesimal surface, S, on the non-material surface $Y(\mathbf{x},t) = \Gamma$. (10) defines its normal unit vector $\mathbf{n}(\mathbf{x},t)$.

The infinitesimal vector, $\mathbf{r}$, joins a point $\mathbf{x}$ at the center of S to a point $\mathbf{x} + \mathbf{r}$ on a neighboring iso-scalar surface $Y(\mathbf{x},t) = \Gamma + \Delta\Gamma$. The two extremes of $\mathbf{r}$ move with velocities $\mathbf{v}^Y(\mathbf{x},t)$ and $\mathbf{v}^Y(\mathbf{x}+\mathbf{r},t)$, where

$$v_i^Y(\mathbf{x},t) = v_i(\mathbf{x},t) + V^Y(\mathbf{x},t)\,n_i\ , \tag{17}$$

$\mathbf{v}$ is the fluid velocity and V^Y is the normal propagation speed the iso-surface relative to the local fluid. The time rate of change of $\mathbf{r}$ is

$$dr_i/dt = s_{ij}\,r_j + w_{ij}r_j + r_j(\partial V^Y/\partial x_j)\,n_i + V^Y r_j(\partial n_i/\partial x_j)\ , \tag{18}$$

where $\mathbf{s}$ and $\mathbf{w}$ are the strain and rotation rate tensors,

respectively, and $(\nabla \mathbf{n})$ is the curvature tensor. $w_{ij}r_j$ can be recast as $(1/2)\varepsilon_{ijk}\omega_j r_k$, in terms of $\omega_i = \varepsilon_{ijk}\,(\partial v_k/\partial x_j)$, the vorticity vector. ε_{ijk} is the alternating Levy-Civita tensor.

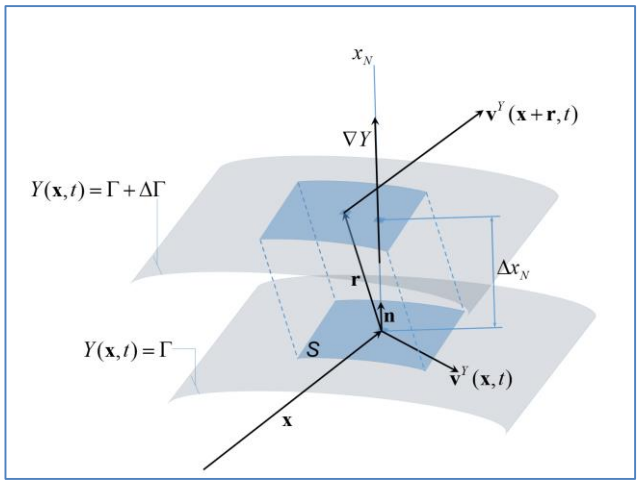

Figure1. Schematic representation of non-material iso-scalar surfaces and infinitesimal vector and area elements.

If $r_i = \Delta x_N n_i$, one can readily obtain from (18)

$$(1/\Delta x_N)\, d\Delta x_N/dt \;=\; a_N + \partial V^Y/\partial x_N, \qquad (19)$$

(11) defines the flow normal strain rate, a_N. $\partial V^Y/\partial x_N$ accounts for differences in the propagation velocity of two adjacent (infinitesimally close) iso-surfaces.

The infinitesimal volume $V = S\,\Delta x_N$, between the two iso-scalar surfaces, changes in time according to

$$(1/V)\, dV/dt \;=\; s_{ii} + \partial V^Y/\partial x_N + 2k_m V^Y, \qquad (20)$$

where $s_{ii} = (\partial v_i/\partial x_i)$, the trace of the strain rate tensor, yields the flow volumetric dilatation rate. The curvature is positive for iso-surfaces convex towards 'fresh gases' $(Y = 1)$ and negative for concave ones. The time rate of change of the infinitesimal surface S can thus be obtained from (19) and (20)

$$(1/S)\, dS/dt \;=\; a_T + 2k_m V^Y, \qquad (21)$$

where

$$a_T = (\delta_{ij} - n_i n_j) s_{ij}, \qquad (22)$$

is the flow strain rate tangential to the iso-scalar surface $Y(\mathbf{x},t) = \Gamma$. δ_{ij} is the Kronecker delta or identity tensor. Expression (21) has been derived for flame stretch by several authors ([65-[68] and references therein).

a_N and a_T add up to

$$a_N + a_T \;=\; \partial v_i/\partial x_i. \qquad (23)$$

For flows of constant density fluids, $\partial v_i/\partial x_i = 0$ and $a_N = -a_T$.

The local molecular flux (mass per unit area and time) vector of $Y(\mathbf{x},t)$ at point $\mathbf{x}$ and time t is

$$f_i^Y \;=\; -\,\rho\, D\, (\partial Y/\partial x_i). \qquad (24)$$

The mass flow rate (mass per unit time) across the infinitesimal surface S is

$$f_i^Y S\, n_i = -\,\rho\, D\, n_i (\partial Y/\partial x_i)\, S = -\,\rho\, D\, S\;\; (\partial Y/\partial x_N), \qquad (25)$$

with the scalar gradient $\partial Y/\partial x_N = \Delta\Gamma/\Delta x_N$.

The mass flow rate per unit volume, which determines the local mixing rate, is

$$f_i^Y S\, n_i\, /\, V = -\,\rho\, D\, (S\,/\,V)\, (\partial Y/\partial x_N), \qquad (26)$$

$\Sigma(\Gamma; x, t) \;=\; S/V \;=\; 1/\Delta x_N$ is the surface density function [68].

Therefore,

$$f_i^Y S\, n_i\, /\, V \sim\; -\,\rho\, D\, \Delta\Gamma/(\Delta x_N)2. \qquad (27)$$

Relation (16) provides a hint at modelling molecular diffusion.

For the two given iso-scalar surfaces, the local mixing rate increases with time if Δx_N diminishes. From eq. (19), $d\Delta x_N > 0$ if $a_N + \partial V^Y/\,\partial x_N > 0$ (scalar gradients decrease with time), and $d\Delta x_N < 0$ if $a_N + \partial V^Y/\,\partial x_N < 0$ (scalar gradients increase with time).

For combusting flows with significant heat release $(\partial v_i/\partial x_i) > 0$, and the probability of finding $a_N > 0$ in most of the flow domain is high. Therefore, for the scalar-gradient and the mass flow rate per unit volume to increase, $\partial V^Y/\,\partial x_N$ should be negative and its absolute value greater than a_N.

On the other hand, (1) can also be written as

$$\partial Y/\partial t \;+ v_j\, (\partial Y/\partial x_j) \;=\; -\,V^Y\, (\partial Y/\partial x_N), \qquad (28)$$

An equation for the evolution of the scalar gradient, $(\partial Y/\partial x_N)$, can be readily obtained from (28),

$$\partial(\partial Y/\partial x_N)/\partial t + v_j^Y \partial/\partial x_j)(\partial Y/\partial x_N) = -(a_N + \partial V^Y/\,\partial x_N)(\partial Y/\partial x_N), \qquad (29)$$

The scalar-gradient associated to a point on a non-material iso-surface, moving with velocity $\mathbf{v}^Y$, decreases or increases depending on positive or negative values, respectively, of the 'effective' normal strain rate, $(a_N + \partial V^Y/\,\partial x_N)$.

Equating the right sides of (1) and (28), and using (2), an expression for V^Y is easily obtained,

$$V^Y \;=\; -\,D\,\partial\,\ln(\rho D\;\partial Y/\partial x_N)/\partial x_N \;-\; 2\,D\,k_m - (\dot{\omega}/\rho)/(\partial Y/\,\partial x_N), \qquad (30)$$

The contributions V_1^Y, from normal molecular diffusion, V_2^Y,

from tangential (due to curvature) diffusion, and V_3^Y, from chemical reaction, correspond to the three terms on the right side of (30). The normal derivative of (30) yields

$$\partial V^Y/\partial x_N = (\partial/\partial x_N)\{-D\,[\partial \ln(\rho D\,\partial Y/\partial x_N)]/\partial x_N\} + (\partial/\partial x_N)(-2\,D\,k_m) + (\partial/\partial x_N)[-(\dot{\omega}/\rho)/(\partial Y/\partial x_N)], \quad (31)$$

The three terms on the right side of (24), $(\partial V^Y/\partial x_N)_1$, $(\partial V^Y/\partial x_N)_2$ and $(\partial V^Y/\partial x_N)_3$, quantify the contributions of normal and tangential diffusions, and chemistry, respectively. Note that $\partial V^Y/\partial x_N$ has dimensions of the inverse of a time scale, to which normal and tangential diffusions, as well as chemistry contributes.

For flows of constant ρ and D fluids,

$$V^Y = -D\,(\partial^2 Y/\partial x_N^2)/(\partial Y/\partial x_N) - 2\,D\,k_m - (\dot{\omega}/\rho)/(\partial Y/\partial x_N), \quad (32)$$

For $(\partial Y/\partial x_N) \longrightarrow 0$, DNS results show that $(\partial^2 Y/\partial x_N^2)/(\partial Y/\partial x_N)$ is finite and so is $(\dot{\omega}/\rho)/(\partial Y/\partial x_N)$. This point deserves a more detailed analysis ([23]-[25]). Similarly

$$\partial V^Y/\partial x_N = (\partial/\partial x_N)[-D\,(\partial^2 Y/\partial x_N^2)/(\partial Y/\partial x_N)] + (\partial/\partial x_N)(-2\,D\,k_m) + (\partial/\partial x_N)[-(\dot{\omega}/\rho)/(\partial Y/\partial x_N)]. \quad (33)$$

A length scale, δ_N, can be defined by the relation

$$\delta_N = (\partial Y/\partial x_N)/|(\partial^2 Y/\partial x_N^2)|, \quad (34)$$

The order of magnitude of δ_N, compared with the Kolmogorov length micro-scale and the laminar flame thickness, should be obtained from DNS results.

2.3 Dimensionless 'effective' normal strain rate equation

Equation (19) can be written as

$$(1/\Delta x_N)\,d\Delta x_N/dt = a_N + (\partial/\partial x_N)\{-D\,[\partial \ln(\rho D\,\partial Y/\partial x_N)]/\partial x_N\} + (\partial/\partial x_N')(-2\,D\,k_m) + (\partial/\partial x_N)[-(\dot{\omega}/\rho)/(\partial Y/\partial x_N)], \quad (35)$$

All term in (35) have dimensions of an inverse of time. In principle, $(1/\Delta x_N)\,d\Delta x_N/dt$ can be considered proportional to the characteristic mixing time. The flow normal strain rate should scale with the Kolmogorov time micro-scale, $\tau_\eta = (\nu/\varepsilon)^{1/2}$. The order of magnitude of the second term on the right side is D_0/δ_N^2, the inverse of a characteristic molecular normal diffusion time (D_0 can be, for example, the value of the molecular diffusion coefficient in the fresh gases and δ_N a characteristic separation of iso-sufaces). $D_0\,k_{m0}/\delta_N$ is the order of magnitude of the third term (k_{m0} stands for the characteristic mean curvature of the iso-surfaces). The last term is of the order of the inverse of a characteristic chemical time, τ_{ch}^{-1}. The orders of magnitude of the second, third and fourth terms of the right side of (35), compared to the first one, are the dimensionless numbers $(D_0\,\tau_\eta/\delta_N^2)$, $(D_0\,\tau_\eta/\delta_N^2)(k_{m0}\,\delta_N)$ and (τ_η/τ_{ch}). The first one is the ratio of the Kolmogorov time micro-scale to a characteristic normal diffusion time. $(k_{m0}\,\delta_N)$ is a dimensionless curvature. The last parameter is the inverse of the Karlovitz number $(Ka = \tau_{ch}/\tau_\eta)$. In general, $(D_0\,\tau_\eta/\delta_N^2)^{-1} = Sc\,Re^{3/2}\,(\delta_N/l)^2$, where $Sc = \nu_0/D_0$, is the Schmidt number (ν_0 is the kinematic viscosity coefficient in the fresh gases), the turbulent Reynolds number is defined by $Re = u'l/\nu_0$ (l is the integral length scale and u' the turbulent fluctuation rms). Should δ_N be of the order of δ_L, the laminar flame thickness, $(D_0\,\tau_\eta/\delta_N^2)^{-1} \sim Ka$.

For $Ka \ll 1$ the fast reaction will determine the characteristic mixing time and the flow strain rate will not influence the process; the importance of the normal and tangential diffusions will depend on the orders of magnitude of (δ_N/δ_L) and $(k_{m0}\,\delta_N)$. At the other extreme, $Ka \gg 1$, a slow reaction will not influence the mixing rate; if $(D_0\tau_\eta/\delta_N^2) \ll 1$ and $(D_0\,\tau_\eta/\delta_N^2)(k_{m0}\,\delta_N) \ll 1$, the flow strain rate will determine the characteristic mixing time; however, the molecular diffusion will control the mixing process if $(D_0\,\tau_\eta/\delta_N^2) \gg 1$ and/or $(D_0\,\tau_\eta/\delta_N^2)(k_{m0}\,\delta_N) \gg 1$.

3. DNS DATASETS EXAMINED

Datasets from the direct numerical simulations of:
- a box of statistically homogeneous and stationary turbulence mixing an inert and a reactive scalar in a constant density fluid,
- a premixed turbulent flame in an inflow-outflow configuration, and
- a turbulent jet premixed flame in a co-flow of hot products,

are examined and compared in this work. The DNS geometries and strategies are next described.

3.1 DNS of inert and reactive scalar mixing in homogeneous turbulence with a constant density fluid

A box of constant density, statistically homogeneous turbulence is simulated. Given the initial turbulent kinetic energy spectrum, a stochastic forcing scheme maintains a statistically stationary turbulence. Boundary conditions are periodic. Numerical simulations are performed using the OpenMP (Open Multi-Processing) parallelized implementation [76] and [77]. A second-order Runge-Kutta numerical integration scheme [78] is used for time-marching. The computational domain, shown in Figure 2, contains $512 \times 512 \times 512$ grid points uniformly distributed in the x, y and z directions. The length of the cube side is 16.57 mm. To reduce aliasing, a spherical filter is applied to data in Fourier space; all nodes corresponding to a wave number larger than 512×0.471 are set to zero. This filter is chosen to suppress the double and triple aliasing contribution ([60] and [61]) caused by convective terms. Two scalars with identical initial distribution, one inert and the other reactive with a prescribed Arrhenius-like chemical reaction, evolve in homogeneous isotropic turbulence. The chemical reaction rate is given by

$$\dot{\omega} = -KY\,exp[-\beta Y/(1-\alpha Y)], \quad (36)$$

where K in this case is taken equal to 13627 s^{-1}, Y represents the reduced mass fraction ($Y = 1$ in the `fresh gases' and $Y = 0$ in the `hot products'), β intends to simulate the activation energy effects ($\beta = 4.5$), and $\alpha = 0.7$. These parameters have been checked in previous DNS [79] and [80]. The dynamically passive scalars do not affect the velocity field and evolve without forcing from a highly unmixed initial condition. The velocity field undergoes a random forcing yielding a statistically stationary flow with no mean gradients. The forcing scheme is that of Eswaran and Pope [62] and [81] with a zero correlation time; all wave numbers with a modulus less than $2\sqrt{2}$, except the zero, receive a stochastic contribution at every time step, while their phase is adjusted to enforce the constant density condition. The turbulent Reynolds number is $Re = u'l/\nu \approx 144$, the integral length scale $l = 2.4$ mm, the kinematic viscosity is set equal to $\nu = 3.5412 \times 10^{-5} m^2/s$, the root mean square velocity $u' = 2.1$ m/s, and the Kolmogorov length micro-scale $\eta = 0.0577$ mm . Numerical values of the characteristic simulation parameters are presented in Table 1.

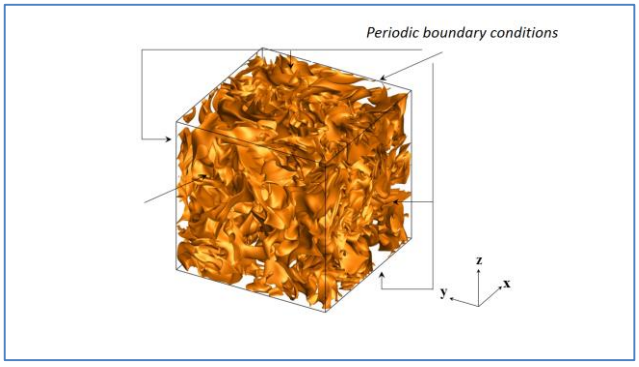

Figure 2. Description of the computational domain for the DNS of inert and reactive scalar mixing in homogeneous turbulence with a constant density fluid. The depicted iso-scalar surfaces are those with Y = 0.5.

3.2 Turbulent premixed flame in an inflow-outflow configuration

A premixed turbulent flame using an inflow-outflow configuration at moderate turbulent Reynolds number (see Figure 3) is simulated. A planar laminar flame, used as initial condition, interacts with a turbulent field of a mixture of $CH_4/O_2/CO_2$ ($70\%O_2$ and $30\%CO_2$) [82], and equivalence ratio $\emptyset_F = 1$. Conservation equations of mass, momentum, energy and chemical species are solved using the fully parallel compressible solver NTMIX3D [83]. The domain is considered periodic in the y and z directions, while non-reflecting inlet-outlet boundary conditions are imposed in the x direction, using the Navier-Stokes Characteristic Boundary Condition (NSCBC) method [84]. The solver [83] uses a 6th order compact Finite-Differences (FD) scheme for space discretization, and a third-order Runge-Kutta explicit method for time integration. The DNS is performed using the MPI (Message Passing Interface) parallelized implementation [85] and [86]. The computational domain, shown schematically in Figure 3, has a size 3π in the x direction and 2π in the y and z directions, and contains $768 \times 512 \times 512$ grid points, uniformly distributed. A single-step Arrhenius chemistry, $Reactants \rightarrow Products$, is used to maintain the computational cost within reasonable limits. The reaction rate expression is:

$$\dot{\omega} = \rho Y B_0 \, exp(-\beta/\alpha) \, exp[-\beta Y/(1-\alpha Y)], \qquad (37)$$

where ρ is the fluid density, $Y = Y_R \,/\, Y_R^u$ is the reduced mass fraction of the mixture (Y_R is the reactants mass fraction and Y_R^u is its value in the fresh gases), B_0 is the pre-exponential factor, $\alpha = (T_b - T_u)/T_b$ is a ratio defined with the temperature, T, in the unburned, T_u, and burnt gases, T_b, β is the reduced activation energy or Zel'dovich number, $\beta = \alpha E_a/RT_b$, E is the activation energy and R is the perfect gas constant. The fluid obeys a perfect gas equation of state, with constant molecular mass and constant specific heat ratio γ. The transport coefficients are temperature dependent, namely,

$$\mu = \mu_u \, (T/T_u)^b. \qquad (38)$$

Schmidt and Prandtl numbers are constant and, therefore, the mass diffusivity D and the thermal diffusivity D_{th} are given by $D = \mu/\rho Sc$ and $D_{th} = \lambda/\rho C_p = \mu/\rho Pr$.

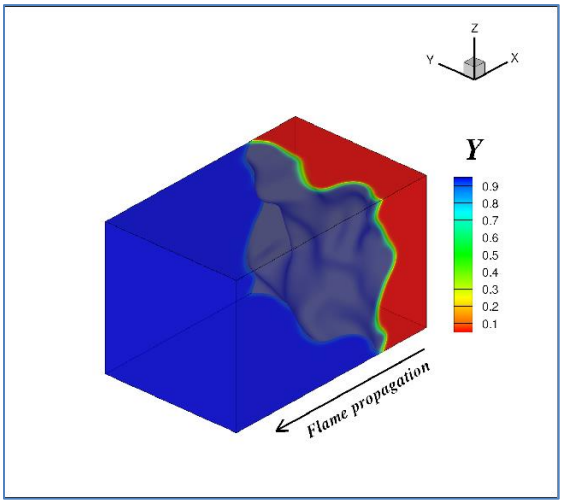

Figure 3. Description of the computational domain for the DNS of a turbulent premixed flame in an inflow-outflow configuration.

Initial conditions correspond to a planar premixed flame propagating in the negative x direction with the laminar flame speed S_L and width $\delta_L = D_{th}/S_L$. A constant-density isotropic turbulent velocity field is initially superposed to the mean velocity on the fresh gases side and evolves without forcing in the compressible solver NTMIX3D. In the subsequent propagation towards fresh gases, the flame encounters a decaying turbulent field, which wrinkles it as it progresses. The

initial constant-density isotropic turbulence is generated with an independent pseudo-spectral numerical code ([60] and [61]), starting from a given spectrum and using a stochastic forcing scheme, to yield a statistically stationary field. In this study, the gas parameters introduced previously are chosen as $b = 0.6$, $Pr = 0.75$, $Sc = 0.75$, $\gamma = 1.4$, and the chemical rate parameters are $\alpha = 0.8$, and $\beta = 6.0$. The rms velocity fluctuations in the 'fresh reactants' decay from $u_0' = 4.80\text{m/s}$ at $t = 0$ to $u' = 3.20\ \text{m/s}$ at t_{final}, in which our data are presented. To estimate the integral length scale, l, in the 'fresh reactants', the transverse autocorrelation coefficients in cross-stream planes, $y - z$, are obtained. The integral scale increases from $l_0 = 0.2612\ \text{mm}$ at $t = 0$ to $l = 0.2962\ \text{mm}$ at t_{final}. The turbulent Reynolds number, $Re = u'l/\nu$, decreases from $Re = 80.36$ at $t = 0$ to $Re = 60.75$ at t_{final}. The initial eddy turnover time is $\tau_0 = l_0/u_0' = 0.0544\text{ms}$. In this study, the initially planar laminar flame is allowed to interact with the turbulence field up to a time $t_{final} = 0.0925\text{ms}$, 1.70 times greater than the initial eddy turnover time. The turbulent Damköhler number, defined as $Da = (l/\delta_L)/(u'/S_L)$, is 11.48 at t_{final}. Therefore, combustion takes place in the `corrugated flamelets' regime ([64] and [65]). Numerical values of the aero-thermo-chemical variables and dimensionless parameters for this simulation are presented in Table 1.

3.3 Turbulent jet premixed flame in a co-flow

A turbulent jet premixed flame is numerically computed with a hybrid Large Eddy Simulation (LES)/DNS approach (see Figure 4). A methane-air mixture is injected through a central jet with a mean velocity $U_{Jet} = 30\text{m/s}$, and equivalence ratio $\emptyset_F = 4.4$. The jet is surrounded by a co-flow of burned products with a mean velocity $U_{coflow} = 5.4\text{m/s}$, and equivalence ratio $\emptyset_c = 1$. The chemistry is tabulated with the FPI (Flame-Prolongation of ILDM) flamelet approach [87]. A reduced mass fraction, Y, based on a single progress variable Y_c defined by Godel et al. [88], $Y_c = Y_{CO} + Y_{CO2} + (Y_{N2} - Y_{N2}^0) + (Y_{H2O} - Y_{H2O}^0) + Y_{NO} + Y_{NO2} + Y_{N2O}$, is used in this case. Y is defined as follows

$$Y = 1 - \left(Y_c/Y_c^{eq}\right), \tag{39}$$

where the 'eq'superscript designates the value in the burnt state of the laminar-premixed flame. Y_{N2}^0 and Y_{H2O}^0 are, respectively, the mass fractions of N_2 and H_2O in fresh gases. Y_{N2}^0 and Y_{H2O}^0 ensures that $Y_c = 1$ in fresh gases for all mixing conditions. The perfect gas law relates thermodynamic variables. The fully parallel compressible solver SiTCom (Simulating Turbulent Combustion) is used to integrate the mass, momentum, energy and reactant mass fraction conservation equations. Viscosity, thermal conductivity, and mass diffusion coefficients are functions of the temperature. The nozzle diameter is $D = 12\text{mm}$ and the computational domain extends 192mm in the streamwise x, and 66mm in the y and z directions, with 802, 466 and 466 grid points, uniformly spaced, in the x, y, and z directions, respectively. Therefore a LES mesh of about 171 million nodes is used, with a resolution varying between $150\mu\text{m}$ and $200\mu\text{m}$. An imbedded zone within the LES mesh features a much higher resolution of $50\mu\text{m}$ (see Figure 3). The DNS zoom box under study contains $243 \times 343 \times 343$ grid points in the x, y, and z directions, respectively, and has physical domain dimensions of 12mm x 18mm x 18mm. Results are analyzed in this DNS zoom, box located at $x/D = 4.5$ from the nozzle, at $t = 80\ \text{ms}$, much greater that the initial eddy turnover time, $\tau_0 = 1.13\ \text{ms}$. Combustion takes place in the `thickened-wrinkled flame' regime [64] and [65]. Numerical values of the aero-thermo-chemical variables for this simulation are presented in Table 1.

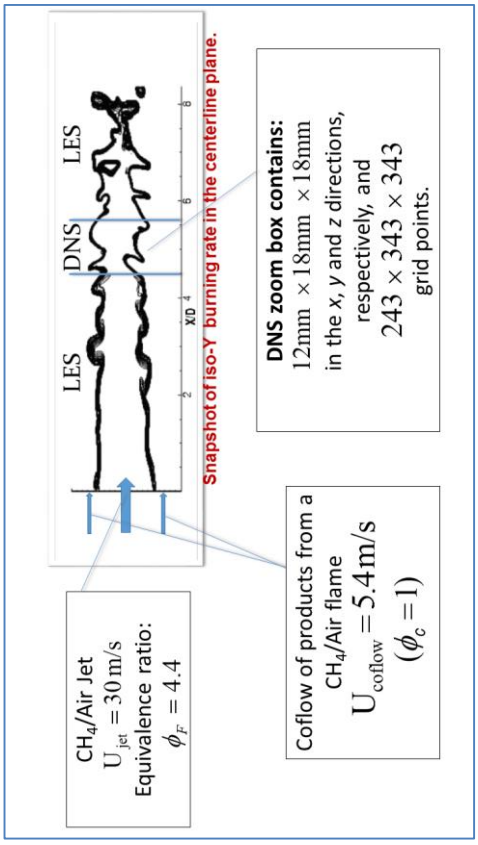

Figure 4. Description of the computational domain for the DNS of a turbulent jet premixed flame in a co-flow.

4. SOME RESULTS

Results obtained from the DNS described in the previous section are examined and compared.

Table 1. DNS dimensional variables and dimensionless parameters

Variables and dimensionless parameters	Scalar field (inert and reactive), homogeneous turbulence (constant density)	Turbulent premixed flame (variable density)	
		Inflow - outflow	Jet in co-flow
DNS grid points	$512 \times 512 \times 512$	$768 \times 512 \times 512$	$243 \times 343 \times 343$
Kinematic viscosity, ν (m^2/s)	3.5412×10^{-5}	1.56×10^{-5}	1.7×10^{-5}
Integral length scale, l (mm)	2.4	0.2962	2.4
Velocity fluctuations rms, u'(m/s)	2.12	3.20	2.12
Turbulent kinetic energy dissipation rate, $\varepsilon = u'^3/l$ (m^2/s^3)	4.0×10^3	1.1063×10^5	4.0×10^3
Kolmogorov length micro-scale, $\eta = (\nu^3/\varepsilon)^{1/4}$ (mm)	0.0577	0.0136	0.0332
Kolmogorov time micro-scale, $\tau_\eta = (\nu/\varepsilon)^{1/2}$ (ms)	0.0940	0.0118	0.0651
Non stretched laminar flame speed, S_L (m/s)	----------	1.60	0.39
Laminar flame thickness, δ_L (mm)	----------	0.0129	0.38
Final velocity ratio, u'/S_L	----------	2.0	5.43
Chemical time scale, $\tau_{ch} = \delta_L/S_L$ (ms)	----------	0.0080	0.9743
Final length ratio, l/δ_L	----------	22.96	6.31
Turbulent Reynolds number, Re	143.68	60.75	300
Karlovitz number, $Ka = \tau_{ch}/\tau_\eta$	----------	0.677	14.96
Damköler number, $Da = (l/\delta_L)/(u'/S_L)$	----------	11.48	1.16
Zeldovich number, β	----------	6.0	----------
Prandtl number, Pr	----------	0.75	0.72
Schmidt number, Sc	1.0	0.75	0.72
Lewis number, Le	----------	1.0	1.0

Figure 5 show the normal and tangential strain rates, a_N and a_T, conditioned on the scalar value at the iso-surfaces. For homogeneous turbulence in a constant density fluid, predominantly $a_N < 0$ and $a_T = -a_N > 0$. The local flow approaches iso-scalar surfaces and, simultaneously, stretches them. The chemistry slightly modifies the strain values at different constant composition surfaces. On the other hand, for the premixed flames a_T is positive everywhere and so is a_N throughout most of the computational domain; only near the extrema of Y, in the fresh gases and in the hot products, a_N can take negative values. In turbulent flames, where significant heat release occurs, $\partial v_i/\partial x_i > 0$ ([70], [74] and [75]), and therefore the probability of both $a_N > 0$ and $a_T > 0$ is high. While $a_T \approx 200\ s^{-1}$ is constant almost everywhere for the flame in the inflow-outflow configuration, a_N displays important variations over the range on compositions; moreover, $a_N > a_T$ for Y in the approximate range (0.05, 0.95), which covers the preheat and burning regions, and a significant part of the fresh gases; the maxima of a_N at $Y \approx 0.4$ (in the preheat region) is about 1200 s^{-1}, around six times the value of a_T [74]. The flow normal and tangential strain rates for the turbulent jet premixed flame display similar trends to those of the inflow-outflow case; $a_T > 0$ everywhere and depicts moderate variations for all mass fractions, reaching a maximum value of about 1500 s^{-1} at $Y \approx 0.25$; a_N is positive except for $Y \leq 0.15$ (hot products) and $Y \geq 0.95$ (fresh gases), and $a_N > a_T$ for $0.2 \leq Y \leq 0.87$ in the preheat and burning regions [75]; $a_N \approx 6100\ s^{-1}$ is the maxima at $Y \approx 0.4$. The significant differences in the local flow between the constant and variable density cases, mainly in the preheat and burning regions, emphasizes the need to account for thermal dilatation of fluid elements in the molecular mixing models for combustion; the

characteristic mixing time must be somehow related to a_N^{-1} and a_T^{-1}.

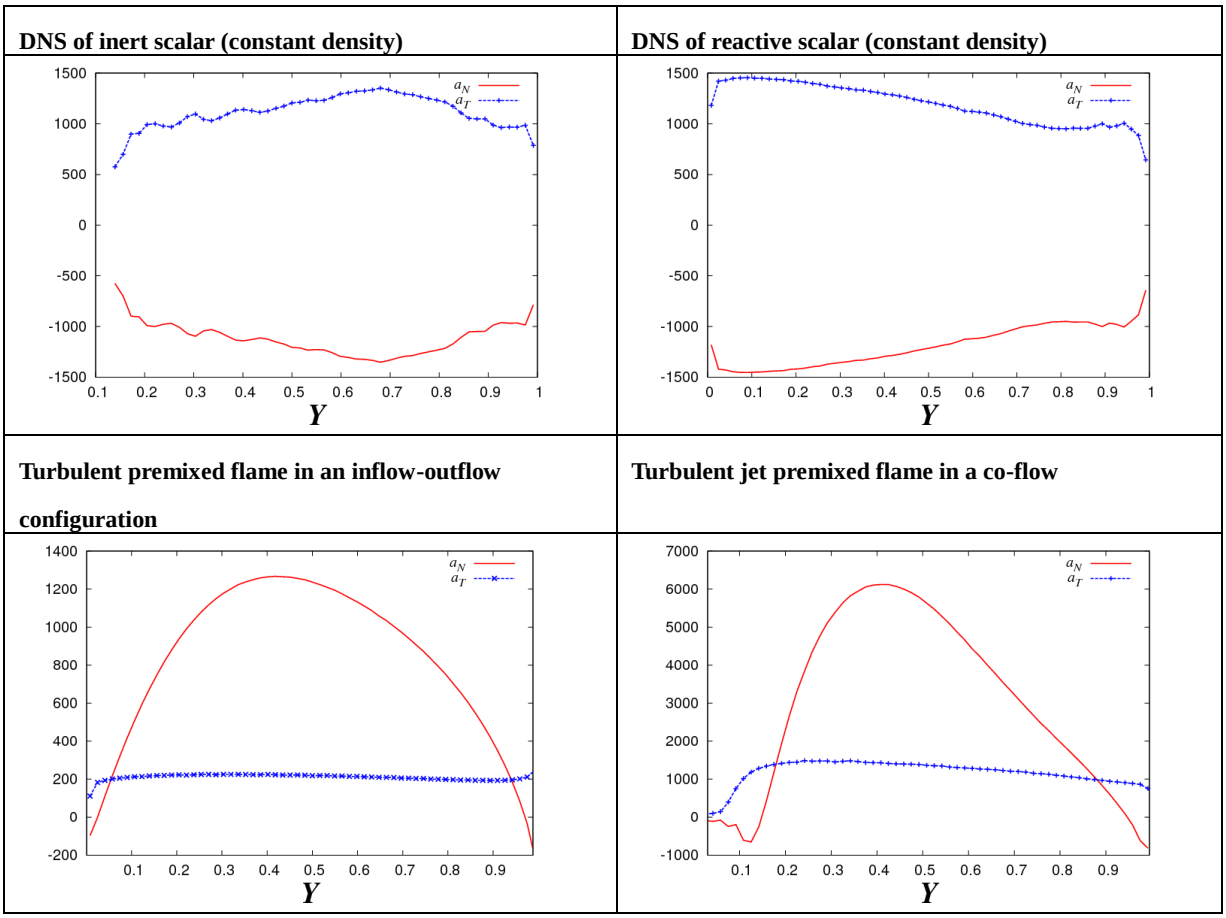

Figure 5. Flow strain rates normal, a_N, and tangential, a_T, to the iso-scalar surfaces, (s^{-1}).

Figure 6 presents the propagation velocity of iso-scalar surfaces, given by equations (30), for variable ρD, and (32), for $\rho D = \text{constant}$, conditioned on the mass fraction Y. The separate contributions of the normal and tangential (due to iso-surface curvature) molecular diffusion rates and of the chemical source term are also presented. For the constant density and inert scalar case, iso-surfaces propagate in the opposite direction of the scalar gradient for $Y < 0.7$ and in the same direction for $Y > 0.7$; the normal and tangential diffusion contributions are of the same order for all compositions. Chemistry causes a drastic change with respect to the inert scalar case, with all iso-surfaces propagating in the direction of the scalar gradient, $V^Y > 0$; the propagation velocity is higher at the scalar extrema and displays a minimum at $Y \approx 0.9$; only the normal diffusion contributes negatively for $Y < 0.25$; the tangential diffusion velocity is comparable to the normal one over most scalar values; the contribution of chemistry to the propagation speed is greater that those of diffusion for $Y < 0.47$. For the two premixed flames the curvature effects are negligible and the normal diffusion negatively contributes to the propagation speed for $Y < 0.3$ (inflow-outflow case) and for $Y < 0.37$ (turbulent jet); moreover, whereas V^Y in the inflow-outflow configuration monotonically decrease from the hot products to the fresh gases, it exhibits a maximum at around $Y = 0.1$ for the turbulent jet; differences in the treatment of the chemical kinetics in both cases can be the reason for the distinct observed behaviors, but this point deserves further attention; normal diffusion and chemical contributions are comparable for most values of Y.

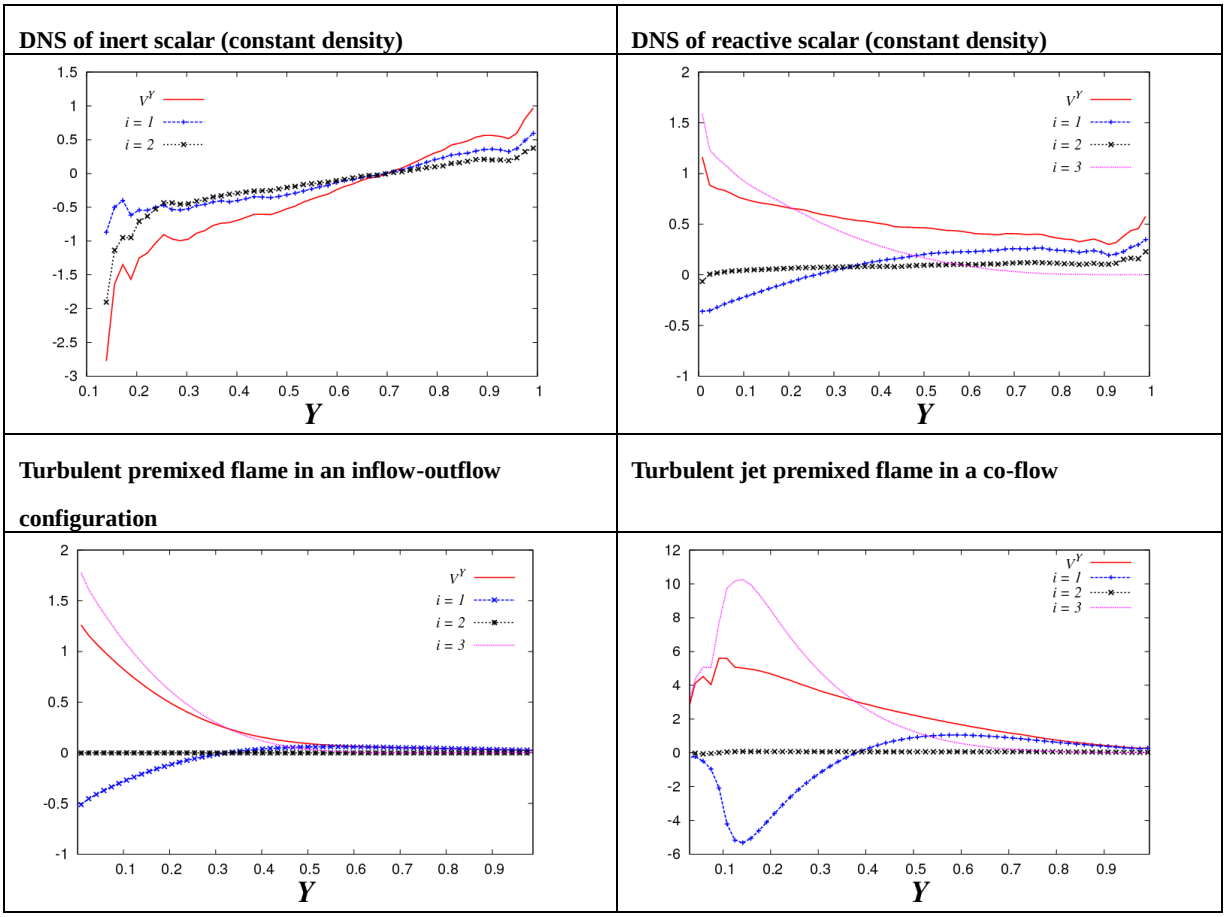

Figure 6. Iso-scalar surface normal propagation speed, V^Y, relative to the fluid (m/s) and contributions to V^Y due to normal diffusion, V_1^Y, tangential diffusion (curvature), V_2^Y, and chemical reaction, V_3^Y.

Figure 7 shows $(\partial V^Y/\partial x_N)$, given by equations (31), for variable ρD, and (33), for $\rho D = \text{constant}$, conditioned on the mass fraction Y, as well as the normal and curvature diffusions and the chemical contributions. $(\partial V^Y/\partial x_N)$ can be interpreted as an added normal strain rate due to the combined action of diffusion and chemistry. The mixing of an inert scalar in the constant density case yields a concave curve, with comparable contributions of normal and tangential diffusion and positive added strain for all compositions; chemistry shows a modest and negative contribution for $0.07 < Y < 0.7$, while the diffusion shares are modified with respect to the inert scalar over all values of the mass fraction. In this context, $(\partial V^Y/\partial x_N) > 0$ means that two adjacent iso-surfaces separate as time increases, whereas a negative value indicates that they get closer to each other; the two constant density cases produce only $(\partial V^Y/\partial x_N) > 0$. The two premixed flames evince a radically different behavior to that of the constant density mixing and reaction, with mostly $(\partial V^Y/\partial x_N) < 0$ (two iso-scalar surfaces tend thus to get closer to each other); curvature effects are negligible while normal diffusion (positive) and chemistry (negative) contributions are comparable in absolute value; for $Y < 0.15$ the two flames show different responses, with chemistry and normal diffusion almost balancing for the turbulent jet.

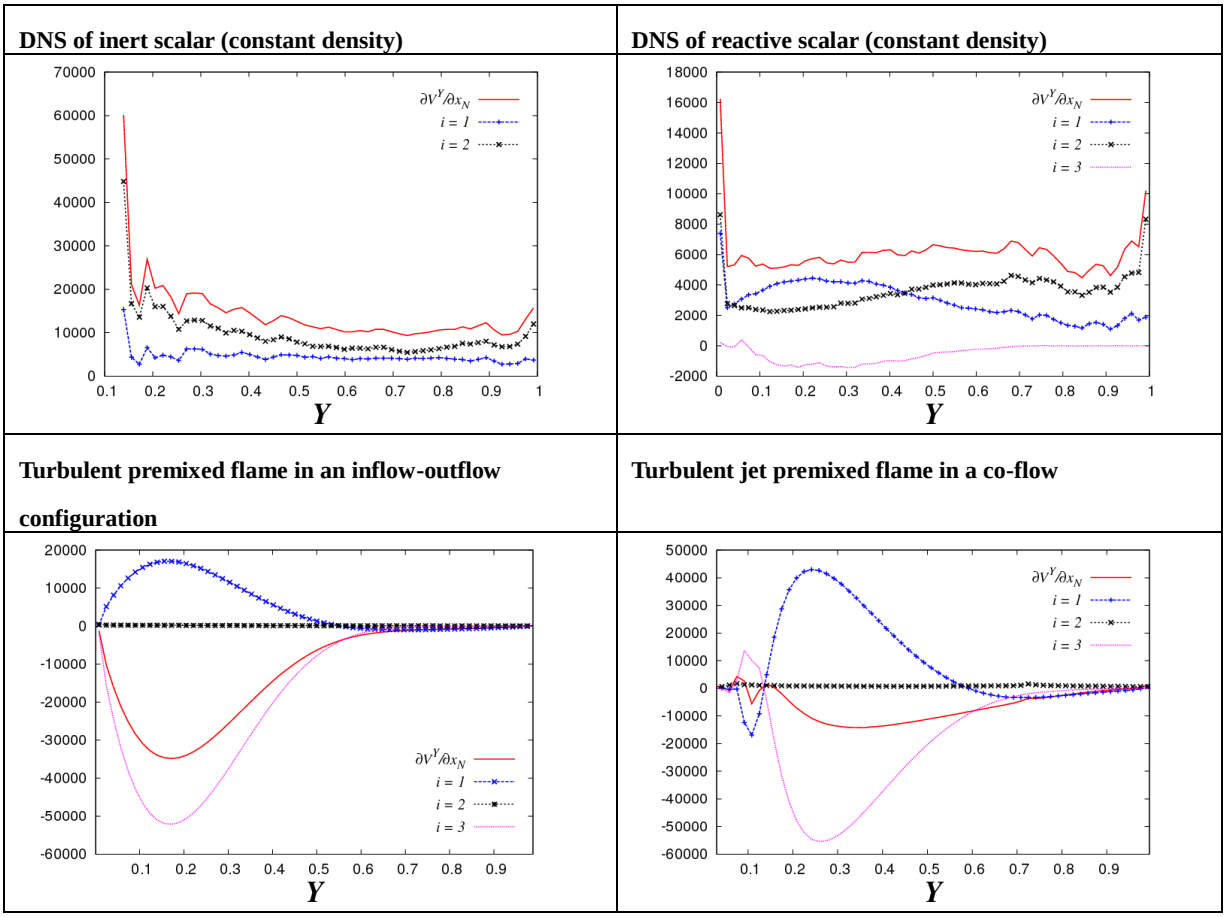

Figure 7. Derivative of V^Y in the direction normal to iso-scalar surfaces, x_N, (s^{-1}) and contributions to $\partial V^Y/\partial x_N$ due to normal diffusion, $(\partial V^Y/\partial x_N)_1$, tangential diffusion (curvature), $(\partial V^Y/\partial x_N)_2$, and chemical reaction, $(\partial V^Y/\partial x_N)_3$.

Figure 8 is a plot of $(a_N + \partial V^Y/\partial x_N)$ conditioned on the mass fraction Y. $(a_N + \partial V^Y/\partial x_N)$ is termed the 'effective' normal strain rate and enters equations (19), describing the time evolution of the infinitesimal distance separating two adjacent iso-scalar surfaces, and (29), governing the scalar gradient modulus. The latter depends on the 'effective' normal strain rate, with negative values leading to gradient enhancement as time evolves, and positive ones implying gradient reduction. The characteristic scalar mixing time must be directly related to $(a_N + \partial V^Y/\partial x_N)^{-1}$. For constant density mixing and reaction, scatter plots in Figure 8 show that positive effective normal strain rates dominate, and hence gradients should be destroyed as time progresses. On the contrary, on average $(a_N + \partial V^Y/\partial x_N) < 0$ for the two premixed flames; for the turbulent jet configuration, positive values are also common, particularly for low and high scalar values; scalar gradients and scalar fluctuation dissipation rates will thus increase with time in combusting flows with significant density variations. The latter is apparent in Figure 9 where the tails of the scalar gradient modulus pdf extends to a wider range of values for increasing times; the opposite is true for the mixing of a reactive scalar in a field of statistically homogeneous and stationary turbulence in a constant density fluid.

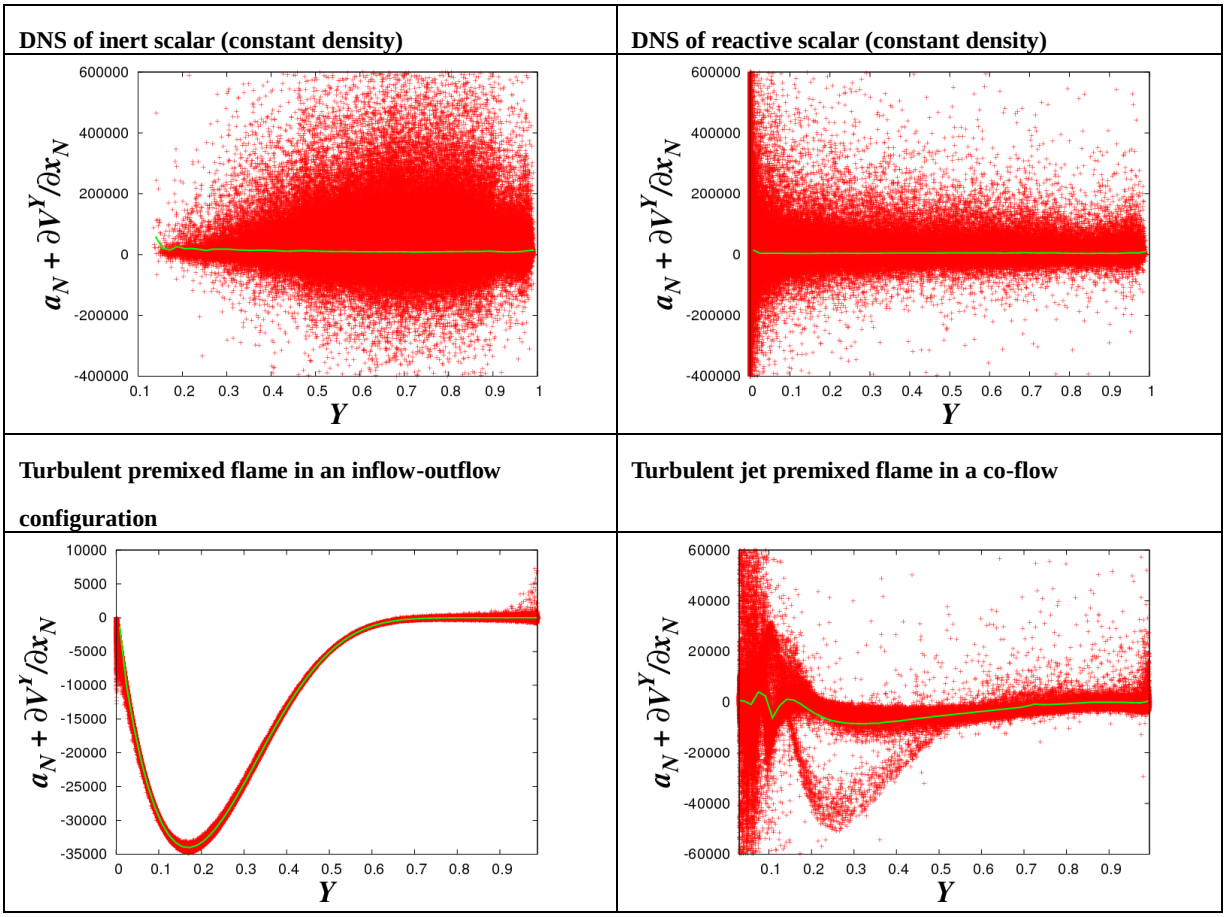

Figure 8. 'Effective' strain rate normal to iso-scalar surfaces, $(a_N + \partial V^Y/\partial x_N)(\mathrm{s}^{-1})$.

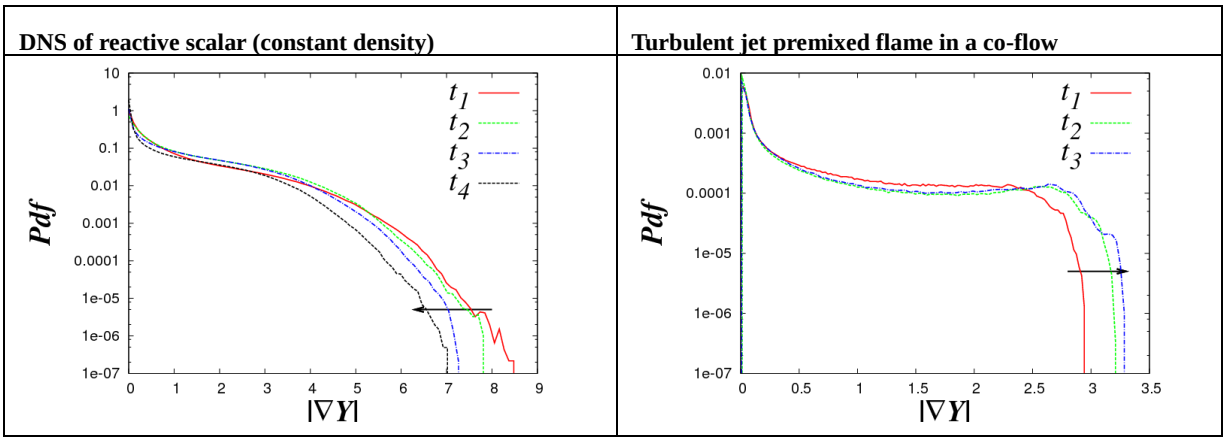

Figure 9. Scalar gradient modulus pdf's at several simulation times, $|\nabla Y|$ (mm^{-1}).

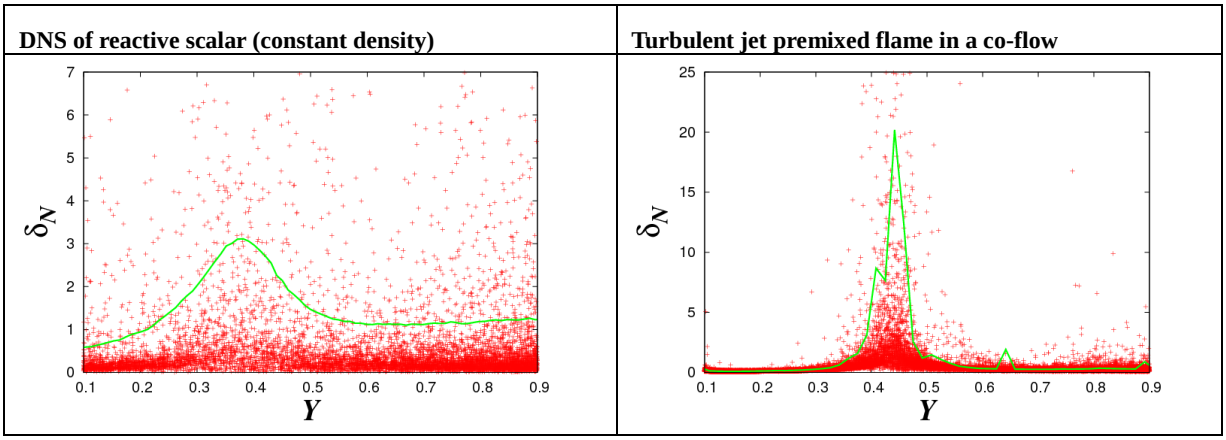

Figure 10. Characteristic iso-scalar surface separation length, δ_N (mm).

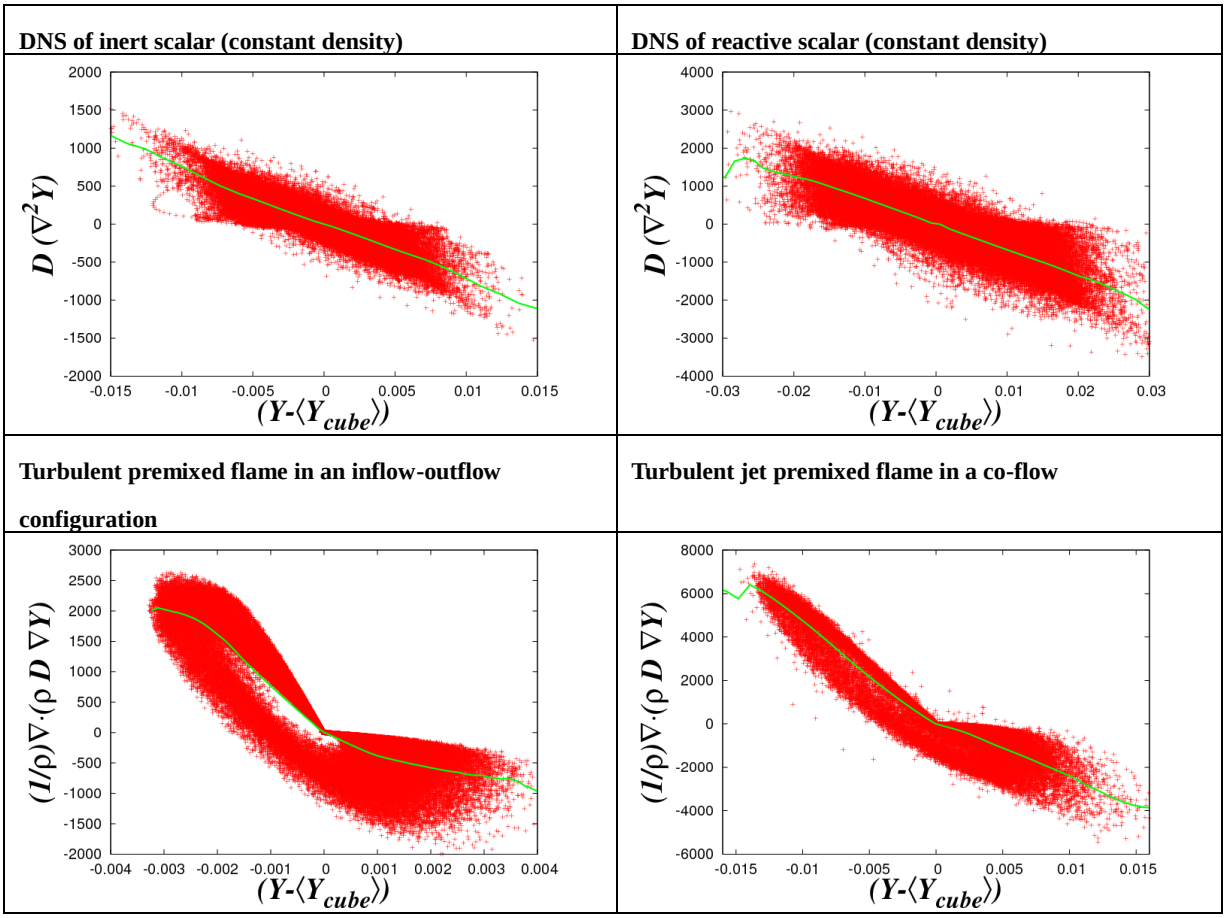

Figure 11. Molecular diffusion rates as a function of the 'scalar local fluctuations', $(1/\rho)\nabla\cdot(\rho D\nabla Y)$ (s^{-1}).

Figure 10 shows the normal length scale δ_N, defined by equation (34), conditioned on the scalar value. For mixing of a reactive scalar in a constant density turbulence, δ_N reaches a maximum value of 3.1 mm. For the turbulent jet premixed flame, δ_N displays a maximum of 20 mm at $Y \approx 0.44$ (preheat region), with much smaller values in the burning region ($0.16 \lesssim Y \lesssim 0.35$)

Figure 11 is a plot of the diffusion rates conditioned upon the scalar mass fraction as a function of $(Y - \langle Y\rangle_{cube})$. $\langle Y\rangle_{cube}$ is the average mass fraction in the neighborhood of a

computational node; in this particular instance, $\langle Y \rangle_{cube}$ is calculated as the average value of Y at 27 nodes, 26 neighboring ones and the chosen node, where the mass fraction is Y. In the limit of infinitesimal grid sizes $(D\,\nabla^2 Y)$ is well approximated by

$$(D\,\nabla^2 Y) \;=\; -\{1/[(\Delta x)^2/6\,D]\}\,[Y \;-\; \langle Y \rangle_{cube}], \qquad (40)$$

when $\Delta x \;=\; \Delta y \;=\; \Delta z$. It is apparent from the two scatter plots for constant density mixing and reaction in Figure 11, that equation (40) is a satisfactory relationship. The negative slope should be the inverse of the diffusive mixing time $[(\Delta x)^2/6\,D]$. For the 512^3 DNS, $\Delta x \;=\; \Delta y \;=\; \Delta z \;=\; 0.0324$ mm and $D \approx 3.54 \times 10^{-5}$ m^2/s. Then, $[(\Delta x)^2/6\,D] \approx 4.9$ μs; on the other hand, from Fig. 11 the estimated value of the mixing time varies around 14 μs. The inverse of the maximum value of the effective normal strain rate is of the order of 100 μs. For the premixed flames, the diffusion rate, $(1/\rho)\,\partial/\partial x_j\,[\rho D\,(\partial Y/\partial x_j)]$, includes, apart from $(D\,\nabla^2 Y)$, the normal variations of ρD, which may modify the linear dependence of equation (40); moreover, two linear dependences with two different slopes are suggested by these plots; further investigation should help to clarify whether these two slopes correspond to the preheat and burning regions of the computational domain. For LES and RANS computations the grid sizes will be much larger than those used in DNS. Should a linear dependence on $[Y - \langle Y \rangle_{cube}]$ hold, one would expect, on intuitive grounds, the slope to be proportional to $-(a_N \;+\; \partial V^Y/\partial x_N)$.

5. CONCLUSIONS AND FUTURE WORK

Scalar mixing has been revisited in the context of simple moment formulation and pdf conservation equations. Understanding the transport of iso-scalar surfaces by turbulence and by molecular diffusion is tantamount to grasp the building blocks of scalar mixing. The kinematics of non-material iso-scalar surfaces has been theoretically analyzed; the time rate of change of the infinitesimal distance between two iso-surfaces is controlled by the value of the 'effective' normal strain, which combines flow and diffusion-reaction induced strain rates. The value and sign of the 'effective' normal strain rate determines whether the modulus of scalar gradients or, equivalently, the scalar fluctuation dissipation rate, increases or decreases with time.

Expressions for the propagation speed of an iso-scalar surface relative to the fluid and its derivative, with respect to the normal direction to the constant composition surface and positive in the direction of the scalar gradient, have been obtained. Flows with constant and variable values of the product of the fluid density and the molecular diffusion coefficient are distinguished. A characteristic length scale normal to an iso-scalar surface emerges from that analysis. A dimensionless equation for the time rate of change of the infinitesimal distance between to iso-surfaces indicates that the mixing rate can be dominated by the small-scale flow features, by chemistry or by molecular diffusion, mainly depending on the value of the Karlovitz number.

DNS experiments for turbulent flows of constant and variable density fluids are described in some detail. Datasets for statistically homogeneous and stationary turbulence, as well as turbulent premixed flames in an inflow-outflow configuration and in a jet with a co-flow of hot products have been examined. Flow normal strain rates, iso-surfaces propagation speeds and normal derivatives are radically different for the homogeneous turbulence and for the premixed flames. While the flow normal strain rate is mainly positive for constant density flows, heat release by flames causes its values to be positive over most of the computational flow domain; the profiles of the propagation speed and its derivative as a function of composition are also drastically different for constant and variable density flows. As a consequence, the 'effective' normal strain rate, whose sign determines the temporal growth or decay of scalar gradients and dissipation rates, are predominantly positive for constant density turbulence and mostly negative in the cases of premixed flames. Scalar gradient pdf clearly shows enhancement with time in turbulent premixed flames, and destruction for constant density mixing-reaction. The approximation of the scalar Laplacian by a linear function of the mass fraction with a negative slope is apparent for constant density turbulence.

The improved physical understanding of mixing resulting from this study should be used in the development of molecular mixing models, particularly those for combusting turbulent flows. The functional dependence of the molecular diffusion term on the mass fraction and the relevance of the 'effective' normal strain rate as a characteristic, mixing rate should be scrutinized. The implementation in the molecular mixing models of the dimensional or dimensionless equations for the time rate of change of the infinitesimal distance between two adjacent iso-surfaces should be one of the main objectives in the short term. The various limits pointed out in our analysis should be scrutinized. The usefulness of the characteristic normal distance defined in this research must be clarified.

6. ACKNOWLEDGEMENTS

This research has been sponsored through the Project CS D2010-00011-SCORE, funded under the CONSOLIDER-INGENIO Program of the Spanish Ministry of Economy and Competitiveness. The authors are indebted to Drs. L. Vervisch and P. Domingo for making available to them their DNS database for a turbulent jet premixed flame. We also thank Dr. M.C. Jimenez, who, apart from allowing the authors to use her DNS dataset for a turbulent flame in an inflow-outflow configuration, has always been willing to provide useful advice and criticism.

REFERENCES

1. 1. R. Everson, D. Manin and L. Sirovich, Quantification of Mixing and Mixing Rate from Experimental Observations, AIAA Journal 36, 121-127, 1998.

2. A.Y. Klimenko, What is mixing and can it be complex?, Phys. Scr T155, 014047, 2013.
3. S. Corrsin, Some statistical properties of the product of a turbulent, first-order reaction, Proc. Symp. Fluid Dynam. Appl. Math, Univ. Maryland, Gordon & Breach, Publ., pp. 105-124, 1961.
4. A. M. Oboukhov, Structure of the temperature field in turbulent flow, Izv. Akad. Nauk SSSR, Geogr. Geophys. Ser., 13, 58-69, 1949.
5. S. Corrsin, On the spectrum of isotropic temperature fluctuations in an isotropic turbulence, J. Appl. Phys. 22, 469-473, 1951.
6. G.K. Batchelor, Small scale variation of convected quantities like temperature in turbulent fluid. Part 1. General discussion and the case of small conductivity, J. Fluid Mech., 5, 113-134, 1959.
7. S. Tavoularis and S. Corrsin, Experiments in nearly homogeneous turbulent shear flow with a uniform mean temperature gradient. Part 1, J. Fluid Mech., 104, 311-347, 1981.
8. S. Tavoularis and S. Corrsin, Experiments in nearly homogeneous turbulent shear flow with a uniform mean temperature gradient. Part 2. The fine structure, J. Fluid Mech., 104, 349-367, 1981.
9. K.R. Sreenivasan, On local isotropy of passive scalars in turbulent shear flows, Proc. R. Soc. London A 434, 165-182, 1991.
10. Z. Warhaft, Passive scalars in turbulent flows, Ann. Rev. Fluid Mech., 32, 203-240, 2000.
11. G. Brethouwer, Mixing of passive and reactive scalars in turbulent flows. A numerical study, Doctoral Dissertation, Technische Universiteit Delft, 2000.
12. P.K. Yeung, S. Xu and K.R. Sreenivasan, Schmidt number effects on turbulent transport with uniform mean scalar gradients, Phys. Fluids 14, 4178-4191, 2002.
13. G.L. Brown and A. Roshko, On density effects and large structure in turbulent mixing layers, J. Fluid Mech. 64, 775-816, 1974.
14. J.C. Lasheras and H. Choi, Three-dimensional instability of a plane free shear layer: an experimental study of the formation and evolution of streamwise vortices, J. Fluid Mech. 189, 53-86, 1988.
15. A. D'Ovidio and C.M. Coats, Organized large structure in the post-transition mixing layer. Part 1. Experimental evidence, J. Fluid Mech., 737, 466-498, 2013.
16. R.D. Moser and M.M. Rogers, Mixing transition and the cascade to small scales in a plane mixing layer, Phys. Fluids A, 3, 1128-1134, 1991.
17. J.E. Broadwell and M.G. Mungal, Large-scale structures and molecular mixing, Phys. Fluids A, 3, 1193-1206, 1991.
18. Dopazo, C., Calvo, P. and Petriz, F., A geometric/kinematic interpretation of scalar mixing, Phys. Fluids 11, 2952-2956, 1999.
19. H.K. Moffatt. The topology of turbulence. Springer, Berlin 2001.
20. Kim, S.H. and Bilger, R.W., Iso-surface mass flow density and its implications for turbulent mixing and combustion, J. Fluid Mech. 590, 381-409, 2007.
21. C. Dopazo, J. Martin, and J. Hierro, Iso–scalar surfaces, mixing and reaction in turbulent flows, C. R. Mecanique, 334, 483–492, 2006.
22. C. Dopazo, J. Martin, and J. Hierro. Local geometry of isoscalar surfaces, Phys. Rev. E, 76, 056316/1–056316/11, 2007.
23. C.H. Gibson. Fine structure of scalar fields mixed by turbulence: I. zero-gradient points and minimal gradient surfaces. Phys. Fluids, 11, 2305–2315, 1968.
24. L. Wang and N. Peters. The length-scale distribution function of the distance between extremal points in passive scalar turbulence, J. Fluid Mech., 554, 457–475, 2006.
25. R.A.C. Griffiths, J.H. Chen, H. Kolla, R.S. Cant and W. Kollmann, Three-dimensional topology of turbulent premixed flame interaction, Proc. Combust. Inst., San Francisco, 2014.
26. R.M. Kerr, Higher-order derivative correlations and the alignment of small-scale structures in isotropic numerical turbulence, J. Fluid Mech., 153, 31–58, 1985.
27. W. Ashurst, A. Kerstein, R. Kerr, and C. Gibson, Alignment of vorticity and scalar gradient in simulated Navier-Stokes turbulence, Phys. Fluids 30, 2343–2353, 1987.
28. M. Chong, A. Perry, and B. Cantwell. A general classification of three-dimensional flow fields, Phys. Fluids 2, 765–777, 1990.
29. A. Ooi, J. Martin, J. Soria, and M. Chong, A study of the evolution and characteristics of the invariants of the velocity-gradient tensor in isotropic turbulence, J. Fluid Mech., 381, 141–174, 1999.
30. E. Elsinga and I. Marusic, Universal aspects of small-scale motions in turbulence, J. Fluid Mech., 662, 514–539, 2010.
31. J. Chen, M. Chong, J. Soria, R. Sondergaard, A. Perry, M. Rogers, R. Moser and B. Cantwell, A study of the topology of dissipating motions in direct numerical simulations of time-developing compressible and incompressible mixing layers, Center for Turbulence Research, pp. 141–164, 1990.
32. M. Tanahashi, M. Fujimura, and T. Miyauchi, Coherent fine-scale eddies in turbulent premixed flames, Proc. Comb. Inst., 28, 529–535, 2000.
33. L. Wang and X. Lu, Flow topology in compressible turbulent boundary layer, J. Fluid Mech., 703, 255–278, 2012.
34. S. Corrsin, Statistical behavior of a reacting mixture in isotropic turbulence, Phys. Fluids 1, 42, 1958.
35. S. Corrsin, The reactant concentration spectrum in turbulent mixing with a first-order reaction, J. Fluid Mech. 11, 407-416, 1961.
36. E.E. O'Brien, On the statistical behavior of a dilute reactant in isotropic turbulence, Doctoral Dissertation, The Johns Hopkins Univ., 1960.
37. E.E. O'Brien, Closure for stochastically distributed second-order reactants, Phys. Fluids 11, 1883-1888, 1968.
38. E.E. O'Brien, Lagrangian History Direct Interaction equations for isotropic turbulent mixing under a

second-order chemical reaction, Phys. Fluids 11, 2328-2335, 1968.
39. C. Dopazo and E.E. O'Brien, Functional formulation of nonisothermal turbulent reactive flows, Phys. Fluids 17, 1968-1975, 1974.
40. C. Dopazo and E.E. O'Brien, An approach to the auto ignition of a turbulent mixture, Acta Astron., 1, 1239-1266, 1974.
41. T.S. Lundgren, Distribution functions in the statistical theory of turbulence, Phys. Fluids 10, 969-975, 1967.
42. C. Dopazo, Relaxation of initial probability density functions in the turbulent convection of scalar fields, Phys. Fluids 22, 20-30, 1979.
43. J. Janicka, W. Kolbe and W. Kollmann, Closure of the transport-equation for the probability density function of turbulent scalar fields, J. Non-Equilibrium Thermodyn., 4, 47-66, 1979.
44. R.L. Curl, Dispersed phase mixing. I. Theory and effects in simple reactors, AIChE J., 9, 175-181, 1963.
45. L. Valino and C. Dopazo, A binomial Langevin model for turbulent mixing, Phys. Fluids A 3, 3034-3037, 1991.
46. R.C. Flagan and J.P., Appleton, A stochastic model of turbulent mixing with chemical reaction: Nitric oxide formation in a plug-flow burner, Combust. Flame 23, 249-267, 1974.
47. S.B. Pope, Pdf methods for turbulent flows, Progress Energy Combust. Sci., 11, 119-192, 1985.
48. E.E. O'Brien, The probability density function (pdf) approach to reacting turbulent flows, in 'Turbulent Reacting Flows', P. Libby and F.A Williams (Eds.), p. 185, Springer-Verlag, Berlin, 1980.
49. C. Dopazo, Recent developments in pdf methods, Ch. 7 in 'Turbulent Reactive Flows', P. Libby and F.A Williams (Eds.), Academic Press, New York, 1994.
50. D.C. Haworth, Progress in probability density function methods for turbulent reacting flows, Progress Energy Combust. Sci., 36, 168-259, 2010.
51. R.O. Fox, Computational models for turbulent reacting flows, Cambridge Univ. Press, 2004.
52. S. Subramanian and S.B. Pope, A mixing model for turbulent reactive flows based on Euclidean Minimum Spanning Trees, Combust. Flame, 115, 487-514, 1998.
53. S.B. Pope, A model for turbulent mixing based on shadow-position conditioning, Phys. Fluids 25, 110803, 2013.
54. D.W. Meyer and R. Deb, Modelling molecular mixing in spatially inhomogeneous turbulent flow, Phys. Fluids 24, 025103, 2012.
55. M.J. Cleary, A.Y. Klimenko, J. Janicka and M. Pfitzner, A sparse-Lagrangian multiple mapping conditioning model for turbulent diffusion flames, Proc. Combust. Inst. 32, 1499-1507, 2009.
56. R.E. Meyers and E.E. O'Brien, The joint PDF of a scalar and its gradient at a point in a turbulent fluid, Combust. Sci. Tech., 26, 123-134, 1981.
57. L. Valino, A field MonteCarlo formulation for calculating the probability density function of a single scalar in a turbulent flow, J. Flow Turb. Combust. 60, 157-172, 1998.
58. A. Kerstein, A linear-eddy model of turbulent scalar transport and mixing, Comb. Sci. Tech., 60, 391-421, 1988.
59. A. Kerstein, One-dimensional turbulence: model formulation and application to homogeneous turbulence, shear flows and buoyant stratified flows, J. Fluid Mech., 392, 277-334, 1999.
60. S. Orszag and G. Patterson, Numerical simulation of three-dimensional homogeneous isotropic turbulence, Physical Review Letters, 12, 76–79, 1972.
61. R.S. Rogallo, Numerical experiments in homogeneous turbulence, NASA TM 81315, NASA Ames Research Center, CA, 1981.
62. V. Eswaran and S.B. Pope, An examination of forcing in direct numerical simulations of turbulence, Comp. Fluids, 16, 3, 257–278, 1988.
63. M. Matalon, Flame dynamics, Proc. Combust. Inst. 32, 57-82, 2009.
64. R. Borghi. On the structure and morphology of turbulent premixed flames, in 'Recent Advances in Aerospace Science', C. Bruno and C. Casci (Eds.), pp. 117–138, 1985.
65. T. Poinsot and D. Veynante, Theoretical and Numerical Combustion, Edwards, 2001.
66. D. Veynante and L. Vervisch, Turbulent combustion modeling, Prog. Energy. Combust. Sci., 28, 193–266, 2002.
67. S.M. Candel and T. Poinsot, Flame Stretch and Balance Equation for the Flame Area, Combust. Sci. and Tech, 70, 1-15, 1990.
68. L. Vervisch, E. Bidaux, K.N.C. Bray and W. Kollmann, Surface density function in premixed turbulent combustion modeling. Similarities between probability density function and flame surface approaches, Phys. Fluids 7, 2496-2503, 1995.
69. G. Hartung, J. Hult, C. Kaminski, J. Rogerson, and N. Swaminathan, Effect of heat release on turbulence and scalar-turbulence interaction in premixed combustion, Phys. Fluids 20, 035110/1–16, 2008.
70. C. Dopazo, L. Cifuentes, J. Martin and C. Jimenez, Strain rates normal to approaching iso-scalar surfaces in a turbulent premixed flame, Combust. Flame (submitted for publication), 2014.
71. N. Chakraborty, N., Comparison of displacement speed statistics of turbulent premixed flames in the regimes representing combustion in corrugated flamelets and thin reaction zones, Phys. Fluids 19, 105109, 2007.
72. N. Chakraborty and N. Swaminathan, Influence of the Damköhler number on turbulence-scalar interaction in premixed flames. I. Physical insight, Phys. Fluids 19, 045103/1-10, 2007.
73. N. Chakraborty, M. Klein and N. Swaminathan, Effects of Lewis number on the reactive scalar gradient alignment with local strain rate in turbulent premixed flames, Proc. Combust. Inst. 32, 1409-1417, 2009.

74. L. Cifuentes, C. Dopazo, J. Martin and C. Jimenez, Local flow topologies and scalar structures in a turbulent premixed flame, Phys. Fluids 26, 065108/1-24, 2014.
75. L. Cifuentes, C. Dopazo, J. Martin, P. Domingo and L. Vervisch, Local volumetric dilatation rate and scalar geometries in a premixed methane-air turbulent jet flame, Proc. Combust. Inst., vol. 35, 2014, http://dx.doi.org/10.1016/j.proci.2014.06.026.
76. R. Chandra, L. Dagun, D. Kohr, J. Maydan, D. Mcdonald, and R. Menon. Parallel programming in OpenMP. Morgan Kaufmann Publishers, 2001.
77. B. Chapman, G. Jost, and R. Van der Pas. Using OpenMP: Portable Shared Memory Parallel Programming. The MIT Press. Library of Congress Cataloging-in-Publication Data, 2008.
78. R. Peyret. Spectral methods for incompressible viscous flow - Applied mathematical sciences, volume 148. Springer-Verlag, 2000.
79. C. Dopazo, J. Martin, and J. Hierro, Iso-scalar surfaces, mixing and reaction in turbulent flows, C. R. Mec. 334, 483–492, 2006.
80. C. Dopazo, J. Martin, and J. Hierro, Local geometry of isoscalar surfaces, Phys. Rev. E 76, 056316, 2007.
81. V. Eswaran and S. Pope, Direct numerical simulations of the turbulent mixing of a passive scalar, Phys. Fluids 31(3), 506–520, 1988.
82. M. Ditaranto and J. Hals. Combustion instabilities in sudden expansion oxy–fuel flames, Combust. Flame 146, 493–512, 2006.
83. B. Cuenot, B. Bedat, and A. Corjon, NTMIX3D User's Guide, volume 1.0. 1997.
84. T. Poinsot and S. Lele. Boundary conditions for direct simulations of compressible viscous flows. J. Comput. Phys., 101, 104–129, 1992.
85. P.S. Pacheco. A User's Guide to MPI. San Francisco, CA 94117, 1998.
86. P.S. Pacheco and W.C. Ming. Introduction to Message Passing Programming: MPI User's Guide in FORTRAN. San Francisco, CA 94117; Hong Kong, 1998.
87. O. Gicquel, N. Darabiha, and D. Thevenin. Laminar premixed hydrogen/air counterflow flame simulations using flame prolongation of ildm with differential diffusion. Proc. Comb. Inst., 28:1901–1908, 2000.
88. G. Godel, P. Domingo, and L. Vervisch. Tabulation of nox chemistry for large-eddy simulation of non-premixed turbulent flames. Proc. Combust. Inst., 32:1555–1561, 2008.

F

Effects of the local flow topologies upon the structure of a premixed methane-air turbulent jet flame

SPEIC14 – Towards Sustainable Combustion
November 19-21, 2014, Lisboa, Portugal

Effects of the local flow topologies upon the structure of a premixed methane-air turbulent jet flame

Luis Cifuentes*, Cesar Dopazo*, Jesus Martin*, Pascale Domingo and Luc Vervisch****

*LIFTEC, CSIC - University of Zaragoza, Calle Maria de Luna 3, 50018, Spain
**CORIA - CNRS, Normandie Université, INSA de Rouen, Saint-Etienne du Rouvray, 76801, France
E-mai: lcifuentes@unizar.es

ABSTRACT

Local flow topologies have been identified and the interactions of them with the iso-scalar surfaces geometries have been investigated using the results of a three-dimensional direct numerical simulation (DNS) of a turbulent premixed methane-air flame in a piloted Bunsen burner configuration with tabulated chemistry. The universal teardrop shape of the joint probability density function (jpdf) of the second and third invariants of the velocity-gradient tensor disappears in the different flame regions under study. A 'canonical' vortex, which affects the fine-scale structure of the turbulent premixed flame, has been identified and analyzed at three times, differing by increments of the order of the Kolmogorov time micro-scale.

***Keywords**: Local flow topologies, iso-scalar surface geometries, invariants of the velocity-gradient tensor, turbulent premixed flame, direct numerical simulation.*

1. INTRODUCTION

Combustion instabilities can be created, in particular, by the effects of differential and preferential diffusion, thermal expansion, or heat losses. For premixed flames, thermal expansion plays an important role in the hydrodynamic instability: it creates sharp folds in the flame front. On the other hand, in a turbulent premixed flame there are external perturbations, different from diffusive-thermal effects, coming from the turbulent field in which the flame front propagates. The effects of these perturbations might be investigated through the small-scale local flow topologies [1], which in interaction with the flame front might create stretching, quenching and high curvature values of the iso-scalar surfaces.

Local flow topology of turbulent flows has been the focus of many discussions. Intuitively, a local topology is a three-dimensional region in the flow over which some properties of the flow exhibit significant correlation in space and time. Theoretical studies and direct numerical simulations have been performed to analyze and visualize these organized small-scale structures of turbulent flow. The seminal ideas were introduced by Perry and Chong [2], and Chong *et al.* [1]. They proposed a topological approach to typify elementary three-dimensional flow patterns using the three invariants, P, Q, R, of the velocity-gradient tensor. In incompressible turbulent flows (constant-density), the first invariant of the velocity-gradient tensor, $P = -\nabla \cdot \mathbf{u}$, is zero due to continuity, and the turbulent flow can be described in the two-dimensional plane of the second Q and third R invariants of the velocity-gradient tensor. A universal teardrop shape of the joint probability density function of Q and R was observed for a wide variety of incompressible turbulence (Soria *et al.* [3]; Blackburn *et al.* [4]; Chong *et al.* [5]; Chacin and Cantwell [6]; Ooi *et al.* [7]; Da Silva and Pereira [8]). In variable-density turbulent flows, the teardrop shape of the jpdf of R and Q remains for zones with $P = 0$ but depending on the region under study (compression or expansion regions, $P > 0$ or $P < 0$, respectively) the statistical distributions are displaced towards the left or the right side (Suman and Girimaji [9]; Wang and Lu [10]; Chu and Lu [11], Cifuentes *et al.* [12]).

Our main concern in this paper is to explore the influence of the local flow topologies characterized by the invariants, P, Q, R, of the velocity-gradient tensor [1,2] upon the iso-scalar surfaces (further details of P, Q, R have been described in Cifuentes *et al.* [12]). For this purpose, a turbulent premixed methane-air flame in a piloted Bunsen burner configuration has been investigated using the results of a three-dimensional direct numerical simulation zoom at three times differing by increments of the order of the Kolmogorov time micro-scale. As a reminder, the local flow topologies are plotted in Figure 1.

2. MATHEMATICAL DESCRIPTION AND IMBEDDED DNS IN LES

The analysis is performed in a jet-flame configuration simulated with a hybrid Large Eddy Simulation (LES)/DNS approach. A methane-air mixture is injected through a central jet with a mean velocity $U_{jet} = 30\ \mathrm{m/s}$, and equivalence ratio $\emptyset_F = 4.4$, surrounded by a co-flow of burned products with a mean velocity $U_{coflow} = 5.4\ \mathrm{m/s}$, and equivalence ratio $\emptyset_c = 1$. The LES mesh has about 171 million nodes, with a resolution varying between $150\mu\mathrm{m}$ and $200\mu\mathrm{m}$. An imbedded zone within the LES mesh features a much higher resolution of $50\mu\mathrm{m}$. Results are analyzed in this DNS zoom box at $t = 80\mathrm{ms}$, which is much greater that one initial integral eddy turnover time, $\tau_0 = 1.13\mathrm{ms}$. The chemistry is tabulated with the FPI (Flame-Prolongation of ILDM) flamelet approach [13]. A reaction progress variable, c, based on a single progress variable Y_c defined by Godel *et al.* [14], $Y_c = Y_{CO} + Y_{CO2} + (Y_{N2} - Y_{N2}^0) + (Y_{H2O} - Y_{H2O}^0) + Y_{NO} + Y_{NO2} + Y_{N2O}$, is used in this case. c is defined as follows:

$$c = \frac{Y_c}{Y_c^{eq}} \ , \tag{1}$$

where the 'eq' superscript designates the value of the corresponding variable in the burnt state of the laminar-premixed flame. Y_{N2}^0 and Y_{H2O}^0 are, respectively, the mass fractions of N_2 and H_2O in fresh gases. Y_{N2}^0 and Y_{H2O}^0 ensures that $Y_c = 0$ in fresh gases for all mixing conditions.

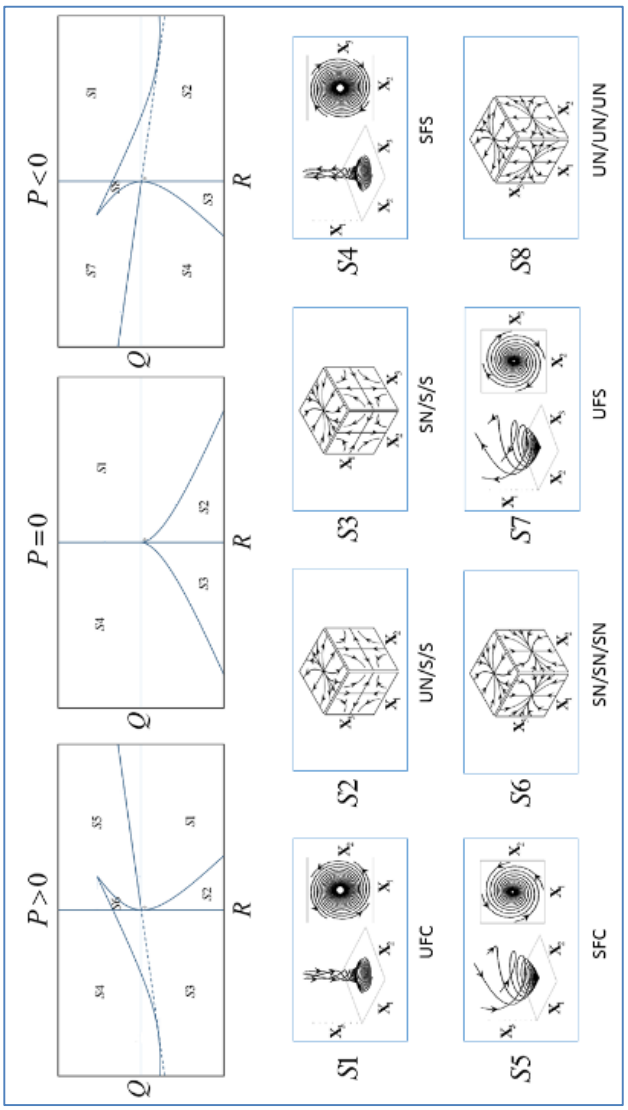

Figure 1. (Color online) Classification of the different topologies in the $Q-R$ plane for: $P>0$ (element compression), $P=0$ (zero dilatation), and $P<0$ (local fluid expansion). The acronyms are as follows: UFC (Unstable focus/compressing), UN/S/S (Unstable node / Saddle / saddle), SN/S/S (Stable node / saddle / saddle), SFS (Stable focus / stretching), SFC (Stable focus / compressing), SN/SN/SN (Stable node / stable node / stable node), UFS (Unstable focus / stretching), and UN/UN/UN (Unstable node / unstable node / unstable node).

The fully parallel compressible solver SiTCom (Simulating Turbulent Combustion) is used to integrate the governing equations, which can then be written in Cartesian tensor notation as mass continuity:

$$\frac{\partial \rho}{\partial t} + \frac{\partial (\rho u_i)}{\partial x_i} = 0 \ , \tag{2}$$

momentum equation:

$$\frac{\partial (\rho u_i)}{\partial t} + \frac{\partial (\rho u_j u_i)}{\partial x_j} = -\frac{\partial p}{\partial x_i} + \frac{\partial \tau_{ij}}{\partial x_j} \ , \tag{3}$$

energy equation in the form of $E = e_s + (u_i u_i)/2$, sensible plus kinetic energy:

$$\frac{\partial (\rho E)}{\partial t} + \frac{\partial (\rho u_i E)}{\partial x_i} = -\frac{\partial (p u_j)}{\partial x_j} + \frac{\partial (\tau_{ij} u_i)}{\partial x_j} + \frac{\partial}{\partial x_i}\left(\lambda \frac{\partial T}{\partial x_i}\right) + \dot{\omega}_T \ , \tag{4}$$

and reaction progress variable Y_c:

$$\frac{\partial (\rho Y_c)}{\partial t} + \frac{\partial (\rho u_i Y_c)}{\partial x_i} = \frac{\partial}{\partial x_i}\left(\rho D \frac{\partial Y_c}{\partial x_i}\right) + \dot{\omega}_{Y_c} \ , \tag{5}$$

In these balance equations, t and x_i stand for time and ith component of the position vector, respectively. ρ denotes density, u_i is the ith component of velocity, p is the pressure, τ_{ij} is the ij component of the viscous stress tensor, given by the Navier-Poisson constitutive relation [15], λ is the thermal conductivity, D is the mass diffusivity, $\dot{\omega}_{Yc}$ is the reaction rate of the progress variable and $\dot{\omega}_T$ is the heat release due to combustion. Thermodynamic variables are related by the perfect gas equation of state, $p = \rho RT/W$, where R is the universal perfect gas constant and W is the mean molecular weight. Table 1 summarizes the numerical values of the aero-thermo-chemical variables for this simulation. The velocity and length ratios are $u'/S_L = 5.43$ and $l/\delta = 6.3$, respectively, therefore combustion takes place in the 'thickened-wrinkled flame' regime [15,16,17], as shown in Figure 2. Further details of computational approach have been described in Cifuentes *et al.* [18].

Table 1. Values of dimensionless parameters and physical variables.

Parameter	Value
Prandtl number, Pr	0.72
Schmidt number, Sc	0.72
Lewis number, Le	1.0
rms of velocity fluctuations, u'	2.12 (m/s)
Integral length scale, l	2.4 (mm)
Turbulent kinetic energy dissipation rate, ε	4.0e+3 (m^2/s^3)
Kolmogorov length micro-scale, η	3.3291e-2 (mm)
Kolmogorov time micro-scale, τ_η	6.5192e-2 (ms)
Non stretched laminar flame velocity, S_L	0.39 (m/s)
Laminar flame thickness, δ_L	0.38 (mm)
Chemical time scale, τ_{ch}	0.97 (ms)
Velocity ratio, u'/S_L	5.43
Length ratio, l/δ_L	6.31
Turbulent Reynolds number, Re_T	300
Damköhler number, $Da = (l/\delta_L)/(u'/S_L)$	1.16
Karlovitz number, $Ka = \tau_{ch}/\tau_\eta$	14.87

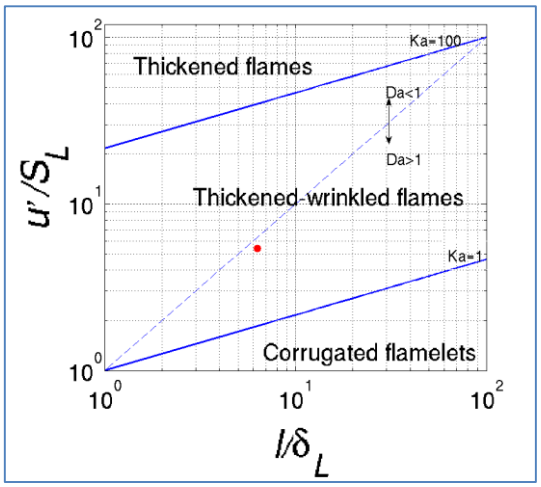

Figure 2. (Color online) Turbulent combustion diagram. The red point indicates the case under study.

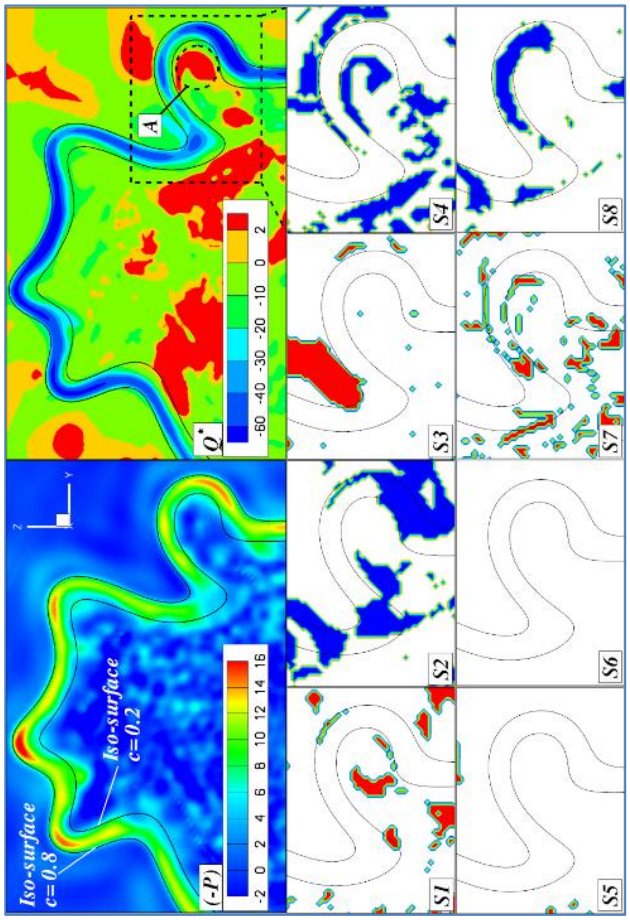

Figure 3. (Color online) $(-P) = \nabla \cdot \mathbf{u}$, Q^* and flow topologies (S1 - S8) in the computational domain. $(-P)$ and Q^* have been normalized with $\langle \nabla \cdot \mathbf{u} \rangle$ and $\langle \nabla \cdot \mathbf{u} \rangle^2$, respectively. $\langle \nabla \cdot \mathbf{u} \rangle$ has been obtained using all the samples of the four reaction-rate conditioned regions summarizes in Table 2.

3. RESULTS AND DISCUSSION

Figure 3 shows the zoom of a $y-z$ plane of the computational domain. This zoom displays two scalar iso-lines, the volumetric dilatation rate $(-P) = \nabla \cdot \mathbf{u}$, the flow topologies from S1 to S8 and the Q^* invariant used by Hunt *et al.* [19],

$$Q^* \equiv \left(-S_{ij}S_{ij} + W_{ij}W_{ij}\right)/2, \quad (6)$$

where S_{ij} and W_{ij} denote symmetric and asymmetric component of the velocity-gradient tensor, respectively. Q^* separates strain dominated regions $(Q^* < 0)$ from coherent fine scale eddies $(Q^* > 0)$.

It can be seen in Figure 3 that local expansion $(-P < 0)$ is significant between the iso-lines, with maximum (minimum) values associated to concave (convex) scalar geometries. These processes can be explained by the heat conduction focussing (defocussing) effect of the scalar concave (convex) structures. High positive values of $(-P)$ also highlight a zone between the scalar iso-lines where an intense thermo-chemical activity prevails. The dotted black circle $'A'$ marks a zone with $Q^* > 0$, which can be considered like a 'canonical' vortex. The identified vortex tends to fold the flame front. It can also be noted high stretching zones $(Q^* < 0)$ found into the flame with joint interactions of unstable topologies, such as S2 (UN/S/S) and S8 (UN/UN/UN). The latter has been identified as a typical topology of combusting flows with significant heat release [12]. It is apparent that the S3 (SN/S/S), S5 (SFC) and S6 (SN/SN/SN) topologies are absent in this flame.

It is clear that, at least locally, geometrical scalar structures and flow topologies change in the normal direction to the iso-surfaces. Thus, it is useful to analyze the results in different regions of the computational domain. Tabla 2 summarizes the intervals for different regions depending on the scalar values: 'fresh reactants', 'preheat region', 'burning region' and 'hot products'. These four reaction-rate conditioned regions have already been investigated in previous works [12,18].

Table 2. Ranges corresponding to scalar values for the different regions of the computational domain.

Region	Range
Fresh reactants	$0.001 < c < 0.200$
Preheat region	$0.200 < c < 0.647$
Burning region	$0.647 < c < 0.841$
Hot products	$0.841 < c < 0.999$

Figure 4 shows the joint pdf's of R and Q in the four regions of the computational domain. The second and third invariants have been normalized with $\langle Q_W \rangle$ and $\langle Q_W \rangle^{3/2}$[12], respectively, where $Q_W (= \boldsymbol{\omega}^2/4)$ is the second invariant of the skew-symmetric rotation-rate tensor, W_{ij}, and $\boldsymbol{\omega}$ is the vorticity vector. It is interesting to note that the universal teardrop shape typical of constant-density turbulent flows is absent in this flow. In the 'fresh reactants', the zone probable values of Q and R displaces towards the right, which indicates flow compressive effects ($P > 0$, see Figure 1) due to the low values of the reaction rate. In the 'preheat' and 'burning' regions the joint pdf's are consistent with the statistical distributions

corresponding to $P < 0$ and the high local expansion between the iso-lines of the progress variable shown in Figure 3. The joint pdf of R and Q in the 'hot products' is completely displaced towards the fourth quadrant, which indicates the lowest values of vorticity over this flow domain. It is important to remark that focal topologies related to high values of vorticity tend to disappear in favor of nodal micro-structures as moving towards the 'hot products'.

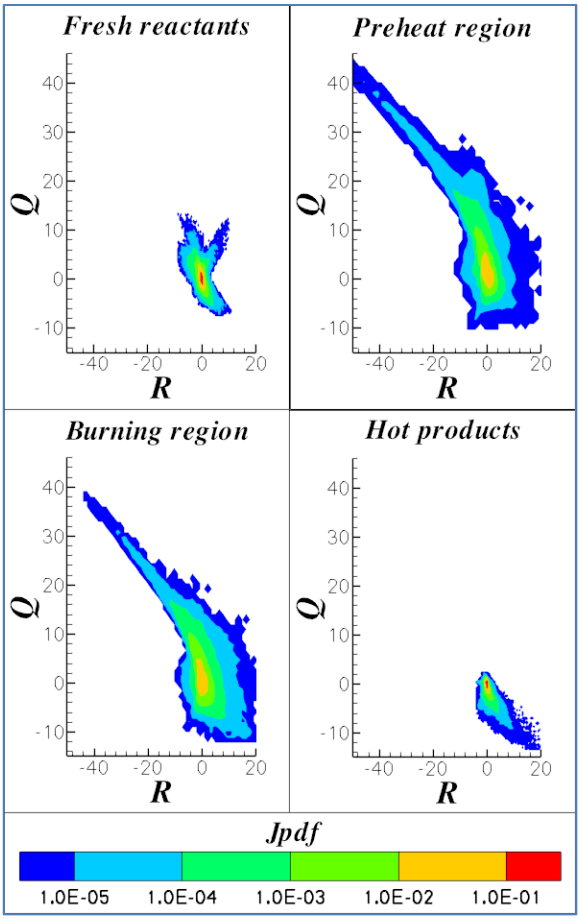

Figure 4. (Color online) Joint pdf of $R - Q$ for the different regions of the computational domain.

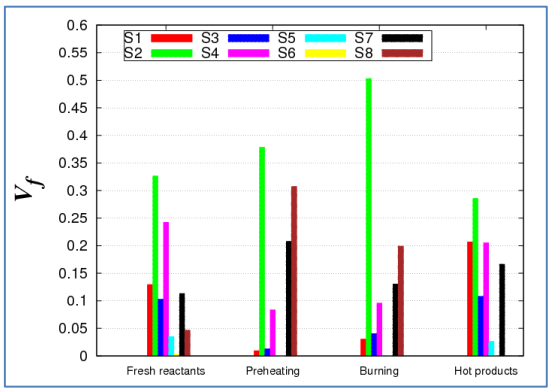

Figure 5. (Color online) Topologies (S1 - S8) belonging to $P - Q - R$ space.

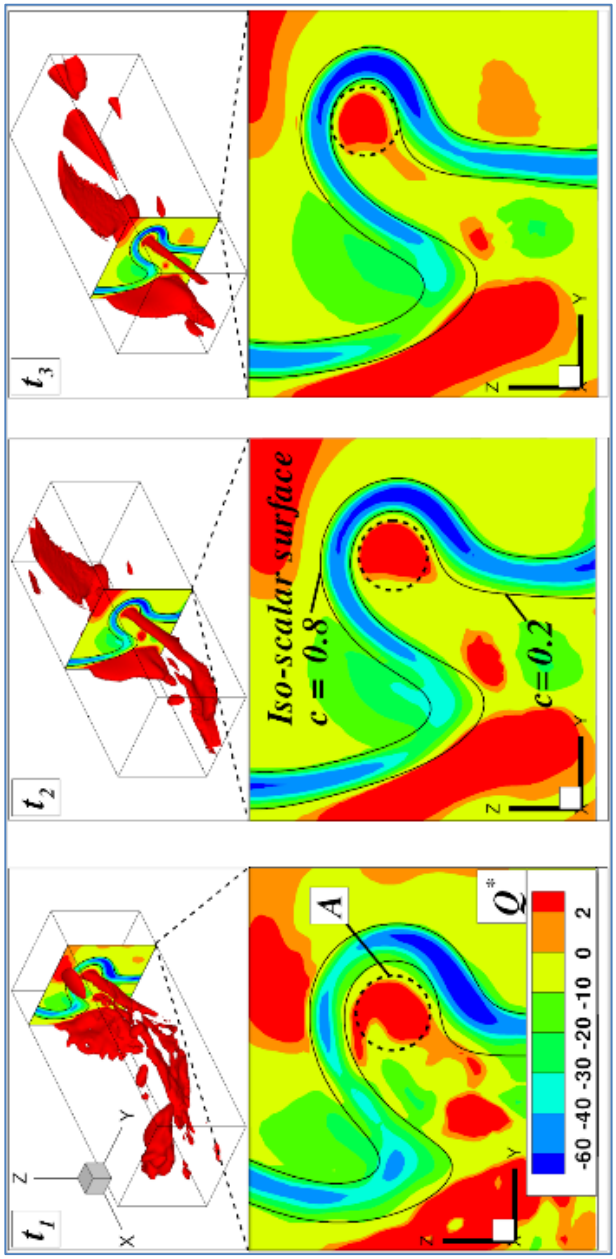

Figure 6. (Color online) Contour surfaces of Q^* at three different times. The three dimensional surfaces shown at the top of the picture correspond to a value $Q^* = 3$. This zoom box coincides with the 'canonical' vortex marked with a dotted black circle $'A'$ in Figure 3.

Figure 5 shows volume fractions of the flow domain pertaining to different flow topologies. It can be seen that S5 (SFC) and S6 (SN/SN/SN) topologies, typical of flows with local negative volumetric dilatation rates, have the lowest share. Topologies S2 (UN/S/S), S4 (SFS), S7 (UFS) and S8 (UN/UN/UN) dominate in the 'preheat' and 'burning' regions, whereas the topologies S1 (UFC), S3 (SN/S/S) and S4 (SFS) are important in the 'fresh reactants' and tend to disappear as moving towards the regions with high chemical activity. The

above is consistent with previous results [12]. In the 'hot products' the share of focal topologies is high, but the shape of the joint pdf of R and Q shown in Figure 4 suggests that in these topologies the vorticity is very low. Moreover, the focal topologies in this region might be created by the co-flow of burned products in the jet flame with values of local enstrophy.

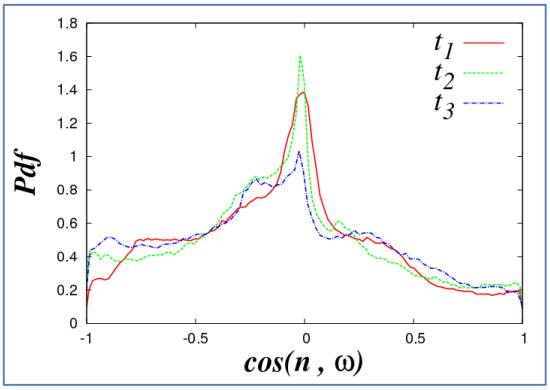

Figure 7. (Color online) Pdf's of the cosine between the flame normal, **n**, and the local vorticity vector, **ω**. These pdf's have been calculated for the zoom box of Figure 6.

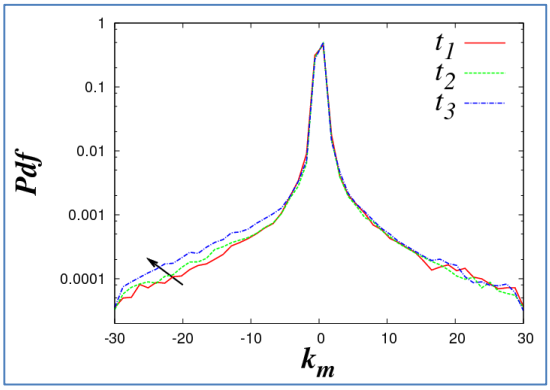

Figure 8. (Color online) Pdf's of the mean curvature, k_m. These pdf's have been calculated for the zoom box of Figure 6.

Contour surfaces of Q^* are shown in Figure 6 at three different times separated by time increments of the order of the Kolmogorov micro-scale. This zoom box captures the 'canonical' vortex shown in Figure 3. The red iso-surfaces at the top of the picture have a value $Q^* = 3$. It can be seen that the `canonical' vortex (dotted black circle $'A'$) interacts with the iso-lines of the progress variable, c. It is important to remark that the diameter of the vortex decreases as well as its length as it evolves; Tsinober *et al.* [20] argue that in the enstrophy dominated regions the curvature radius of vortex lines increases. Visually, it seems that all these iso-surfaces $Q^* = 3$ are preferentially perpendicular to the unit vector normal to the iso-scalar surfaces: $\mathbf{n} = -\nabla c/|\nabla c|$. To calculate the alignment of these focal topologies respect to the iso-scalar surfaces, Figure 7 plots the pdf's of the cosine between the flame normal, **n**, and the local vorticity vector, **ω**, at the three different times. The results of this alignment do not change and the probability of finding the vorticity vector parallel to the plane of the iso-scalar surfaces is high. These results are in agreement with DNS calculations [21], where the vorticity vector is found to lie preferentially in the plane of the flame.

It can also be seen in Figure 6 that where the identified vortex acts the concavity of the iso-scalar surface geometries increases. In order to quantify the increase of curvature of the iso-scalar surfaces, Figure 8 shows the pdf's of the mean curvature, k_m. The mean curvature is defined as $k_m = (\nabla \cdot \mathbf{n})/2$ [22] (For a positive (negative) flame curvature, $k_m > 0$ ($k_m < 0$), the scalar surface is convex (concave) towards the fresh gas side. $k_m = 0$ are flat iso-scalar structures). k_m has been made non-dimensional by the laminar flame thickness, δ_L. All the pdf's display maxima for nearly flat iso-scalar surfaces, in agreement with experimental results [23] and three-dimensional DNS calculations [12,24,25] of premixed turbulent flames. It is important to note that concave iso-surfaces increase their probability as they evolves, whereas convex ones remains equal for the three times under study. These results provide evidence that the local flow topologies have an influence in the geometry of flame structure apart from its diffusive-thermal effects.

4. CONCLUSIONS

The influence of local flow topologies upon the scalar structures have been studied in a three-dimensional DNS of a premixed methane-air turbulent jet flame. The computational domain has been divided into four reaction-rate conditioned regions, corresponding to 'fresh reactants', 'preheating', 'burning' and 'hot products'. Local expansion, $-P > 0$, between iso-lines of the progress variable has been identified with maximum (minimum) values associated to concave (convex) scalar geometries. The joint pdf's of the second Q and third R invariants of the velocity-gradient tensor suggest that the characteristic teardrop shape, typical of constant-density turbulent flows, disappears in the different regions. Focal topologies related to high values of vorticity tend to disappear in favor of nodal micro-structures as moving towards the 'hot products'. A 'canonical' vortex has been identified and its time evolution has been analyzed considering three different times separated by increments of the order of the Kolmogorov time micro-scale. This vortex is found to lie most probably in the plane of the iso-scalar surfaces. The local concave scalar structures increases where the identified vortex acts.

The results presented here support the influence of the local flow topologies upon the scalar structures. The effects of these topologies upon the scalar gradient field evolution will be also studied in future work.

5. ACKNOWLEDGMENTS

This research was sponsored through Project CS D2010 – 00011 – SCORE, funded under the CONSOLIDER – INGENIO Program of the Spanish Ministry of Economy and Competitiveness.

REFERENCES

1. M. Chong, A. Perry and B. Cantwell, A general classification of three-dimensional flow fields, *Phys. Fluids*, vol. 2, pp. 765-777, 1990.
2. A. Perry and M. Chong, A description of eddying motions and flow patterns using critical-point concepts, *Ann. Rev. Fluid Mech.*, vol. 19, pp. 125-155, 1987.
3. J. Soria, R. Sondergaard, B. Cantweel, M. Chong and A. Perry, A study of the fine-scale motions of incompressible time-developing mixing layers, *Phys. Fluids*, vol. 6, pp. 871-884, 1994.
4. H. Blackburn, N. Mansour and B. Cantwell, Topology of fine-scale motions in turbulent channel flow, *J. Fluid Mech.*, vol. 301, pp. 269-292, 1996.
5. M. Chong, A. Perry, J. Chacin and B. Cantweel, Turbulence structures of wall-bounded shear flows found using DNS data, *J. Fluid Mech.*, vol. 357, pp. 225-247, 1998.
6. J. Chacin and B. Cantwell, Dynamics of a low Reynolds number turbulent boundary layer, *J. Fluid Mech.*, vol. 404, pp. 87-115, 2000.
7. A. Ooi and J. Martin and J. Soria and M. Chong, A study of the evolution and characteristics of the invariants of the velocity-gradient tensor in isotropic turbulence, *J. Fluid Mech.*, vol. 381, pp. 141-174, 1999.
8. C. Da silva and J. Pereira, Invariants of the velocity-gradient, rate-of-strain, and rate-of-rotation tensors across the turbulent/nonturbulent interface in jets, *Phys. Fluids*, vol. 20, pp. 055101/ 1-8, 2008.
9. S. Suman and S. Girimaji, Velocity gradient invariants and local flow field topology in compressible turbulence, *J. Turbul.*, vol. 11, pp. 1-24, 2010.
10. L. Wang and X. Lu, Flow topology in compressible turbulent boundary layer, *J. Fluid Mech.*, vol. 703, pp. 255-278, 2012.
11. Y. Chu and X. Lu, Topological evolution in compressible turbulent boundary layers, *J. Fluid Mech.*, vol. 733, pp. 414-438, 2013.
12. L. Cifuentes and C. Dopazo and J. Martin and C. Jimenez, Local flow topologies and scalar structures in a turbulent premixed flame, *Phys. Fluids*, vol. 26 (6), pp. 065108/ 1-24, 2014.
13. O. Gicquel, N. Darabiha and D. Thevenin, Laminar premixed hydrogen/air counterflow flame simulations using flame prolongation of ILDM with differential diffusion, *Proc. Combust. Inst.*, vol. 28, pp. 1901-1908, 2000.
14. G. Godel, P. Domingo and L. Vervisch, Tabulation of NOx chemistry for Large-Eddy Simulation of non-premixed turbulent flames, *Proc. Combust. Inst.*, vol. 32, pp. 1555-1561, 2008.
15. T. Poinsot and D. Veynante, Theoretical and Numerical Combustion, RT Edwards, Philadelphia, PA, 2005.
16. R. Borghi, On the structure and morphology of turbulent premixed flames, *Recent advances in aerospace sciences: in honor of Luigi Crocco on his seventy-fifth birthday*, pp. 117-138, Plenum Press, New York, 1985.
17. D. Veynante and L. Vervisch, Turbulent combustion modeling, *Prog. Energy. Combust. Sci.*, vol. 28, pp. 193-266, 2002.
18. L. Cifuentes and C. Dopazo and J. Martin and P. Domingo and L. Vervisch, Local volumetric dilatation rate and scalar geometries in a premixed methane-air turbulent jet flame, *Proc. Combust. Inst.*, vol. 35, 2014, http://dx.doi.org/10.1016/j.proci.2014.06.026.
19. J. Hunt, A. Wray and P. Moin, Eddies, streams, and convergence zones in turbulent flows, Studying Turbulence Using Numerical Simulation Databases II Rept. CTR-S88, Stanford, Calif., Dec. 1988.
20. A. Tsinober, M. Ortenberg and L. Shtilman, On depression of nonlinearity in turbulence, *Phys. Fluids*, vol. 11 (8), pp. 2291-2297, 1999.
21. C. Rutland and A. Trouve, Direct simulations of premixed turbulent flames with nonunity Lewis numbers, *Combustion and Flame*, vol. 94, pp. 41-57, 1993.
22. C. Dopazo, J. Martin and J. Hierro, Local geometry of isoscalar surfaces, *Phys. Rev. E*, vol. 76, pp. 056316/1-11, 2007.
23. B. Renou, A. Boukhalfa, D. Puechberty and M. Trinite, Effects of strech on the local structure of freely propagating premixed low-turbulent flames with various Lewis numbers, *Proc. Comb. Inst.*, vol. 27, pp. 841-847, 1998.
24. N. Chakraborty and R. Cant, Influence of Lewis number on curvature effects in turbulent premixed flame propagation in the thin reaction zones regime, *Phys. Fluids*, vol. 17, pp. 105105/1-20, 2005.
25. R. Sankaran, E. Hawkes, J. Chen, T. Lu and C. Law, Structure of a spatially developing turbulent lean methane-air Bunsen flame, *Proc. Comsbust. Inst.*, vol. 31, pp. 1291-1298, 2007.

G

Effects of scalar isosurfaces curvatures on turbulent combustion

Effects of Scalar Isosurfaces Curvatures on Turbulent Combustion

Jesus Martin[a,*], Cesar Dopazo[a], Juan Hierro[b], Luis Cifuentes[c]

[a] *Universidad de Zaragoza-LIFTEC (CSIC), Zaragoza, Spain*
[b] *Centro Universitario de la Defensa-LIFTEC (CSIC), Spain*
[c] *Universidad de Zaragoza, Zaragoza, Spain*

Turbulent scalar mixing and combustion phenomena are investigated in terms of the local principal curvatures of the scalar field isosurfaces. Direct numerical simulations of both inert and reactive scalars at three different Schmidt numbers have been performed with a mesh size 256^3. Results show that high chemical reaction rates occur for small curvature values -isosurface flat zones- and for 'tile'-like structures convex towards the isosurface propagation direction. Further work is in progress, using 512^3 DNS databases, to investigate with greater detail this behavior, and also to explore its correlations with the velocity field small scale structures.

*Corresponding author
Email address: jjmartin@unizar.es

H

An analysis of the correlation of chemically active scalar fields

SPEIC14 – TOWARDS SUSTAINABLE COMBUSTION

AN ANALYSIS OF THE CORRELATION OF CHEMICALLY ACTIVE SCALAR FIELDS

Juan Hierro*, Luis Cifuentes and Jesús Martín****

* Centro Universitario de la Defensa, AGM. Crta. Huesca s/n, 50090 Zaragoza Spain.
** Área de Mecánica de Fluidos, LIFTEC/CSIC, Universidad de Zaragoza. María de Luna, 3. 50018 Zaragoza Spain.
E-mai: hierro@unizar.es

ABSTRACT

Direct Numerical Simulation (DNS) data about the different terms which appear in the evolution of the scalar correlation function of a premixed chemically active scalar field is presented in this paper. The behaviour of a previous model which had been initially proposed to handle passive scalars is studied.

***Keywords**: correlation function, chemically active scalar, turbulence*

1. INTRODUCTION

In the computational simulation of turbulent reactive flows, see Eq. (1), it is usual that both micromixing and chemical reaction terms need modeling.

$$\frac{\partial Y}{\partial t} + u_i \frac{\partial Y}{\partial x_i} = D \frac{\partial^2 Y}{\partial x_i \partial x_i} + \dot{W}(Y) \qquad (1)$$

The terms which appear in Eq.(1) are from left to right: inertial evolution, convective transport, mixing transport and chemical reaction.

Whereas chemical reaction is a local, highly nonlinear phenomenon; micromixing is a typical multipoint process which depends on the values of the scalar field in a neighbourhood of any given point. This means that closures which represent acceptably one of them, have trouble with representing the effect of the other one. For instance, one-point PDF methods handle in an exact form any local term [1], including chemical reaction; however, they need some external closure in order to represent micromixing. The first natural choice would be to try and use two-point PDF methods, however the closure problem shows in the need to model three-point statistics.

If the attention is focused in one-point PDF closures, the two-point information that they need could be provided by either the correlation function or by the spectrum (the Fourier transform of the correlation function) of the scalar field. Typical time and length mixing scales, to be used by a a one-point closure, may be derived from them.

Since the pioneering work of Obukhov and Corrsin [2, 3, 4], there has been a great number of publications related to the study of the correlation function of a chemically passive scalar field. However, chemically active scalars have not received as much attention as passive ones. In the end, the correlation is a second-order statistical moment whose chemical closure suffers from the well known problem of moment closures: a model about higher order moments must be provided.

In this contribution, Direct Numerical Simulation (DNS) data of homogeneous, isotropic, turbulence with highly non-linear active scalar species will be analyzed in order to measure the contribution from the different terms of Corrsin's equation[5,6], see Eq. (2), to the global evolution of the correlation function. It should be pointed out that there are no thermal effects, that is to say density and transport coefficients are treated as constant terms. This is, of course, an unreal assumption; anyway, this contribution is only focused in the coupling between chemistry and turbulent transport.

$$\begin{aligned}\frac{\partial \langle Y_1 Y_2 \rangle}{\partial t} = 2\left(\frac{\partial}{\partial r} + \frac{2}{r}\right)\left(\langle \delta u_r Y_1 Y_2 \rangle + D \frac{\partial \langle Y_1 Y_2 \rangle}{\partial r}\right) \\ + Y_1 \dot{W}(Y_2) + \dot{W}(Y_1) Y_2\end{aligned} \qquad (2)$$

In Eq.(2), Y_1 and Y_2 refer to the value of a scalar field at position x_1 and x_2, respectively; r is the modulus of the separation between both points; is one half of the projection of the velocity difference between points 1 and 2 along the line which links them (the radial component of the velocity at point 2, as seen from a reference situated on 1); D is the diffusion coefficient and $W(Y_1)$ and $W(Y_2)$ stand for the chemical reaction rate at points 1 and 2.

In a previous work of two of the authors [7], passive scalar fields obtained from a DNS were studied in order to elucidate whether Prandtl hypothesis [6] could be used to close the third-order moment, transport term in Corrsin's equation. Prandtl hypothesis merely proposes that

$$\langle \delta u_r Y_1 Y_2 \rangle \propto L(r) \langle \delta u_r \rangle \frac{\partial \langle Y_1 Y_2 \rangle}{\partial r} \qquad (3)$$

which could always be true provided that zeros of the cross third-order moment coincide with zeros of the radial component of the gradient of scalar correlation. In principle, L(r) may have any functional dependence on r. However, the authors of reference [6] proposed a model for the value of L(r)

$$L(r)\langle \delta u_r \rangle = C_\delta u' L\big(1 - \exp(-(r/\lambda)^2)\big) \quad (4)$$

where L and u' are related to the integral length and velocity scales of the velocity turbulent field, whereas is related to the correlation length of the scalar field which, in its turn, is expected to depend on the Prandtl (Schmidt) number.

Although, for an arbitrary initial scalar field, the model represented by Eq.(4) did not provided a good fit of the third-order, transport moment[7]; it must be pointed out that, after a very short time of evolution of that field under the Navier-Stokes equations, the fitting was very good, though with time dependent parameters.

2. DIRECT NUMERICAL SIMULATION (DNS) FEATURES.

All the DNS were realized in a cubic, computational grid with an edge of size cm. A pseudospectral code was used for the numerical integration. Wave numbers between 1 and were randomly forced until a statistically stationary state was reached. The main features of the turbulent velocity field are provided in Table 1.

Table 1. Turbulent Velocity data.

Reynolds number, Taylor-based	65 ~ 69
Kolmogorov length scale	0.0242 cm ~ 0.0249 cm
Integral length scale	0.91 cm ~ 0.96 cm
Large-eddy turn-over time	0.006 s ~ 0.0063 s
Spatial resolution	5.83 ~ 6.00

The spatial resolution is the maximum wave number times the Kolmogorov length scale. Its value is wide higher than in other DNS because these data were also used to compute isosurface statistics whose requirements about the quality of first and second derivatives are higher than usual, too.

Scalar fields were initialized as an almost unpremixed initial condition with mean 0.7, minimum 0.0 and maximum 1.0. The word 'almost' refers to the fact that a fully umpremixed initial condition (either 0.0 or 1.0) shows a strong numerical dispersion during the first computational steps with values which may enter into the forbidden zones of Y<0 and Y>1. It is necessary to allow for the scalar and velocity field to evolve for, approximately, 0.2 large-eddy turn-over times, while all the forbidden values of the scalar field are truncated to either 0 or 1, before numerical dispersion is reduced to an acceptable level. This process means that initial scalar fields have a 0.7 mean value, yet a 0.132 initial variance of its fluctuations, whereas a fully segregated initial state of 0,7 mean value should have a variance of 0.21.

Three different values of the Schmidt number were considered for the scalar fields: 0.5, 1.0 and 1.5. For each Schmidt number both a passive and a chemically active situation were computed. All in all, there were a total of six simulations which shared the same velocity field, yet had different scalar field properties.

The chemical reaction obeyed the following Arrhenius law

$$\dot{W}(Y) = -30Y \exp\big(-4.5Y/(1-0.7Y)\big) \quad (5)$$

which corresponds [8] to a Damköhler number of 0.5, with laminar flame speeds (Blint model, [8]) and flame thicknesses which are recorded in Table 2.

Table 2: Laminar flame data.

	Sc=0.5	Sc=1.0	Sc=1.5
Laminar flame speed	0.2618 m/s	0.1851 m/s	0.1512 m/s
Flame thickness	0.3194 cm	0.2259 cm	0.1844 cm
Reaction thickness	0.07098 cm	0.05019 cm	0.04098 cm

Two different time steps were analysed for each simultaion: the initial time and the time step when the variance of the fluctuations of the inert scalar field had lowered to a value of 0.053. Since Schmidt numbers are different, such a state is reached at a different time instance for each run; however, the overall rate of chemical reaction is very much alike: mean values of the chemically active scalar fields are 0.45 for Sc=0.5 and 0.48 for Sc=1.0 and Sc=1.5; variance values of the chemically active scalar fields are 0.146 for Sc=0.5, 0.149 for Sc=1.0 and 0.151 for Sc=1.5.

3. RESULTS AND DISCUSSION

3.1 Correlation function.

In Figure 1, the values of the initial correlation functions in the interval are plotted. Since boundary conditions are periodic, for values higher than the influence of the boundary conditions starts to be felt. No data for correlation lengths larger than are presented since the aim of the simulation is to analyze data as free as possible from the particular set of boundary conditions chosen.

In Figure 2, the correlation functions at the final step are represented for the six simulations. Values have been normalized by its maximum (the fluctuation scalar variance) to ease comparison. It can be checked that the initial correlation was a bit broader for Sc=1 and that this feature is kept as time evolves. Sc=0.5 and Sc=1.5 show an alike evolution of their normalized correlation function regardless of the presence of a chemical reaction.

In Figure 3, the correlation of the chemical term at one point with the scalar field at another point (chemical term in Corrsin's equation, Eq.(2)) is plotted for the last step. Since the chemical term has a sign opposite to that of the scalar, this correlation is negative.

In Figure 4, a plot of the ratio between the third-order cross moment and the gradient term in Corrsin's equation, Eq. (2), is

Figure 1. Initial correlation functions.

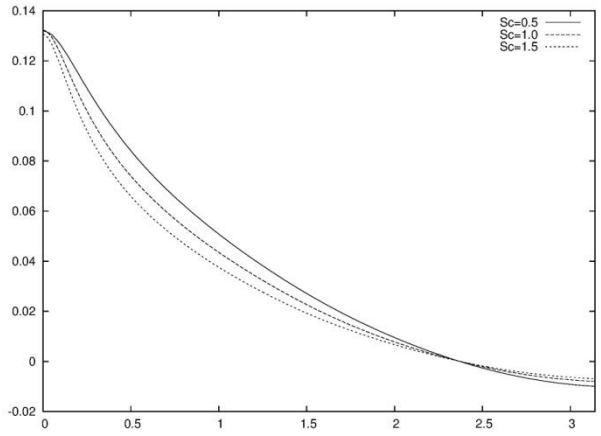

Figure 2. Normalized correlation functions, last step.

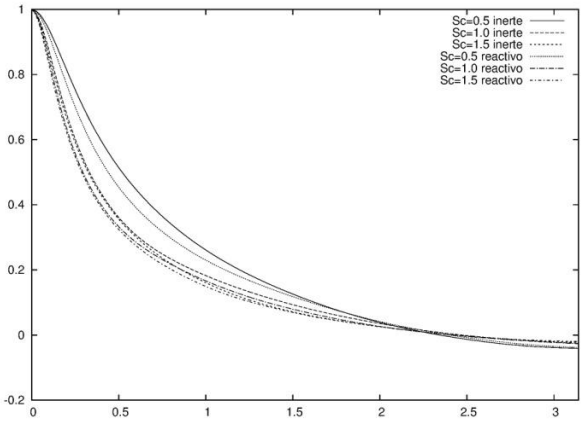

In Figure 4, a plot of the ratio between the third-order cross moment and the gradient term in Corrsin's equation, Eq. (2), is plotted for the initial and the final time steps and scalar fields with Sc=0.5. The same data is plotted in Figures 5 and 6 when Sc=1.0 and Sc=1.5, respectively.

The model is represented as a function of a term which may depend on the properties of the velocity field, K, which should be the same with these data, plus a term which may depend on the Schmidt number, l.

$$C_\delta u' L\left(1-\exp(-(r/\lambda)^2)\right) = -K\left(1-\exp(-K(r/l)^2)\right) \quad (6)$$

A good fit was found with K=0.8 and l=1.75 for Sc=0.5, l=1.7 for Sc=1.0 and l=1.8 for Sc=1.5. The same K was taken for all Schmidt numbers since it should depend only on velocity field properties.

4. CONCLUSIONS

A model developed a few years ago to represent turbulent transport in the evolution equation of the correlation function of a passive scalar shows a good qualitative behaviour when applied to represent the same term in an active scalar up to distances of order .

Of course, the question of the closure of the chemical reaction term remains open. The shape of the normalized correlation function does not change very much with the reaction used in these simulations, however the variance used to normalize is strongly affected

Figure 3. Chemical term of Corrsin's equation.

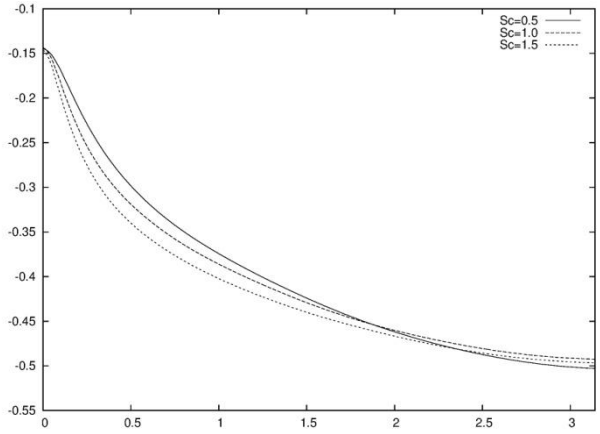

Figure 4. Model of transport. Sc=0.5.

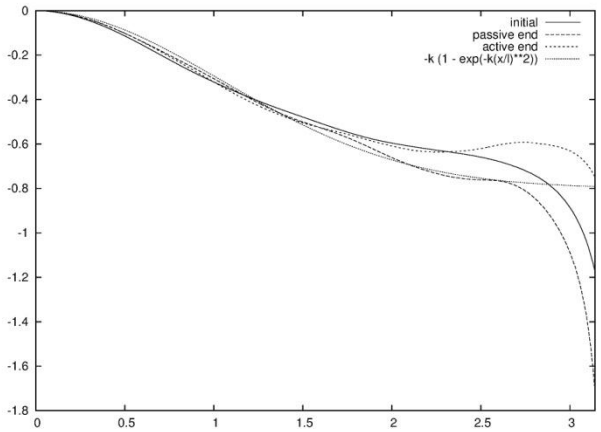

Figure 5. Model of transport. Sc=1.0.

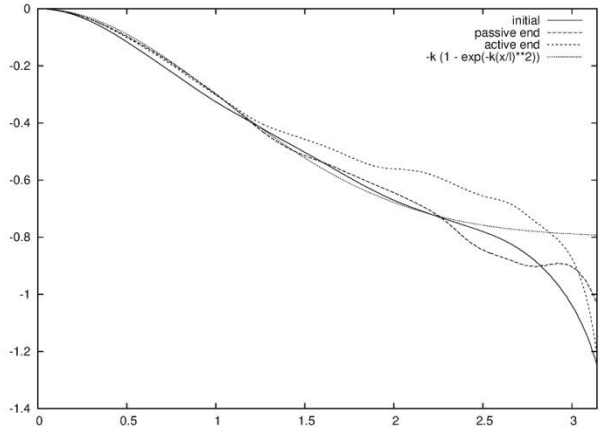

Figure 6. Model of transport. Sc=1.5.

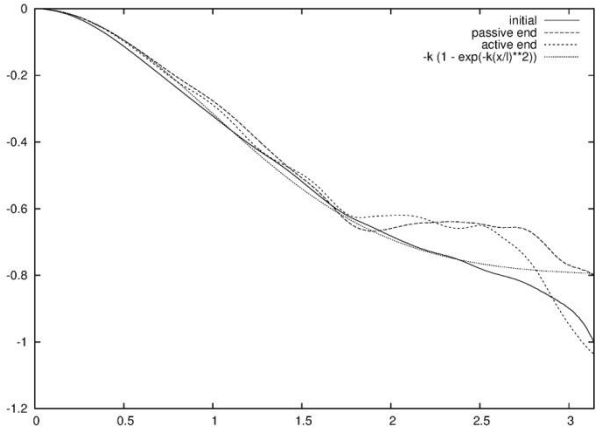

REFERENCES

1. R. O. Fox, *Computational models for turbulent reactive flows,* Cambridge University Press, 2003.
2. A. M. Obukhov, The structure of the temperature field in a turbulent flow, *Izv. Akad. Nauk SSR Geophr. Geofiz.,* vol. 13, pp. 58, 1949.
3. S. Corrsin, *On the spectrum of isotropic turbulent fluctuations in isotropic turbulence,* J. Appl. Phys., vol. 22, pp. 469, 1951.
4. A. S. Monim and A. M. Yaglom, *Statistical Fluid Mechanics vol. II*, MIT Press, Cambridge, 1975.
5. V. Eswaran, E.E. O'Brien and A.Deckert, *The modelling of the two-point probability density function of a reacting scalar in isotropic turbulence,* Combust. Sci. Tech., vol. 65, pp. 1-18, 1989.
6. V.P. Krasitskii and V. Frost, *Molecular transfer in turbulent flows,* Fluid Dynamics, vol. 42, pp. 190-200, 2007.
7. J. Hierro, V. Frost, C. Dopazo and J. Marín. *An analysis of the correlation of scalar fields from DNS data,* Khimicheskaya Fizika, vol. 24, pp. 38-46, 2005.
8. T. Poinsot and D. Veynante, *Theoretical and numerical combustion,* Edwards, Philadelphia, 2001.

I

‘Effective’ normal strain rate and scalar gradient enhancement

'Effective' normal strain rate and scalar gradient enhancement

L. Cifuentes[a,*], C. Dopazo[a], J. Martin[a], P. Domingo[b], L. Vervisch[b], M. C. Jimenez[c]

[a] *LIFTEC, CSIC-University of Zaragoza, Spain*
[b] *CORIA - CNRS, Normandie Université, INSA de Rouen, France*
[c] *Department of Energy, CIEMAT, Spain*

Two DNS datasets for turbulent premixed flames (Flame-A: inflow-outflow configuration; Flame-B: Jet in a co-flow) are used to investigate local flow topologies and scalar iso-surface geometries [1]. The scalar-gradient modulus, $|\nabla Y|$, evolution depends on the sign of $(a_N + \partial V^Y/\partial x_N)$, the 'effective' strain rate normal to the iso-scalar surfaces [2]. This study aims at characterizing the 'effective' normal strain rate for different scalar field geometries and flow topologies for Flame-A [1] and Flame-B [3].

References

[1] L. Cifuentes, C. Dopazo, J. Martin, and C. Jimenez. Local flow topologies and scalar structures in a turbulent premixed flame. *Phys. Fluids*, 26 (6):065108, 2014.

[2] C. Dopazo, L. Cifuentes, J. Martin, and C. Jimenez. Strain rates normal to approaching iso-scalar surfaces in a turbulent premixed flame (under review). *Combustion and Flame*, 2014.

[3] L. Cifuentes, C. Dopazo, J. Martín, P. Domingo, and L. Vervisch. Local volumetric dilatation rate and scalar geometries in a premixed methane-air turbulent jet flame. *Proc. Combust. Inst.*, 35, 2014.

*Corresponding author
Email address: lcifuentes@unizar.es (L. Cifuentes)

J

Scalar field geometries and small-scale flow features in turbulent premixed flames

SCALAR FIELD GEOMETRIES AND SMALL-SCALE FLOW FEATURES IN TURBULENT PREMIXED FLAMES

Luis Cifuentes*, Cesar Dopazo*, Jesus Martin*, Carmen Jimenez, Pascale Domingo*** and Luc Vervisch*****

lcifuentes@unizar.es

*LIFTEC, CSIC-University of Zaragoza, Spain

**Department of Energy, CIEMAT, Spain

***CORIA - CNRS, Normandie Université, INSA de Rouen, France

Abstract

Direct Numerical Simulation (DNS) datasets of turbulent premixed flames (inflow-outflow and jet in a co-flow) are used to study interactions of the flame thermochemical processes with scalar field geometries in terms of their mean and Gauss curvatures, k_m and k_g, and local flow topologies characterized by the three invariants of the velocity-gradient tensor. Four regions ('fresh reactants', 'preheating', 'burning' and 'hot products'), singled out by their reaction rate levels, are examined. Nearly flat scalar iso-surfaces are the most probable geometries in all four regions. The second invariant of the velocity-gradient tensor, Q, which represents the balance between the physical enstrophy and local dissipation of kinetic energy, is governed by the second invariant of the symmetric strain-rate tensor, S_{ij}. Focal topologies tend to disappear in favor of nodal micro-structures towards the 'hot products'.

Introduction

Compared to constant-density turbulent reacting flows, the scalar field geometries and the small-scale flow features of variable-density turbulent reacting flows have been much less studied.

Candel and Poinsot [1] deduced an expression of the flame surface stretch in terms of the tangential strain rate, a_T, and the mean curvature of the flame, k_m; they proved that a_T and k_m correlate with the extinction mechanisms of turbulent flames. Echekki and Chen [2] simulated turbulent premixed stoichiometric methane/air flames and evaluated, among other things, the effects of strain rate and mean curvature of the flame upon radicals concentration and heat release. Renou *et al.* [3] tested experimentally different mixtures with different Lewis numbers, and performed measurements of the flame curvature and tangential strain rate varying the turbulence conditions. Chakraborty and Cant [4, 5] used three-dimensional DNS of premixed turbulent flames, and obtained a detailed statistical analysis for the displacement speed, strain rate, dilatation rate and flame curvature; the mean curvature of the flame is negatively correlated with the local volumetric dilatation rate and the displacement speed of the iso-scalar surfaces. Dopazo *et al.* [6, 7] used results from constant-density turbulent flow DNS to describe the local geometry of iso-scalar surfaces in terms of either main curvatures, k_1 and k_2, and mean and Gauss curvatures, k_m and k_g. Cifuentes *et al.* [8] explored the flow fine-structure and the iso-scalar surface geometries in terms of the mean and Gauss curvatures of a turbulent premixed flame and observed that there are significant occurrence of flow topologies with divergent characteristic interacting with concave iso-scalar surfaces, where heat-conduction focusing effects enhance chemical reaction.

On the other hand, theoretical studies and direct numerical simulations have been carried out to analyze and visualize the physical-space local flow structures of small-scale turbulence. Kuo and Corrsin [9, 10] investigated the nature of small-scale turbulence and

suggested that the small-scale vorticity structure is cylindrical rather than sheet-like as suggested by Betchov [11] and observed by Schwarz [12]. Siggia [13] observed cylindrical or tube-like structures of vorticity using a direct spectral simulation for a stationary, homogeneous, isotropic turbulence field. Perry and Chong [14], and Chong *et al.* [15] proposed a topological approach to typify elementary three-dimensional flow patterns using the three invariants of the velocity-gradient tensor. In incompressible flows, the first invariant of the velocity-gradient tensor P is zero due to continuity, and the turbulent flow can be described in the two-dimensional plane of the second Q and third R invariants of the velocity-gradient tensor. A universal teardrop shape of the Joint Probability Density Function (JPDF) of R and Q was observed for a wide variety of incompressible turbulence (Soria *et al.* [16]; Ooi *et al.* [17]). Dopazo *et al.* [7] explored the possible relationship between the structures of an inert dynamically passive scalar, in terms of the local mean and Gauss curvatures, k_m and k_g, of the iso-scalar surfaces, and the invariant Q. Cifuentes *et al.* [8] studied a three-dimensional variable-density DNS of a turbulent premixed propagating flame in an inflow-outflow configuration and observed that positive volumetric dilatation rates, $-P = \nabla \cdot \mathbf{u}$, display maxima for elliptic concave and minima for convex scalar micro-structures.

This study aims at exploring the small-scale geometry of the scalar field and the flow fine-structure in turbulent premixed flames. A systematic investigation of the scalar field geometries, the features of invariants of the velocity-gradient, rate-of-strain, and rate-of-rotation tensors is undertaken by means of conditional averages and JPDF's. The conditional statistics reported here will serve to guide the development of accurate models of variable-density turbulent reacting flows. A summary of flow topologies and local scalar field geometries is first presented. The DNS of Flame-A (inflow-outflow configuration) and Flame-B (turbulent jet in a co-flow) are then described. Results are analyzed and some conclusions are presented.

Flow topologies

According to the topological classification of Chong *et al.* [15], the local flow patterns are fully characterized by three invariants of the velocity-gradient tensor, $\mathbf{A}$, with components $A_{ij} = \partial u_i/\partial x_j$. P, Q and R are, respectively, the first, second and third invariants of $\mathbf{A}$, which are defined by

$$P = -tr(\mathbf{A}) = -(\lambda_1 + \lambda_2 + \lambda_3) = -S_{ii} = -(\Lambda_1 + \Lambda_2 + \Lambda_3) = -\nabla \cdot \mathbf{u}\,, \tag{1}$$

$$Q = \frac{1}{2}\left([tr(\mathbf{A})]^2 - tr(\mathbf{A}^2)\right) = \frac{1}{2}\left(P^2 - S_{ij}S_{ij} + W_{ij}W_{ij}\right)\,, \tag{2}$$

$$R = -\det(\mathbf{A}) = \frac{1}{3}\left(-P^3 + 3PQ - S_{ij}S_{jk}S_{ki} - 3W_{ij}W_{jk}S_{ki}\right)\,, \tag{3}$$

λ_1, λ_2 and λ_3, are the eigenvalues of $\mathbf{A}$, W_{ij} is the skew-symmetric rotation-rate tensor, S_{ij} is the symmetric strain-rate tensor and Λ_1, Λ_2, and Λ_3 its eigenvalues. The invariants of S_{ij} and W_{ij} provide information about the enstrophy and local dissipation, as well as the dissipation production rate and enstrophy generation rate. The invariants of S_{ij} and W_{ij} are given by

$$P_S = P = -S_{ii}\,, \quad Q_S = \frac{1}{2}\left(P^2 - S_{ij}S_{ij}\right)\,, \quad R_S = \frac{1}{3}\left(-P^3 + 3PQ_S - S_{ij}S_{jk}S_{ki}\right)\,, \tag{4}$$

$$P_W = 0\,, \quad Q_W = \frac{\boldsymbol{\omega}^2}{4} = \frac{1}{2}W_{ij}W_{ij}\,, \quad R_W = 0\,, \tag{5}$$

where $\boldsymbol{\omega}$ is the vorticity vector.

$-P = \nabla \cdot \mathbf{u}$, represents the local volumetric dilatation rate, namely, the rate of change of an infinitesimal fluid volume per unit volume. $-P < 0$ implies element compression, $-P = 0$ means zero dilatation and $-P > 0$ entails local fluid expansion. As a reminder, the local flow topologies are plotted in Figure 1.

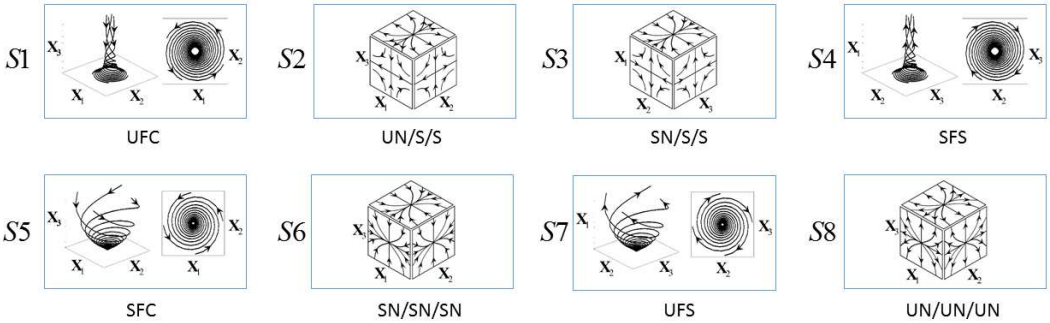

Figure 1: Classification of the different topologies belonging to $P - Q - R$ space.. The acronyms are as follows: UFC (Unstable focus/compressing), UN/S/S (Unstable node/Saddle/saddle), SN/S/S (Stable node/saddle/saddle), SFS (Stable focus/stretching), SFC (Stable focus/compressing), SN/SN/SN (Stable node/stable node/stable node), UFS (Unstable focus/stretching), and UN/UN/UN (Unstable node/unstable node/unstable node).

Geometries of scalar fields

Iso-scalar surfaces, $Y(\mathbf{x}, t) =$ constant (where Y is, for example, the normalized reactant mass fraction: $Y = 1$ in the 'fresh gases' and $Y = 0$ in the 'hot products'), can be described in terms of their mean and Gauss curvatures, k_m and k_g, respectively [7]. The unit normal vector to those surfaces, pointing towards the reactants, is given by $\mathbf{n} = \nabla Y / |\nabla Y|$.

The expressions for k_g and k_m are,

$$k_g = k_1 k_2 \ , \tag{6}$$

$$k_m = \frac{k_1 + k_2}{2} = \frac{1}{2} \nabla \cdot \mathbf{n} \ , \tag{7}$$

where k_1 and k_2 are the main surface curvatures, namely, the eigenvalues of the curvature tensor, $\partial n_i / \partial x_j$, corresponding to its eigenvectors, the main directions of curvature.

Iso-scalar surface geometries in the $k_m - k_g$ plane can be readily characterized [7, 8]; the region $k_g > k_m^2$ implies non-physical complex curvatures. Positive mean curvatures imply convex surfaces towards the fresh reactants, while $k_m < 0$ indicate concave ones.

Numerical simulation

Two datasets from Direct Numerical Simulations of turbulent premixed flames are used in the present work.

The first database is termed Flame-A [8] and uses an inflow-outflow configuration (see Figure 2(a)) at moderate turbulent Reynolds number with single-step Arrhenius chemistry:

$$\dot{\omega} = \frac{\dot{\omega}_R}{Y_R^u} = \rho Y B_0 \, exp\left(-\frac{\beta}{\alpha}\right) exp\left[\frac{-\beta(1-\theta)}{1-\alpha(1-\theta)}\right] \ , \tag{8}$$

where ρ is the density of the mixture, $Y = Y_R / Y_R^u$ is the reduced mass fraction, defined with Y_R, the reactants mass fraction and its value in the fresh gasses, Y_R^u, B_0 is the pre-

exponential factor; the ratio $\alpha = (T_b - T_u)/T_b$ is defined with the temperature, T, in the unburned, T_u, and burnt gases, T_b, β is the reduced activation energy or Zel′dovich number, $\beta = \alpha E_a/RT_b$, E is the activation energy and R the universal gas constant, and $\theta = (T - T_u)/(T_b - T_u)$ is the reduced temperature. A planar laminar flame used as initial condition interacts with a turbulent field of fresh gases, which was initialized by a precomputed incompressible homogeneous isotropic turbulence field. Thermodynamic variables are related by the perfect gas law and the conservation equations for mass, momentum, energy and chemical species, are solved using the fully parallel compressible solver NTMIX3D [18, 19]. The full set of governing equations is made dimensionless using reference characteristic variables and molecular transport coefficients in the fresh gases. All the parameters and results reported below for Flame-A are made dimensionless using the speed of sound a_{ref}, the density and temperature in the fresh gases and a characteristic length, L_{ref}, defined as $L_{ref} = (Re_{ac}\nu_{ref})/a_{ref}$, where ν_{ref} is the kinematic viscosity in the fresh gases and $Re_{ac}(= 5000)$ is a scaling parameter. The domain is considered periodic in the y and z directions, while non-reflecting inlet-outlet boundary conditions are imposed in the x direction, using the Navier-Stokes Characteristic Boundary Condition (NSCBC) method [20]. The computational domain has a size 3π in the x direction and 2π in the y and z directions, and contains 768 x 512 x 512 grid points, uniformly distributed. The rms velocity fluctuations in the 'fresh reactants' decay from $u'_0 = 0.016$ in $t = 0$ to $u' = 0.010$ in $t_{final} = 90$, in which our data are presented. To estimate the integral length scale, l, in the 'fresh reactants', the transverse autocorrelation coefficients in cross-stream planes, $y - z$, are obtained. The integral scale increases from $l_0 = 1.058$ in $t = 0$ to $l = 1.200$ in t_{final}. Combustion takes place in the 'corrugated flamelets' regime [21, 22]. Numerical values of the aero-thermo-chemical variables and dimensionless parameters for this simulation are presented in Table 1. Further details of computational approach have been described in Cifuentes *et al.* [8].

Table 1: Values of dimensionless parameters and physical variables at the end of the simulation.

Parameter	Flame-A	Flame-B
Prandtl number, Pr	0.75	0.72
Schmidt number, Sc	0.75	0.72
Lewis number, Le	1.0	1.0
rms of velocity fluctuations, u'	0.01	2.12 (m/s)
Integral length scale, l	1.20	2.4 (mm)
Turbulent kinetic energy dissipation rate, ε	8.333e-7	4.0e+3 (m2/s)
Kolmogorov length micro-scale, η	0.055	3.3291e-2 (mm)
Kolmogorov time micro-scale, τ_η	15.36	6.5192e-2 (ms)
Non stretched laminar flame velocity, S_L	0.005	0.39 (m/s)
Laminar flame thickness, δ_L	0.0526	0.38 (mm)
Chemical time scale, τ_{ch}	10.52	0.97(ms)
Velocity ratio, u'/S_L	2.0	5.43
Length ratio, l/δ_L	22.81	6.31
Turbulent Reynolds number, Re_t	61	300
Damköhler number, $Da = (l/\delta_L)/(u'/S_L)$	11.41	1.16
Karlovitz number, $Ka = \tau_{ch}/\tau_\eta$	0.68	14.87

The second database, termed Flame-B [23], uses a jet-flame configuration. A hybrid Large Eddy Simulation (LES)/DNS approach is performed (see Figure 2(b)). A methane-air mixture is injected through a central jet with a mean velocity $U_{jet} = 30$ m/s, and equivalence ratio $\phi_F = 4.4$, surrounded by a co-flow of burned products with a mean velocity $U_{coflow} = 5.4$ m/s, and equivalence ratio $\phi_c = 1$. The chemistry is tabulated with the FPI (Flame-Prolongation of ILDM) flamelet approach [24]. A reaction progress variable, c, based on a single progress variable Y_c defined by Godel *et al.* [25], $Y_c = Y_{CO} + Y_{CO_2} + (Y_{N_2} - Y^0_{N_2}) + (Y_{H_2O} - Y^0_{H_2O}) + Y_{NO} + Y_{NO_2} + Y_{N_2O}$, is used in this case. c is defined as follows:

$$c = \frac{Y_c}{Y_c^{eq}} \ , \tag{9}$$

where the 'eq' superscript designates the value of the corresponding variable in the burnt state of the laminar-premixed flame. $Y^0_{N_2}$ and $Y^0_{H_2O}$ are, respectively, the mass fractions of N_2 and H_2O in the fresh gases. $Y^0_{N_2}$ and $Y^0_{H_2O}$ ensures that $Y_c = 0$ in fresh gases for all mixing conditions. Thermodynamic variables are related by the perfect gas law and the fully parallel compressible solver SiTCom (Simulating Turbulent Combustion) is used to integrate the mass, momentum, energy and reaction progress variable conservation equations. Viscosity, thermal conductivity, and mass diffusion coefficients are given functions of the temperature. The nozzle diameter is $D = 12$ mm and the computational domain extends 192 mm in the streamwise (x), and 66 mm in the (y) and (z) directions, with 802, 466 and 466 grid points, uniformly spaced, in the x, y, and z directions, respectively. Therefore a LES mesh of about 171 million nodes is used, with a resolution varying between 150 µm and 200 µm. An imbedded zone within the LES mesh features a much higher resolution of 50 µm (see Figure 2(b)), where small scales can rapidly develop to complete the turbulence cascade of the already well-resolved LES. Results are analyzed in this DNS zoom box located at $x/D = 4.5$ from the nozzle, which corresponds essentially to the potential core of the jet, and at $t = 80$ ms, which is much greater that one initial integral eddy turnover time, $\tau_0 = 1.13$ ms. Combustion takes place in the 'thickened-wrinkled flame' regime [22, 21]. Numerical values of the aero-thermo-chemical variables for this simulation are presented in Table 1. Further details of computational approach have been described in Cifuentes *et al.* [23].

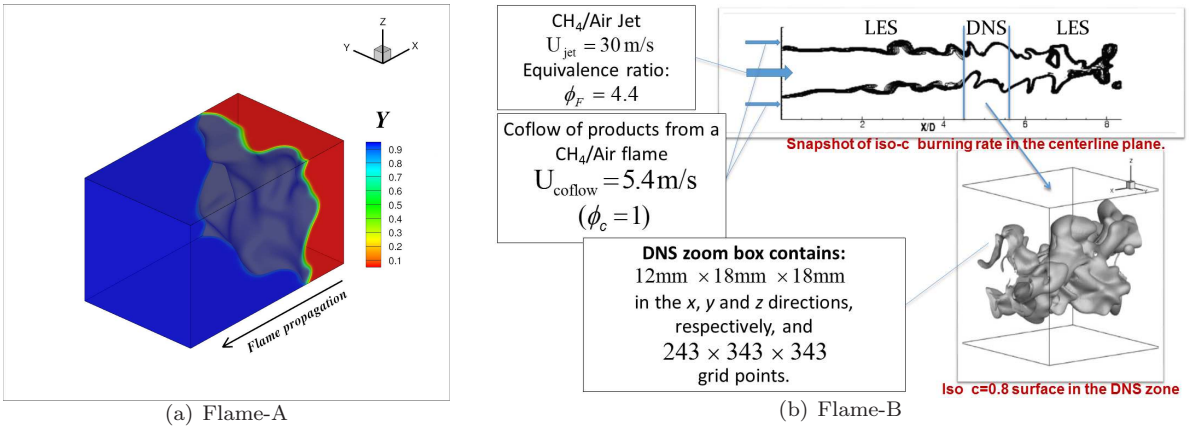

(a) Flame-A (b) Flame-B

Figure 2: Description of the computational domain.

Results and discussion

Local geometrical scalar structures and flow topologies change in the normal direction to the iso-surfaces. Results will then be analyzed considering four different regions of the computational domain based on the reaction rate. The regions are termed as follows: 'fresh reactants', 'preheat region', 'burning region' and 'hot products'. Figure 3 shows the reaction rates, $\dot{\omega}_Y = \dot{\omega}/\rho$, and $\dot{\omega}_c = \dot{\omega}/\rho$, as function of the scalar value for the Flame-A and Flame-B, respectively. Vertical dotted lines demarcate the four regions of the computational domain. The reaction rates have been normalized with their root-mean-square using all the samples in the domain under study. These four reaction-rate conditioned regions have been investigated in previous works [8, 23].

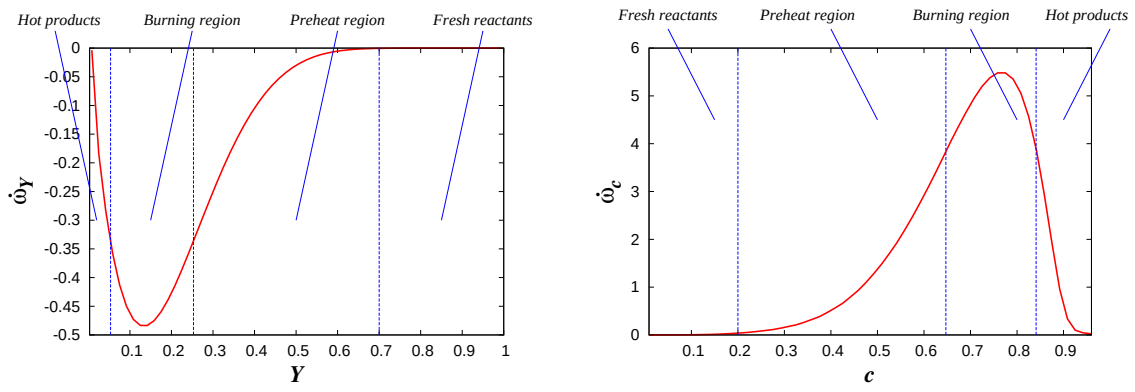

(a) Flame-A (b) Flame-B

Figure 3: (a) Flame-A: Reaction rate, $\dot{\omega}_Y$, conditional upon the mass fraction, Y. (b) Flame-B: Reaction rate, $\dot{\omega}_c$, conditional upon the progress variable, c. Vertical dotted lines mark the limits of the four regions of the computational domain.

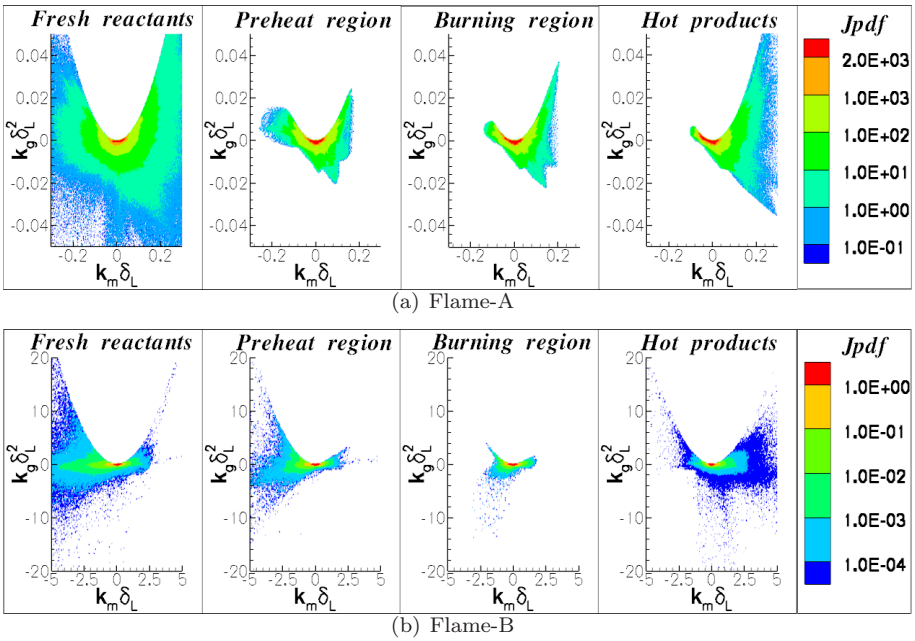

(a) Flame-A

(b) Flame-B

Figure 4: Joint PDF of the mean and Gauss curvatures, k_m and k_g. Joint PDF magnitudes decrease from the center to the circumference. k_m and k_g have been normalized with the flame thickness, δ_L.

To explore the scalar structure, the geometries of the scalar field in terms of mean and Gauss curvatures of the iso-scalar surfaces in the different regions of the computational domain have been obtained (see Figure 4). This analysis yields information about the small-scale scalar geometries and helps to understand the turbulent scalar mixing mechanisms. k_m and k_g, in Figure 4, have been normalized with the laminar flame thickness, δ_L. All the JPDF's display maxima for nearly flat iso-scalar surfaces, in agreement with experimental results [3] and three-dimensional DNS calculations [5] of premixed turbulent flames. In the 'fresh reactants' of Flame-A, the joint PDF is slightly skewed towards positive values of k_m (convex iso-surfaces), reflecting the features of the initially imposed and evolving small-scale turbulent structures and scalar field upstream of zones of intense heat and mass diffusive/reactive activity; these processes drastically discriminate against large

values of k_m and k_g in both the 'preheat' and 'burning' regions; the probability of highly concave and convex iso-scalar surfaces, of a marked either elliptic ($k_g > 0$) or hyperbolic ($k_g < 0$) nature, significantly decreases as the heat transfer and chemical processes become important. Slightly concave scalar iso-surfaces occur in the 'preheat' region, but they become less probable in the 'burning' zone and 'hot products', very likely due to the heat conduction enhancement or focusing, with a reduction of $k_m < 0$, by concave geometries. Convex iso-surfaces with moderate values of k_m, predominantly of an elliptic cup-like structure, survive in the 'hot products'. Concave iso-surfaces in Flame-B are much more probable than convex ones except in the 'hot products'; this result seems to agree with the intuitive notion that concave geometries are predominant within the jet flame; it seems that the high chemical activity and the heat release smooth the large concave curvatures as moving towards the 'burning' region; this behavior is similar to that obtained for Flame-A. The probability of convex scalar structures increases in the 'hot products'. The radius of convex geometries decrease towards the 'hot products', which could be induced by the vortices that survive in this region of the computational domain; Tanahashi *et al.* [26] argue that strong coherent fine-scale eddies, perpendicular to the flame front, can survive behind it and create low pressure zones, which increase the probability of finding large-curvature convex geometries in the 'hot products'.

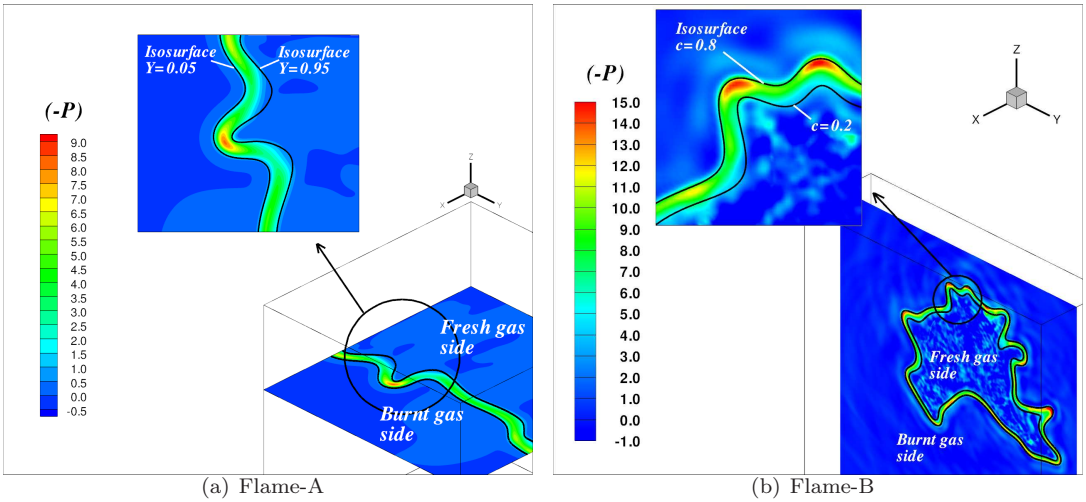

(a) Flame-A (b) Flame-B

Figure 5: Fluid element dilatation rate, $-P = \nabla \cdot \mathbf{u}$, in the computational domain. The volumetric dilatation rate has been normalized with $\langle Q_W \rangle^{1/2}$, where Q_W is the second invariant of the skew-symmetric rotation-rate tensor (see Eq. (5)).

Figure 5 shows zooms of $x - y$ and $y - z$ planes of the computational domain for both flames. They display two scalar iso-lines and the volumetric dilatation rate, $-P = \nabla \cdot \mathbf{u}$. It can be seen that local expansion ($-P > 0$) is significant between the iso-lines, with maximum (minimum) values associated to concave (convex) scalar geometries. This behavior between $-P$ and the scalar geometries is in agreement with previous results [5, 8, 23], and seems to be common to the two flames under study. Expansive (compressive) volumetric dilatations rates are mainly associated to concave and flat (convex) iso-scalar surfaces; these processes can be explained by the heat conduction focussing (defocussing) effect of the scalar concave (convex) structures.

According to Eq. (1), the local volumetric dilatation rate, $-P = \nabla \cdot \mathbf{u}$, results from the addition of the eigenvalues of the strain rate tensor Λ_1, Λ_2 and Λ_3, which are ordered from the largest to the smallest value. For variable-density flows the three eigenvalues can add up to non-zero, $\nabla \cdot \mathbf{u} = \Lambda_1 + \Lambda_2 + \Lambda_3 \neq 0$. Fluid element dilatation rate, $-P = \nabla \cdot \mathbf{u}$

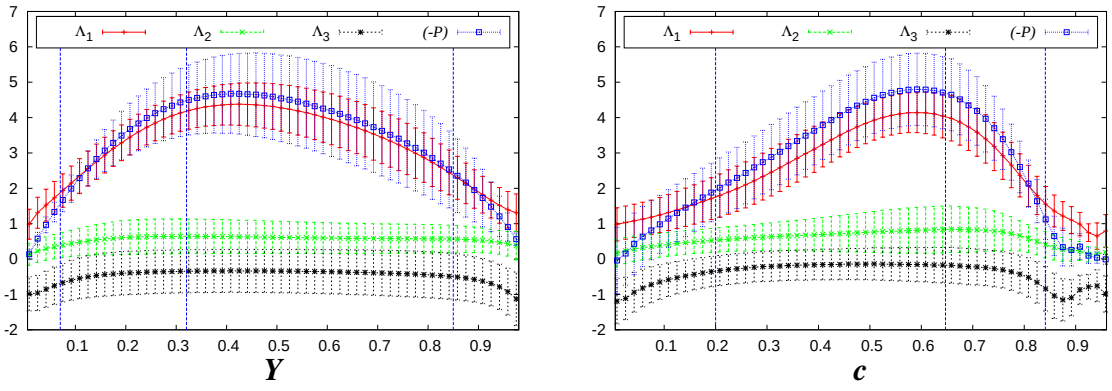

(a) Flame-A (b) Flame-B

Figure 6: Fluid element dilatation rate, $-P = \nabla \cdot \mathbf{u}$ and eigenvalues of the strain rate tensor conditional upon: (a) the mass fraction, Y, and (b) the progress variable, c. Variables have been normalized with $\langle Q_W \rangle^{1/2}$.

and eigenvalues of the strain rate tensor conditional upon the scalar field are shown in Figure 6 for both flames. It is important to remark that the variables in both cases display the same trends. The probability of high dilatation rate is greater near the regions with high chemical activity. Positive values for Λ_1 and Λ_2 (due to flow expansion effects) are greater in the 'preheat' and 'burning' regions, due to high chemical reaction rates. On the other hand, negative eigenvalues (compressive effects) might occur in the 'fresh' and 'burnt' gases. The mean value of the most extensive eigenvalue, Λ_1, is positive for all regions of the computational domain, and displays an almost identical variation to that of $-P$. Variation of Λ_2 for both flames are similar, with positive mean values, and small tails toward negative ones. It is important to note in Figure 6(b) that approximately for $c > 0.88$ the eigenvalues depict only a small dependence on c. This behavior might be due to the fact that there is a co-flow of burned products in the jet flame.

The second invariant of the velocity-gradient tensor, Q, represents the additive contribution of enstrophy, $Q_W (\equiv \omega_i \omega_i / 4)$, and dilatation/dissipation, $Q_S (\equiv (P^2 - S_{ij} S_{ij})/2)$. For flows with variable density, the governing equations for the enstrophy and the strain are as follows [27]:

$$\frac{1}{2}\frac{D\boldsymbol{\omega}^2}{Dt} = \omega_i S_{ik} \omega_k - \omega_i \omega_i S_{kk} - \frac{\omega_i}{\rho^2} \nabla\rho \times \nabla p + \omega_i \, curl \left(\frac{1}{\rho} \frac{\partial \tau_{ik}}{\partial x_k} \right) , \tag{10}$$

$$\begin{aligned} \frac{1}{2}\frac{D\mathbf{s}^2}{Dt} = & -S_{ik} S_{ij} S_{jk} - \frac{1}{4} \omega_i S_{ik} \omega_k + \frac{1}{4} \omega_i \omega_i S_{kk} \\ & - \frac{S_{ik}}{2} \left[\frac{\partial}{\partial x_k} \left(\frac{1}{\rho} \frac{\partial p}{\partial x_i} \right) + \frac{\partial}{\partial x_i} \left(\frac{1}{\rho} \frac{\partial p}{\partial x_k} \right) \right] + \frac{S_{ik}}{2} \left[\frac{\partial}{\partial x_k} \left(\frac{1}{\rho} \frac{\partial \tau_{ij}}{\partial x_j} \right) + \frac{\partial}{\partial x_i} \left(\frac{1}{\rho} \frac{\partial \tau_{kj}}{\partial x_j} \right) \right] , \end{aligned} \tag{11}$$

where $\boldsymbol{\omega}^2 = \omega_i \omega_i$ and $\mathbf{s}^2 = S_{ik} S_{ik}$.

The terms $\omega_i S_{ik} \omega_k - \omega_i \omega_i S_{kk}$ in (10) account for the enstrophy production and enter the definition of the third invariant, R, as well as the dissipation generation rate, $-S_{ik} S_{ij} S_{jk} (\equiv -\Lambda_1 \Lambda_2 \Lambda_3)$, of Eq. (11). Figure 7 depicts Q, Q_S, Q_W, R, R_S, and $(\omega_i \omega_i S_{kk} - \omega_i S_{ik} \omega_k)/4$ as functions of the scalar fields for both flames. The second and third invariants have been normalized with $\langle Q_W \rangle$ and $\langle Q_W \rangle^{3/2}$, respectively. The behavior of the invariants

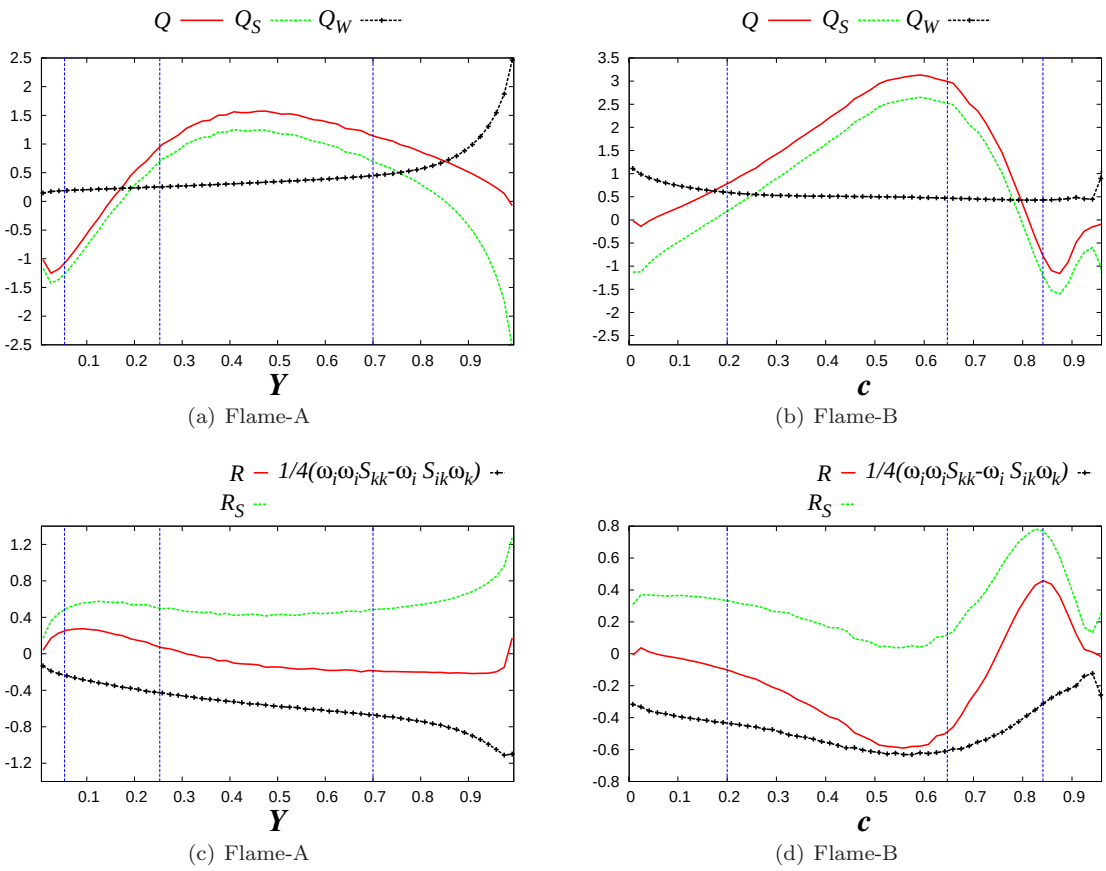

(a) Flame-A (b) Flame-B

(c) Flame-A (d) Flame-B

Figure 7: (a), (b) Q, Q_S, Q_W, and (c), (d) R, R_S, $1/4(\omega_i\omega_i S_{kk} - \omega_i S_{ik}\omega_k)$ as functions of the scalar field. Vertical dotted lines mark the limits of the four regions of the computational domain.

is similar for both flames, as shown in Figures 7(a) and 7(b). The mean of Q_S is negative in the 'fresh' reactants, where the heat release is weak, similar to turbulent mixing in constant-density flows. With decreasing (increasing) of mass fraction (progress variable), Q_S attains a maximum within the 'preheat' region and then starts decreasing; the maximum value is due to the dilatation term, P^2. Q_S changes sign in the 'burning' region, where a balance between flow expansion and strain is reached, and attains a minimum within the 'hot products'. The local enstrophy, Q_W, monotonically decreases from 'fresh' gases towards the 'hot products'. Obviously, the increment of kinematic viscosity with increasing temperature and the local volumetric expansion destroy vorticity. On the other hand, the invariants in Figures 7(c) and 7(d) behave differently for Flames-A and -B. $R_S(\equiv (-P^3 + 3PQ_S - S_{ik}S_{ij}S_{jk})/3)$ seems to be dominated by $-P^3 > 0$ and $-S_{ik}S_{ij}S_{jk}(\equiv -\Lambda_1\Lambda_2\Lambda_3)$. The latter is always positive due to the fact that $\langle\Lambda_1\rangle > 0$, $\langle\Lambda_2\rangle > 0$ and $\langle\Lambda_3\rangle < 0$, according to results in Figure 6. On the other hand, the enstrophy production, $\omega_i S_{ik}\omega_k - \omega_i\omega_i S_{kk}$, defined in Eq. (10), is always positive. The balance between this term and the annihilation of enstrophy due to the increment of kinematic viscosity, leads to an almost constant budget of Q_W towards the 'hot products'.

Nodal and focal topologies can also be investigated through the study of the invariants of the velocity-gradient tensor. Figure 8 shows the joint PDF of the second and third invariants of the velocity-gradient tensor, R and Q, in the four regions of the computational domain. It is interesting to note that the universal teardrop shape, typical of constant-density turbulent flows, remains in the 'fresh' reactants region for Flame-A, where the heat transfer and chemical reaction are weak, whereas in Flame-B the teardrop

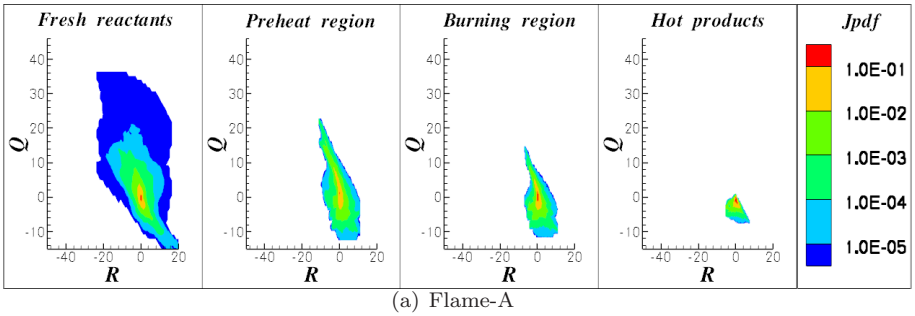

(a) Flame-A

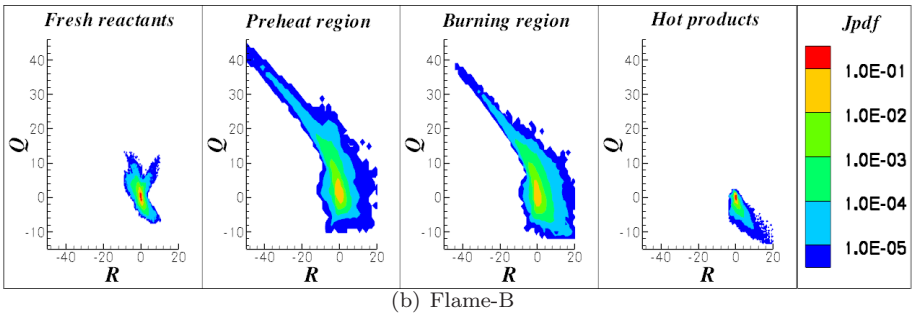

(b) Flame-B

Figure 8: Joint PDF of $R - Q$. Joint PDF magnitudes decrease from the center to the circumference.

shape disappears. For both flames, the statistical distributions displace towards the left side in the regions with high chemical activity; this behavior is consistent with the high volumetric dilatation rates, $P < 0$, in these regions. JPDF's tails decrease with decreasing (increasing) of mass fraction (progress variable), which indicates that the local dissipation and enstrophy diminish towards the 'hot products'. This is in agreement with the reduction of Q_S and Q_W towards the burnt gas side (see Figures 7(a) and 7(b)). S5 (SFC) and S6 (SN/SN/SN), typical of flows with local negative volumetric dilatation rates, seem to be absent in these premixed combustion cases. The unstable topology S2 (UN/S/S) is the most probable, whereas the compressive topology S1 (SN/S/S) and stable topology S3 (SFC) have the lowest share. Topologies S2 (UN/S/S), S4 (SFS), S7 (UFS) and S8 (UN/UN/UN) dominate over the flow domain. In general, focal topologies tend to disappear in favor of nodal micro-structures towards the 'hot products'. Obviously, positive volumetric dilatation rates and flow laminarization, due to increments of kinematic viscosity with increasing temperature, destroy vorticity.

Conclusions

The behavior of local scalar field geometries and small-scale flow topologies is investigated using DNS datasets for two turbulent premixed flames (Flame-A: inflow-outflow configuration; Flame-B: jet in a co-flow). Mean and Gauss curvatures, and invariants of the velocity-gradient, rate-of-strain, and rate-of-rotation tensors have been analyzed. The computational domain has been divided into four reaction-rate conditioned regions, corresponding to 'fresh reactants', 'preheating', 'burning' and 'hot products'. Regardless of the configuration under study, nearly flat scalar iso-surfaces are the most probable geometries in all four regions. Thermochemical processes in the regions with high chemical activity smooth out highly contorted iso-scalar surfaces and annihilate large curvatures. Expansive (compressive) volumetric dilatations rates, $-P = \nabla \cdot \mathbf{u}$, are mainly associated to concave and flat (convex) iso-scalar surfaces. The most extensive eigenvalue, Λ_1, is positive for all regions of the computational domain, and displays an almost identical variation to that of $-P$. Evolution of the invariants as a function of the scalar field have been studied.

The most extensive eigenvalue, Λ_1, is positive for all regions of the computational domain, and displays an almost identical variation to that of $-P$. Evolution of the invariants as a function of the scalar field have been studied. The behavior of the second invariant of the velocity-gradient tensor, Q, is governed by the local dissipation of kinetic energy, Q_S. The physical enstrophy, Q_W, always decreases towards the regions with high chemical activity. Furthermore, the enstrophy production, $\omega_i S_{ik} \omega_k - \omega_i \omega_i S_{kk}$, is always positive as well as the dissipation rate generation, $-S_{ik} S_{ij} S_{jk} (\equiv -\Lambda_1 \Lambda_2 \Lambda_3)$, due to the fact that $\langle \Lambda_1 \rangle > 0$, $\langle \Lambda_2 \rangle > 0$ and $\langle \Lambda_3 \rangle < 0$. The universal teardrop shape typical of JPDF's of R and Q in constant-density turbulent flows disappear in regions with high chemical activity. Flow topologies S5 (SFC) and S6 (SN/SN/SN), typical of flows with local negative volumetric dilatation rates, are absent, whereas the topologies S2 (UN/S/S), S4 (SFS), S7 (UFS) and S8 (UN/UN/UN) dominate over the flow domain. Focal topologies are important in the 'fresh reactants' and tend to disappear in favor of nodal structures as moving towards the 'hot products'. Finally, the behavior of the invariants in two-time studies, separated by time increments of the order of the Kolmogorov micro-scale, will also be undertaken in future work.

Acknowledgments
This research was sponsored through Project CS D2010-00011-SCORE, funded under the CONSOLIDER-INGENIO Program of the Spanish Ministry of Economy and Competitiveness.

*

References

[1] S. Candel and T. Poinsot. Flame stretch and the balance equation for the flame area. *Combust. Sci. and Tech.*, 70:1–15, 1990.

[2] T. Echekki and J. Chen. Unsteady strain rate and curvature effects in turbulent premixed methane - air flames. *Combustion and Flame*, 106:184–202, 1996.

[3] B. Renou, A. Boukhalfa, D. Puechberty, and M. Trinite. Effects of strech on the local structure of freely propagating premixed low-turbulent flames with various lewis numbers. *Proc. Comb. Inst.*, 27:841–847, 1998.

[4] N. Chakraborty and Cant R. Unsteady effects of strain rate and curvature on turbulent premixed flames in an inflow-outflow configuration. *Combustion and Flame*, 137:129–147, 2004.

[5] N. Chakraborty and R. Cant. Influence of lewis number on curvature effects in turbulent premixed flame propagation in the thin reaction zones regime. *Phys. Fluids*, 17:105105/1–105105/20, 2005.

[6] C. Dopazo, J. Martín, and J. Hierro. Iso - scalarsurfaces, mixing and reaction in turbulent flows. *C. R. Mecanique*, 334:483–492, 2006.

[7] C. Dopazo, J. Martín, and J. Hierro. Local geometry of isoscalar surfaces. *Phys. Rev. E*, 76:056316/1–056316/11, 2007.

[8] L. Cifuentes, C. Dopazo, J. Martin, and C. Jimenez. Local flow topologies and scalar structures in a turbulent premixed flame. *Phys. Fluids*, 26 (6):065108, 2014.

[9] A. Kuo and S. Corrsin. Experiments on internal intermittency and fine-structure distribution functions in fully turbulent fluid. *J. Fluid Mech.*, 50:285–319, 1971.

[10] A. Kuo and S. Corrsin. Experiments on the geometry of fine-structure regions in turbulent fluid. *J. Fluid Mech.*, 56:447–479, 1972.

[11] R. Betchov. An inequality concerning the production of vorticity in isotropic turbulence. *J. Fluid Mech.*, 1:497–504, 1956.

[12] K.W. Schwarz. Evidence for organized small-scale structure in fully developed turbulence. *Phys. Rev. Lett.*, 64:407, 1990.

[13] E. Siggia. Numerical study of small-scale intermittency in three-dimensional turbulence. *J. Fluid Mech.*, 107:375–406, 1981.

[14] A. Perry and M. Chong. A description of eddying motions and flow patterns using critical-point concepts. *Ann. Rev. Fluid Mech.*, 19:125–155, 1987.

[15] M. Chong, A. Perry, and B. Cantwell. A general classification of three-dimensional flow fields. *Phys. Fluids*, 2:765–777, 1990.

[16] J. Soria, R. Sondergaard, B. Cantweel, M. Chong, and A. Perry. A study of the fine-scale motions of incompressible time-developing mixing layers. *Phys. Fluids*, 6:871–884, 1994.

[17] A. Ooi, J. Martín, J. Soria, and M. Chong. A study of the evolution and characteristics of the invariants of the velocity-gradient tensor in isotropic turbulence. *J. Fluid Mech.*, 381:141–174, 1999.

[18] T. Poinsot, D. Haworth, and G. Bruneaux. Direct simulation and modelling of flame-wall interaction for premixed turbulent combustion. *Combustion and Flame*, 95:118–132, 1993.

[19] B. Cuenot and T. Poinsot. Asymptotic and numerical study of diffusion flames with variable Lewis number and finite rate chemistry. *Combustion and Flame*, 104:111–137, 1996.

[20] T. Ponsot and S. Lele. Boundary conditions for direct simulations of compressible viscous flows. *J. Comput. Phys.*, 101:104–129, 1992.

[21] T. Poinsot and D. Veynante. *Theoretical and Numerical Combustion*, volume 2. Edwards, Philadelphia, 2005.

[22] R. Borghi. On the structure and morphology of turbulent premixed flames. *in Recent Advances in Aerospace Science (ed. Bruno C. and Casci C.)*, pages 117–138, 1985.

[23] L. Cifuentes, C. Dopazo, J. Martín, P. Domingo, and L. Vervisch. Local volumetric dilatation rate and scalar geometries in a premixed methane-air turbulent jet flame. *Proc. Combust. Inst.*, 35, 2014.

[24] O. Gicquel, N. Darabiha, and D. Thévenin. Laminar premixed hydrogen/air counterflow flame simulations using flame prolongation of ildm with differential diffusion. *Proc. Comb. Inst.*, 28:1901–1908, 2000.

[25] G. Godel, P. Domingo, and L. Vervisch. Tabulation of nox chemistry for large-eddy simulation of non-premixed turbulent flames. *Proc. Combust. Inst.*, 32:1555–1561, 2008.

[26] M. Tanahashi, M. Fujimura, and T. Miyauchi. Coherent fine-scale eddies in turbulent premixed flames. *Proc. Comb. Inst.*, 28:529–535, 2000.

[27] A. Tsinober. *An informal introduction to turbulence*, volume 63. Springer, 2001.

Bibliography

[1] S. Corrsin. Some statistical properties of the product of a turbulent, first-order reaction. *Proc. Symp. Fluid Dynam. Appl. Math., Univ. Maryland, Gordon and Breach, Publ.*, pages 105–124, 1961.

[2] T. Von Kárman. Some remarks on the statistical theory of turbulence. volume 5, page 347. Proc. 5th Int. Congr. Appl. Mech., Cambridge, 1938.

[3] Bradshaw P. Turbulence: the chief outstanding difficulty of our subject. *Experiments in Fluids*, 16:203–216, 1994.

[4] Osborne Reynolds and Internationaler Binnenschifffahrts-Congress. *On certain laws relating to the regime of rivers and estuaries, and on the possibility of experiments on a small scale.* Osterrieth, 1888.

[5] Lewis Fry Richardson. *Weather prediction by numerical process.* Cambridge University Press, 1922.

[6] A.N. Kolmogorov. The local structure of turbulence in incompressible viscous fluid for very large reynolds numbers. *C.R. Acad. Sci. USSR*, 30:301, 1941.

[7] A. Kuo and S. Corrsin. Experiments on internal intermittency and fine-structure distribution functions in fully turbulent fluid. *J. Fluid Mech.*, 50:285–319, 1971.

[8] A. Kuo and S. Corrsin. Experiments on the geometry of fine-structure regions in turbulent fluid. *J. Fluid Mech.*, 56:447–479, 1972.

[9] R. Betchov. An inequality concerning the production of vorticity in isotropic turbulence. *J. Fluid Mech.*, 1:497–504, 1956.

[10] K.W. Schwarz. Evidence for organized small-scale structure in fully developed turbulence. *Phys. Rev. Lett.*, 64:407, 1990.

[11] E. Siggia. Numerical study of small-scale intermittency in three-dimensional turbulence. *J. Fluid Mech.*, 107:375–406, 1981.

[12] R. M. Kerr. Higher-order derivative correlations and the alignment of small-scale structures in isotropic numerical turbulence. *J. Fluid Mech.*, 153:31–58, 1985.

[13] Z. She, E. Jackson, and S. Orszag. Intermittent vortex structures in homogeneous isotropic turbulence. *Nature*, 344:226–228, 1990.

[14] A. Vincent and M. Meneguzzi. The spatial structure and statistical properties of homogeneous turbulence. *J. Fluid Mech.*, 225:1–25, 1991.

[15] G. Ruetsch and M. Maxey. Small scale features of vorticity and passive scalar fields in homogeneous isotropic turbulence. *Phys. Fluids*, A 3:1587–1597, 1991.

[16] J. Jiménez, A. Wray, P. Saffman, and R. Rogallo. The structure of intense vorticity in isotropic turbulence. *J. Fluid Mech.*, 255:65–90, 1993.

[17] A. Perry and M. Chong. A description of eddying motions and flow patterns using critical-point concepts. *Ann. Rev. Fluid Mech.*, 19:125–155, 1987.

[18] M. Chong, A. Perry, and B. Cantwell. A general classification of three-dimensional flow fields. *Phys. Fluids*, 2:765–777, 1990.

[19] A. Perry and M. Chong. Topology of flow patterns in vortex motions and turbulence. *Appl. Sci. Res*, 53:357–374, 1994.

[20] J. Soria, R. Sondergaard, B. Cantweel, M. Chong, and A. Perry. A study of the fine-scale motions of incompressible time-developing mixing layers. *Phys. Fluids*, 6:871–884, 1994.

[21] H. Blackburn, N. Mansour, and B. Cantwell. Topology of fine-scale motions in turbulent channel flow. *J. Fluid Mech.*, 301:269–292, 1996.

[22] M. Chong, A. Perry, J. Chacin, and B. Cantweel. Turbulence structures of wall-bounded shear flows found using dns data. *J. Fluid Mech.*, 357:225–247, 1998.

[23] J. Chacin and B. Cantwell. Dynamics of a low reynolds number turbulent boundary layer. *J. Fluid Mech.*, 404:87–115, 2000.

[24] A. Ooi, J. Martín, J. Soria, and M. Chong. A study of the evolution and characteristics of the invariants of the velocity-gradient tensor in isotropic turbulence. *J. Fluid Mech.*, 381:141–174, 1999.

[25] Y. Andreopoulos and A. Honkan. An experimental study of the dissipative and vortical motion in turbulent boundary layers. *J. Fluid Mech.*, 439:131–163, 2001.

[26] G. Elsinga and I. Marusic. Evolution and lifetimes of flow topology in a turbulent boundary layer. *Phys. Fluids*, 22:015102, 2010.

[27] E. Elsinga and I. Marusic. Universal aspects of small-scale motions in turbulence. *J. Fluid Mech.*, 662:514–539, 2010.

[28] A. Tsinober. *Vortex stretching versus production of strain/dissipation.* Cambridge University Press., 2000.

[29] C. Dopazo, J. Martín, and J. Hierro. Local geometry of isoscalar surfaces. *Phys. Rev. E*, 76:056316/1–056316/11, 2007.

[30] B. Lüthi, M. Holzner, and A. Tsinober. Expanding the q-r space to three dimensions. *J. Fluid Mech.*, 641:497–507, 2009.

[31] C. Da silva and Pereira J. Invariants of the velocity-gradient, rate-of-strain, and rate-of-rotation tensors across the turbulent/nonturbulent interface in jets. *Phys. Fluids*, 20:055101/1–055101/18, 2008.

[32] M. Khashehchi, G. Elsinga, A. Ooi, J. Soria, and I. Marusic. Studying invariants of the velocity gradient tensor of a round turbulent jet across the turbulent/nonturbulent interface using tomo-piv. pages 1–12. 15th Int. Symp. on Applications of Laser Techniques to Fluid Mechanics, Lisbon, Portugal, 2010.

[33] P. Gualtieri and C. Meneveau. Direct numerical simulations of turbulence subjected to a straining and destraining cycle. *Phys. Fluids*, 22:065104/1–065104/15, 2010.

[34] M. Bijlard, R. Oliemans, L. Portela, and G. Ooms. Direct numerical simulation analysis of local flow topology in a particle-laden turbulent channel flow. *J. Fluid Mech.*, 653:35–56, 2010.

[35] W. Feiereisen, W. Reynolds, and J. Ferziger. Numerical simulation of a compresssible, homogeneous turbulent shear flow. *Rep. TF-13, Thermosci. Div., Dept. Mech. Eng., Stanford*, 1981.

[36] J. Chen, B. Cantwell, and N. Mansour. The topology and vorticity dynamics of a three-dimensional plane compressible wake. pages 5.1–5.4. Proceedings of the Tenth Australasian Fluid Mechanics Conference, Melbourne, Australia, 1989.

[37] R. Sondergaard, J. Chen, J. Soria, and B. Cantweel. Local topology of small scale motions in turbulent shear flows. pages 16/1.1–16/1.6. Eighth symposium on turbulent shear flows, Technical University of Munich, 1991.

[38] H. Maekawa, T. Hiyama, and Y. Matsuo. Study of the geometry of flow patterns in compressible isotropic turbulence. *JSME Intl J.*, 42:846–864, 1999.

[39] M. Tanahashi, M. Fujimura, and T. Miyauchi. Coherent fine-scale eddies in turbulent premixed flames. volume 28, pages 529–535. Proc. Comb. Inst., 2000.

[40] S. Suman and S. Girimaji. Velocity gradient invariants and local flow field topology in compressible turbulence. *J. Turbul.*, 11 n 2:1–24, 2010.

[41] R. Grout, A. Gruber, C. Yoo, and J. Chen. Direct numerical simulation of flame stabilization downstream of a transverse fuel jet in cross-flow. volume 33, pages 1629–1637. Proc. Comb. Inst., 2011.

[42] L. Wang and X. Lu. Flow topology in compressible turbulent boundary layer. *J. Fluid Mech.*, 703:255–278, 2012.

[43] G.K. Batchelor. The effect of homogeneous turbulence on material lines and surfaces. *Proc. R. Soc. Lond. A*, 213:349–366, 1952.

[44] W.J. Cocke. Turbulent hydrodynamic line stretching: Consequences of isotropy. *Phys. Fluids*, 12:2488, 1969.

[45] A. Orszag. Comments on 'turbulent hydrodynamic line stretching: Consequences of isotropy'. *Phys. Fluids*, 13:2203, 1970.

[46] C. H. Gibson. Fine structure of scalar fields mixed by turbulence: I. zero-gradient points and minimal gradient surfaces. *Phys. Fluids*, 11:2305–2315, 1968.

[47] A.M. Obukhov. Structure of the temperature field in turbulent flow. *Izv. Akad. Nauk., SSSR. Ser. Geogr. Geofiz.*, 13:58–69, 1949.

[48] S. Corrsin. On the spectrum of isotropic temperature fluctuations in an isotropic turbulence. *J. Appl. Phys.*, 22:469–473, 1951.

[49] P. Clavin and F.A. Williams. Effects of leiws number on propagation of wrinkled flames in turbulent flow. *Prog. Astronaut. Aeronaut.*, 76:403–411, 1981.

[50] P. Clavin and F.A. Williams. Effects of molecular diffusion and of thermal expansion on the structure and dynamics of premixed flames in turbulent flows of large scale and low intensity. *J. Fluid Mech*, 116:251–282, 1982.

[51] S.B. Pope. The evolution of surfaces in turbulence. *Int. J. Engng. Sci.*, 26:445–469, 1988.

[52] S.B. Pope, P.K. Yeung, and S.S. Girimaji. The curvature of material surfaces in isotropic turbulence. *Phys. Fluids A 1*, 12:2010–2018, 1989.

[53] S. Candel and T. Poinsot. Flame stretch and the balance equation for the flame area. *Combust. Sci. and Tech.*, 70:1–15, 1990.

[54] C. Rutland, J. Ferziger, and S. Tahry. Full numerical simulations and modeling of turbulent premixed flames. pages 621–627. Proceedings

of the Twenty-Third Symposium (International) on Combustion, The combustion Institute, Pittsburgh, 1990.

[55] T. Poinsot, D. Veynante, and S. Candel. Quenching processes and premixed turbulent combustion diagrams. *J. Fluid Mech.*, 228:561–606, 1991.

[56] D. Haworth and T. Poinsot. Numerical simulations of lewis number effects in turbulent premixed flames. *J. Fluid Mech.*, 244:405–436, 1992.

[57] M. Baum, T. Poinsot, D. Haworth, and N. Darabiha. Direct numerical simulation of h2/o2/n2 flames with complex chemistry in two-dimensional turbulent flows. *J. Fluid Mech.*, 281:1–32, 1994.

[58] T. Echekki and J. Chen. Unsteady strain rate and curvature effects in turbulent premixed methane - air flames. *Combustion and Flame*, 106:184–202, 1996.

[59] I. Gran, J. Chen, and T. Echekki. Negative flame speed in an unsteady 2-d premixed flame: A computational study. pages 323–329. Twenty-sixth symposium (international) on combustion, The combustion institute, 1996.

[60] B. Renou, A. Boukhalfa, D. Puechberty, and M. Trinite. Effects of strech on the local structure of freely propagating premixed low-turbulent flames with various lewis numbers. volume 27, pages 841–847. Twenty-Seventh symposium (international) on combustion, The combustion institute, 1998.

[61] T. Echekki and J. Chen. Analysis of the contribution of curvature to premixed flame propagation. *Combustion and Flame*, 118:308–311, 1999.

[62] N. Chakraborty and Cant R. Unsteady effects of strain rate and curvature on turbulent premixed flames in an inflow-outflow configuration. *Combustion and Flame*, 137:129–147, 2004.

[63] N. Chakraborty and R. Cant. Influence of lewis number on curvature effects in turbulent premixed flame propagation in the thin reaction zones regime. *Phys. Fluids*, 17:105105/1–105105/20, 2005.

[64] C. Dopazo, J. Martín, and J. Hierro. Iso - scalarsurfaces, mixing and reaction in turbulent flows. *C. R. Mecanique*, 334:483–492, 2006.

[65] I. Han and K.Y. Huh. Effects of the karlovitz number on the evolution of the flame surface density in turbulent premixed flames. volume 32, pages 1419–1425. Proc. Comb. Inst., 2009.

[66] M. Matalon. Flame dynamics. *Proc. Comsbust. Inst.*, 32:57–82, 2009.

[67] J. Chen and H. G. Im. Stretch effects on the burning velocity of turbulent premixed hydrogen/air flames. volume 28, pages 211–218. Proc. Comsbust. Inst., 2000.

[68] L. Vervisch, E. Bidaux, K. Bray, and W. Kollmann. Surface density function in premixed turbulent combustion modeling, similarities between probability density fucntion and flame surface approaches. *Phys. Fluids*, 7 n 10:2496–2503, 1995.

[69] L. Cifuentes, C. Dopazo, J. Martín, P. Domingo, and L. Vervisch. Local volumetric dilatation rate and scalar geometries in a premixed methane-air turbulent jet flame. *Proc. Combust. Inst.*, 35:1295–1303, 2014.

[70] N. Chakraborty. Comparison of displacement speed statistics of turbulent premixed flames in the regimes representing combustion in corrugated flamelets and thin reaction zones. *Phys. Fluids*, 19:105109/1–045103/20, 2007.

[71] W. Ashurst, A. Kerstein, R. Kerr, and C. Gibson. Alignment of vorticity and scalar gradient in simulated navier-stokes turbulence. *Phys. Fluids*, 30:2343–2353, 1987.

[72] N. Chakraborty, M. Klein, and N. Swaminathan. Effects of lewis number on reactive scalar gradient alignment with local strain rate in turbulent premixed flames. volume 32, pages 1409–1417. Proc. Comsbust. Inst., 2009.

[73] B. Cuenot, B. Bédat, and A. Corjon. *NTMIX3D User's Guide*, volume 1.0. 1997.

[74] F.A. Williams. *Combustion theory*, volume 2. The benjamin/Cummings Publishing Company, Inc., 1985.

[75] R. Aris. *Vectors, Tensors and the Basic Equations of Fluid Mechanics*. Prentice-Hall, 1962.

[76] T. Poinsot and D. Veynante. *Theoretical and Numerical Combustion*, volume 2. Edwards, Philadelphia, 2005.

[77] K.K. Kuo. *Principles of combustion*. New York: Wiley, 1986.

[78] R. Borghi. On the structure and morphology of turbulent premixed flames. *in Recent Advances in Aerospace Science (ed. Bruno C. and Casci C.)*, pages 117–138, 1985.

[79] N. Peters. The turbulent burning velocity for large-scale and small-scale turbulence. *J. Fluid Mech.*, 384:107–132, 1999.

[80] D. Veynante and L. Vervisch. Turbulent combustion modeling. *Prog. Energy. Combust. Sci.*, 28:193–266, 2002.

[81] Irvin Glassman. *Combustion*, volume 2. Department of Mechanical and Aerospace Engineering; Princeton University; School of Engineering and Applied Science; Academics Press, INC., 1987.

[82] Stephen R. Turns. *An introduction to combustion: Concepts and applications*, volume 2. Mc Graw-Hill Higher Education, 2000.

[83] Jürgen Warnatz, Ulrich Maas, and Robert W Dibble. *Combustion: physical and chemical fundamentals, modeling and simulation, experiments, pollutant formation.* Springer, 2006.

[84] U. Maas and S.B. Pope. Implementation of simplified chemical kinetics based on low-dimensional manifolds. volume 24, pages 719–729. Proc. Comb. Inst., 1992.

[85] U. Maas and S.B. Pope. Simplifying chemical kinetics: intrinsic low-dimensional manifolds in composition space. *Combustion and Flame*, 88:239–264, 1992.

[86] O. Gicquel, N. Darabiha, and D. Thévenin. Laminar premixed hydrogen/air counterflow flame simulations using flame prolongation of

ildm with differential diffusion. volume 28, pages 1901–1908. Proc. Comsbust. Inst., 2000.

[87] L. Vervisch, R. Hauguel, P. Domingo, and M. Rullaud. Three facets of turbulent combustion modelling: Dns of premixed v-flame, les of lifted nonpremixed flame and rans of jet-flame. *Journal of Turbulence*, 4:1–36, 2004.

[88] B. Fiorina, R. Baron, O. Gicquel, D. Thevenin, S. Carpentier, and N. Darabiha. Modelling non-adiabatic partially premixed flames using flame-prolongation of ildm. *Combustion Theory and Modelling*, 7(3):449–470, 2003.

[89] S. Orszag and G. Patterson. Numerical simulation of three-dimensional homogeneous isotropic turbulence. *Physical review letters*, 12:76–79, 1972.

[90] R.S. Rogallo. Numerical experiments in homogeneous turbulence. *NASA TM 81315, NASA Ames Research Center, CA*, 1981.

[91] R. Peyret. *Spectral methods for incompressible viscous flow - Applied mathematical sciences*, volume 148. Springer-Verlag, 2000.

[92] E.O. Brigham. *The Fast Fourier Transform.* Englewood Cliffs, NJ: Prentice-Hall, 1974.

[93] M. Frigo and S. Johnson. *FFTW User's Manual*. Massachusetts Institute of Technology, 2003.

[94] S.B. Pope. *Turbulent Flows*. Cambridge University, 2000.

[95] B.A. Crespo. *Código DNS: Simulación numérica directa de escalares inertes y reactivos*. PhD thesis, Universidad de Zaragoza, España, 1994.

[96] J. Hierro. *Métodos estadísticos para simular la evolución de campos escalares y de gradientes en turbulencia homogénea e isótropa*. PhD thesis, Universidad de Zaragoza, España, 2002.

[97] R. Chandra, L. Dagun, D. Kohr, J. Maydan, D. Mcdonald, and R. Menon. *Parallel programming in OpenMP*. Morgan Kaufmann Publishers, 2001.

[98] B. Chapman, G. Jost, and R. Van der Pas. *Using OpenMP: Portable Shared Memory Parallel Programming*. The MIT Press. Library of Congress Cataloging-in-Publication Data, 2008.

[99] V. Eswaran and S. Pope. An examination of forcing in direct numerical simulations of turbulence. *Comp. Fluids*, 16, n 3:257–278, 1988.

[100] V. Eswaran and S. Pope. Direct numerical simulations of the turbulent mixing of a pasive scalar. *Phys. Fluids*, 31, n 3:506–520, 1988.

[101] R. Sankaran, E. Hawkes, J. Chen, T. Lu, and C. Law. Structure of a spatially developing turbulent lean methane-air bunsen flame. volume 31, pages 1291–1298. Proc. Comsbust. Inst., 2007.

[102] R Betchov. An inequality concerning the production of vorticity in isotropic turbulence. *Journal of Fluid Mechanics*, 1(05):497–504, 1956.

[103] Arkady Tsinober. *An informal introduction to turbulence*, volume 63. Springer, 2001.

[104] Beat Lüthi, Arkady Tsinober, and Wolfgang Kinzelbach. Lagrangian measurement of vorticity dynamics in turbulent flow. *Journal of Fluid mechanics*, 528:87–118, 2005.

[105] C. Rutland and A. Trouvé. Direct simulations of premixed turbulent flames with nonunity lewis numbers. *Combustion and Flame*, 94:41–57, 1993.

[106] J Soria, A Ooi, and MS Chong. Volume integrals of the qa-ra invariants of the velocity gradient tensor in incompressible flows. *Fluid dynamics research*, 19(4):219, 1997.

[107] T. Ponsot and S. Lele. Boundary conditions for direct simulations of compressible viscous flows. *J. Comput. Phys.*, 101:104–129, 1992.

[108] M. Baum. *Étude de l'allumage et de la structure des flammes turbulentes.* PhD thesis, Ecole Centrale de Paris, France, 1994.

[109] M. Baum. *NTMIX/CHEMKIM - Release2, User's Guide*, volume 1.0. 1995.

[110] K.W. Thompson. Time dependent boundary conditions for hyperbolic systems. *Journal of computational physics*, 68:1–24, 1987.

[111] P.S. Pacheco. *A User's Guide to MPI.* San Francisco, CA 94117, 1998.

[112] P.S. Pacheco and W.C. Ming. *Introduction to Message Passing Programming:MPI User's Guide in FORTRAN.* San Francisco, CA 94117; Hong Kong, 1998.

[113] N. Chakraborty and N. Swaminathan. Influence of the damköhler number on turbulence-scalar interaction in premixed flames. i. physical insight. *Phys. Fluids*, 19:045103/1–045103/10, 2007.

[114] S. Kim and H. Pitsch. Scalar gradient and small-scale structure in turbulent premixed combustion. *Phys. Fluids*, 19:115104/1–115104/14, 2007.

[115] G. Hartung, J. Hult, C. Kaminski, J. Rogerson, and N. Swaminathan. Effect of heat release on turbulence and scalar-turbulence interaction in premixed combustion. *Phys. Fluids*, 20:035110/1–035110/16, 2008.

[116] F. Drucos, F. Laporte, T. Souléres, V. Guinot, P. Moinat, and B. Caruelle. High-order fluxes for conservative skew-symmetric-like schemes in structured meshes: Application to compressible flows. *J. Comput. Phys.*, 161:114–139, 2000.

[117] S. Gottlieb and C. Shu. Total variation diminishing runge-kutta schemes. *Math. Comput*, 67:73–85, 1998.

[118] G. Lodato, P. Domingo, and L. Vervisch. Three-dimensional boundary conditions for direct and large-eddy simulation of compressible viscous flows. *J. Comput. Phys.*, 227:5105–5143, 2008.

[119] J. Ferziger and M. Perić. *Computational Methods for Fluid Dynamics.* Springer-Verlag, 2002.

[120] G. Godel, P. Domingo, and L. Vervisch. Tabulation of nox chemistry for large-eddy simulation of non-premixed turbulent flames. *Proc. Combust. Inst.*, 32:1555–1561, 2008.

[121] Y. Chen, N. Peters, G. Schneemann, N. Wruck, U. Renz, and M. Mansour. The detailed flame structure of highly stretched turbu-

lent premixed methane-air flames. *Combustion and Flame*, 107:223–244, 1996.

[122] P. Domingo, L. Vervisch, and D. Veynante. Large-eddy simulation of a lifted methane-air jet flame in a vitiated coflow. *Combust. Flame*, 152(3):415–432, 2008.

[123] M. Klein, A. Sadiki, and J. Janicka. A digital filter based generation of inflow data for spatially developing direct numerical or large eddy simulations. *J. Comput. Phys.*, 186:652–665, 2003.

[124] K. Bray, P. Libby, and J. Moss. Unified modeling approach for premixed turbulent combustion - part i: General formulation. *Combustion and Flame*, 61:87–102, 1985.

[125] J. Hunt, A. Wray, and P. Moin. Eddies, streams, and convergence zones in turbulent flows. *Center for turbulence research*, pages 193–208, 1988.

[126] L. Cifuentes, C. Dopazo, J. Martin, and C. Jimenez. Local flow topologies and scalar structures in a turbulent premixed flame. *Phys. Fluids*, 26 (6):065108, 2014.

[127] A Tsinober, M Ortenberg, and L Shtilman. On depression of nonlinearity in turbulence. *Physics of Fluids (1994-present)*, 11(8):2291–

2297, 1999.

[128] C. Dopazo, L. Cifuentes, J. Martin, and C. Jimenez. Strain rates normal to approaching iso-scalar surfaces in a turbulent premixed flame. *Combustion and Flame*, 2014.